

NASA Contractor Report 189158

11-57  
10-7  
P-430

# Probabilistic Structural Analysis Methods for Select Space Propulsion System Components (PSAM)

## Volume II—Literature Surveys of Critical Space Shuttle Main Engine Components

Southwest Research Institute  
*San Antonio, Texas*

and

K.R. Rajagopal  
*Rockwell International*  
*Canoga Park, California*

April 1992

Prepared for  
Lewis Research Center  
Under Contract NAS3-24389



(NASA-CR-189158) PROBABILISTIC STRUCTURAL  
ANALYSIS METHODS FOR SELECT SPACE PROPULSION  
SYSTEM COMPONENTS (PSAM). VOLUME 2:  
LITERATURE SURVEYS OF CRITICAL SPACE SHUTTLE  
MAIN ENGINE COMPONENTS Final Report

N92-24804

Unclass  
G3/39 0089337



## Table of Contents

### Section

1	LOX Posts	1
2	Turbine Blades	103
3	Transfer Ducts and Preburner Liners	245
4	SSME Ducts and High Pressure Oxidizer Duct	306
5	Nozzle Feed Line	376
6	Main Combustion Chamber Liner	407





## Section 1

### LOX Posts

## INJECTORS (LOX POST)

### 1. Purpose

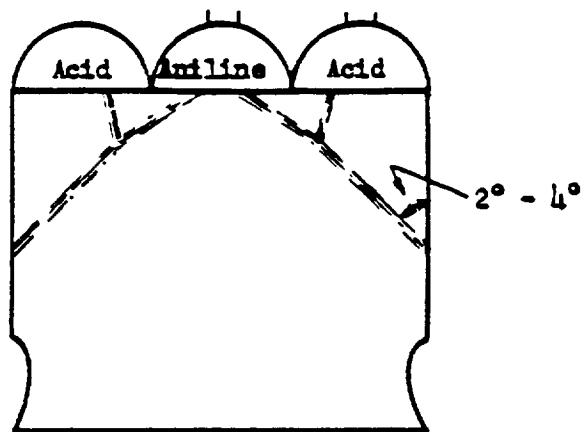
The function of an injector, which is located in the forward end of the combustion chamber is similar to that of carburetor in an internal combustion engine. The injector introduces and meters the propellant flow to the combustion chamber after atomization and mixing. Design of injectors require a thorough understanding of chemical and physical process encountered in the combustion chamber. The injector design has a major impact on both engine performance and combustion stability.

### 2. Injector Patterns

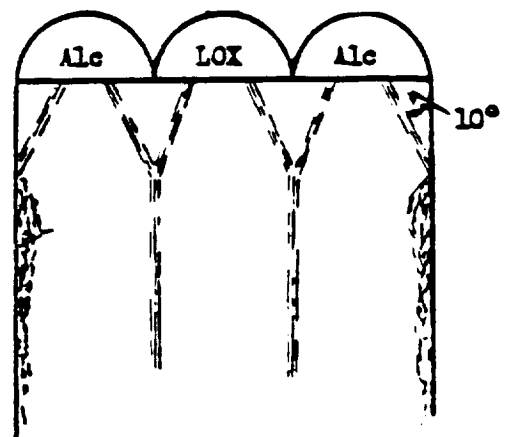
A variety of injector patterns have been designed to satisfy the needs of various propellant combinations. Some of the injector concepts that have been used in practice include 1) impinging (Fig. 1), 2) uniform coaxial (Fig. 2 & Fig. 3), 3) spray bar coaxial (Fig. 4), 4) coaxial with swirl (Fig. 5), and 5) micro orifice showerhead (Fig. 1). A comparison of injector pattern is shown in Table 1. For liquid oxygen hydrogen engines, coaxial injection elements have proven to provide favorable combustion performance and stability. The current SSME configuration utilizes uniform coaxial pattern in both the preburners and injectors.

### 3. Coaxial Element Description

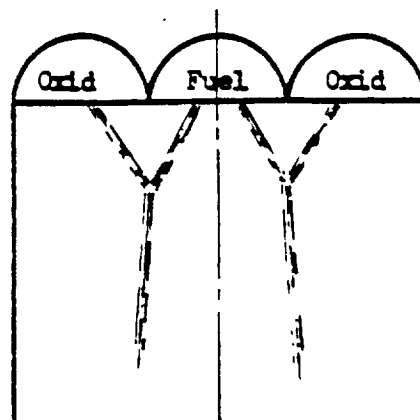
A qualitative description of the coaxial element design is shown in Fig. 6. The coaxial elements are particularly adapted to mixing of gaseous propellants such as hydrogen, with liquid propellants such as oxygen. Coaxial elements consist of tubes or drilled posts that provide the flow area for one propellant, and the concentric annuli that provide the flow area for the second propellant. Proper propellant atomization and mixing which is central to combustion efficiency is promoted by momentum exchange due to high differential velocities between the fuel and oxidizer. Recess cup region where the Lox post stops short of being flush with the face plate and a thin Lox post trailing edge have definite positive influences on the combustion performance of the injector.



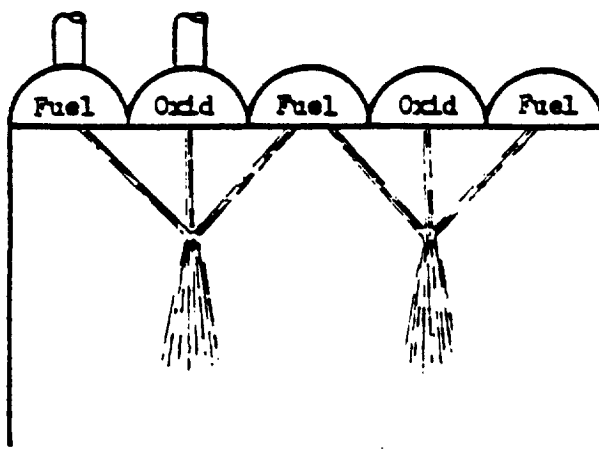
A. Acid-aniline Impinging on Chamber Wall



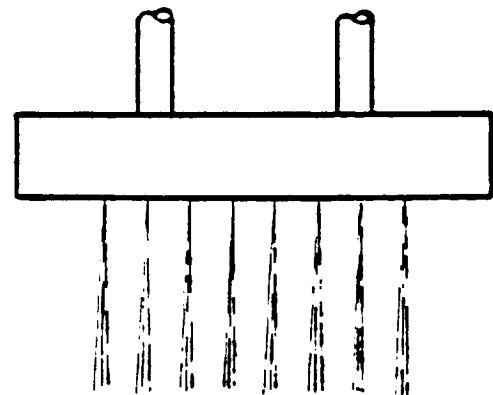
B. Fuel Film Cooling at Injector



C. Doublet Impingement

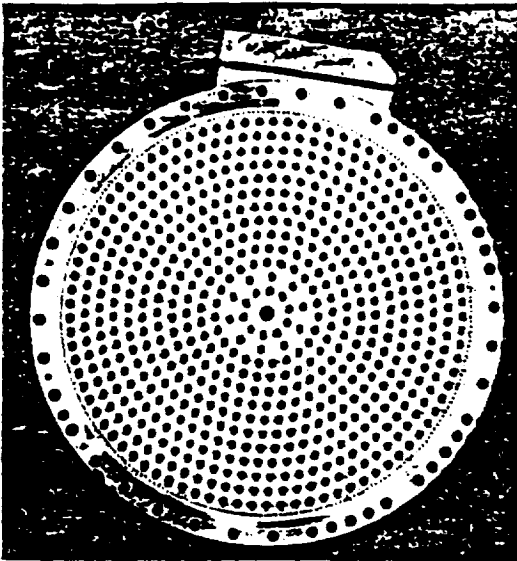


D. Triplet Impingement

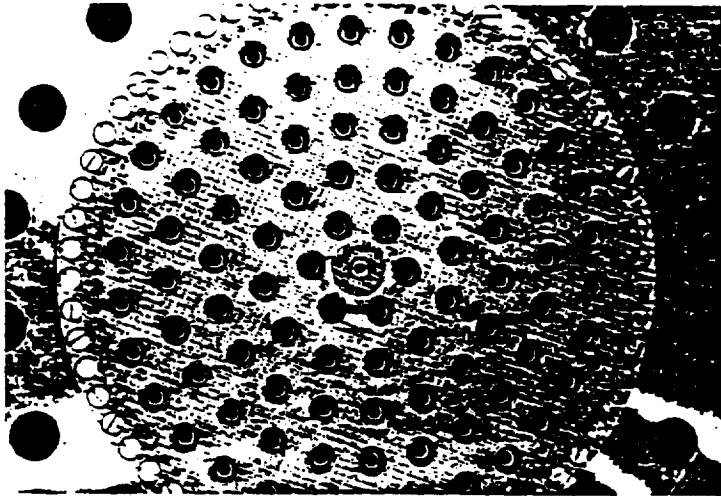


E. Shower Head Injector

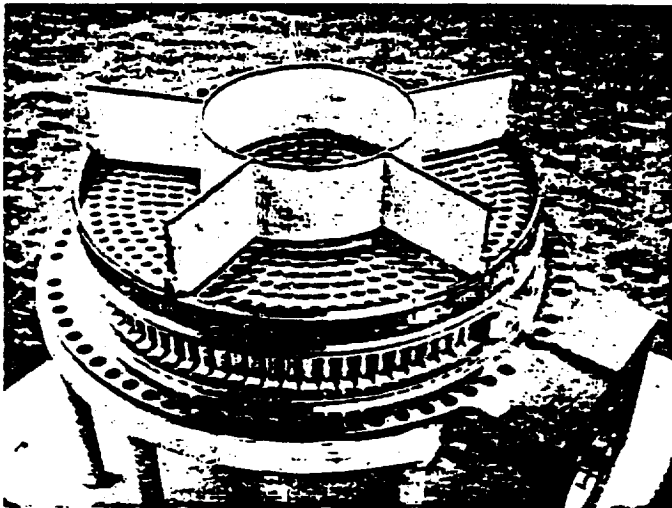
Fig. 1. Examples of Injector Patterns



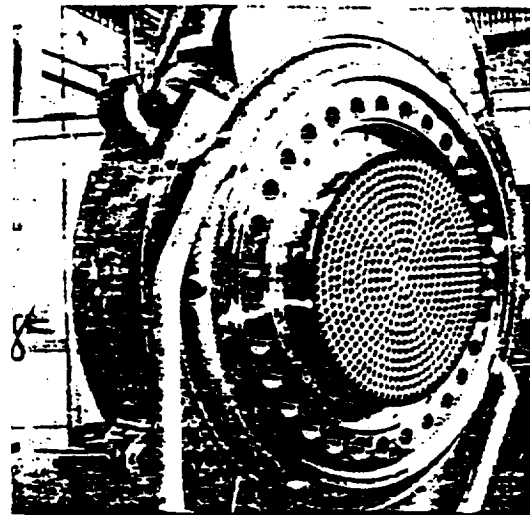
J-2 Injector Assembly



BORD 1 Injector Assembly



J-2S Baffled Injector Assembly



SSME Full-Scale Test  
Injector Assembly

Fig. 2. Examples of Uniform Coaxial Injector Patterns

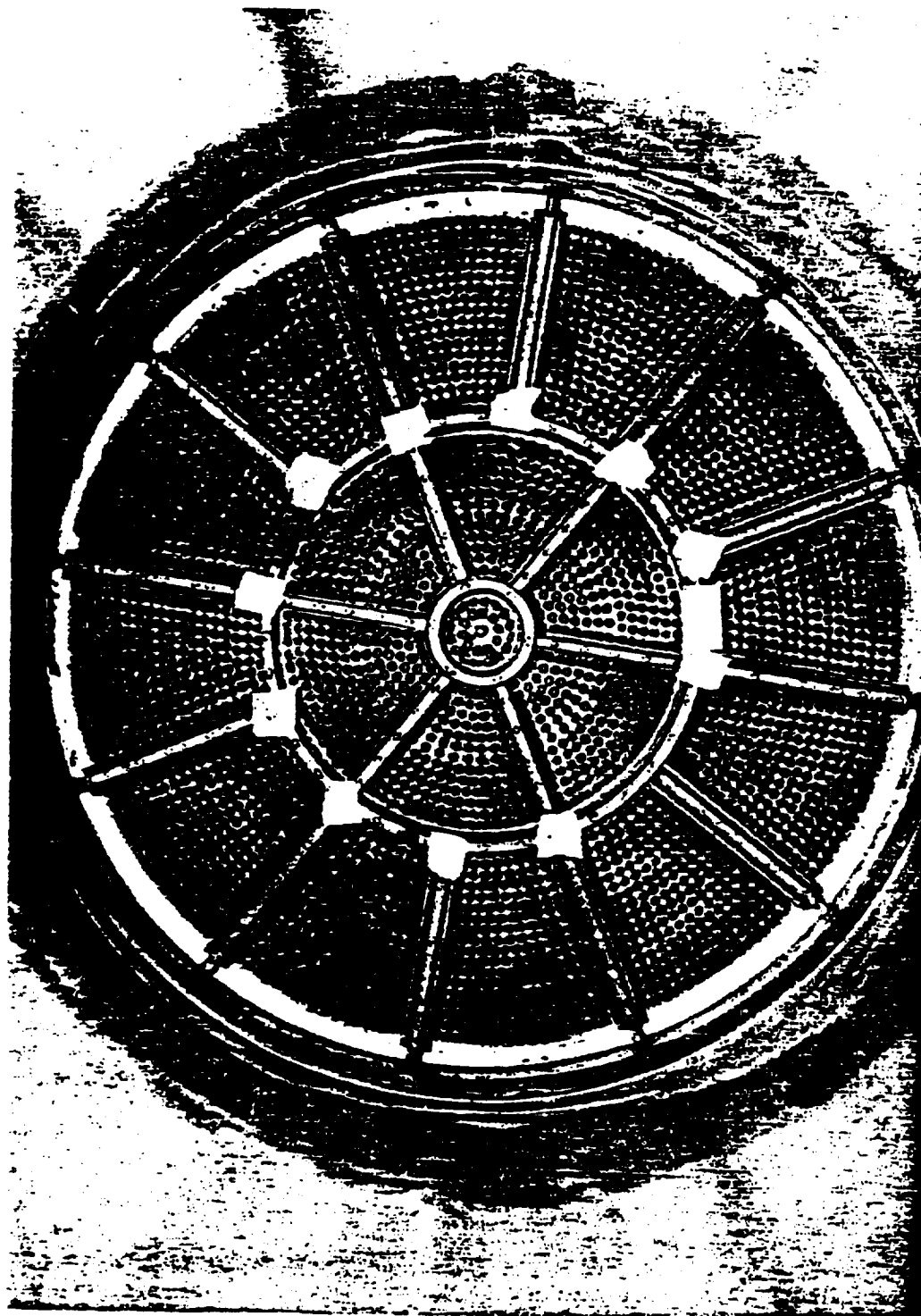


Fig. 3. Million Pound M1 Engine Coaxial Injector Pattern

ORIGINAL PAGE IS  
OF POOR QUALITY

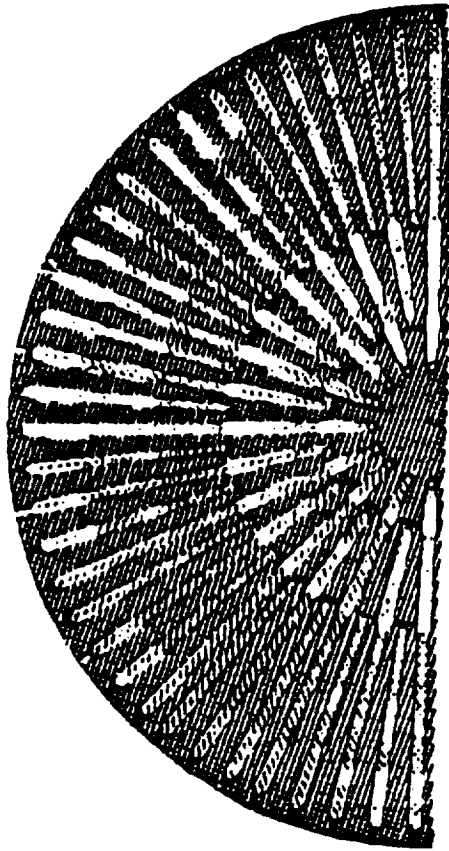
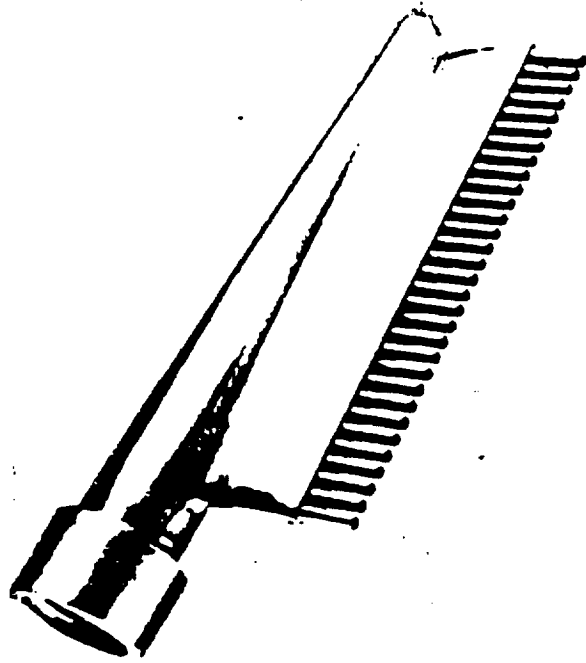


Fig. 4. Spray Bar Injector Pattern

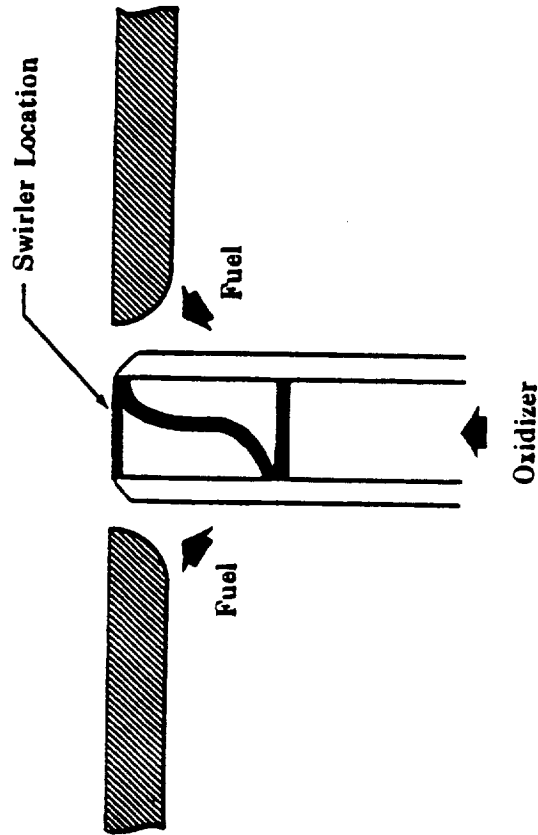
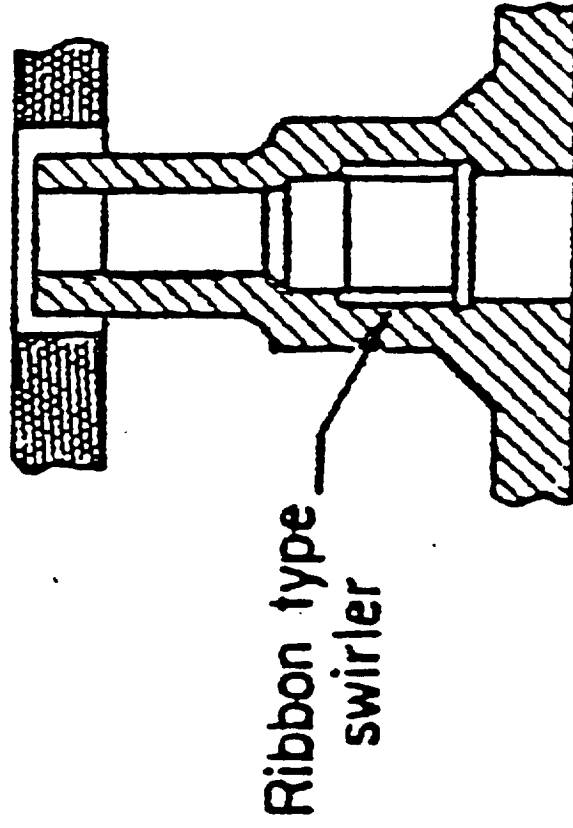


Fig. 5. Injectors with Swirler for LOX

SELECTION CRITERIA	UNIFORM COAXIAL	SPRAY-BAR COAXIAL	COAXIAL WITH SWIRL	IMPINGING	MICRO-ORIFICE SHOWERHEAD
PERFORMANCE	GOOD OVER OPERATING RANGE BECAUSE OF HIGH SHEAR VELOCITY AND UNIFORM FACE SPACING	SUBJECT TO MIXTURE RATIO DISTRIBUTION (MAD) LOSSES BECAUSE OF NONUNIFORM FACE SPACING	DEPENDENCE ON SWIRL IMPINGEMENT RESULTS IN ELEMENT MIXING LOSSES BECAUSE OF NONPROPORTIONAL GAS/LIQUID MOMENTUM VARIATION DURING $P_c$ AND MR EXCURSION	DEPENDENCE ON STREAM IMPINGEMENT RESULTS IN ELEMENT MIXING LOSSES BECAUSE OF NONPROPORTIONAL GAS/LIQUID MOMENTUM VARIATION DURING $P_c$ AND MR EXCURSION	"STREAM-TUBE" FLOW CHARACTERISTICS SUBJECT TO ELEMENT MIXING LOSSES
STABILITY (I.E., SENSITIVITY TO TRANSVERSE PRESSURE WAVE)	REASONABLY INSENSITIVE TO TRANSVERSE PRESSURE WAVE BECAUSE OF PROTECTION AFFORDED OXYGEN STREAM BY HIGH-VELOCITY GAS SHROUD	REASONABLY INSENSITIVE TO TRANSVERSE PRESSURE WAVE BECAUSE OF PROTECTION AFFORDED OXYGEN STREAM BY HIGH-VELOCITY GAS SHROUD	SENSITIVE TO TRANSVERSE PRESSURE WAVE BECAUSE DISTORTION OF ORIFICE SWIRL SPRAY-FIELD RESULTS IN ERRATIC COMBUSTION BEHAVIOR	HIGHLY SENSITIVE TO TRANSVERSE PRESSURE WAVE BECAUSE DISTORTION OF PROPELLANT STREAMS RESULTS IN ERRATIC COMBUSTION BEHAVIOR	HIGHLY SENSITIVE TO TRANSVERSE PRESSURE WAVE BECAUSE DISTORTION OF PROPELLANT STREAMS RESULTS IN ERRATIC COMBUSTION BEHAVIOR
FACE HEATING	LOW HEAT FLUX BECAUSE OF UNIFORM MASS INJECTION ACROSS THE FACE AND PROTECTION AFFORDED BY EXTERNAL FUEL-RICH GAS ANNULUS	MODERATE HEAT FLUX BECAUSE OF NONUNIFORM MASS INJECTION ACROSS FACE, RESULTS IN ADVERSE RECIRCULATION	MODERATE HEAT FLUX BECAUSE OF ORIFICE SWIRL PENETRATION DURING PERIODS OF $P_c$ AND MR EXCURSION	HIGH HEAT FLUX BECAUSE OF EXPOSURE OF FACE TO LOCALIZED HIGH MIXTURE RATIO COMBUSTION	SUBJECT TO "FLASH FIRE" DAMAGE DURING STARTING AND CUTOFF TRANSIENTS BECAUSE OF LOW HEAT-SINK CAPABILITY
THRUST CHAMBER COMPATIBILITY	GOOD OVER OPERATING RANGE BECAUSE OF TOTAL CONTAINMENT OF ORIFICE STREAM BY A FUEL-RICH GAS ANNULUS	POOR BECAUSE OF PROPELLANT MIXTURE RATIO AND MASS UNBALANCE RESULTING FROM "WAGON-WHEEL" INJECTION PATTERN	RISK OF LOCAL WALL BURNING BECAUSE OF ORIFICE SWIRL PENETRATION OF FUEL-RICH GAS ANNULUS	POOR IN APPLICATIONS INVOLVING $P_c$ AND MR EXCURSIONS BECAUSE NONPROPORTIONAL GAS/LIQUID MOMENTUM VARIATION RESULTS IN LOCAL ORIFICE-RICH COMBUSTION AT THRUST CHAMBER WALL	RISK OF LOCAL WALL BURNING BECAUSE OF ORIFICE PLUGGING FROM FOREIGN MATERIAL OR ICE

Table 1 Comparison of Relative Merits of Injector Patterns



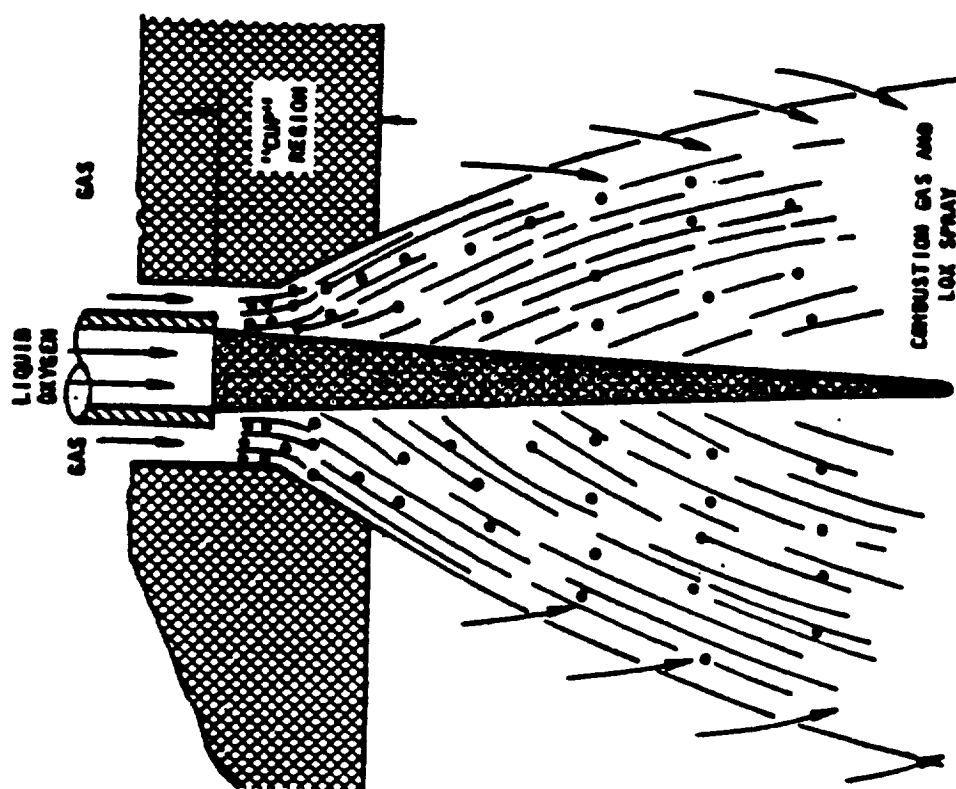


Fig. 6. Atomization Concept of Coaxial Injectors

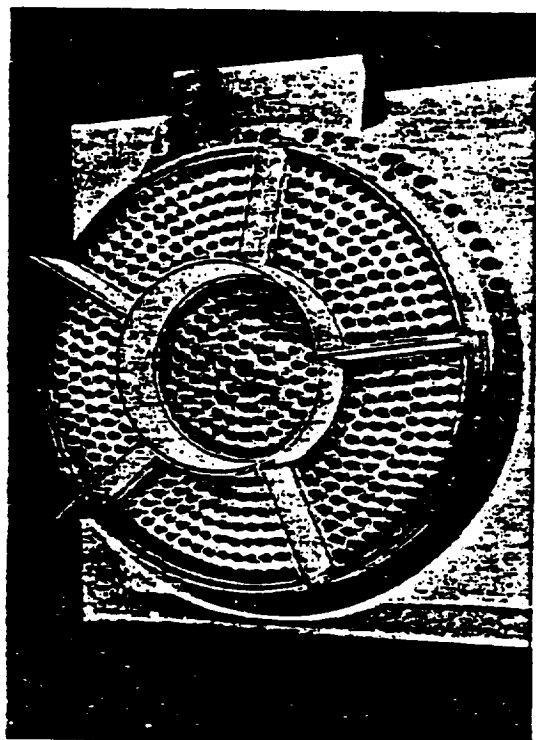
#### 4. Baffle Elements

Baffle elements is one of the common features that appear in many rocket engines manufactured to date (Fig. 7). Even though every measure is generally taken in the design of injection elements for stable operation, dynamic stability cannot be guaranteed over a wide range of operating requirements with a stringent verification requirement. Therefore, combustion baffles and acoustic absorbers are generally incorporated for added insurance for damping instability under wide operating conditions. Baffles can be either separate plates or injector elements themselves can be extended to form baffle barriers.

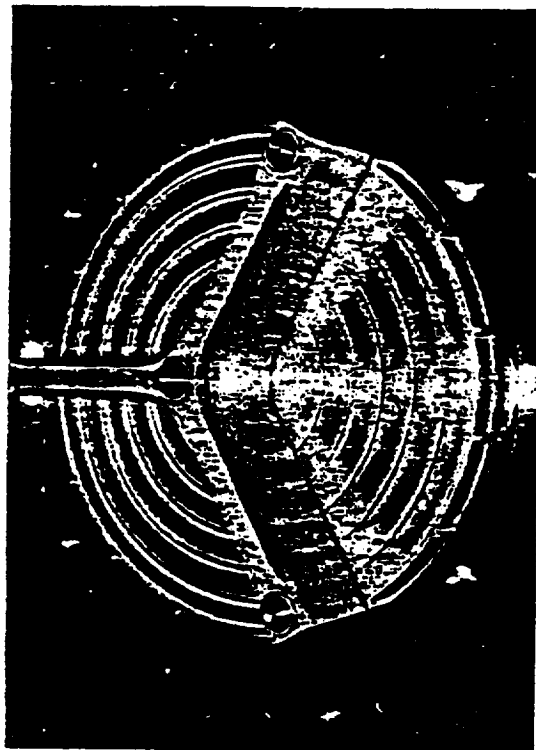
#### 5. SSME Main Injector Elements

General Design Description: The main injector is configured of 600 injection elements, combustion baffles, a faceplate assembly and a manifold-body structure (Fig. 8). The injection elements are of the coaxial type with the liquid oxygen injected at low velocity at the center of the element and the gaseous fuel injected at high velocity through the surrounding annulus. This high velocity difference enhances propellant atomization and mixing for maximum performance. The coaxial elements are spaced uniformly across the face, both radially and circumferentially. This provides for uniform mass flow and mixture ratio across the chamber, as well as maximum vaporization and mixing, provided in this well characterized main injector assembly.

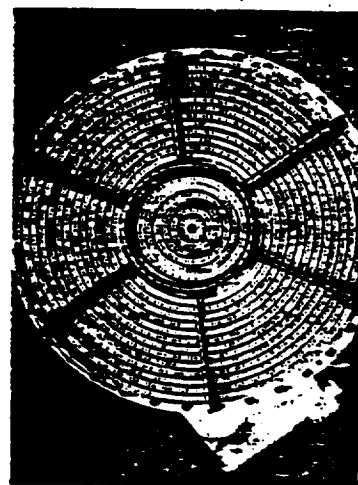
The baffles are formed by 75 of the injection elements extending 2 inches below the face (Fig. 9). These baffles prevent combustion instability modes below a frequency of 4300 Hz. The 75 baffle-forming injection elements give the same propellant mass flux and mixture ratio as the remaining 525, but they differ in configuration. The major difference is that the baffle elements inject hydrogen gas, whereas the main elements inject combusted hydrogen-rich gases. This is done because the baffle elements are convectively cooled where they extend below the injector face. The cooling is more effectively accomplished with hydrogen than with the hot-gas.



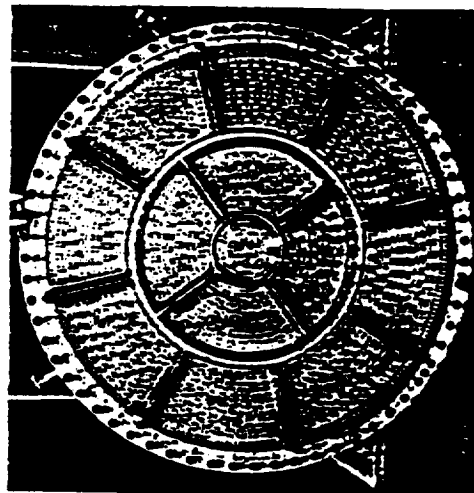
J-35 BAFFLED INJECTOR  
(a)



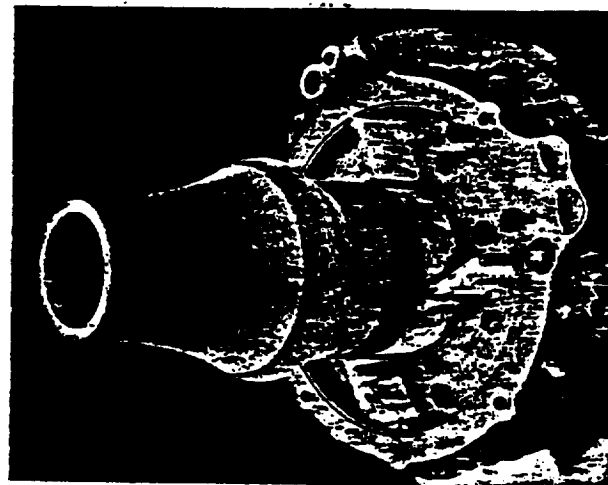
LMA BAFFLED INJECTOR  
(b)



ATLAS, H-1, THOR BAFFLED INJECTOR  
(c)



F-1 BAFFLED INJECTOR  
(d)



LANCE HML BOOSTER BAFFLED COMBUSTOR  
(e)

Fig. 7. Some Examples of Baffled Elements Used In Rocket Engines

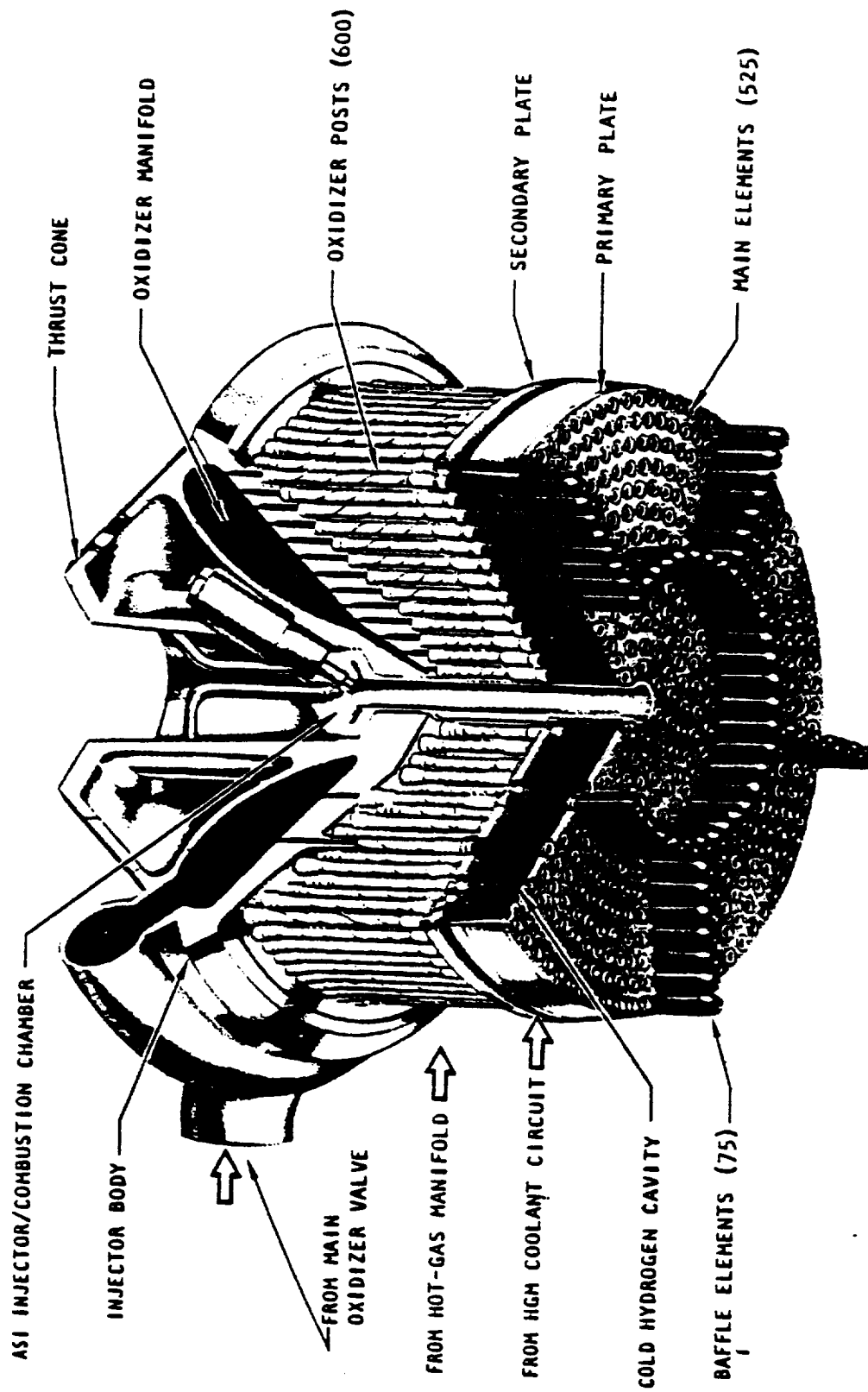
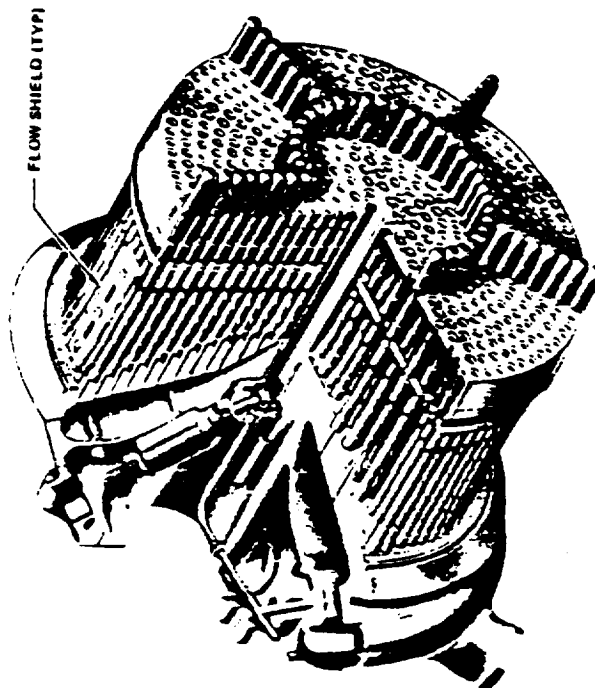


Fig. 8. SSME Main Injector and Manifolds



## GEOMETRY

■ 347 CRES RIGIMESH FACEPLATES	
■ DUAL SPARK IGNITER	
■ FACE DIAMETER	17.74 IN.
■ INJECTOR CONFIGURATION	CONCENTRIC ORIFICE
■ NUMBER OF ELEMENTS	525
■ NUMBER OF FLOW SHIELDS	42
■ NUMBER OF BAFFLE ELEMENTS	75
■ BAFFLE ELEMENT LENGTH	2 IN.

## OPERATING PARAMETERS (RPL, MR-6.0)

■ CHAMBER PRESSURE	2995 PSIA
■ OXIDIZER FLOWRATE	784.6 LB/SEC
■ HOT GAS FLOWRATE	224.8 LB/SEC
■ COOLANT FLOWRATE	
■ PRIMARY FACEPLATE	5.1 LB/SEC
■ SECONDARY FACEPLATE	3.8 LB/SEC
■ BAFFLES	15.3 LB/SEC

Fig. 9. Some Geometry and Operating Parameters of SSME Main Injector

The injector faceplate assembly is transpiration cooled with cold gaseous hydrogen. It is especially designed to allow freedom of expansion and to maintain low face temperatures. This enhances life and prevents distortion of the elements. This is achieved with a dual-faceplate configuration. The primary faceplate separates the cooling hydrogen from the combustion chamber, and the secondary faceplate separates the cooling hydrogen from the hot gas (Fig. 10). The faceplates are uniformly supported by the oxygen posts, which are threaded into both porous faces. A sliding joint is provided between the faceplate assembly and the adjacent hot-gas manifold/main combustor interface. Sealing of this location is effected by two contracting-ring seals, one on each face.

Hydrogen enters the dual-faceplate assembly radially around the full circumference. It flows inward around the injection elements and divides into three paths (Fig. 11). Part of the total passes through the porous primary faceplate. This hydrogen cools the face and then enters the combustion chamber. Another portion of the total passes forward through the porous secondary faceplate. This hydrogen cools the face and then mixes uniformly with the incoming hot-gas from the turbines and aids in achieving maximum performance. The remaining hydrogen enters the 75 baffle elements through holes in the retainer.

The injector body (Fig. 12) forms the two main propellant manifolds, one for the hot-gas and the other for the liquid oxygen. The hot-gas manifold exists between the contoured body and the secondary faceplate. The body is contoured to maintain a uniform velocity of the hydrogen-rich hot-gas which enters around the injector circumference and flows radially inward. The injection element posts pass axially through this hot-gas manifold. The hot-gas enters each element through 6 slots in the retainer just forward of the secondary faceplate.

The liquid oxygen torous manifold covers the forward end of the body and provides uniform static pressure at all elements. The liquid oxygen is transferred from the manifold directly to the center post of the coaxial element through orifices (Fig. 10). The oxygen posts inertia are welded into the body. Flow is controlled at the entrance to each oxygen post by

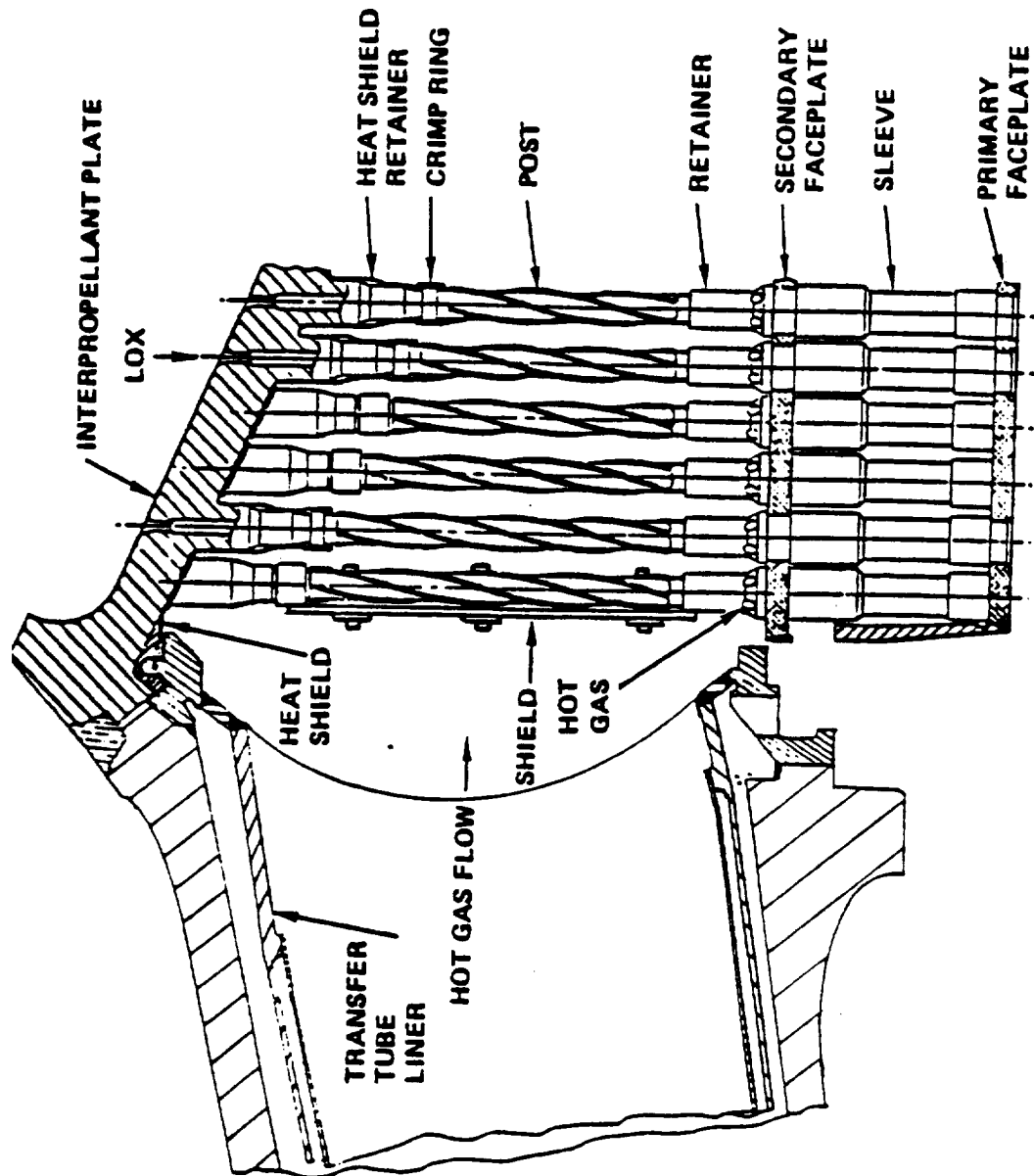


Fig. 10. Main Injector View With Cold Hydrogen Cavity Between The Face Plates

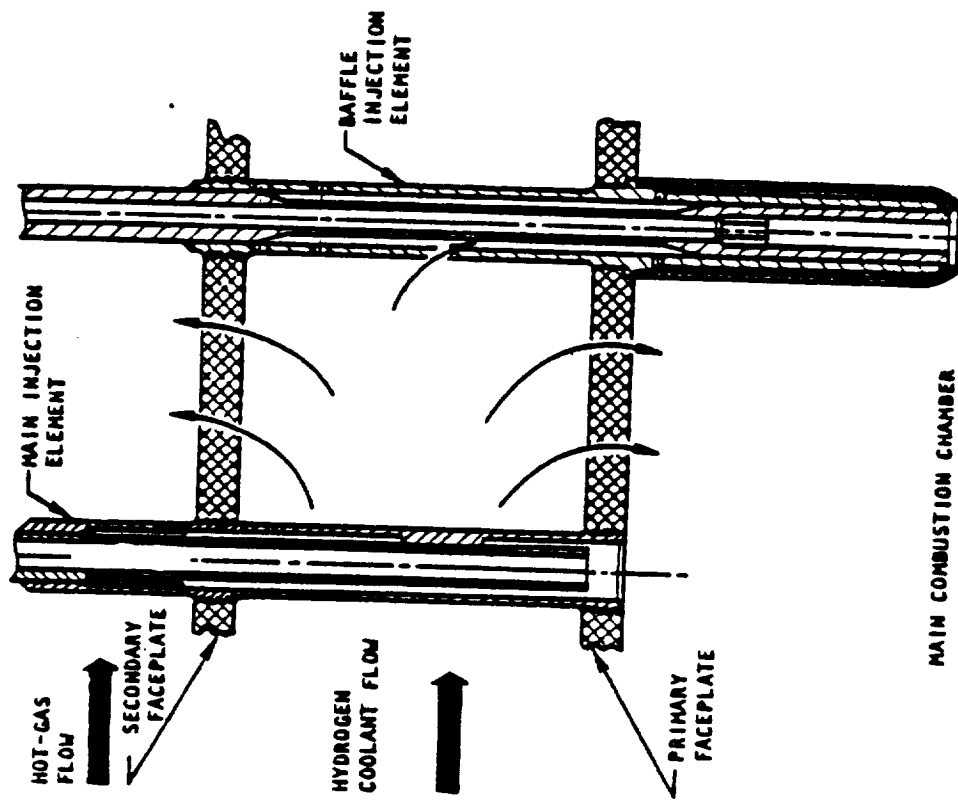


Fig. 11. Schematic Representation of Cold Hydrogen Flow Through in the Cold Cavity



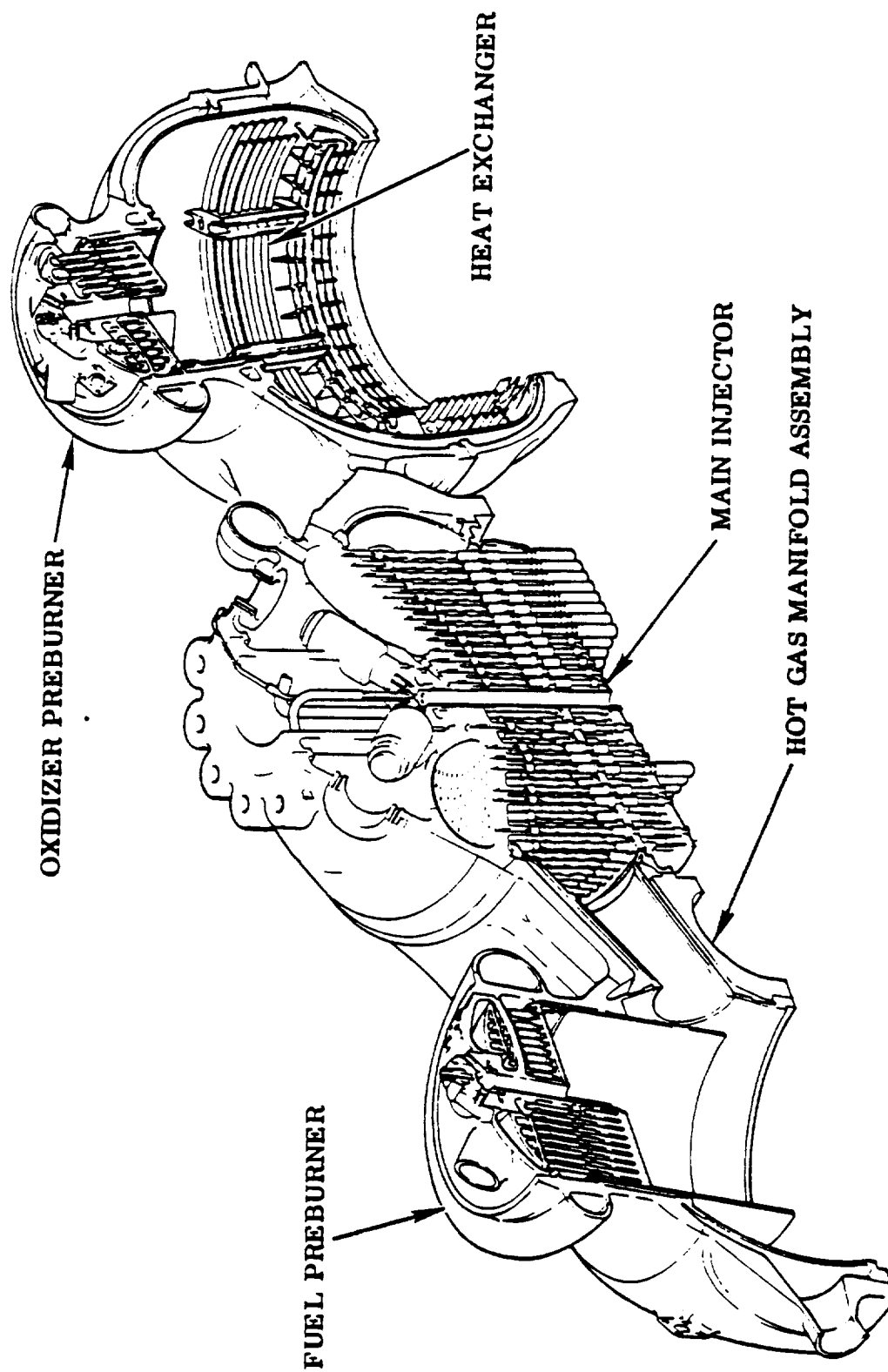


Fig. 12. Cutaway View of Hot Gas and LOX Manifolds

a high-impedance orifice which provides uniform oxygen flow to each element for maximum performance. Major portion of the pressure drop occurs in this orifice. The toroidal liquid oxygen manifold also permitted the installation of the augmented spark igniter at the center of the injector.

#### 6. Face Cooling

Face cooling is a major consideration in the design of a high-performance long-life injector. A low face temperature is required to preclude performance-degrading thermal distortion within the injection element and life-degrading thermal strains within the faceplate structure.

To minimize the risk in this critical area, a cooling concept with a broad technology base is used for the main injector design. Transpiration injector face-cooling with cold gaseous hydrogen is employed and has been successfully demonstrated with coaxial injectors during several hydrogen-oxygen engine development programs. These include:

<u>Program</u>	<u>Maximum Chamber Pressure, PSIA</u>
RL-10	300
J-2	800
M-1	1000
J-2S	1300
AEA SEGMENT (NAS8-20349)	2000
BORD 1	4000
SSME	3000

A porous material (Rigimesh) which allows for simple and effective transpiration cooling of the faceplate is used for the main injector. Cold hydrogen gas was selected as the cooling media because the use of hot-gas would result in a face temperature greater than 1400F and a radial thermal expansion of 0.120 inch. The design hydrogen flowrate results in a low injector face temperature of 200F and a radial thermal growth of less than 0.015 inch, thus having a negligible effect on the injection elements.

## 7. Thermal Expansion Provisions

The dual-faceplate structure is attached to the injector body through the individual oxidizer injection posts (Fig. 10). Heat exchange between the liquid oxygen posts and the hot-gas within the injector body manifold results in the thermal expansion of the longer posts in the outer rows being greater than the shorter posts near the center of the injector. However, the variable thermal expansion of the oxidizer posts is partially compensated by the greater cooling of the hot-gas sleeves within the outer rows by the cold hydrogen flowing between the primary and secondary faceplates. The net axial thermal deflection of the faceplate between the center and outer region of the injector is therefore small. This small differential axial movement is well within the expansion capability of the main injector threaded faceplate structure. Because the baffle elements experience different heating characteristics than the main elements within the cold cavity, the baffle elements are threaded into the secondary faceplate only and are free to contract in an axial direction at the primary faceplate joint.

The bending flexibility of the liquid oxygen posts is sufficient to comply with the radial thermal expansion and contraction of the injector face. The shorter stiffer posts are located near the center where the radial movements are small and the longer flexible posts are located in the outer region of the injector where the radial movements are a maximum. The maximum radial deflection at the faceplate outside diameter is  $-0.014$  inch during prechill and  $+0.024$  inches during mainstage operation.

The relative injector-combustor axial and radial movement at the periphery of the dual-faceplate is accommodated by two contracting-ring seals. The seals are retained within the groove by a spring-loaded carrier ring which provides a positive bearing load on the face of the ring seals.

## 8. Components of Main Injector Post

The major components of the injector element include:

- 1) LOX Post
  - 2) Retainer
  - 3) Fuel Sleeve
  - 4) Face Nut
- Fig. 13

- 5) Heat Shield Retainer
  - 6) Swage Ring
- Fig. 14

In addition, Row 13 posts contain:

- 7) Flow Shields
  - 8) T-Bolt and Nuts
- Fig. 15

The main injector LOX post consists of hollow post within a sleeve that is secured by a retainer and nut between primary and secondary plates of the main injector.

The upper ends of the post have four helically wound spoilers machined in their outer perimeter to reduce vibration induced by hot gas flow due to vortex shedding.

The retainer clamps the secondary faceplate to the sleeve and contains six equally spaced orifices that direct the hot gas into the annulus surrounding the post.

The sleeve with the post forms the annulus for the hydrogen rich gas between primary and secondary faceplates.

The face nut secures the primary faceplate to the sleeve and forms the cup in which the initial contact between liquid oxygen and hot gas takes place. The face nut also presents a convenient way of changing the metering of hot gas into the combustion chamber if necessary. The assembly of major main injector elements is schematically illustrated in Fig. 16.

A heat shield is placed between the interpropellant plate and hot gas manifold to protect the interpropellant plate from hot gases (Fig. 14). The heat shield is kept in place by a heat shield retainer and a heat shield swage ring retainer.

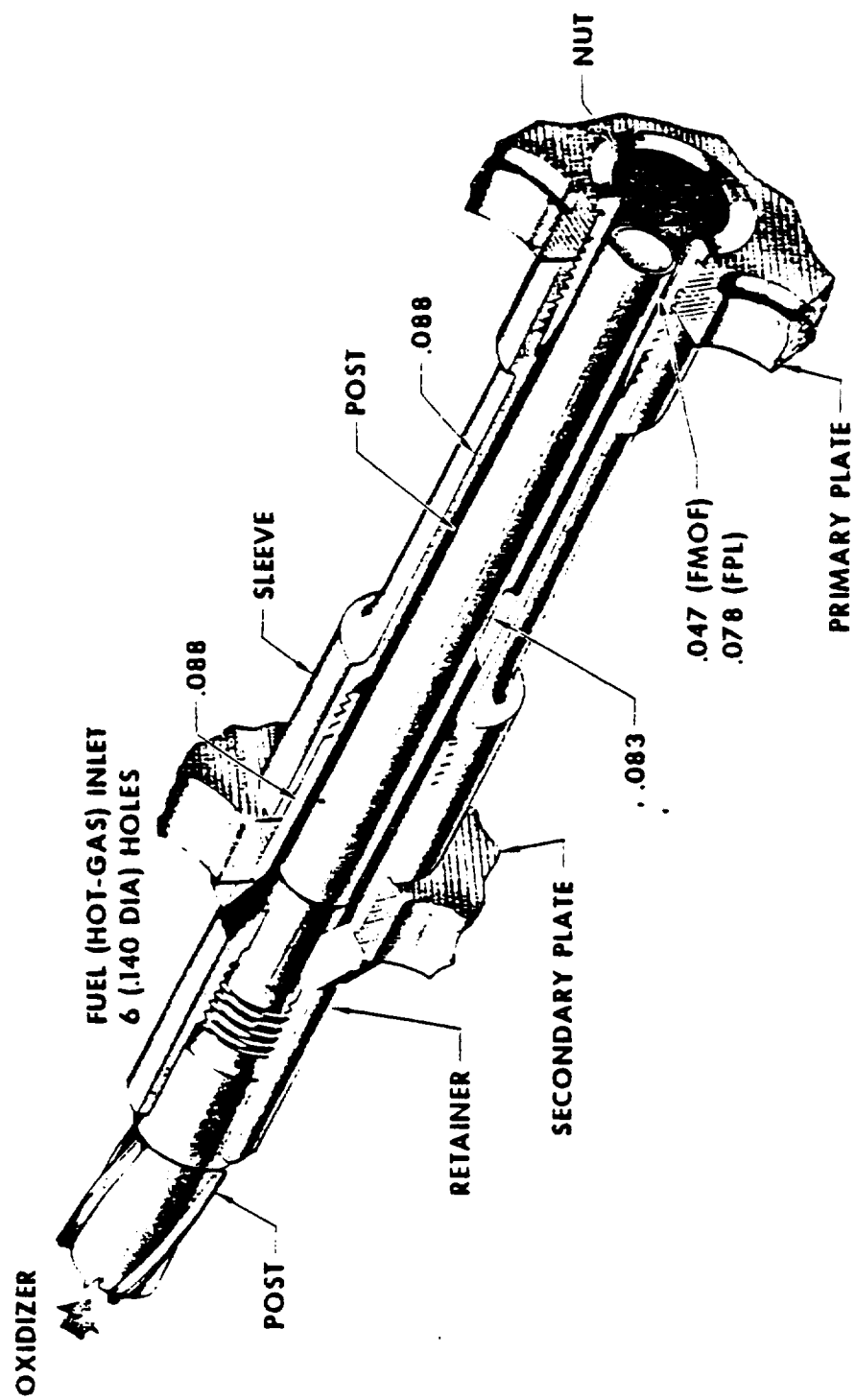


Fig. 13. Main Injector Assembly

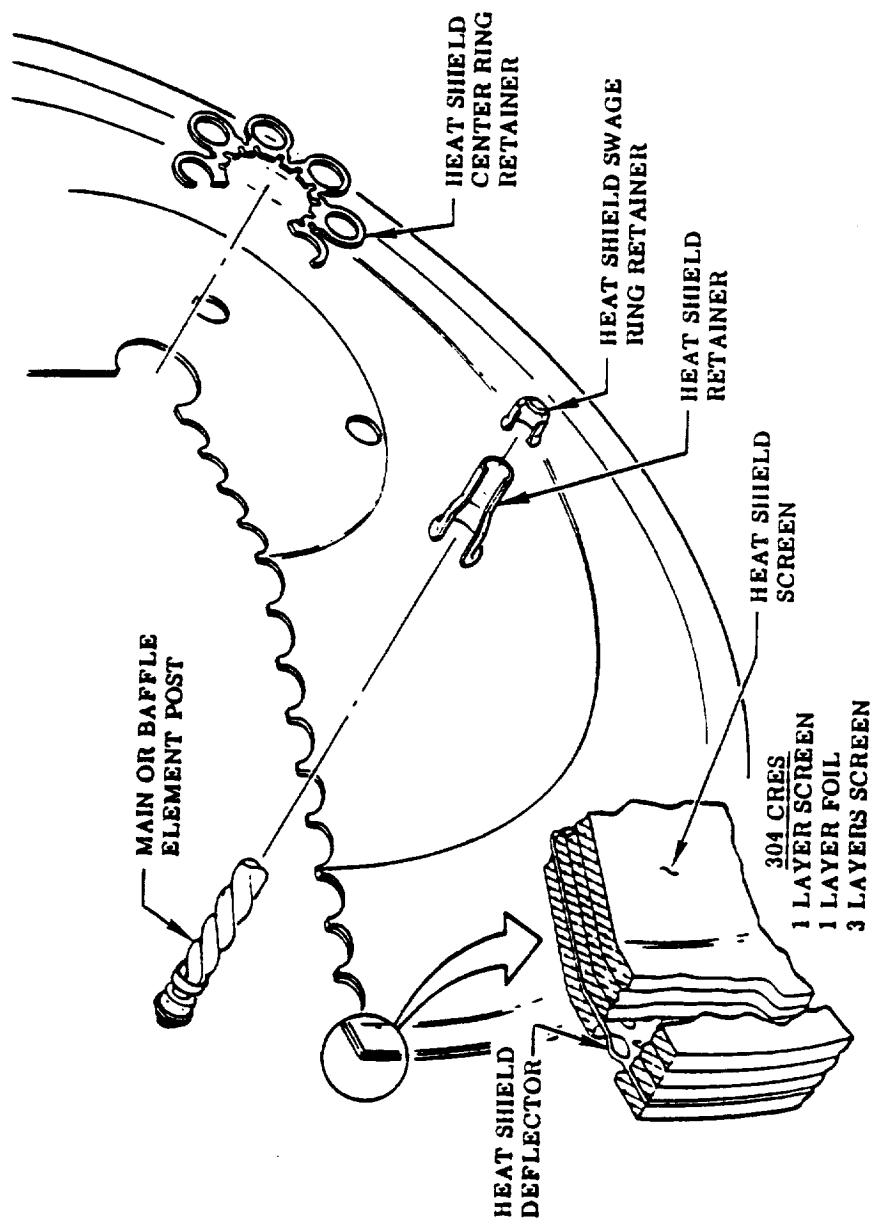


Fig. 14. Function of Heat Shield Retainer and Swage Ring

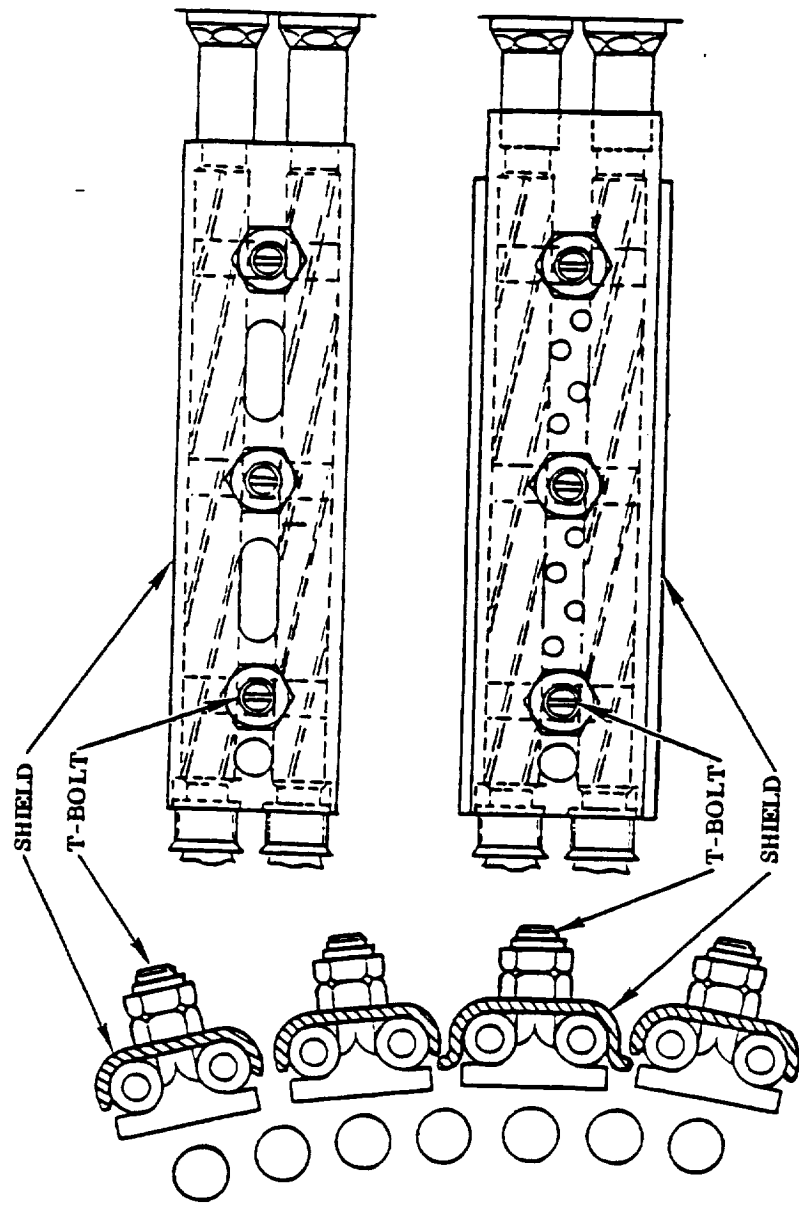


Fig. 15. Flow Shields, T-Bolt and Nut for Row 13 Posts

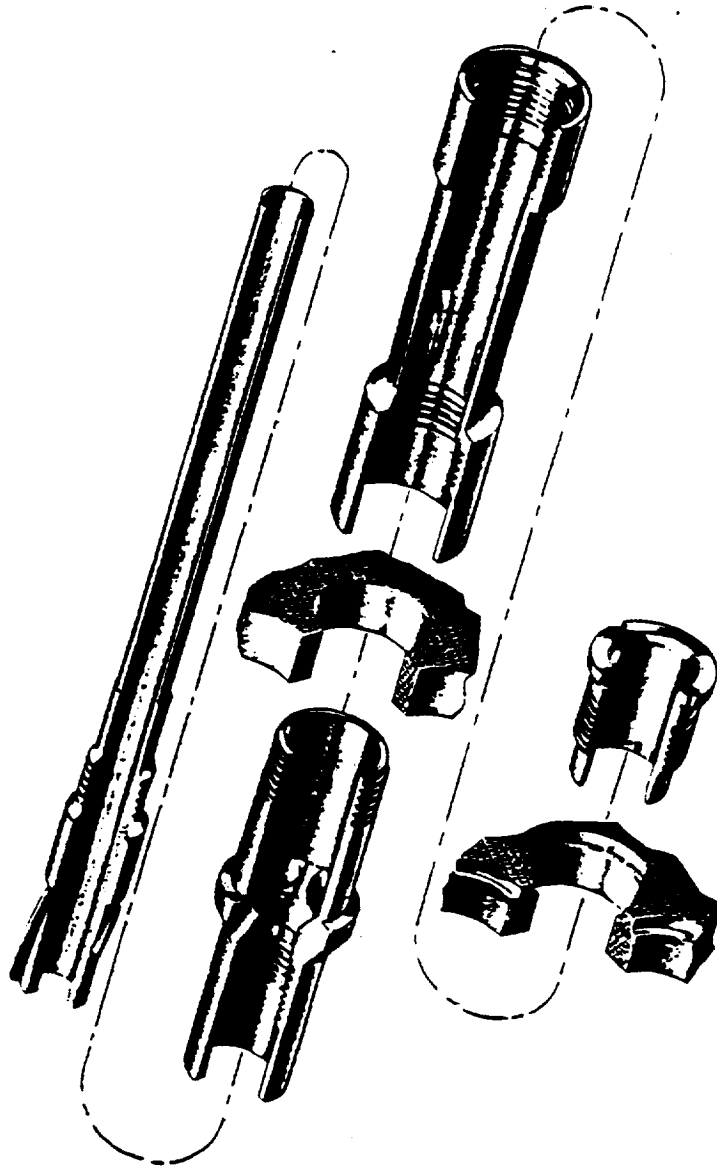


Fig. 16. Assembly Schematic of Loxpost Components



The flow shield assembly is used in the Row 13 Lox posts only (Fig. 9 and Fig. 15) to protect the Row 13 posts from direct impinging of hot gases. In addition, flow shields reinforce the row 13 posts.

#### 9. Comparison of Main Injectors Between Various Rocket Engines

A comparison of geometric dimensions of Lox posts for J2, J2-S, M1, SSME and RL-10 engines are given in Table 2. The variations in number of elements, post ID/OD diameter ratios, must be observed. The large variation in combustion chamber pressure ( $P_c$ ) and variation in Fuel temperatures must be noted. The comparatively stable Lox temperature around 200°R must also be observed. The large  $\Delta t$  observed in SSME is due to the fact SSME uses the staged combustion process involving hot gases (hydrogen rich steam), whereas the other engines use cold hydrogen gas as the fuel. The commonality of the injectors in J2, M1 and SSME (Fig. 16, 17 and 18) having brazed or welded connection at the top dome and the threaded connection at bottom for the fuel sleeve must be noted. The presence of helical whirlers in SSME injector in the outer diameter to act as spoilers (Fig. 13) or in the inside diameter to give a whirling action to Lox (Fig. 18), must be observed.

#### 10. Main Injector Baffle Elements General Design Description

As described earlier, baffle elements are stability aids used in the main injector (Fig. 9). The baffle injection element is also coaxial and consists of liquid-oxygen core which is surrounded by gaseous hydrogen annulus (Fig. 19). The propellant flowrate and mixture ratio from baffle element is equal to that of main injection element; consequently, the overall mass and mixture ratio balance within the combustion chamber is not disturbed by the incorporation of combustion baffles.

Cooling of combustion baffles within a high chamber pressure environment is a serious consideration. A cooling concept very similar to main combustor is used because of similar heat transfer environment at the baffle and in the upper region of the combustion chamber. Hydrogen cooling with milled channel walls has demonstrated failure free operation at chamber pressures and at

TABLE 2. DESIGN GEOMETRY OF CO-AXIAL ELEMENTS ( $\text{CH}_4/\text{LO}_2$ ) FOR VARIOUS ROCKET ENGINES

ENGINE ELEMENTS	/COAX ELEMENTS (O.D.)	FUEL SLEEVE DIA. (IN)	OR. POST DIA. (IN)	AREA (IN <sup>2</sup> )	OR/FUEL	LB/S FLOWRATE PER ELEMENT	OR/FUEL	LBS. THRUST/ELEMENT	CUP RECESS	A <sub>POX</sub>	A <sub>FUEL</sub>	P <sub>C</sub>	INJECTOR DIA. (IN)	INJECTOR FACE TO THROAT LENGTH	CONTR. RATIO	AT THERMAL LOX FUEL TEMP
J2	614	.332	.182	.244	15.97/25.26	.741/.118	325.0	.200	207	102	787	16.50	17.926	2.30	180°R	195°R
M1	3248	.334	.210	.290	159.5/10.15	.831/.153	300.0	.231	335	175.0	1000.0	42.17	30.0	1.74	180°R	140°R
SSME M.C.C. (FPL)	600	.389	.188	.220	16.66/46.38	1.42/.4298	783.0	.255	641.7	251.2	3000.0	17.74	14.0	2.96	191	1444
J2S	614	.323	.119	.254	19.10/19.20	.849/.132	431.0	.200	210	130.0	1245	18.50	17.926	1.57	180	257
RL-10	216	.186	.014	.120	.9289/3.426	.130/.024	70.3		52.4	77.6	395.0	10.30	15.0	4.0	167	451

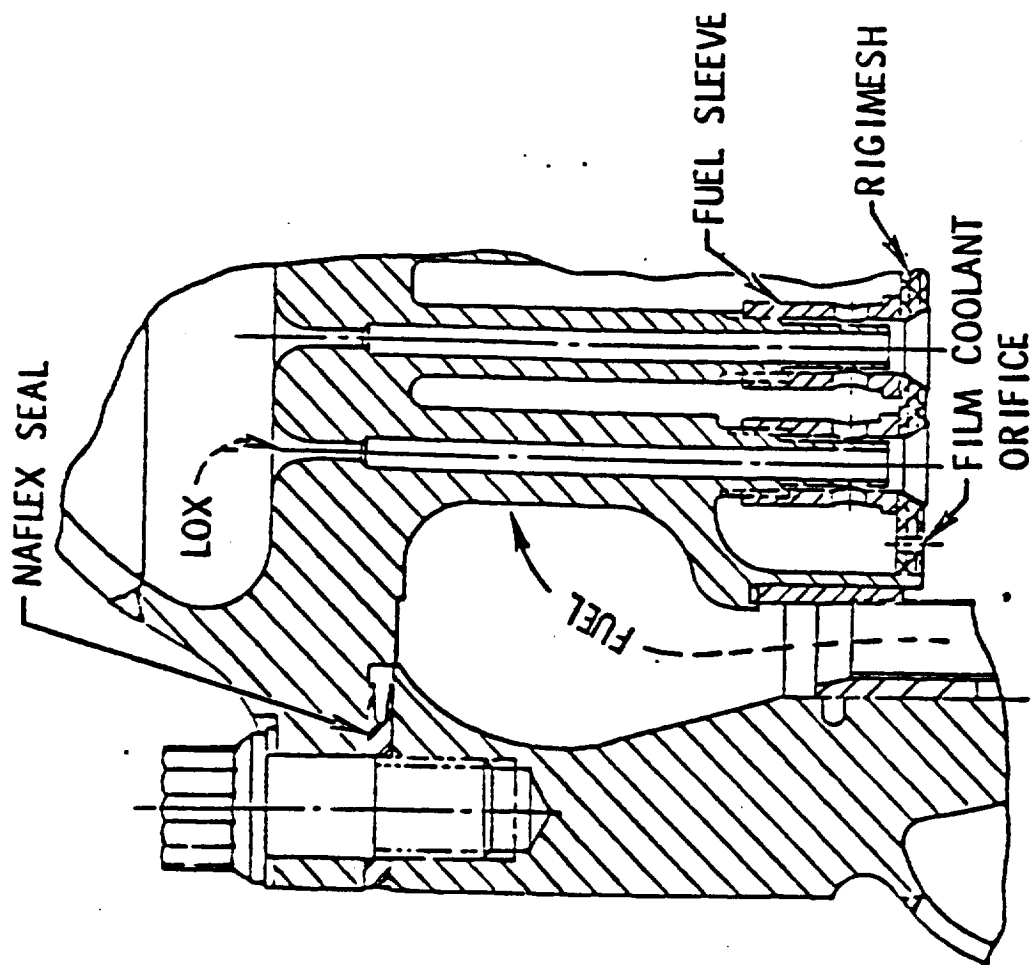


Fig. 17. J2 Injector Configuration

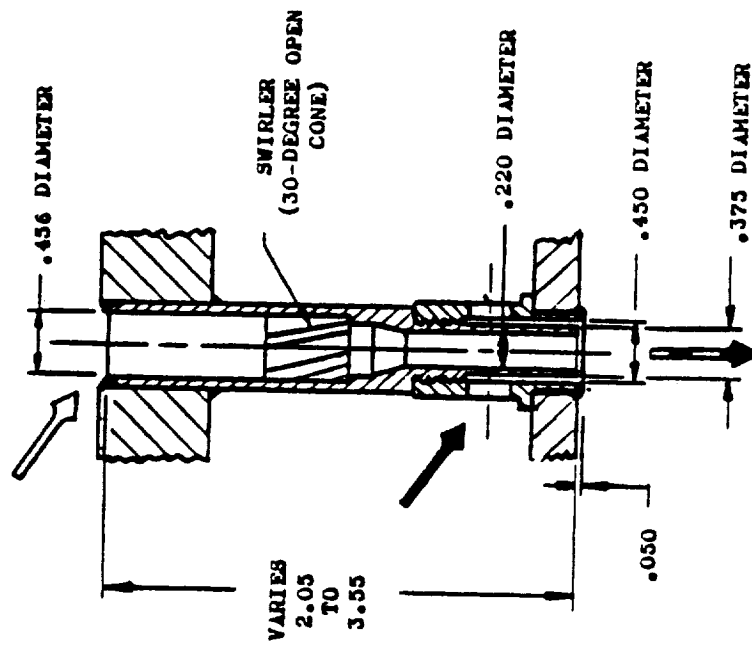


Fig. 18. M1 Injector Configuration

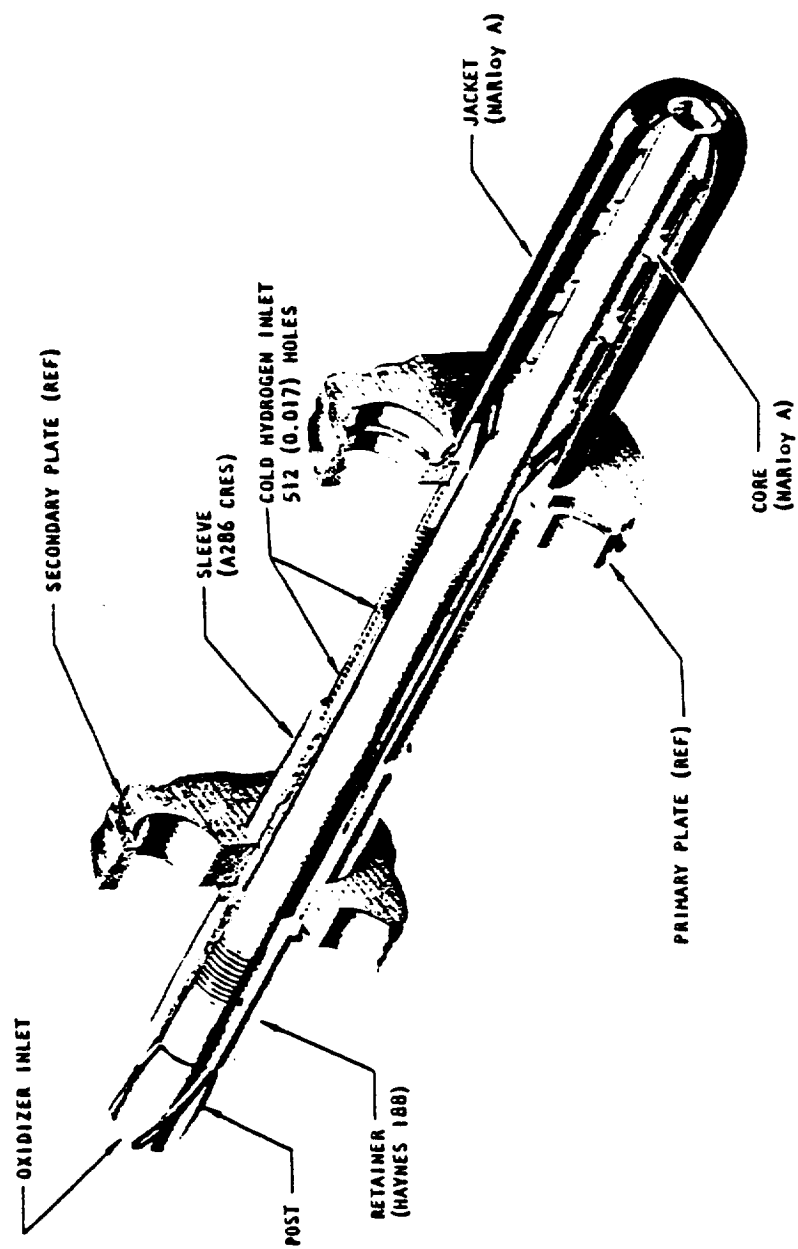


Fig. 19. Main Injector Baffle Elements

upper combustion environments. The baffle coolant channel geometry is optimized to provide uniform low hot gas surface temperature. A baffle length of 2" is used to provide dynamic stability over all operating conditions.

Each main injector baffle element assembly consists of a post, a retainer, a sleeve, a jacket and a core (Fig. 20). The sleeve, jacket and the core are brazed together into an integral component.

Similar to the normal main injector element, the post is hollow, welded to the injector body and ported to the injector oxidizer manifold through a metering orifice in the injector body. The upper end of the posts have four helically wound spoilers machined to the outer diameter to act as spoilers to vortex shedding resonance phenomena. Unlike the regular injector retainer, the retainer in the baffle element has no holes and threads to the posts and clamps the secondary plate to the sleeve which is threaded to the retainer.

The sleeve is hollow throughout its length and has 16 rows of orifices, which direct cold hydrogen gas into the annulus formed by post and sleeve. From this annulus the cold hydrogen gas is redirected through holes in the sleeve and into the annulus formed by the jacket and core.

The inner wall of the jacket has milled rectangular channels (Fig. 20) to provide convective cooling of the baffle element exposed to high temperature in the MCC. The geometry of the baffle tip provides both a smooth external gas transition and initiates early propellant interaction at the baffle tip.

#### 11. Failure History of Main Injector Lox Posts

The SSME's have demonstrated excellent performance for the 15 space flights to date and have undergone over 1000 successful firings. However, SSME's experienced main injector failures in early test stand firings. Evolution of main injector configuration is a direct result of Lox post failures.

In early Lox post designs, the material used was 316L cres. These injectors failed in early engine firings (engine 0002 and 0005) due to cracking in thread and tip regions (Fig. 21). Fig 22 indicates the failure occurred in

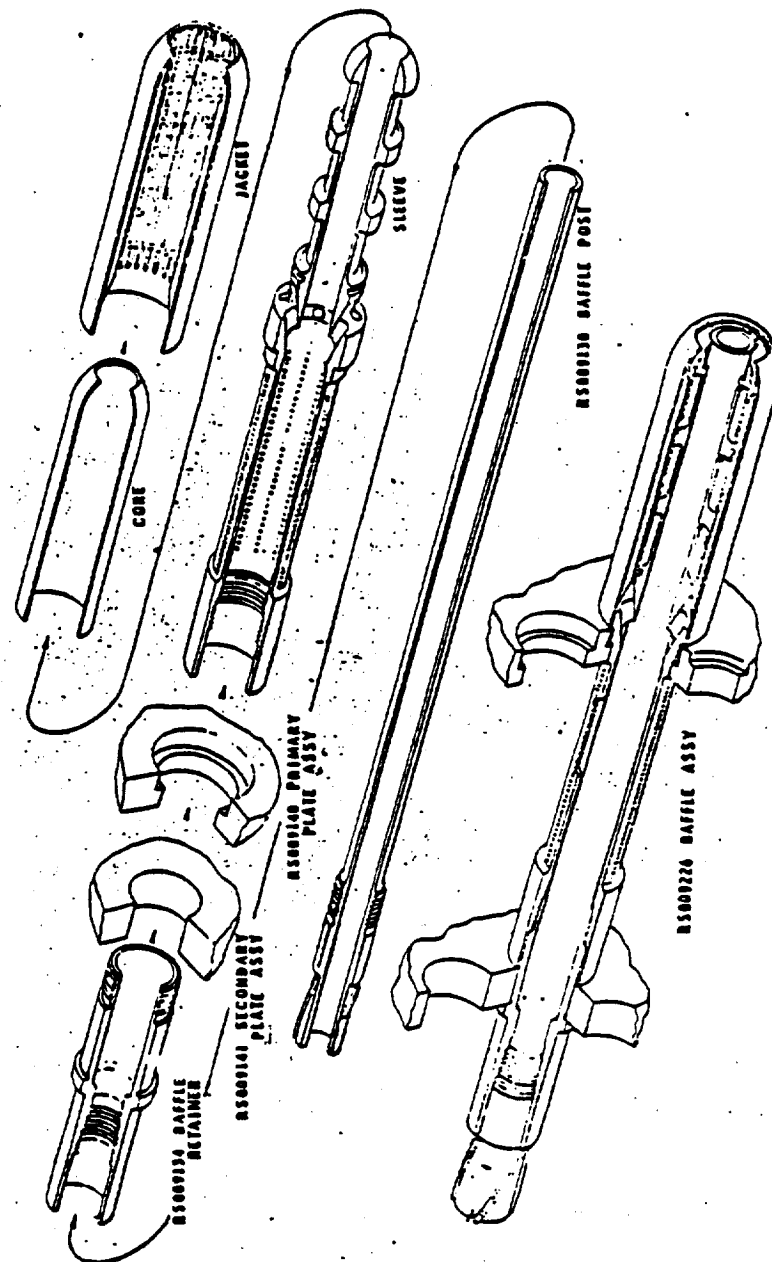


Fig. 20. Assembly Schematic of Main Injector Baffle Element Assembly

high flow regions at the fuel side transfer duct exits. The main injectors in engines 0002 and 0005 had approximately 780 seconds of equivalent RPL (100% or rated power level) at the time of failure. Flow shields were added (Fig. 15) to reinforce the flow 13 posts, modify the injector flow distribution and cool the outer row posts. At approximately 20,000 secs equivalent RPL time, shielded engine 2004 experienced failure in a row 12 post tip region. At that time, existing cres posts were reworked to put a material more suited to high temperature fatigue environment (Haynes 188 vs. 316L cres) in the thread and tip regions. Two later engines, 2108 and 0110, both of which had some run time at the full (109%) power lever (FPL) experienced failures as a result of cracks in the inertia weld region (Fig. 23). These cracks occurred approximately 2800 secs of equivalent FPL time. To attain the goal of infinite life, the entire post is now made of Haynes 188 material. The only failure of this configuration has been the cracking of secondary face plate retainers (Fig. 24) at 4500 secs at FPL (109% RPL). This resulted in a design modification to have a stronger retainer with more material and a radius to reduce the stress in the stress concentration area where the cracking occurred. This configuration is calculated to have infinite life at FPL.

The failure log of the main injector posts to date include two thread failures, two tip failures, two inertia weld failures, and two retainer failures. On another occasion, the Lox post had permanent deformation due to bending result of high drag loads. Current expert opinion on Lox post failures is due to HCF resulting from unknown random flow induced pressure loading.

## 12. Loads on SSME Lox Post

The outer row 13 (Fig. 25) is subjected to the most severe loading conditions. The following loadings need to be considered in the analysis of Lox post.



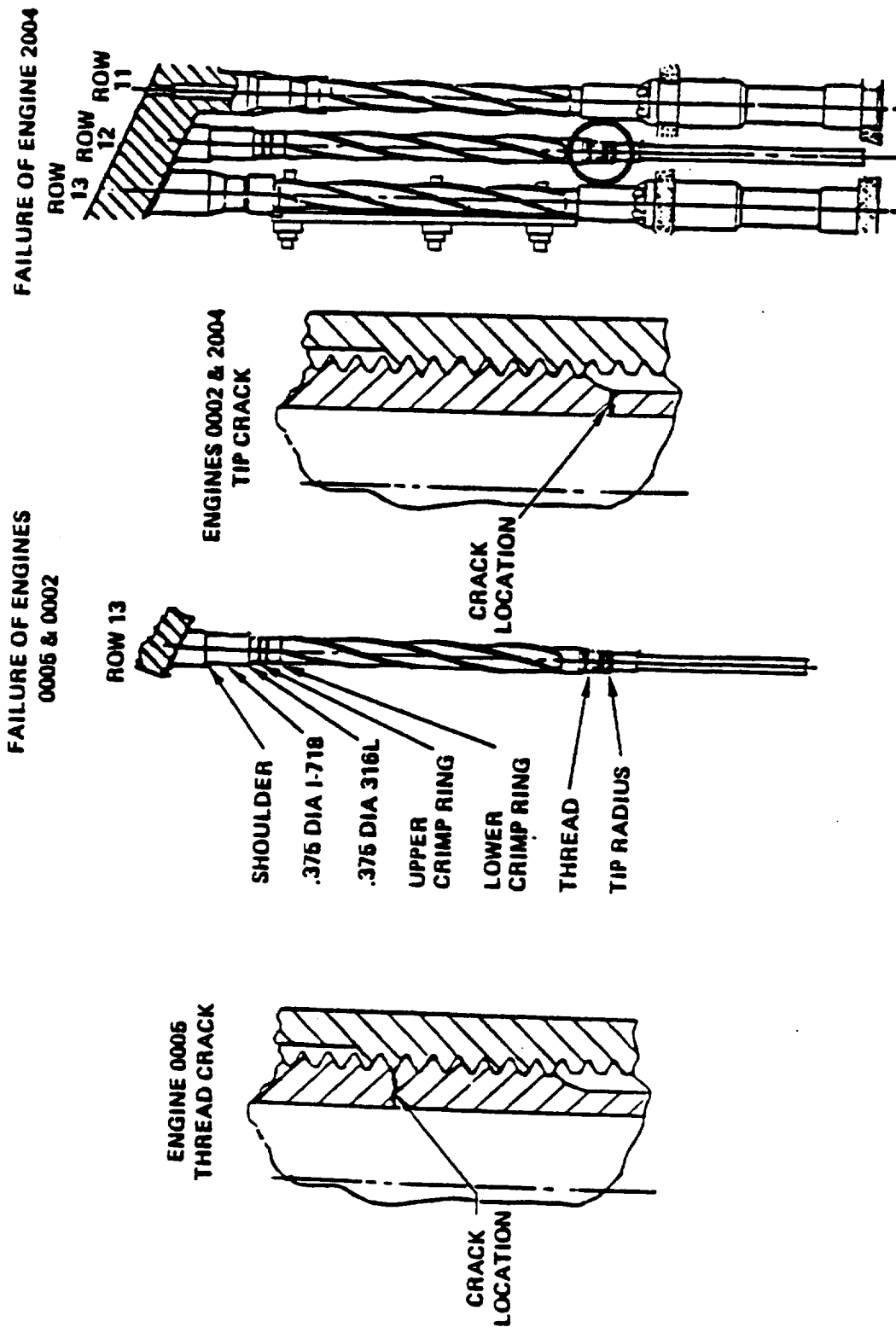


Fig. 21. Failure Location of 316-L Cres Main Injector LOX Post Elements

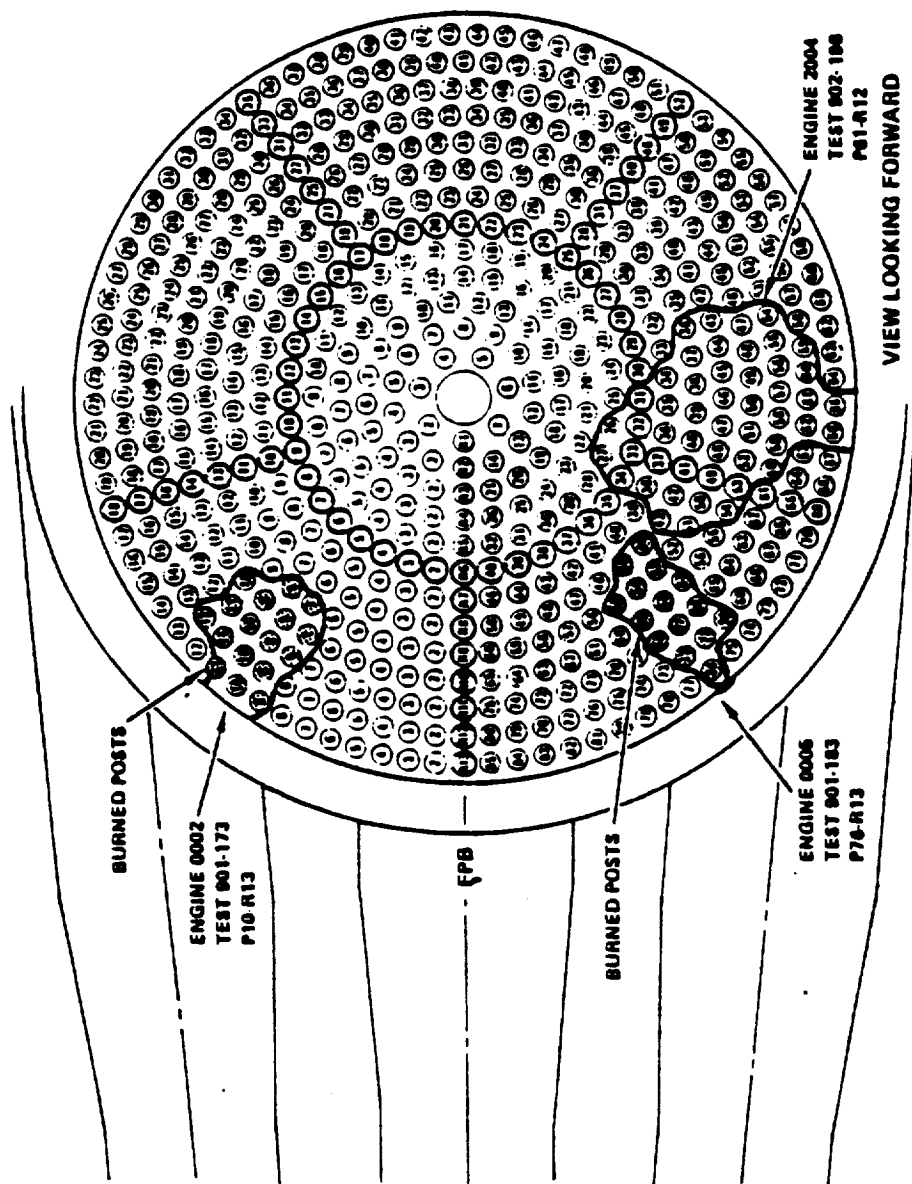


Fig. 22. Failure Location of LOX Posts Relative to Hot Gas Manifold Exits

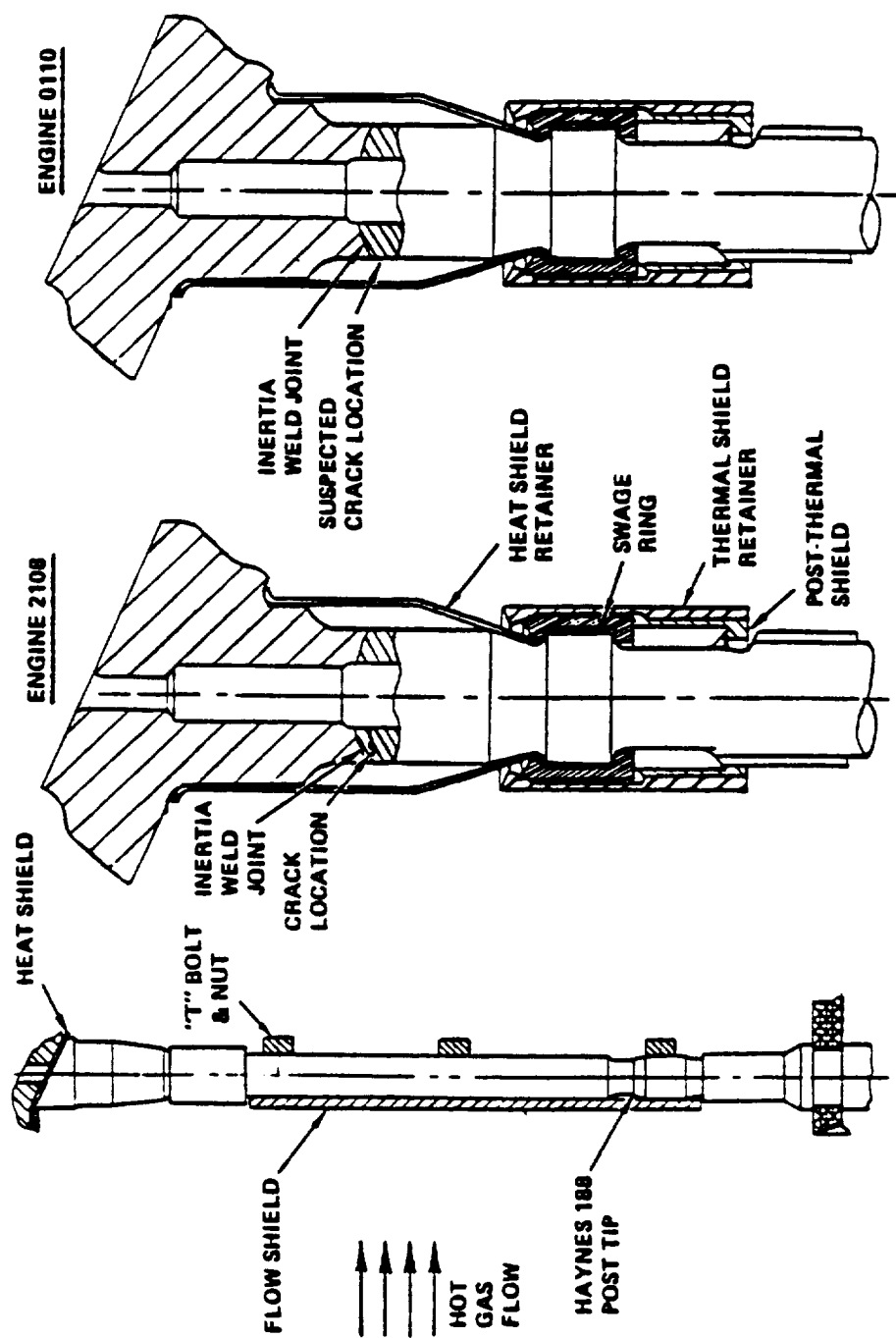


Fig. 23. Failure Location of 316-L Cres Main Injector Posts With Haynes 188 Tip

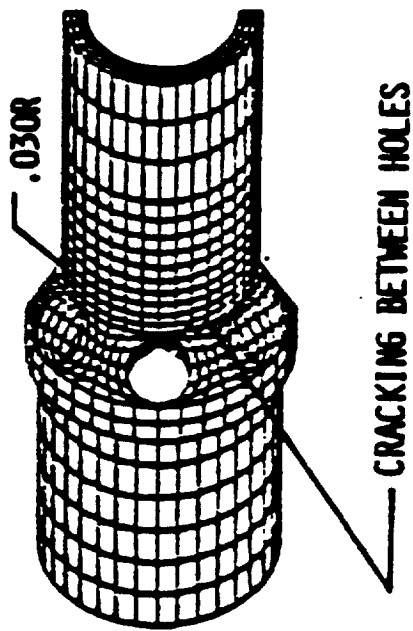
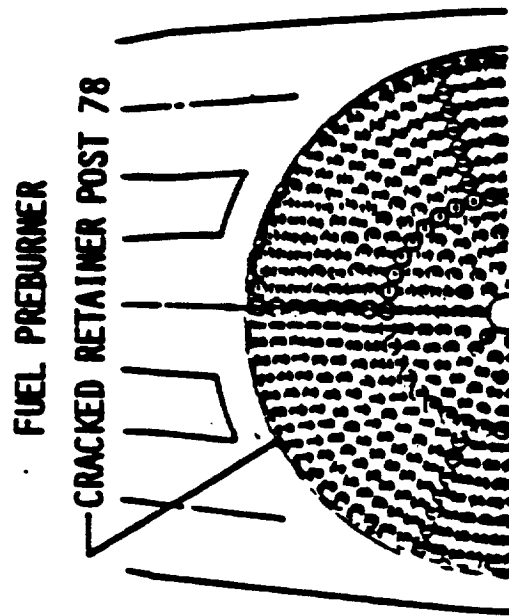


Fig. 24. Failure Location on Secondary Face Plate Retainers

# HGM/MAIN INJECTOR POST RELATIONSHIP

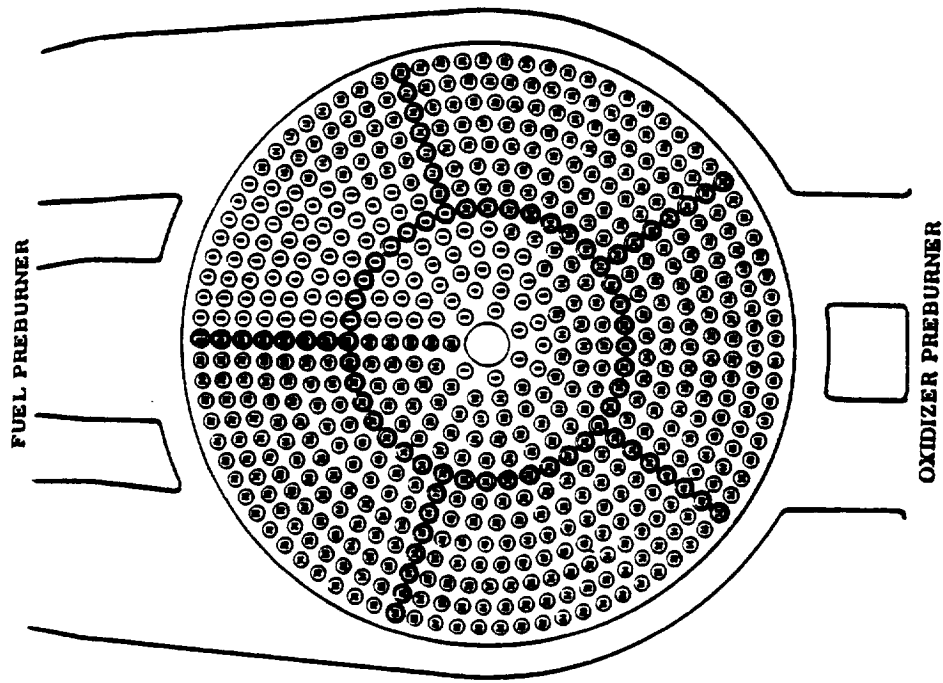


Fig. 25. Critical Row 13 Post Locations Relative to Hot Gas Manifold

Steady state loads:

- 1) thermal loads from high temperature gradient,
- 2) static drag loads from hydrogen rich steam impinging in the post,
- 3) direct loads from differential pressure across the face plate,
- 4) differential pressure between I.D. and O.D. of the Lox post.

Dynamic loads:

- 1) mechanical vibration of the powerhead,
- 2) flow-induced vibration,
  - a) fluid elastic excitation
  - b) turbulence,
  - c) vortex shedding.

The contribution of loads to the Lox post analysis best summarized as follows:

LOAD	STRENGTH	LCF	HCF
Thermal	X	X	X
Static Pressures	X	-	-
Mechanical Vibrations	X	-	X
Flow Induced Vibrations	X	-	X
External Loads	X	-	X
Residual Loads	-	-	X

### 13. Thermal Loads

The Lox post experience severe thermal gradients. These thermal gradients vary along the post length. The heat transfer through the post, from hot gas to Lox, is affected by six factors: 1) exterior hot-gas temperature, 2) exterior hot-gas film coefficient, 3) thermal conductivity of the post walls, 4) peripheral parts on the post surface (heat shield retainer, swage ring, secondary faceplate retainer), 5) interior Lox temperature, and 6) interior Lox film coefficient.

Hot-gas temperature is measured at the turbine exit, upstream of the injector post field. The hot gas is cooled slightly as it travels to the Main Injector, but it is a good assumption to base the Main Injector hot gas temperature on the measured value at the turbine exit as it is a recorded data point that closely approximates the actual temperature. The hot-gas temperature changes slightly from test to test, with more significant variations between engines, engine configurations, and power levels. These variations can be up to hundreds of degrees apart due to all the influencing factors.

The hot-gas heat transfer coefficient is based on characteristics of cross flow over tube banks (as encountered in many heat exchanger arrangements), where results of various investigations have been correlated into a formula. This correlation is for smooth, regularly spaced tubes in cross-flow. The main injector Lox posts are not smooth, the hot-gas flow has a significant axial component, and although tube spacings are generally regular, they are not in a uniform pattern. A test program in the year 1982 verified that in the main body section of the posts, this cross-flow over tube banks correlation was applicable to the Lox posts in the outer four rows. Therefore, the hot-gas heat transfer coefficient in the outer rows, where failures have predominantly taken place, can be closely modeled by established and verified analytical methods.

At the ends of the post (near the interpropellant plate and the secondary faceplate), the film coefficient is modified following classical trends. This modification of the "main body" film coefficient then allows the ends of the post to be analyzed with high confidence.

Thermal conductivity through the post wall is a well-defined phenomenon. The thermophysical properties of the post have been documented and with the geometry of the post known, the thermal resistance through the post is established.

Additional parts added onto the post affect the heat transfer into the post. Added material acts either to increase the path length of heat transfer through the metal, or as a convection shield to the post, protecting it from

the impingement of high velocity hot gas. Thus, for an accurate analysis, thermal loads are derived from detailed local heat transfer models. There are heat transfer models with 1) details near the interpropellant and inertia weld, 2) models of the retainer threaded connection and assembly, 3) models of Lox post tip zone, and 4) cross-section models of swirler areas to study nonaxisymmetric loading. Temperature loads cause large strain range (1 to 2.5%) on the post resulting in low cycle fatigue considerations.

Uncertainties of thermal load on the Lox post are caused by improper mounting of heat shield retainer near the Lox dome and the variation in turbine discharge temperatures. In addition, because of the complex flow regime, the velocity and direction of flow is not well defined, results in variation in heat transfer coefficients used in the heat transfer analysis.

#### 14. Flow Loads

Due to the importance of flow loads on the main injector, a large amount of effort has been devoted to understanding the flow in and approaching the main injector. Determination of flow loads analytically in the complicated geometry of hot gas manifold and main injector consisting of tube bundle is at best a difficult task. Because of the complexity of loading, the accuracy of flow loads and their variation is not well understood. Therefore, flow analysis on the post is a combination of analytical computational fluid dynamic results, cold flow tests, hot fire test measurements, and failure analysis studies combined with expert opinion polling.

Cold flow tests have been conducted on full scale SSME hardware. The fluctuating hot fire pressure measurements have been compared with cold flow tests using appropriate scaling and good agreements have been obtained.

In addition to the flow test, computational fluid dynamics is used to understand and improve flow in the SSME powerhead. The procedure includes the solution of incompressible Navier-Stokes equations in a generalized curvilinear coordinate system. The main injector Lox post core is modelled as



a volume averaged porous media. A typical computation fluid mesh for main injector core is shown in Fig. 26. The analytical flow field descriptions are shown in Fig. 27 representing a vertical section and in Fig. 28 representing a horizontal direction.

Flow induced vibration mechanisms consist of a) fluid-elastic coupled excitation, b) turbulence, and c) vortex shedding. Because of the similarity of flow conditions around tube bundles in heat exchangers and the flow around the main injector configuration, many lessons learned in heat exchanger designs can be applied to main injector flow. Large amplitude tube vibration has resulted in rapid deterioration in tubes in heat exchangers when certain critical velocity is needed. The vibration is sinusoidal occurring at the natural frequency of the tube.

Turbulence causes narrow band random vibration at about natural frequencies of the tubes in the fluid. Vibration amplitudes can vary randomly in time and direction. Turbulence is thought to be the main cause of tube vibration in heat exchangers when the possibility of fluid elastic excitation has been eliminated.

When a fluid flows across a circular cylinder, the wake behind the cylinder contains vortices. The vortices are shed from cylinder in a regular manner. The alternating force associated with vortex shedding can cause resonance when its frequency matches the post frequency. In early phases of SSME injector design, this phenomenon was considered as a potential problem resulting in the addition of spoilers to the outer diameter of the posts.

Major uncertainty associated with fluid-elastic coupling calculations is the structural damping associated with the posts. Major variations associated with drag loads include turbine discharge temperatures and variation in vibration and from turbine to turbine.

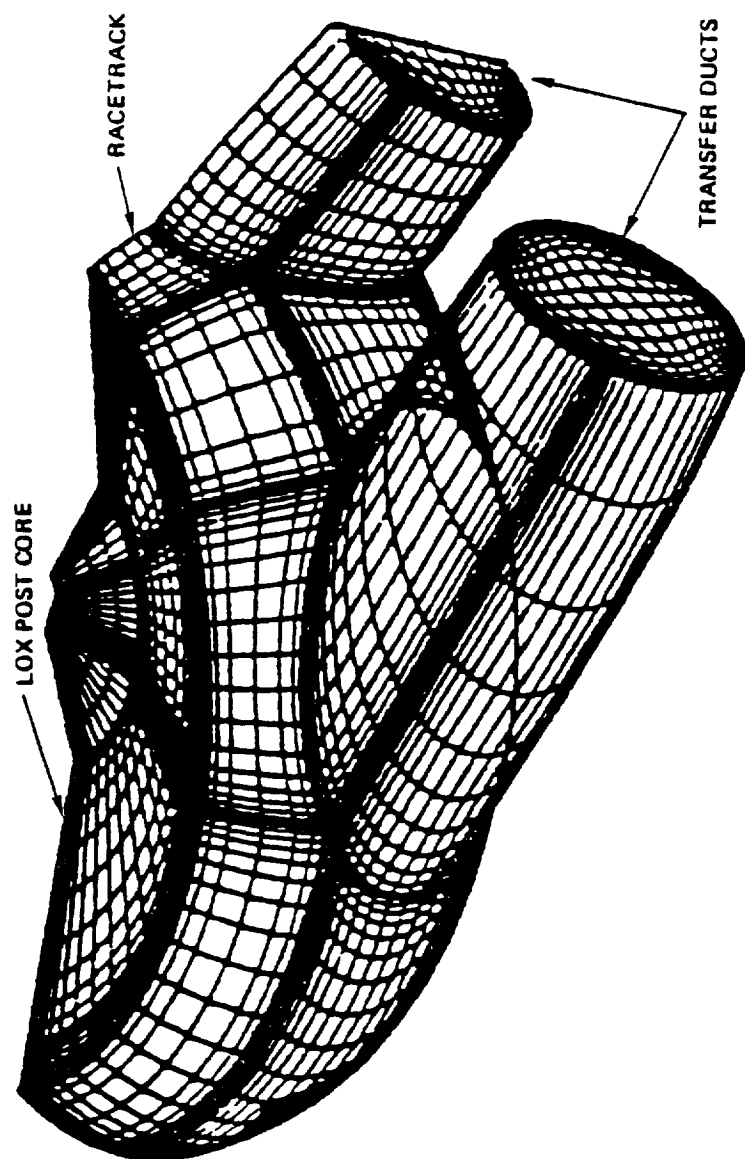


Fig. 26. Computational Fluid Dynamics Mesh of Hot Gas Manifold with LOX Post Core

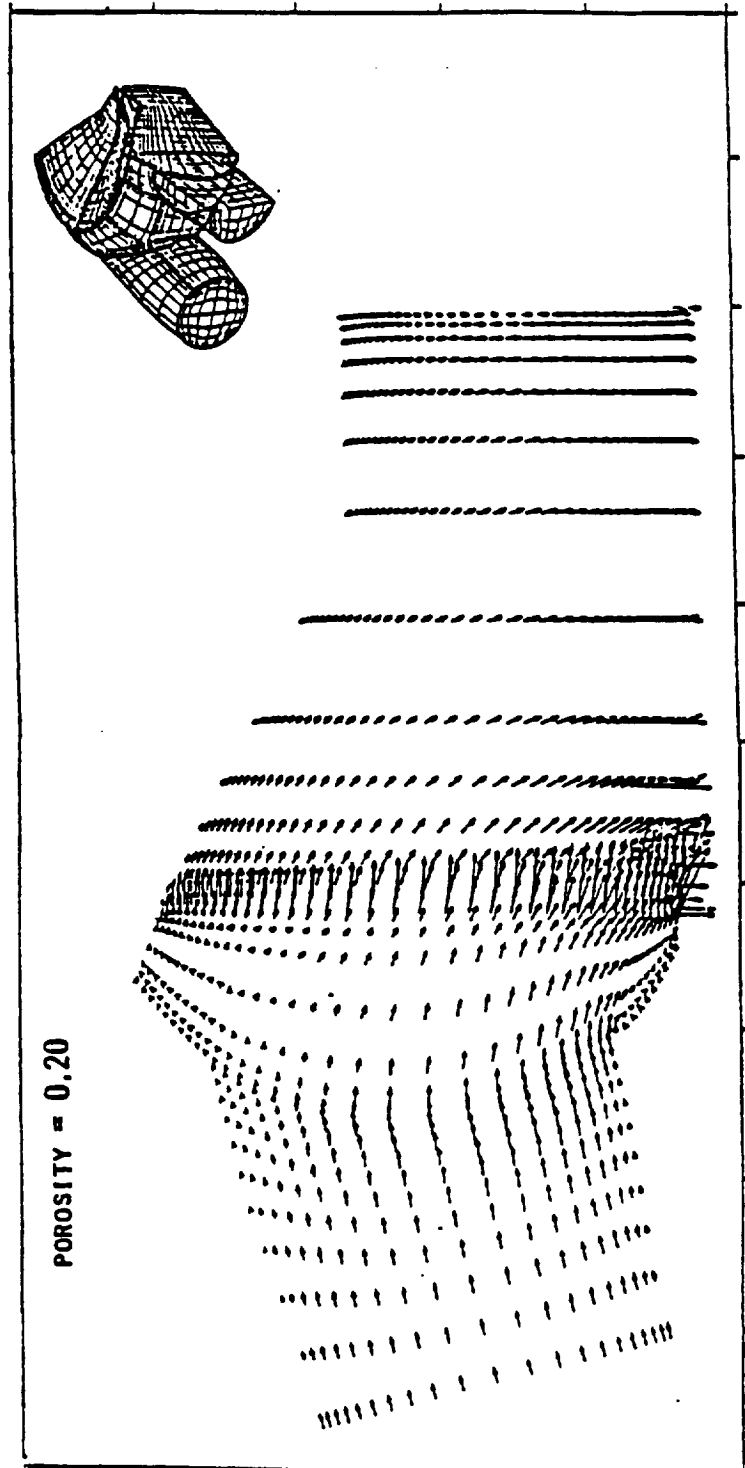


Fig. 27. Analytical Flow Distribution in the Main Injector Through a Vertical Cross Section

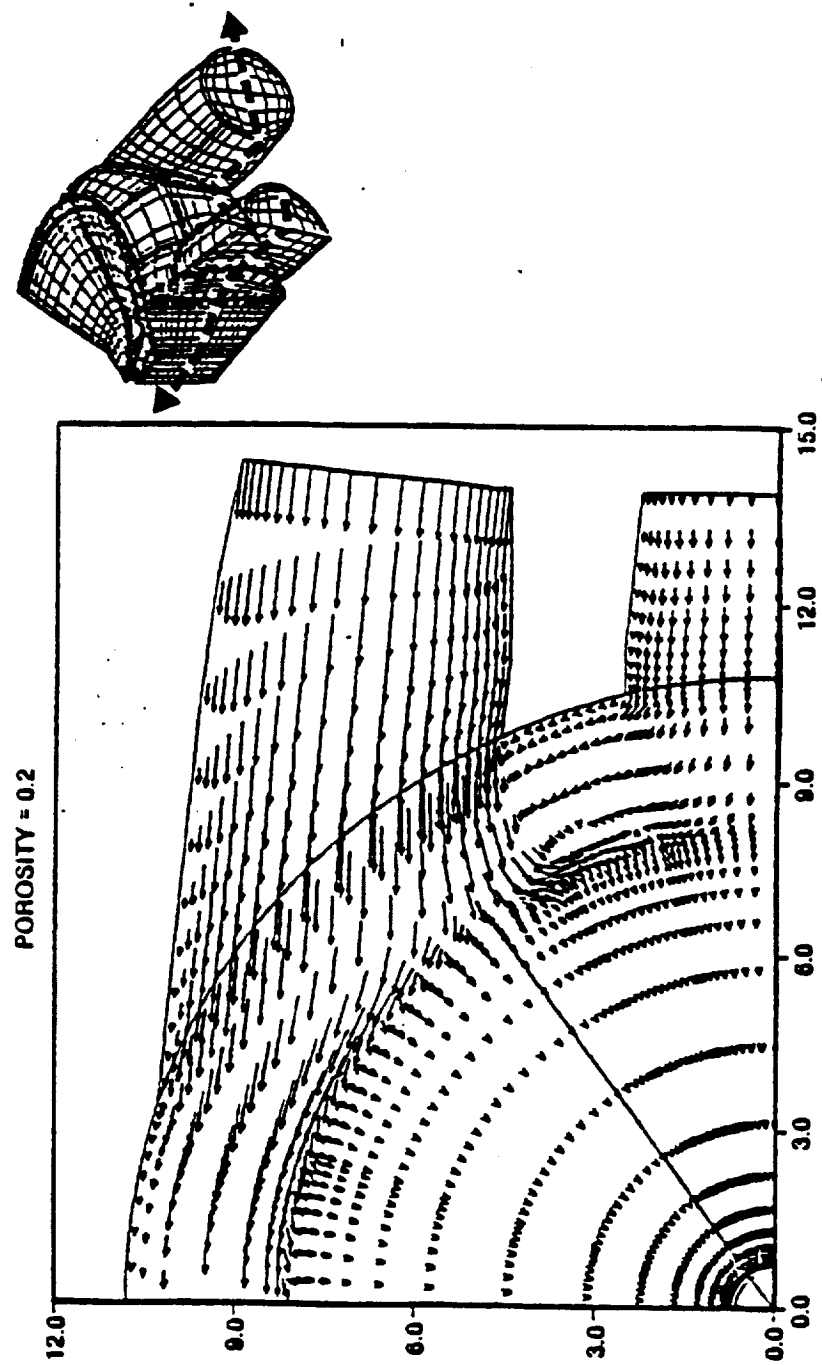


Fig. 28. Analytical Flow Distribution in the Main Injector Through a Horizontal Cross Section

## 15. Mechanical Vibration

Effect of mechanical vibration loads on main injector Lox posts is small compared to the flow induced dynamic loads. Mechanical base acceleration environment on the Lox posts are obtained from accelerometer readings on the engine (Fig. 29).

## 16. Materials in Lox Post

Evolution of materials used in Lox post design is a direct result of lessons learned from Lox post failures. Initial Lox post made out of 316L cres material exhibited HCF failures in the threaded region of the tip. A design change was made in which 316L cres was used in the main body of the Lox post except at the tip where Haynes 188 was used. The Haynes 188 material has comparatively higher strength at high temperatures. However, the Haynes tip Lox posts failed in the inertia weld region on subsequent tests. Thus, the current configuration uses Haynes 188 material for the entire post. There have been no Lox post failures with the new configuration using strengthened secondary plate retainers. The interpropellant plate to which the Lox post are inertia welded are made out of Inconel 718L. The relevant material properties for Haynes 188 are included in Fig. 30 through Fig. 35.

## 17. Static Analysis Survey

Extensive static analysis database exists for main injector Lox post. The scope of static analysis include hand analysis, 2-D axisymmetric analysis, and 3-D analysis. The breadth of analysis vary from standard handbook equations to linear analysis to material nonlinear analysis to material and geometric nonlinear analysis. The static analysis include temperature loads, external loads and flow induced drag loads. Due to the complexity of geometry, of Lox post assembly, and because of the level of detail of the stress regime that is necessary for practical life prediction, global model and local fine models exist. The size of FEM models vary from 500 to 15000 degrees of freedom. Details of the static finite element models are covered later. The analysis program that was used for static analysis included APSA (inhouse axisymmetric and plane stress 2-D program), ANSYS and Stardyne.

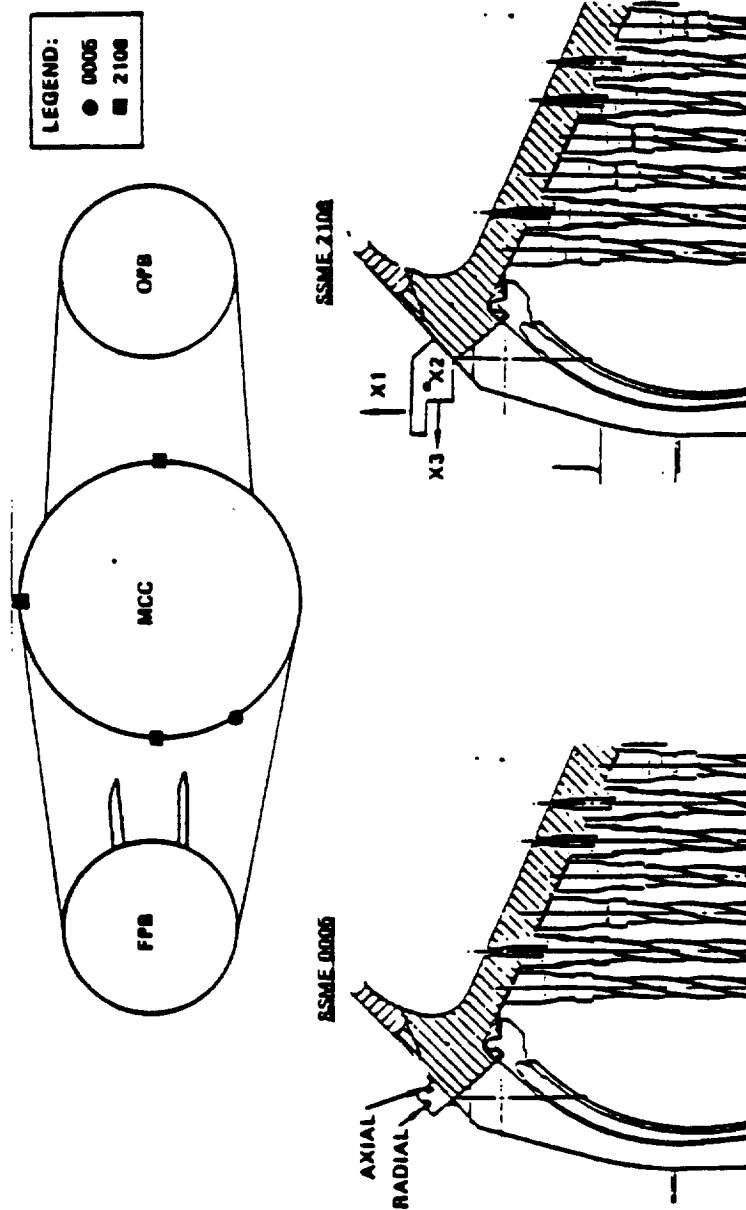


Fig. 29. Measurement Accelerometer Locations at the Hot Gas Manifold

ROCKWELL  
INTERNATIONAL  
ALLOY DIVISION  
MATERIALS  
PROPERTIES  
MANUAL

TYPICAL

0002 27.14.74-31

DAVIDS  
STRESS-STRAIN DIAGRAM  
PROPORTIONAL  
710 STA-1  
DATE: 03-28-84  
REFERENCE:  
REVISION: 002

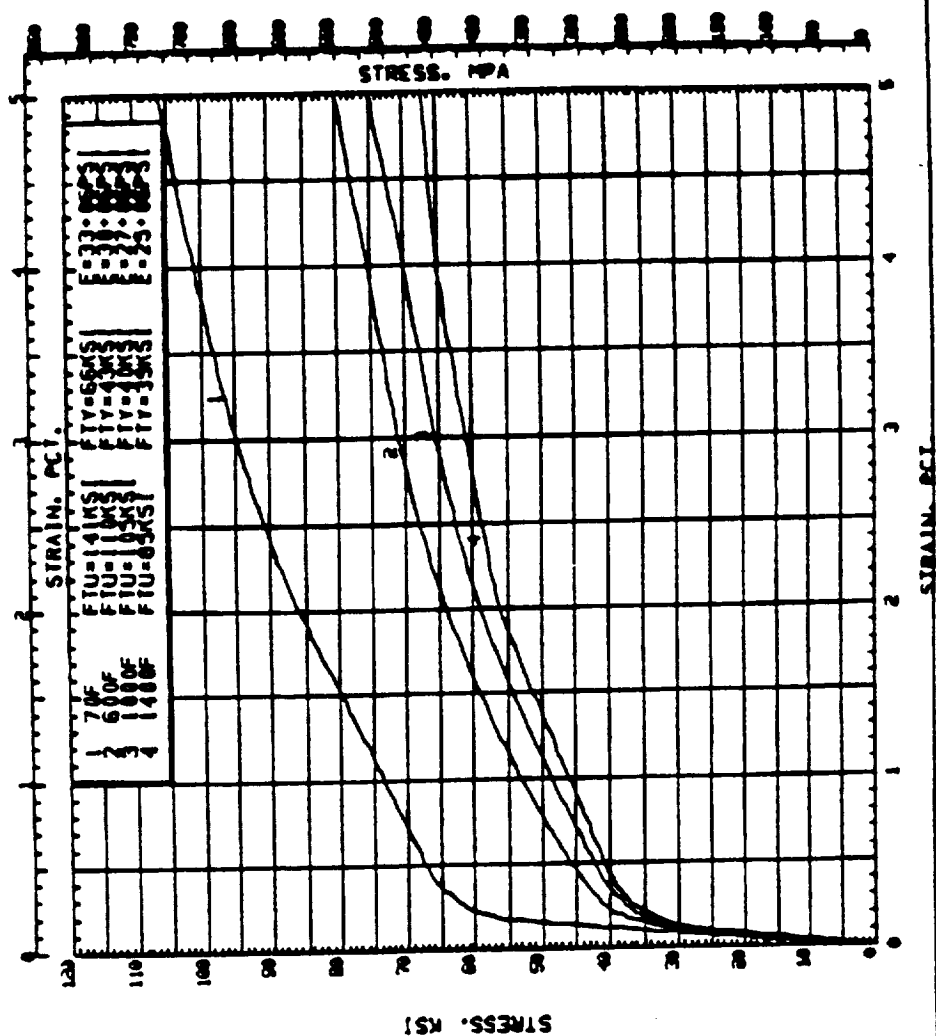


Fig. 30. Stress-Strain Diagram of Haynes 188



# MATERIALS PROPERTIES MANUAL

TYPICAL

ANNEALED 2150F

DATE- 9-1-77

REFERENCE- 8002-13.14

2ND EDITION PAGE- 5.4.2.1.2.13

8002.25.10.50-01

HAYNES 188	8002
POISSON'S RATIO	.25
BROUGHT	.10
ANNEALED	.30
PAGE NUMBER	-01

SPC 4-56772

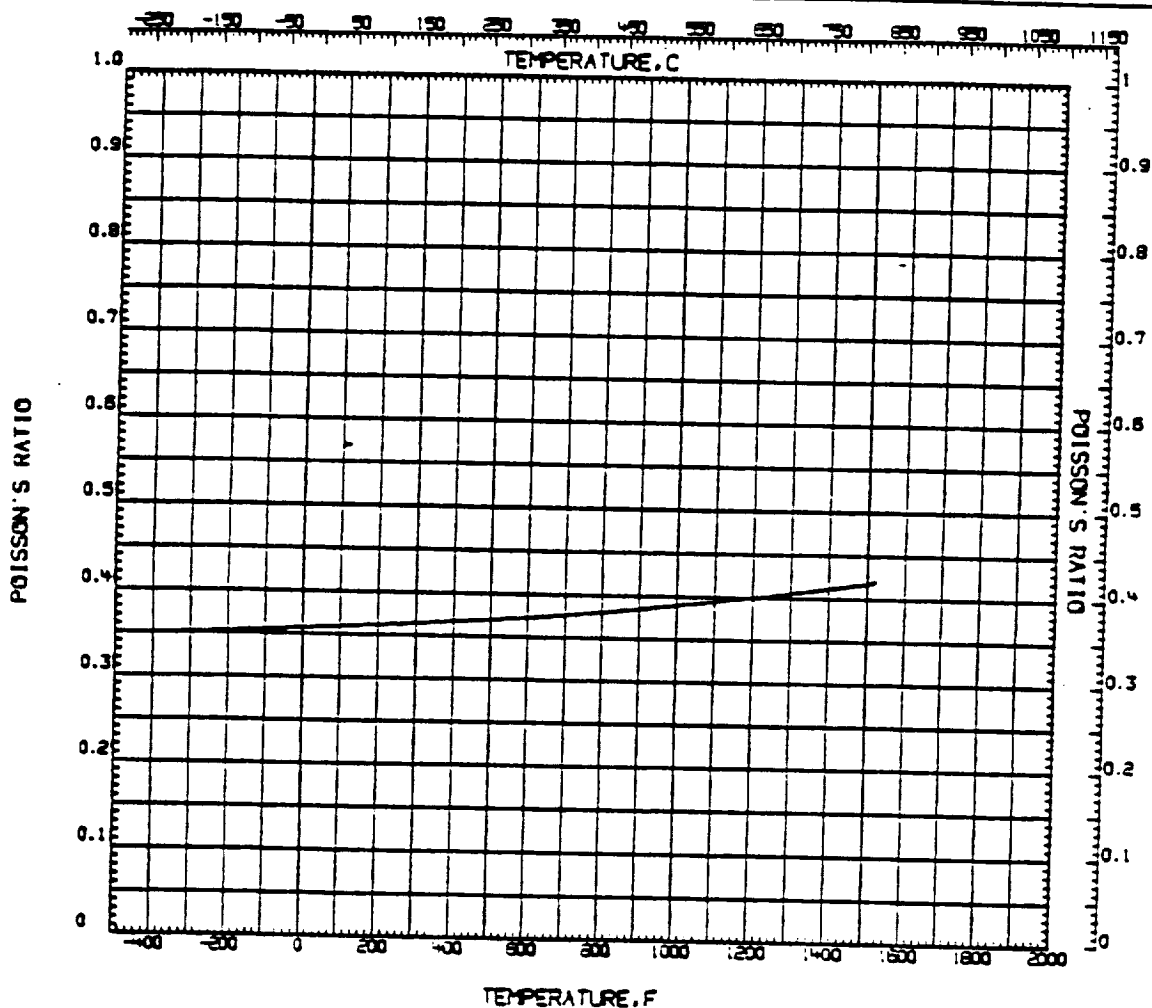


Fig. 31. Poisson's Ratio of Haynes 188





# MATERIALS PROPERTIES MANUAL

TYPICAL \_\_\_\_\_  
ANNEALED 2150F \_\_\_\_\_

DATE- 9-1-77 \_\_\_\_\_  
REFERENCE- 9002-01 \_\_\_\_\_  
2ND EDITION PAGE- 8.4.2.1, 2, 3 \_\_\_\_\_

8002.21.10.50-01

HAYNES 188	9002
ELASTIC MODULUS	.21
BROUGHT	.10
ANNEALED	.50
PAGE NUMBER	-01

SPEC 44887/2

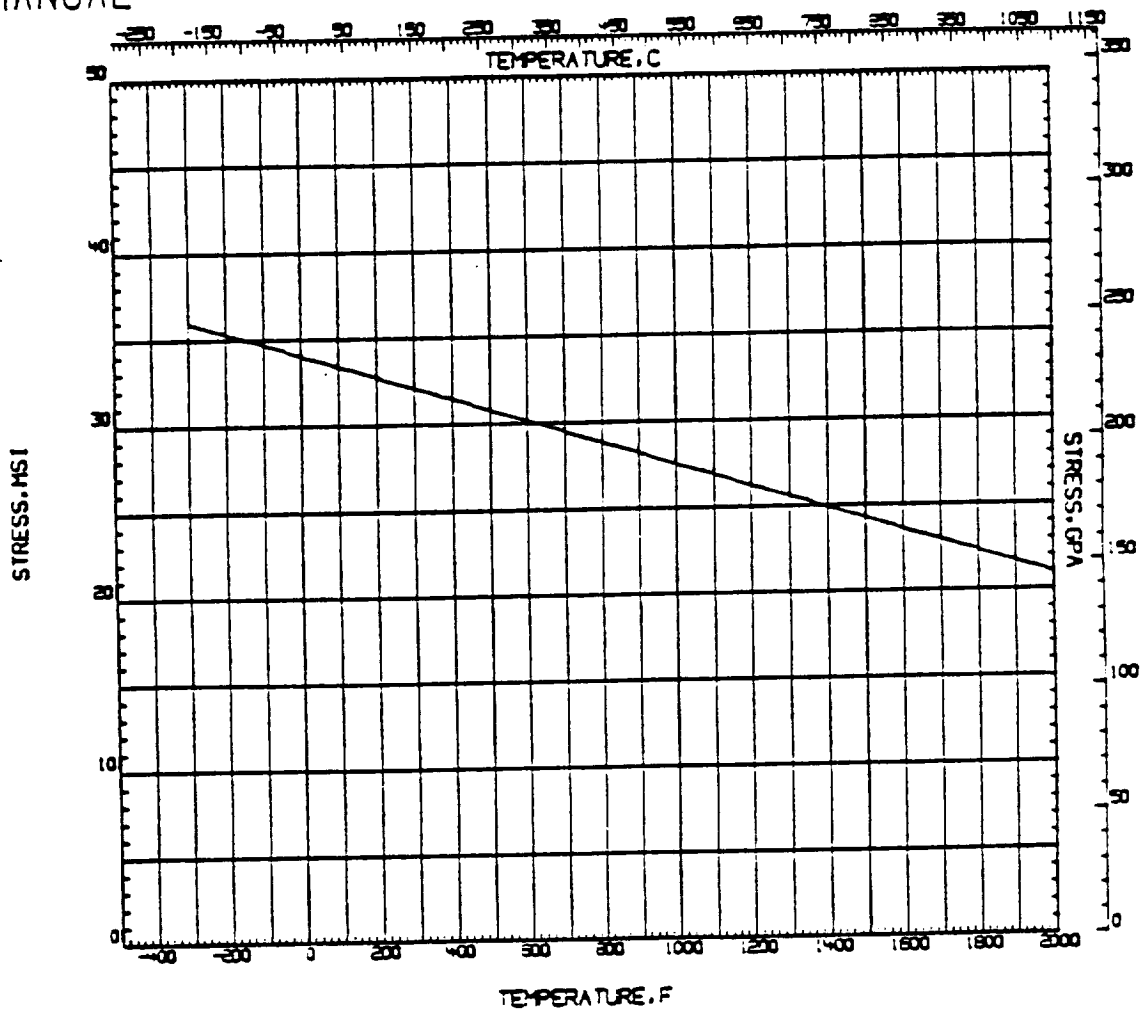


Fig. 32. Young's Modules for Haynes 188



# MATERIALS PROPERTIES MANUAL

TYPICAL

ANNEALED 2150F

DATE- 9-1-77

REFERENCE- 8002-01.13.17

2ND EDITION PAGE- 5.4.2.1.1.18

8002.13.10.50-01A

HAYNES 188	8002
THERMAL EXPANSION	.13
POUR	.10
ANNEALED	.50
PAGE NUMBER	-01A

SPEC 485772

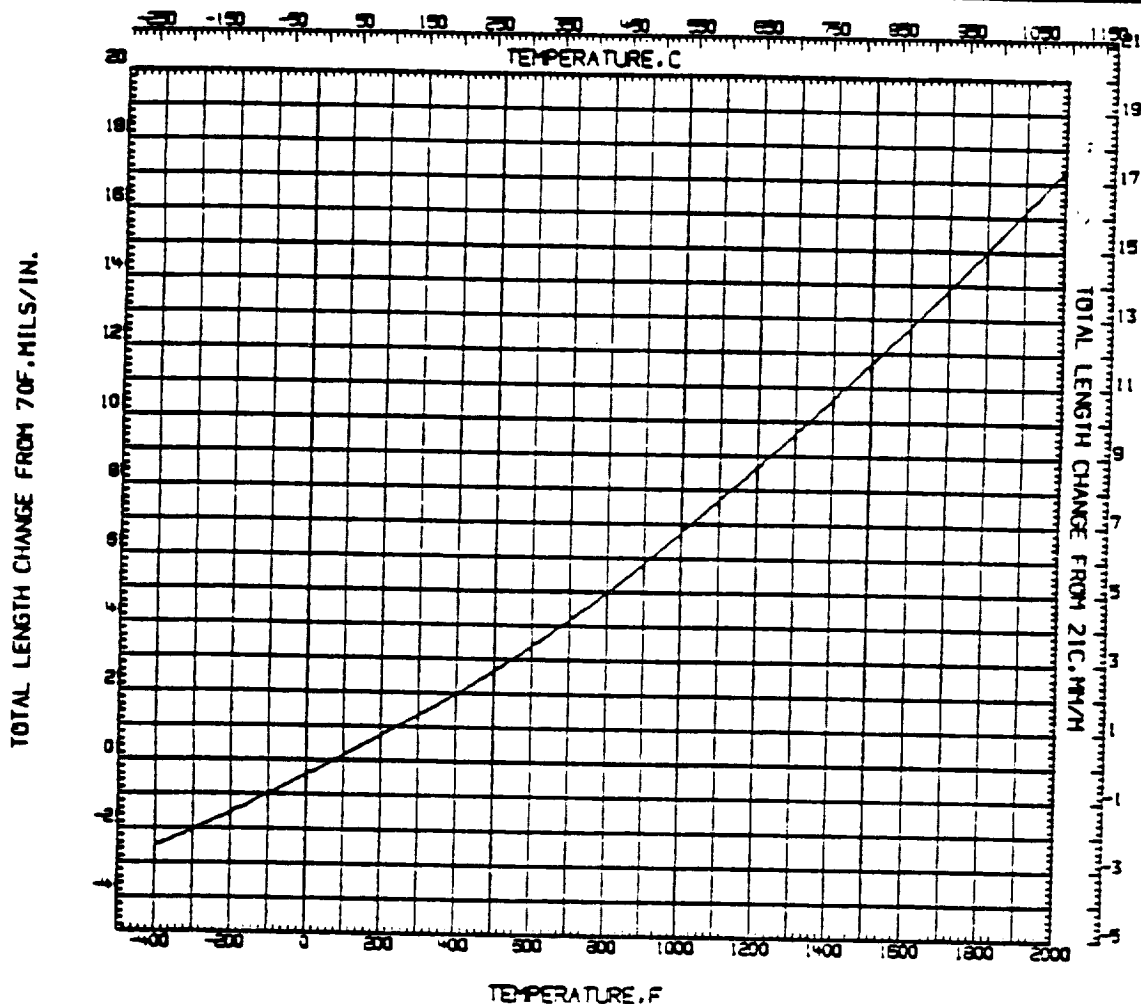


Fig. 33. Thermal Expansion for Haynes 188



# MATERIALS PROPERTIES MANUAL

PREDICTED MINIMUM 70F TO 1600F  
EXPECTED MINIMUM BELOW 70F  
AND ABOVE 1600F  
ANNEALED 2150F

DATE- 2-1-78

REFERENCE- 8002-17

2ND EDITION PAGE- 5.4.2.1.2.4

8002.25.11.50-01A

-AYNES 188	8002
TENSILE STRENGTH	25
9-DET	11
ANNEALED	50
PAGE NUMBER	-01A

SECT. 4.1.1.1.1.1.1

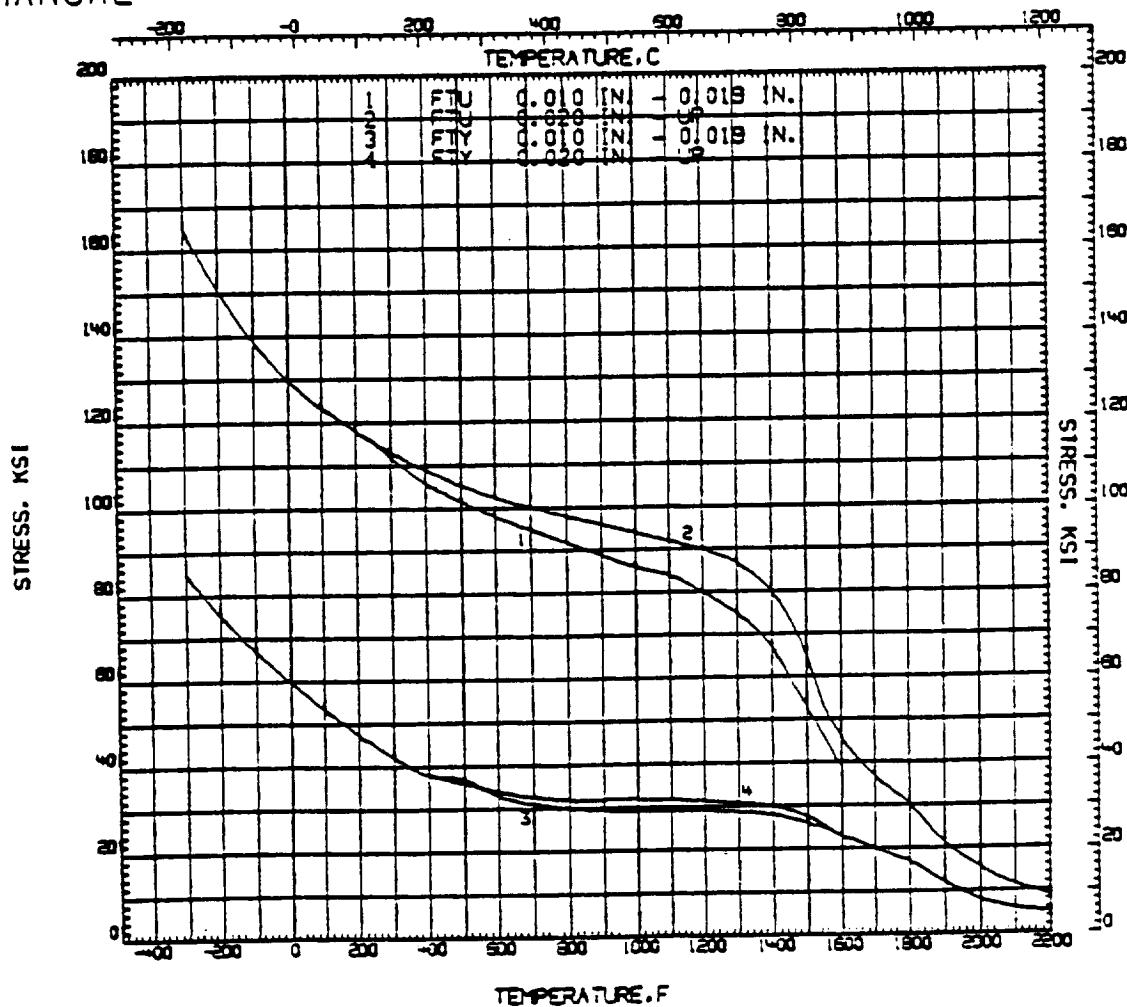
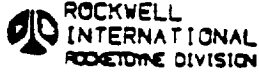


Fig. 34. Tensile Strength for Haynes 188



# MATERIALS PROPERTIES MANUAL

## PREDICTED MINIMUM

AXIAL, T=-1.0, AIR OR O2 ENV

MACHINED SURFACE 32 FINISH

HT 1900F 1400F/1200F 20HRS

DATE- 10-1-80

REFERENCE- 9002-17

2ND EDITION PAGE- 464

9002.33.10.74-02

HAYNES-188	9002
HIGH CYCLE FATIGUE	.33
POURHT	.10
718 STA-1	.74
PAGE NUMBER	-02

SPEC. 4458772

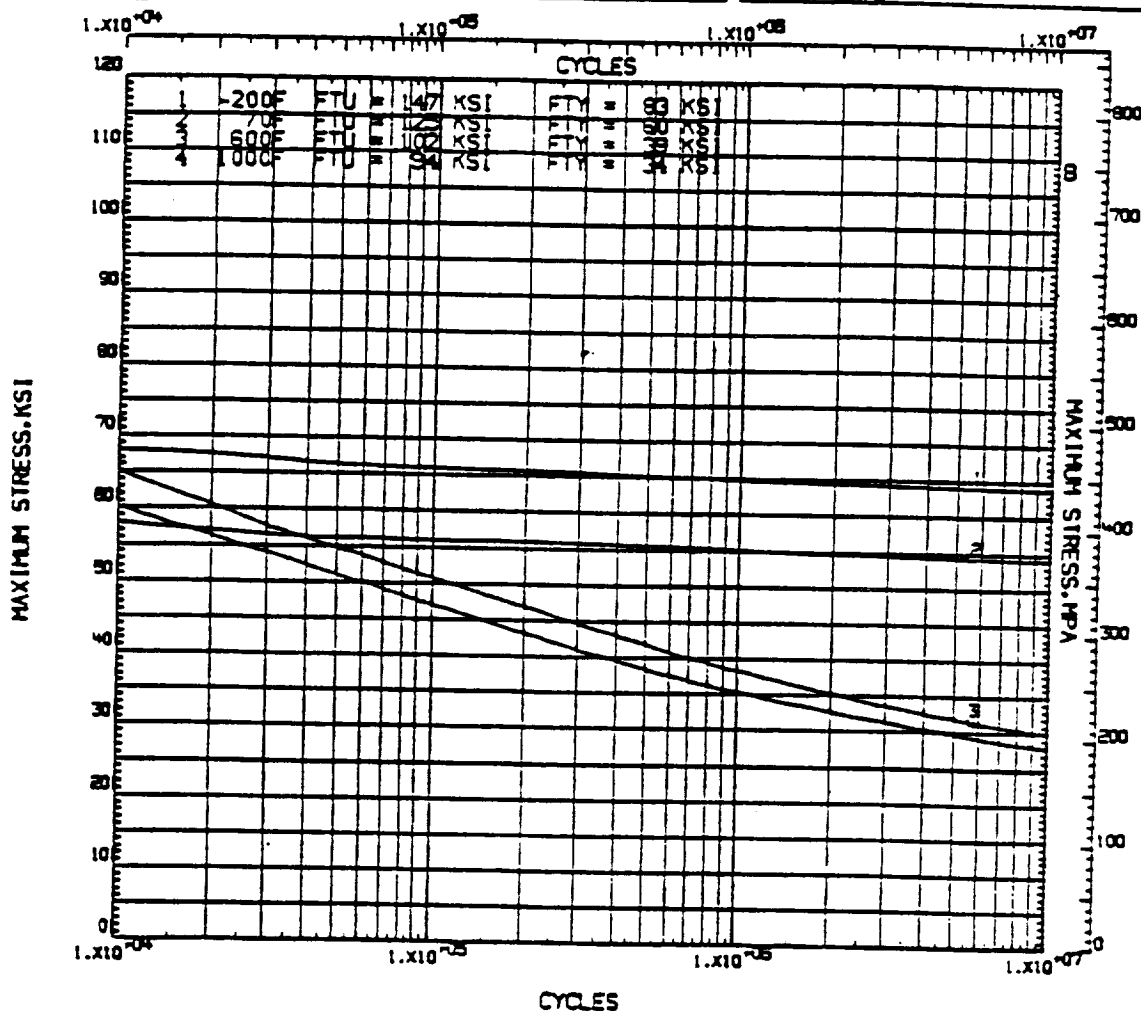


Fig. 35. High Cycle Fatigue Data for Haynes 188

## 18. Dynamic Analysis Survey

Extensive dynamic analysis results are available for the main injector Lox post. The range of dynamic analysis include modal analysis, random base excitation analysis and random flow load analysis. The hand analysis include sample beam analysis checks for mode shapes and a limited checking for random vibration analysis from shock and vibration handbooks. The dynamic finite element analysis include finite element models using beam and shell elements using Sturdyne computer program. The size of the models is about 1000 dynamic degrees of freedom. The details of the finite element model are covered separately later.

## 19. Random Vibration Loads

Background: Random vibration processes are necessarily treated in a probabilistic manner. A stationary random process is described in the amplitude domain by its probability density function, and in the frequency domain by the power spectral density (PSD) function. Non-stationary random processes are difficult to analyze, since the probability density and spectral content vary with time; however, stationarity is quite often a reasonable and necessary assumption under steady-state engine operating conditions. The unavoidable presence of shock transients and periodic components must be well defined and separately treated in probabilistic analysis of the entire process.

The amplitude probability density curve gives a description of the amplitude characteristics of the random process, and can be used to estimate the probability of occurrence of a given amplitude.

Empirical estimates of the probability density function for finite observation times and discrete magnitude intervals are made by digital analysis of the available data.

The most common amplitude probability density function found in nature is the Normal, or gaussian. Analysis of the spectral content of the data is

accomplished by Fast Fourier Transform, followed by multiplication of the transform conjugate pairs and division by the analysis bandwidth to produce a PSD result.

Statistical confidence in the PSD analysis is a function of the total number of time records analyzed, and the analysis bandwidth. Ensemble-averaging increases the statistical confidence in the PSD analysis to a stationary random process, as does an increase in the analysis bandwidth. Assuming a gaussian process, or one which can be approximately described by a gaussian probability density function, the distribution of the measured PSD magnitudes about the true PSD magnitude is chi-squared with degrees of freedom  $n$ , where  $n$  is determined by the relationship:

$$n = 2BT,$$

where:

$B$  = the analysis bandwidth

$T$  = the total analysis time, including all ensembles.

The SSME random vibration load spectra were initially obtained by using vibration data from existing J-2 and J-2S engines, the amplitude scaled using criteria developed by R. E. Barrett at NASA-MSFC. This criteria assume that the mechanical vibration environment of a rocket engine is primarily generated by combustion processes and is directly proportional to the thrust and exhaust gas velocity of the engine and inversely proportional to the weight of the engine. No frequency scaling is provided by the Barrett criteria. The criteria used were:

$$\frac{\text{Random Vibration Spectra}_N}{\text{Random Vibration Spectra}_R} = \frac{T_N V_N W_R}{T_R V_R W_N}$$

where:

$N$  = new rocket engine

$R$  = reference rocket engine

$T$  = thrust

$V$  = exhaust velocity

$W$  = weight of the engine

Experience with the SSME program indicates the Barrett method overpredicted the SSME vibration environments particularly in the low-frequency (below 200 Hz) range. This was due primarily to the conservative enveloping techniques used for the reference engine data. In addition, other factors that can affect vibration environments such as flow effects, structural responses and acoustic resonances are not accounted for in Barrett's method.

Initial SSME testing was accomplished at operational levels below rated power level, and vibration measurements were made during these tests to evaluate the predicted random and periodic vibration environments. These data were then scaled to full engine power level for structural dynamic analysis and testing of components. The Barrett method was again used for this scaling.

When the SSME was operated at full power level, it was found that the scaled data tended to overpredict the vibration environments. Some environments particularly in the oxidizer turbopumps and oxidizer propellant feed system displayed higher than predicted amplitudes at full power level, possibly due to increased flow turbulence. Hence, the SSME experience has shown that the Barrett method is not entirely satisfactory for predicting vibration environments. However, in a majority of cases the method does provide a conservative loads estimate for random and periodic vibration. The prediction method must be revised to account for variables such as flow turbulence, mixture ratio effects, structural resonances, acoustic resonances, and turbomachinery configuration effects.

Definition of the random vibration environments to be used in structural analysis is ultimately based on all available measurements of the relevant responses. An enveloping process is applied to the data to define maximum expected spectra, and to account for uncertainties in the spectral distributions. Normally, the enveloping includes data at all engine power levels, and the resulting dynamic environment specifications are used in structural analyses at all engine power levels. This conservative approach can be modified by application of the Barrett criterion

(described above) to define an environment specification applicable at a power level less than the maximum, or full power level. This scaling works well for a given engine, although there are frequencies, corresponding to dominant system modes and turbomachinery critical speeds, which do not scale in this manner.

Vibration zones are established as a means of describing the vibration environment experienced by components as a function of their spacial location on the SSME. These vibration zones are divided into two categories: source zones and response zones. Source zones are principal areas of energy generation, including all turbomachinery and combustion devices. Nine source zones have been defined for the SSME (Table 3).

Response zones have been defined for locations which contain relatively passive engine components, such as valves, actuators, and sensors. Many response zones have been specified for the SSME. Table 3 lists 13 of the most significant ones.

Evolution of the SSME zonal vibration criteria followed the growth of the SSME from early design phase through rated-power level (RPL) development (initial hot-fire tests, RPL operation, and flight certification) to current effort of full-power level (FPL) development. The process of updating, as new data became available, ensured that the most recent knowledge of the environment was being used to verify the design--whether by analysis or by test.

Vibration sources resulting from non-nominal engine operation are not accounted for in the standard vibration zones. Instead, these sources of severe vibration are deliberately engineered out of the system and attentively monitored during engine service. The physical phenomena that can cause exceedence in vibration levels include:

1. Subsynchronous rotor whirl in turbomachinery
2. Hot-gas flow separation instabilities
3. Propellant feedline severe transient vibration



SOURCE  
ZONES

CONTENTS

A	MAIN COMBUSTION CHAMBER (MCC)
B	MCC THROAT AND INPUT TO ENGINE CONTROLLER
C	THRUST CHAMBER NOZZLE
D	OXIDIZER PREBURNER
E	FUEL PREBURNER
F	LOW-PRESSURE OXIDIZER TURBOPUMP (LPOTP)
G	HIGH-PRESSURE OXIDIZER TURBOPUMP (HPOTP)
H	LOW-PRESSURE FUEL TURBOPUMP (LPFTP)
I	HIGH-PRESSURE FUEL TURBOPUMP (HPFTP)

RESPONSE  
ZONES

J	MAIN FUEL VALVE (MFV) AND ACTUATOR
K	MAIN OXIDIZER VALVE (MOV) AND ACTUATOR
L	PNEUMATIC CONTROL ASSEMBLY
M	CHAMBER COOLANT VALVE (CCV) AND ACTUATOR
N	FUEL PREBURNER OXIDIZER VALVE (FPOV) AND ACTUATOR
O	OXIDIZER PREBURNER OXIDIZER VALVE (OPOV) AND ACTUATOR
P	OXIDIZER AND FUEL BLEED VALVES
Q	VEHICLE ATTACH PANEL
R	PRESSURE SENSORS
S	ANTIFLOOD VALVE
T	CHECK VALVE
U	NOT USED
V	POGO ACCUMULATOR AND VALVES
W	TURBINE TEMPERATURE SENSORS

TABLE 3. PRINCIPAL SSME SOURCE AND RESPONSE VIBRATION ZONES

4. Cavity resonances in duct transitions (particularly at the main oxidizer valve)
5. Vortex shedding excitation of main injector LOX posts
6. Sheet metal component fatigue

Lox Post Random Loads: The mechanical random vibration response of Lox post is calculated from acceleration PSD diagrams Fig. 36 derived from actual engine firings. The flow induced random vibration response is calculated from measured pressure PSD diagrams (Fig. 37) from CGIP or CGIC location (Fig. 38) from hot fire testings. One of the key parameters in random vibration analysis is the effective damping of the post-shield-retainer-heat shield assembly. From the measured Lox post strain gage response and using analytical models (Fig. 39), the effective damping present in row 13 posts have been calculated to be 6.7% (Fig. 40). Response data on Row 12 Lox posts during engine operation is estimated to be 3%. Variations in damping parameter can occur when variations in pretension of T-bolt assembly occur and due to variations in thread-fit assembly.

## 20. Structural Dynamics Data Base

All of the above environments, including the vibration zone criteria, are determined from engine acceleration measurements. Many of these environments are based on the minimum of 6 tests of 2 engines (12 measurements), while several are defined by acceleration measurements made on every engine test conducted. However, most environments are defined by 9 tests of 3 engines (27 measurements). In all, approximately 200 vibration measurements are included in the structural dynamics data base.

Data from these measurements are available to define the vibration environments as a function of the engine mission history profile, as example of which is shown in Fig. 41. One approach is as follows:

1. The initial startup sequence (0 to 4 seconds) is analyzed by means of complex trace records and shock spectra analysis to define start transients.

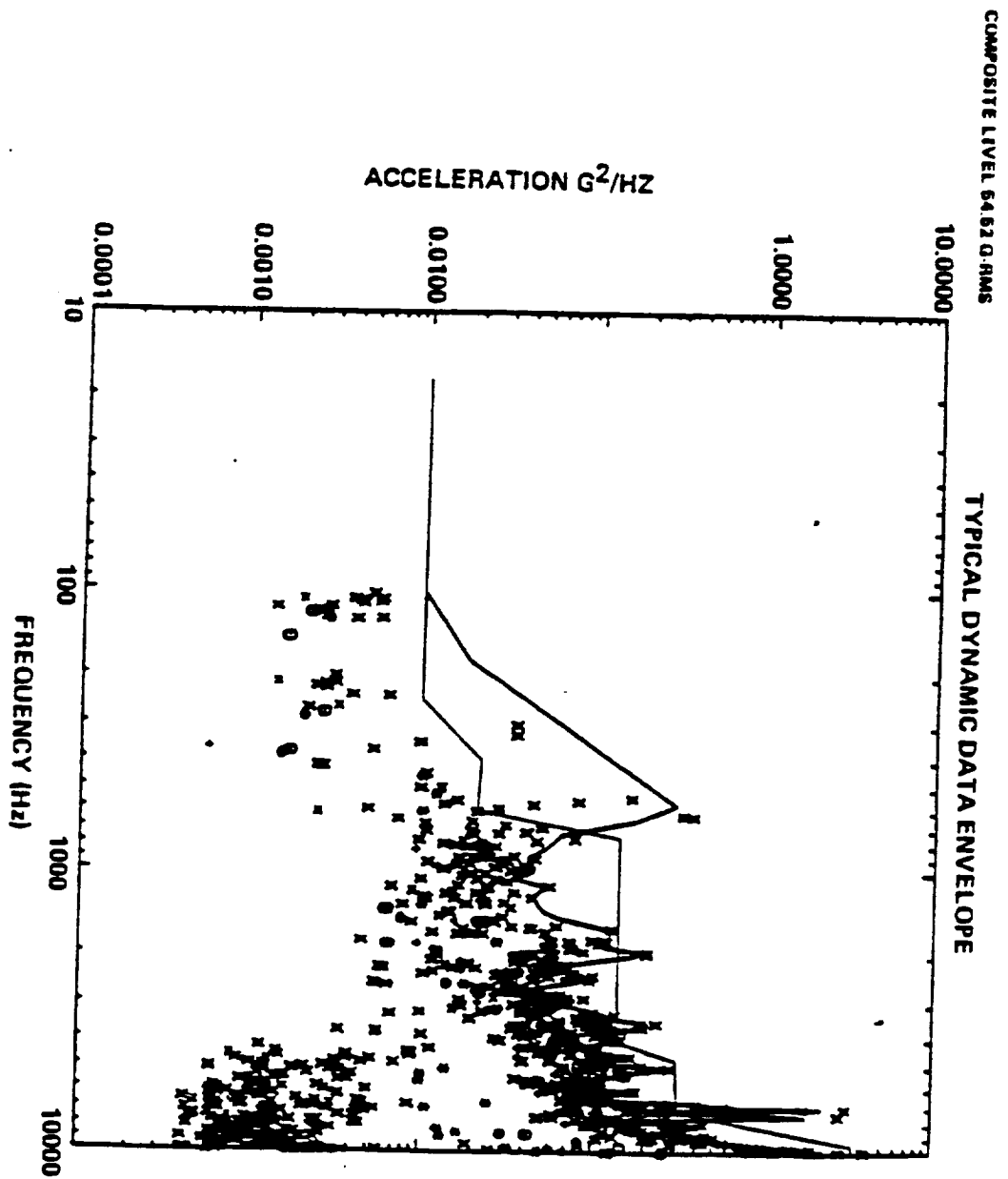


Fig. 36. PSD Diagram For Mechanical Vibration

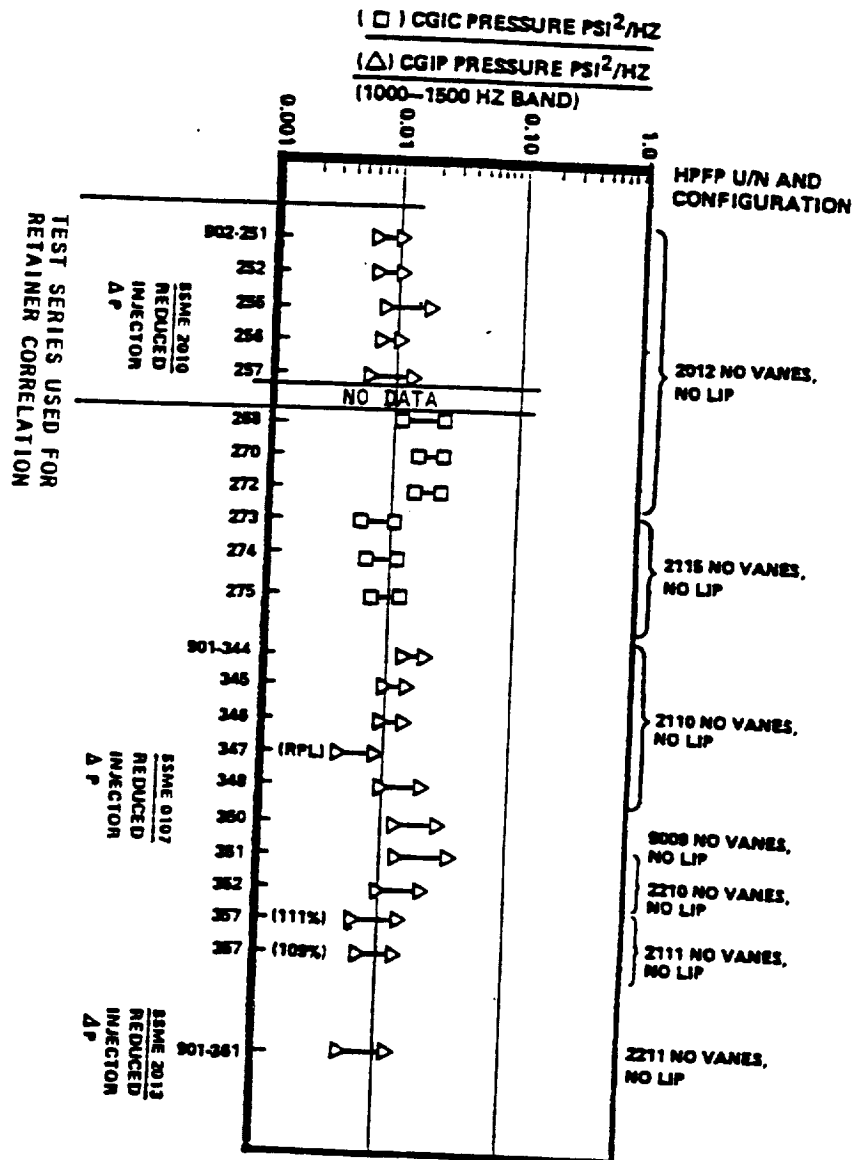


Fig. 37. PSD Diagram for HGM Pressure

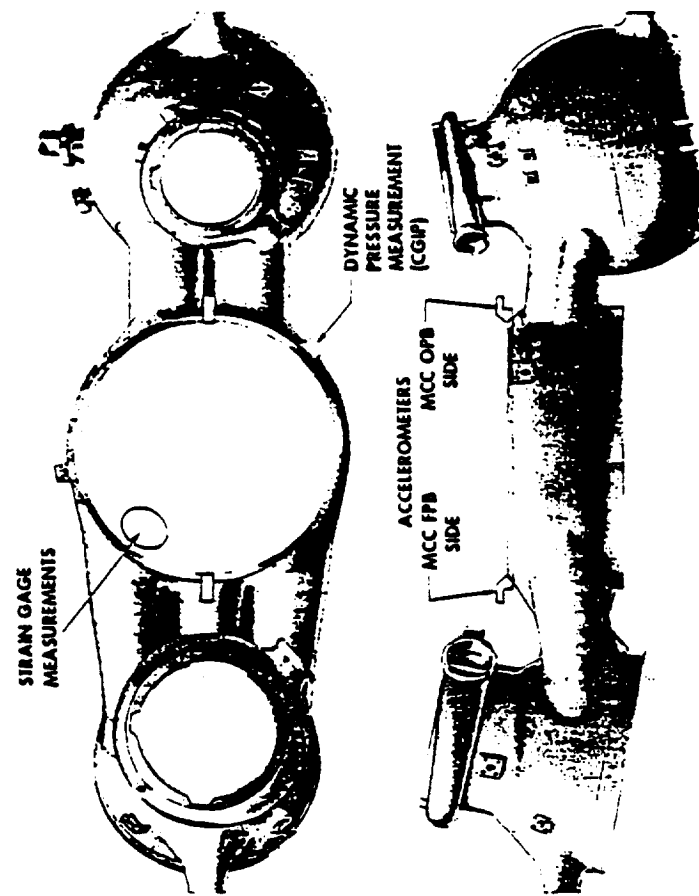


Fig. 38. Accelerometer and Pressure Location on HGM

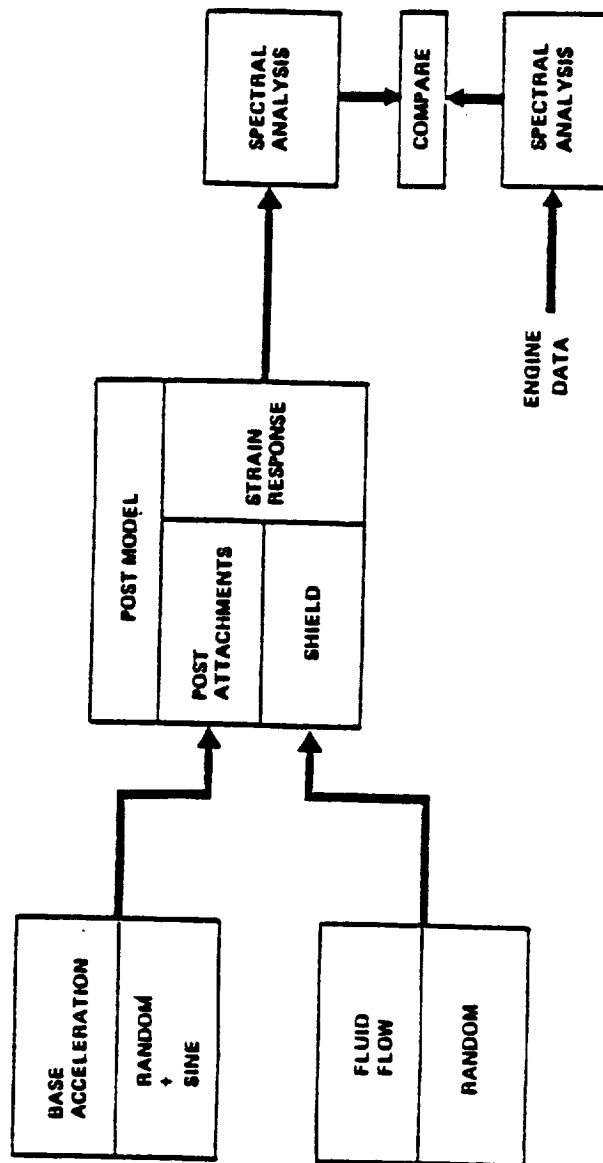


Fig. 39. Correlation Logic Diagram for Experimental and Analytical Results for Damping Calculations

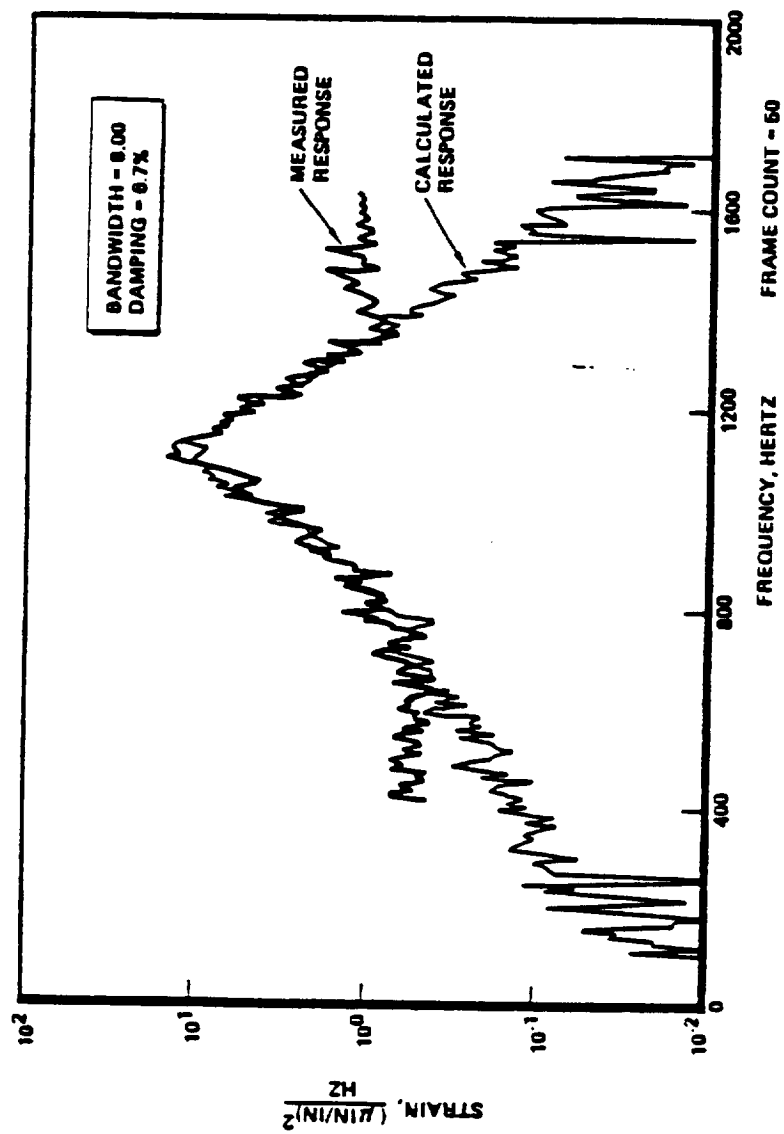


Fig. 40. Correlation of Measured LOX Post Strain Gage Response With Analysis

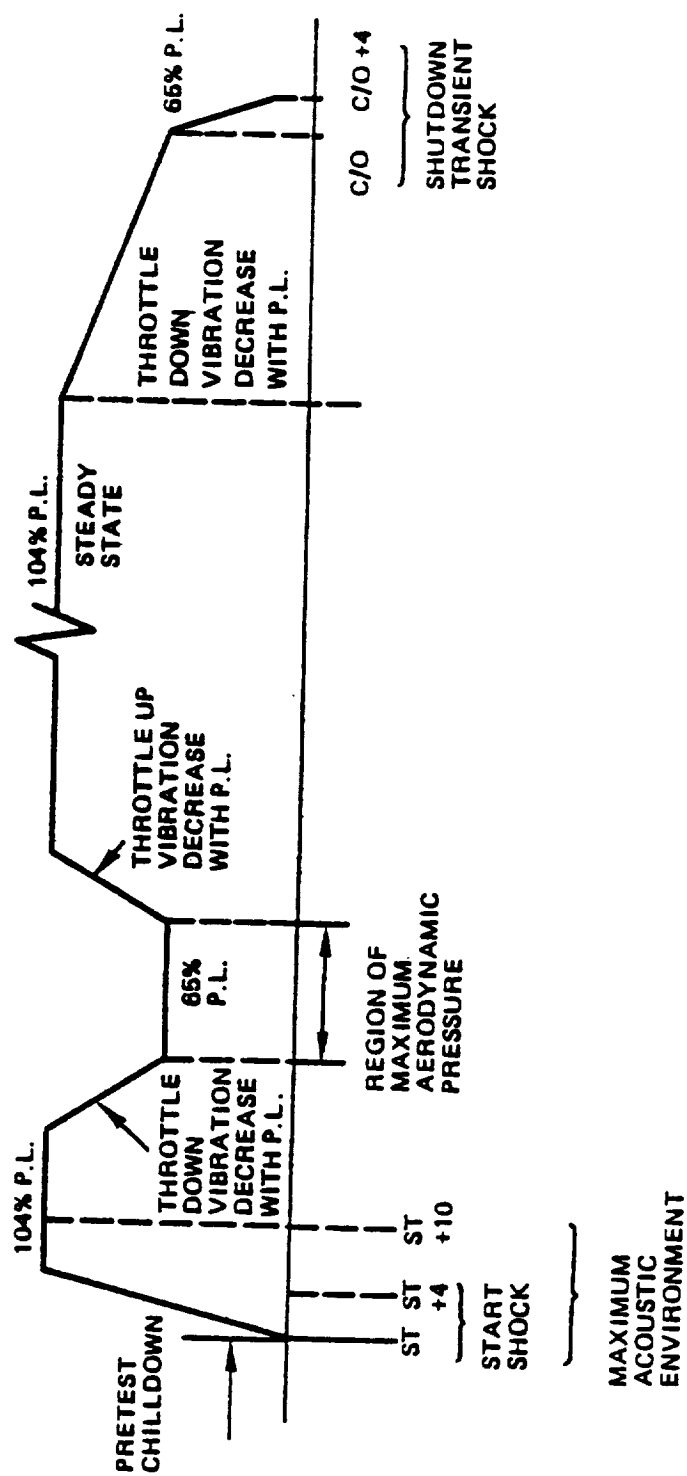


Fig. 41. Typical Mission History Thrust Profile



2. Each mainstage steady-state operation time is characterized by power spectral density analyses conducted for each operational power level (i.e., 65% to 109%).
3. The shutdown transient data are analyzed by means of complex trace records and shock spectra analysis to define the post mainstage transient shocks.

Thus data are available to specify the engine operation vibration environments as a function of the mission duty cycle.

## 21. Survey of Finite Element Models

Due to the criticality of main injector component, numerous finite element models and analysis results are available. The variations in models include different types of flow shields (currently there are three different types mounted on each engine), numerous models to satisfy a material review condition (material review condition analysis is performed when a manufactured component deviates from drawing specification) and models to perform sensitivity studies when the actual values are known only within certain bounds.

Static Finite Element Models: Broadly there are two different types of finite element models are available. They are:

- 1) Global or overall models,
- 2) Local models.

Global Models: The objective of the global models is to study the overall response of the structure, understand the mechanism of load transfer and to compute gross cross-sectional forces and stresses that exist in the post.

The axisymmetric model shown in Fig. 42 represents the Lox dome and Lox post forest in an approximate way. A solidity factor is used to model to discontinuities present in the circumferential direction. This model is

used to model the load transfer from face plates to the Lox dome, the effect of varying thermal expansion of the Lox posts on the dome, and interaction between Lox post bundle and interpropellant plate.

The global 3-D model shown in Fig. 43 comprises of beams and shells modelling accurately the varying cross-sections of the Lox post along its length. This model is used to do dynamic analysis as well and for combining the results with static analysis load combinations. It has also been used to correlate experimentally observed strain gage results.

Local Models: Numerous local models have been constructed to study the local stress region more accurately including stress concentration factors. The models were also constructed to support failure analysis. The axisymmetric model shown in Fig. 44 is used to model more accurately the inertia weld region area of the Lox post. The model approximately represents in an axisymmetric way the interpropellant plate junction.

The axisymmetric model shown in Fig. 45 is used to study the stress field in the threaded region of Lox pot.

The eighth of a sector model shown in Fig. 46 is used to model the swirler region accurately to study stress concentrations using a refined temperature distribution in the area.

While all the above local models described were axisymmetric in nature, 3-D local solid models are also available. The retainer solid model shown in Fig. 47 is used to study the stress concentrations between the holes of the retainer and the effect of smooth radius on the stress concentrations.

The detailed solid model shown in Fig. 48 is used to study in detail the effect of inclination of interpropellant plate to the Lox post and the resulting stress concentrations on the toe and the heel of the connection.

A summary static finite element models that can be used for validation and verification purposes is shown in Table 3.

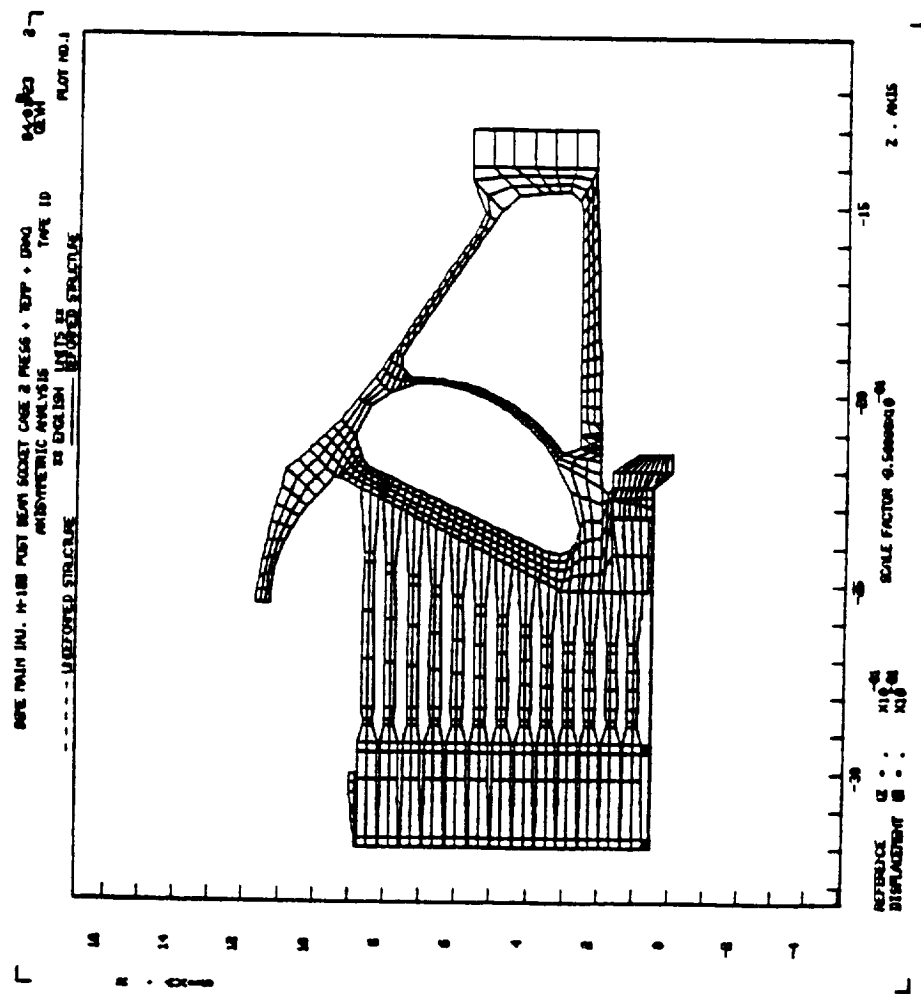


Fig. 42. Axisymmetric Model of LOX Post Dome and Injectors

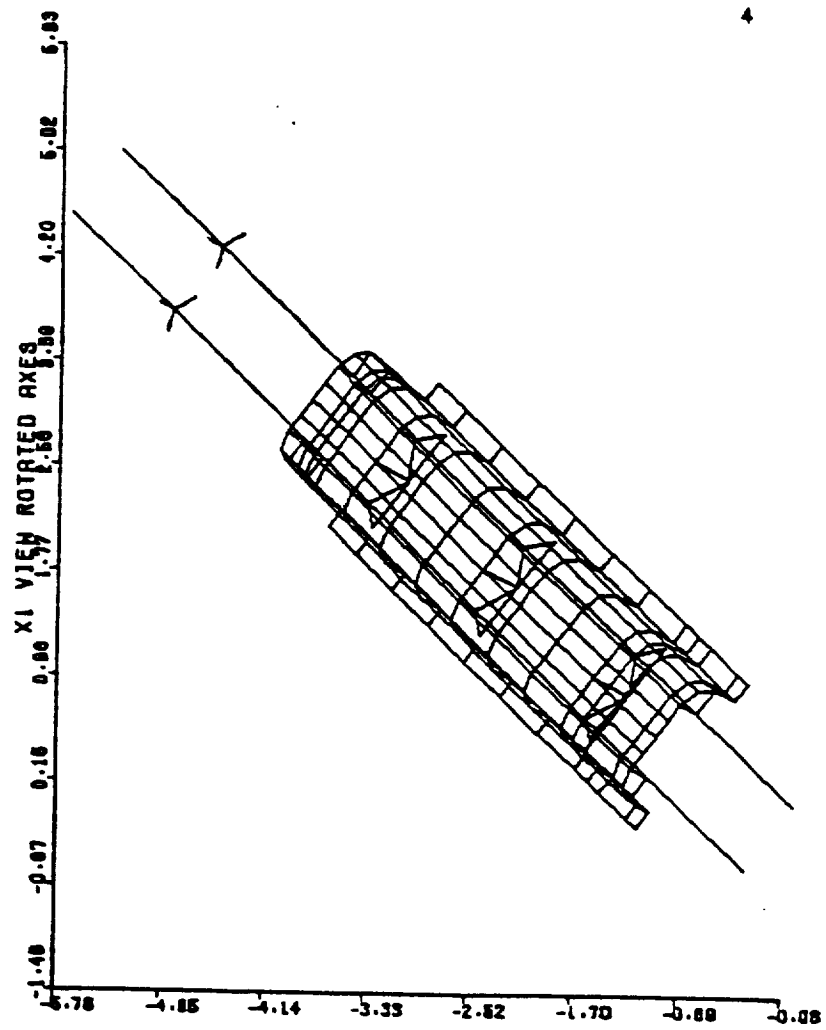


Fig. 43. Beam and Shell Model of LOX Post and Flowshield

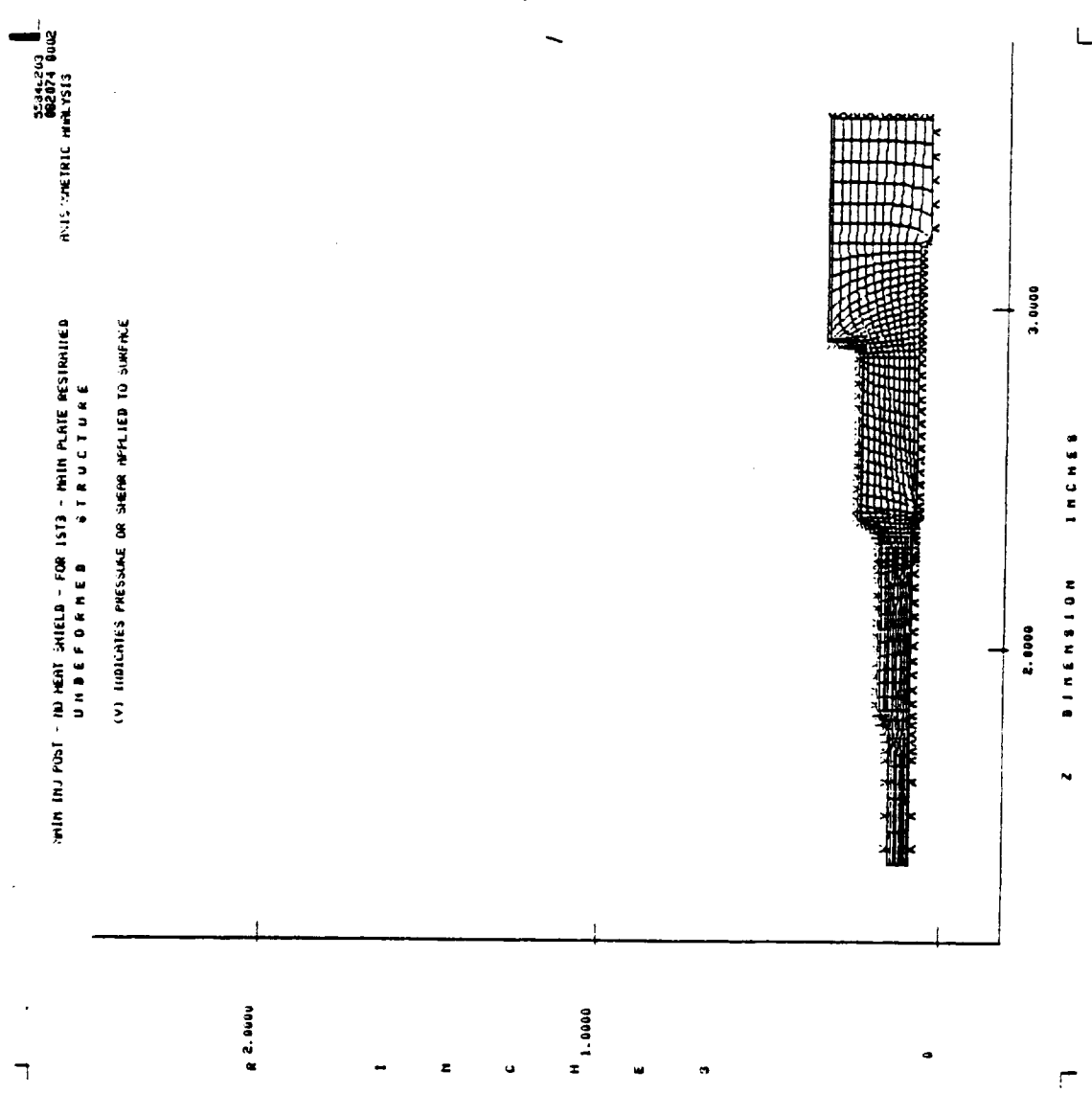


Fig. 44. Local Model of Inertia Weld Region

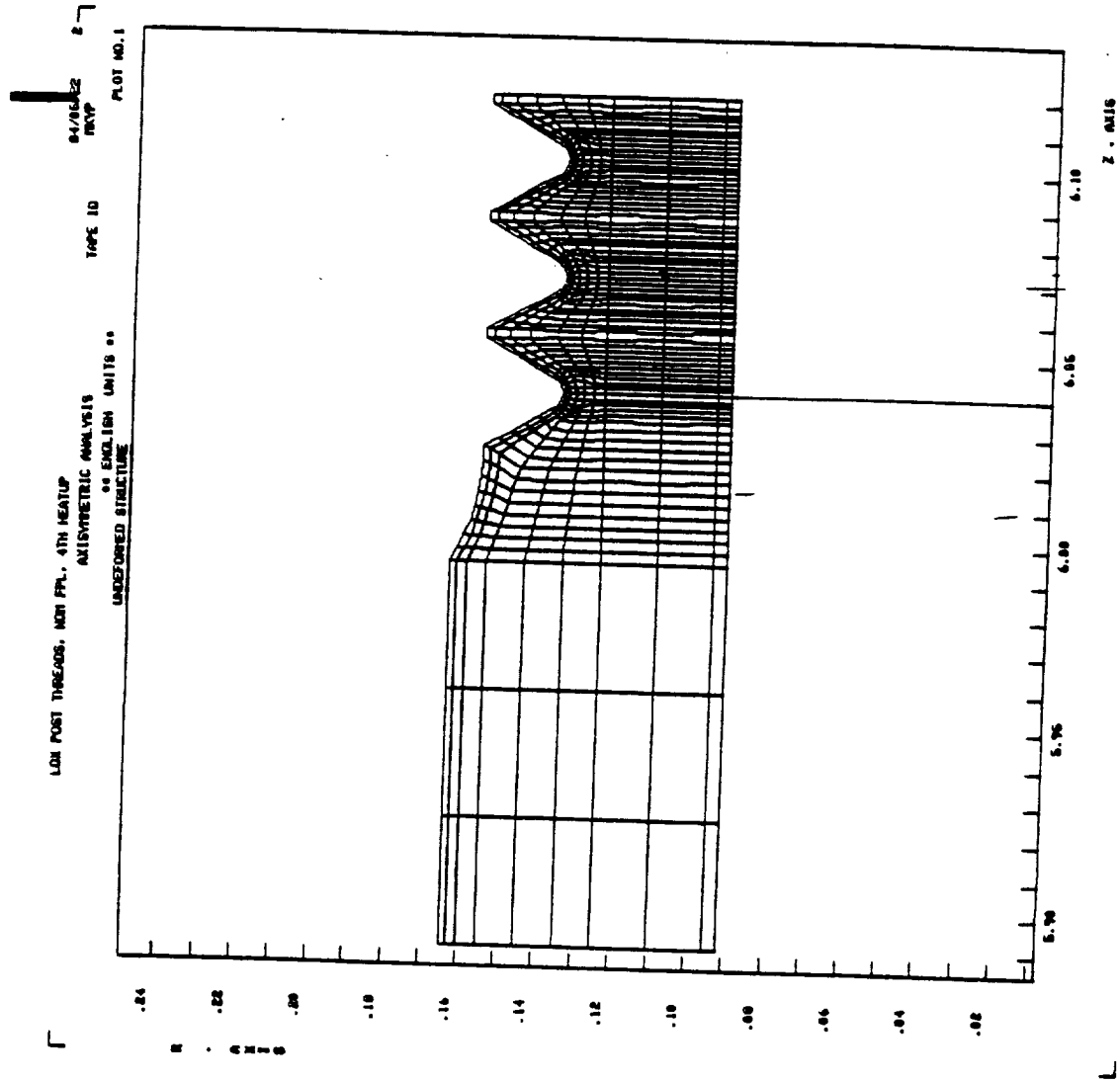


Fig. 45. Axisymmetric LOX Post Model for the Threaded Region

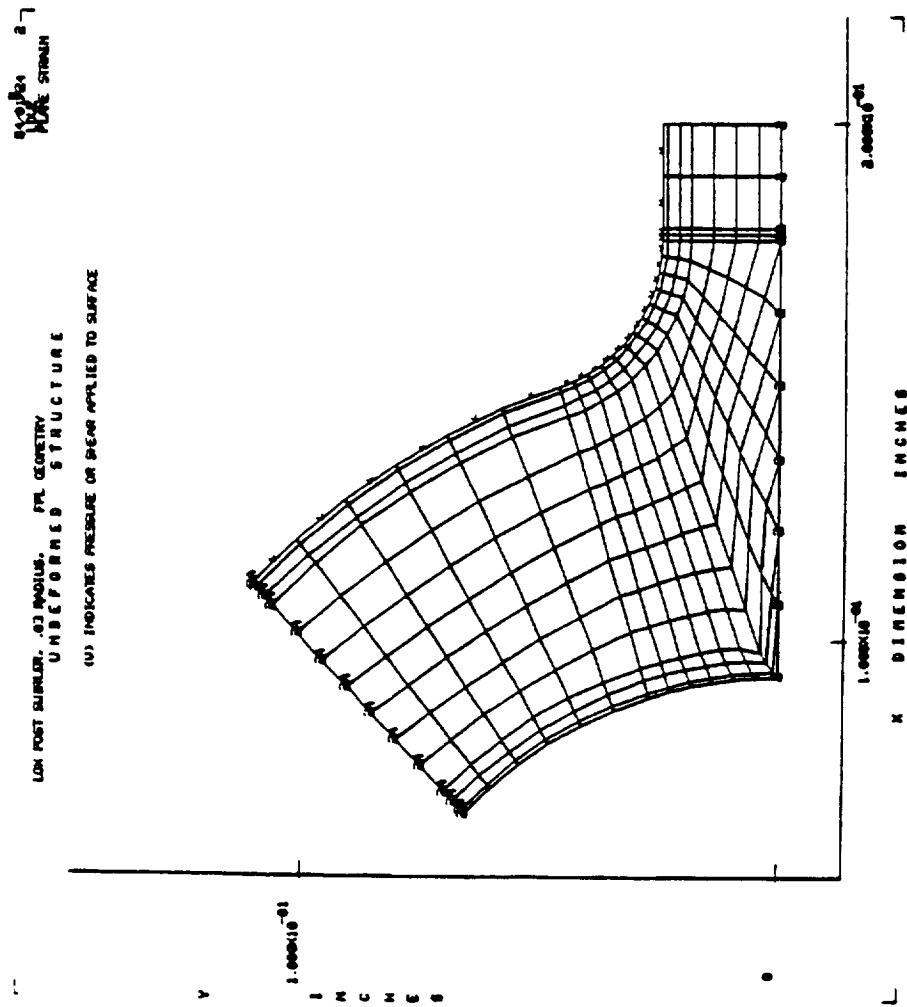


Fig. 46. Eighth of a Sector Model for LOX Post Swirler Region

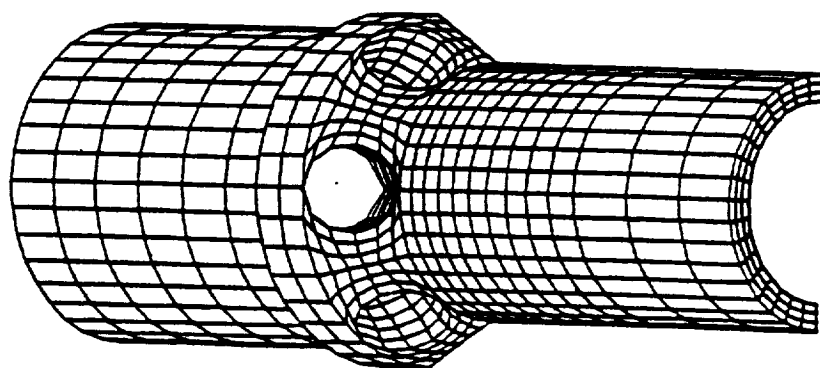


Fig. 47. Secondary Face Plate Retainer Solid Model



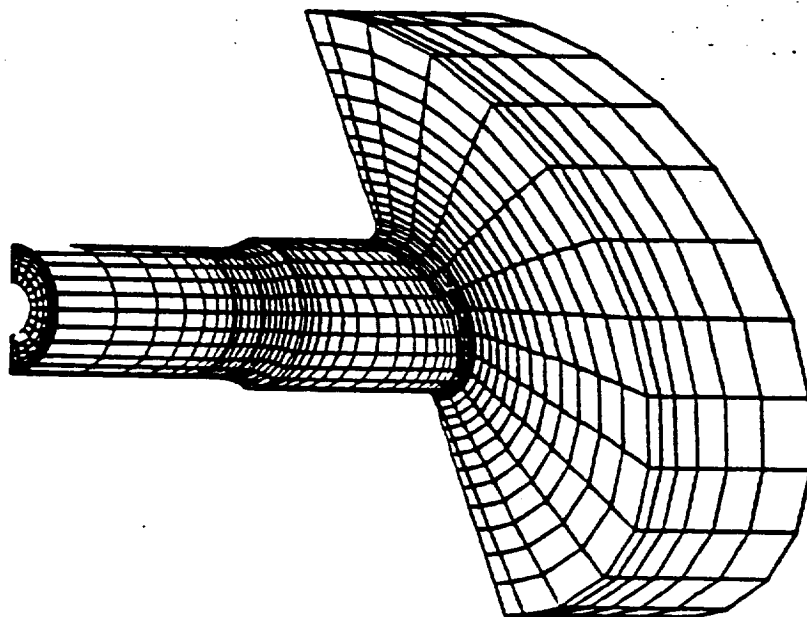


Fig. 48. LOX Post 3-D Model of Post and Inter-Propellant Plate Junction

## MAIN INJECTOR

# FINITE ELEMENT MODELS SURVEY

## STATIC AND DYNAMIC MODELS

[illegible]

• Was also used to aid in cold flow resistance at 145°

**THE UNIVERSITY OF CHICAGO**

Dynamic Models: There are numerous dynamic models available representing single Lox post, Lox post and different types of shield assemblies. One of the commonly used dynamic models is shown in Fig. 43 representing a pair of Lox posts and shield. This model has been used for modal analysis and random analysis of flow loads and mechanical vibration. A summary of dynamic finite element models that can be used for validation and verification purposes is also shown in Table 3.

## 22. Geometric Variations in Main Injector Loxpost

Geometric uncertainties in main injector Lox post, in addition to the usual tolerances in dimensions, include weld offset, surface scratches and thread fit. The effect of these geometric uncertainties have a bearing on fatigue life of main injector Lox post. This is due to the fact that at yield operating mean stress that is present in the Lox post due to high radial thermal gradient. Any stress raiser has an adverse effect on the life of the post due to more than allowable alternating stresses.

The geometric weld offset occurs when the posts are inertia welded to the stub in the interpropellant plate. The notch thus created acts as a stress raisers (Fig. 49). The geometric uncertainty in thread fit occurs due to potential variation of thermal gradients. The threads are used to adjust the secondary face plate retainer and are not preloaded during assembly. The variation in the tightness of fit results in variations in contact, and the number of threads engaged affect the response of entire post to external loads, and locally the thermal response.

Whenever a critical flaw is discovered in an injector of an existing assembled engine, then it is possible to deactivate the particular post such that fatal failure of that post can be eliminated. This is accomplished by either pinning or plugging and rodding the post. The three procedures have evolved during the years to increase the confidence in the structural integrity of the deactivated Lox post. In the first procedure, a gold plated pin is used to plug the orifice in the interpropellant plate. The orifice dimensions have tight tolerances from combustion performance point of view.

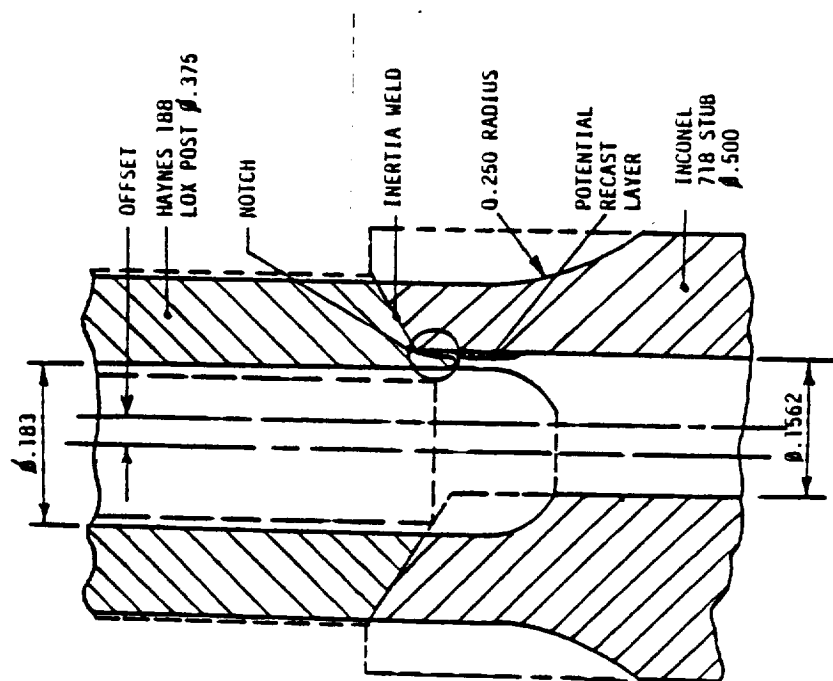


Fig. 49. Main Injector LOX Post Offset

To prevent destructive missile generation during operation, due to through crack developing at inertia welds, the posts are rodded internally using multiple rods in series and the last rod is welded onto the face plate. The geometry of multiple rods used are such that they accomodate for the large thermal expansions and contractions. It must be noted that plugged posts run much hotter under operating conditions due to the absence of Lox. This results in plugged posts buckling under large thermal axial loads. After several cycles, plugged Lox post can develop failure at the threads.

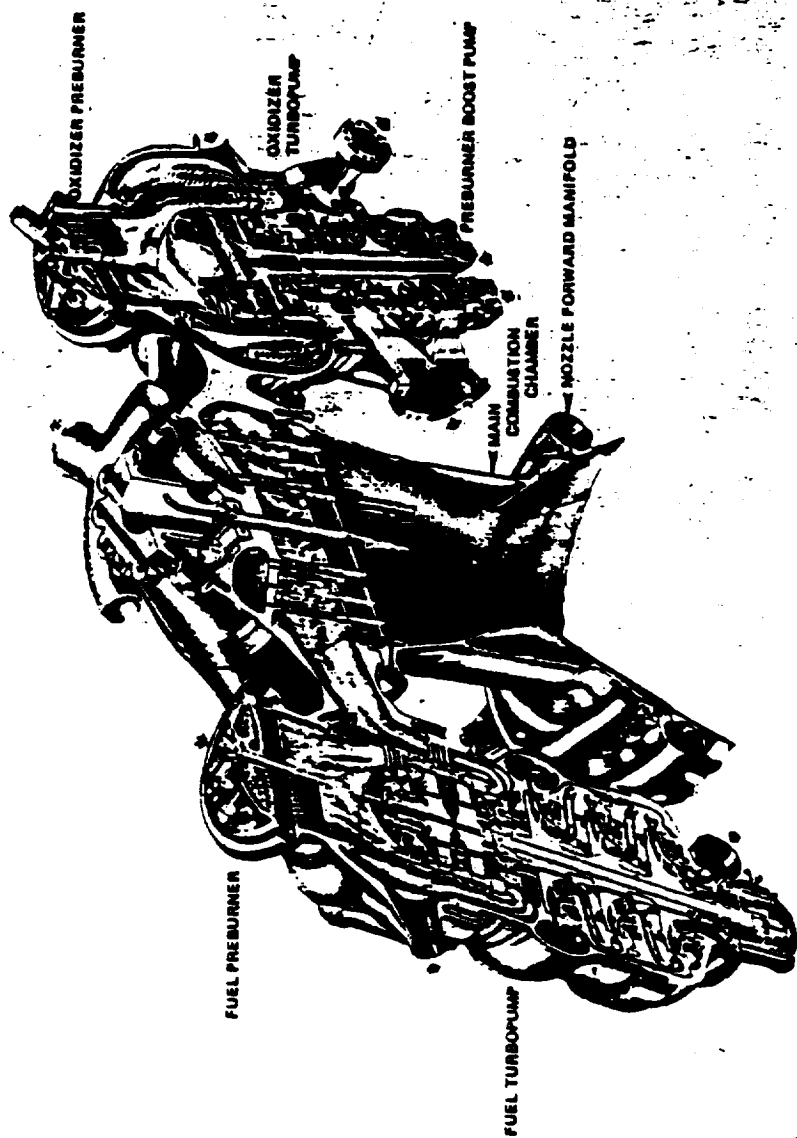
### 23. Preburner Injection Elements

Design Description: The major goal in preburner design is to provide reliable, repeatable power to the turbopump. Dual preburner assemblies are used on the main engine for hot gas supply to power the turbopumps. A preburner is mounted above each of the turbines of the turbopump assemblies (Fig. 50). They operate at a low mixture ratio with gaseous hydrogen from nozzle coolant circuit and liquid oxygen from the preburner oxidizer pump. Specific operating levels of the preburner are used to achieve engine system mixture ratios and power level variations. This is achieved by regulating the oxidizer flow rate with preburner oxidizer valves. For example, with the opening of preburner oxidizer valves, higher preburner mixture ratios and temperatures result, and the engine power level increases in response to the higher energy available to the turbines, and a new balance point is reached.

The design features of typical assemblies of fuel and oxidizer preburner are illustrated in Fig. 51 through Fig. 54. Basically, the two preburners are the same concept, but because of lower flow rate requirements, the oxidizer preburner diameter is 7.43" diameter, whereas the fuel preburner diameter is 10.43". Some of the sailent geometry features of the two preburners are:

	<u>FPB</u>	<u>OPB</u>
Internal Diameter	10.43"	7.43"
Combustor, Length	4.37"	4.25"
Injector Configuration	Concentric Orifice	Concentric Orifice
Number of Elements	264	120
Baffle, Length, Inches	2.25"	2.25"

## SSME POWERHEAD



5C306-896  
 Richard  
 International  
 Aerospace Division

Fig. 50. Preburner Locations Relative to Engine

# FUEL PREBURNER

## GEOMETRY

- INTERNAL DIAMETER
- COMBUSTOR LENGTH
- INCO 625 FACEPLATE
- INJECTOR CONFIGURATION
- NUMBER OF ELEMENTS
- BAFFLE LENGTH

10.43 IN.  
4.37 IN.

## CONCENTRIC ORIFICE

264  
2.26 IN.  
MARLOY-A

## OPERATING PARAMETERS (FPL MR-6.0)

- CHAMBER PRESSURE
- COMBUSTION TEMPERATURE
- HOT GAS MIXTURE RATIO (O/F)
- OXIDIZER FLOWRATE (INCLUDING IGNITER)
- FUEL FLOWRATE (INCLUDING IGNITER)

5572 PSIA  
1918 R  
0.99  
85.27 LB/SEC  
98.16 LB/SEC

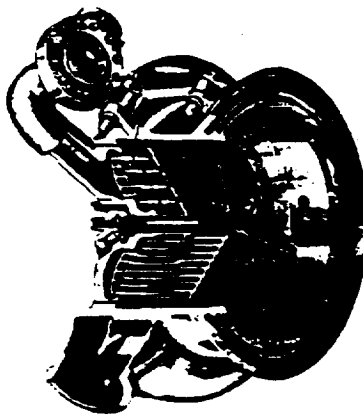


Fig. 51. Fuel Preburner Geometry and Operating Parameters

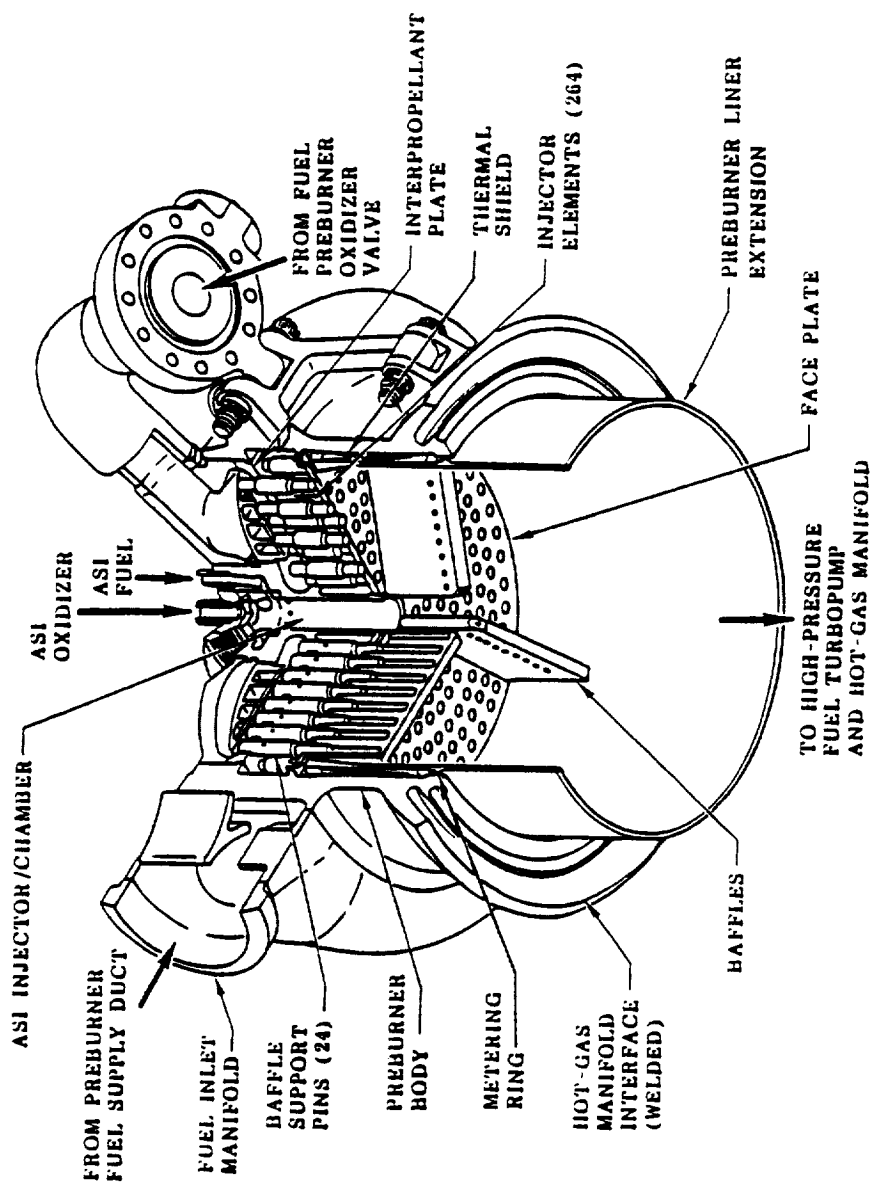


Fig. 52. Components of Fuel Preburner



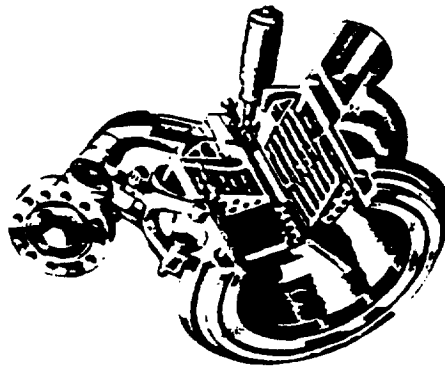
# OXIDIZER PREBURNER

## GEOMETRY

■ INTERNAL DIAMETER	7.43 IN.
■ COMBUSTOR LENGTH	4.26 IN.
■ INCO 825 FACEPLATE	
■ INJECTOR CONFIGURATION	
■ NUMBER OF ELEMENTS	120
■ BAFFLE LENGTH	2.25 IN.
■ MATERIAL	NARLOY-A
	CONCENTRIC ORIFICE

## OPERATING PARAMETERS (FPL, MR-6.0)

■ CHAMBER PRESSURE	5648 PSIA
■ COMBUSTION TEMPERATURE	1546 R
■ HOT GAS MIXTURE RATIO (O/F)	0.76
■ OXIDIZER FLOWRATE (INCLUDING IGNITER)	29.61 LB/SEC
■ FUEL FLOWRATE (INCLUDING IGNITER)	40.87 LB/SEC



100-55A  
Rockwell International Corporation

Fig. 53. Oxidizer Preburner Geometry and Operating Parameters

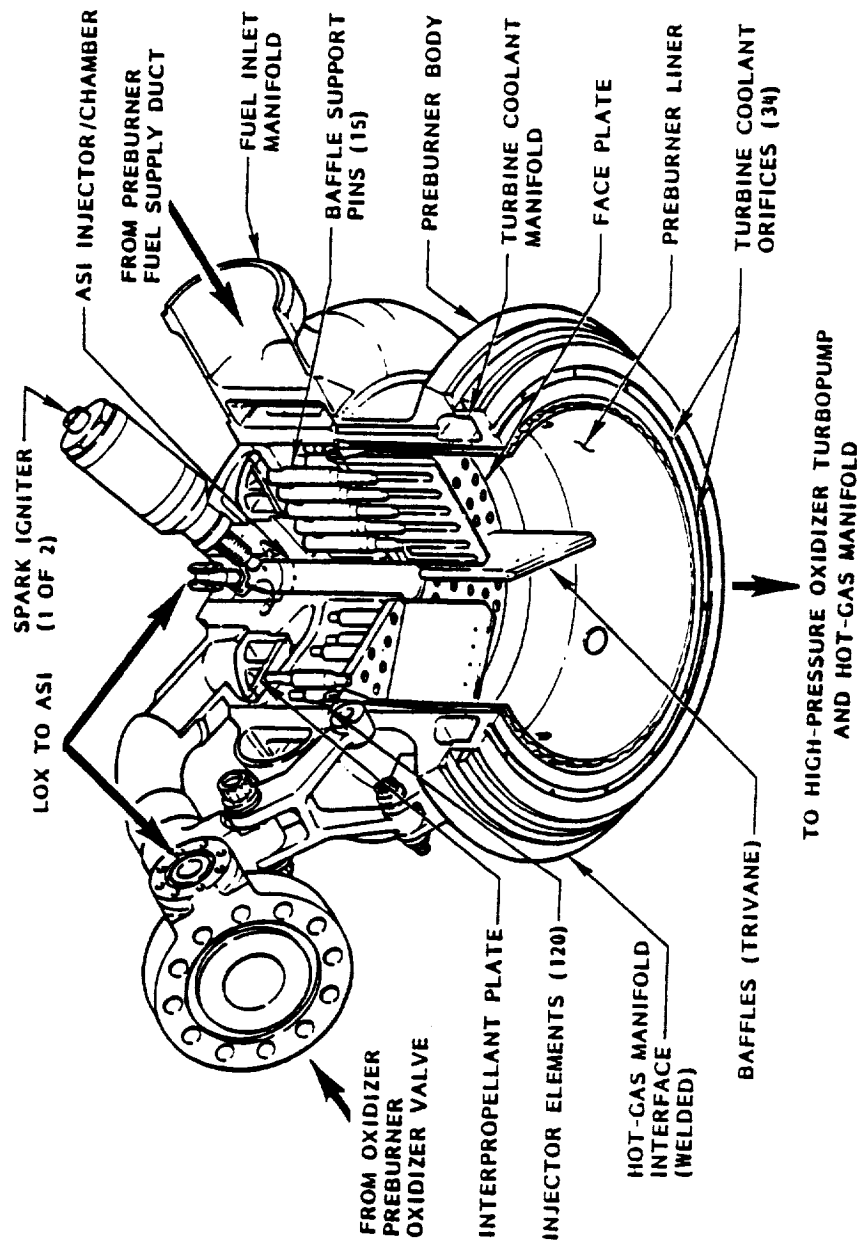


Fig. 54. Components of Oxidizer Preburner

The preburner injector is a baffled, coaxial-element injector that mixes the gaseous hydrogen and liquid oxidizer in correct proportions and uniformly distributes and injects the propellants into the combustion chamber (Fig. 55). The coaxial elements are contained by the upper interpropellant plate and a lower faceplate in a closely spaced pattern of concentric rows. Each element consists of an orificed center tube (oxidizer post) and an outer fuel sleeve that has a series of orifices in its periphery. Oxidizer entering the oxidizer manifold is uniformly distributed within the oxidizer dome fuel passes radially into the injector fuel cavity formed by the interpropellant plate and the faceplate. From the fuel manifold, the hydrogen enters the annulus of the coaxial elements through the fuel sleeve orifices. The high velocity of the low-density fuel, relative to the density and velocity of the oxidizer, produces a high rate of atomization and thorough mixing. Coaxial injection and baffles maintain stable combustion in the preburners. Hydrogen flows through passages in each baffle for cooling and is discharged radially into the combustion chamber.

#### Fuel Preburner

The fuel preburner (FPB) is supported by the hot-gas manifold (HGM), to which it is welded, and is close-coupled to the high-pressure fuel turbopump (HPFTP). The FPB consists of three major parts: 1) augmented spark igniter (ASI), 2) injector, and 3) combustion chamber.

The augmented spark igniter (ASI) unit is a small injector and combustion chamber with two spark igniters located in the center of the injector. It initiates ignition of propellants in the preburner. The injector has a single pair of impinging oxidizer orifices and eight hydrogen orifices directed tangentially around the oxidizer. The propellants are ignited by dual, redundant spark igniters.

The FPB combustion chamber is a fuel-cooled, double-walled chamber in which hot gas (hydrogen-rich steam) is generated to power the HPFTP. The chamber, consisting of an outer wall and a liner, is welded to the injector/dome and

HGM. Fuel coolant is provided between the outer wall and liner by hydrogen from the fuel manifold. The fuel coolant is discharged at the lower end of the liner into the hot gas powering the HPFTP turbine.

#### Oxidizer Preburner

The oxidizer preburner (OPB) is supported by the hot-gas manifold (HGM) to which it is welded, and is close-coupled to the high-pressure oxidizer turbopump (HPOTP). The OPB consists of three major parts: 1) augmented spark igniter, 2) injector, and 3) combustion chamber.

The augmented spark igniter (ASI) unit is small injector and combustion chamber with two spark igniters located in the center of the injectors. It initiates ignition of propellants in the preburner. The injector has a single pair of impinging oxidizer orifices and eight hydrogen orifices directed tangentially around the oxidizer. The propellants are ignited by dual, redundant spark igniters.

The OPB combustion chamber is a fuel-cooled double-walled chamber in which the hot gas (hydrogen-rich steam) is generated to power the HPOTP. The chamber, consisting of an outer wall and a liner, is welded to the injector/dome and HGM. Fuel coolant is provided between the outer wall and liner by hydrogen supplied from the fuel manifold. The fuel coolant is discharged at the lower end of the liner into the hot-gas powering the HPOTP turbine. Fuel from the fuel inlet manifold is conducted through the preburner body to a turbine coolant manifold for use in cooling HPOTP turbine components.

#### Preburner Baffles

The tri-vane NARALOY-A baffles (Fig. 52, Fig. 54) on the preburners are cooled with hydrogen to minimize weight and produce high durability. The baffles are 2.25 inch long and extend to within 0.5 inch radius of the center ASI injector.

The opening at the center of baffles provides an exit and direct communication to each compartment of augmented spark igniter hot gas. The baffles are structurally attached by brazing to post pins which extend through fuel cavity, each of which occupies an equivalent element location on each element row. The pins are brazed to the faceplate and interpropellant plate in the same manner as the elements. Each pin has flow passages (Fig. 52) which supply fuel to axial coolant passages in the baffles. Coolant flow is discharged at the side of the baffles through orifices and is mixed with the main hot gas stream. The flow from the innermost coolant passages near the center of injector is injected into the hot gas stream from ASI. This is done to provide additional hydrogen to the oxidizer core of ASI.

#### 24. Operating Environment

The preburner operating environments are quite different from that of main injector though similarity in the type of loadings exist. A comparison of the operating environment's critical parameter values are shown in Table 4. The much higher operating pressures in the preburners as opposed to main injectors and much lower hydrogen gas temperature in preburners as opposed to main injectors must be noted. Severe thermal gradient present in the walls of the main injector is absent in the preburner injectors, as cold hydrogen is the fuel in the preburner. The oxidizer and fuel flow rates are also much lower compared to the main injector environment.

#### 25. Geometry

The geometry of the preburner injector elements is different from that main injector elements in the sense that posts themselves are much smaller and the assembly is all brazed devoid of any threaded assemblies (Fig. 55). The preburner injector elements are much stiffer structurally (mainly due to smaller size). As a comparison while the fundamental frequency of main injector Lox post is around 1200 Hz, the fundamental frequency of a similar preburner injector element is of the order of 4800 Hz to 8000 Hz depending upon configuration. The stress concentration areas are brazed fillet joint radius location between elements and interpropellant plate, between element and face plate and at the base of cantilever Lox post (Fig. 56).

TABLE 4. COMPARISON OF PREBURNER INJECTOR AND MAIN INJECTOR ENVIRONMENT

	109% Power Level		
	FPB	OPB	MCC
Hot Gas Temp (°R)	1671	1560	1449
P <sub>c</sub> (Psi)	4925	5164	2981
Lox Temp (°R)	209	211	194
Fuel Temp (°R)	265	265	1444
Fuel Flow Rate (lbm/s)	90.40	37.3	239.56
Ox. Flow Rate (lbm/s)	76.35	27.70	865.75
Lox Pressure In (Psi) Lox Post	5098	5325	3077
Average Fuel Pressure	5457	5508	3232

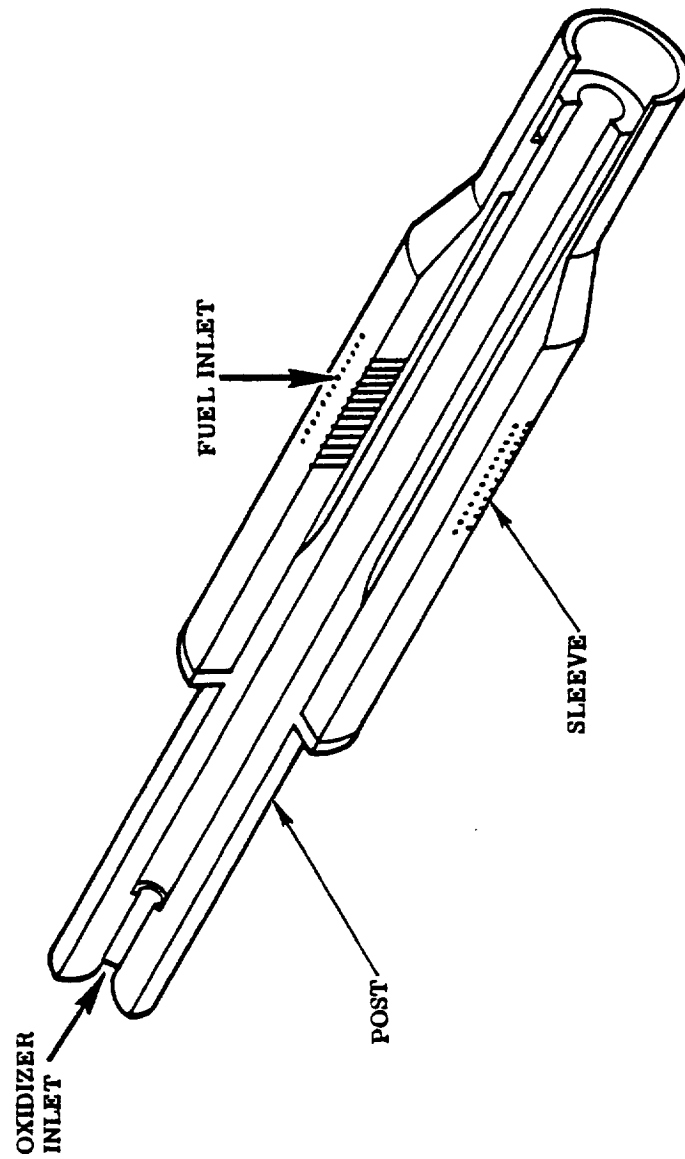


Fig. 55. A Typical Preburner Injector Element

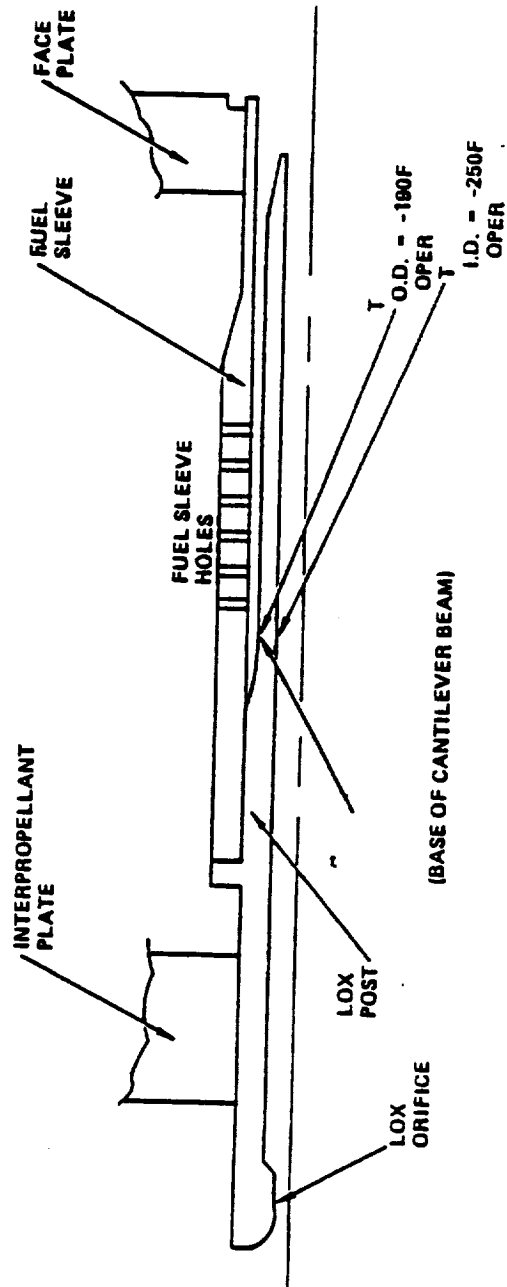


Fig. 56. Preburner Element Geometry and Stress Concentration Areas



## 26. Loads on the Preburner

The static loads in the preburner include the differential pressure and thermal gradient across the Lox post wall. The mechanical vibration loads include random vibration due to combustion noise and sinusoidal vibration at multiples of shaft speeds of high pressure turbopumps. Mechanical vibration is the predominant load source for alternating stresses. This is contrast to main injector post environment where the flow loads are dominant. The transfer function test accelerometer locations are shown in Fig. 57.

The contribution of the dynamic flow loads result from gaseous hydrogen flow through fuel sleeves. The ability of flow to excite the Lox post have been demonstrated using unelement flow test fixtures (Fig. 58). The results indicate annular flow over cantilever post can be unstable. Offset holes (Fig. 29) as opposed to correctly aligned radial holes decreases the stability margin due to tangential swirling action. In addition, cutoff transients create more unstable flow conditions than the main stage flow condition.

## 27. Failure History of Preburner Injector Elements

The failure history of preburner Lox post elements operating on a different environment than the main injector elements offer an insight into the variety of conditions that can become critical in a "generic" Lox post. As opposed to main injector Lox post failure, the failure of preburner injector elements are not always necessarily fatal to the engine. There are two incidents of fuel preburner Lox post failure. There have been no failures in oxidizer preburner injection elements. A fuel preburner injection element failure occurred in engine 0009 after 41 tests with an accumulated time of 11,842 seconds. On engine 0204, a preburner injection element failure occurred after 20 tests with an accumulated time of 4,692 seconds (Fig. 60). The hardware damage in both the failures were similar. The engines had gone through a variety of power levels before the failure occurred. The failure investigation revealed Lox post cracking identified as the problem (Fig. 61), and the crack is high cycle fatigue initiated. Metallurgical examination of the Lox posts exhibited

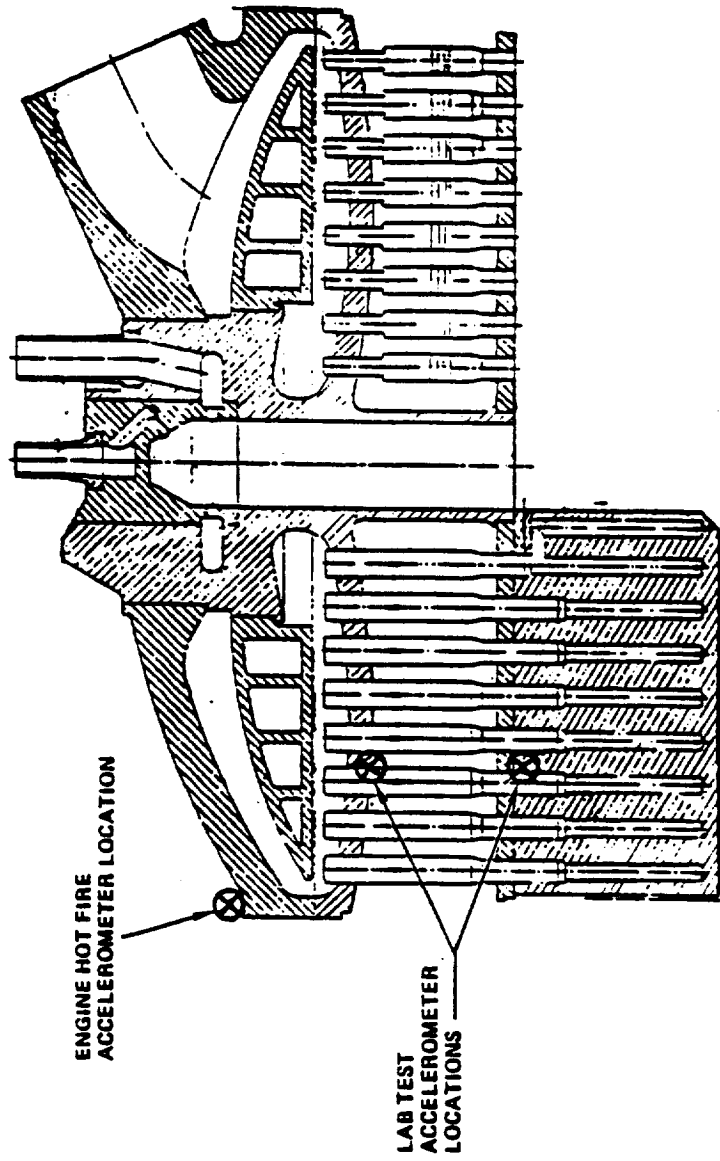


Fig. 57. Transfer Function Test Accelerometer Locations

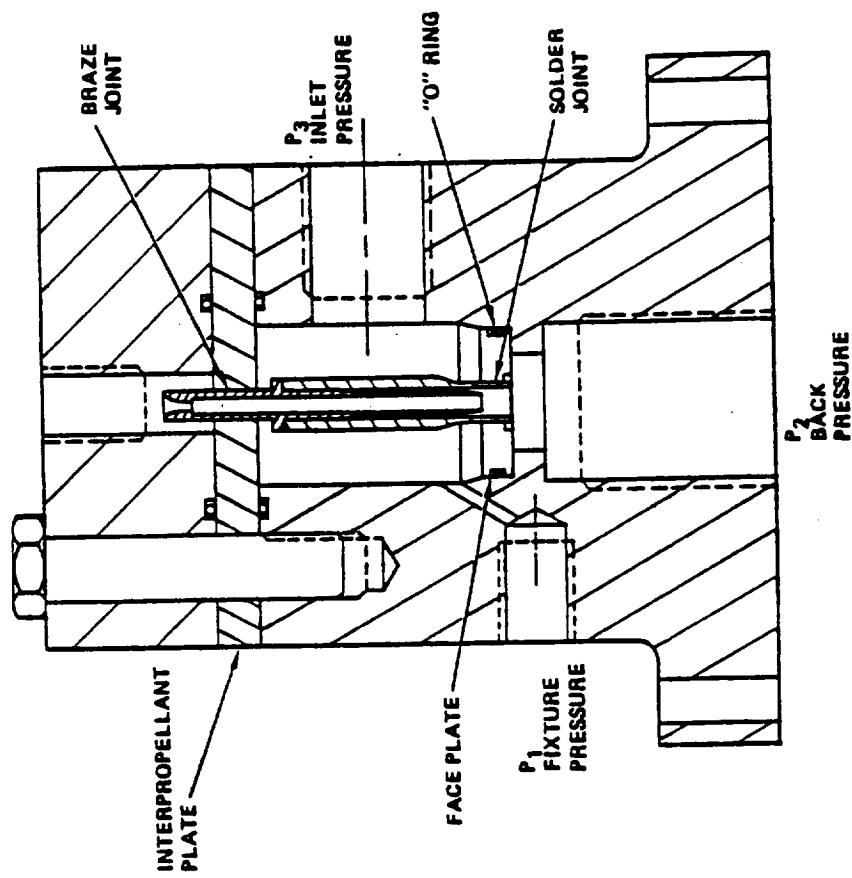


Fig. 58. Unielement Flow Test Fixture

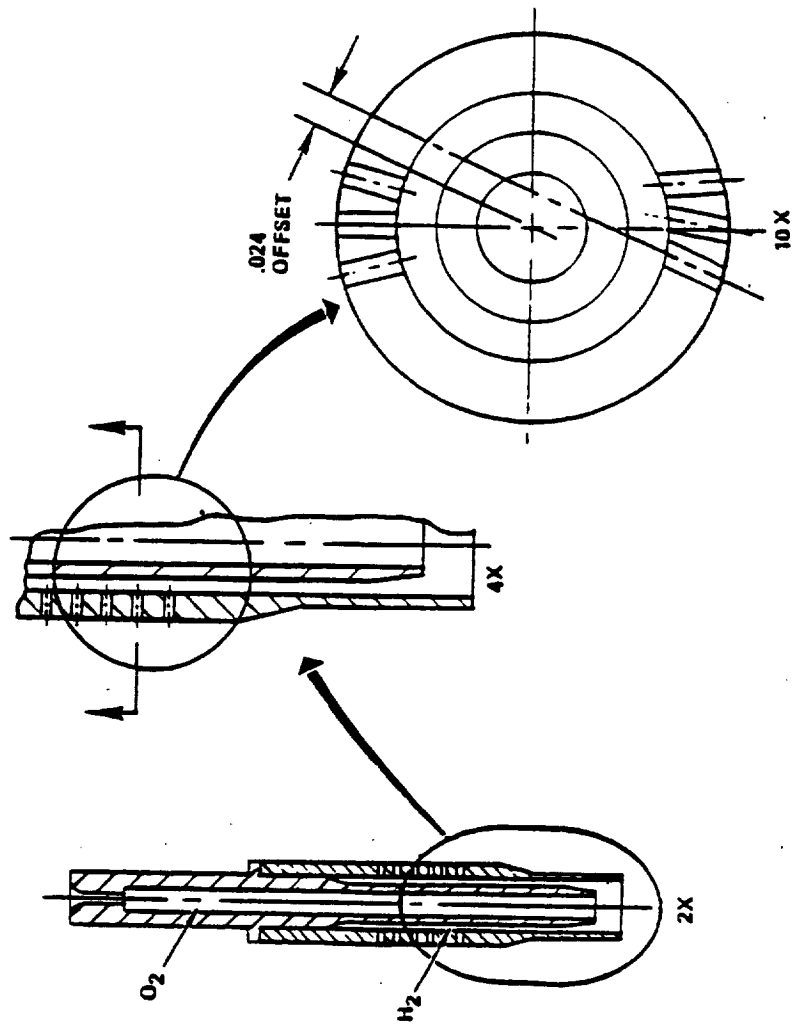


Fig. 59. Offset Holes in Preburner Fuel Sleeves

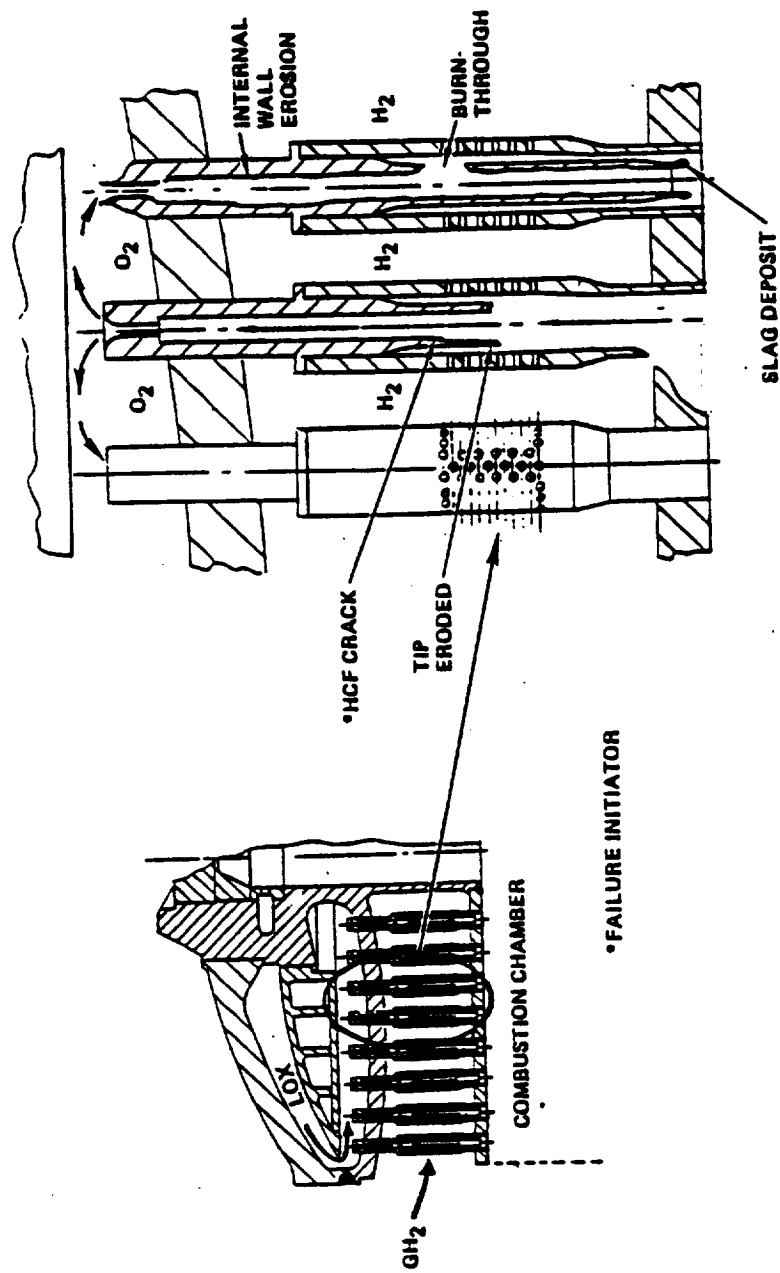


Fig. 60. Failure Locations in Fuel Preburner Elements

• I.D. OF LOX POST C-8 SHOWS BURNING IMMEDIATELY D/S OF THROUGH CRACK - ENGINE 0204

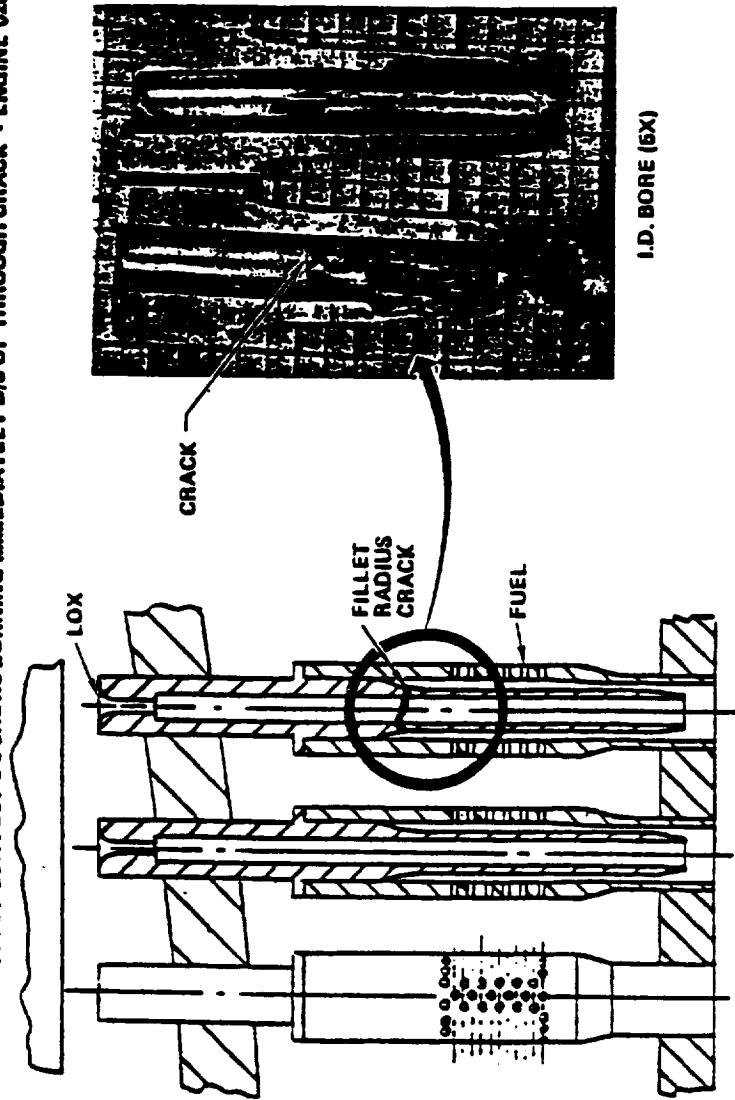


Fig. 61. LOX Post High Cycle Fatigue Crack

cold work at fracture location. The problem was fixed by the inclusion of three preloaded pin supported located between the Lox post and the fuel sleeve (Fig. 62).

## 28. Survey of Preburner Finite Element Models

Single element finite element models of the fuel and oxidizer preburner elements exist and due to the simplicity of the models, they are not covered in the survey the finite element models.

The finite element models include global and local models. In the global models, an example of the axisymmetric approximate fuel preburner models is shown in Fig. 63. They are used to calculate the approximate load transfer bath and stresses between Lox post assembly and the surrounding manifolds. Many refined local finite element models also exist (Fig. 64) to calculate the local effects. Because of the nature of the vibration environment in the fuel preburner, an 180° model containing the Lox post forest, baffle elements, face plate and the interpropellant (Fig. 65) was also used for static and dynamic analysis. Table 5 gives an overall view of the breadth of finite element models available for fuel preburner Lox post assembly.

## 29. Scoping of Finite Element Analysis

Finite Element Types: From the survey of static and dynamic finite element analysis done, the finite element library should contain for a complete Lox post analysis:

- a) Pipe or beam element.
- b) Axisymmetric 2-D solid quad and triangle.
- c) Shell element (4 noded quad and triangle).
- d) Solid element (8 noded solid, tetrahedron and prism).
- e) 2-D and 3D gap elements.

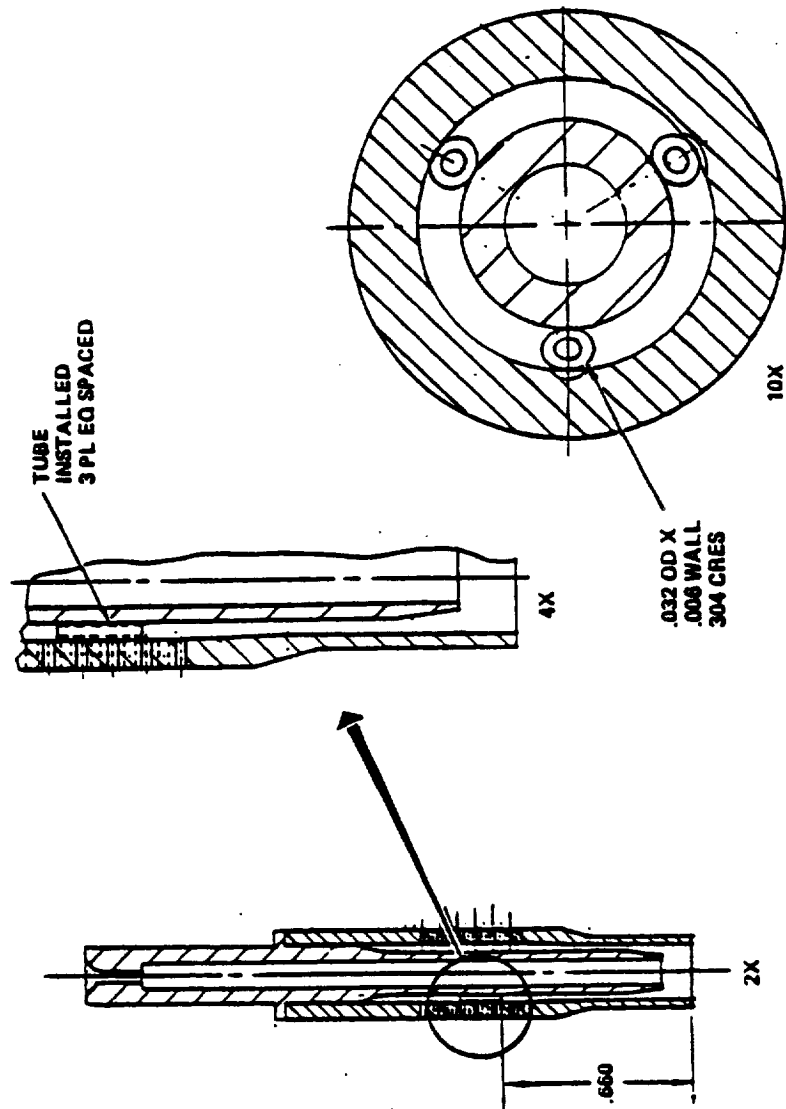


Fig. 62. Pin Support Configuration for Fuel Preburner Elements



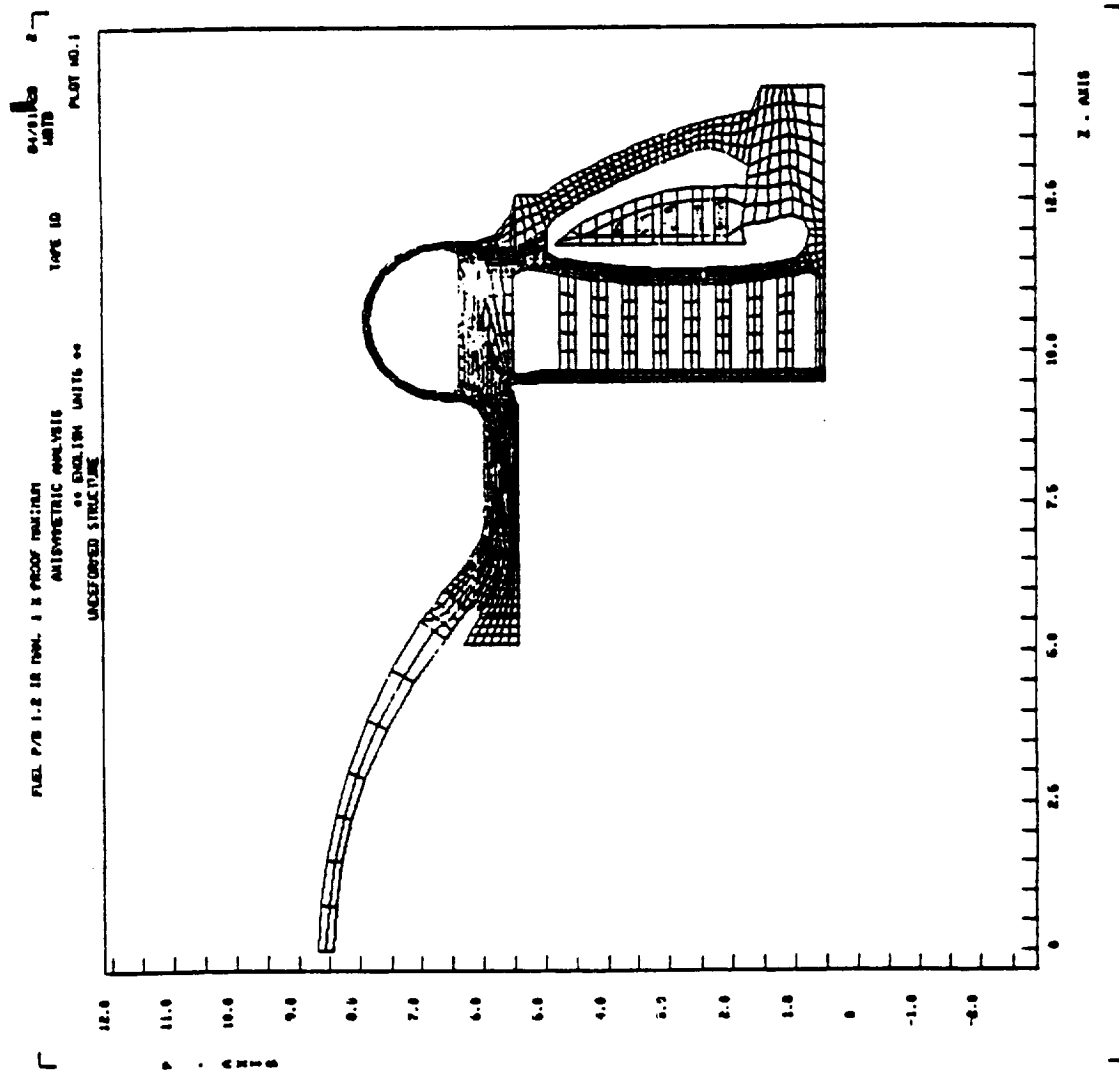


Fig. 63. Global Finite Element Model of Fuel Preburner

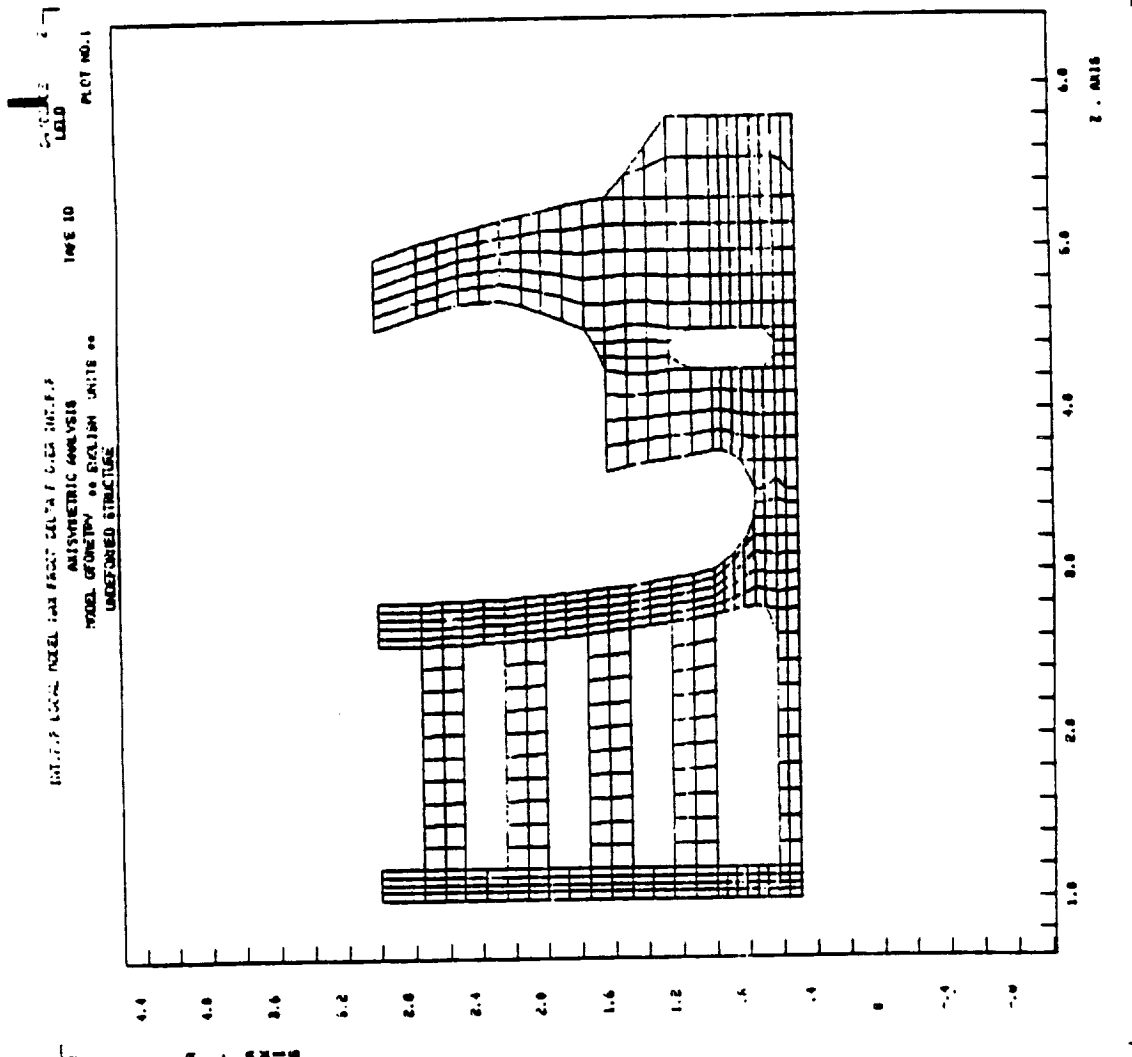


Fig. 64. Refined Local Model of Preburner LOX Manifold

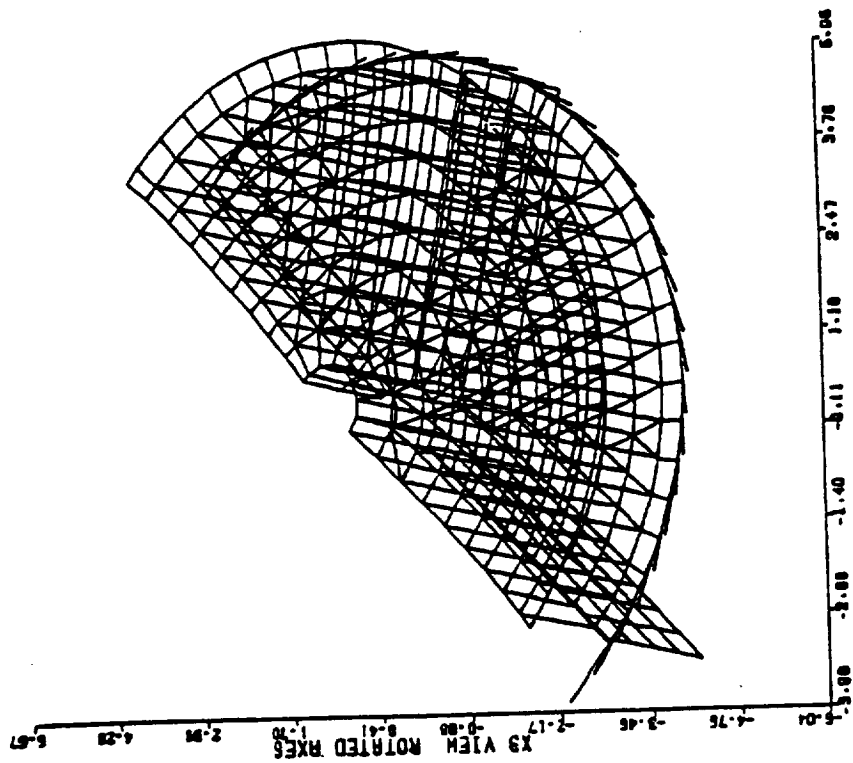


Fig. 65. LOX Post Forest Global Model of Fuel Preburner

# FINITE ELEMENT MODELS SURVEY

J M - Jahr 1910-1911.  
B P - Ende Prior

Material Nonlinearity: The material library should include:

- a) Temperature dependent properties.
- b) Account for material nonlinearity by having provisions for
  - 1) Defining a stress-strain curve point by point
  - 2) bilinear representation.
  - 3) and thermal creep buckling

Geometric Nonlinearity: Geometric nonlinearity enters the Lox post analysis in three ways. The response of Lox post and the effective damping of Lox post is controlled by the threaded correction to the secondary face plate retainers. Thus, accurate modelling of the boundary condition may require the use of gap elements to model the contact phenomenon and for modelling preloaded T-nuts and bolts.

The presence of high axial loads on the Lox post results in the consideration of the second order geometric stiffness matrix in modal response analysis of the Lox post. In fact, such analysis has been done to study the responses of Lox post under axial loads. For certain configurations, higher order geometric stiffness matrix is a necessity to calculate approximate buckling loads or exact buckling loads using incremental analysis.

Scoping of Solution Strategies: The solution strategies should include:

- a) Linear analysis.
- b) Incremental and iterative nonlinear analysis to include material and geometric nonlinearity using Newton, quasi-Newton or self-adoptive procedures.
- c) Linear Modal analysis.
- d) Linear random analysis using modal superposition and PSD diagrams.
- e) Nonlinear transient dynamic analysis using stable time integration procedures.

- f) Development of efficient procedures to predict accurately random response in nonlinear structural analysis domain that can be cost effective to do in practical sized finite element models.

Section 2  
Turbine Blades

## 1. TURBOPUMP SYSTEMS

### GENERAL

Turbomachinery is required on pump fed rocket engines as opposed to pressure fed rocket engines. Pressure fed engines are less complex and less development effort is required but they require high tank pressures. The pumped systems have the advantages of lower weight, higher payload capability and has a significant advantage at higher velocities. As an example in space shuttle transportation system, pressure fed solid boosters are used at lift off, while pump fed SSME's are required at orbit insertion.

Basic elements of turbomachinery include pump, turbine, bearings, seals, thrust balance device, casing, and gears or splines. As in an example, crossectional view of MARK-15F turbopump, used in J-2 engine is shown in Fig. 2.1 where the different components are identified. Depending upon operating requirements, the key parameters of pump design can vary over a wide range as shown in Fig. 2.2.

Because of emphasis on high performance and weight requirements rocket engine turbines run at a very high speed. Advances in bearings and seals have resulted in direct drive turbo-pump systems with no need for reduction gears. Liquid rocket engine turbopumps have one of the highest power to weight ratio in the entire field of turbomachinery and this is illustrated in Fig. 2.3.

Turbines which is the drive mechanism for the turbopumps provide the required shaft power for the pump. Of the two major types of turbines, impulse and reaction, reaction turbines have been used extensively in oxidizer and fuel turbopumps in rocket engines. Other design options in turbine design include single vs. multistage, full vs. partial admission and axial vs. radial flow. Actual turbine installation used in a rocket engine is very dependant on the engine system used. Schematics of basic turbine drive cycles are shown in Fig. 2.4. Earlier versions of rocket engines have used the gas-generator (GG)



# CROSS-SECTIONAL VIEW OF MARK 15-F TURBOPUMP

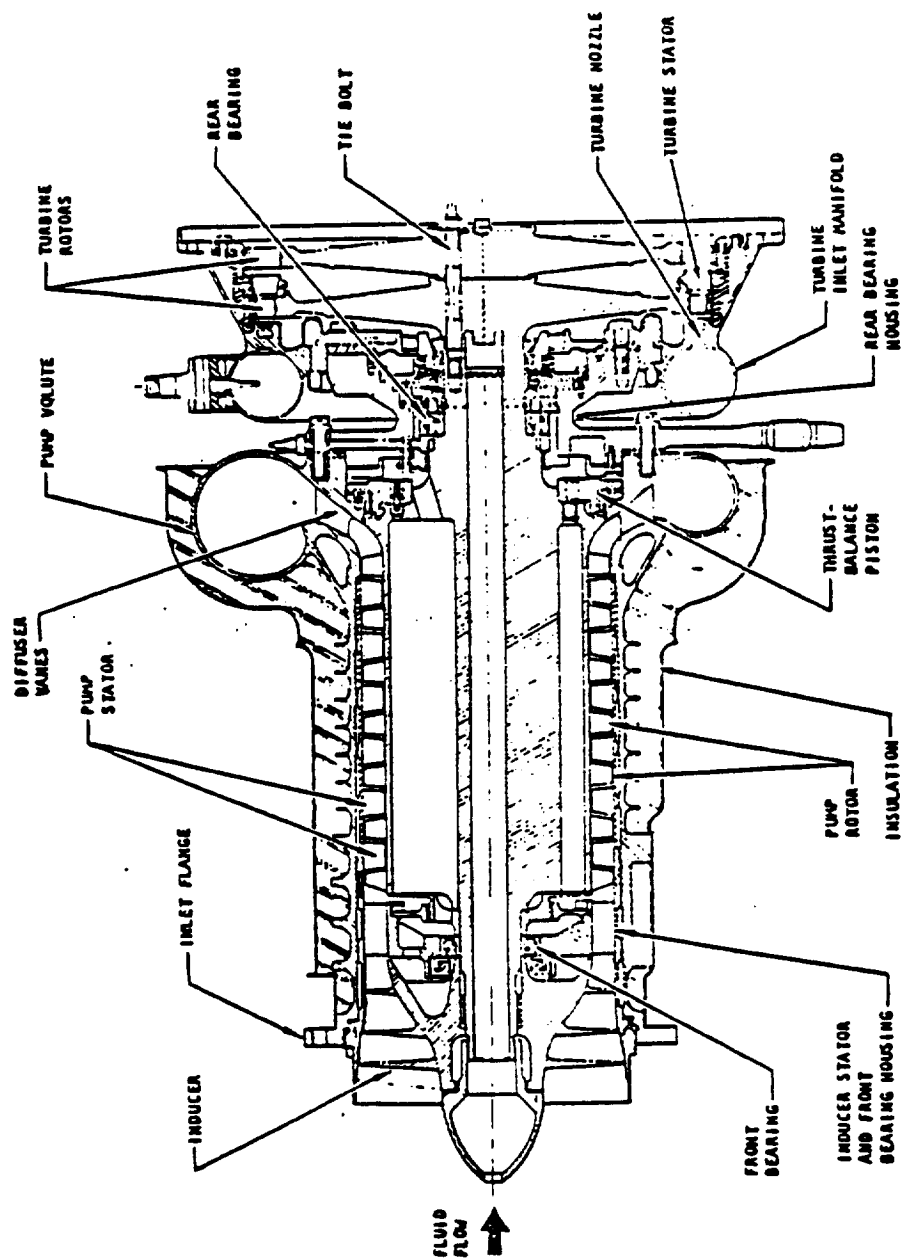


Fig. 2.1 Cross-Sectional View of Mark 15-F Turbopump

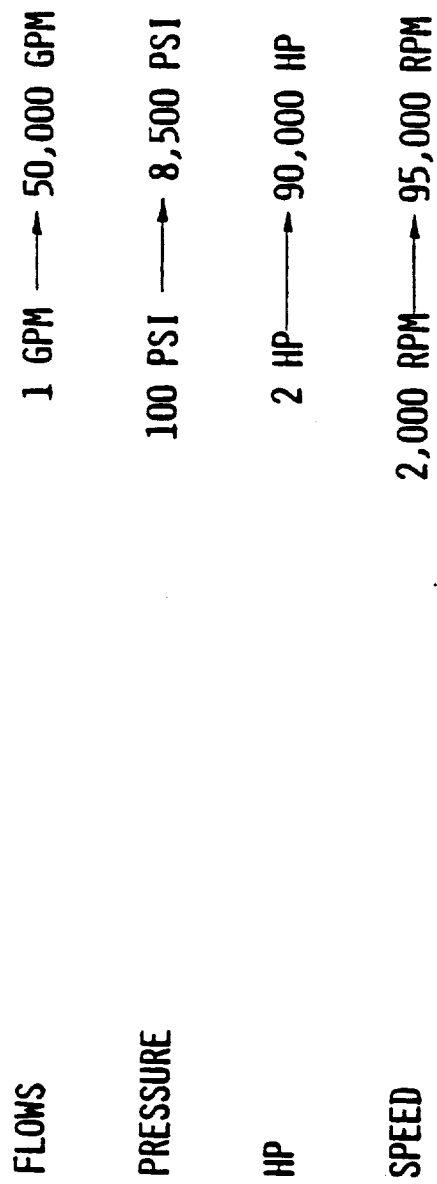


Fig. 2.2 Range of Design of Rocketdyne Turbopumps

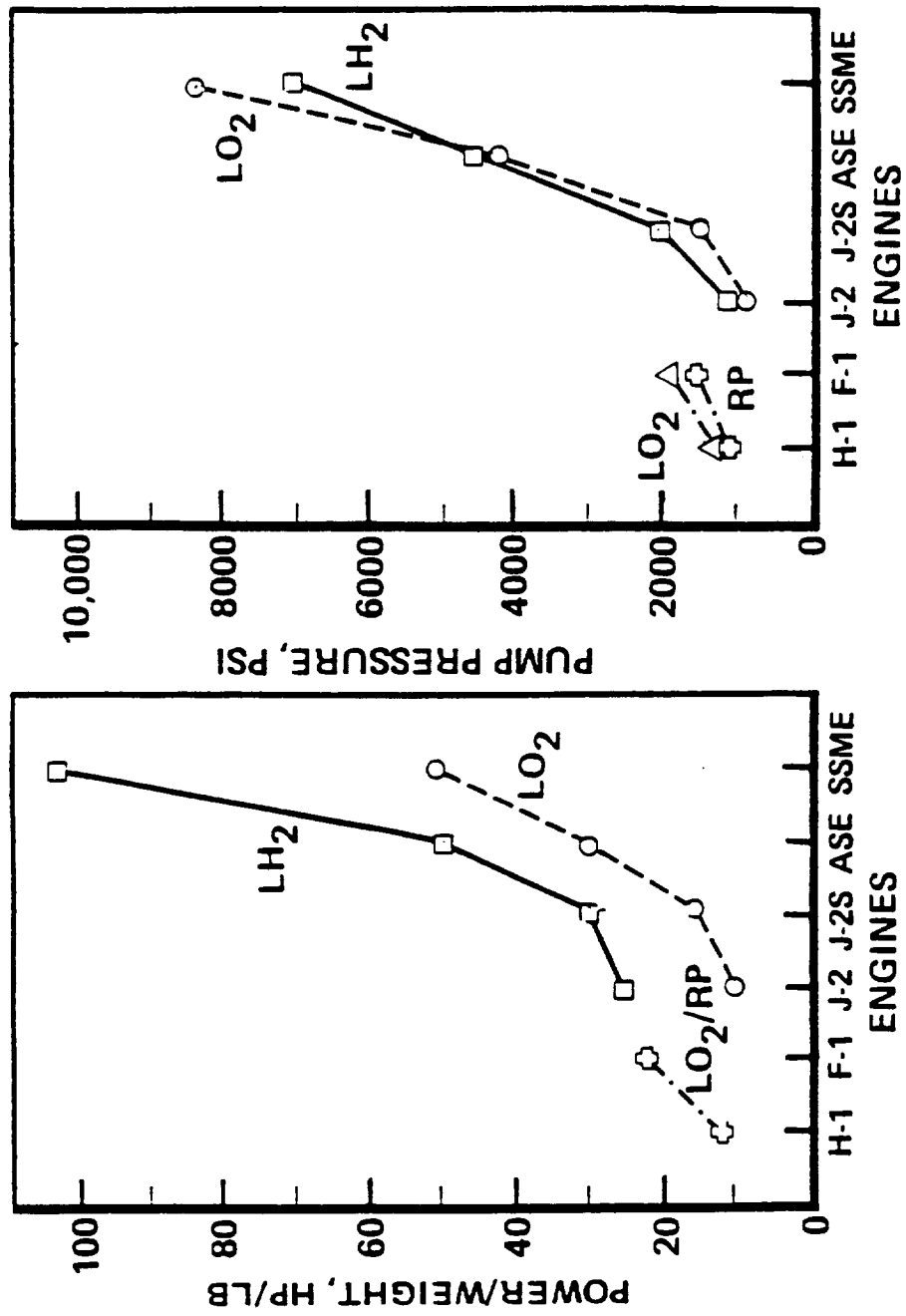


Fig. 2.3 Power Growth of Rocket Engine Turbopumps

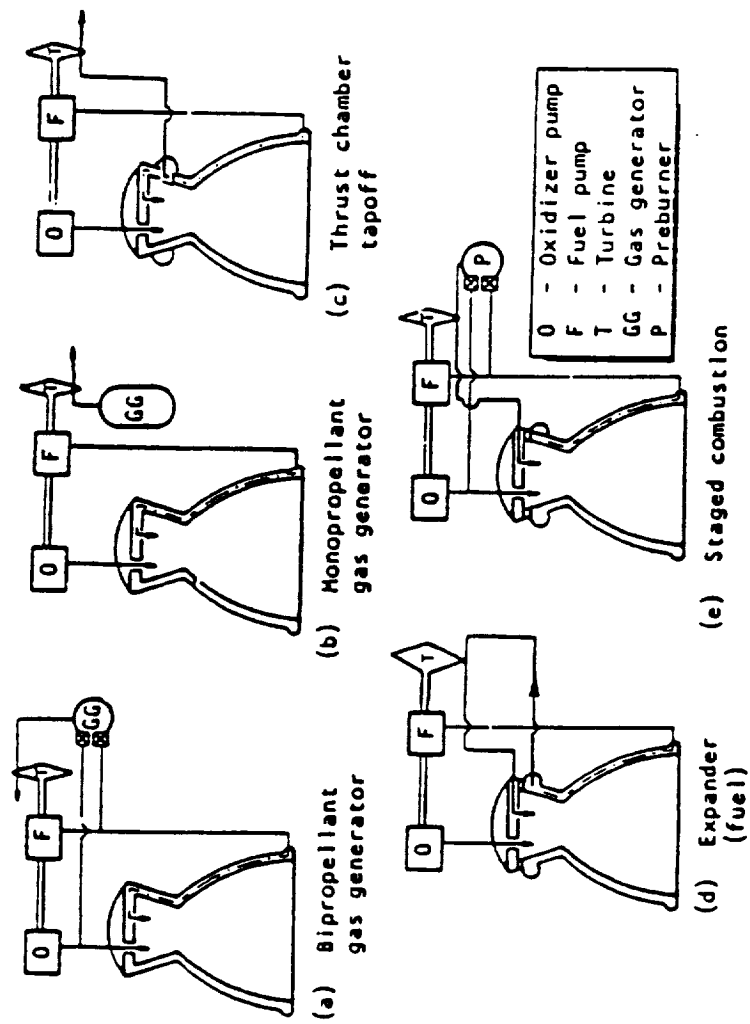


Fig. 2.4 Rocket Engine Cycles and Turbine Installations

cycle in which the turbine working fluid is derived by combustion of main propellents in the GG at a temperature below the turbine temperature limits. If the turbine exhaust is after burned by the introduction of additional oxidizer higher performance can be obtained from the GG cycle. The J2-S development engine utilized the variation of the GG cycle called the tap off cycle (Fig. 2.4) in which the turbine working fluid is tapped off near the face of injector at a location where relatively cool gas is available. In the expander or hot fuel tap off cycle which is used for the RL-10 engine, the hydrogen that is evaporated and heated in the thrust chamber regenerative jacket is used to drive the turbines. The turbine exhaust is then fed to the main combustion chamber for combustion. In the staged combustion cycle, a preburner generates the turbine working fluid which then discharges into the main combustion chamber, where the second stage of combustion occurs. Virtually all the fuel and 10% of the oxidizer is routed to preburner where it is burned at a low mixture ratio. The turbine discharge pressure is established by main combustion chamber pressure and working backwards considering all the pressure drops. Key elements of the turbine are shown in Fig. 2.5.

Distinguishing factors of rocket engine turbine include:

- a) Comparatively short but severe service life
- b) Strict limitations on size and weight
- c) High energy content of fluids
- d) High specific work output
- e) Rapid start and short run duration
- f) Severe thermalshock conditions
- g) High stage loading and stress

Turbine working fluids can be a) Combustion products (LOX/RP1, LOX/LH2, LOX/CH4) b) Compressible fluids (Ambient hydrogen or nitrogen) c) Mono propellents (Hydrogen peroxide) and d) for hydraulic turbines liquid oxygen, or liquid fuel.

A comparison of turbine flow rate and horse power for various turbopumps is shown in Table 2.1.

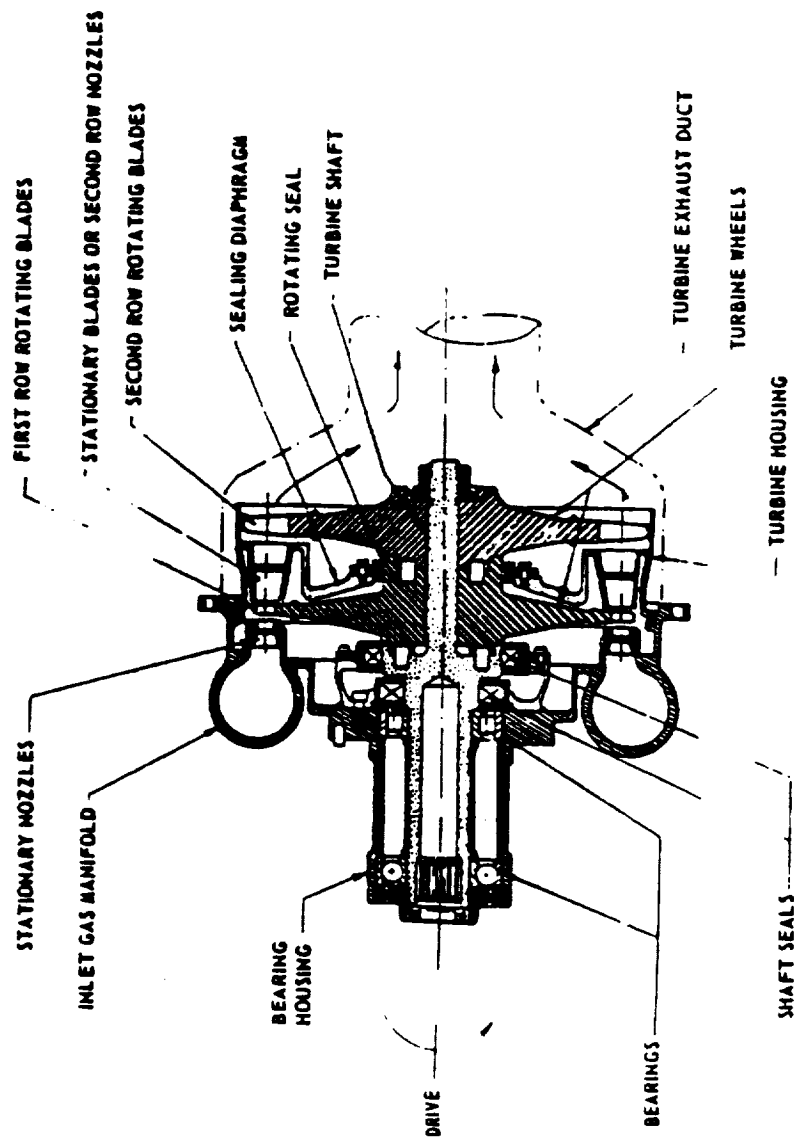


Fig. 2.5 Elements of a Turbine

1 OF 2

MODEL	TYPE	NO. STGS	ENGINE	FLUID	HP	RPM	D <sub>m</sub> INCH.	U <sub>m</sub> FT/SEC	T <sub>11</sub> F	P <sub>11</sub> PSIA	PR	U <sub>m</sub> /C <sub>0</sub>	η <sub>1</sub> (TS) %
MARK 3	PC	2	H-1	O <sub>2</sub> /HP-1	4,007	32,800	9.00	1290	1200	800	17.7	0.42	82.6
MARK 4	PC	2	ATLAS	O <sub>2</sub> /RP-1	1,680	38,000	8.00	896	1075	760	25	0.39	48.3
MARK 6	VC	1	E-1	O <sub>2</sub> /RP-1	14,860	8,900	22.04	867	1400	660	26	0.20	82.0
MARK 10	VC	1	F-1	O <sub>2</sub> /FP-1	64,358	6,480	34.80	840	1650	929	16.3	0.20	80.6
MARK 14	VC	1	H-2	O <sub>2</sub> /FP-1	7,660	14,300	16.07	1000	1700	626	11.8	0.21	68.9
MARK 16-0	VC	1	J-2	O <sub>2</sub> /H <sub>2</sub>	2,604	8,650	16.60	685	740	62	3.16	0.11	48.4
MARK 16F	VC	1	J-2	O <sub>2</sub> /H <sub>2</sub>	8,748	26,062	12.60	1448	1200	820	6.36	0.18	60.1
MARK 18-0	IMPULSE	1	X-8	O <sub>2</sub> /H <sub>2</sub>	760	32,800	6.00	880	1200	460	9.0	0.102	19.7
MARK 18F	PC	2	X-8	O <sub>2</sub> /H <sub>2</sub>	4,000	27,000	9.00	1160	1200	410	16.4	0.116	40.7

NOTES:  
VC - VELOCITY COMPOUNDED; 2 ROW  
PC - PRESSURE COMPOUNDED  
D<sub>m</sub> - PITCH DIAMETER  
U<sub>m</sub> - PITCHLINE VELOCITY  
PR - PRESSURE RATIO  
U<sub>m</sub>/C<sub>0</sub> - VELOCITY RATIO

Table 2,1 Design Parameters of Rocketdyne Turbines

2 OF 2

MODEL	TYPE	NO. STGS	ENGINE	FLUID	HP	RPM	D <sub>m</sub> INCH	U <sub>m</sub> FT/SEC	T <sub>11</sub> °F	P <sub>11</sub> PSIA	PR	U <sub>m</sub> /C <sub>0</sub>	η <sub>1</sub> (T.S) %
MARK 29F (MOD MK-16/F)	VC	1	J-24	O <sub>2</sub> /H <sub>2</sub>	12,700	28,060	12.50	1535	1050	920	7	0.181	54.1
MARK 29F	VC	1	J-25	O <sub>2</sub> /H <sub>2</sub>	10,810	28,000	10.6	1288	1200	889	7.30	0.161	56.1
MARK 29-0 (MOD MK-16/O)	VC	1	J-25	O <sub>2</sub> /H <sub>2</sub>	3,283	9,050	15.6	613	740	100	2.68	0.119	46.0
H-1/O	VC	1	H-1	O <sub>2</sub> /H <sub>2</sub>	24,866	3,530	33.0	508	763	194	1.82	0.12	54.0
H-1/F	VC	1	H-1	O <sub>2</sub> /H <sub>2</sub>	74,138	12,861	23.18	1310	1000	904	3.87	0.19	65.0
MARK 38 (HPOTF)	REACT.	2	SSME	O <sub>2</sub> /H <sub>2</sub>	26,700	31,200	10.08	1374	1107	5848	1.552	0.308	0.768 (T-T)
MARK 38 (HPFTP)	REACT.	2	SSME	O <sub>2</sub> /H <sub>2</sub>	76,700	38,000	10.19	1589	1468	5916	1.68	0.357	0.791 (T-T)
MARK 48-0	IMPULSE PARTIAL ADMISS.	1	ASE	O <sub>2</sub> /H <sub>2</sub>	858	70,000	4.7	1435	1414	3368	1.424	0.343	0.588
MARK 48F	REACT.	2	ASE	O <sub>2</sub> /H <sub>2</sub>	2,543	95,000	3.5	1451	1400	3420	1.443	0.483	0.74 (T-T)

## NOTES

VC - VELOCITY COMPOUNDED, 2 ROW

PC - PRESSURE COMPOUNDED

D<sub>m</sub> - PITCH DIAMETER  
U<sub>m</sub> - PITCHLINE VELOCITYPR - PRESSURE RATIO  
U<sub>m</sub>/C<sub>0</sub> - VELOCITY RATIO

Table 2.1 (Cont'd) Design Parameters of Rocketdyne Turbines



## 2. SSME TURBOMACHINERY DESCRIPTION

SSME requirement of high discharge pressures necessitate high pump rotating speeds to operate with good efficiencies while keeping the pump weight and sizes to a minimum. Suction performance requirements, however, limit the pump speed. Thus performance requirements in SSME are achieved through a low pressure pump and a high pressure pump for each propellant. The low pressure pumps which operate at low pump speeds consistent with low suction pressures, boost the propellant pressures such that high pressure props operate at optimum speeds. The turbomachinery in relation to other engine components are shown in Fig. 2.6.

### Low Pressure Oxidizer Turbopump (LPOTP)

The low pressure oxidizer turbopump is fixed mounted to the vehicle. The low pressure oxidizer turbopump (Fig. 2.7) is a compact and simple machine, consisting of a four bladed axial inducer driven by small diameter hydraulic turbine. The key performance parameters of the low pressure oxygen turbopump is shown in Fig. 2.7.

The pumped fluid and the drive fluid are both liquid oxygen. This results in operational safety and eliminates the need for a seal package, drain lines and purges. The oxygen which drives the turbine comes from high pressure turbopump discharge, and is returned to the main flow stream by being exhausted into the low pressure pump discharge, which then is routed to the high pressure oxidizer turbopump inlet.

The pump and the turbine are both contained in a single case aluminum housing. The inducer is machined of K-Monel and a K-Monel liner is used to protect the aluminum housing from tip cavitation damage. The inducer is driven by a full admission six stage hydraulic turbine. The turbine flow is introduced into the distribution manifold, and routed through the passages in the pump diffuser vanes to the first stage nozzle. After passing through the turbine, the flow is reunited, via volute collection scroll with the inducer discharge and returned to high pressure main pump inlet. The turbine rotor

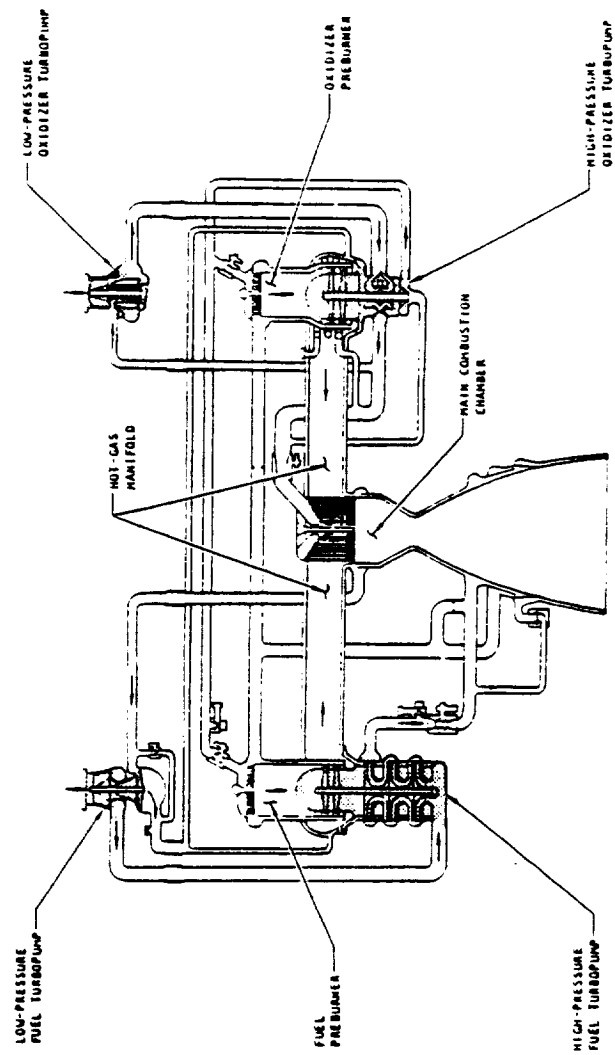
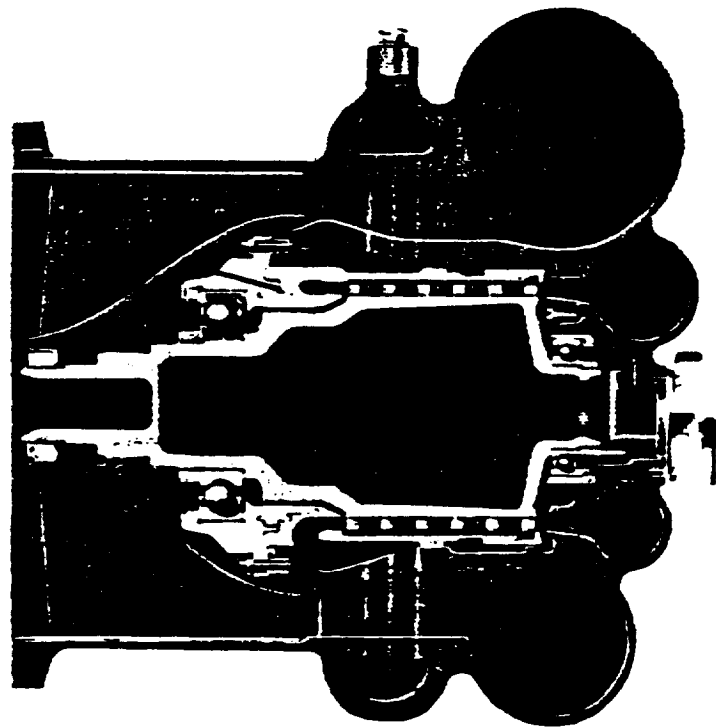


Fig. 2.6 Schematic Arrangement of SSME Turbomachinery



KEY PERFORMANCE PARAMETERS		
	RPL	FPL
PUMP INLET FLOWRATE (LB/SEC)	887.5	969.3
PUMP INLET PRESSURE (PSIA)	100.0	100.0
PUMP DISCHARGE PRESS (PSIA)	410.8	430.7
PUMP EFFICIENCY	.632	.615
TURBINE FLOWRATE	181.1	192.0
TURBINE INLET PRESSURE (PSIA)	4114.0	4594.3
TURBINE INLET TEMP (DEG R)	192.2	195.8
TURBINE PRESSURE RATIO	—	—
TURBINE EFFICIENCY	.644	.644
TURBINE SPEED (RPM)	4968.4	5252.0
TURBINE HORSEPOWER	1609.5	1919.5

Fig. 2.7 SSME Low Pressure Oxidizer Turbopump (LPOTP)

blades and shafts are machined integrally from K-Monel which was selected for its superior nonsparking, oxidization resistance, and cavitation damage resistance characteristics.

The turbine nozzles are retained in an Inco 718 cylindrical barrel which is secured to the primary housing. The nozzles are made in three 120-degree segments of a cylindrical shell and are joined to form a complete cylinder over the rotor prior to installation. The nozzles are aligned and secured by cylindrical barrel.

The primary housing supports the turbine inlet manifold. The turbine inlet flow is routed into the constant velocity distribution passage from which it flows inwards through the eleven diffuser vanes into the turbine manifold.

The rotor is supported by two liquid oxygen cooled ball bearings. The turbine end bearing coolant path is from the last stage of turbine, through the bearing, hollow rotor, radial holes in the rotor, and to the inducer discharge. Coolant for the inducer end bearing is from the turbine inlet, through the labyrinth seal, through the bearing and to the inducer discharge.

A redundant element magnetic tape speed inducer is installed on the turbine end of the turbopump housing.

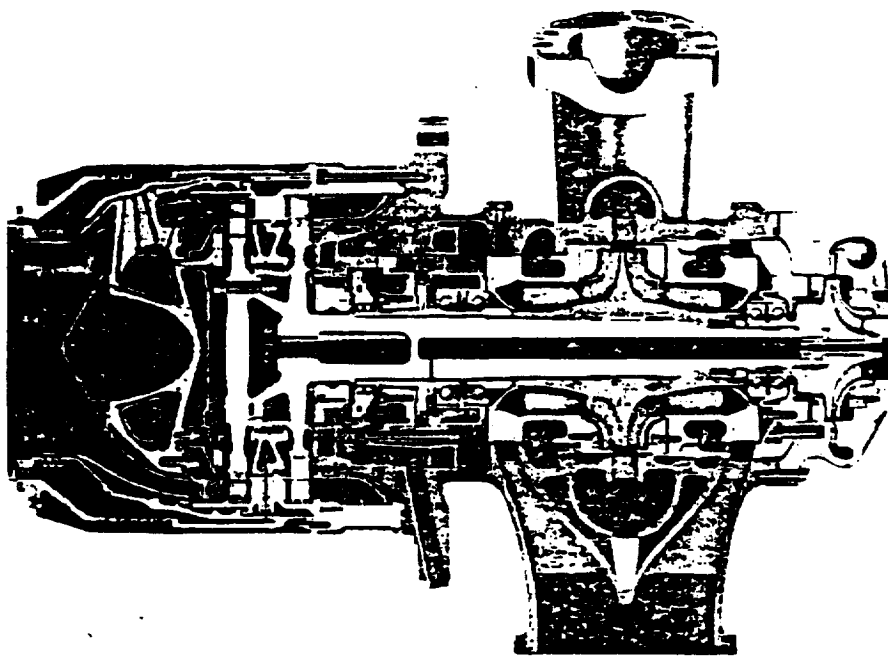
#### High Pressure Oxidizer Turbopump (HPOTP)

The high pressure oxidizer turbopump receives the oxidizers from the low pressure oxidizer turbopump and boosts the pressure to sufficient level to supply the oxidizer to the thrust chamber, low pressure oxidizer turbopump turbine, the heat exchanger and the preburners. The turbopump assembly consists of three major elements: 1) main pump, 2) preburner pump, and 3) turbine. Because of the safety hazards inherent in the oxidizer pumping machinery, safe operation is achieved through careful attention to design details. It includes the use of oxidization resistant materials, positive rotor operating clearances, elimination of fretting and positive separation of oxygen and hydrogen rich gas.

The HPOTP (Fig. 2.8) has a single inlet with a 50-50 flow split into a double entry, common outlet impeller. The liquid oxygen enters the main pump through the main pump housing where the flow split is made. Inlet vanes direct the flow to the inducer/impeller inlet guide vanes, which in turn direct the flow to the flow to inducer/impeller inlet. There are four inducer blades and four full and four partial impeller blades on each side of the combined inducer/impeller. After passing through the impeller, the flow is redirected into discharge volute by diffuser vanes. The main impeller/inducer is made of Inconel 718.

Since only 10% of oxidizer flow needs to be delivered at the higher preburner pressures, a substantial saving in total power requirement and engine pump weight is achieved through the use of preburner pump stage. The preburner pump receives only the preburner flow from the main pump discharge via an engine duct, and boost the pressure to meet the inlet pressure requirements. The preburner pump has a single entry impeller made of Inconel 718 that discharges oxidizer through diffuser vanes into discharge volute. The preburner pump housing is flange mounted to the main housing.

Turbopump shaft bearings are cooled by liquid oxygen from the preburner pump. Coolant flow for the pump-end bearings is through the preburner pump impeller hub labyrinth seal, through the bearings, and to the main pump inducer/impeller inlet. The turbine-end bearings coolant flow is through the preburner impeller bolt, through the hollow shaft, through the bearings, and to the main pump inducer/impeller inlet. Pump shaft axial thrust is balanced in that the double-entry main inducer/impeller is inherently balanced and the thrusts of the preburner pump and turbine are equal but opposite. Residual shaft thrust is controlled by a self-compensating, non-rubbing, balance piston which utilizes orifices located at the tip and inner diameter of the main shrouds to control the leakage and, consequently, the pressure acting on the respective shrouds. Mixing of oxidizer and turbine gas is prevented by a dynamic shaft seal package that is between the main pump and the turbine. The seal package consists of a labyrinth-type primary oxidizer seal, a purged controlled-gas intermediate seal, and two controlled-gap turbine hot-gas seals. Drain cavities with overboard drain lines are located between the



KEY PERFORMANCE PARAMETERS			
	RPL		FPL
	MAIN	BOOST	MAIN   BOOST
PUMP INLET FLOWRATE (LB/SEC)	1068.5	106.5	1161.2   122.0
PUMP INLET PRESS (PSIA)	376.7	4172.8	390.3   4647.9
PUMP DISCHARGE PR (PSIA)	4290.8	7279.8	4793.3   8078.0
PUMP EFFICIENCY	.681	.803	.678   .809
TURBINE FLOWRATE (LB/SEC)		63.6	
TURBINE INLET PR (PSIA)		4963.6	
TURBINE INLET TEMP (DEG R)		1392.9	
TURBINE PRESS RATIO		1.511	
TURBINE EFFICIENCY		.733	
TURBINE SPEED (RPM)		28349	
TURBINE HORSEPOWER		23973	
			5569.9   1499.7   1.546   .772   30.381   29471

Fig. 2.8 SSME High Pressure Oxidizer Turbopump (HPOTP)

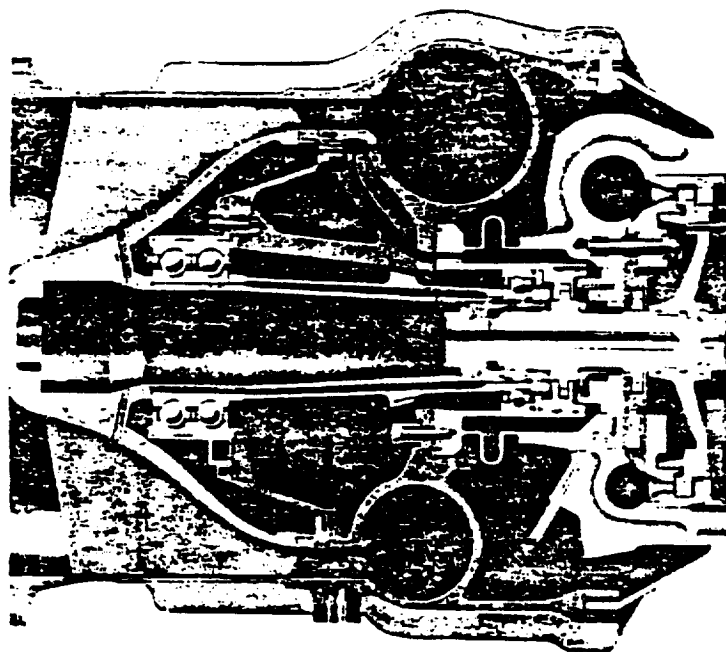
primary oxidizer seal and the intermediate seal, between the intermediate seal and secondary turbine seal, and between the secondary and primary turbine seals. To further ensure against the mixing of oxidizer and turbine gas, a helium purge is applied between the elements of the intermediate seal during engine operation.

The high pressure oxidizer turbopump turbine, which is a two stage turbine is powered by hot gas (hydrogen rich steam) generated by the oxidizer preburner. That gas enters the turbine and flows across shielded support struts, through the first and second stage nozzles and blades, and is discharged into the hot gas manifold. The nozzles are made of conventionally cast MAR-M-246 material and turbine blades are made out of directionally solidified MAR-M-246 (Hf). The turbine rotors are mated through curvic coupling and are held together with a circle of bolts. The second stage rotor is integral with the pump shaft. Turbine blade bypass is minimized by lands in the outer perimeter of blade shrouds that run against honeycomb seals in the turbine housing. The HPOTP is flange attached to the hot-gas manifold and is canted 10 degree angle out of the engine centerline.

#### Low Pressure Fuel Turbopump (LPFTP)

The low pressure fuel turbopump is a compact simple machine which operates at low inlet pressures and boost the pressure to a sufficient level such that high pressure fuel turbopump (HPFTP) can operate efficiently. Both the pumped fluid and turbine drive gas are hydrogen resulting in operational safety. The turbopump assembly (Fig. 2.9) consists of an axial inducer driven by a two stage turbine. The turbine gaseous hydrogen comes from main combustion chamber coolant pass.

The inducer and the shaft are supported by three liquid hydrogen cooled ball bearings. The bearing coolant is the leakage from the inducer discharge labyrinth seal. The coolant flow through the pump end bearings and turbine bearing and is returned to the pump inlet through passages in the shaft, bearing-bearing spacer and inducer. The inducer and turbine blade are made of corrosion resistance A-286 steel.



KEY PERFORMANCE PARAMETERS		
	RPL	FPL
PUMP INLET FLOWRATE LB/SEC	147.9	161.1
PUMP INLET PR PSIA	30.0	30.0
PUMP DISCH PR PSIA	261.8	282.6
PUMP EFFICIENCY	.674	.679
TURBINE FLOWRATE LB/SEC	28.7	32.2
TURBINE INLET TEMP R	459.	455.
TURBINE PRESSURE RATIO	1.30	1.32
TURBINE EFFICIENCY	.536	.530
TURBINE SPEED RPM	15370.	16249.
TURBINE HORSEPOWER	3003.	3536.

Fig. 2.9 SSME Low Pressure Fuel Turbopump (LPFTP)



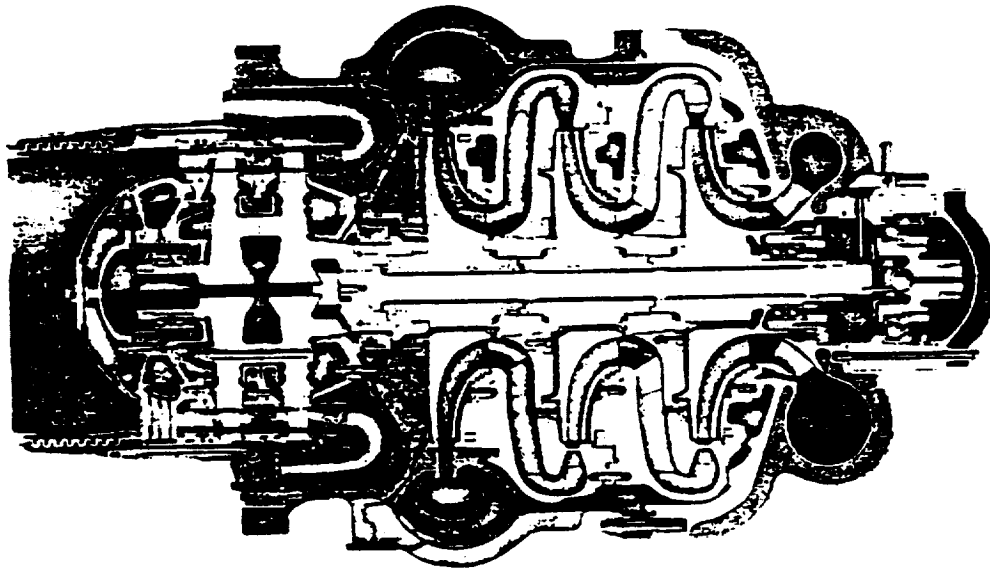
### High Pressure Fuel Turbopump (HPFTP)

The high pressure fuel turbopump (Fig. 2.10) receives the flow from the low pressure fuel turbopump and boosts the pressure to the level required for preburner supply through the main fuel valve and through thrust chamber assembly coolant circuit. The turbopump consists of three stage centrifugal pump driven by two stage reaction turbines. The HPFTP develops some 70% of the total turbomachinery power.

The titanium inlet receives the flow from the low pressure fuel pump discharge duct and directs it to the inlet of the first stage impeller. Fuel flows in series through the three impellers from pump inlet to outlet, with flow being redirected between impellers by interstage diffusers. The interstage diffusion is efficiently accomplished within the turbopump housing. The flow from first and second stage impeller is passed through radial vanes, turned 180 degrees, then turned inward and further diffused by tandem set of vanes for entry into next stage impellers. The flow from third stage impeller is diffused by a like set of radial vanes, then collected in volute for delivery to the high pressure fuel system. The impellers are made of titanium alloy, the diffusers are made of aluminum alloy and the turbine housing is made of Inconel 718.

Coolant flow across the pump end bearings is provided by the first stage impeller backplate wear-ring flow. The coolant is returned to the inlet of the first stage impeller. Coolant flow to the turbine end bearing is supplied from the pump balance piston cavity through the shaft static lift-off seal.

Axial rotor thrust is controlled by a balance piston feature (Fig. 2.11). The balance piston operates between a high pressure orifice and a low pressure orifice and absorbs the rotor axial forces so that bearings operate at all times with only preloads. Any unbalanced load which tends to move the rotor towards the inlet reduces the high pressure orifice area, thus, reducing the pressure in the balance piston cavity between orifices. The higher differential pressure across the piston restores equilibrium. Similarly, an unbalanced force towards the turbine increases the high pressure orifice area



KEY PERFORMANCE PARAMETERS		
	RPL	FPL
PUMP INLET FLOWRATE LB/SEC	148.4	161.7
PUMP INLET PR PSIA	204.1	214.0
PUMP DISCH PR PSIA	6254.8	7036.8
PUMP EFFICIENCY	.758	.757
TURBINE FLOWRATE LB/SEC	147.5	164.0
TURBINE INLET TEMP R	1898.4	1989.2
TURBINE PRESSURE RATIO	1.522	1.558
TURBINE EFFICIENCY	.770	.780
TURBINE SPEED RPM	34931.	37076.
TURBINE HORSEPOWER	63288.	77142.

Fig. 2.10 SSME High Pressure Fuel Turbopump (HPFTP)

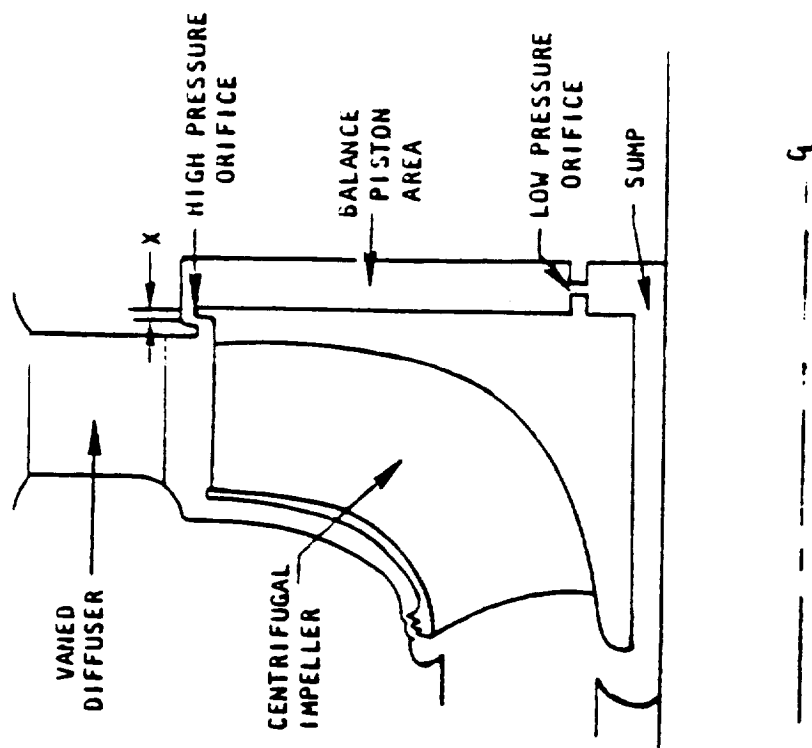


Fig. 2.11 Balance Piston Design Concept

and reduces the low pressure orifice area; the increase in cavity pressure reduces the balance piston force and restores equilibrium.

The HPFTP turbine is powered by hot gas generated by the fuel preburner. Hot gas enters the turbine and flows across the shielded support struts, through first and second stage nozzles and blades is discharged into hot gas manifold. The two stage turbine transmits the torque to the pump by a splined coupling between the second stage wheel and the pump third stage impeller. Turbine to FPB sealing is accomplished by a bellows that loads a Naflex seal against the FPB flange and the whole pump is canted out from the engine centerline at a 10 degree angle.

### 3. Blade Geometry Description:

The major geometrical features in a turbine blade include (Fig. 2.12):

- 1) Shroud
- 2) Airfoil
- 3) Platform
- 4) Shank
- 5) Fixture
- 6) Damper Pockets
- 7) Cooling Passages

All the features may or may not be present in a single blade. The airfoil design deals with the development of blade profile that will develop the required gas path vector diagram relationships and pass the working fluid mass flow at design operating conditions (Fig. 2.13). Numerous geometrical design parameters (Fig. 2.14) are used to evolve design blade profiles. Circular arcs and straight lines can be used to define the airfoil shape as was the case with rotors of Mark 3, Mark 4, and Mark 15 turbines. Turbine airfoils are also designed with tangent parabola curves which introduce more gradual curvature change thereby lessening the potential for suction surface separation. Elliptical leading edges and conic curves were used in SSME and other subsequent designs.

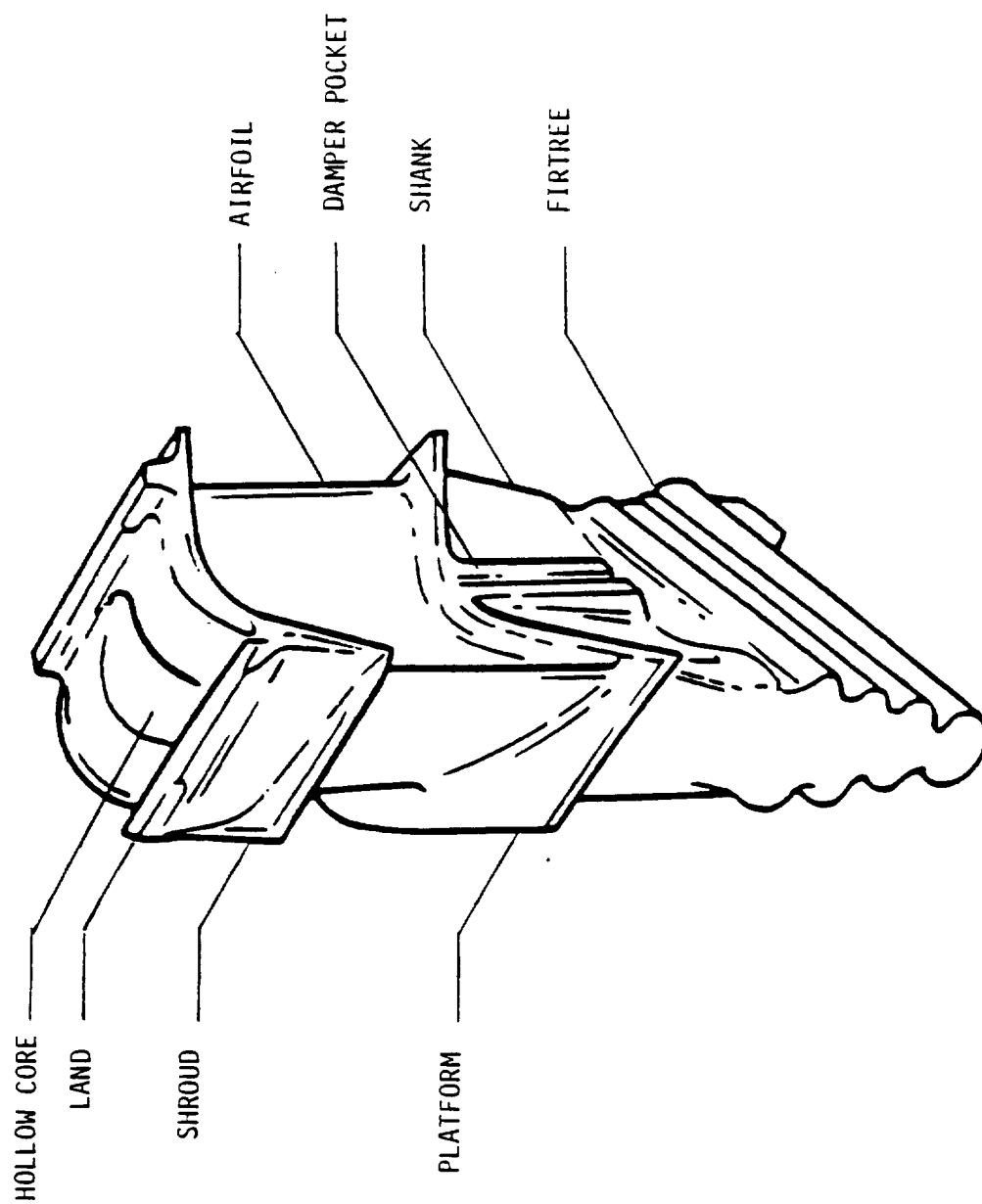


Fig. 2.12 Turbine Blade Geometry Description

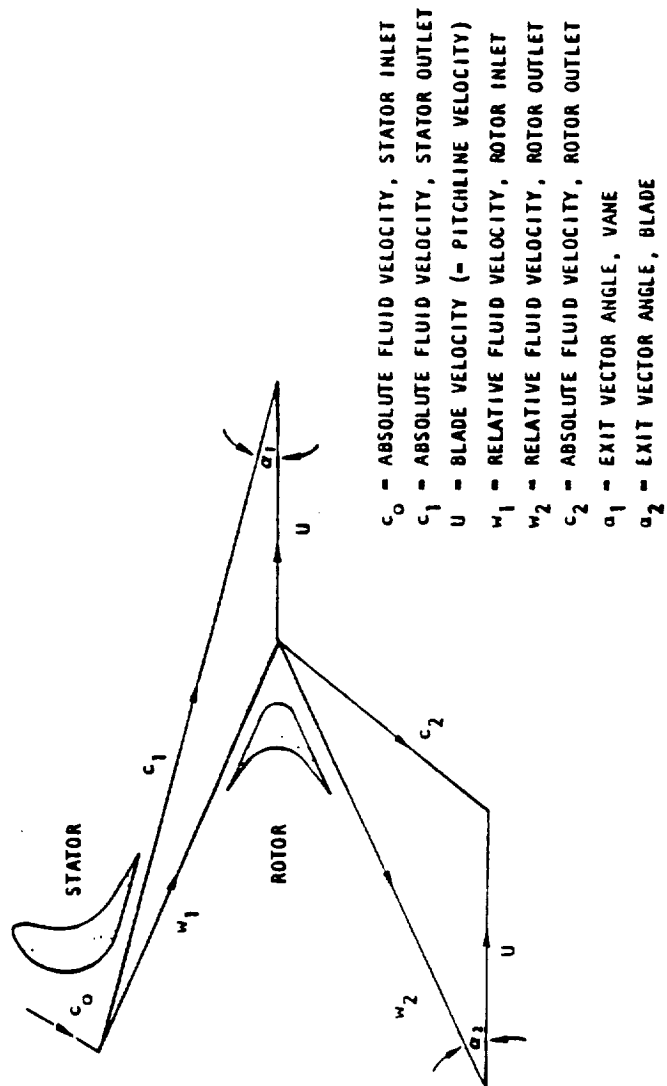


Fig. 2.13 Turbine Velocity Diagram

$p$	Pitch
$b$	Axial width
$o$	Throat opening
$r_1$	Leading-edge radius
$r_2$	Trailing-edge radius
$\phi$	Chord angle
$\beta_{1p}$	Inlet angle (pressure surface)
$\beta_{1s}$	Inlet angle (suction surface)
$\beta_1$	Blade inlet angle
$\Delta\beta_1$	Leading-edge divergence
$\beta_{2p}$	Discharge angle (pressure surface)
$\beta_{2s}$	Discharge angle (suction surface)
$\beta_2$	Blade discharge angle
$\Delta\beta_2$	Trailing-edge divergence
$p/b$	Pitch-width ratio
$o/p$	Opening coefficient
$\alpha_2$	Exit vector angle = $\arcsin(o/p)$
$\Theta$	Blade deflection angle = $180^\circ - (\beta_1 + \alpha_2)$
$t_1$	Leading-edge thickness = $2r_1$
$t_2$	Trailing-edge thickness = $2r_2$
$c_e$	Edge coefficient = $o/(o + t_2)$

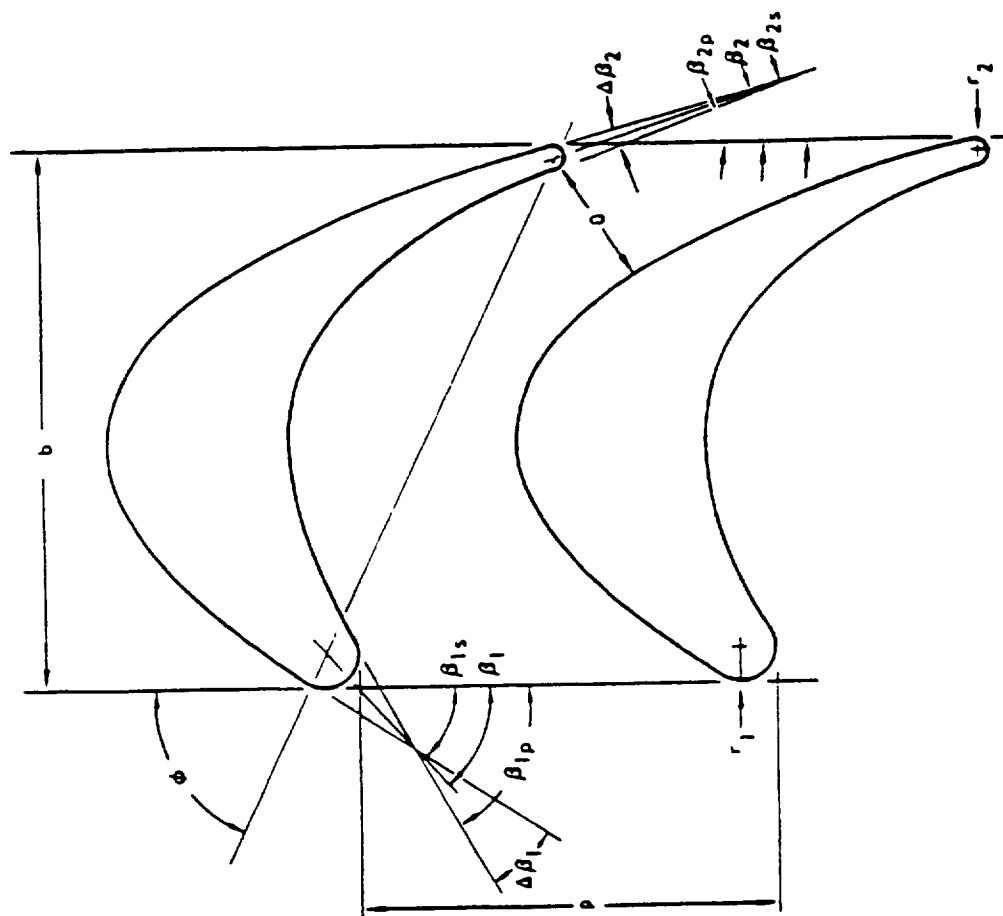


Fig. 2.14 Nozzle, Vane and Blade Design Parameters

## Blade Twist

Blading losses resulting from root-to-tip velocity (and flow) variations in parallel-sided blades with constant entrance and exit angles are minimized when the blading is designed for radial-equilibrium conditions. Parallel-sided blades normally are developed with state conditions and vector quantities that exist at the pitch line. In reality the blading experiences velocity changes that affect the vector diagram at all radii away from the pitch diameter. Past experience with both supersonic and subsonic turbines indicates that this variation is not significant in typically short, untwisted blading; no blading redesigns have been required to correct for effects of blade radial velocities and static-pressure gradients.

However, all state-of-the-art high performance blades that are longer than one inch in height are designed to comply with requirements for radial equilibrium, viz., the product of blade radius  $R$  and the respective tangential velocity  $c_{u1}$  is constant at all radii along the blade length:

$$Rc_{u1} = \text{constant}$$

This condition is based on the assumption that stagnation temperature and pressure are constant at all radii and that equal quantities of working-fluid energy are available along the length of the blade to develop a uniform work output. Flow conditions are in radial equilibrium along the entrance and discharge of each blade. The free-vortex blade profile that results is twisted from root to tip and provides for more turning at the blade root than at the tip, as illustrated in Fig. 2.15. Note that the pictured blade design is tapered; radial equilibrium can be applied to either tapered or straight blading.

## Blade Shrouding

Experimental data indicates that turbine rotors with shrouds, when compared to unshrouded blade designs, offer an efficiency advantage. The performance



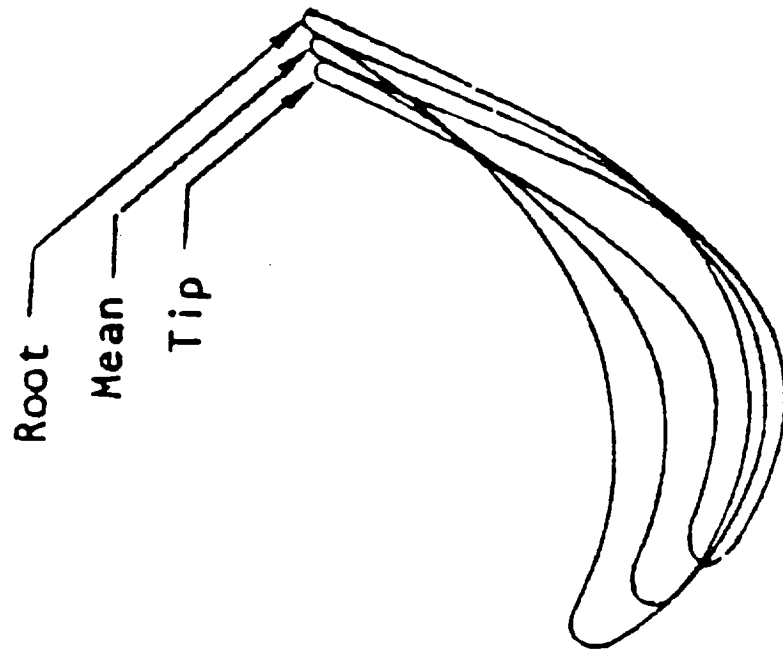


Fig. 2.15 Twist in the Blades Designed for Radial Equilibrium

advantage is attributed to the reduced amount of leakage. In some turbine designs, shrouds are used for structural damping purposes. In SSME HPOTP, shrouds are used to increase the performance as well as for mounting two lands facing the honeycomb seal.

#### Blade Platform

The blade platform performs the function similar to the shrouds by minimizing leakage losses. In addition they are generally fitted with damper pockets which support precision dampers. Dampers are used to reduce the blade stresses due to mechanical vibration. The turbine blades in both the HPOTP and HPFTP of SSME have platforms.

#### Blade Shank

The main purpose of the blade shank is to give a smooth transition between the airfoil and the fir tree mounting of the blade. The two crosssections between which the shank spans have crosssections which have widely varying curvature. Shanks also serve the dual purpose of supporting blade dampers. Shanks are not present in blades that are integrally machined or welded to the disk.

#### Fir Tree

The fir tree mechanical blade attachment to the disk has been used for most of the production turbines for high thrust engines (Fig. 2.16). The fir tree geometry varies from configurations with two or three relatively large lobes to configurations containing a large number of small lobes. The geometry and tolerances of the fir tree are adjusted to distribute the load between the lobes. The fir tree manufacturing tolerances are very tight in the order of 0.0005 in the loaded side and .002 in the unloaded side.

#### Cooling Passages:

For future high performance space vehicles, high temperature turbines offer an attractive way of increasing engine performance. While cooled turbine blades

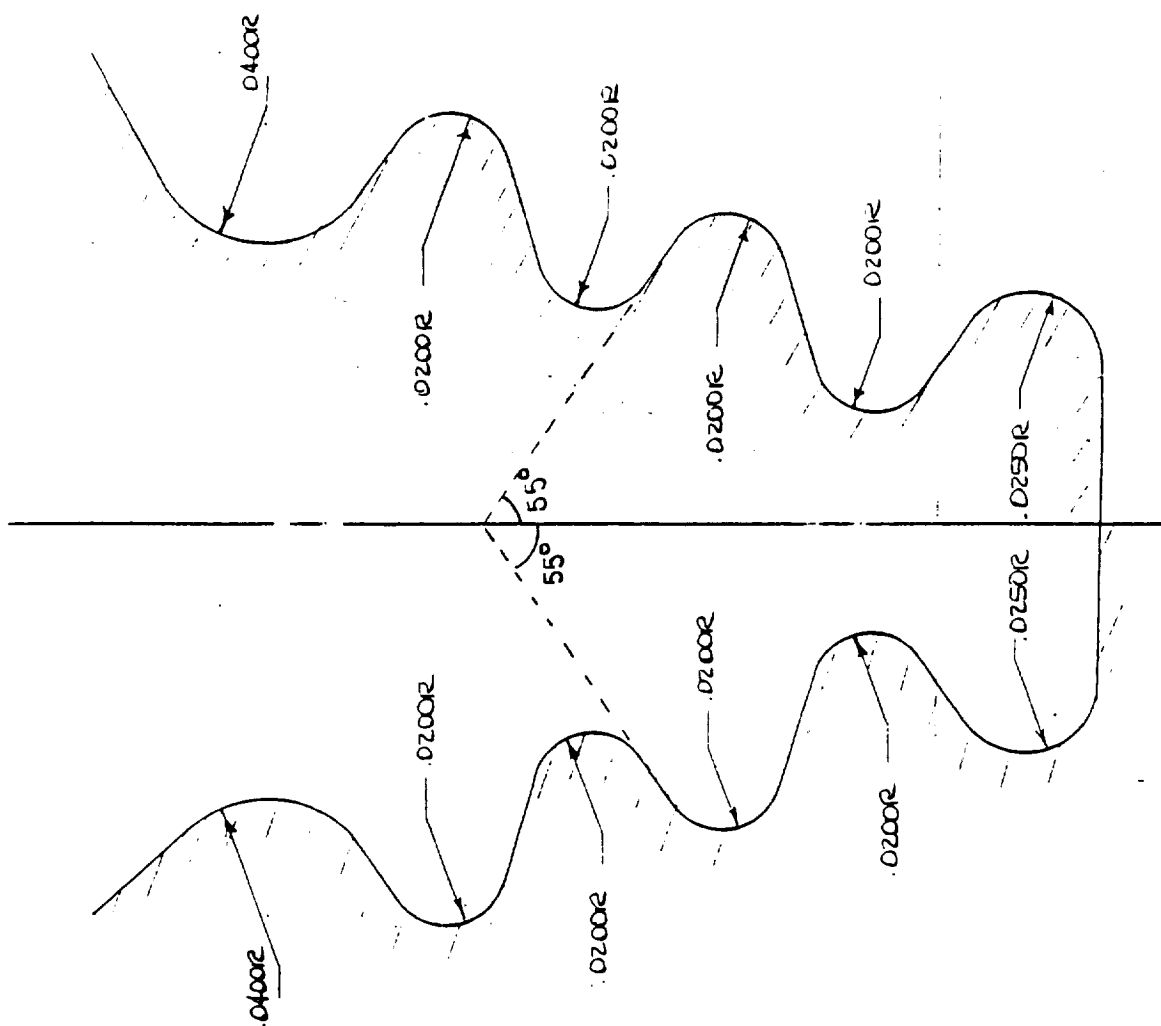


Fig. 2.16 Fir-tree Design of the J2-S Turbine Blade

have been used extensively in air breathing engines, they have not been used up to now in rocket engines. Since there is potential for cooled turbine blade designs in future rocket engines, the possible geometrical features of a cooled rocket engine turbine blade are presented here. The actual cooled blade geometry is a function of type of cooling used. The various cooling schemes that can be used include, convective cooling, film and transpiration cooling, impingement cooling and convective impingement cooling. Some of these cooled blade concepts are schematically represented in Fig. 2.17 through Figure 2.18.

#### Comparison of Blade Geometry

Turbine blades are designed to meet a specific set of operating requirements in its respective turbine gas path. Thus the turbine blades geometrical characteristics can vary widely. Of the many rocket engines developed to date, sizing data for a representative rocket turbine appear in Table 2.2. Of significance to note are the variation in pitch diameter, blade height and width.

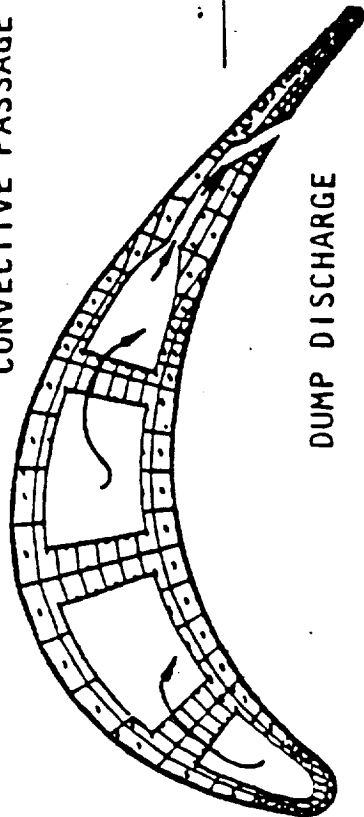
#### 4. Loading Environment

The major load types that are present in the turbine blades are

- 1) Centrifugal loads
- 2) Gas bending loads
- 3) Temperature loads

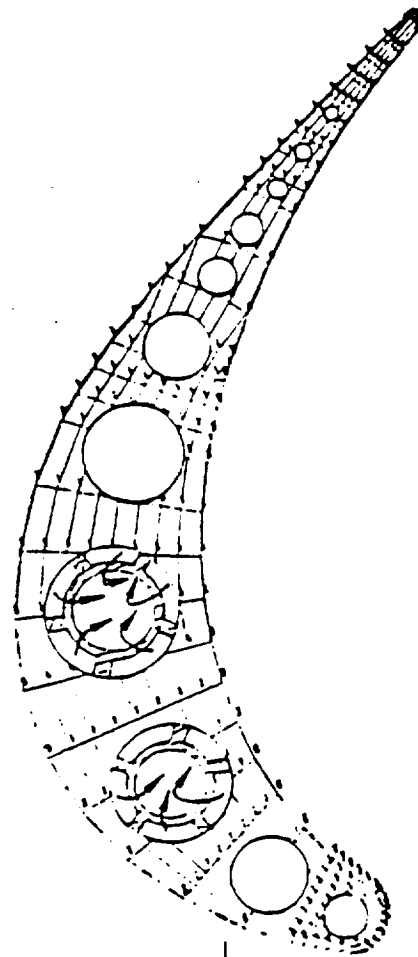
The turbine blades design loads are determined for the maximum required power conditions as specified in the engine performance prediction model. The engine model incorporates the performance characteristics of all rocket engine components. Thrust chamber, injector, valves, ducts, pumps, turbine, etc. to predict the operating conditions for each component. The maximum turbine power conditions represent the highest values of speed, torque, flow, steady state inlet temperature and pressure drops for the turbine.

CONVECTIVE PASSAGE



Ribbed Multipass Cooled Blade  
with Trailing Edge Dumping

DUMP DISCHARGE



Hollow Blade with Variable Circular  
Cooling Holes with Inserts

Fig. 2.17 Cooled Blade Concepts with Convective Cooling

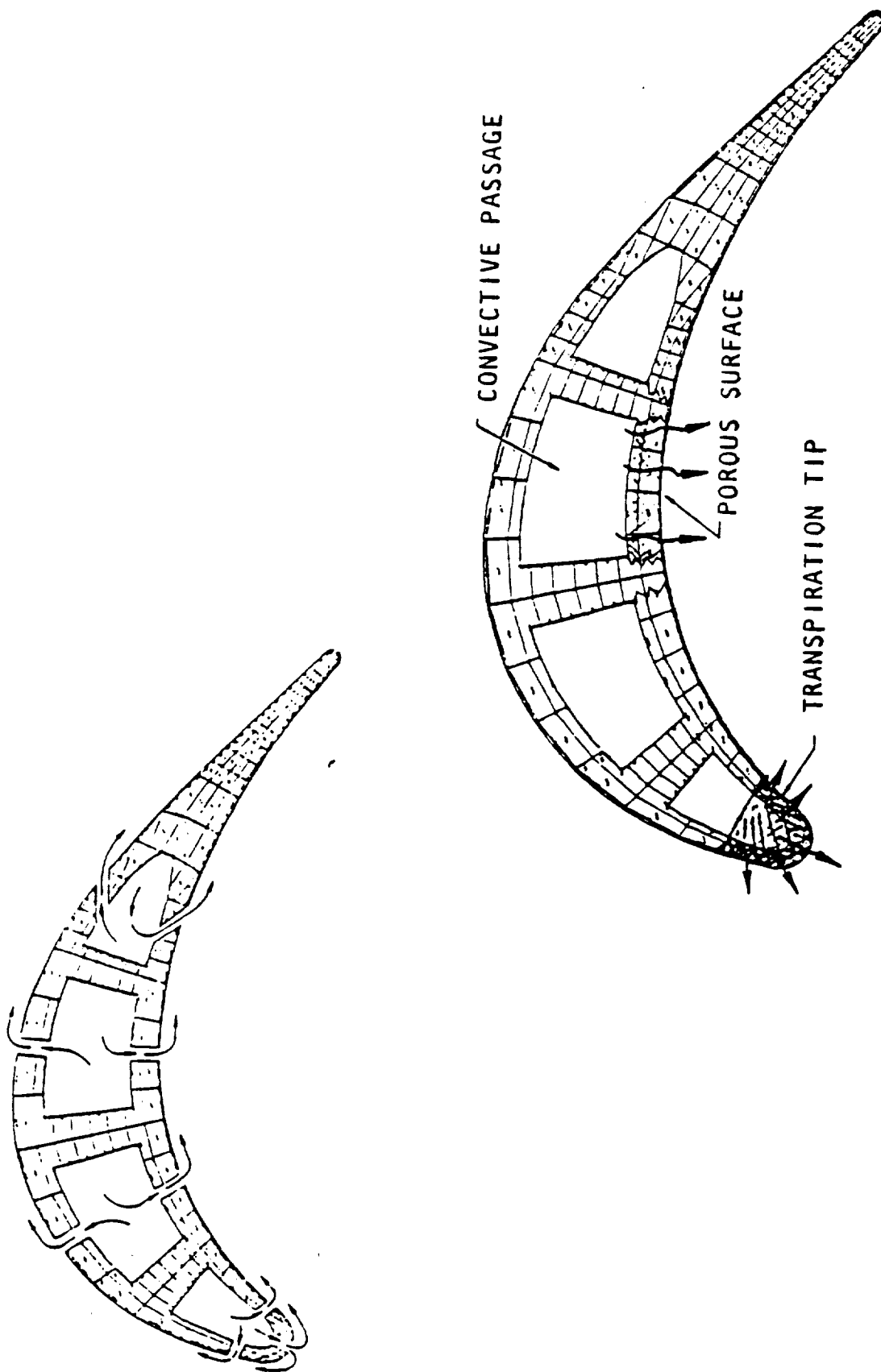


Fig. 2.18 Film and Transpiration Cooled Blade Design Concepts



### Centrifugal Loads

Rocket engine turbine pumps typically run at high speed to achieve maximum efficiency. The pitch line velocity can be up to 1700 ft/sec. The blades are generally tilted such that centrifugal bending stresses compensate for the power bending. The mission history profile for the speed of a turbopump follows very closely the power profile of the engine. A typical time history for HPFTP speed is shown in Figure 2.19. The HPOTP first and second stage blades have a hollow core to reduce the centrifugal stresses. For blades with high aspect ratio, the contribution of centrifugal stresses to stress stiffening can be significant enough to affect the frequencies of the blade. In general, the operating mean stresses in the turbine blades are mostly governed by the centrifugal stresses.

### Pressure Bending

The turbine aerothermodynamic design is performed using the turbine design gas path calculation. The gas path model includes representative blade row loss correlations as well as tip clearance and configuration losses, and other parasitic losses (Fig. 2.20). The model determines the turbine performance and geometry for the input overall and interstage design conditions to produce the highest efficiency within the structural and envelope limits. The design energy distribution between stages and blade rows and radially from hub to tip sets the overall blade row loads. These loads are distributed on the turbine blade as the pressures, temperatures, and torques on the upstream and downstream surfaces of the blade. The velocity vector diagrams (Fig. 2.13) indicate the resultant inlet and outlet velocities and flow angles from which the overall loading at a specific radius is calculated.

The design of each profile section is meant to satisfy the gas path performance requirements within the structural limits. The profile design is an interactive procedure using a blade profile design computer program to define a profile with gradual surface curvature to satisfy the design turning, flow and diffusion requirements. The defined profile suction and pressure surface distributions of velocity, pressure, and temperature are determined



764 HPFP SPD MFD

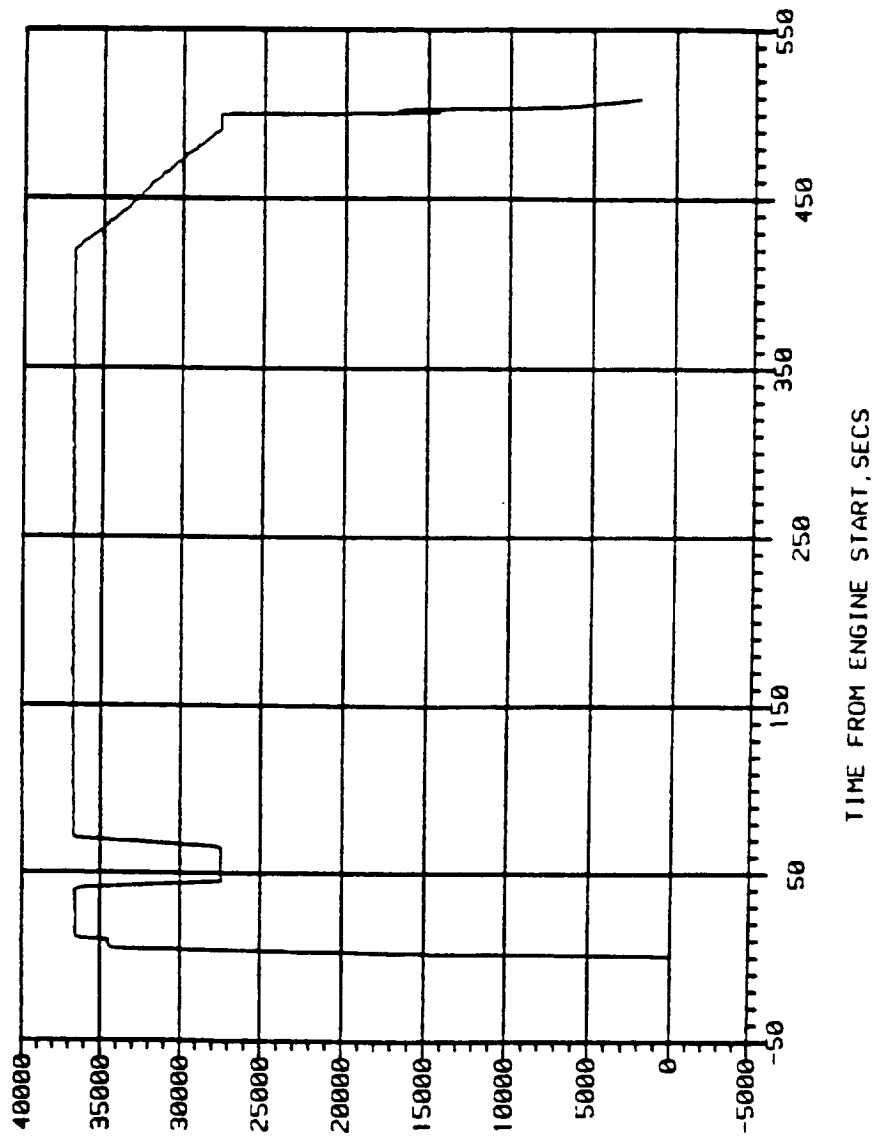
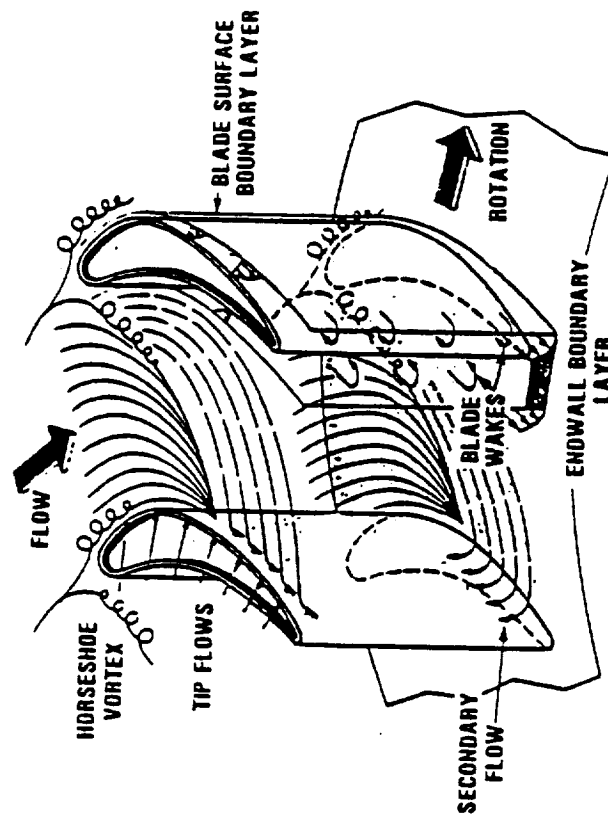


Fig. 2.19 Typical Mission History of HPFP Rotor Speed

## TURBINE BLADE ROW FLOW PHENOMENA



## FACTORS AFFECTING TURBINE EFFICIENCY

- EXPANSION ENERGY LOSSES
  - DEPENDENT ON BLADE TURNING AND WIDTH
  - REFLECTS LOSSES DUE TO FRICTION ALONG FLOW PATH DUE TO SECONDARY MOTIONS IN TURNING FLOW
- INCIDENCE LOSSES
  - RESULT FROM MISMATCH OF FLUID AND BLADE ANGLES
- MACH NUMBER LOSSES
- TIP CLEARANCE LOSSES
  - DEPENDENT ON CLEARANCE TO BLADE HEIGHT RATIO
- INTERSTAGE SEAL LOSSES

Fig. 2.20 Turbine Flow Phenomena and Potential Losses

using an exact, compressible blade to blade computer calculation. Fig. 2.21 shows a blade model indicating the blade streamline locations, one example of which is illustrated in Fig. 2.22. Fig. 2.23 and Fig. 2.24 show an example of the corresponding surface velocity and static pressure distributions. The detailed loading of the design profile at a streamline radius is shown by the surface distribution curves. The time history of pressures follow very closely the powerlevel requirement. A typical mission history profile of oxidizer preburner and fuel preburner chamber pressures are shown in Fig. 2.25 and Fig. 2.26 which is indicative of turbine inlet pressures.

### Temperature Loads

Rocket engine turbine blades see a severe thermal shock as opposed to air breathing engines due to severe start and cutoff transient. Rapid start of rocket engines is necessitated by a number of reasons. Some of the reasons for rapid start and cutoff include:

- 1) Slow start of soft systems results in the phenomenon called chugging.
- 2) Due to the high expansion ratio used in SSME (77.5:1) nozzle if the engine dwells below 92% powerlevel the resulting flow separation in the nozzle induces severe side loads.
- 3) To avoid the resonance problems associated with turbomachinery, the engines start and reach operating speeds quickly.
- 4) It is efficient from payload point of view to reach full powerlevel and liftoff.
- 5) Rapid cutoff to have control over correct orbital insertion.
- 6) A normal rapid cutoff also serves the abort sequence.

Operating temperatures of turbine blades in rocket engine turbopumps are primarily a function of hot gas flow and coolant if any is used. The

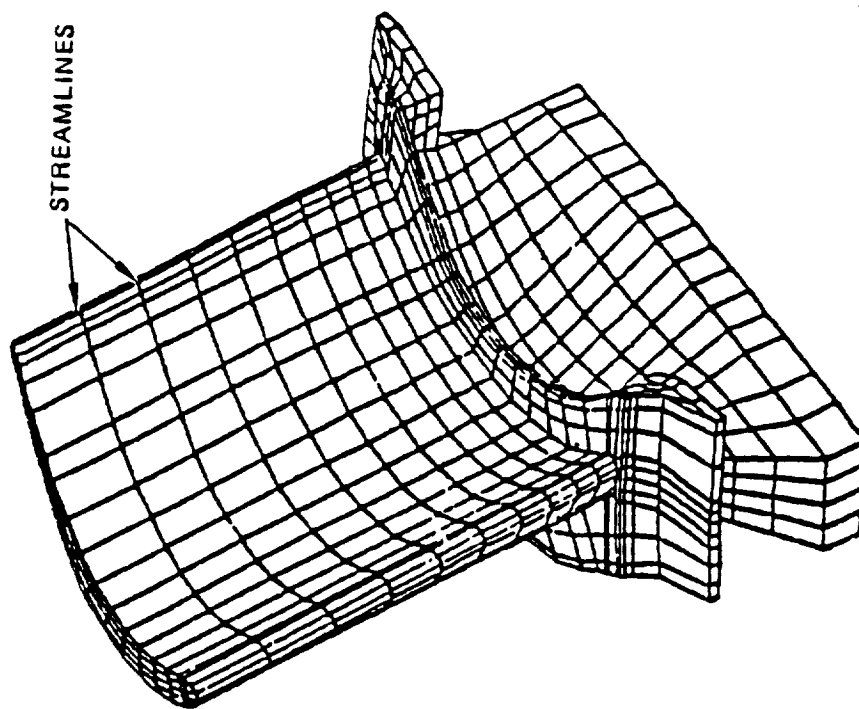
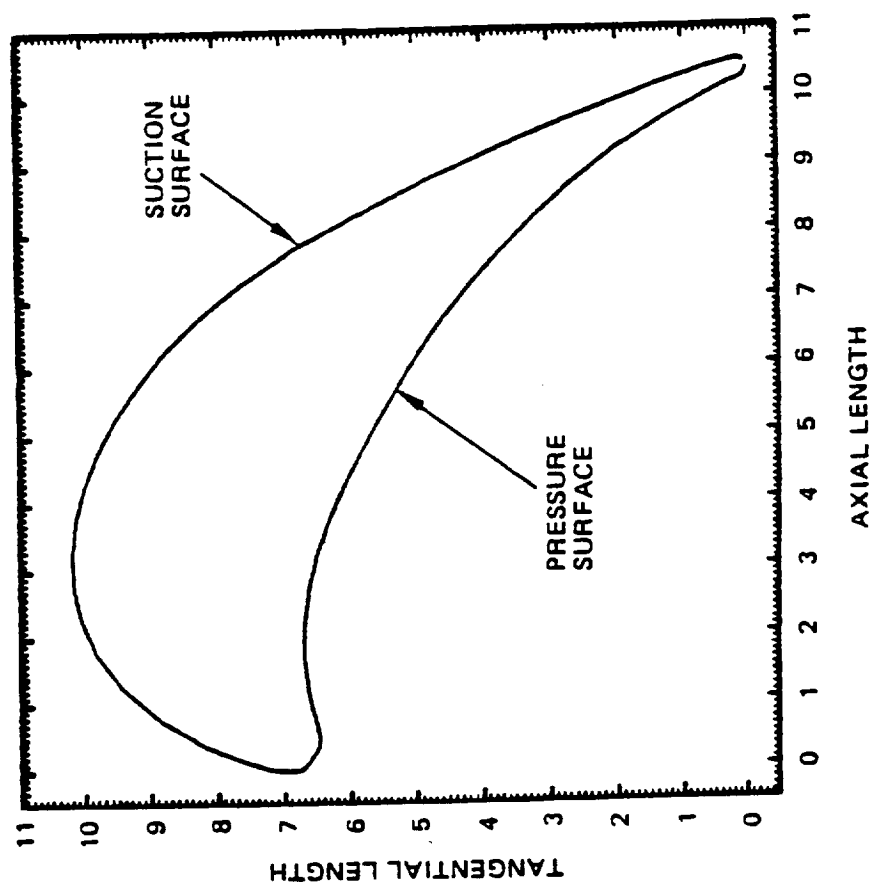


Fig. 2.21 Blade Finite Element Model Showing Stream Lines



Fig, 2.22 Typical Turbine Blade Stream Line Profile

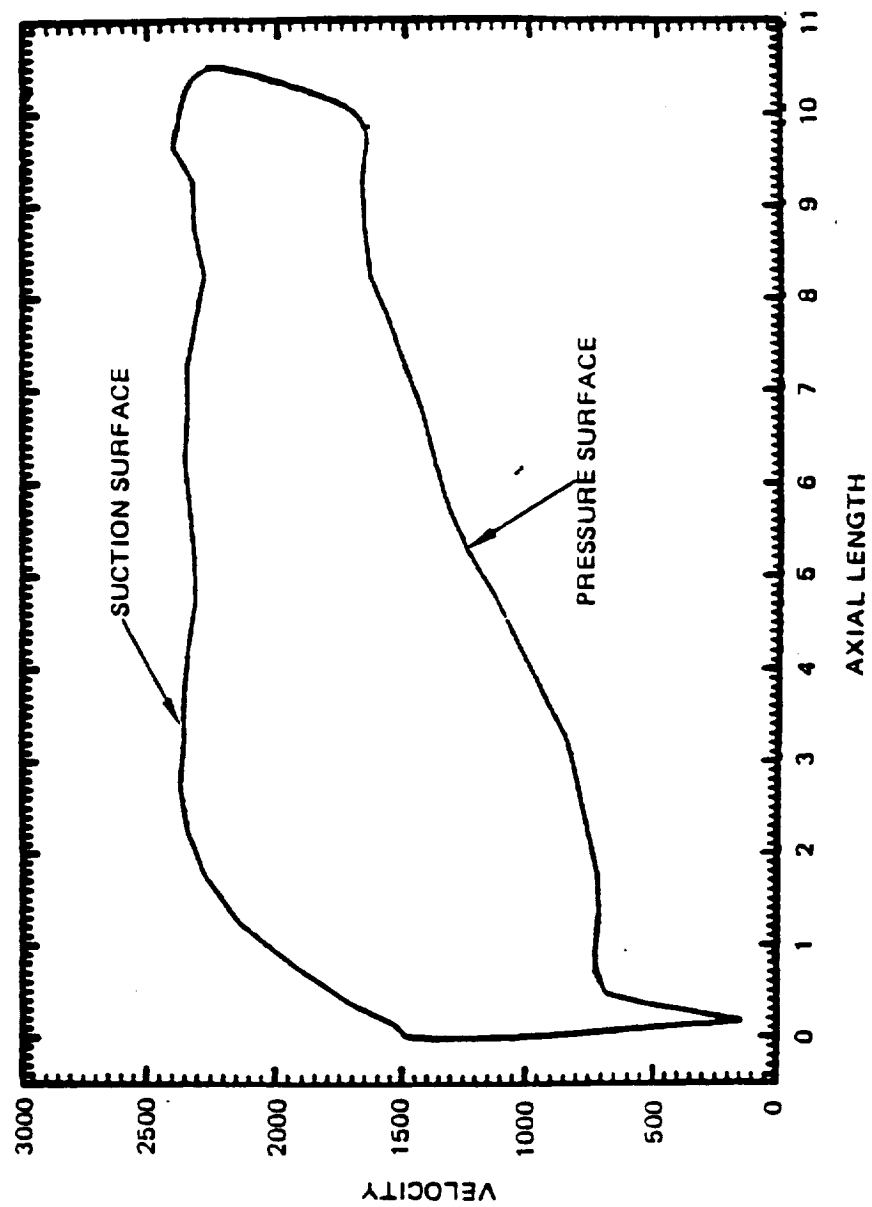


Fig. 2.23 Typical Turbine Blade Stream Line Velocity Profile

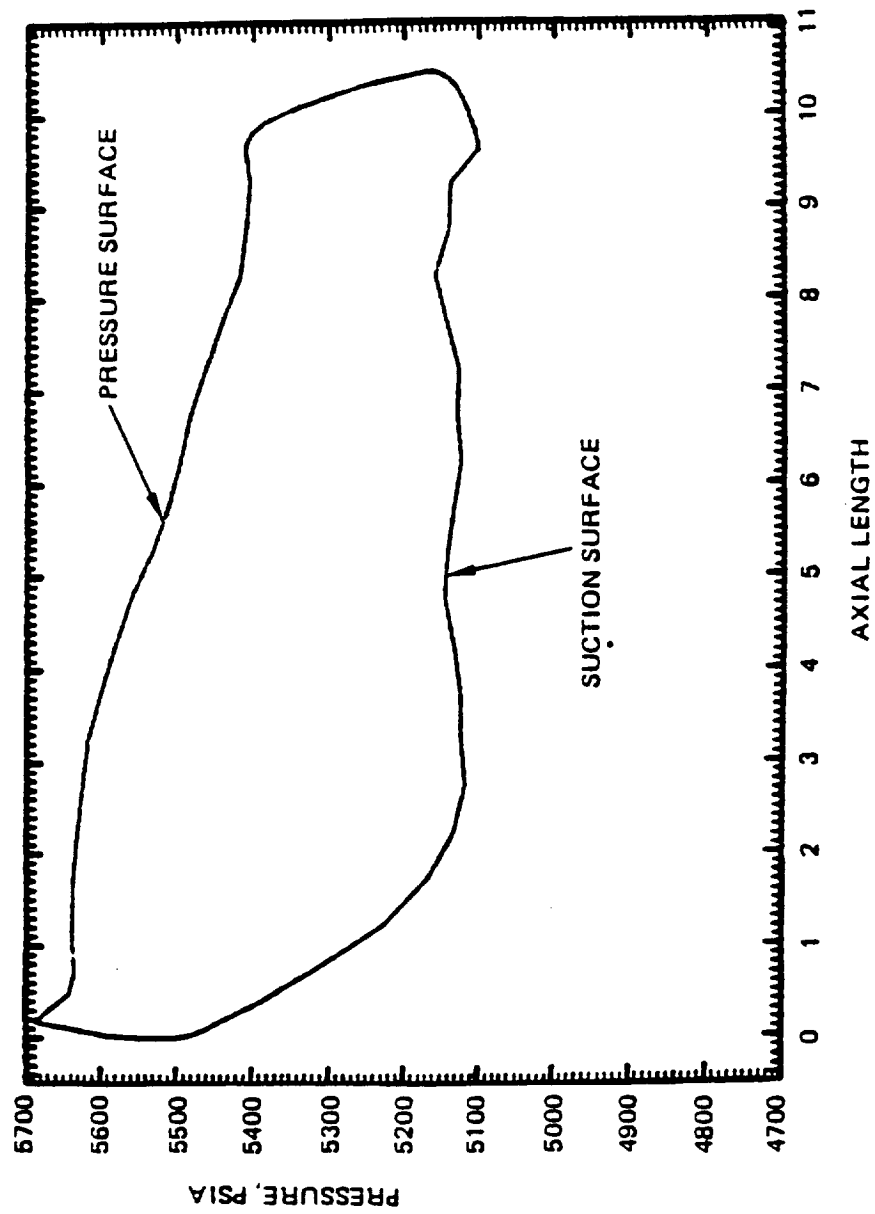


Fig. 2,24 Typical Turbine Blade Streamline Pressure Profile

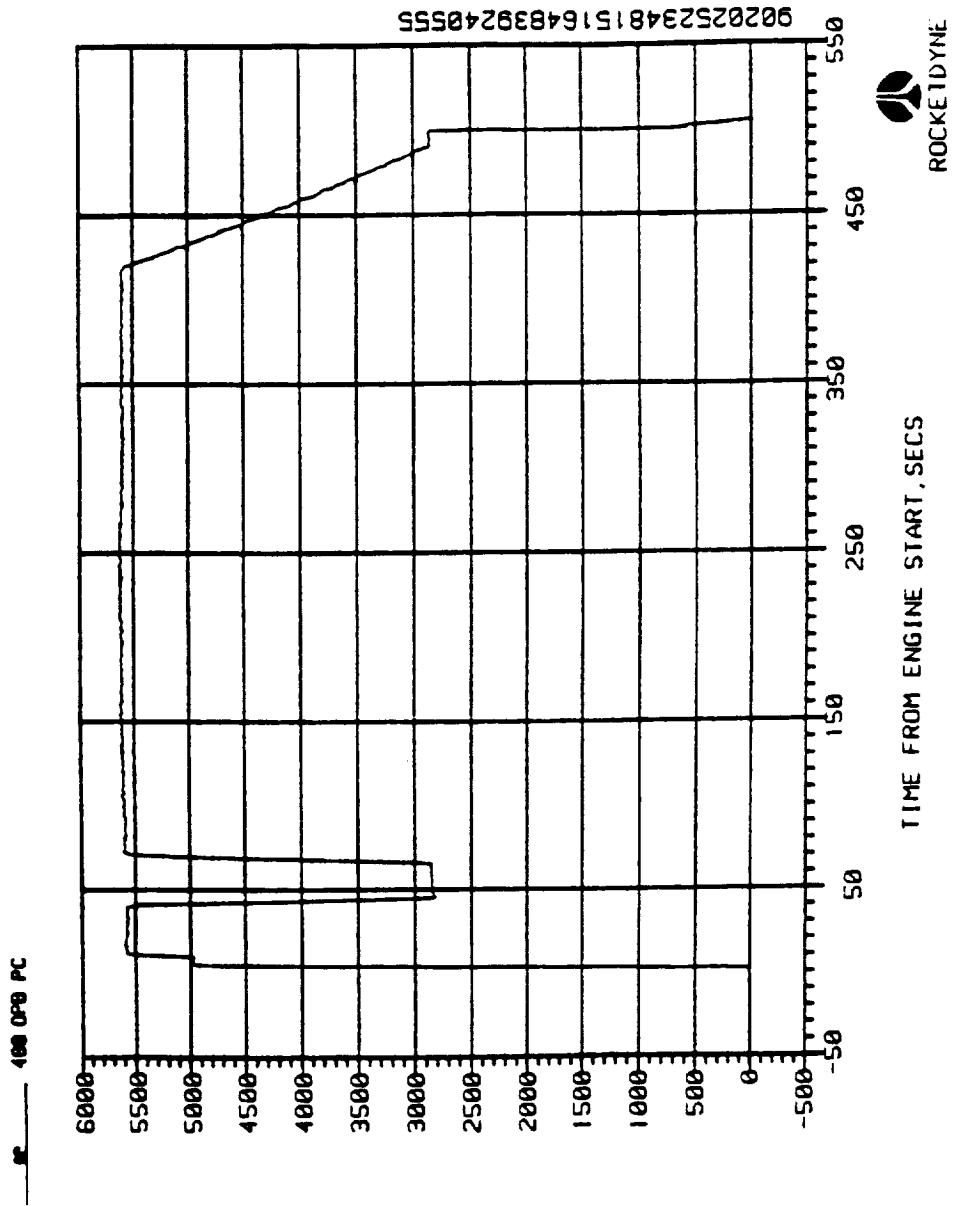


Fig. 2.25 Mission History Profile of Oxidizer Preburner Chamber Pressure



FILE 50 FP8 PC A

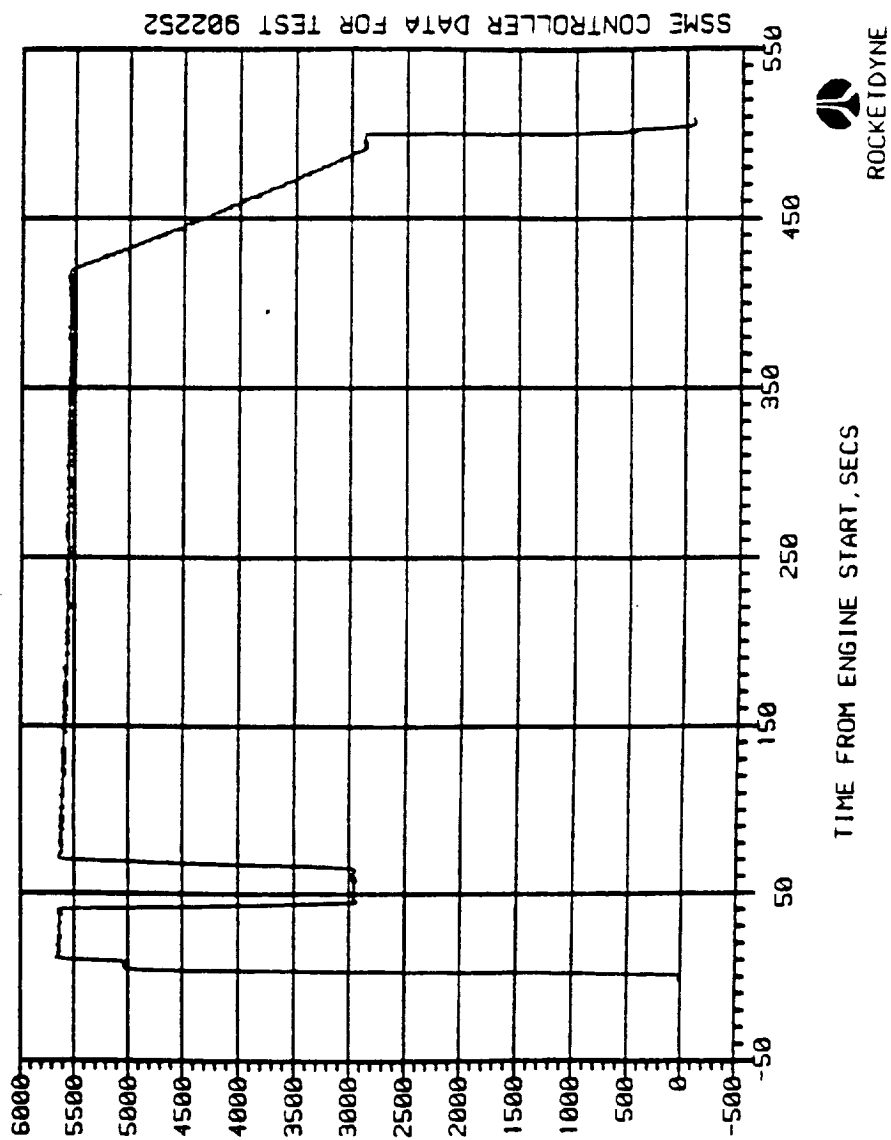


Fig. 2,26 Mission History Profile of Fuel Preburner Chamber Pressure

temperature gradient through a blade is governed by such factors as blade geometry location of shrouds, platform, dampers, etc. and the presence of coating material. A good definition of blade temperatures at start and cutoff is difficult primarily due to the complex nature of flow through an accelerating turbine. Thus, the time-temperature history profile at start transient, steady state and cutoff is obtained through a combination of analytical and experimental results. It is necessary to point out that instrumentation of rocket engine turbines is especially a difficult task due to high pressure lines and the extreme temperatures the lead wires are required to traverse through the region.

The first step in a blade thermal analysis involves obtaining the free stream mach numbers as a function of chord length for both suction and pressure sides of the airfoil. This information is used as input for a boundary layer analysis program that calculates the convection heat transfer coefficients on the blade (Fig. 2.27 and 2.28). Since both the flow and boundary layer analyses are steady state, the resulting convection coefficients are scaled according to flowrate for start and cutoff values.

The temperature of the hot gas must also be determined in order to obtain the blade temperature profiles. In the design stage, the gas temperatures are predicted using engine simulation programs at steady state and transient conditions. The calculated hot gas convection coefficients and temperature time histories are used as inputs to thermal models to determine blade temperatures. A number of different models have been constructed to analyze various parts of the SSME turbine blades. The models generally represent some relatively small but critical part of a blade. A few models have been made of the entire blade, but in general, these models are unsatisfactory in the sense that they do not have the necessary detail to accurately define the local temperature gradients. Constructing profiles of the blade temperature distribution is often best accomplished by combining results of a number of small detailed models.

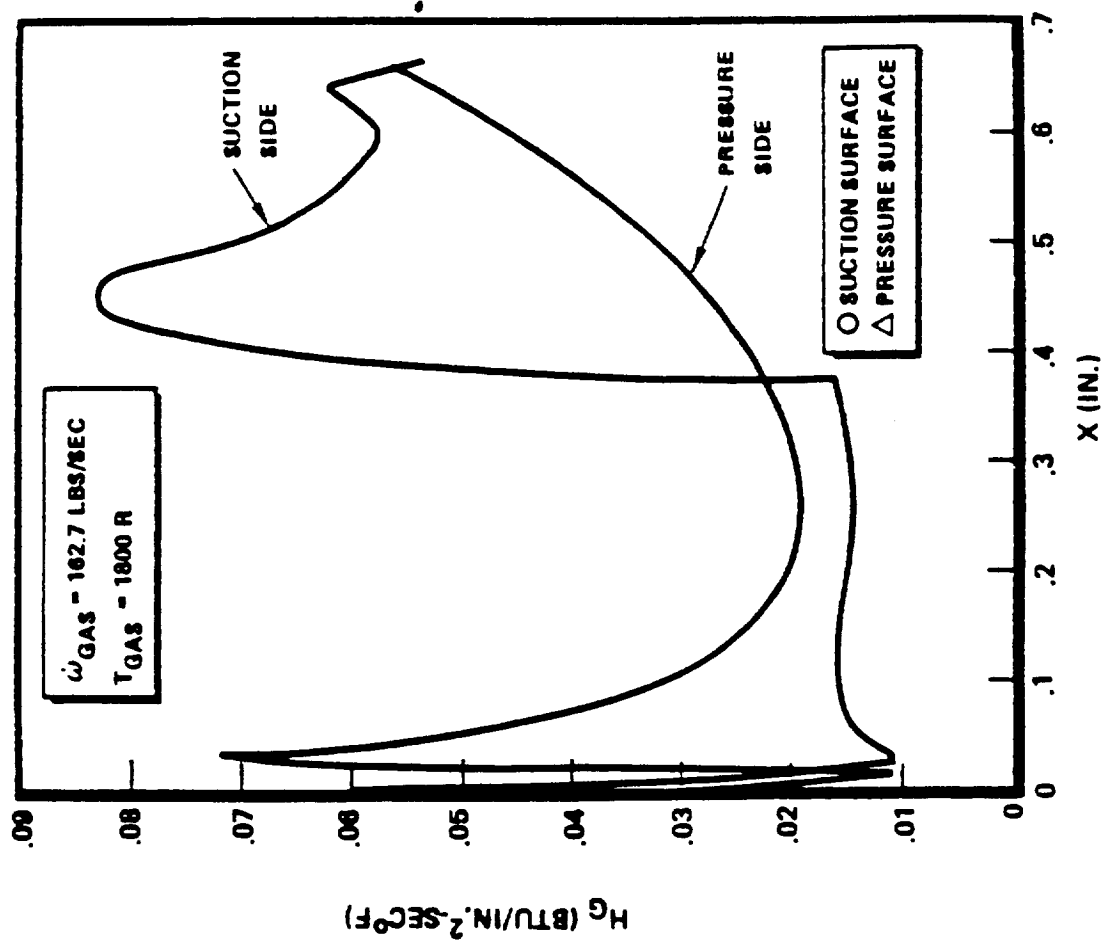


Fig. 2.27 Typical HPFTP First Stage Airfoil Tip Hot Gas Film Coefficient Distribution

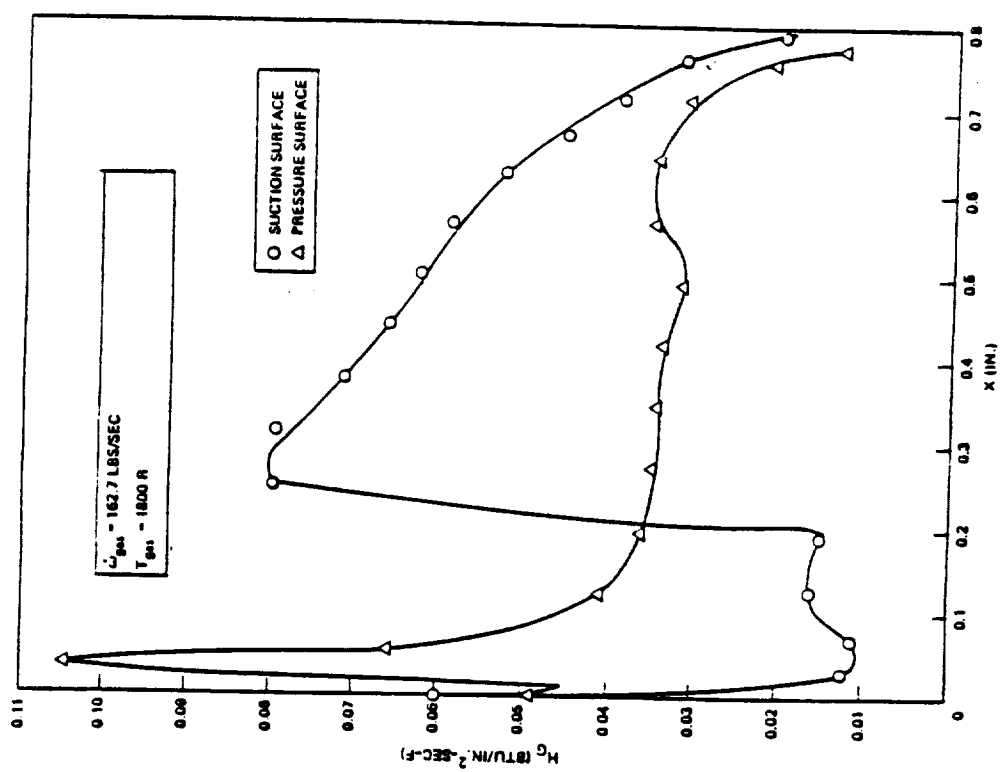


Fig. 2.28 Typical HPFTP First Stage Airfoil Root Hot Gas Film Coefficient Distribution

## Forcing Functions

The flow in turbomachinery is unsteady by nature because of the relative motion of adjacent blade rows. In a typical multistage turbomachine fluctuating velocity and pressure fields are generated by potential flow interactions between stator and rotor blade rows, vortex shedding from blade tips, viscous wake formations, rotating stall and cavitation. In addition, inlet flow distortions resulting in circumferentially nonuniform inlet velocity may lead to large pressure pulsations and highly three dimensional flow effects which are difficult to predict. The problem is further complicated by the fact that pump flows are subsonic so that a downstream blade row induces dynamic loading on an upstream blade row.

Numerous investigators have established analytical approaches to attempt to calculate these dynamic load effects but all these approaches are limited in their application. One approach that is used extensively in the industry is based on potential flow solution of a two dimensional isolated airfoil or an axial cascade of zero camber, zero thickness airfoils (flat plates) at zero mean incidence angle (zero load). Other solutions include camber effects but again valid for thin, low cambered axial cascade. There is very little experimental data available for formulating a general empirical approach. The majority of data available in literature more closely represent the limitations imposed by analytical procedures rather than for actual turbomachinery hardware. Almost no data exist for dynamic loads induced by downstream blade rows. Development 2-D and quasi 3-D analytical procedure with experimental correlations that can be used economically in the design process may be available in the near term. At a more complex level and from long term objective it is necessary to develop 3-D computational fluid dynamics model for unsteady flow around cascades of blades.

The actual forcing function that is used for turbine blade analysis depends upon the type of analysis. For normal design considerations certain percentage of steady state pressure is used as the alternating pressure. For damper optimization studies, a sinusoidal forcing function with certain percentage amplitude of the steady state pressure is used exciting the blades

various modes. For failure analysis, for experimental correlation and for evaluating the effectiveness of actual damper, forcing functions obtained through a combination of experimental measurements and analytical approach is used. This procedure is illustrated below for the high pressure fuel turbopump first stage blade analysis. The flow elements in the HPOTP consists of (Fig. 2.29) 13 upstream struts, first stage consisting of 41 nozzles and 63 blades, and the second stage consisting of 39 vanes and 59 blades. A schematic representation of wake development in flow about cascade blade section is shown in Fig. 2.30. This velocity description has been measured for SSME high pressure fuel turbine first stage nozzle and upstream strut combination. The test was conducted by flowing air through nozzle/strut combination and measuring the circumferential variation of velocity at a section downstream of nozzle using boundary layer probe. Fig. 2.31 is plot of this velocity variation over a portion of the circumference. Another approach to assessing the wake velocity is to simulate the blade nozzle geometry on a rotating water table. This type of test has been conducted for SSME high pressure fuel turbine first stage nozzle with limited success (Fig. 2.32).

An analytical approach to quantifying the forcing function amplitude is to utilize the wake velocity description. The pressure distribution over the blade can be calculated from static fluid dynamic theory using these data. An example of the pressure distribution across the blade at the tip is shown in Figure 2.33. An interpolating scheme can then be used that smoothly switches between wake and free stream distribution following a time history trace similar to velocity trace of Fig. 2.31 where time between each peak is  $1/N$  of the rotor speed where  $N$  is the number of blades. The actual forcing function used for HPOTP first stage analysis is shown in Fig. 2.34.

## 5. Turbine Blade Mission History Profile

A typical turbine blade mission history profile consists of both start/stop transients as well as steady state operation with throttling over a range of power levels. This can be illustrated as shown in Fig. 2.35. Turbine inlet temperatures closely follow the power level profile except for transients.

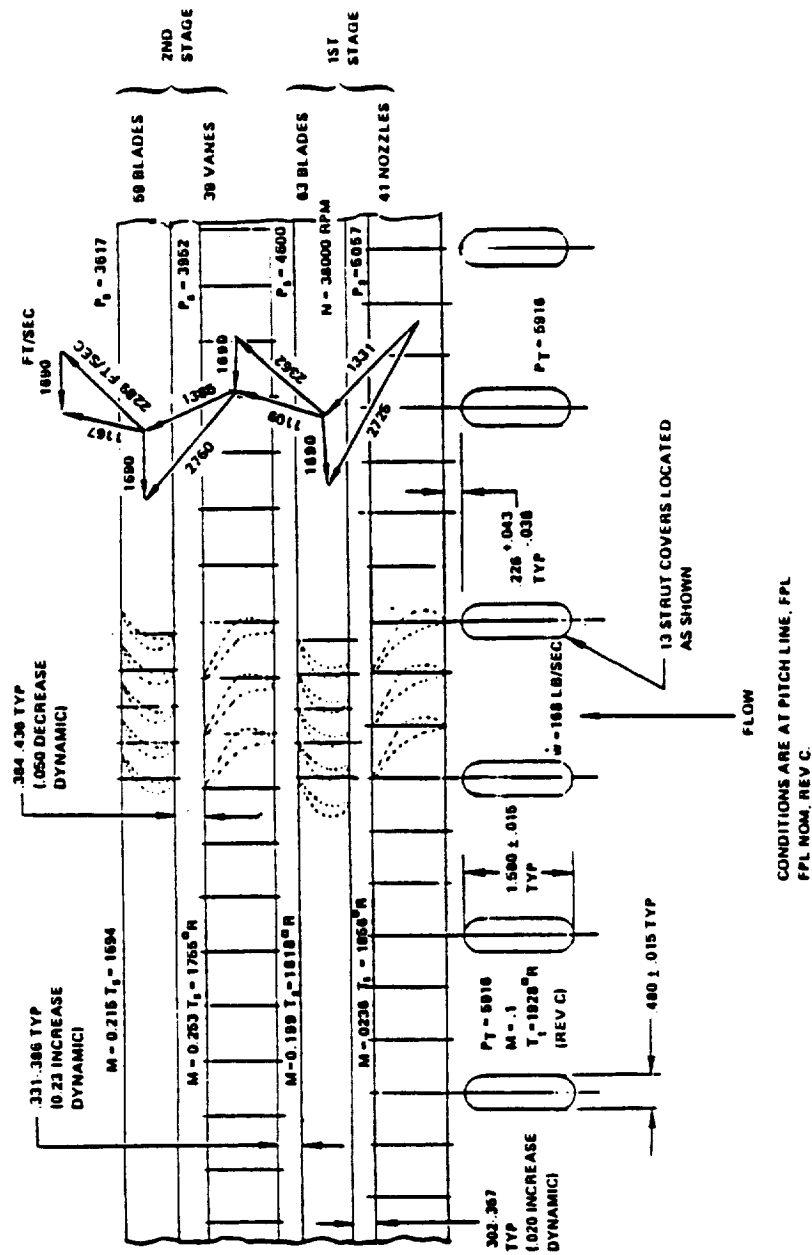


Fig. 2.29 Flow Elements for SSME HPFTP Turbine

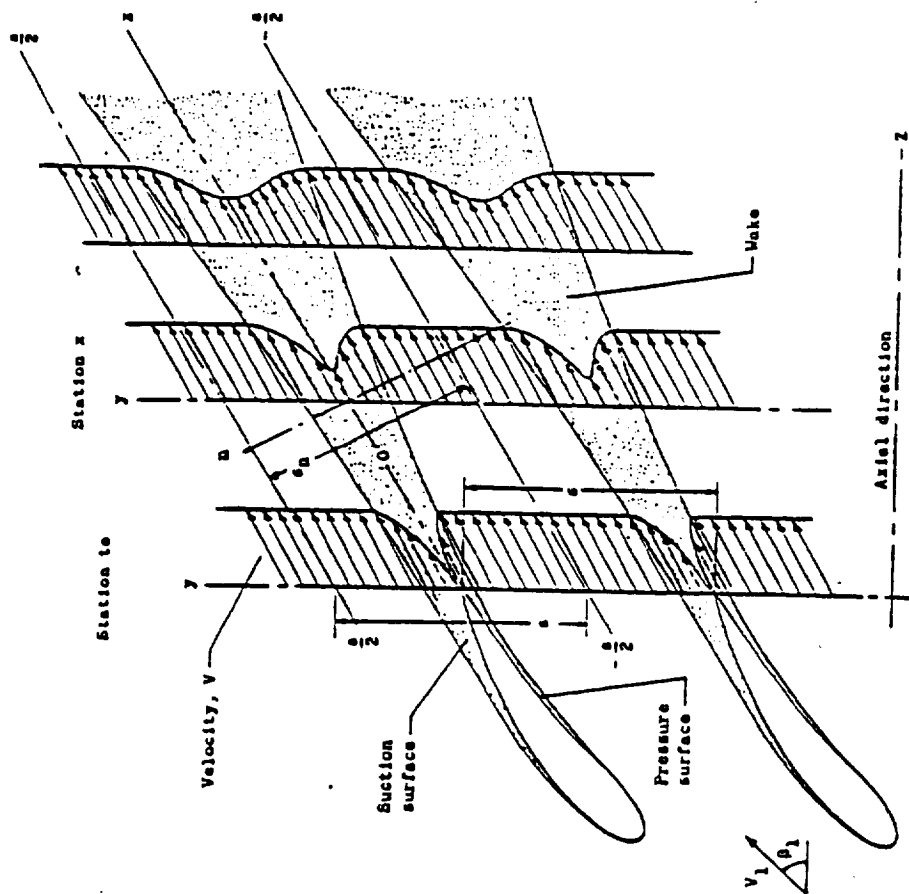


Fig. 2.30 Schematic Representation of Wake Development in Flow about Cascade Blade Sections



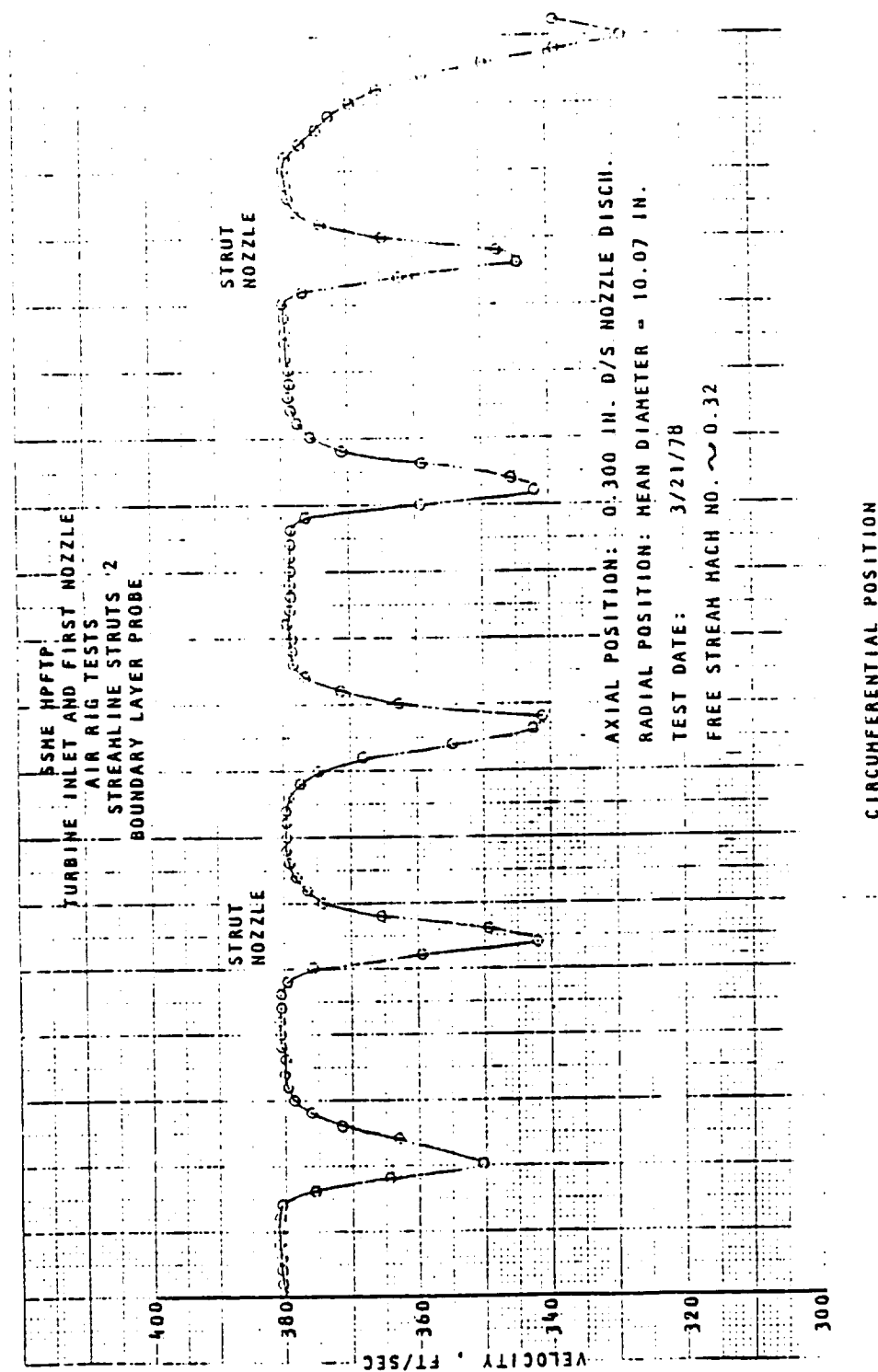


Fig. 2.31 SSME HPFTP Velocity Profile behind Turbine Inlet and First Nozzle



Fig. 2.32 SSHE Turbine Water Table Test

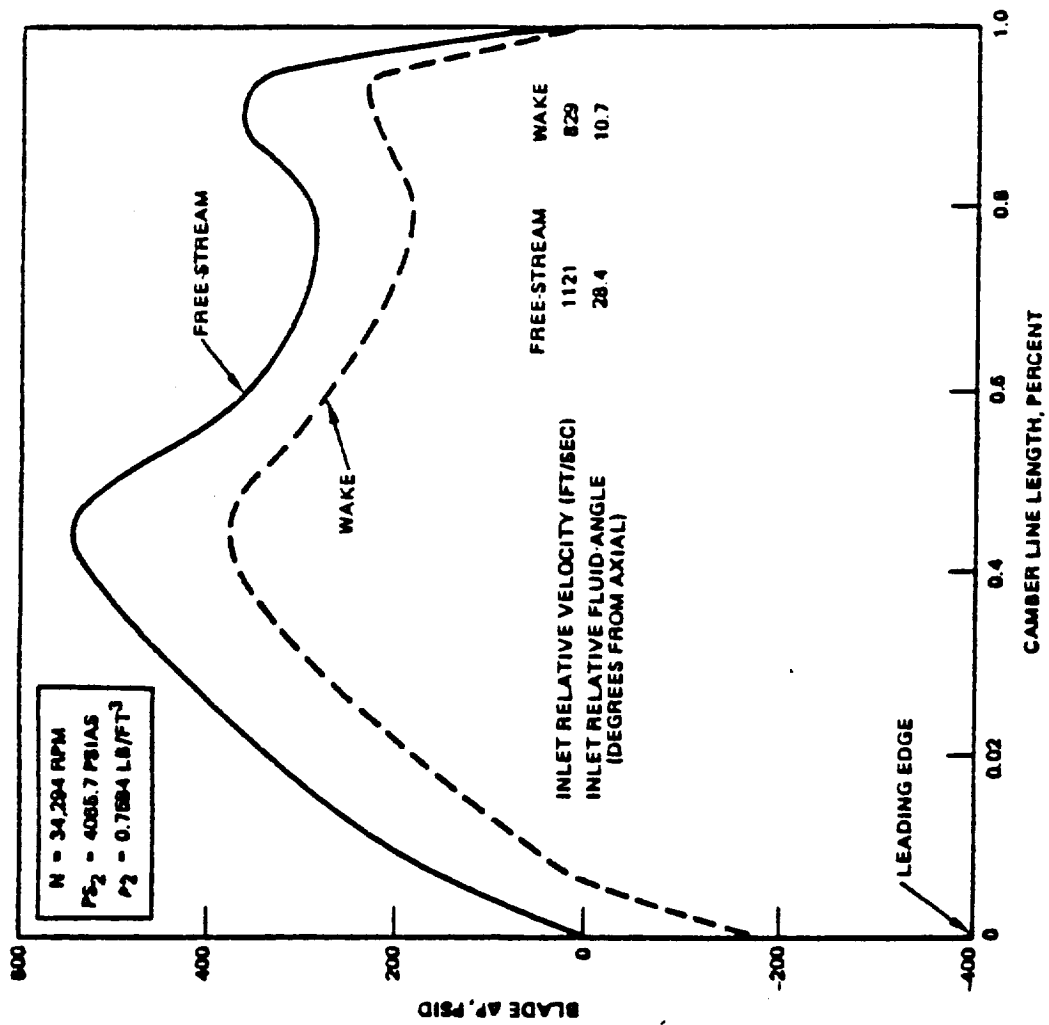


Fig. 2.33 SSME HPFTP First Stage Blade Loading Variations

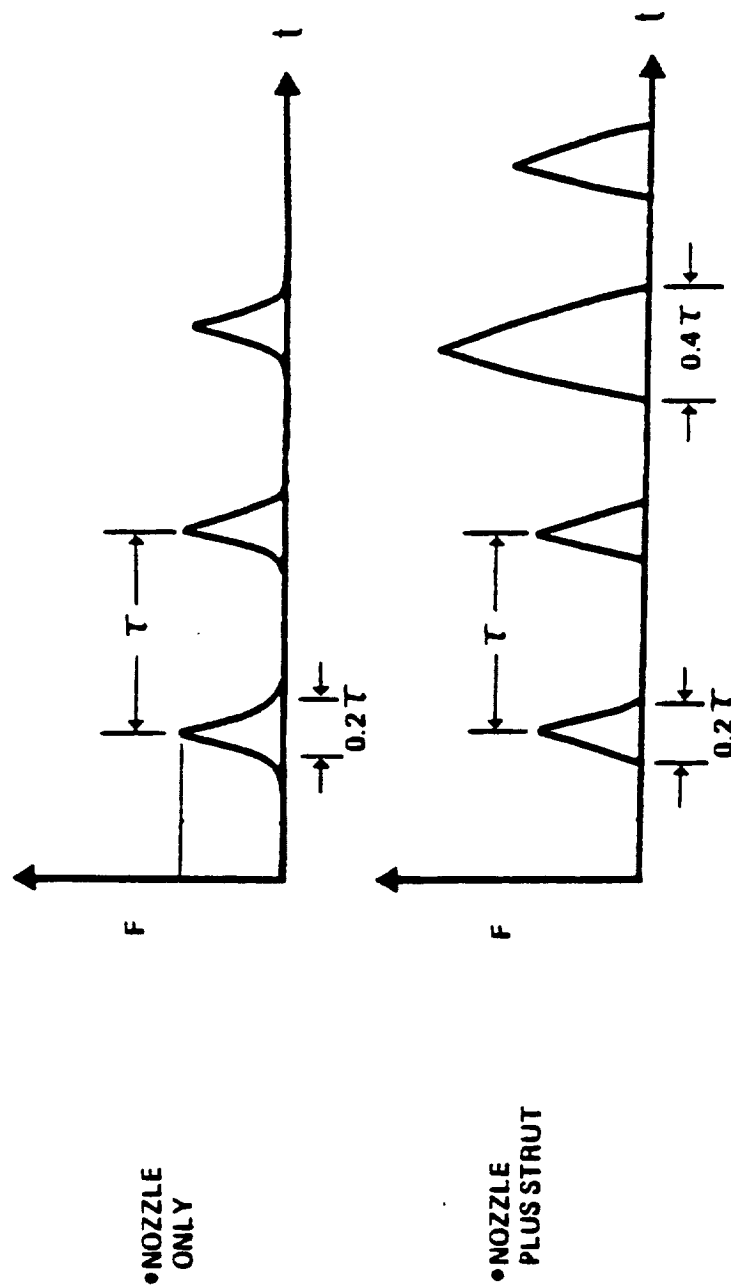


Fig. 2.34 Forcing Functions from Nozzle Strut Wake for HPFTP First Stage Blade

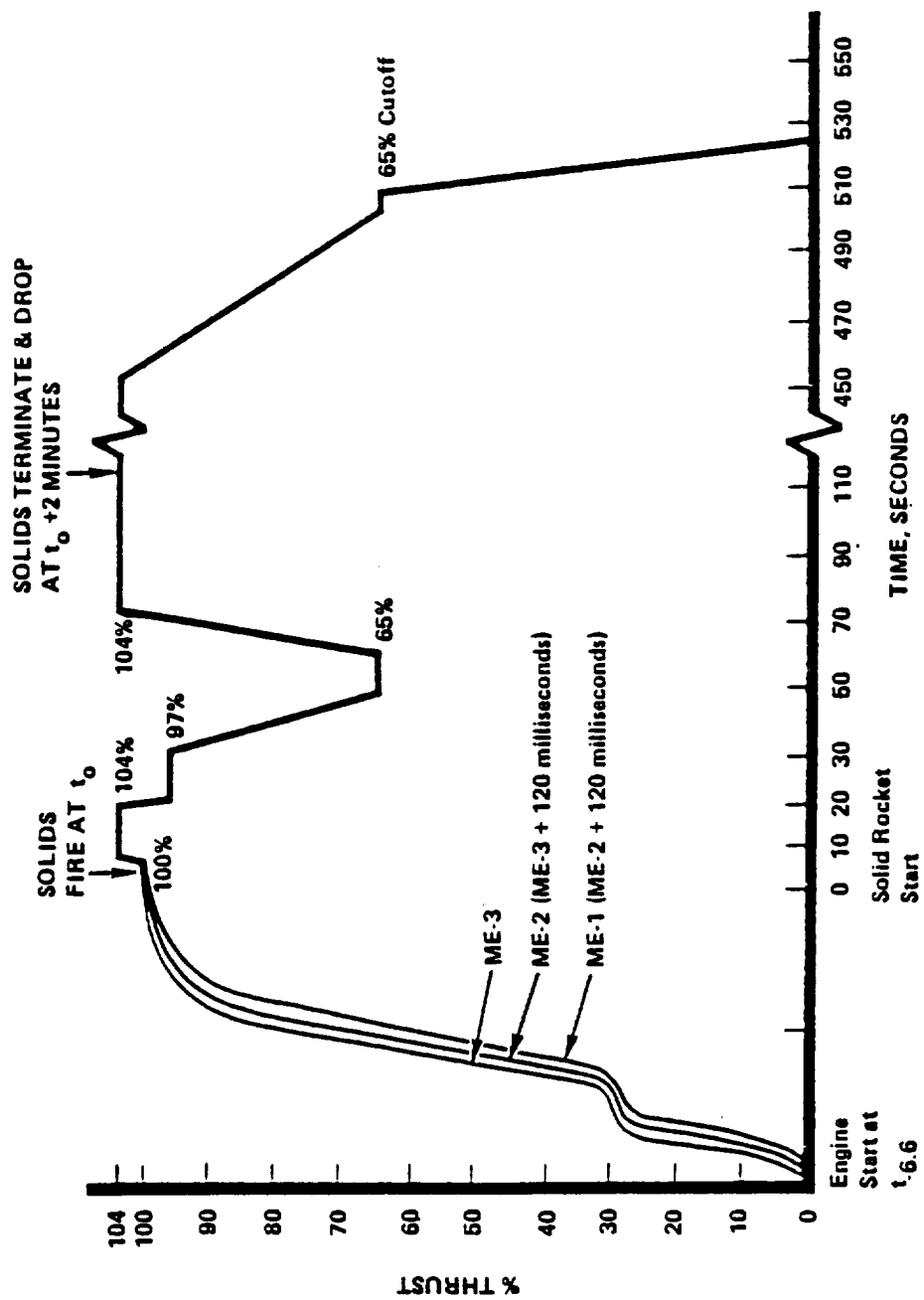


Fig. 2.35 Typical Power Level Mission History Profile

There are specific types of loading associated with the various segments of the mission history profile.

Fig. 2.36 schematically illustrates blade stress variation through the mission history profile. The segment 0-1 represents the transient thermal stress response of the blade surface to the temperature variation as indicated in Fig. 2.35. Segment 1-2 is the superposition of mechanical stresses due to speed and gas forces. If the rate of temperature change is sufficiently high, the blade surface can yield, as shown in Fig. 2.36, and result in residual stresses during main stage operation. Superimposed on Fig. 2.36 are cyclic dynamic stresses resulting from gas force variations experienced by the blade.

Turbine blades are generally designed to avoid coincidence of natural frequencies with harmonic excitation sources in the gas path. These sources usually are upstream and downstream wakes from nozzles, struts, and gas generator maldistributions. However, during transient conditions, avoiding resonant speed is not usually possible. Therefore, superimposed on the stresses in Fig. 2.36 are cyclic dynamic stresses. These stresses can be quite high, depending on ramp rates and damping, but typically occur for only a few cycles. This is also the case for other situations such as tip rubbing during transient clearance changes.

The steady-state loading consists of centrifugal stresses, gas force static stresses, steady-state thermal stresses, and dynamic stresses resulting from gas path wakes. It is presumed that power level excursions of a properly designed blade will avoid stability problems such as flutter. The actual state of stress in the blade can be dependent upon the start transient history. Presuming yielding occurs during the start transient, as inferred from Fig. 2.36, the situation in Fig. 2.37 can exist, i.e., the maximum stress is limited by the yield strength. Therefore, the dynamic stress shakes down the mean stress. Further, the mean stress can decay with time by a creep mechanism. The assumption is made that the stresses are not primary (load dependent) and stress redistribution can take place. The stress versus time can also be influenced by power level excursions, i.e., operation at a high power level can reduce the mean stress for subsequent operation at a reduced power level.

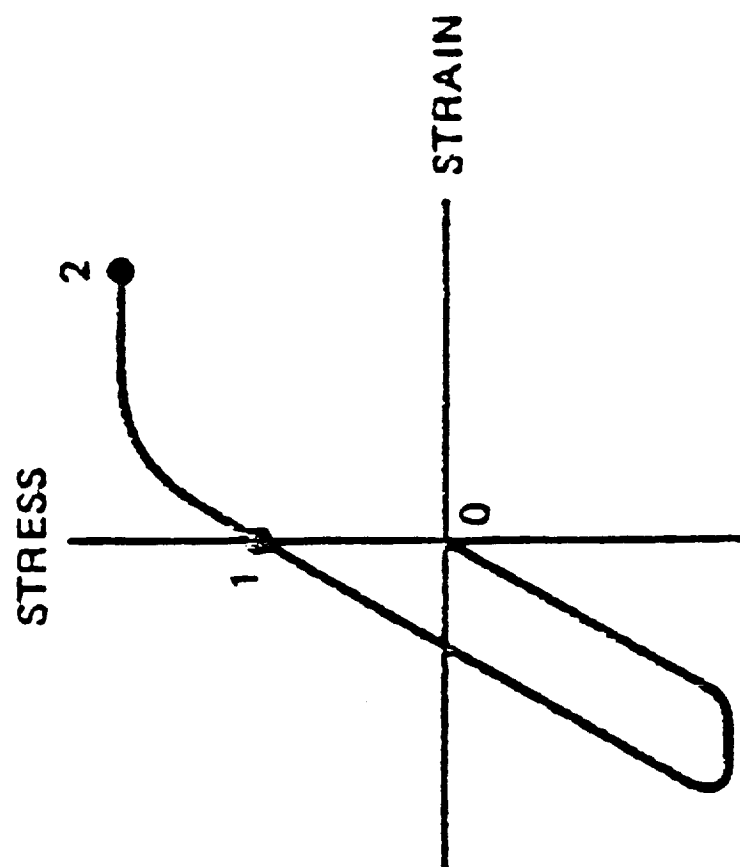


Fig. 2.36 Schematic Representation of Blade Stress Variation Through the Mission History Profile

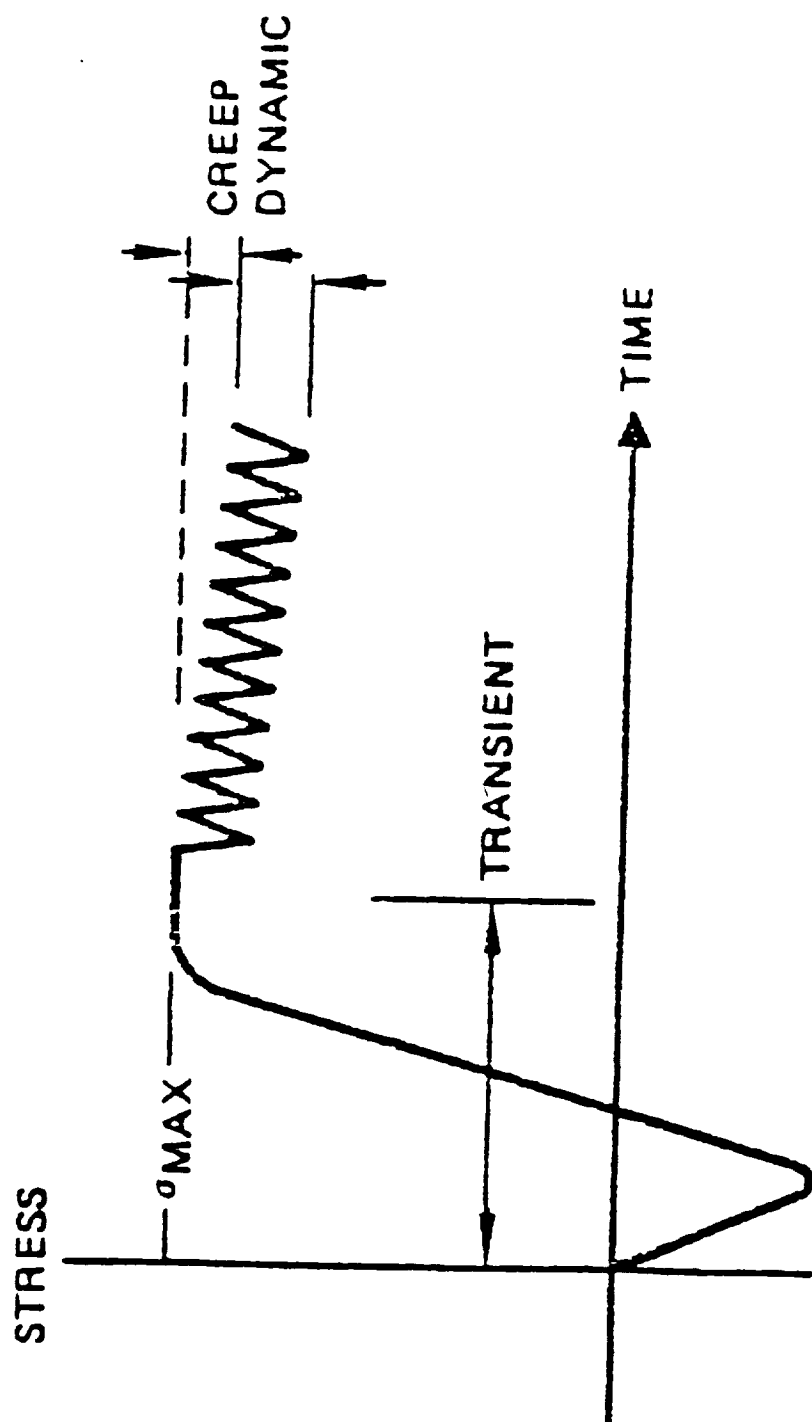


Fig. 2.37 Start Transient Response



The last segment of the mission history profile is the cutoff sequence. As illustrated in Fig. 2.38, the blade is subjected to rapid temperature change in the cooling direction. Similar to the start transient, the blade passes through resonance speeds during deceleration, and dynamic stresses are superimposed on the general stress behavior. Subsequent duty cycles will follow the behavior described. The first few duty cycles will shake the blade down in to a stable stress-strain loop.

In summary, the blade is exposed to various types of loading during the segments of a mission history profile as follows:

- Start Transient--(1) Rapid temperature excursions, (2) Transition through blade resonances - upstream and downstream disturbances, (3) potential for rubbing, (4) Centrifugal and gas forces, (5) Gas generator disturbances
- Steady State--(1) Centrifugal and gas forces, (2) Steady-state thermal stresses, (3) Flow disturbances, (4) Power level excursions
- Cutoff--(1) Rapid temperature excursion, (2) Transition through blade resonances, (3) Potential for rubbing, (4) Gas generator disturbances

## 6. Material Aspects

In the advanced liquid rocket engines of the like of SSME, demands have been placed on turbine blades to perform under extreme conditions for long periods of time with many starts. The currently used turbine blades are subject to fatigue cracks which limit their lives. The fatigue problems in turbine blades may become even more critical with advanced version of SSME and other liquid rocket engines when they impose even more severe thermal and stress conditions. Of the many avenues being investigated to extend the turbine blade lives, the one avenue that has received much attention is the material with which turbine blades are made of.

Historically, the rocket engine industry has relied for its turbine blade materials, on materials developed for aircraft gas turbines. The selection of MAR-M-246 (HF, DS) was no exception. However, there are significant differences in the requirements placed on turbine blade materials in rocket

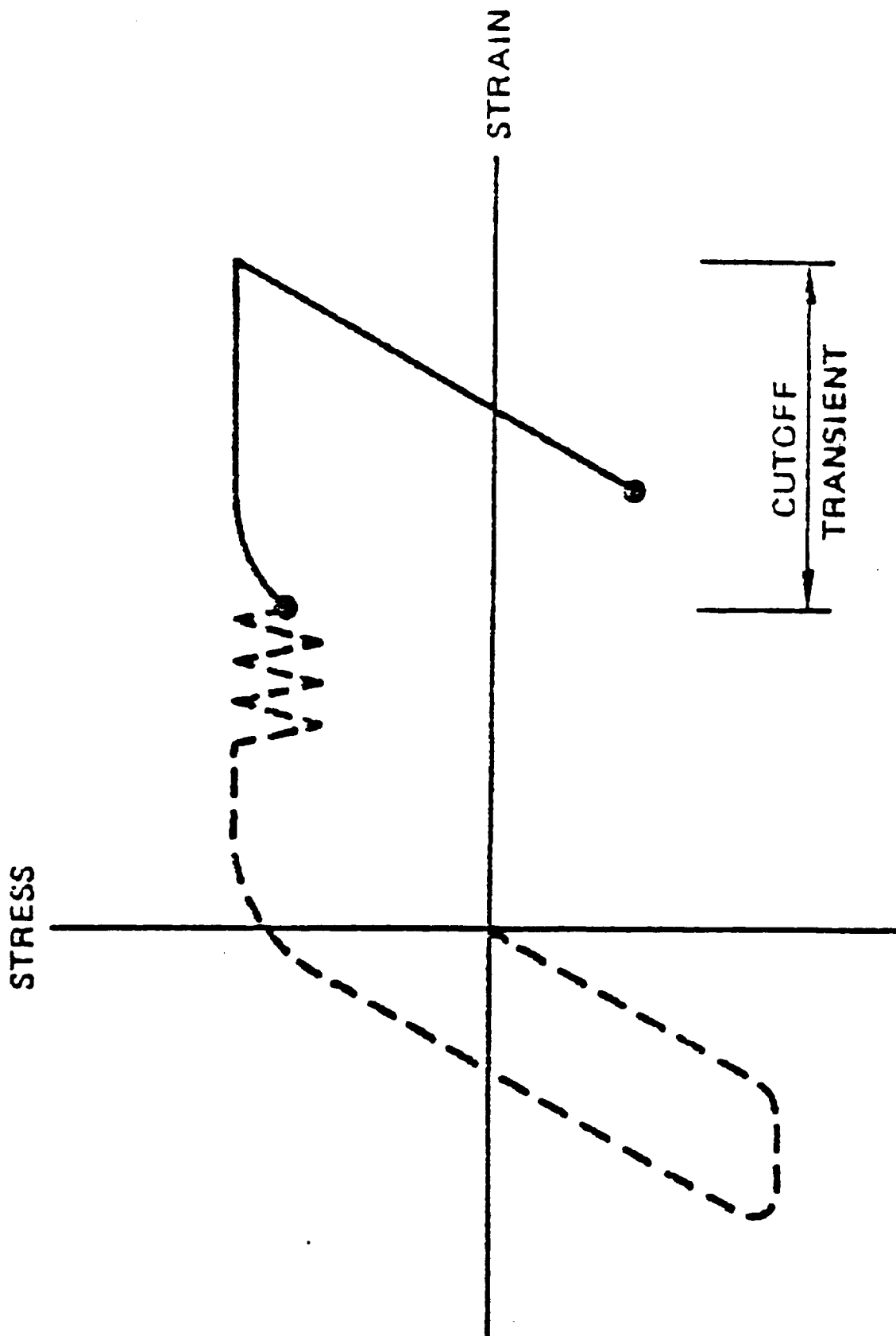


Fig. 2.38 General Turbine Blade Stress Strain Behavior

engines, compared to aircraft gas turbines as shown in Table 2.3. It has become apparent based on SSME experience that the turbine blade materials used by the aircraft gas turbine industry does not necessarily meet rocket engine requirements.

Compared to aircraft gas turbines, rocket engines operate at considerably higher speeds. As a rule, the rocket engines start and reach full power in a matter of seconds. The rapid start results in severe thermal shock which might set the stage for high cycle fatigue cracking problems under steady state conditions. From rocket engines point of view desirable material properties include high tensile and short term creep strengths, high thermal strain low cycle fatigue, high mean stress high cycle fatigue strengths and thermal shock resistance. With regards to environment effects, rocket engine turbine materials are not exposed to sulfidation, but there is potential for hydrogen environmental embrittlement (HEE) when components are exposed to the high pressure hydrogen fuel. The active candidates for oxygen/fuel combination in advanced engines include oxygen/hydrogen and oxygen/methane. Thus environmental effects on the turbine blade materials must be considered before a material selection can be made.

#### Past experience on turbine blade materials:

Table 2.4 highlights number of materials that have potential for being used in a high temperature environment. These materials have all been in use in existing rocket or air breathing engines and have been varying amount of physical properties data base. Conventionally cast alloys can be treated as isotropic and D.S. alloys are generally treated as orthotropic material with isotropic properties in the transverse direction.

#### New material consideration in turbine blades:

The fatigue life of the order of about  $10^7$  cycles for MAR-M-246 (HF) (DS) presently used in SSME turbines need to be improved to  $10^8$  cycles so that

ITEM	ROCKET ENGINE TURBINES	AIRCRAFT GAS TURBINES
FUEL	HYDROGEN OR CH <sub>4</sub>	PETROLEUM DISTILLATE
OXIDIZER	OXYGEN	AIR
OPERATING SPEED (RPM)	UP TO - 110,000	15,000
BLADE TIP SPEED (FT/SEC)	1,850	1,850
HORSEPOWER/BLADE	700	200 - 470
TURBINE INLET TEMP (R)	UP TO 2,160R (UNCOOLED)	2,600 (COOLED)
HEAT TRANSFER COEFFICIENT (BTU/FT <sup>2</sup> -HR-F)	54,000	500
THERMAL SPIKE-TRANSIENTS (°F/SEC)	UP TO 30,000	100
ENGINE STARTS	55 - 300	2,400
OPERATIONAL LIFE (HRS)	7.5 - 100	8,000

Table 2.3 A Comparison of Rocket Engine and Airbreathing Engine Environment

PROPERTY	CAST ALLOYS								WROUGHT
	DIRECTIONALLY SOLIDIFIED				CONVENTIONALLY CAST				
	MAN M 246 (H/F) D.S. (3)	MAN M246 (H/F) S.C. (3)	MAN M200 (H/F) D.S. (3)	MAN M247 (H/F) D.S. (3)	RENE 80	MAN M 200	MAN M 200	UNIMET 700	
TENSILE AT 1860°R									
ULTIMATE, KSI	151	~ 151	148	146 (8)	119	128	120	123	
YIELD KSI	136	~ 136	125	119 (8)	81	4	118	108	
ELONGATION, %	5		4	7 (8)	10	4	3.6	21	
REDUCTION OF AREA, %				18 (8)	17.6	4		28	
STRESS RUPTURE AT 1860°R									
(STRESS FOR RUPTURE IN 7.5 HOURS)	114	~ 114	103	103	90	90	92	65	
CREEP AT 1860°R									
(STRESS FOR 1% CREEP IN 7.5 HOURS)	> 500	> 500	> 500	> 500	5	22.5	1	1	
THERMAL FATIGUE RESISTANCE - RELATIVE (7)	0.84	~ 0.84							
LOW CYCLE FATIGUE (8) AT 630°R, 25 @ 240 ~	38	~ 38							
CYCLE LIFE @ 1% STRAIN RANGE	44 (1)	~ 44 (1)	38 (2)		51			52	
HIGH CYCLE FATIGUE AT 1860°R	38 (1)	~ 38 (1)	32 (2)		41				
10 <sup>7</sup> CYCLES, R = -1.0, 30 Hz					23.5	24.5	24.5	22.5	
10 <sup>6</sup> CYCLES, R = -1.0, 30 Hz	14.5	~ 14.5	13.8		~ 5200	~ 5200	~ 5200	~ 5200	
MODULUS OF ELASTICITY AT 1860°R (10 <sup>6</sup> PSI)	21.1	21.1	24		1.4 X 10 <sup>8</sup>				
LONGITUDINAL DIRECTION	4000	~ 4000	~ 4000	~ 4000					
TRANSVERSE DIRECTION	1.1 X 10 <sup>8</sup>								
1ST FLEX. MODE CYCLIC RATE, Hz									
NUMBER OF CYCLES IN 7.5 HOURS									
K <sub>IC</sub>									
44 KIN									
HYDROGEN ENVIRONMENT EFFECTS									
IMPACT RESISTANCE									
MARGINS									
STRESS RUPTURE (4)									
1860°R	1.4	1.4	1.2	1.2	1.1	1.1	1.1	0.8	
2160°R	0.8	0.8	0.8	0.8	0.6	0.7	0.7	0.5	
HIGH CYCLE FATIGUE, 7.5 HOUR LIFE (6)	1.0	~ 1.0	0.8		1.1				
1860°R									
2160°R									
THERMAL FATIGUE									
CRITICAL DESIGN PARAMETERS									
USER/EXPERIENCE	ROCKET DYNE	ROCKET DYNE	P&W JTD ENGINE (DC-9, 727 & 737)		THERMAL FATIGUE G.E.	P&W	THERMAL FATIGUE	THERMAL FATIGUE G.E.	
FOUNDRY EXPERIENCE	HOWMET DOVER	HOWMET DOVER	P&W FOR HOWMET DOVER		HOWMET MISCO	HOWMET MISCO & DOVER			

NOTES:  
 (1) 2010°R  
 (2) 2000°R  
 (3) LONGITUDINAL DIRECTION  
 (4) TYPICAL PROPERTY X 0.9 1860°R  
 (5) 7 MEAN ± 20 ALT  
 (6) 7 MEAN ± 20 ALT  
 (7) STRAIN RATE - N THAT OF SSME BLADE  
 (8) 1860°R  
 (9) BASED ON:  
 CONSTANT LIFE (GOODMAN) DIAGRAM  
 90% TYP PROP (SPECIMEN)  
 MEAN - 15 7.5 ALT - 20 Hg AT 1860°R  
 (10) MINIMUM (DATA) OR MAX (2)

Table 2.4 Turbine Blade Material Comparison - Typical Data

blade life is not fatigue limited. Recent studies have looked into a number of alternative materials with the objective of meeting the design life of reusable rocket engines. The promising material candidates include:

- 1) Single crystal super alloys.
- 2) Fiber reinforced super alloy composite.
- 3) Ceramics

### Single Crystal Super Alloys

A significant improvement in certain mechanical properties and environmental resistance may be achieved by a complete elimination of all grain boundaries from a turbine blade. Single crystal turbine blades have demonstrated improvements in creep and stress rupture capability over polycrystalline directionally solidified blades. Corrosion resistance is also improved by elimination of grain boundaries and their associated chemical inhomogeneity. Carbides are usually added to conventional high temperature alloys to improve creep resistance at grain boundaries. It is known that fatigue cracks initiate at the carbides present in their alloys. With the entire blade made out of single crystal, carbides can be entirely eliminated.

Absence of carbides permit higher solution treatment temperatures with a high volume fraction of fine, evenly dispensed gamma prime precipitate, resulting in better tensile, creep, fatigue and stress rupture properties. With improvements in industrial process development PWA 1480 and CM SX materials show promise of being used in the manufacture of rocket engine turbine blades.

### Fiber reinforced super alloy composite:

Recent investigations of fatigue behavior of composite materials indicate that when the strength of the fiber is significantly greater than that of matrix, then both low cycle fatigue and high cycle fatigue are controlled by the fibers. Combined with the above desirable property the relatively high thermal conductivity of FRS composite and better strength properties at high temperatures makes FRS an attractive candidate for turbine blade material for

future systems. The candidate reinforcing filament that is frequently mentioned is a strong tungsten alloy (W-4RE-0.38HF-0.02C). The candidate matrix alloys that might be considered include Fecraly, 316L stn1, INC0903, Waspaloy and Astroloy.

#### Ceramics:

The appeal of ceramics as turbine blade materials, compared to metals, lies in three distinguishing features: (1) high-melting or dissociation temperature, (2) tolerance of aggressive environments, and (3) low density.

The most obvious advantage of ceramics is their capability for uncooled high-temperature operation to temperatures well above the limits for nickel-base alloys. Ceramics such as silicon nitride and silicon carbide are characterized by low coefficients of thermal expansion and thus, by reduced thermal stresses. In addition, silicon nitride and silicon carbide are stable at elevated temperatures and resistant to oxidation. Limited data on silicon nitride materials showed that exposure to the combustion products of LOX/H<sub>2</sub> and LOX/CH<sub>4</sub> rocket engine propellants at 1116 C (2040 F) resulted in little, if any, effect on mechanical properties.

Finally, the low density of ceramics is another significant asset because it not only provides a direct weight saving, but also conveys the benefit of reduced centrifugal loads on rotating components. Ceramics also offer the added advantage that they contain no strategically scarce materials.

The design approach for ceramics differs from that for metals because of their brittle nature and inherent sensitivity to local stress concentrations. Compared with metals, ceramics are characterized by lower strain tolerance, reduced fracture toughness, and greater scatter in strength. A notable feature of ceramics is the lack of a mechanism for plastic relief of local stresses.

## Impact of Material Types on Structural Analysis

### D.S. and S.C. Material.

The directionally solidified blades may have anywhere from 2 to 20 crystals forming the blade. In the directionally solidified polycrystal form, the direction of the longitudinal axis can not be very closely controlled. Hence to avoid inordinate amounts of rejection, the crystal orientation axis usually has a tolerance of 0 to  $10^\circ$  with the blade stacking axis. In addition there might be other restrictions on crystal boundaries intersecting leading or trailing edges. In D.S. form there are no controls over the secondary axis orientation. It is usual to assume for directionally solidified materials, they are transversely isotropic, though this is not strictly true. For single crystal blade materials, the longitudinal axis as well as the transverse axis orientations can be controlled within certain range of values. One way to improve the fatigue life of the blade is to reduce the shear stress in the slip direction of the slip plane of the crystal. If the material is treated as transversely isotropic, five independent elastic constants and two coefficients of thermal expansions are required.

### FRS Material

The mechanical properties for the FRS composite is governed by the properties of the reinforcing wire and the properties of the matrix.

The influence of constituent material properties can be identified at a macromechanics level by a three dimensional finite-element model with orthotropic properties. However, local influences on structural behavior must be addressed at the micromechanics level to make a reasonable assessment of a design. These local effects are contributions due to the volume ratio of fiber to matrix, orientation of fibers, number of plies, type of reinforcement (fiber, particle, and whisker) and packing with either discrete and/or continuous filament, and manufacturing method, specifically, on joints and



attachments. Thermal strains that occur due to mismatch of coefficient of thermal expansion is another important consideration. Micromechanical considerations include:

1. Interlaminar Shear. Primarily an in-plane stress between plies in a multiply component.
2. Debonding. Incompatibility of displacements between plies, fiber and matrix, and initial inhomogeneity in matrix.
3. Stress Concentration. Nonuniform stress distribution at the packing of fiber due to the difference in material properties of matrix and its reinforcement.
4. Fracture. Interface bond irregularity among plies, void in matrix, loss of continuous support between the fiber and matrix, and imperfect fiber.

#### Ceramic Material

Due to the sensitivity of ceramics to local stress riser, much design emphasis is placed on local thermal gradients and stress concentrations combined with a probabilistic determination of design strength properties.

The generally accepted basis for statistical analysis of ceramic strength is based on Weibull's weakest link model, which holds that the probability of survival of a structural element is:

$$p_{s_i} = \exp \left( - \frac{\sigma}{\sigma_0} \right)^m \quad (1)$$

where

$p_{s_i}$  = probability of survival for a given element

$\sigma$  = applied stress  
 $\sigma_0$  = a normalizing factor (the "characteristic strength" of the material)  
 $m$  = Weibull modulus

The foregoing equation can be extended to calculate the probability of survival for a particular structure of known volume or surface as represented in a finite element analysis. If we assume independence among the various elements, and that the local elements of the structure have the same size, stress level, and flaw distribution, then the probability of survival of the total structure becomes the product of the local elements:

$$p_{s_t} = (p_{s_i})^n \quad (2)$$

where

$p_{s_t}$  = probability of survival for the total structure  
 $p_{s_i}$  = probability of survival for an element "i"  
 $n$  = number of elements in the structure

The strength of a structural material is determined through measurements on laboratory test specimens. If we assume, for example, that the unit elements of Eq. 1 and 2 are of a size equal to that of a standard laboratory test specimen, then the number of elements ("n") in a structure becomes:

$$n = \frac{\text{total structure volume}}{\text{volume of test specimen}}$$

This permits us to express the probability of survival in terms that consider structural size as related to laboratory test data, so that

$$p_{s_t} = \exp \left[ - \frac{v_i}{v_t} \left( \frac{\sigma}{\sigma_0} \right)^m \right] \quad (3)$$

where

$p_{s_t}$  = probability of survival for the structure  
 $v_i$  = volume of test specimens upon which the values of  $\sigma$ ,  $\sigma_0$ , and  $m$  are based  
 $v_t$  = volume of the engine component (e.g., turbine blade)

Analogous equations can be employed for adjustments in  $p_{s_t}$  to compensate for surface area effects as well as volume.

In the foregoing equations, the Weibull modulus ("m") describes the scatter of the strength distribution, with a high value indicating a small degree of scatter. Thus, the Weibull modulus is an important parameter that must be known in company with the values for average strength. Accurate determination of "m" requires sizable numbers of strength tests. For example, an "m" value calculated from 30 samples is reliable to only  $\pm 20\%$ . Thus, the number of samples used should be recorded along with the value for "m".

### Plasticity

It is known that due to severe thermal shock during start and cutoff transients, surface yielding of turbine blades occur, resulting in residual stresses. Thus for an accurate analytical evaluation of blade life, it is necessary to do a material nonlinear analysis. The material library should contain plasticity formulations for general anisotropic bodies.

### 7. Fatigue Failure of SSME Turbine Blades

Turbine blades in SSME, the most advanced, large, liquid propellant rocket engine currently in service, are subjected to fatigue cracking problems that limit their life to less than design life. The first and second stage fuel turbine blades and the first stage oxidizer turbine blades exhibited cracking. Though the fatigue cracking problem is attributed to different causes in each blade, the primary reason is the severe thermal shock these blades experience during start and cutoff transient.

The HPFTP first stage blades must be inspected periodically and are limited to 4,000 secs. of operation at 109% rpl due to shank cracking. The characteristics indicate three influences.

1. Corner Stress Riser
2. Surface Carbides
3. Thermal Cycles

The first stage blade high cycle fatigue cracks propagate from cracked carbides typically located in areas of incipient surface melting at a cast to

machined surface stress riser. The short term design changes that address the extension of first stage blade include 1) Recontouring of the shank in the critical area and 2) insulate the shank with ceramic coating. Recontouring in the critical area is accomplished (Fig. 2.39) to reduce the stress concentration factor. By applying a coating around the shank (Fig. 2.39), the incipient surface melting can be eliminated and thermal gradients reduced.

The HPFTP second stage blades are limited 1375 secs of operation at 109% rpm due to shank cracking. They are caused by a combination of high thermal and mechanical stresses aggravated by geometrical stress concentration. A mixture of turbine hot gases and hydrogen coolant at a temperature of approximately 1760°R flows between the blade shanks. Hydrogen at approximately 250°R flows along the downstream end of the shanks. The high-temperature differential produces high thermal stresses in the shank. The cast surface at the downstream end of the shank and underside of the platform are machined to provide the tolerance control desired for the platform seal clearance. A stress concentration is produced at the line of intersection between the machined surface and the cast surface at the curvature of the shank. These conditions are shown in Fig. 2.40. Some of the design changes that are being considered to extend the life of second stage fuel blade include:

- 1) Recontour and shotpeen in the critical area.
- 2) Insulate the downstream end of shank with a ceramic coating.
- 3) Development of a practical method for selecting blade castings with superior fatigue properties.
- 4) Development of single crystal alloy with improved properties.
- 5) And a diverter to the second stage aft platform seal to direct the cold hydrogen from the blade shanks.

Recontouring of critical area reduces the stress concentration factors thereby increasing the fatigue life. Shotpeening the shank will include a substantial residual stress which will then reduce the mechanical operating stress. By applying a thermal insulating coating to the aft end of the blade shank as

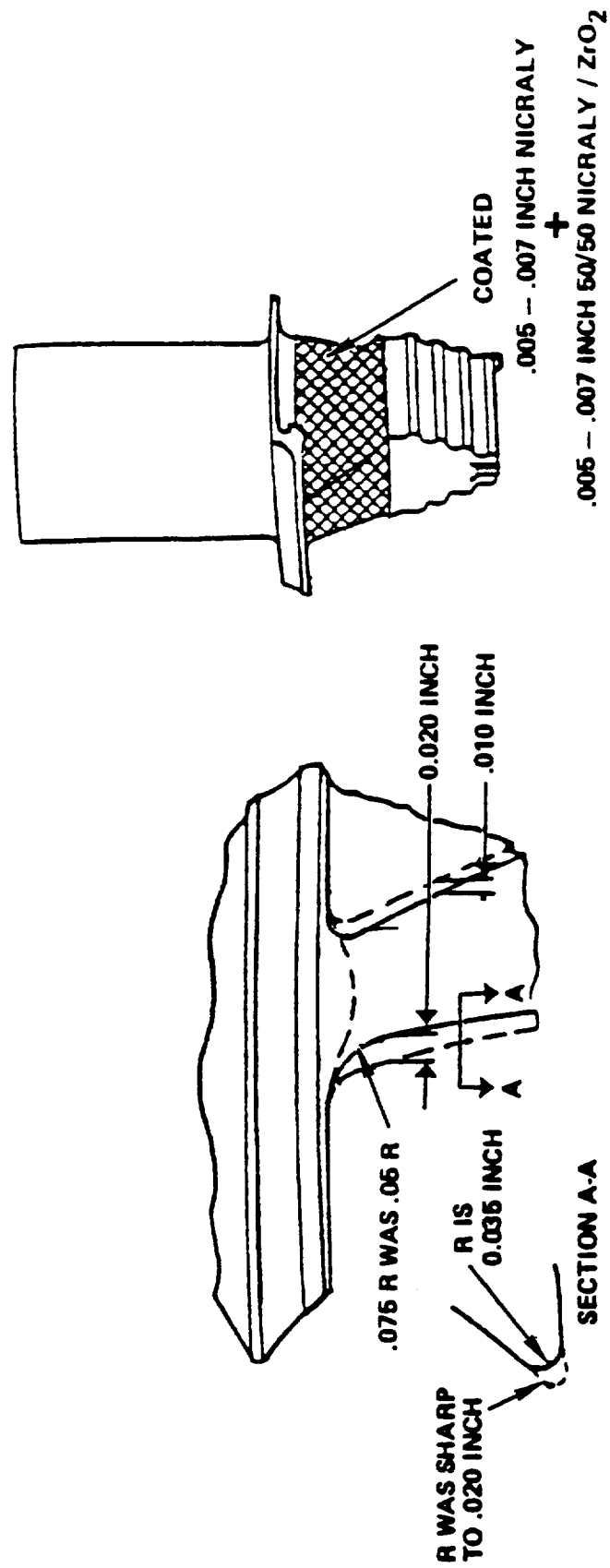


Fig. 2.39 HPFTP First Stage Blade Shank Recontour and Coating

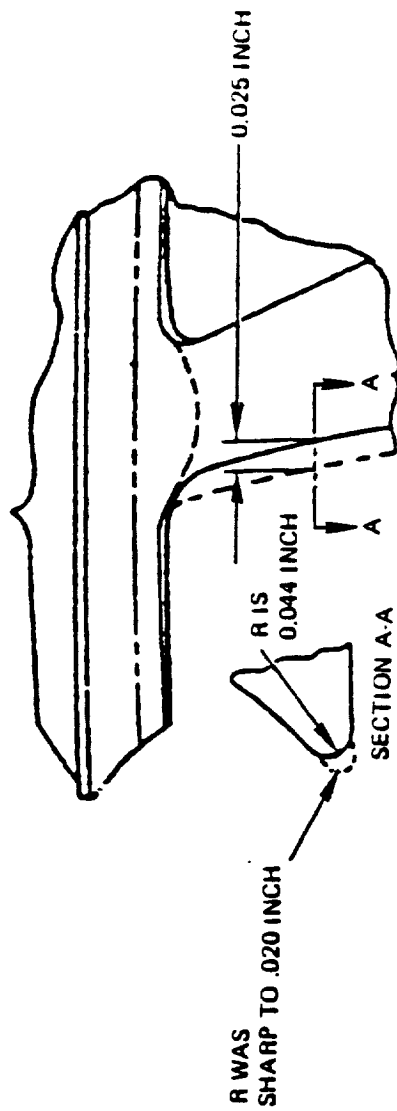
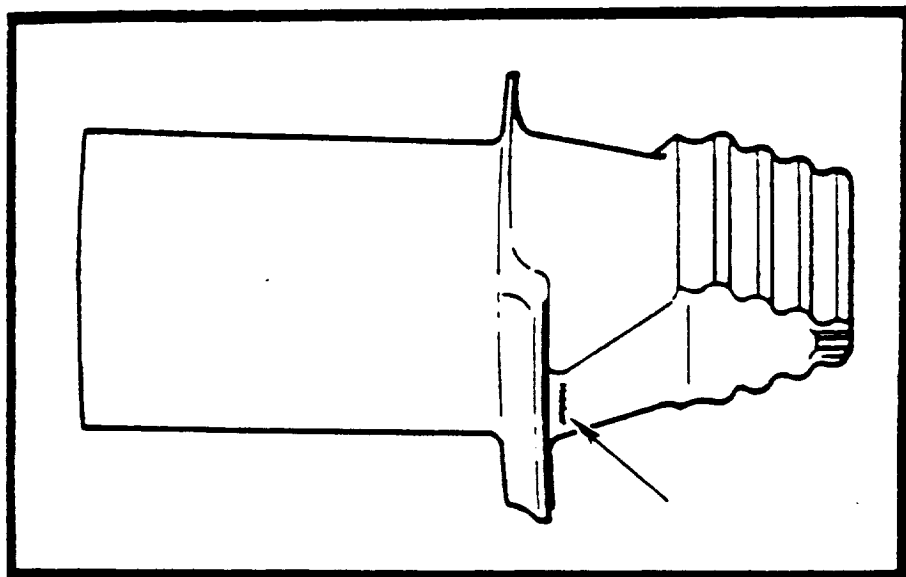


Fig. 2.40 HPFTP Second Stage Blade Shank Cracking and Recontouring

shown in Fig. 2.41 the steep thermal gradient through the trailing edge of shank can be substantially reduced as shown in Fig. 2.41. Laboratory examination has established a correlation between blade cracking and crystallographic orientation of grain at the shank trailing edge. The MAR-M-246 (Hf) blade material has face centered cubic crystallography (Fig. 2.42). In all cases examined, the high cycle fatigue crack has occurred in the crystallographic slip plane. By controlling the grain orientation, the resolved stresses in the slip plane might be reduced to a value that can increase the blade life considerably.

The function of the divertor will be to remove the cold hydrogen from the downstream surface of the shank. This will reduce the temperature differential with mixed gases that flow between the shanks. The average temperature in the cavity adjacent to the downstream face of the shank will be increased from the baseline value of 250°R to approximately 1400°R thereby substantially reducing the thermal stress.

High pressure oxidizer turbopump first stage turbine blades exhibit transverse trailing edge shank transition cracks that limit their life to 3000 seconds of flight operation. The cracks are due to Stage 1 HCF, crystallographic in nature initiated at carbides. The primary objective in the design changes is to reduce the alternating stresses through more effective damping. This is achieved by a two-piece damper (Fig. 2.43 ). While one piece acts as a seal to prevent bypass of hot gas flow between the blade shanks, the second piece provides the damping function. Current analysis indicates that the two-piece damper configuration will reduce the alternating stress in the blade significantly, thereby increasing the blade life.

## 8. Static Analysis

The scope of static finite element analysis of turbine blades include the evaluation of blade stresses due to centrifugal load, temperature load, pressure load and due to severe thermal transients. In general stresses due to centrifugal loading, pressure loading, and vibratory stresses are classified as primary stresses. The secondary stresses are those caused by discontinuity stresses, thermal stresses and certain types of bending or

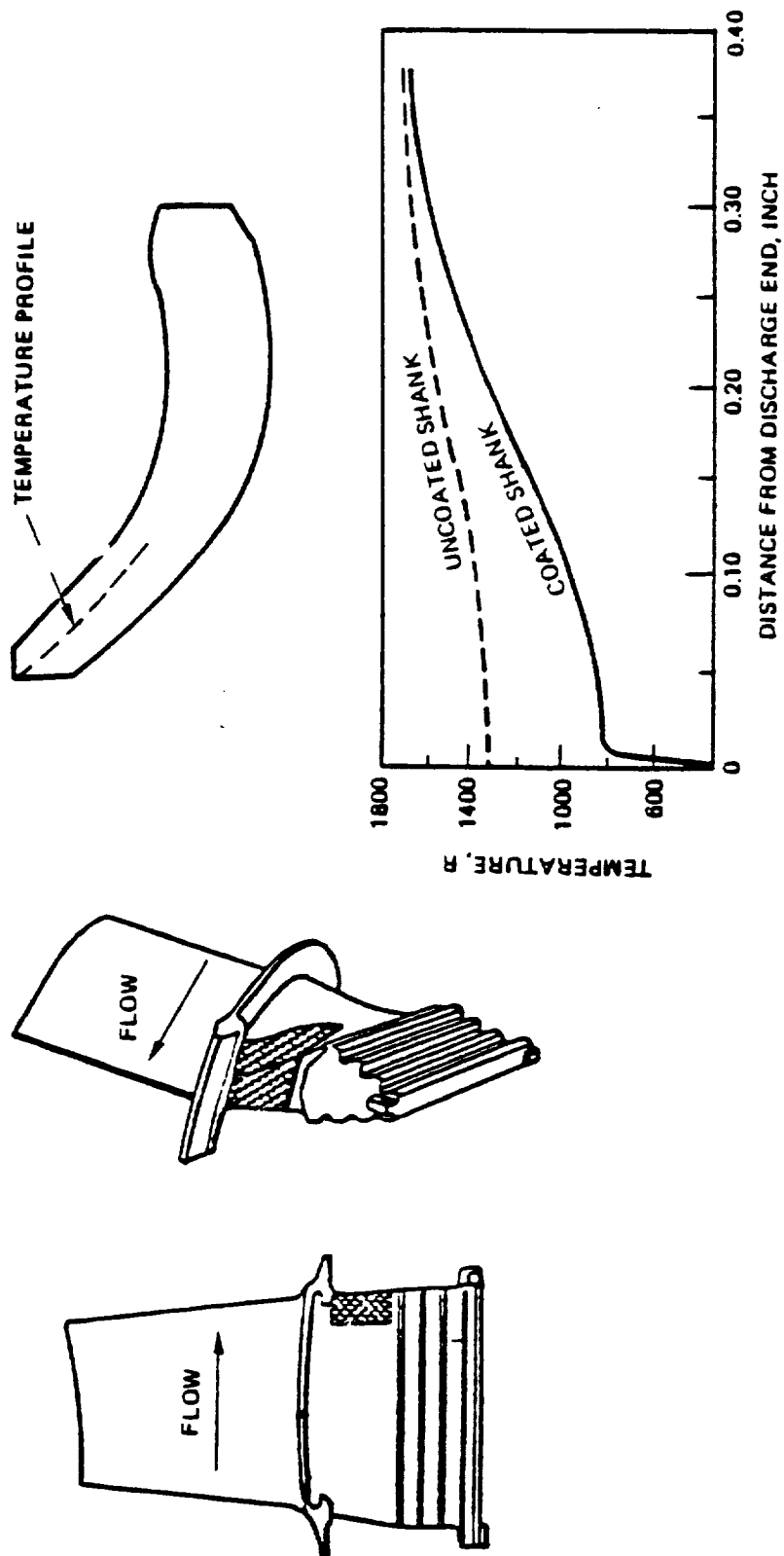


Fig. 2.41 HPFTP Second Stage Blade Shank Coating Temperature Analysis



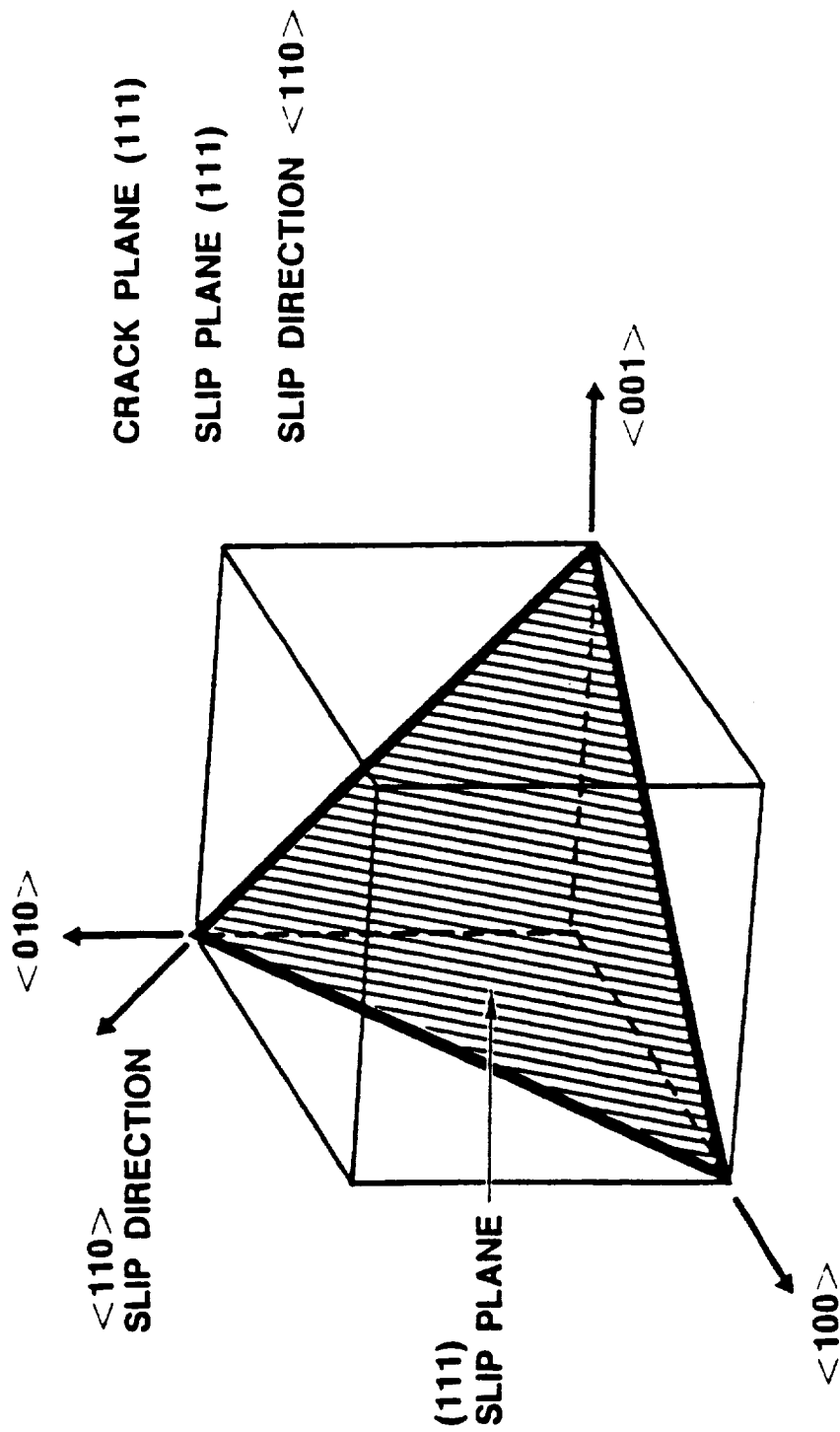


Fig. 2.42 Face Centered Cubic Crystallography

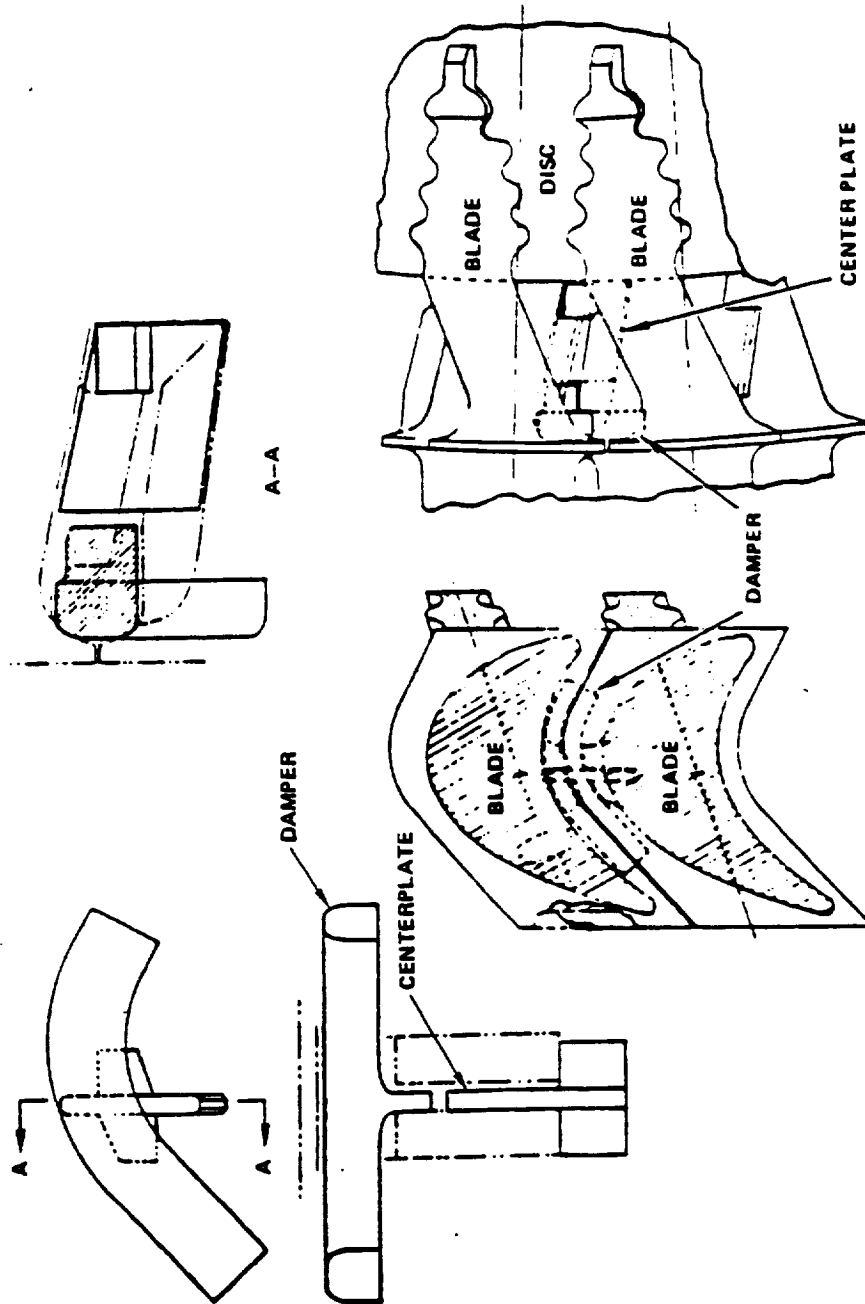


Fig. 2.43 HPOTP First Stage Two Piece Damper Design

deflection limited stresses. However, with the first reusable rocket engine like that of SSME, the design life is limited by the secondary stresses and thermal stresses. In general static linear analysis is done for each of the individual loading cases ie. centrifugal load, temperature load and pressure load. The combined results for the baseline steady state are obtained by principle of superposition. In general there is insufficient details in large 3-D models to define the local stress concentration factors. In such cases a separate substructure model approach is used to define the local stress concentration factor.

Due to the severity of thermal transients that exist at rocket engine turbines, a material nonlinear analysis may be required for accurate life prediction not only in turbine blades but in other turbine components. A material nonlinear analysis done for the HPFTP nozzle is illustrated here for a typical start and shut down transient, using a 2-D finite element model (Fig. 2.44). The thermal transient loading on the nozzle a start and cutoff are shown in Fig. 2.45 and Fig. 2.46.

These are average temperatures in which the bulk temperature of the nozzle has been subtracted out and the key turning points in temperatures have been marked. The temperature contours of the nozzle at key time steps are shown in Fig. 2.47 and Fig. 2.49. The resulting effective stress-strain history obtained at a reference point at the nose of the nozzle is shown in Fig. 2.50 with key steps corresponding to load curve marked. The ignition spike causes the material to go plastic in compression (Segment 1-2). Subsequent oscillation in temperature in start transient, results in the material going plastic in the tension region (Segment 5-6).

During subsequent oscillations during time steps 6 through 16, the material essentially behaves elastically with loading and unloading. During the reverse thermal shock during shut down transient 16-17, the material goes further plastic in the tension region. Subsequent oscillations in shutdown thermal transient results in elastic unloading and loading (17-22). The nozzle at the end of one duty cycle has residual stresses and strains. Subsequent start and cutoff transients should shake down the stress-strain curve into a stable loop.

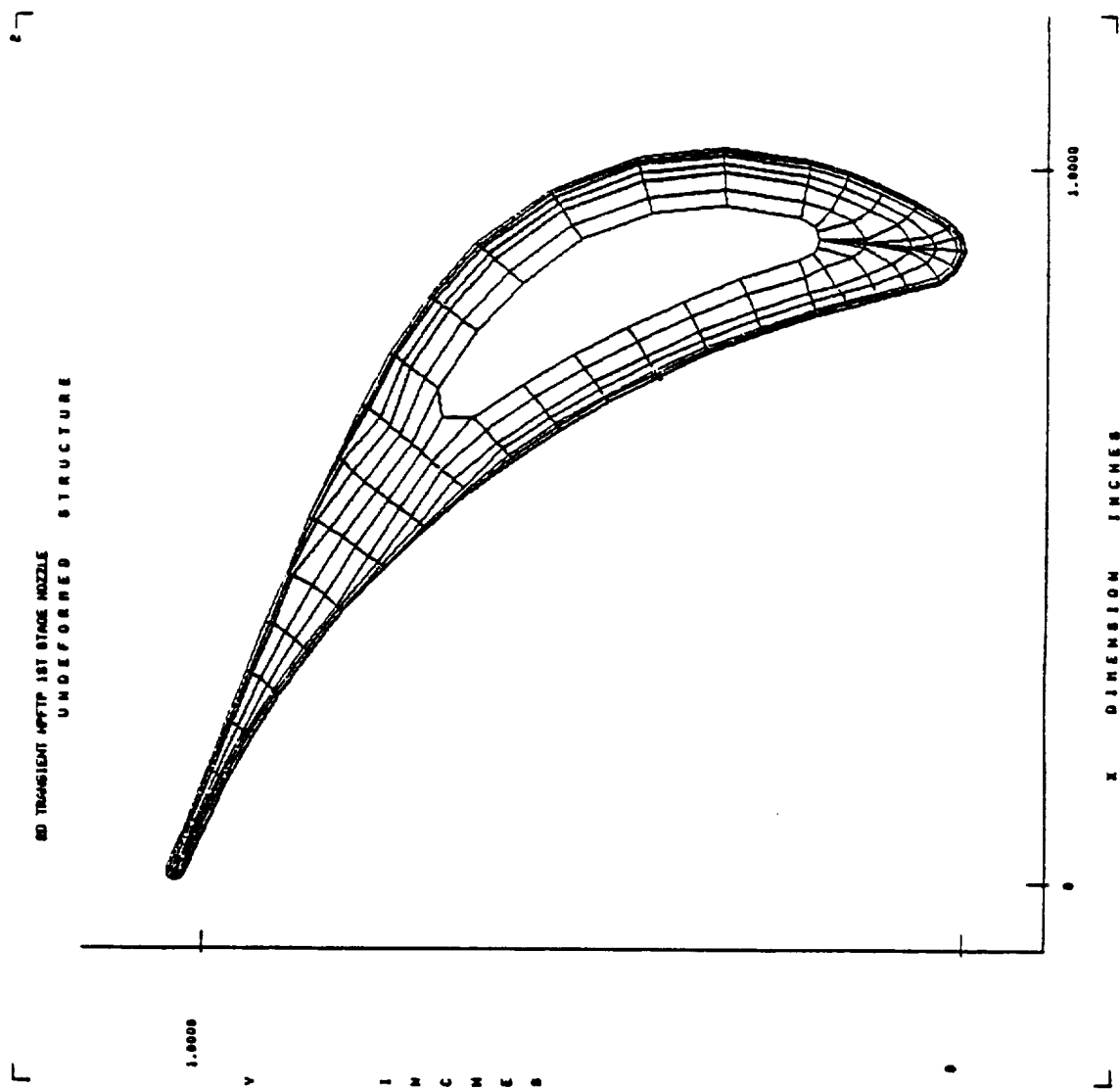


Fig. 2.14 HPFTP First Stage 2-D Finite Element Model

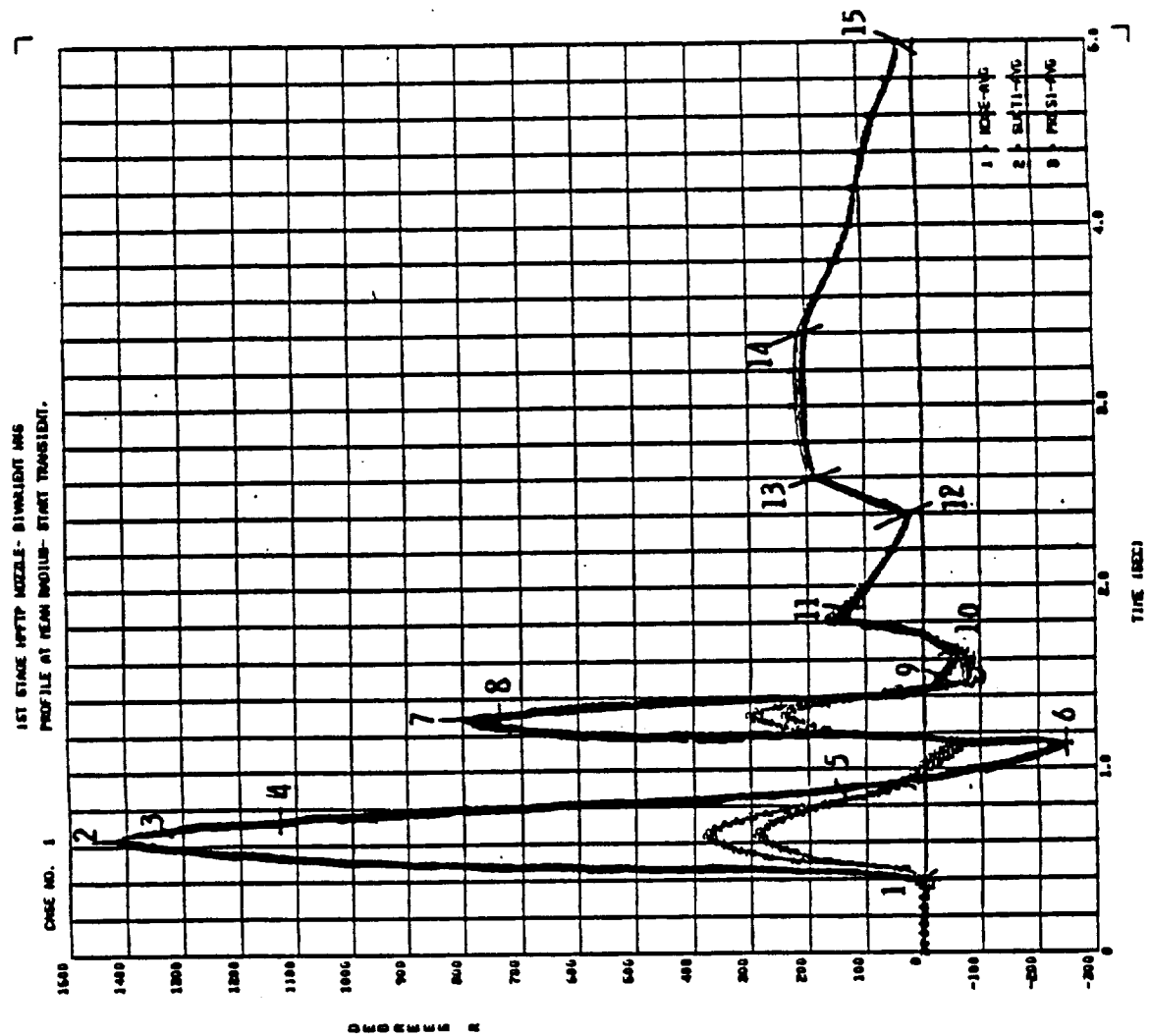


Fig. 2.45 HPFTP First Stage Nozzle Start Temperature Transient

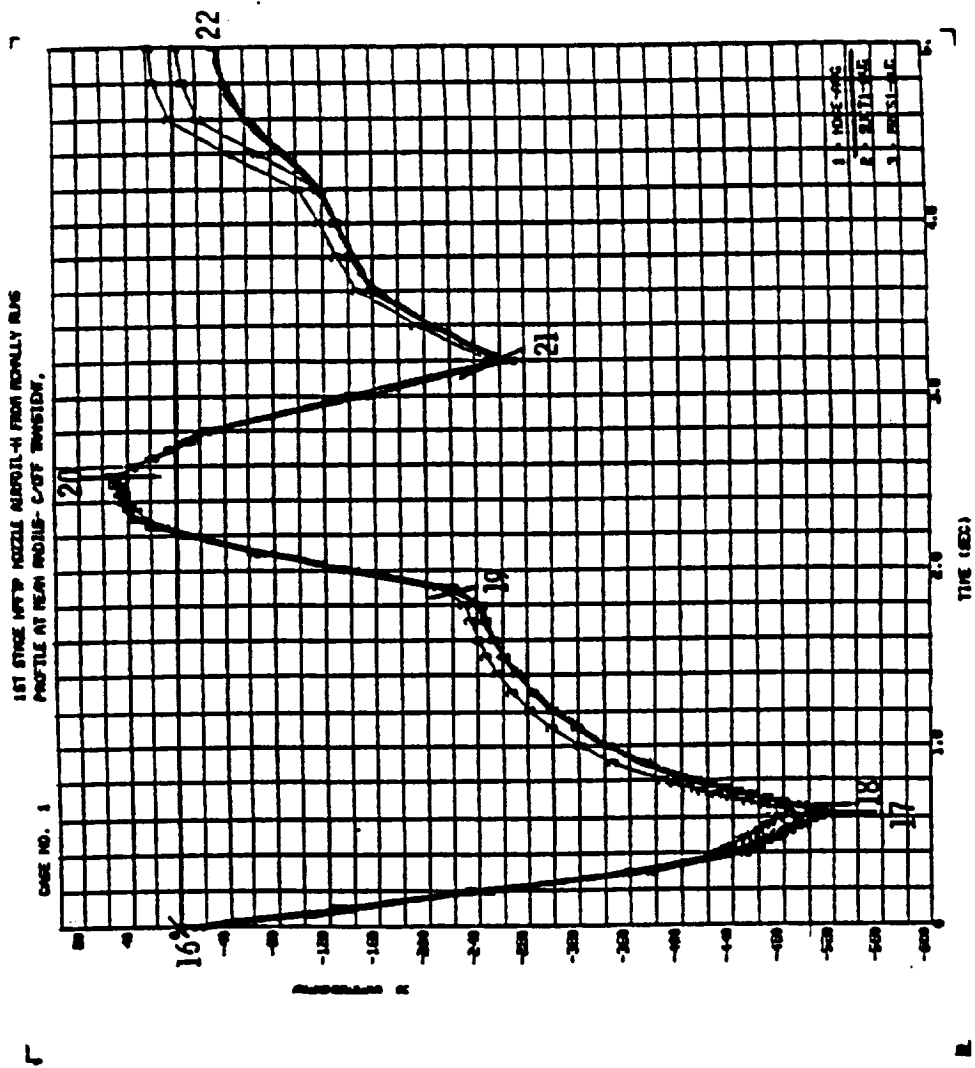


Fig. 2.46 HPFTP First Stage Nozzle Cutoff Temperature Transient

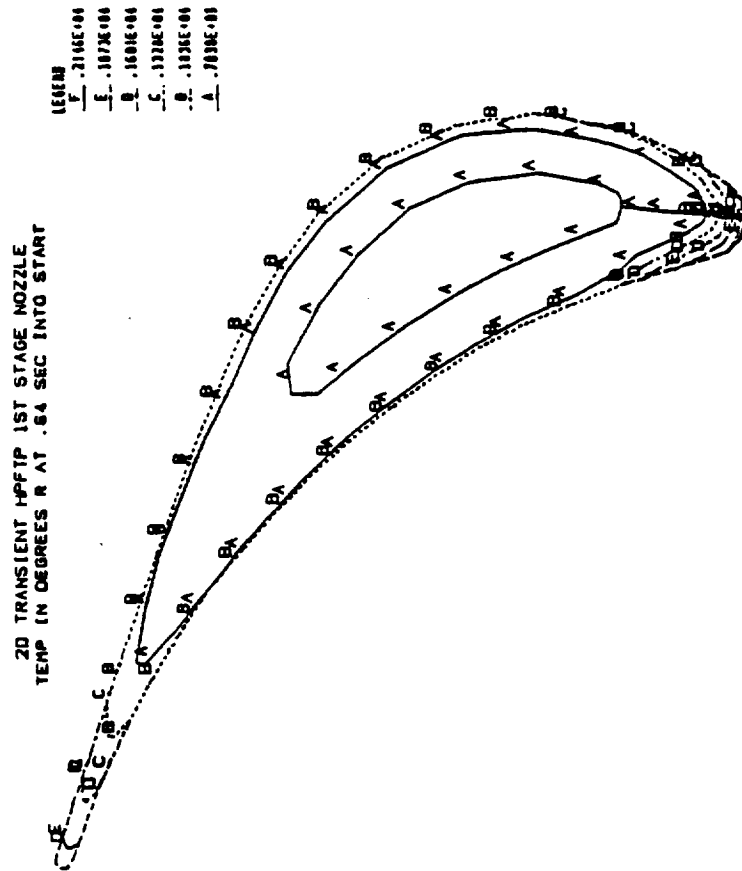


Fig. 2.47 HPFTP First Stage Nozzle Temperature Contour at 0.64 Sec. Temperature Spike at Start

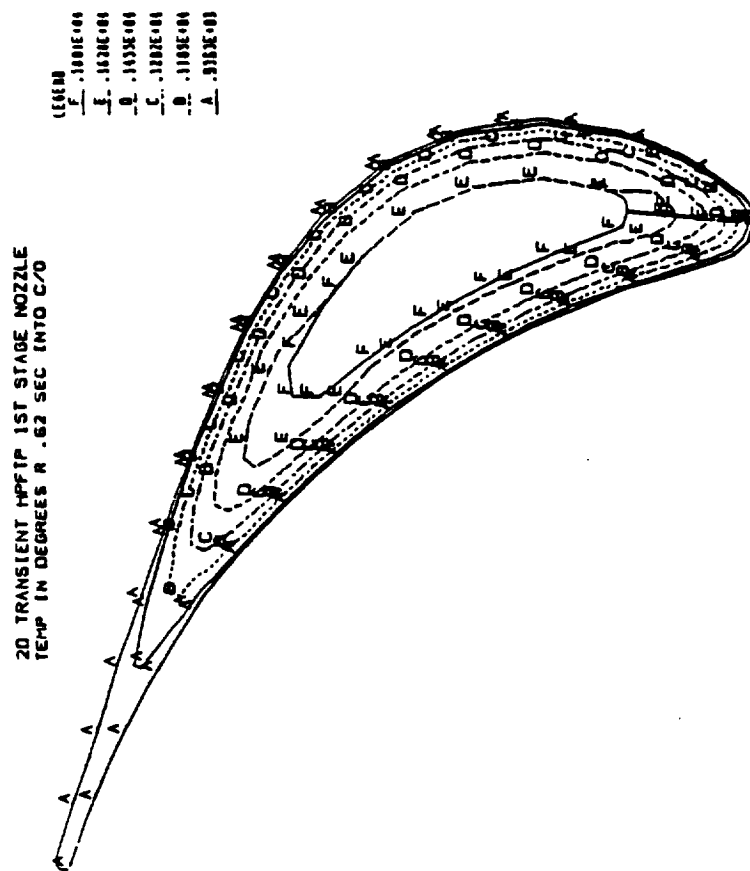


Fig. 2.48 HPFTP First Stage Nozzle Temperature Contour at 0.62 Sec. Temperature Spike



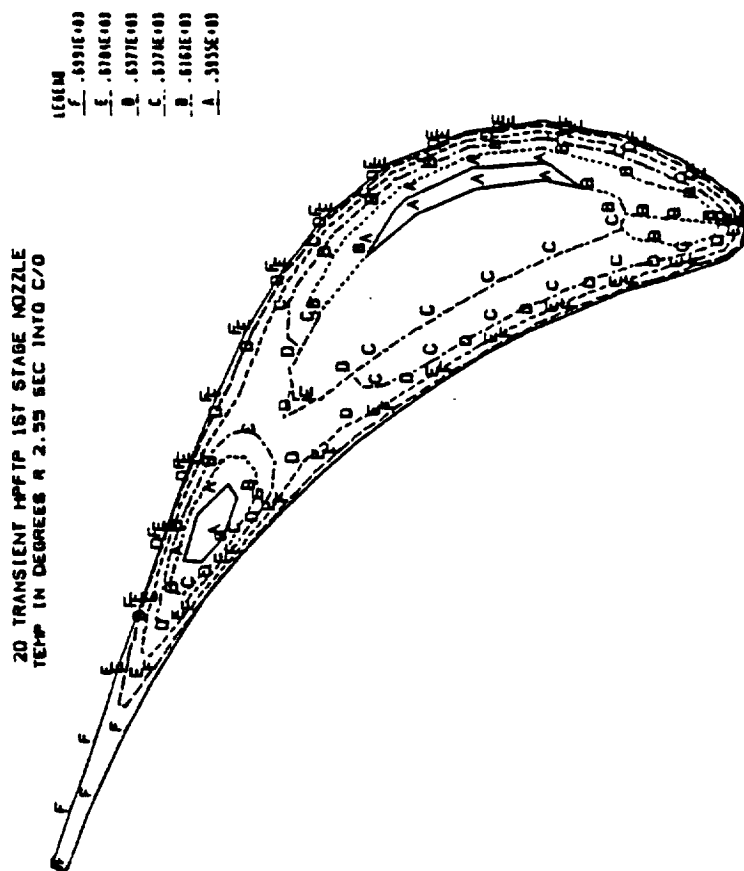


Fig. 2.49 HPFTP First Stage Nozzle Temperature Contour  
at 2.55 Sec. Temperature Spike at Cutoff

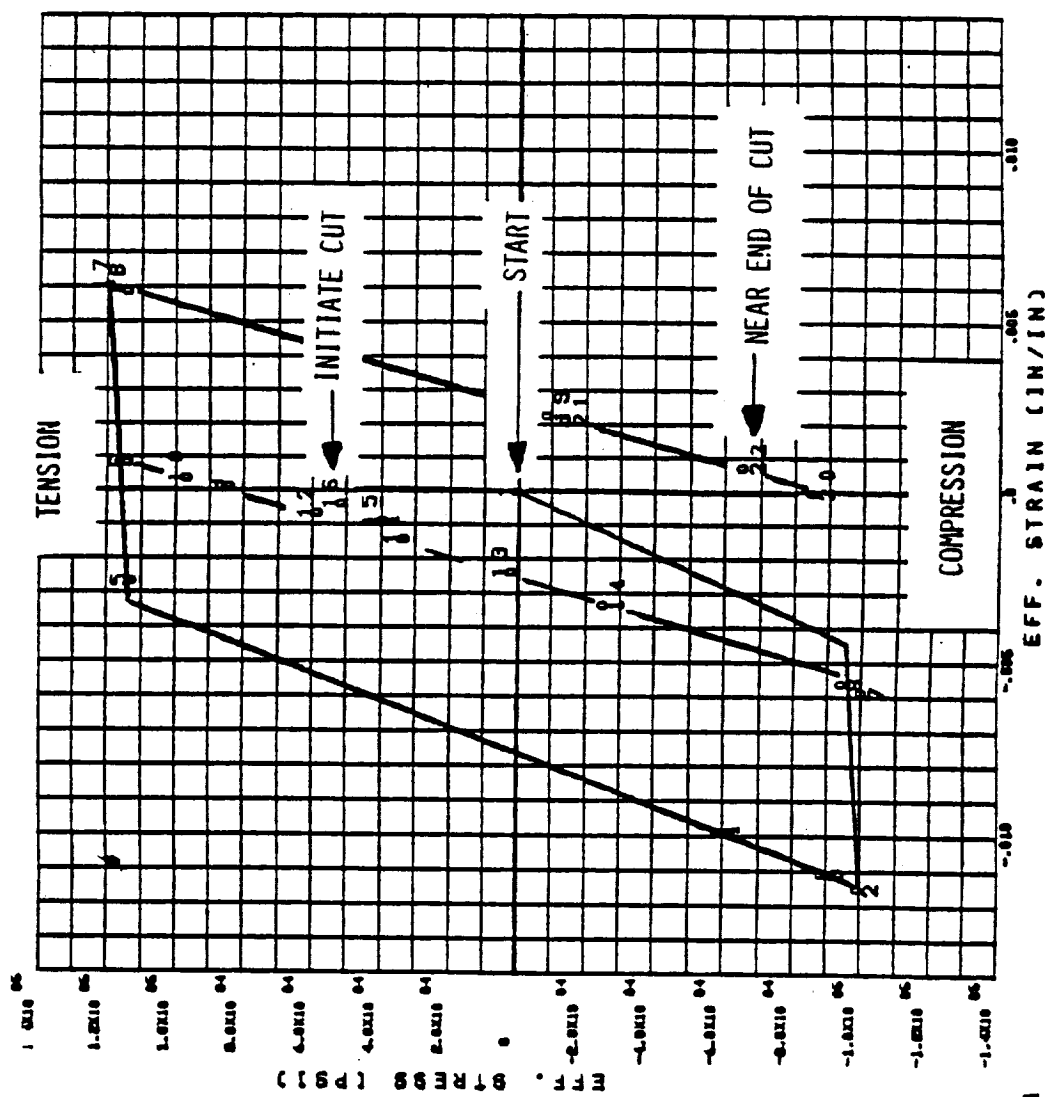


Fig. 2.50 Effective Stress-Strain Curve at a Reference Point at Nozzle Nose During One Temperature Duty Cycle

## Fir Tree Attachment Analysis

Rocket engine turbines have been designed successfully with blades integrally welded with the disk and welded. However, for most of the high thrust production engines fir tree attachment has been used. The goal of the fir tree attachment is to distribute the load uniformly to the disk. A typical profile of the fir tree arrangement is shown in Fig. 2.16. Initial sizing of the fir tree arrangement is done using strength of materials approach, but the design is verified using extensive finite element analysis. The load distribution problem is complicated due to tolerance envelope on the fir tree profiles which can result in all lobes not touching simultaneously and the number of loading conditions that need to be considered. This can happen inspite of the tight manufacturing tolerances in the loaded flat of the order of 0.0005". Thus a detailed sensitivity analysis is done using finite element techniques. Some of the objectives of the analysis include:

- 1) Optimum biasing of loaded flat tolerances to assure the desired ordered sequence to pick up the load.
- 2) Investigation of worst case conditions of tolerances to maintain adequate safety.
- 3) To design optimum loaded flat angle that can result in optimum stress distribution in blade and disk.
- 4) To design optimum fir tree tolerances in hoop direction to account for thermal hoop stresses in disk.

The details of the finite element model is relegated to a later chapter. The finite element analysis analysis requirement include material and geometric nonlinear analysis under steady state and transient conditions. The material nonlinear analysis is necessitated when only one lobes initiate the contact. In general single lobes, either the disk or the blade have insufficient strength to carry the entire load and therefore plastically yields until other contact points get into the mechanism of load transfer.

The actual value of the plastic strain limit used is a function of material, life requirement, and the environment (Hydrogen embrittlement effect). The geometric nonlinear analysis requirement is introduced through the use of interface or gap elements. It is necessary to note the many levels of sophistication of contact elements which include 1) Small deflection gap/no gap element with axial stiffness and friction with stick slip option 2) Large deflection contact element with axial stiffness and friction with coordinate update and stick/slip option in which gap condition is always checked between two predefined nodes and 3) Contact surface element which permits large lateral displacement between surfaces. The transient analysis is necessitated due to the ramp in rotor speed, pressure bending, and temperature field in disk and fir tree. It must be noted that the circumferential tolerances in the fir tree lobes and the unloaded bottom flats are generally based on different criteria. During the start, while the rim is hot, the center of the disk is cool resulting in compressive stresses in the rim of the disk. This has the effect of locking or unlocking the blade or both during a transient time history. This effect has to be considered appropriately based on design philosophy. For designs which rely on fir tree damping, locking is undesirable. Fir tree designs which do not rely on fir tree damping, the effect of unlocking resulting in fretting and its effect on the resulting fatigue or the effect of locking and its effect on vonmises stresses at the critical area of the root must be considered. While many successful designs have been completed using 2-D analysis, many approximations inherent in the 2-D analysis can be eliminated using a 3-D analysis. With a 3-D analysis the effect of blade bending on fir tree interface forces may be more effectively studied. The effect of skew of the blade with respect to the disk can be considered. In addition, the nonuniform distribution of the interface load along the chord length of the blade may be evaluated. The use of cycle symmetric option can be effectively used to reduce the size of the problem.

## 9. Dynamic Analysis

### Turbine Blade Vibration Damping

During normal operation, turbine blades are subjected to both steady-state and alternating stresses. The steady-state stresses are primarily due to

centrifugal and gas bending forces, while alternating stresses are due to harmonic variations in the flow stream. Struts, nozzles, and coolant jets are typical causes of flow stream variations. In the case of the SSME high-pressure fuel turbine (HPFT) first-stage blades, forcing functions are generated by the blades passing 41 upstream nozzles and 13 unequally spaced structural support vanes which are located upstream of the nozzles.

The attainable service life of a blade is a function of the combination of alternating and steady-state stress levels. This may be best illustrated with a Goodman diagram, as presented in Fig. 2.51 for MAR-M-246-DS at 1550 F. The calculated operating mean stress for the SSME HPFTP first-stage blade leading edge at full power level is noted on the diagram at 30 ksi. As evident, life (the number of cycles to failure) is very sensitive to the alternating stress level. The lowest blade frequency is approximately 5000 Hz. Using this as a counter, only 2000 seconds of turbine operation is necessary to accumulate  $10^7$  cycles.

It is clear then, that a reduction in the alternating stress level is desirable to increase operating life, or increase reliability for a given life. There are several methods which can be used to decrease alternating stress. The forcing function can be attenuated by increasing the axial space between the rotating blade and the impulse generating member; however, this is generally not an acceptable solution because of performance reduction or rotor dynamic side effects. Alternating stresses are also minimized by designing to avoid coincidence of natural blade frequencies with probable harmonic excitation forces. This becomes difficult because of the complexity of the turbine hardware, variable concerning the forcing functions, and the requirement for a wide operating range.

For the above reasons, and because the inherent damping of turbine blades is small, effective damping must be added to the blades. A certain amount of damping may be provided by mounting the blades to the disk by means of a fir tree arrangement with an appropriately engineered tolerance. The amount of motion in the fir tree is usually small and, therefore, the energy dissipated is limited. As a result, it has been frequently found necessary to incorporate a mechanical damper design operating some distance from the

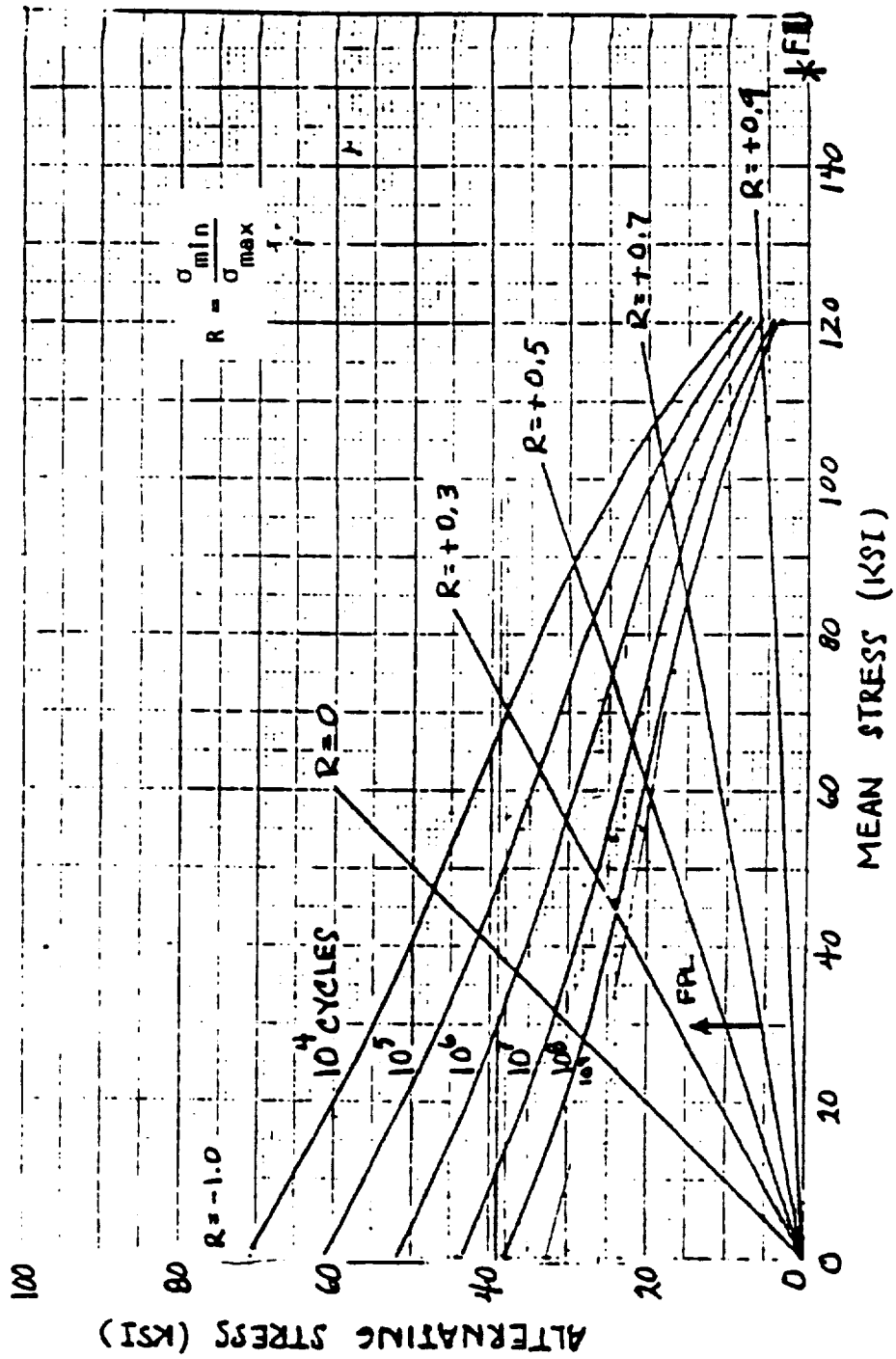


Fig. 2.51 Typical Goodman Diagram (1550F, MAR-M-246 DS (HF); Longitudinal)

fulcrum of the blade motion, i.e., at the blade platform or shroud. The design of such dampers has in the past, been based to a large extent on empirical data, which generally has been treated as proprietary by turbine companies. The most common damper concept used consists of a relatively small piece of metal which under centrifugal load is forced radially out, and is supported equally by the platforms of two adjacent blades where relative motion occurs between the blades due to vibration, and energy is dissipated at the damper-to-blade interface. This energy is proportional to the mass of the damper, the coefficient of friction at the contacting surfaces, the square of rotational speed, and the relative sliding velocity between the contacting surfaces.

As the weight of the damper or the rotational speed increases beyond a critical value, the damper locks up, provides no damping, and acts as an added mass. This effect establishes mass as a critical parameter, and shows quite clearly that:

- 1) There is a distinct optimum damper mass.
- 2) An extremely heavy damper is worse than no damper at all.

3) If a blade locks up so that one blade is supported at the damper location by another blade, stresses will be quite large. This is a condition that occurred on the SSME, where molten plating material (nickel) was trapped between platforms during an overtemperature start, (Fig. 2.52) forming a solid path during a subsequent lower temperature test; and in a separate instance, when two blades were installed such that they were touching at the platforms. Both instances led to premature cracking of the blades involved.

The second partially controllable parameter is the friction factor at the damper contacting surfaces. The observation made above relative to optimizing the mass of the damper is also applicable to the friction factor. Thus, a very high friction factor would tend to have the same effect as excessive mass, and would lead to blade lockup. Very low friction factors would limit the energy absorbed in damping. In analysis, the selection of friction factor values is important to obtain a realistic simulation of damper effectiveness. In practice, surface conditions must be controlled to realize optimum benefits from damping.

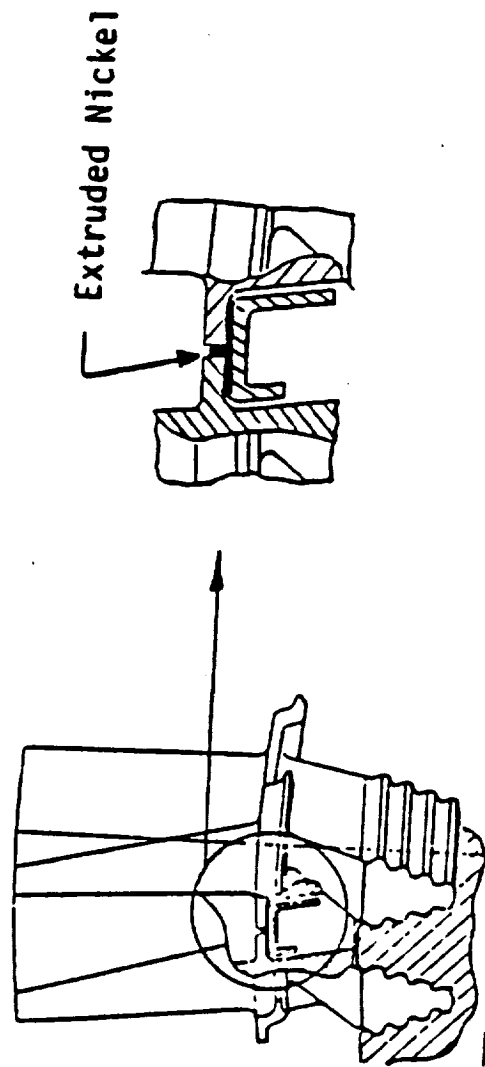


Fig. 2.52 Lock up of HPFTP Blade Due to a Overtemperature Start



The geometry of the damper and locations where the loads are applied to the blades also are parameters which have a direct bearing on the effectiveness of the damping concept. As discussed later, blades can vibrate in any of a number of modes depending on the frequency of the forcing function. These must be identified, and the damper must be designed such that the damping load is applied away from the nodes of the predominant modes, i.e., those which are potentially most detrimental. This consideration makes it imperative that the vibration characteristics of the subject blade be known to the damper designer, either from analysis or preferably confirmed by experimental effort.

Although rotational speed and sliding velocity are important terms in the damping analysis equation, they are fixed by performance requirements of the turbine, and by blade frequency and vibration amplitude, respectively. Therefore, these parameters cannot be adjusted to effect a more efficient damper.

Usually a parametric study is done by forcing the blade sinusoidally at each of its natural frequencies and varying the damper weight (friction force) until the stress in the blade is minimized. As would be expected, each mode would require a different damper weight for a minimum stress. Therefore the problem becomes one of determining which mode is more predominant in the overall blades response. The damper weight is then chosen to minimize stresses in the mode which is most likely to respond highly.

#### SSME HPFTP FIRST STAGE TURBINE BLADE DAMPING ANALYSIS

A substantial effort has been expended by Rocketdyne in analyzing the vibration characteristics of the SSME high-pressure fuel pump first-stage turbine blade. The analytical work was supported by nonrotating static tests of individual blades and by whirligig tests of strain gaged blades in a wheel at full operating speed. The blade vibration modes, frequencies, and the formulation of finite element models have been defined, and analytical codes have been developed to predict blade dynamics, including damping effects.

A finite element analytical model of the HPFTP first-stage turbine blade and wheel has been developed for use in STARDYNE computer code with plate type

elements. The model has been used extensively to perform natural frequency and mode shape computations in addition to detailed linear and nonlinear response analyses to evaluate the current dampers in support of the SSME program. Of particular interest is the nonlinear capabilities of the analytical model. Friction damping was introduced and optimum damper weight was computed for several damper configurations. Figure 2.53 shows a typical result of an analysis where blade alternating stress is plotted as a function of damper mass. Note the optimum damper mass is at the point of minimum stress. Any further increase in weight only serves to decrease the effectiveness of the damper and increase blade stresses. Another typical example of the results of nonlinear analysis is presented in Fig. 2.54 where peak blade stress is plotted versus rotor speed for various damper configurations.

#### ANALYSIS TECHNIQUE

One of the analysis technique that is used to determine damper effectiveness employs the use of a large finite element model of the turbine blade and wheel. The model was analysed using the STARDYNE computer program. This program is widely at Rocketdyne with excellent correlation between analysis and test. Both the blade and wheel and modeled primarily with plate elements which describe, in detail, the stiffness, mass, and geometric properties of the actual hardware.

The STARDYNE program is used to form the basic stiffness and mass matrices and extract eigenvalues from the finite element model. Output from STARDYNE is then used in a Rocketdyne developed response program called DYNREN. This is a nonlinear modal analysis program which operates in the time domain. It uses modal analysis as a transformation to a coordinate system in which the equations of motion are easier to solve, and then transforms back to physical coordinates to output results. It is not a modal superposition technique when nonlinearities are encountered, since the vibration modes are coupled. The technique employed is exact within the limits of:

- 1) The accuracy of the finite element model employed
- 2) The accuracy of the numerical integration time step specified
- 3) The number of modes retained in the solution

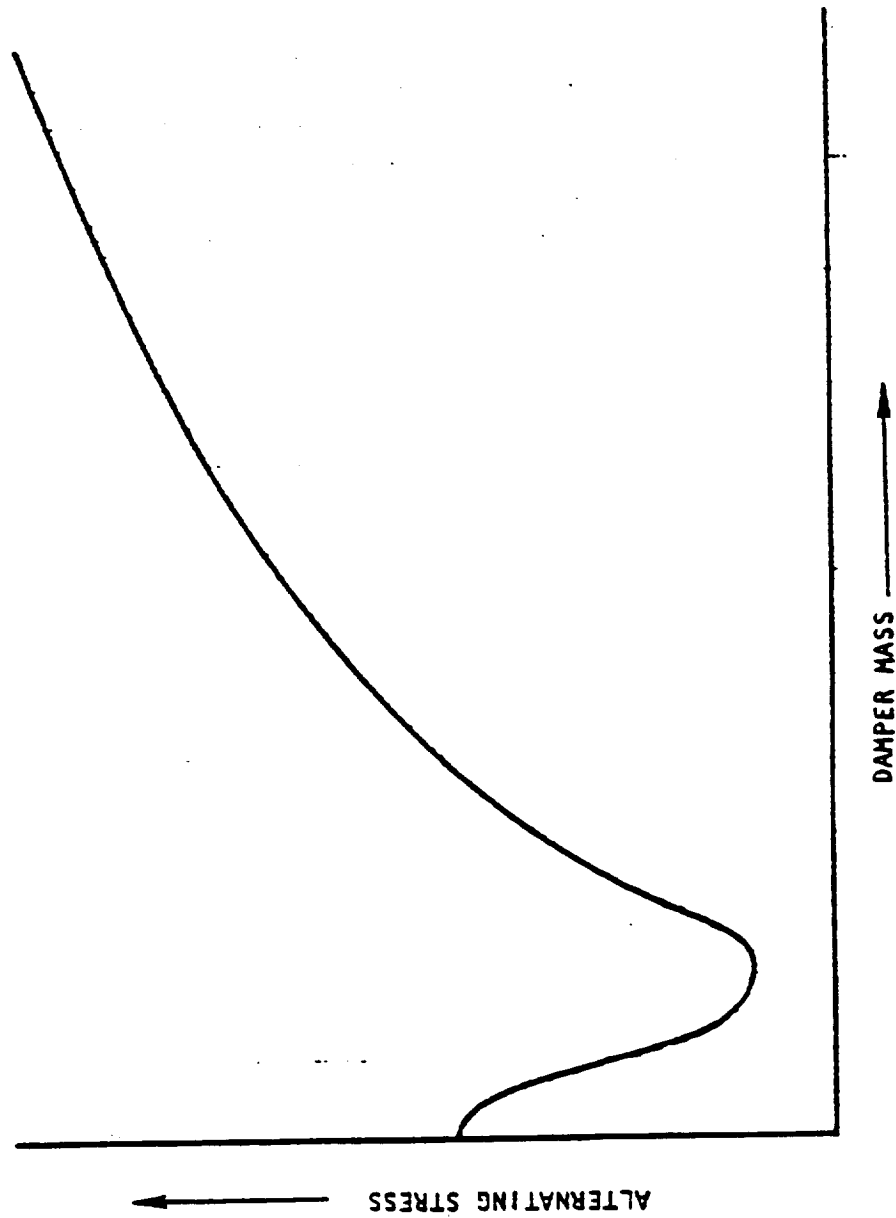


Fig. 2.53 Alternating Stress vs Damper Weight

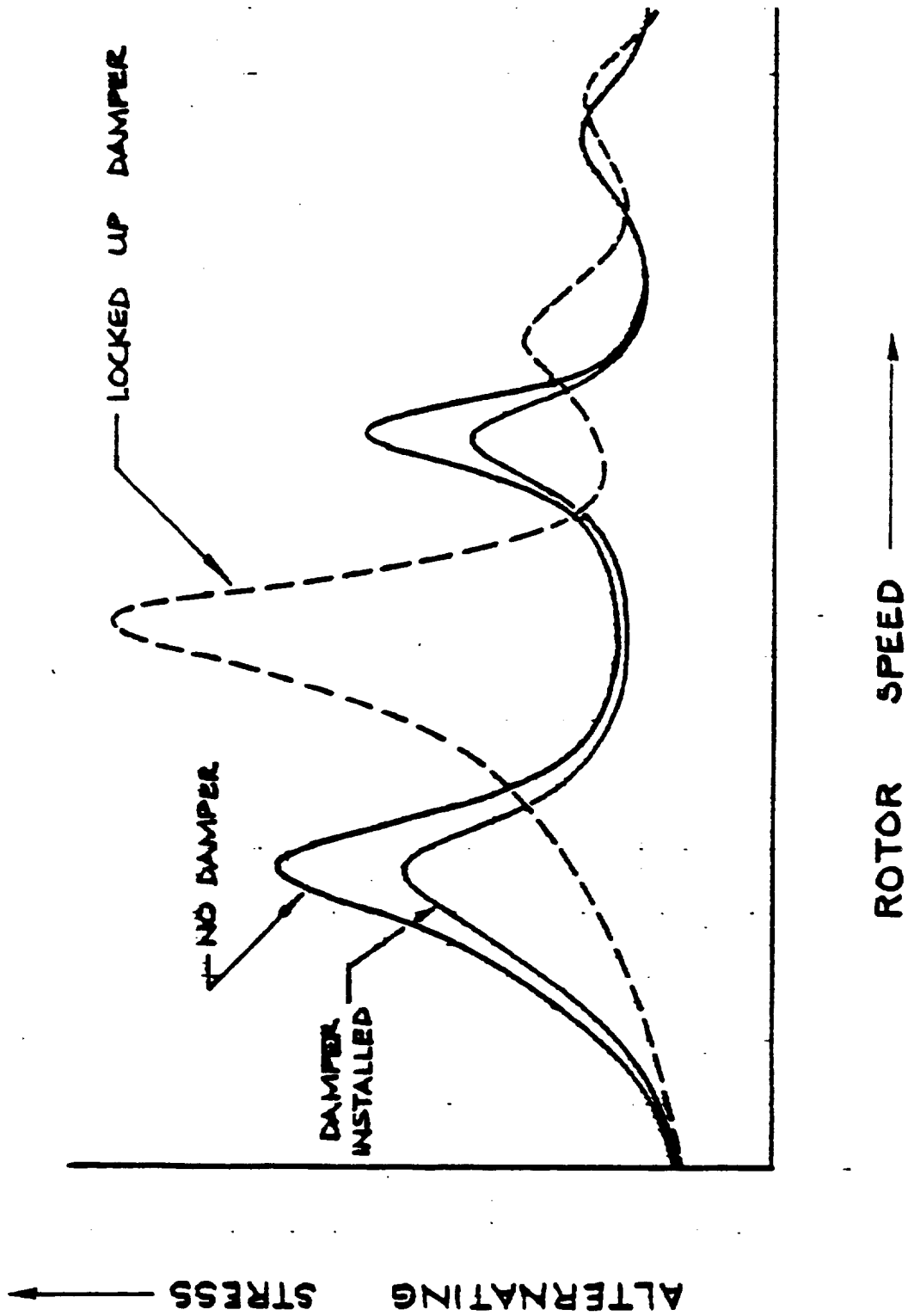


Fig. 2.54 Turbine Blade Response as a Function of Damper Configuration

If a sufficiently large number of modes are selected (enough to accurately describe the motion where nonlinearities occur), the model is sufficiently fine, and a reasonably fine time step is used for numerical integration, excellent results have been obtained with this procedure as compared to other linear and nonlinear computer programs.

The basic equations employed in the problem solution are as follows:

Given a system,

$$[m] \{\ddot{x}\} + [c] \{\dot{x}\} + ([K_1] + [K_2]) \{x\} = \{F\}$$

Using STARDYNE, the eigenvalue problem is solved for,

$$[m] \{\ddot{x}\} + [K_1] \{x\} = 0$$

This gives natural frequencies and mode shapes,

$$[\omega^2], [\Phi]$$

The modes and frequencies are then input to the DYNREN program. In this program the physical coordinates  $\{x\}$  are transformed to modal coordinates.

$$\{x\} = [\Phi] \{q\}$$

The new equations of motion become,

$$\{\ddot{q}\} + [2\zeta\omega] \{\dot{q}\} + ([\omega^2] + [\Phi]^T [K_2] [\Phi]) \{q\} = [\Phi]^T \{F\}$$

$[K_2]$  can be any linear or nonlinear stiffness matrix.

For the blade-damper problem  $[K_2]$  will represent coulomb friction damping,

$$[K_2] = [F_f \text{ sign}\{\dot{x}\}],$$

where  $F_f$  is the friction force due to the damper rubbing on the blade,  $F_f$

is a function primarily of rotor speed, damper mass, geometry, and friction coefficient.

After rearranging, the final equations become,

$$[\ddot{q}] + [-2\zeta\omega_n][\dot{q}] + [\omega_n^2][q] = [\Phi]^T[F] - [\Phi]^T[F_f \text{sign}(\dot{x})][\Phi][q]$$

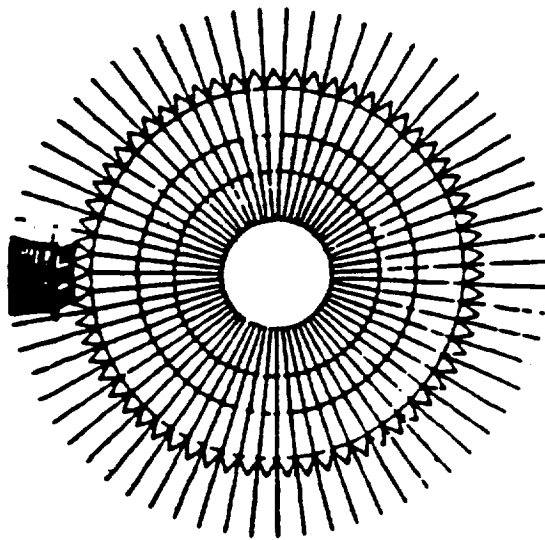
This system of nonlinear differential equations is then solved using a standard integration routine.

### Some Variations in Damping Analysis Technique

Initial efforts in analysis of coupled disk blade problems involved modeling only a few blades with detailed blade models and the rest of them with multiple beam elements (Fig. 2.55). The coupling between the blades were examined by a response analysis in which only one blade was excited and studying the response of the others. The results indicated:

- 1) Wheel modes were highly coupled with blade modes in the same frequency range.
- 2) There is significant coupling between all blades (even 180 degrees across the wheel) in most modes where wheel blade interaction is strong.
- 3) The response of the blades modeled with beam elements is so different from the response of modelled with plate elements that it was concluded that all blades must be modeled with plate elements.

Due to the nonlinear characteristics of the friction-dampers the results of the damper weight optimization study are dependant on the magnitude of the forcing function. As is always the case with unsteady pressure loading of blade surfaces, the forcing function is not well known. For most turbine blade analysis work the alternating pressure component is taken to be 10 to 20% of steady state pressure exerted in the blades. However, the frequency content of the forcing function is better understood because the turbine



WHEEL WITH THREE FULL BLADES  
AND 60 BALANCE BLADES

Fig. 2.55 SSME HPFTP First Stage Blade Model

geometry is well known. For example HPFTP has 13 and 41 upstream nozzles. Therefore each blade will be pulsed 13 and 41 times during one revolution of the turbine disk. In addition, since pulses are not sine waves, higher harmonics can be present. Again the relative magnitude of primary as well as secondary harmonics is not well known. These uncertainties present in the single blade analysis are compounded tremendously when multiple blade studies are attempted. Thus there is another school of experts who believe that it is sufficient to model single blade and perform the analysis with the goal of discovering general trends. In either case the analysis results should be carefully studied and compared with extensive experimental testing of the type used at Rocketdyne (whirlgig).

#### Key Features of a Finite Element Program for Turbine Blade Analysis

A finite element program specifically tailored for turbine blade analysis must first have the capability to accurately define the blade geometry and compute natural frequencies and associated mode shapes. As when strong coupling between the disk and the blade is suspected, it will be necessary to model the disk with all the blades attached. A modal coupling approach may be necessary since typical turbine disks have on the order of 60 blades. The computer capacity of most large systems would be overwhelmed by such a problem not to mention the prohibitively high costs of computing eigenvalues for large structural models. However, if the modal characteristics of a typical single blade and if any rogue blade that may be present were computed and coupled with the modes of the turbine disk and with the other blades then the complete system modes could be defined at a relatively low cost. Other techniques such as substructure analysis or cyclic symmetry may be useful in simplifying the problem to a manageable size. When using cyclic symmetric options it is important to consider the complexity of forcing function produced by upstream and downstream wakes, free stream distributions, and the phasing needed between the blades.

The response part of the finite element program must be capable of handling the nonlinear forces produced by friction damping. Many programs that handle coulomb friction do not address the stick-slip phenomenon. The assumption in these programs is that the friction force is in effect only as long as the



element is in motion. This is adequate for low values of friction where the rubbing surface is slipping during most of the cycle. However, as the damper weight increases stick-slip action becomes very important. Any new response program must account for stick-slip by computing the friction force which occurs when the rubbing surface is not in motion as well as when it is in motion.

For the analysis of multiple blades on a disk the response program must have the capability of handling up to 100 phased forcing functions. This is necessary because of the fact that the turbine wheel is rotating within a stationary pattern of flow field disturbances. Each blade gets pulsed by a force that has a time lead or lag from the force that an adjacent blade was hit by.

## 10. Experimental Correlation

### Temperature Data

Engine firing data and failure history of HPFTP turbine blades have indicated that SSME HPFTP first stage blades see much higher temperatures than the nominal design values. Post test inspection of blades have further given an indication of temperature gradients present in the blade by surface condition and decoloration. The detection of incipient melting conditions through optical devices show that some blades have seen temperatures greater than 2715°R. The standard flight instrumentation measures temperatures at turbine exhaust and that too at only two locations. The measurement devices used in flight (transducers) are too slow to respond to rapid temperature spikes and thus, are unsuitable for measurement of rapid thermal transients. In order to obtain a better understanding of the temperature environment in the turbine, three turbopumps were extensively instrumented with thermocouples and tested on two engines (Table 2.5). The instrumentation was designed to measure rapid thermal transients, gas temperatures at turbine outlet as well as at inlet and at several clock positions. Other objectives of the test included modification to fuel preburner and fuel preburner oxidizer valve start sequence. An overview of the global locations of the instrumentation is shown in Fig. 2.56. Fig. 2.57, section CC, shows the locations of sensors at Kaiser

MPFTP	ENGINE	TEST	TEST PROFILE	PRE-TEST CONFIGURATION CHANGES
9208R2	2010	902-278	Ignition	Fuel Preburner Modification #1
"	"	902-279	RPL-FPL-65	No change
"	"	902-280	Ignition	Fuel Preburner Modification #2
"	"	902-281	Ignition	FP0V Start Modification #1
"	"	902-282	Ignition	FP0V Start Modification #2
"	"	902-283	RPL-FPL-65	FP0V Start Modification #3
9208R3	"	902-285	RPL	Final (Present) Configuration
"	2208	750-169	Ignition	No Change
"	"	750-170	RPL-90	" "
9307	"	750-171	RPL-FPL-90	" "
"	"	750-172	RPL-FPL-90	" "
"	"	750-173	RPL-FPL	" "
"	"	750-174	RPL-FPL-90	" "
"	"	750-175	RPL-FPL-111	No Change

Table 2.5 Instrumented MPFTP Tests

hat, Fig. 2.58, section BB, shows the locations of sensors at turbine inlet nozzles, and Fig. 2.59, section AA, shows the location of sensors at turbine exhaust.

A typical start temperature transient for the HPFTP is examined first. The start temperature transient is plotted to an expanded scale in Fig. 2.60 for the first 10 seconds at the Kaiser hat location. The transient is characterized by two temperature spikes, the first one being termed as the ignition spike at 0.75 seconds and the second one as the fuel oscillation spike at approximately 1.3 seconds.

The first spike is caused by the too rich mixture as a result of reduced fuel flow due to the sudden increase in fuel preburner chamber pressure at ignition. The second spike is due to fuel oscillation which is a cyclic phenomenon observed in SSME. The net effect of this phenomenon is the reduction in fuel flow to the fuel preburner at about 1.3 seconds. As the engine pressure increases, the oscillation vanishes and the engine reaches the main stage operation. Fig. 2.61 through Fig. 2.67 illustrate several aspects of this start transient phenomenon.

There are variations in data between firing to firing, engine to engine and from turbopump to turbopump. The inlet temperature can vary between firings appreciably for the same spatial location. This is illustrated by comparing the PID 1319 measurement between 750-171 and 902-279 test measurements (Fig. 2.61 and Fig. 2.62). Both the firings used the same start sequence but the engines and turbopumps were different. Fig. 2.62 illustrate the variation in turbine inlet temperatures at transient due to modifications in start sequence. Turbine blades may experience large cyclic temperature changes at start transient and to a lesser extent at mainstage operation. This is illustrated in Fig. 2.63 where  $T_1$  through  $T_7$  are temperature measurements at different clock positions (Fig. 2.59). The temperature spikes as measured in the turbine exhaust is much less than that observed in turbine inlet. This is illustrated by comparison of Fig. 2.63 and Fig. 2.64 which were measurements from test 750-171. There is also a variation in gas temperature based on clock positions. The regular flight transducers instrumentation (Fig. 2.65) is too slow to follow the start transients and thus shows no spikes.

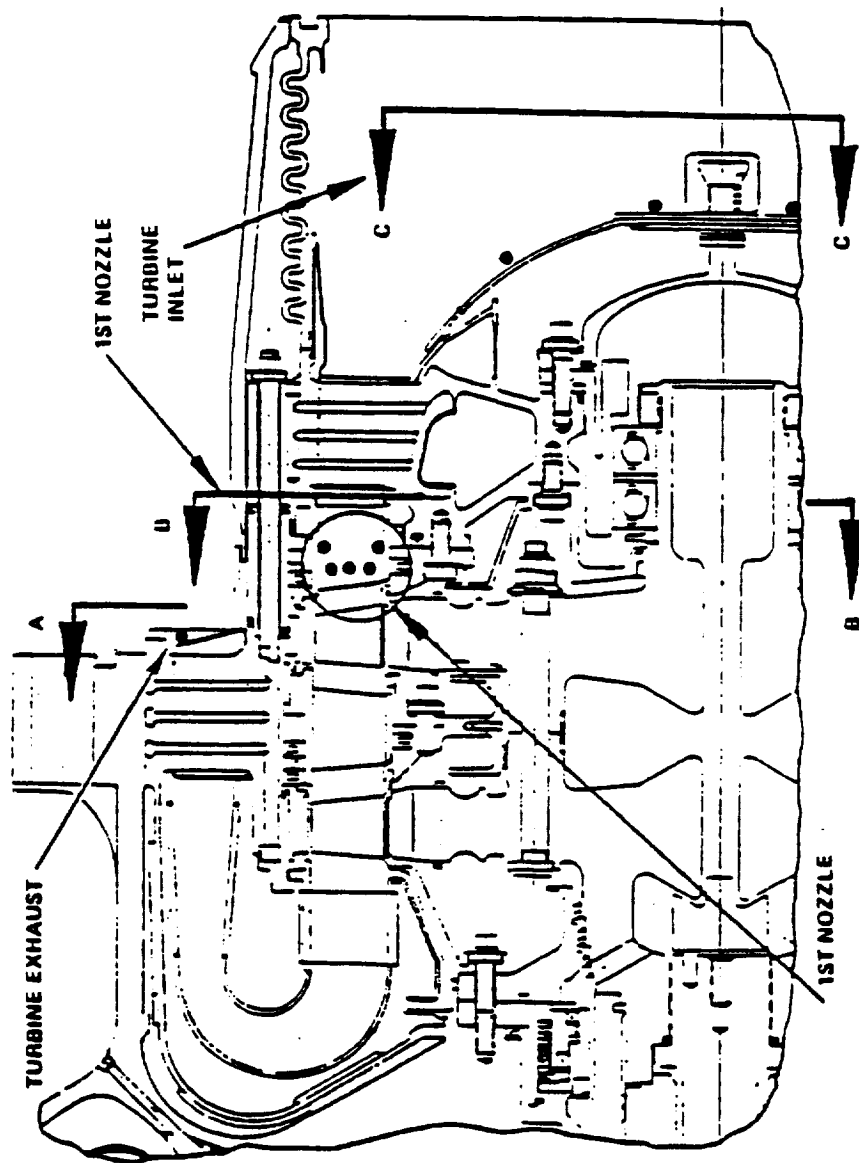


Fig. 2.56 Cross-Sectional View of the Instrumented HPFTP Turbopump

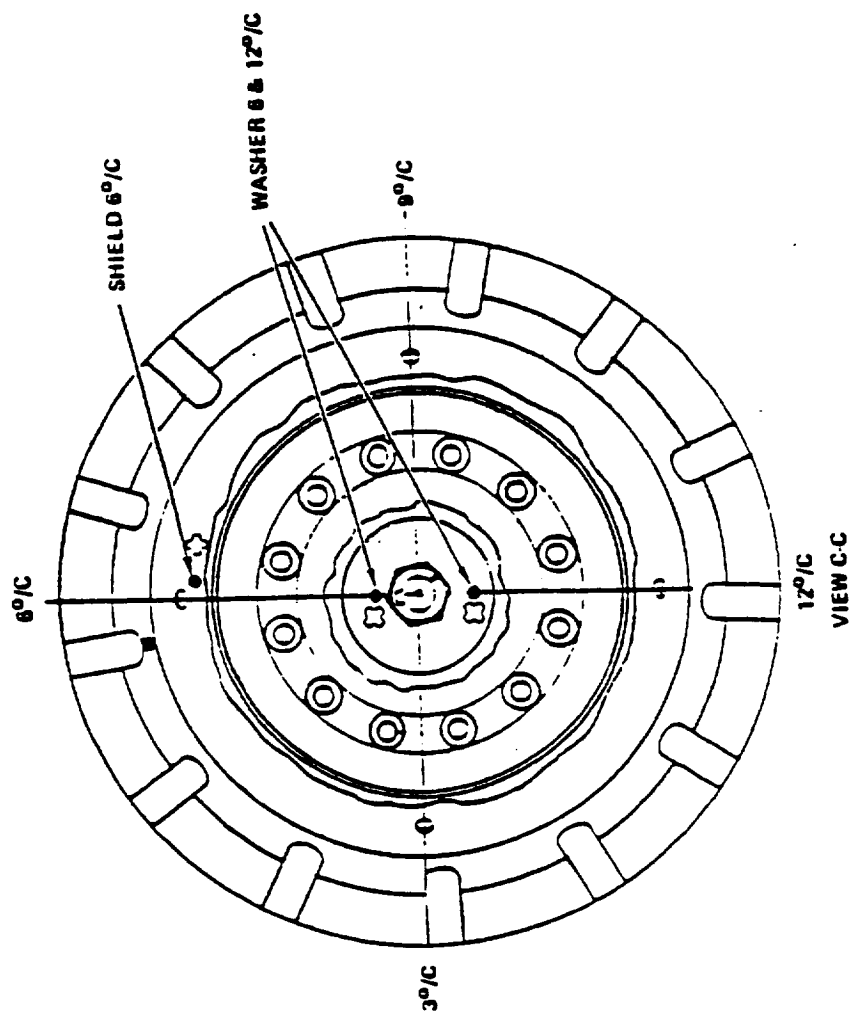


Fig. 2.57 Turbine Inlet Temperature Sensors at Kaiser Hat

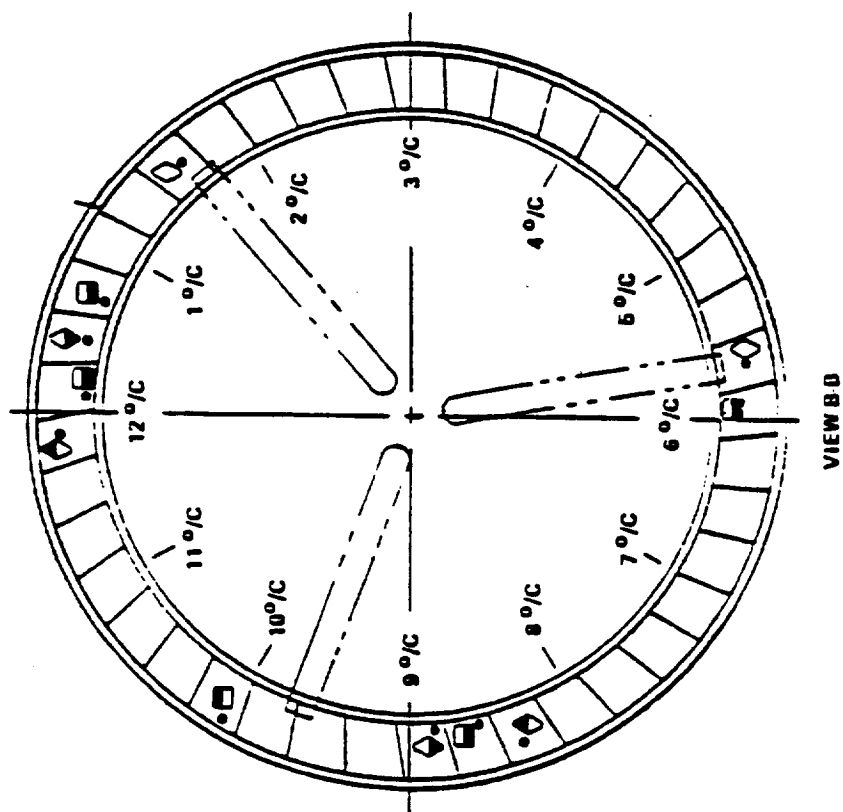


Fig. 2.58 Turbine Inlet Temperature Sensors at Turbine First Stage Nozzle

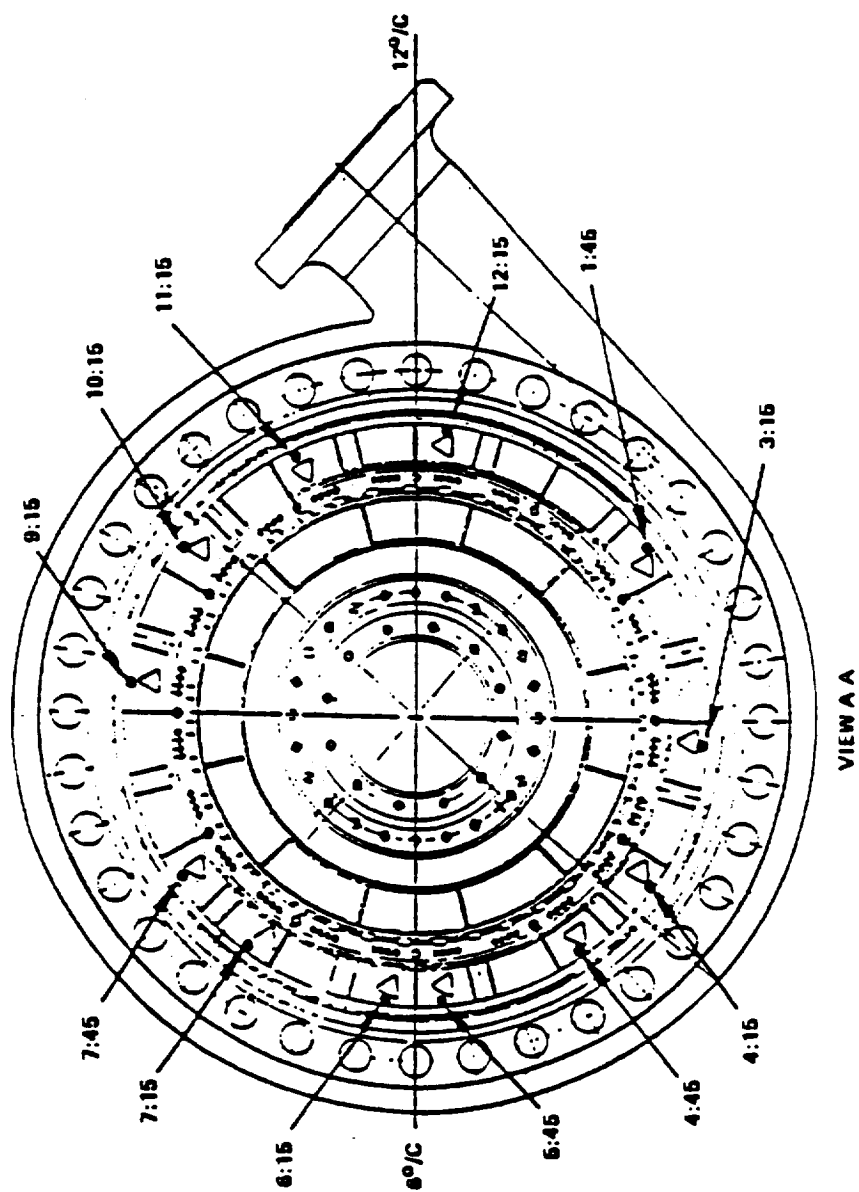


Fig. 2.59 Turbine Exhaust Temperature Sensors

52 1319 HPFT KSR NUT USH

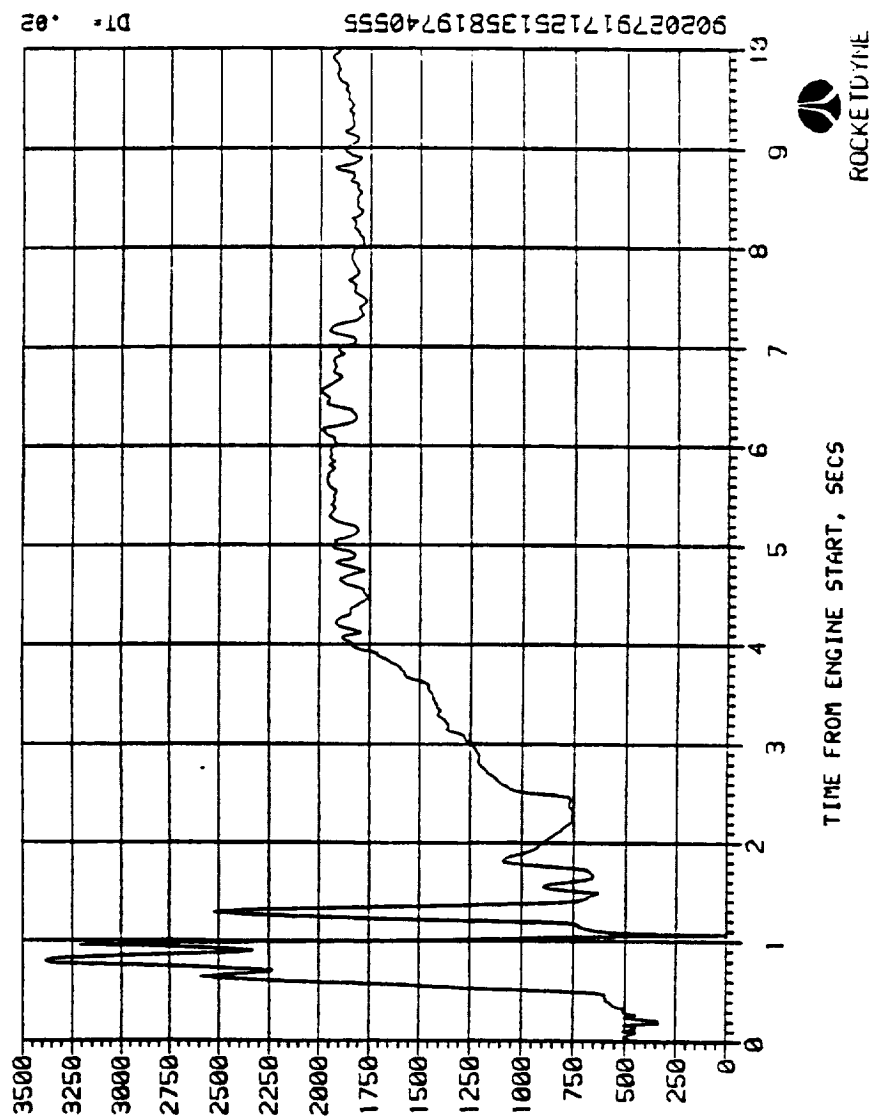


Fig. 2.60 Temperature Spike at Start Transient at Kaiser Hat Location



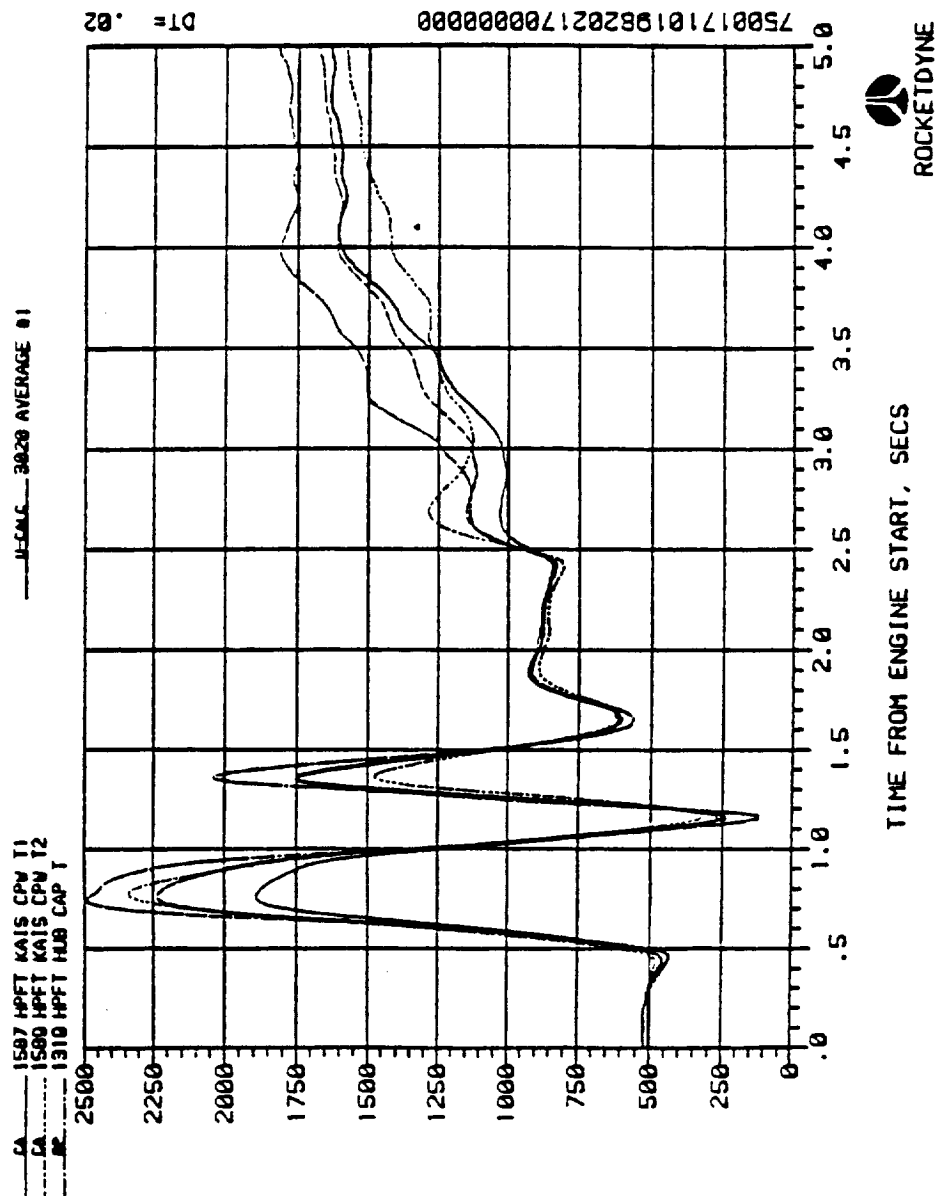


Fig. 2.61 Start Transient Temperature Measurements at Kaiser Hat for Test 750-171

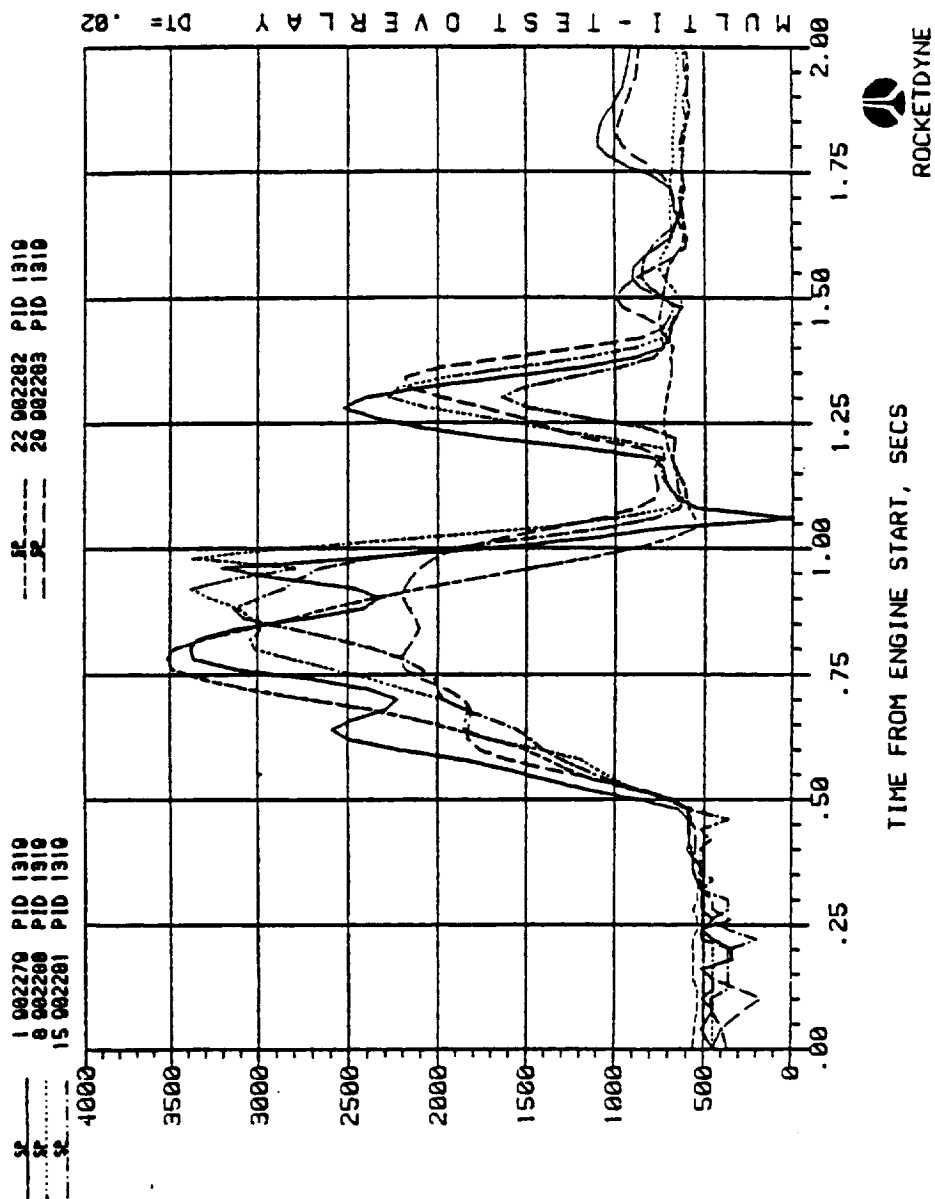


Fig. 2.62 Comparison of Kaiser Hat Temperature Measurements with Variations in Start Sequence



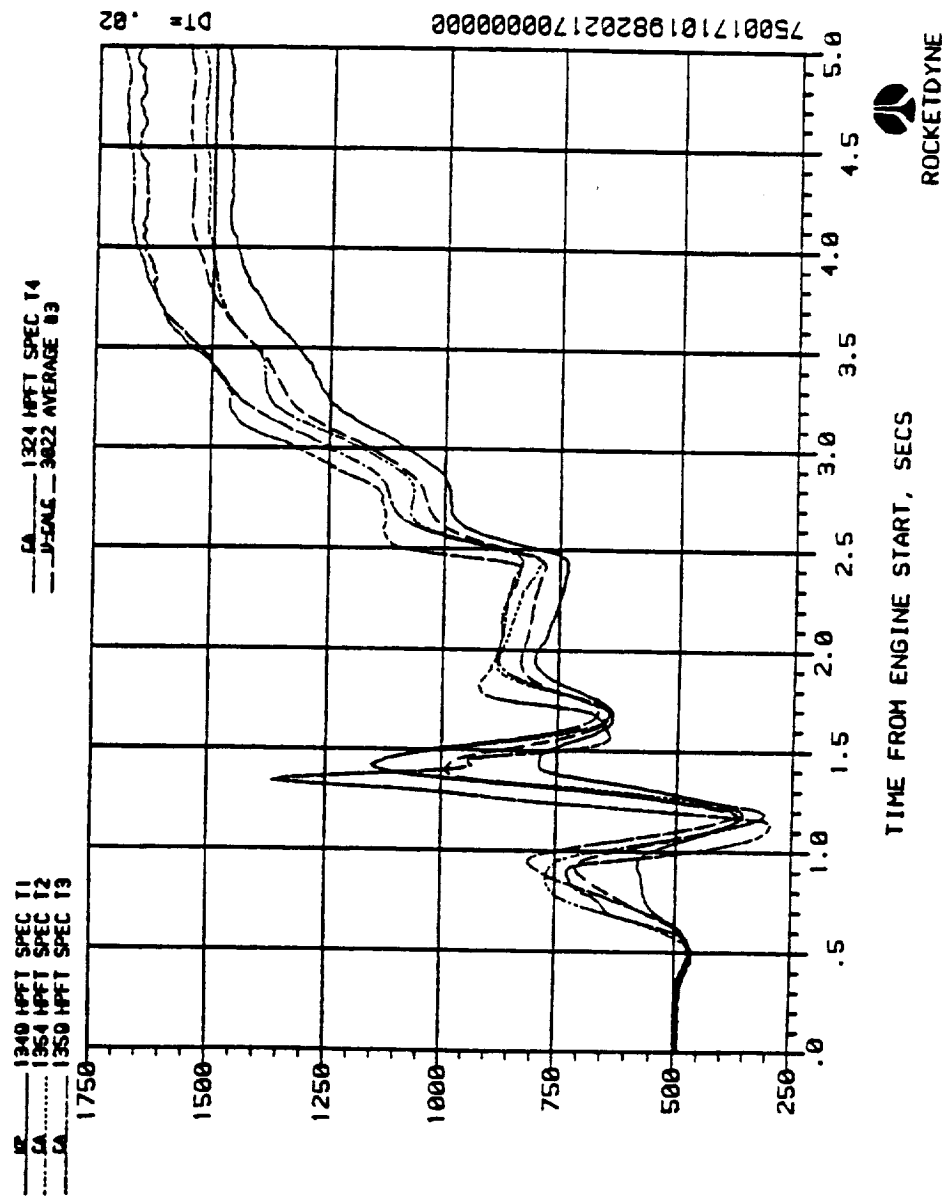


Fig. 2.64 Turbine Exhaust Temperature Measurements at Start Transient

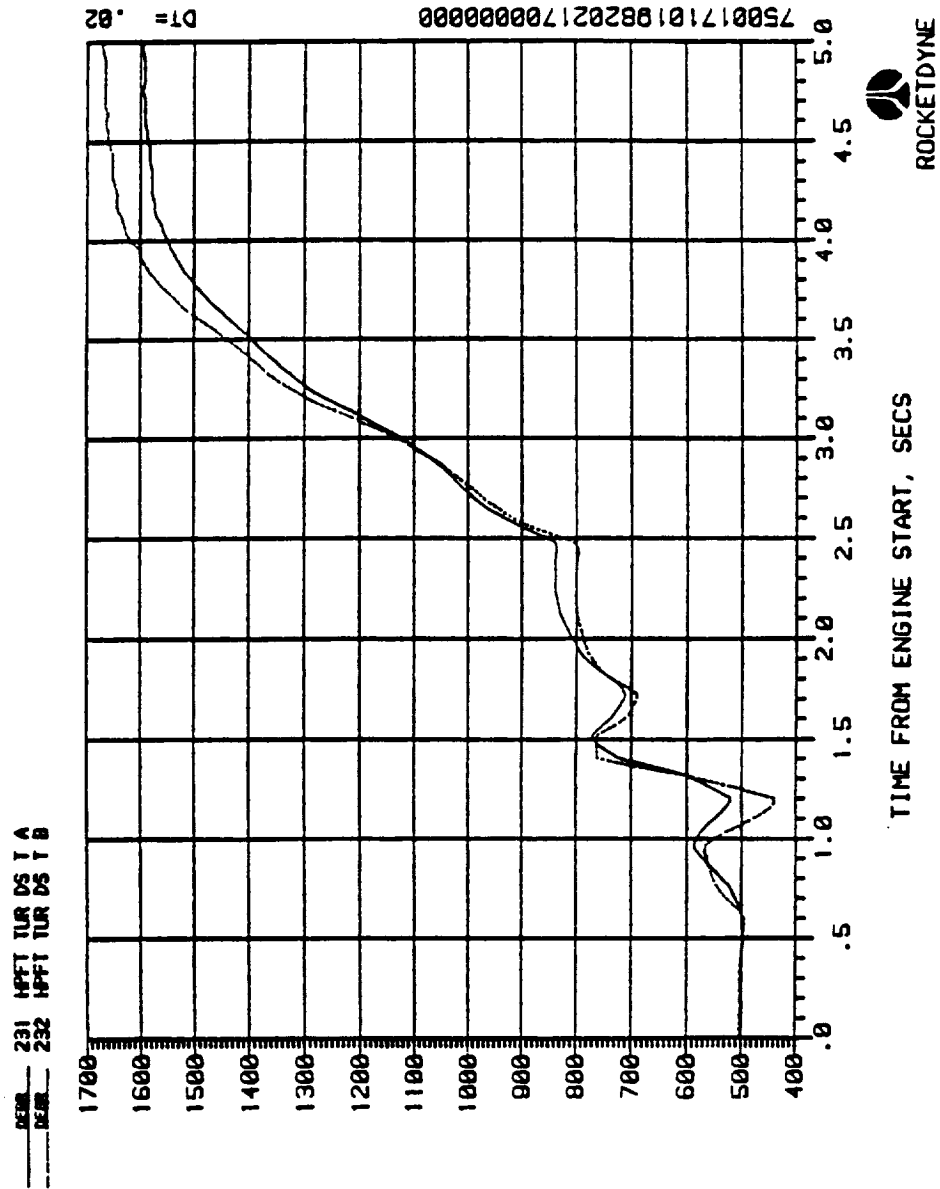


Fig. 2.65 Temperature Measurements at Turbine Exhaust using A and B Transducers

The effects of rapid cutoff transient is illustrated in Fig. 2.66 and Fig. 2.67. For safety reasons at shutdown oxidizer valve is activated first resulting in quenching of hot turbine components in cold hydrogen in a time period of five seconds. The rapid temperature decrease at nozzle and the turbine exhaust is illustrated in Fig. 2.66 and Fig. 2.67.

## MODAL TESTING

Holographic modal testing as it applies to turbine blades is done to determine the natural frequencies and corresponding mode shapes of a blade. This information is used to assess the Validity of the blade finite element model. Most testing is done with a single blade specimen brazed to a block. The blade is painted white for good optical properties and the block is secured to a small crystal shaker. All excitation forces are input at the blade base.

The holographic method employs a low power laser light beam which is split into two beams. The reference beam is directed at a holographic plate and the other beam is focused on the test specimen undergoing vibration. Reflected light from the vibrating test specimen also falls on the holographic plate. The reflected light when strikes the holographic plate forms an interference pattern with the reference beam. The interference pattern is formed because the reflected light has been doppler shifted by the vibrating test specimen. The interference pattern clearly shows the mode shape of the vibrating blade (Fig. 2.68). A comparison of analytical results from a finite element model with that of Helographic testing can be made using Fig. 2.68 and Fig. 2.69.

## Whirligig Testing

Rocketdyne's high speed diagnostic laboratory testing facility is used to determine blade excitation modes and stresses at full operating speeds and to determine the effectiveness of several damper designs. The tester is named "whirligig", and is shown in Fig. 2.70.

Whirligig testing consists of strain gaging turbine blades and running them in a turbine disc, exciting the blades to resonance with gas directed through orifice jets onto the blades, and monitoring the response using strain gages

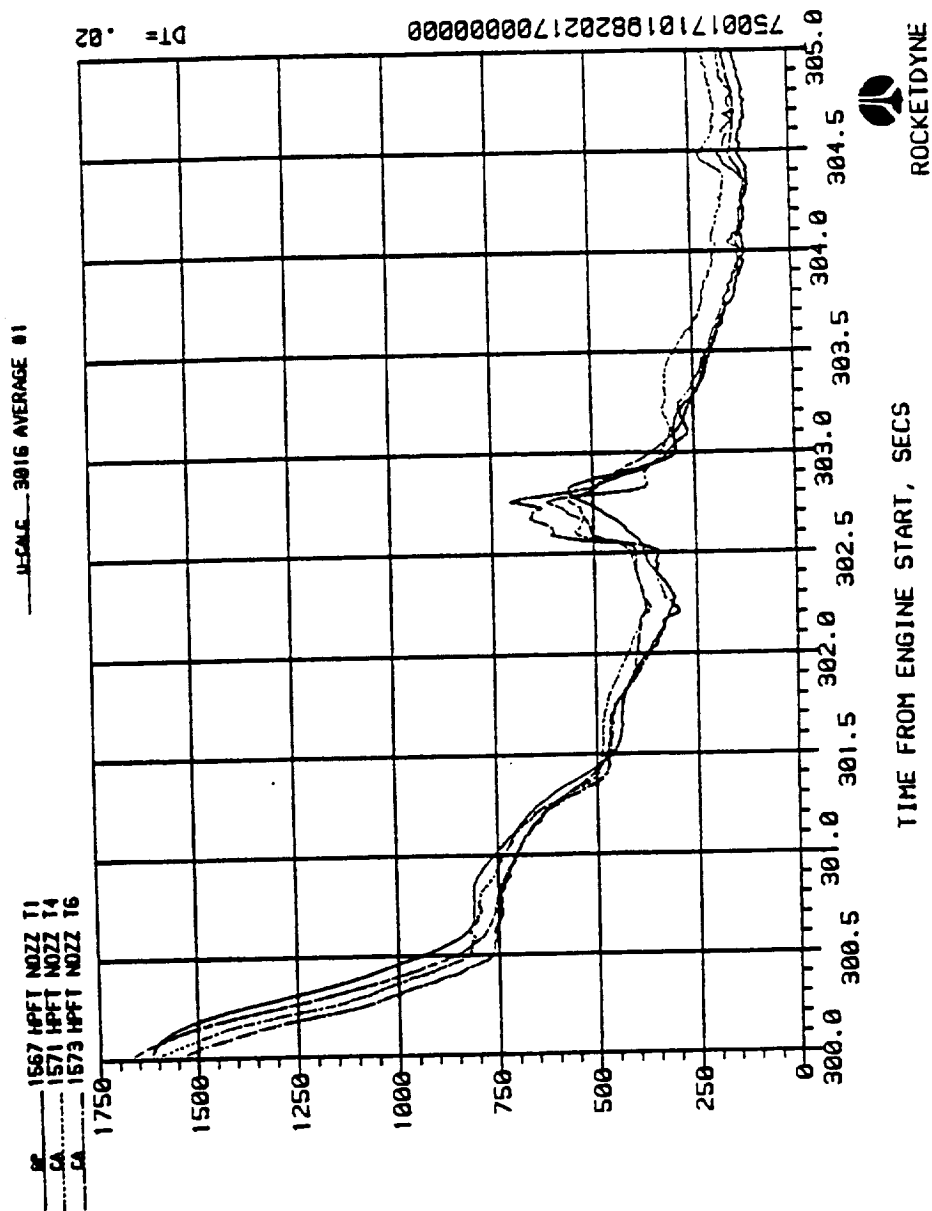


Fig. 2.66 Turbine Nozzle Temperatures at Cutoff Transient

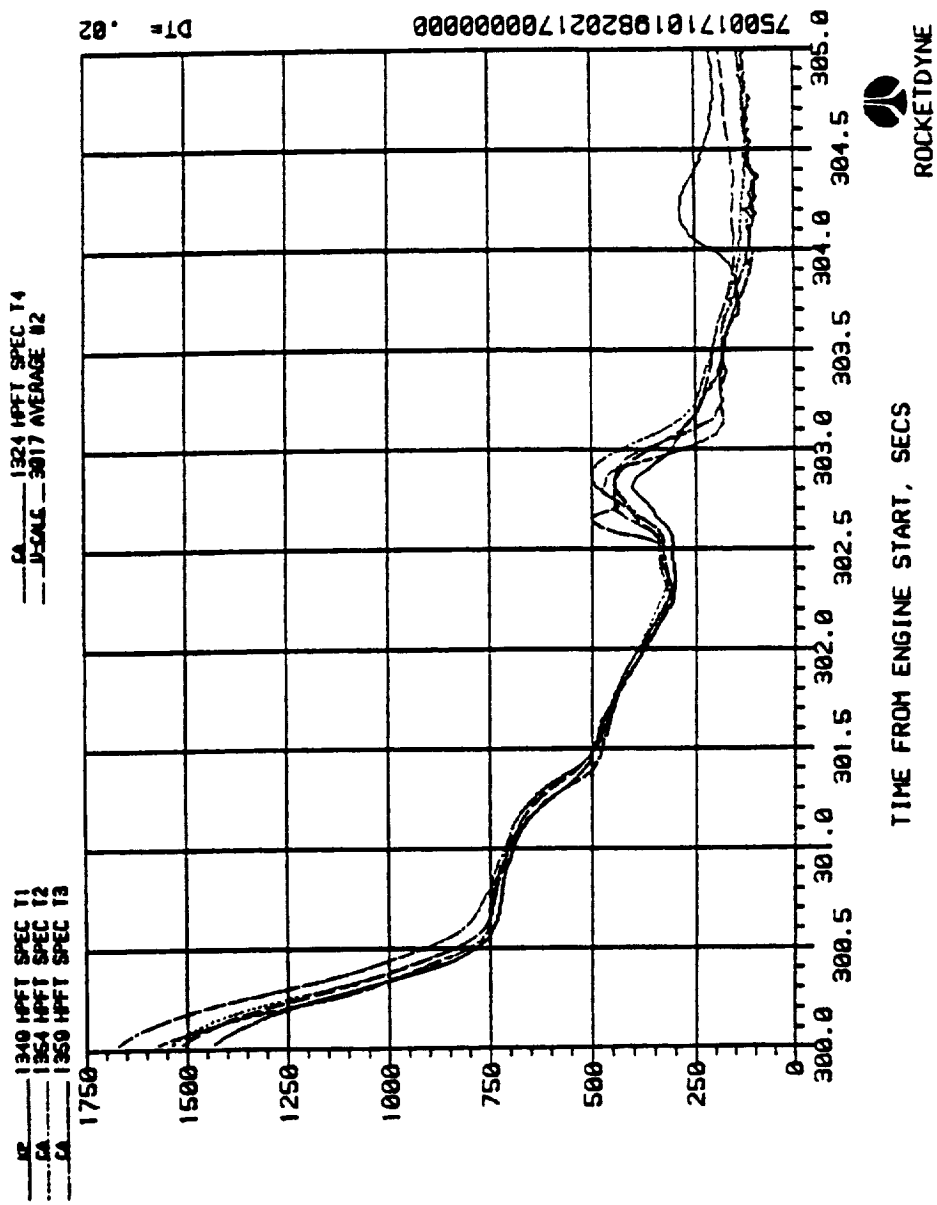


Fig. 2.67 Turbine Exhaust Temperatures at Cutoff Transient



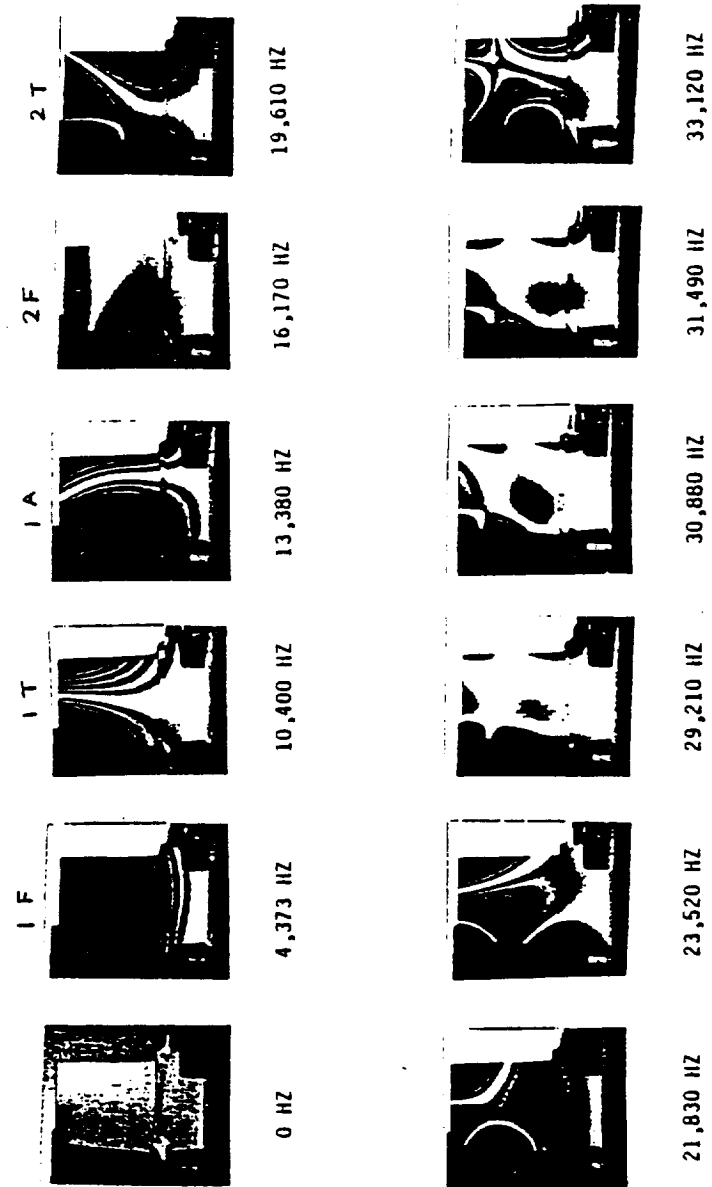


Fig. 2.68 Holographic Modal Testing of HPFTP First Stage Blade

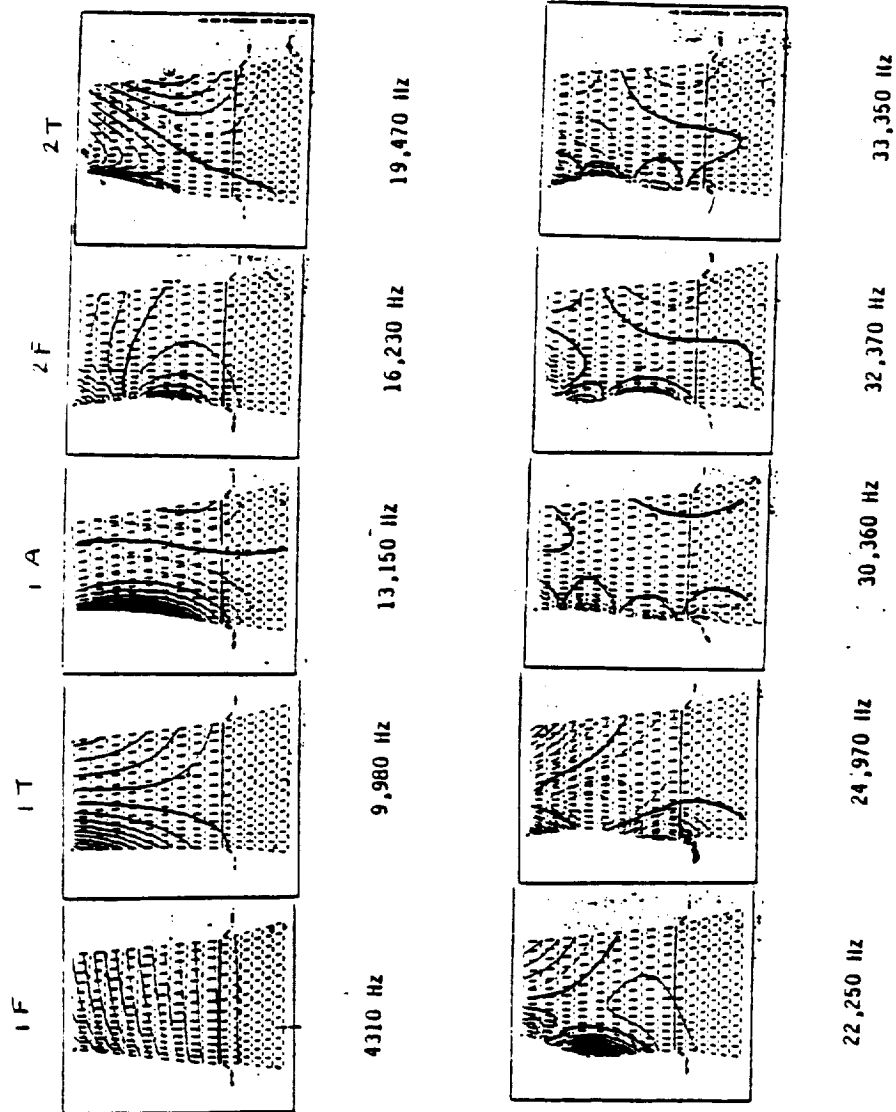


Fig. 2.69 Finite Element Analysis Results of HPFTP First Stage Blade

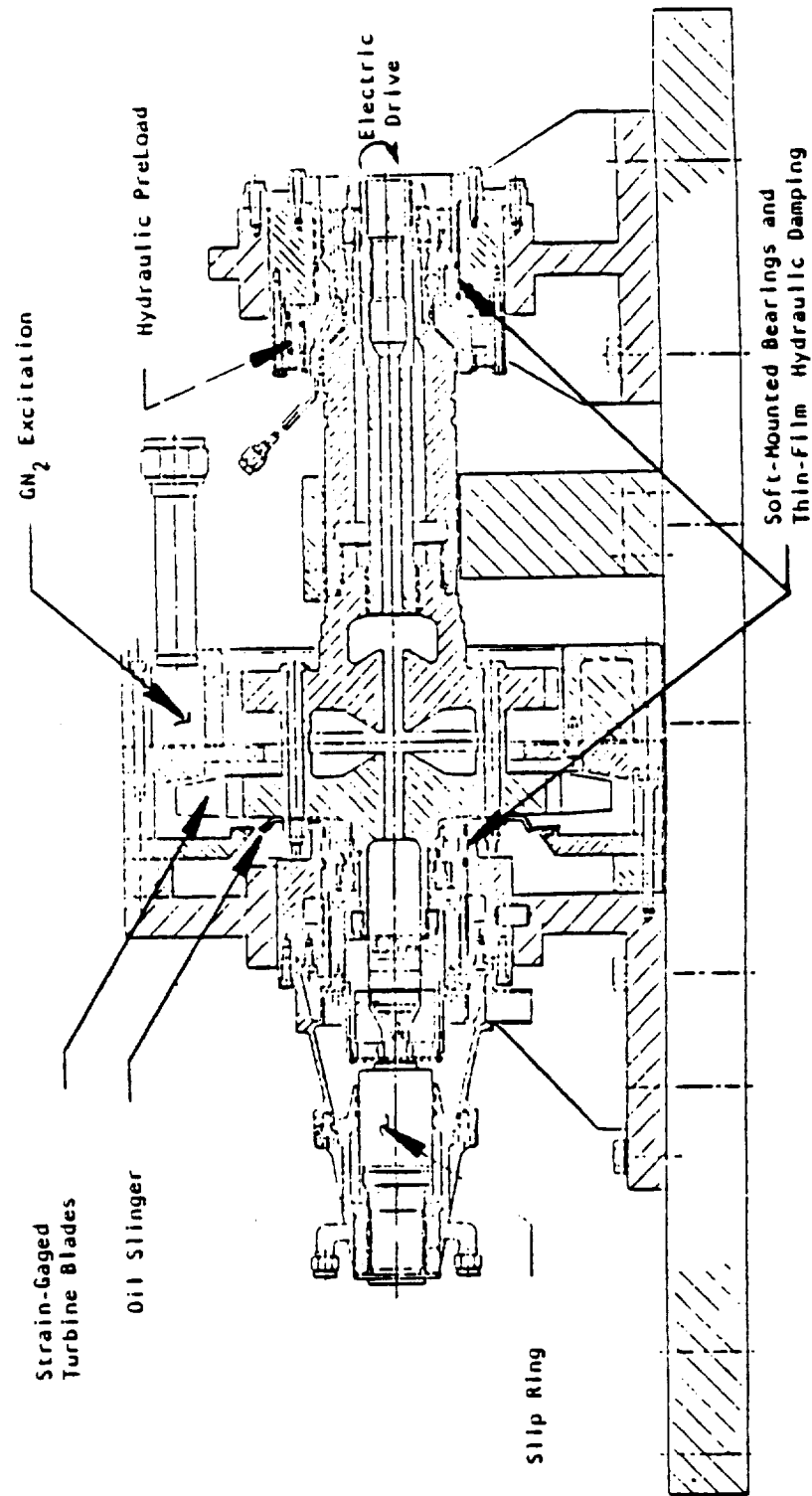


Fig. 2.70 Rocketdyne Whirligig Features

attached to selected blades. The strain gage lead wire are routed through a slip ring to permit high-speed data acquisition. One of the principal objectives of this type of test rig is for the comparison of the vibration characteristics of different blade-damper configurations. Another important objective of the program would be for the verification of analytical models. It must be emphasized that this type of testing is a comparative type of test and the actual strain amplitudes obtained do not simulate actual engine conditions.

The principle design features of the whirligig test rig are the following:

- 1) Steady-state rotor operating speeds can be from 25,000 to 38,000 rpm
- 2) The pulsing gas will be gaseous nitrogen to provide an inert atmosphere within the test chamber and preclude detonation of hot oil with an ambient environment.
- 3) Minimum duration at full operating speed is at least 10 minutes
- 4) Wheel rotation is either direction
- 5) Drive system: electric motor (300 hp) through a gearbox and connecting quill shaft with an estimated 250 hp available at the quill shaft
- 6) Bearings: single assembly each end (wheel, drive), ball bearings (Barden), oil-film damped, soft-mounted, variable axial preload
- 7) Lubrication: Rotor Bearings - DTE 797 or Brayoil No. 1015. Slip Ring Assembly - Mixture of Freon (F113) and MIL-L-7808 oil, the actual mixture ratio determined based on shaft speed.

The description of a typical test on SSME HPOTP is given here to give an idea of the type of information that can be obtained using these tests. The whirligig tester was intended to be operated in a partial vacuum (200 to 600 mm Hg or 3.9 to 11.6 psia) to reduce the windage horsepower. Design maximum speed for the SSME HPOTP whirligig was 32,000 rpm, which corresponds to a nominal power requirement of about 110 hp.

Blade excitation is obtained by passing a flow of  $\text{GN}_2$  through a discrete number of jets, then impinging each jet stream on the trailing edge of the turbine blade. The whirligig was designed for excitation at the trailing edge

(blade easily excited), but with a mod-option to excite at the leading edge. Fig. 2.71 shows the gas path vector diagram which was used to design the blade excitation method. The gas jet strikes the blade normal to the minimum moment of inertia axis.

The blades are instrumented with foil-type strain gages attached by epoxy and covered by fiberglass. Soldered connections between the gages and lead wire are made to withstand the radial loads and windage heating imposed by the high rotor speeds. The lead wires are routed to a 100-channel rotating slip ring assembly in which two channels per gage are normally utilized. Four channels are allocated for blade thermocouples (for d-c shift compensation), leaving a total capability of 48 strain gage measurements. Normally more than one blade/damper configuration is tested at one time, thus the 48 gages are divided between several (3 to 5) sectors of differing blade/damper configuration to maximize data/test sampling. The blade forcing frequency is fixed by the rpm times the number of jets.

The strain gage signal from a whirligig test is processed by a real time data analyzer (RTDA). A typical output is displayed in Fig. 2.72. The program decomposes the signal into its Fourier components and displays both frequency and amplitude as a function of rotational speed. Fig. 2.72 is a Campbell diagram for the whirligig environment. The frequencies can be adjusted for operating temperatures as shown in Fig. 2.73, which is a Campbell diagram for the HPOTP first-stage blade under operating conditions.

Such testing methods can be used for the future verification of probabilistic models developed.

### 11. Geometrical Variations in Turbine Blades

Manufacture of turbine blades are characterized by the strict geometric tolerances that are enforced. These tolerance limits are imposed by stress considerations and aerodynamic considerations in that order. It is not unusual for the scrap rates of turbine blades to be very high. Variations in geometric dimensions result in shift of mass center of the blade which in turn

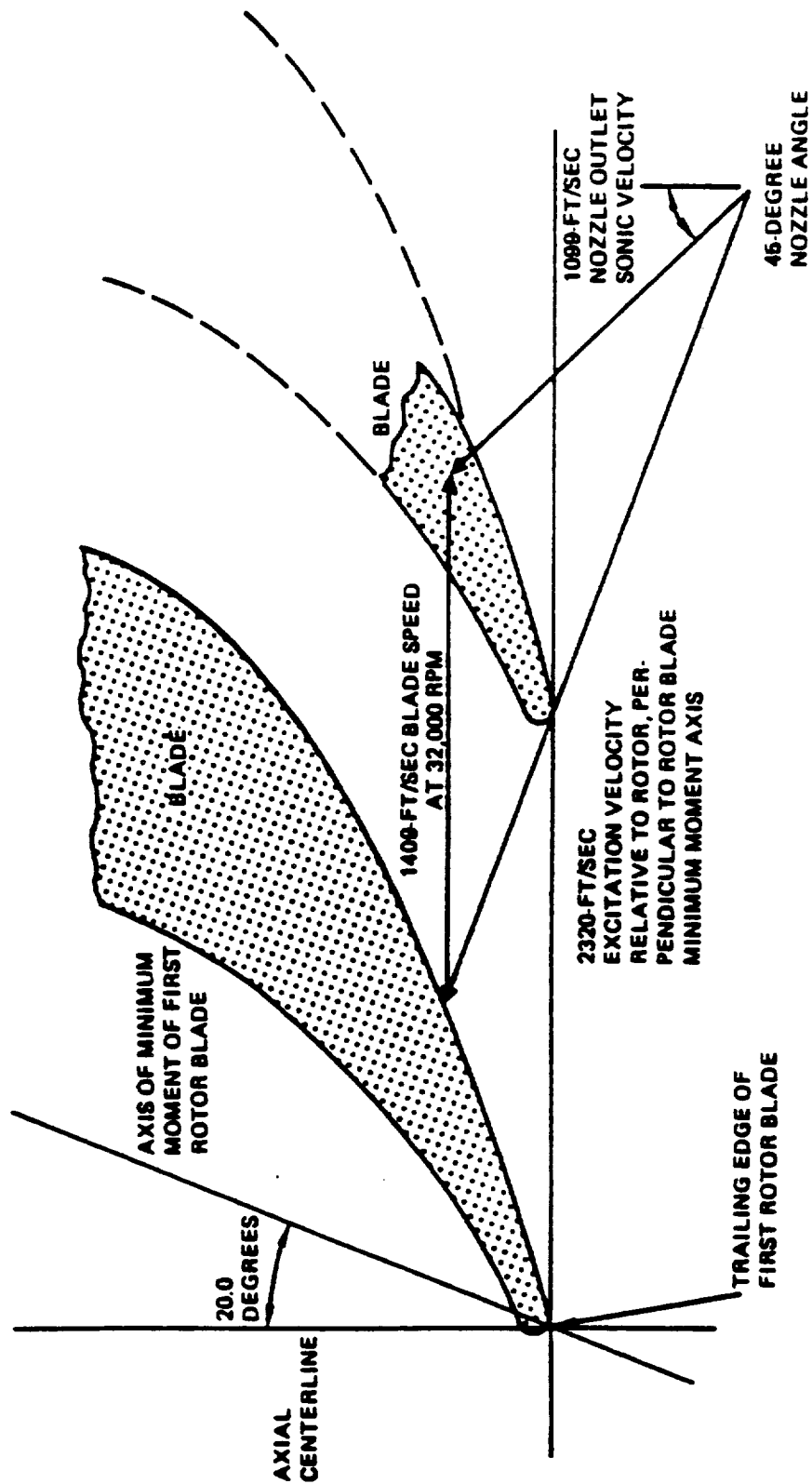


Fig. 2.71 HPOTP Turbine First Rotor Whirligig

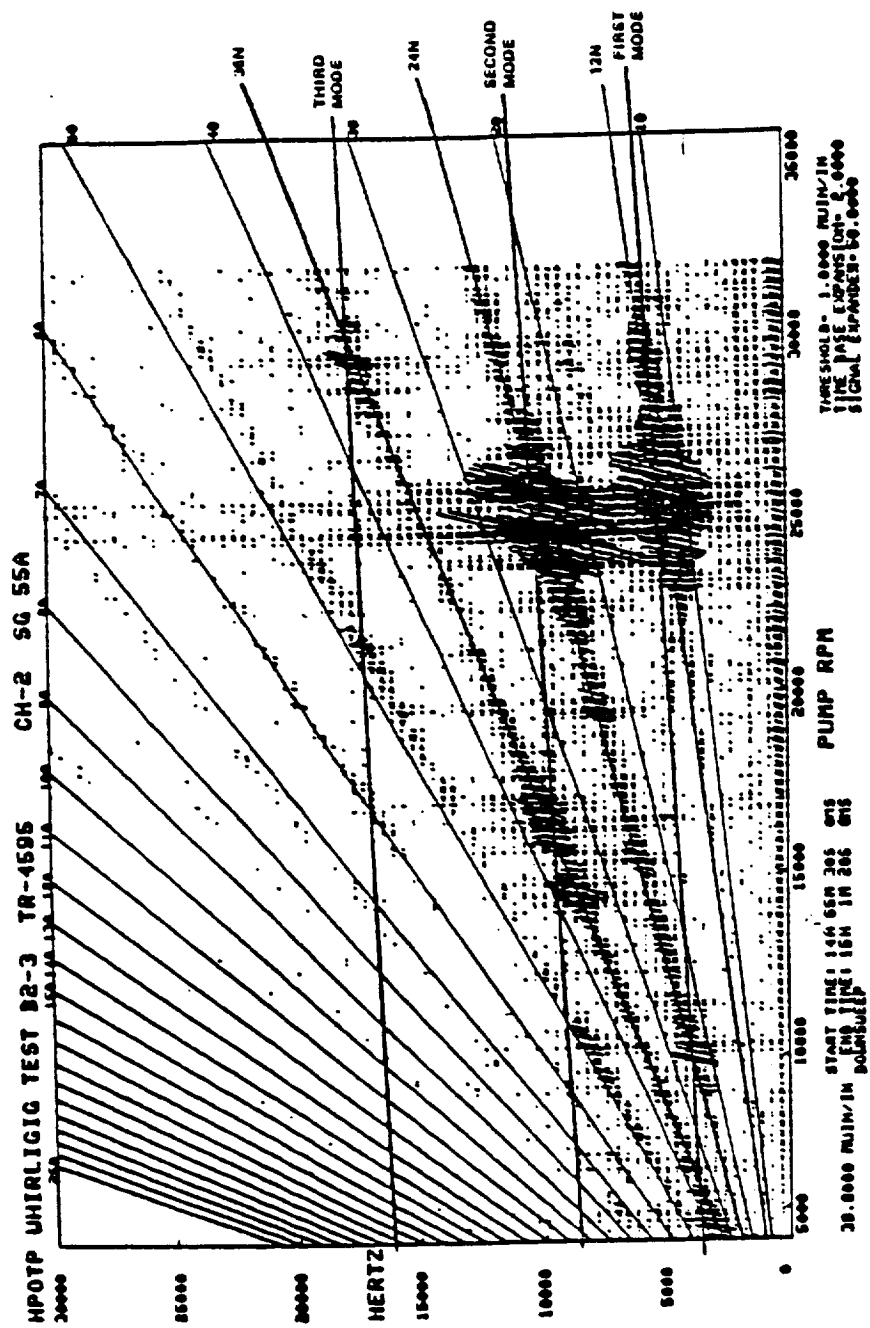


Fig. 2.72 HPOTP Whirligig Test Result

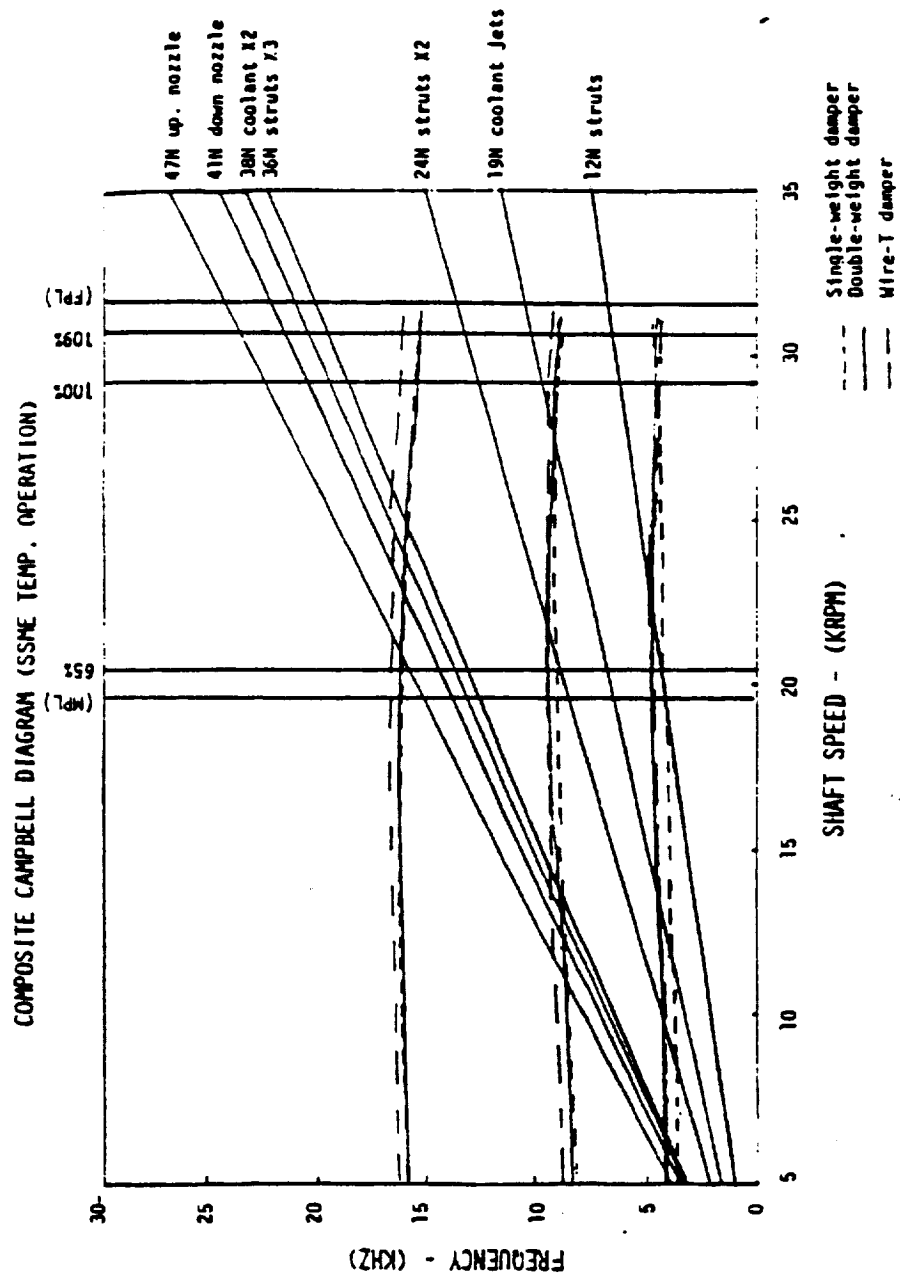


Fig. 2.73 Composite Campbell Diagram for HPOTP First Stage Blade at Operating Temperature



affect centrifugal stresses. An analysis of geometric variations and their effect on stresses is illustrated here. The example chosen is the second stage blades of the high pressure oxidizer turbopump (HPOTP). The analysis presented is based on strength of materials approach. A similar analysis could be done using a more rigorous FEM analysis.

The HPOTP turbine blades geometry is defined by an upper platform, airfoil, lower platform, shank, damper slot, and fir tree. (Fig. 2.12). The blade also has a hollow core section. The blade contours are usually inspected by contour tracing machines or more recently by "Defracto" laser inspection machine. The laser inspection machines which are used exclusively now has the advantage of storing x and y coordinates automatically in a file that can be machine processed for blade acceptability. Typically the points are those that are specified in master dimension chart. An example of contour and laser output is shown in Fig. 2.74 for four sections. Based on contour measurements the blades are evaluated for profile area, blade twist and lean and tilt. The designed lean and tilt are critical dimensions as any variation in the location of center of mass affect the designed centrifugal stresses. This becomes an important criterion as blades are designed such that centrifugal stress are to counteract power bending stresses. Variations in centrifugal stresses result in variations in mean and alternating stresses that affect the fatigue life of the blade.

An analysis of the variations in geometry and their effect on equivalent alternating stress is presented in Fig. 2.75. for a critical point. Similar study is done for all the critical stress points in the blade. Fig. 2.75 compares the results of the analysis of blades manufactured after a tooling change and of those blades that have been actually used in engines, to investigate the range of operating experience. Such geometric tolerance analysis is more critical in blades of small size as compared to bigger blades. Other critical dimensions that are routinely inspected include root and valley discrepancies in fir tree, core offset, damper slot depth and upper and lower platform discrepancies.

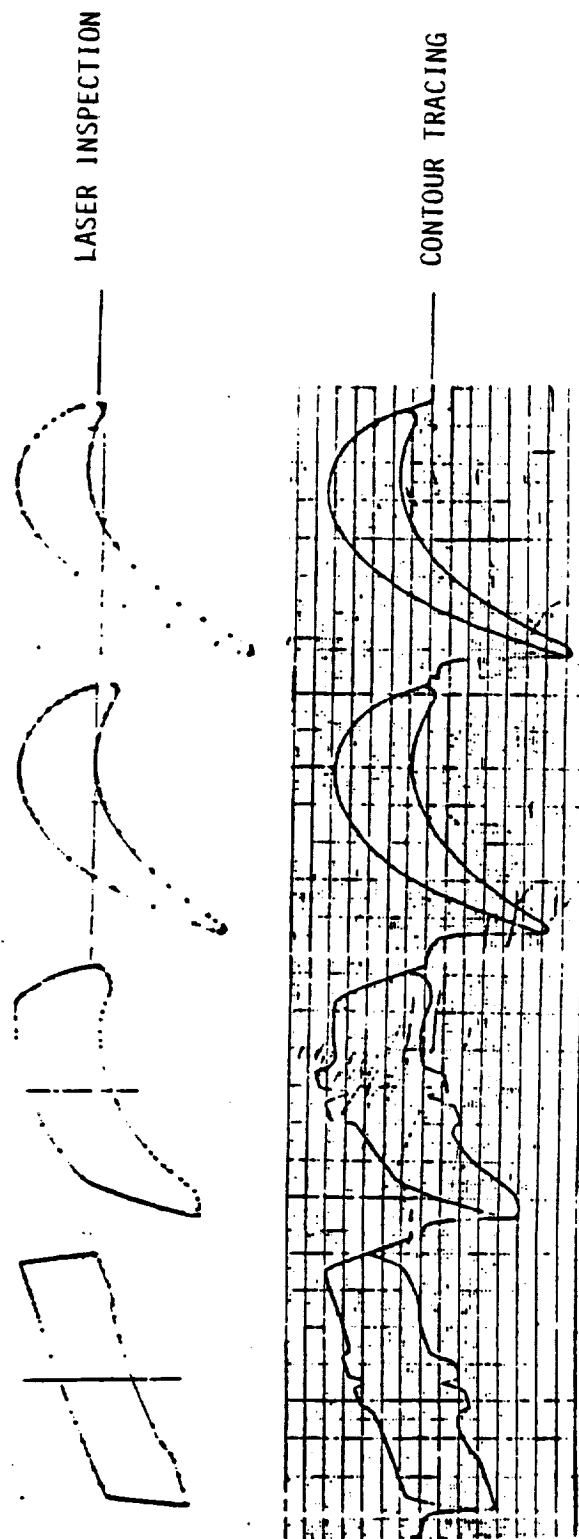


Fig. 2.74 A Typical Output from Laser Machine and Tracing Machine of HP0TP Second Stage Blade

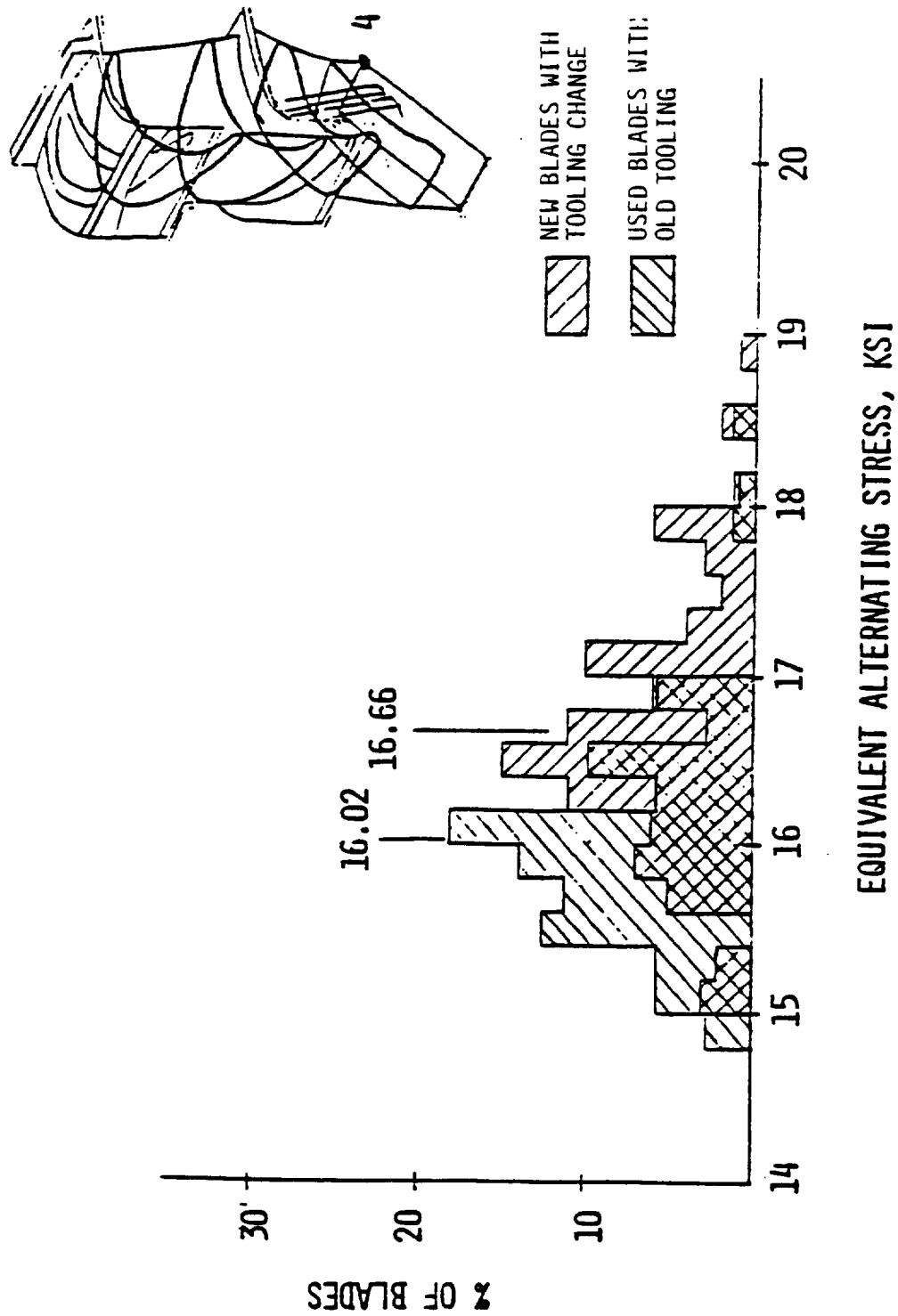


Fig. 2.75 Impact of Geometrical Variations in Alternating Stresses on HP01P Second Stage Blade

## 12. Hydraulic Turbine Considerations

Hydraulic turbines have been used in low pressure turbopumps of rocket engines which typically operate at low speed. The SSME low pressure oxidizer turbopump (LOX) uses a hydraulic turbine. Hydraulic turbines concepts have also been proposed for low pressure fuel pumps ( $\text{LH}_2$  or Hydrocarbon). Unlike in high temperature gas turbines, keeping the number of stages to a minimum is less of a concern in hydraulic turbines. The SSME LPOTP has six stages. The hydrodynamic codes that design the flow passage of hydraulic turbines treat the flow as incompressible.

While axial flow turbines have been exclusively used in high pressure turbopumps of rocket engines, radial flow hydraulic turbines can be used in low pressure turbopumps. The turbine blade geometrical configuration differ substantially from axial flow blades as shown in Fig. 2.76. They are more like a pump impellor blade. The blade can be shrouded or unshrouded, the later being more common.

The biggest impact in stress analysis of hydraulic turbine blade design is the density of the working fluid. Significant fluid structure interaction may be present. In general, the virtual mass of the fluid must be considered in the dynamic analysis of the blade. This virtual mass can alter the natural frequencies of the blade by as much as 20%. Because of the presence of fluid damping, no additional damping provisions are generally provided.

There has been no failures of the SSME LPOTP blades. However, potential for trailing edge flap phenomenon under resonance has been studied for these blades.

## 13. Approximate Analysis Techniques

For initial rough sizing, turbine blades have been effectively analysed as cantilever beams. The section properties of the airfoil section are generally calculated through computer programs which include areas, centroids, moment of inertia and section modulus. The approximate stresses using beam analogy can

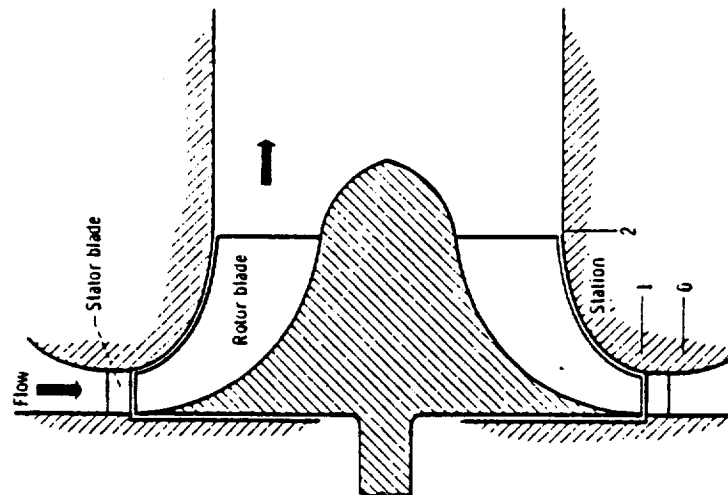
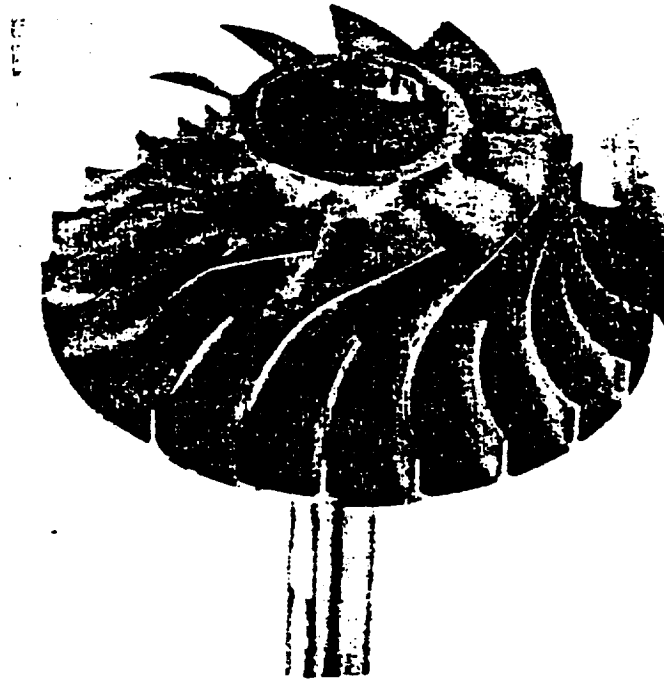


Fig. 2.76 Radial Inflow Turbine Blade Geometry

be used to calculate centrifugal stresses including bending and, stresses due to power bending. Simplified inputs usually include defining the profile point by point or by defining it through geometric entities like straight lines, arcs, conics, and parabolas. The approximate method include calculation of natural frequencies for cantilever with varying crosssections including centrifugal stiffening effect.

Several improvements to component specific approximate analysis of turbine blades may be possible. The beam analogy can be replaced by a more accurate shell analysis. The approximate dynamic analysis capability can be improved to include response analysis for the blade damper configuration. The recent improvements in approximate dynamic analysis published in literature include two parameter lumped mass model for frequency response analysis of multiple blade systems with blade to blade and blade to disk coupling (Fig. 2.77). The springs in the model represent the sections between root and platform and above the platform.

#### 14. Survey of Finite Element Models

A number of finite element models and analysis results are available for high pressure turbopump blades. Though many other models might have been constructed to review a MR condition and for sensitivity analysis, they are not presented here. The models presented in this survey can be used to test specific features for validation and verification of PSAM code. Broadly there are two different types of finite element models available. They are:

- 1) Global Models
- 2) Local Models

The objective of the global models is to study the overall response of the structure, load path and gross crosssectional forces and stresses that exist in the blade. The model shown in Fig. 2.78 represents the second stage blade of the HPFTP. The model comprising fully of linear cube elements was used to analyse stresses due to centrifugal, pressure, and temperature loadings at steady state. This model has further been used for material orientation

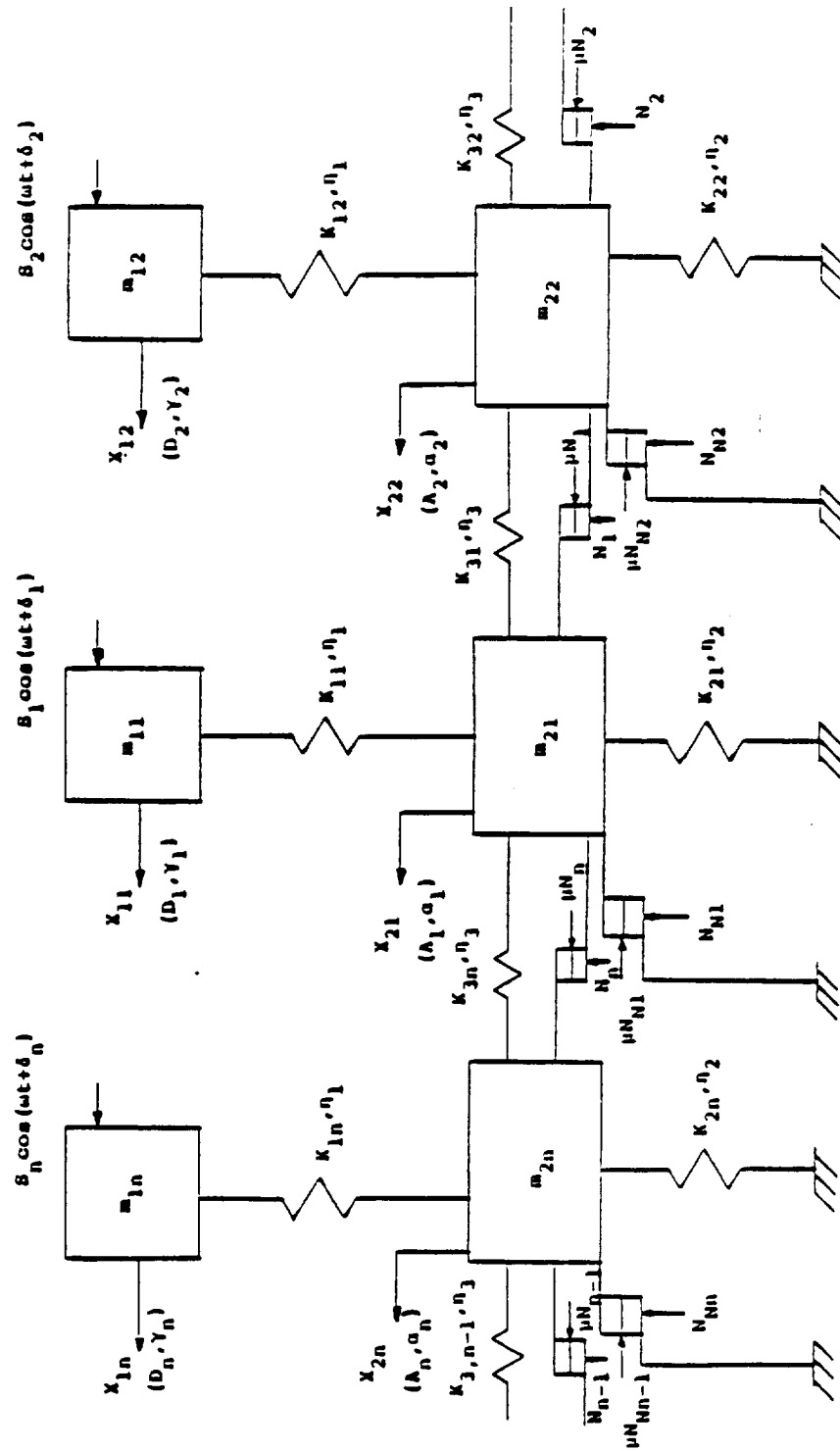


Fig. 2.77 An Approximate Lumped Mass Dynamic Model for Blade Damping Study

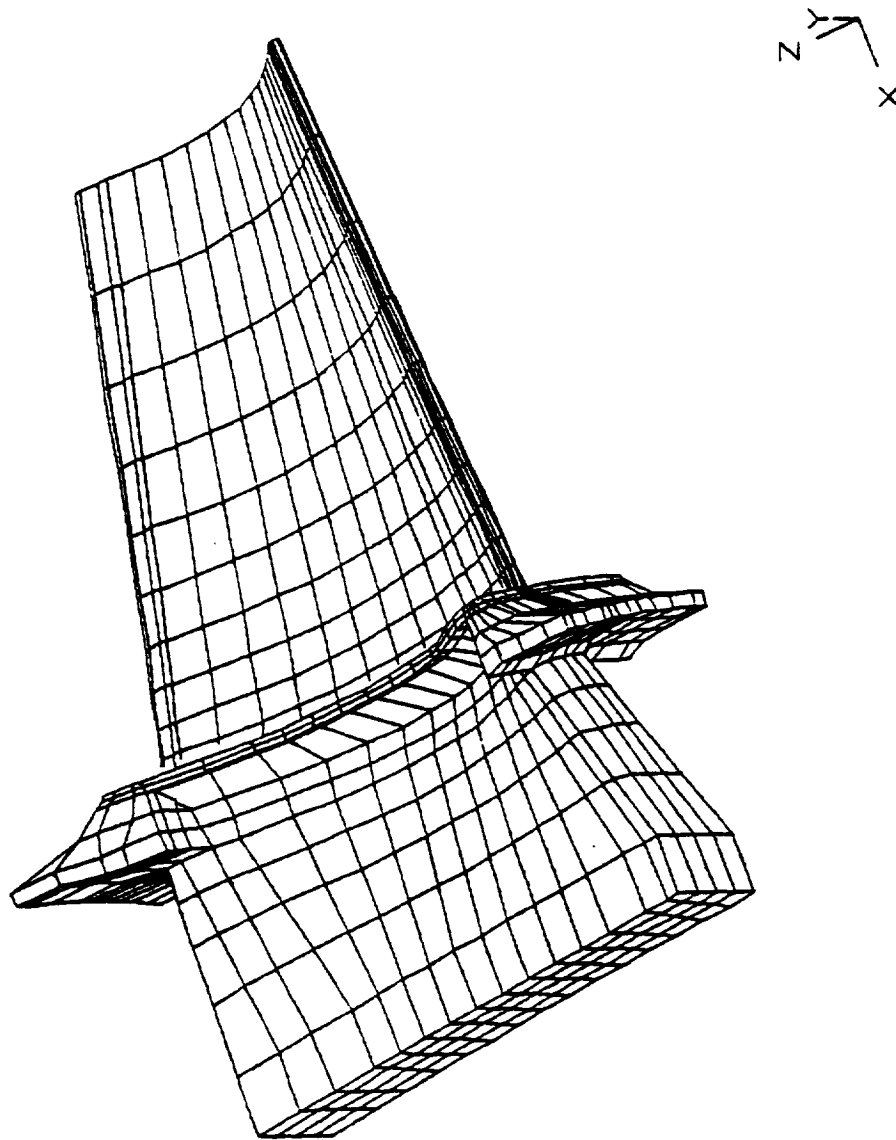


Fig. 2.78 A Global Finite Element Model of HPFTP Second Stage Blade used for Static Analysis



sensitivity studies. The model represented in Fig. 2.79 is a plate model of the same second stage fuel turbine blade that was used for dynamic analysis. The dynamic included, model analysis and damping analysis. The model shown in Fig. 2.80 is that of HPOTP first stage blade. It is model composed fully of solid elements and used for static analysis. The loadings analyzed included centrifugal, pressure and temperature loadings at steady state. The same first stage HPOTP blade has been modeled using plate elements for dynamic analysis. The dynamic analysis included model analysis and damping analysis. The model for the first stage nozzle of the HPFTP is illustrated in Fig. 2.82. This 2-D model was used to model the response of the nozzle due to start and cutoff transients. The 2-D model of the HPFTP second stage blade shown in Fig. 2.83 illustrates the use of approximate global models that can be used effectively to study the blade response. The thickness of the elements are modeled appropriately to suit the hardware. Such techniques can be used to obtain quick approximate answers as accurate 3-D models of turbine blades can be quite time consuming.

A number of local models also exist of the turbine blades which are used to obtain a better definition of stress concentration factors. The model shown in Fig. 2.84 is a more detailed model of the shank-platform junction of the second stage HPFTP blade which has experienced failure at this location. This model was used to determine stress concentration factors under steady state as well to study the effect of various fillet radii to reduce the stress concentration factors. The techniques used was a two stage approach in which the global model boundary conditions were extracted by interpolation at cut sections and were imposed in the local model. There was no one to one correspondence of nodes between models at cut boundary. This technique is different in some respects to a rigorous substructure analysis. In a rigorous substructure analysis, exact match of boundary nodes is required and thus the two step approach is rigorous. But then along with the accuracy comes the complications of smooth transition between coarse and fine grid in a complex 3-D model. In the zoom model approach used, the interpolations in the boundary introduces some approximations, but if the cut planes are sufficiently away from the point of interest, the effect of approximation can be minimal. This model has further been used for material orientation sensitivity studies.

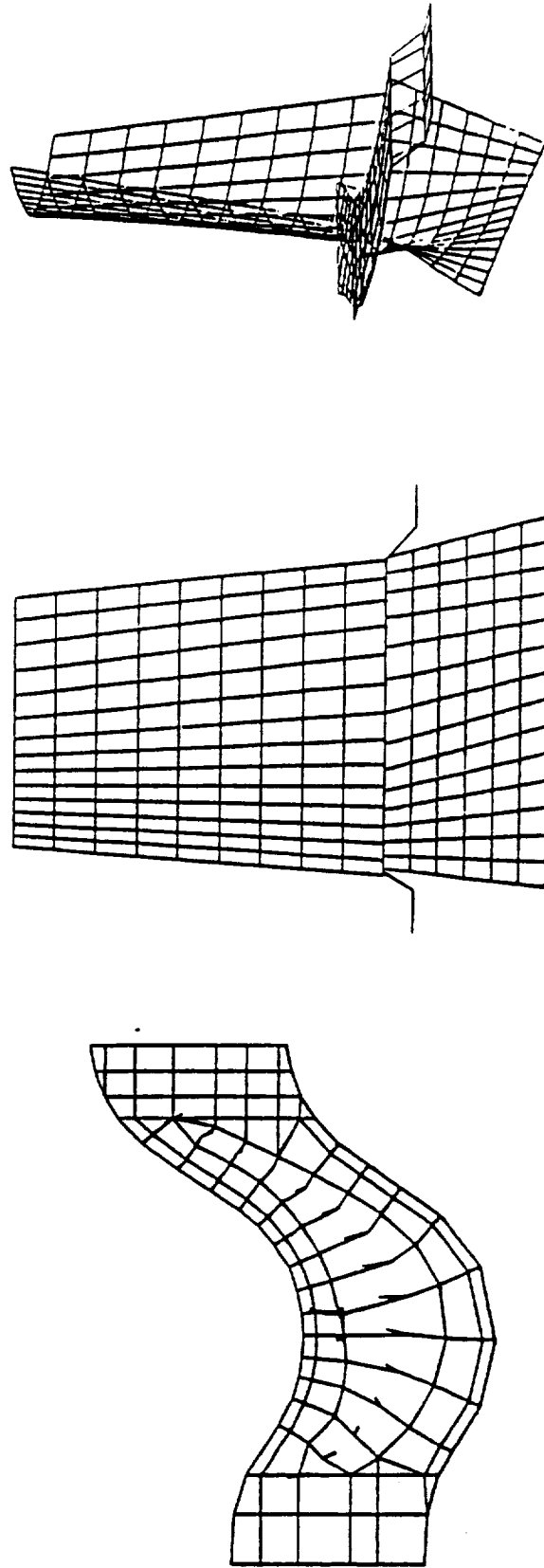


Fig. 2.79 A Global Finite Element Model of HPFTP  
Second Stage Blade used for Dynamic Analysis

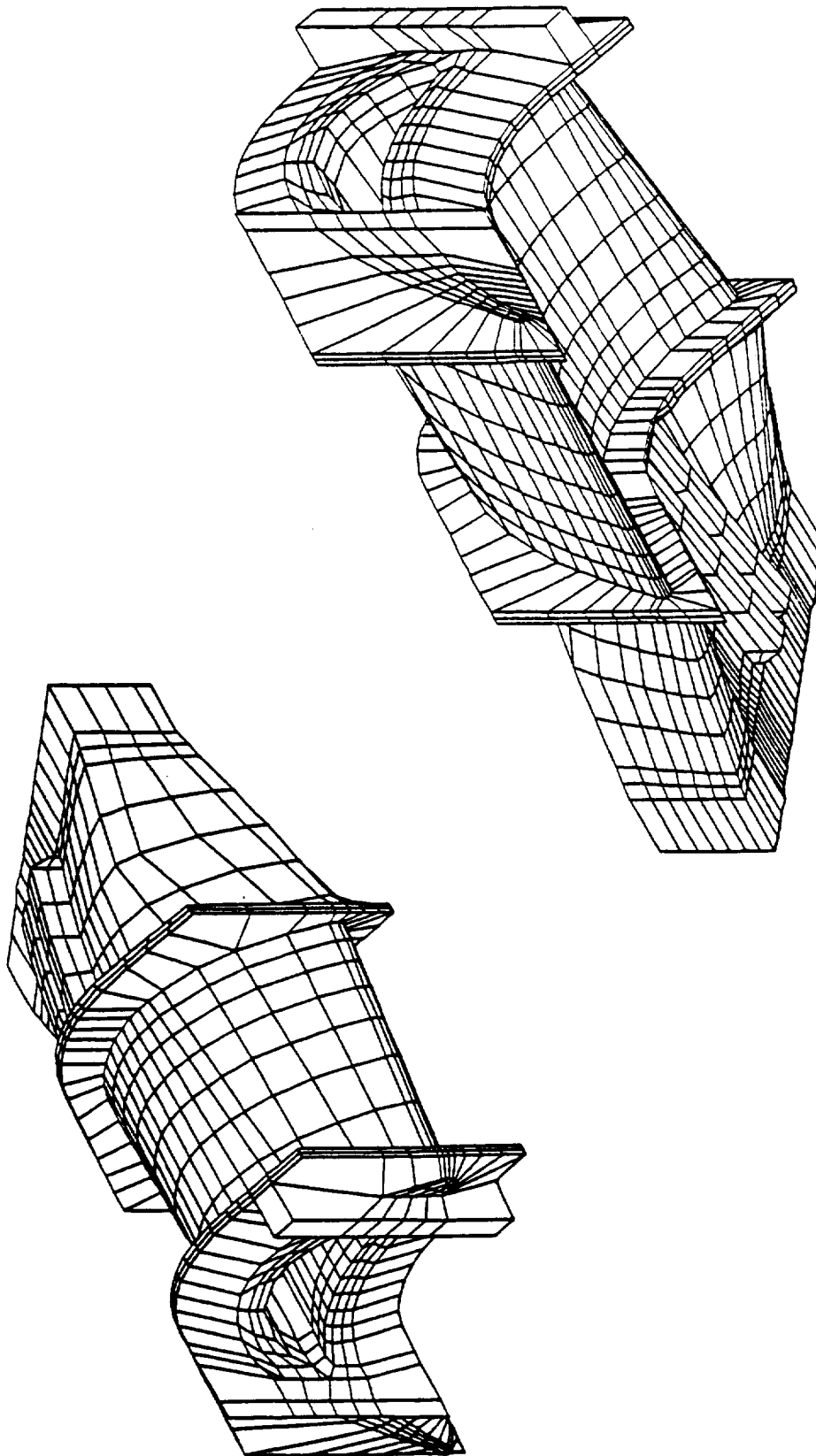


Fig. 2.80 A Global Finite Element Model of the HPOTP First Stage Blade used for Static Analysis

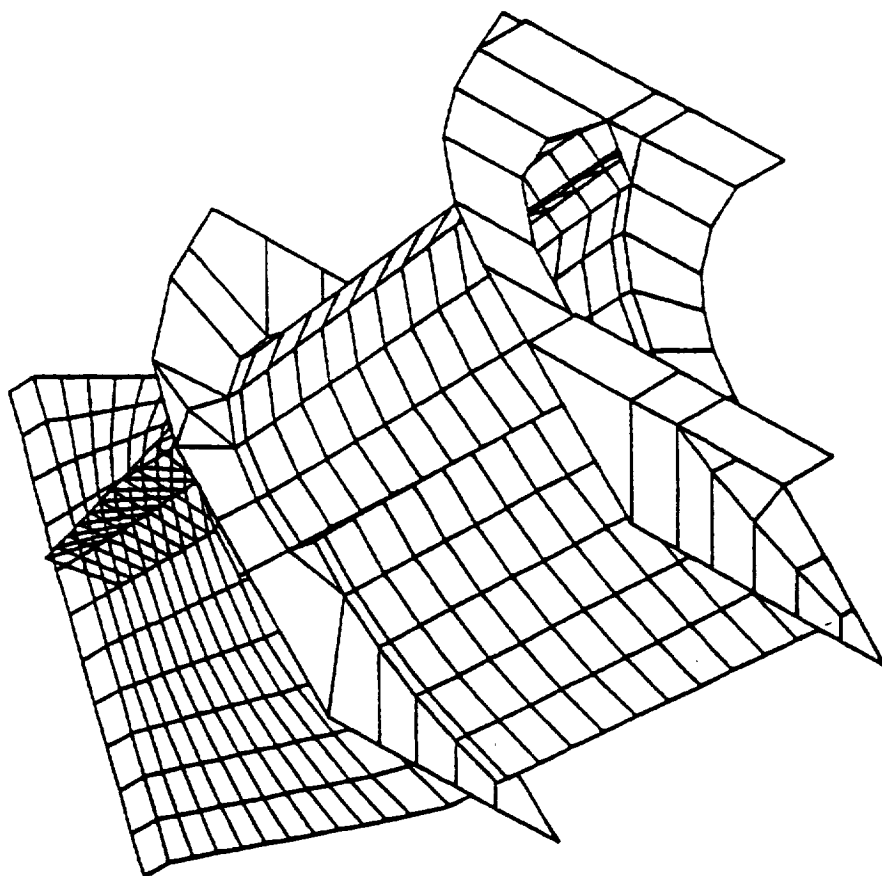


Fig. 2.81 A Global Finite Element Model of the HPOTP First Stage Blade used for Dynamic Analysis

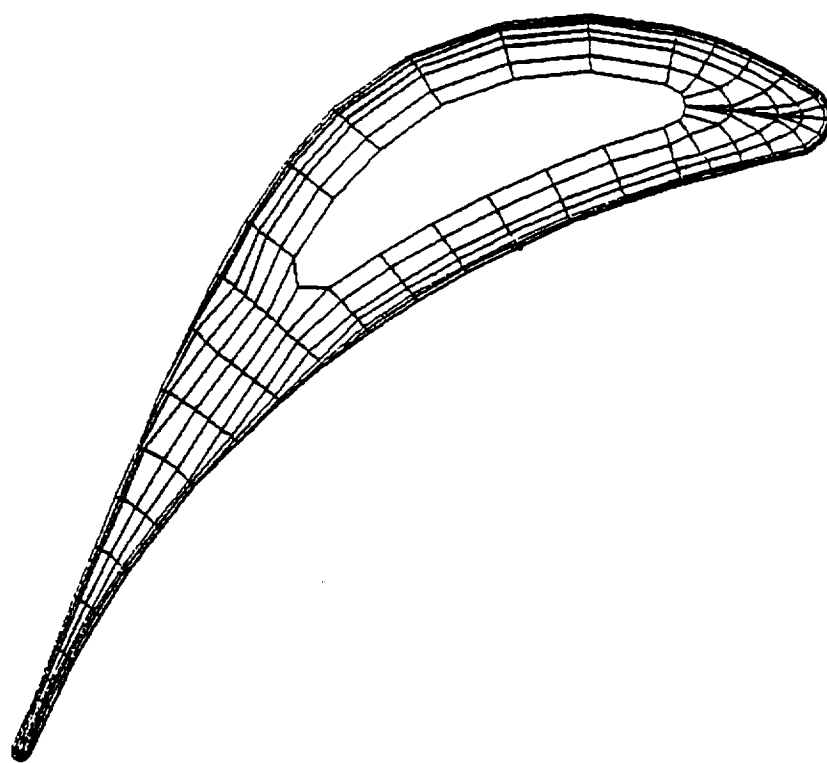


Fig. 2.82 A 2-D Finite Element Model of the HPFTP First Stage Nozzle

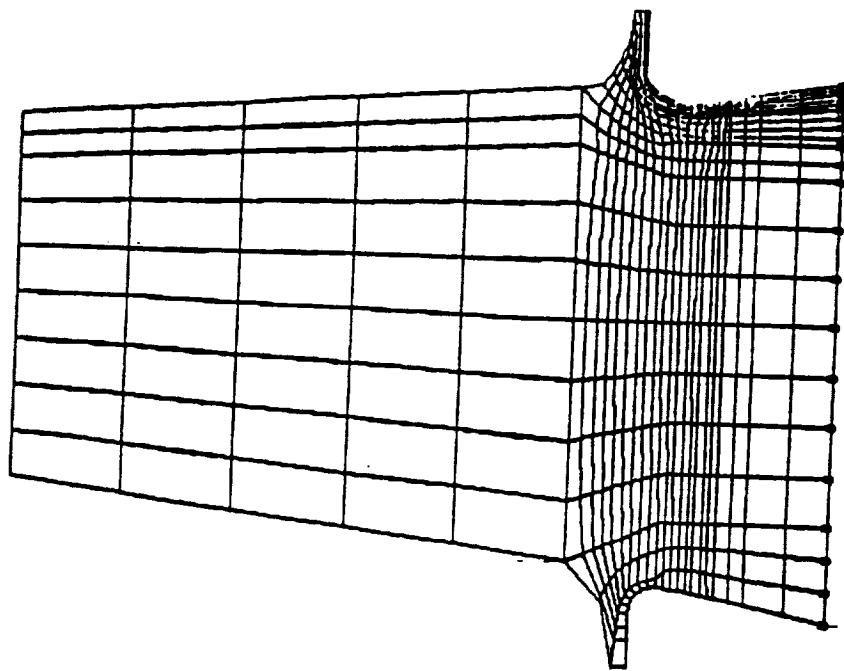


Fig. 2.83 An Approximate 2-D Model of the HPFTP Second Stage Blade

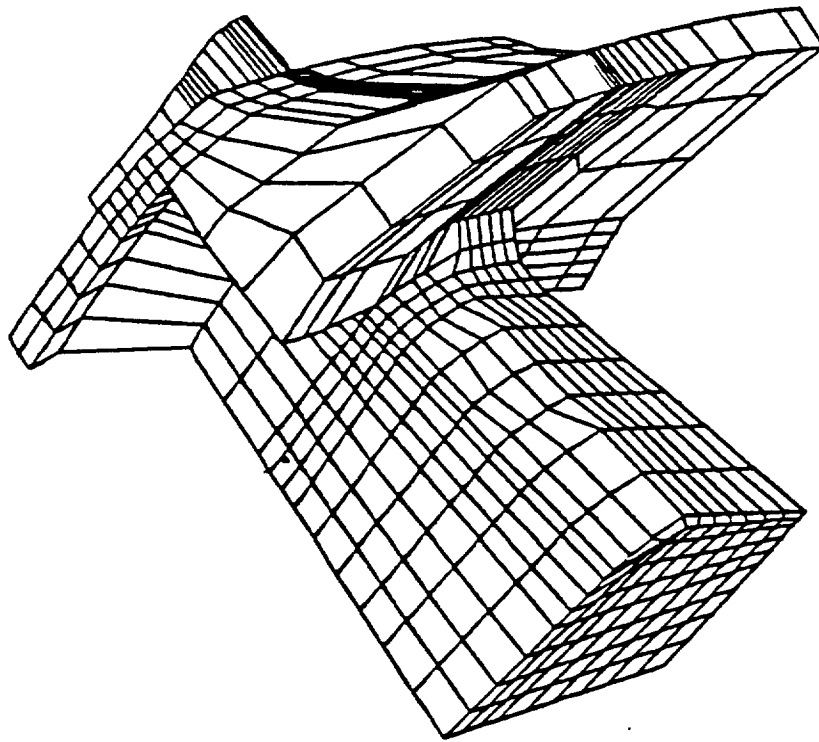


Fig. 2.84 A Local Finite Element Model of the HPFTP  
Second Stage Turbine Blade

The local 2-D model of the fir tree region of the HPFTP first stage blade is shown in Fig. 2.85. This model was used for sensitivity studies on the tolerances as well to optimize the fir tree profile. Table 2.5 and Table 2.6 lists the finite element models available for high pressure turbopump blades.

#### 15. Scoping of Finite Element Analysis

From the survey of static and dynamic finite element analysis done, the finite element library should contain for a complete blade analysis:

- 1) Plate Shell Element
- 2) 2-D Plane Stress Element
- 3) 3-D Solid or Shell Element
- 4) 2-D or 3-D Gap Elements

#### Scoping of Linear and Nonlinear Analysis Requirements

##### Material Library

- a) Include provisions for isotropic, orthotropic and anisotropic materials. Angular orientation of the material must be one of the random variables. For future applications a convenient method of inputting composite materials and ceramic materials may be necessary. A material nonlinear analysis treatment is needed when an accurate analysis of thermo-mechanical stresses is necessary.
- b) Temperature dependant material properties.

##### Geometric Nonlinearity:

Geometric nonlinearity enters the turbine blade analysis in two ways. The centrifugal stress cause stiffening of the blade altering the natural frequency. The geometric nonlinearity enters in a detailed analysis of fir tree interaction with turbine disk.



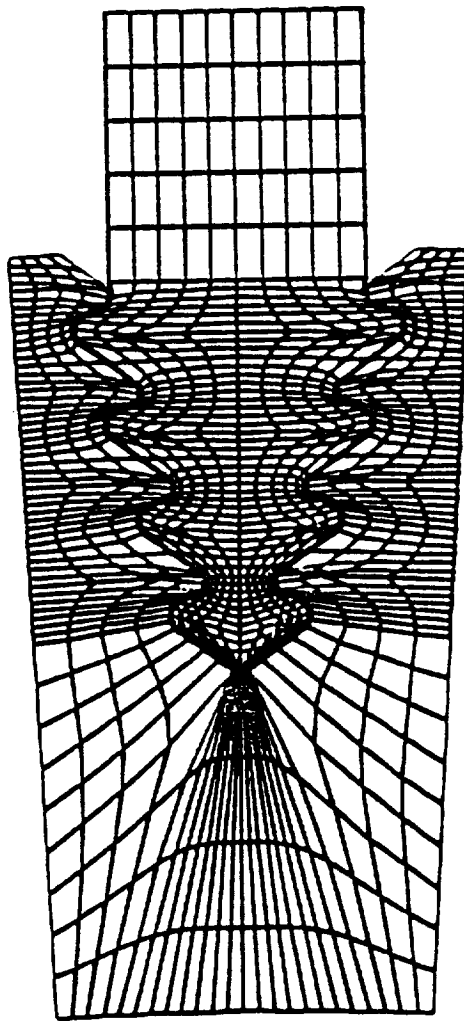


Fig. 2.85 A Local 2-D Model of the Firtree Detail for HPFTP First Stage Blade

Table 2.5 HPOTP  
Turbine Blade Finite  
Element Models

PART	MODEL	GEOMETRY	ANALYSIS		MODEL CUSTOMER	MODEL DETAILS		NO. OF ELEMENTS	NO. OF HOLES	NO. OF R.F.T.	ANALYSIS TYPE	STEADY STATE	TRANSIENT	LOAD CYCLES	REASONS FOR ANALYSIS
			PROGRAM	RESULTS		TYPE	ELEMENTS								
WIPF 2ND STAGE	1) WHOLE	1) TYPICAL	1) PERMANENT FILE	1) PRINTOUT	M.R.	1) 2-D	1) BAR	1876	2019	1257	1) LINEAR - STATIC	1) THERMAL	---	---	ORIGINAL DESIGN
	2) LOCAL	2) ANALYSIS	2) PERMANENT FILE	2) POST PROCTAPE		2) 3-D	2) BEAM				2) THERMAL - STATIC	2) PRESSURE			
	3) SECTION	3) STRESSING	3) STRESSING	3) TAPING		3) 4-D	3) TRIANGLE				3) THERMAL - STATIC	3) ERT. LOADS			
	4) STIM	4) STRAIN	4) CARD DECK ONLY	4) 5-D		4) SOLID	4) DYNAMIC								
WIPF 2ND STAGE	WHOLE	TYPICAL	PERMANENT FILE	POST PROCTAPE	G.D.	3-D	1, 3, 4	335	374	2154	5, 6, 9, NONLINEAR FRICTION BUMPING	3, 4	3, 4	---	ALTERNATING STRESS OPTIMUM DAMPER MOUNT
	WHOLE	TYPICAL	PERMANENT FILE	PRINT OUT											
WIPF 2ND STAGE	LOCAL	TYPICAL	ANALYSIS	PERMANENT FILE	M.R.	3-D	SOLID	1749	1899	5697	LINEAR-STATIC	1) THERMAL PRESSURE	---	---	FAILURE ANALYSIS, REQUEST
	LOCAL	TYPICAL	AFSA	CARD DECK		3-D	3, 4				LINEAR-STATIC	ROTATION			
WIPF 2ND STAGE	LOCAL	TYPICAL		PRINT OUT		3-D	3, 4	507	556	= 1000	LINEAR-STATIC	ROTATION	---	---	FIREBEE DESIGN

Table 2.6 HPOTP  
Turbine Blade Finite  
Element Models

PART	MODEL	GEOMETRY	ANALYSIS PROGRAM	AVAILABILITY		MODEL	MODEL DETAILS		NO. OF DOF	ANALYSIS TYPE	STEADY STATE	TRANSIENT LOAD CYCLES	REASONS FOR ANALYSIS
				INPUT	RESULTS		TYPE	ELEMENT TYPES					
ROTP STAGE	1) WHOLE	1) TYPICAL	1) APOST	1) PRINTOUT ONLY	1) PRINTOUT	1) CUBIC	1) 2-D	1) BAR		1) LINEAR - STATIC	1) TIME	1) TIME	1) DETERMINING STRESS
	2) LOCAL	2) LOCAL	2) APOST	2) PERMANENT FILE	2) POST PROCTAPE	2) CUBIC	2) 3-D	2) BEAM		2) GEOM. NONLINEAR - STATIC	2) PRESSURE	2) PRESSURE	2) DETERMINING OPTIMUM DAMPING
	3) SECTION	3) SECTION	3) APOST	3) PERMANENT FILE	3) POST PROCTAPE	3) CUBIC	3) 3-D	3) TRIANGLE		3) GEOM. NONLINEAR - STATIC	3) EXT. LOADS	3) EXT. LOADS	3) DETERMINING OPTIMUM DAMPING
	4) STYM	4) STYM	4) APOST	4) PERMANENT FILE	4) POST PROCTAPE	4) CUBIC	4) 3-D	4) QUAD		4) GEOM. NONLINEAR - STATIC	4) DYNAMIC	4) DYNAMIC	4) DETERMINING OPTIMUM DAMPING
ROTP STAGE	1) WHOLE	1) TYPICAL	1) APOST	1) PRINTOUT ONLY	1) PRINTOUT	1) CUBIC	1) 2-D	1) 3-D	742	1) LINEAR - STATIC	1) TIME	1) TIME	1) DETERMINING STRESS
	2) LOCAL	2) LOCAL	2) APOST	2) PERMANENT FILE	2) POST PROCTAPE	2) CUBIC	2) 3-D	2) TRIANGLE	2558	2) GEOM. NONLINEAR - STATIC	2) PRESSURE	2) PRESSURE	2) DETERMINING OPTIMUM DAMPING

### Scoping of Solution Strategies

The solution strategies should indicate:

- a) linear analysis.
- b) Efficient eigen value and eigen vector extraction for large systems.
- c) Incremental and iterative analysis using newton, quasi-newton or self adaptive procedures.
- d) Turbine blade damping analysis using coulomb damping. Analysis of single blade damping or coupled blade/ blades and disk damping. Provisions for analysis of damping problem using time integration of modal generalized displacements and coulomb damping if necessary. Provisions for inputting large number of phased forcing functions.

Section 3  
Transfer Ducts and Preburner Liners

•

## HOT GAS MANIFOLD TRANSFER DUCTS

### 1. INTRODUCTION

A highly efficient arrangement of the engine major components (preburners, turbopumps, main injector, thrust chamber, and heat exchanger) is necessary to achieve the engine system goals of light weight and accessibility. The main engine hot gas manifold assembly is designed to perform two primary functions: to conduct hot gas flow from the preburners through the turbines to the main injector and to serve as a structural nucleus for the engine system.

The engine packaging concept that has been extensively tested and used in the SSME is shown in Fig. 3.1 and Fig. 3.2. Fig. 3.1 shows the manifold configuration and Fig. 3.2 indicates how the component integration with the manifold is achieved. Hot gas from preburners is ducted directly to high pressure turbines which then discharges the gas to a toroidal manifold. The high pressure, high flow rate, high temperature hydrogen rich gas then enters the hot gas transfer ducts, three on the fuel side and two on the oxidizer side. The gas is then routed to main injector torus manifold where it is radially directed into hot gas cavity of the main injector.

A different engine packaging concept was explored in the XLR129-P-1 reusable rocket engine which was subjected to very limited testing. Fig. 3.3 shows the transition case and Fig. 3.4 shows how the components are attached or plugged into the transition case. Similar to the hot gas manifold of SSME the transition case also serves as the mounting structure for three major components, the preburner, oxidizer pump and fuel pump. It contains internal ducting that routes preburner discharge gases through the fuel and oxidizer turbines and to the main injector.

Thus a manifold design consists of structurally efficient spheres and cylinders. Cooled structural shell concepts are invariably used to minimize the system weight. This is achieved by having a structural liner which forms an annular passage between the liner and the outer casing, through which the

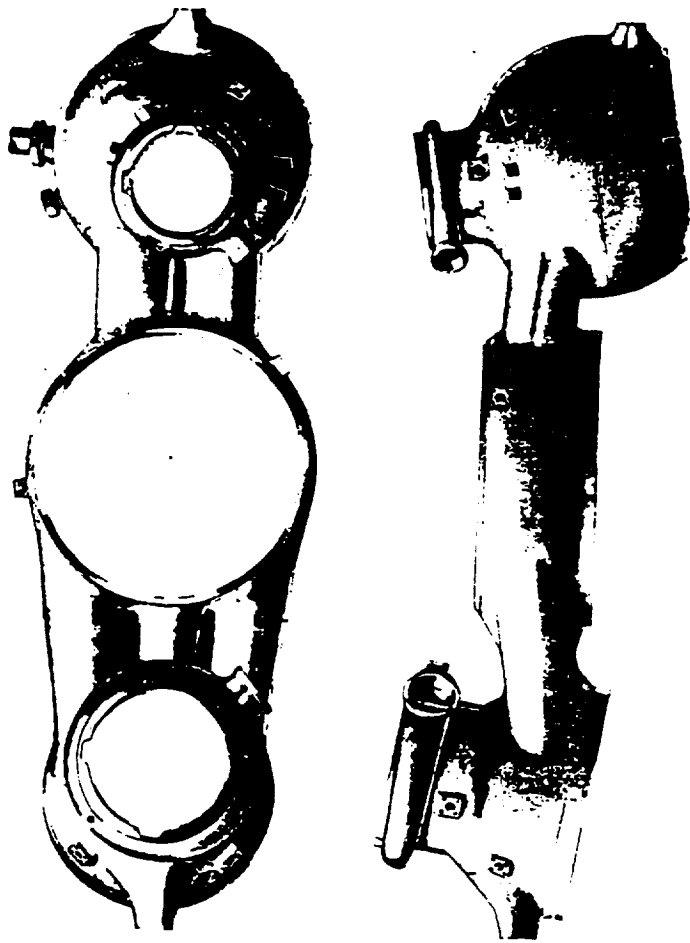


Fig. 3.1 SSME Hot Gas Manifold

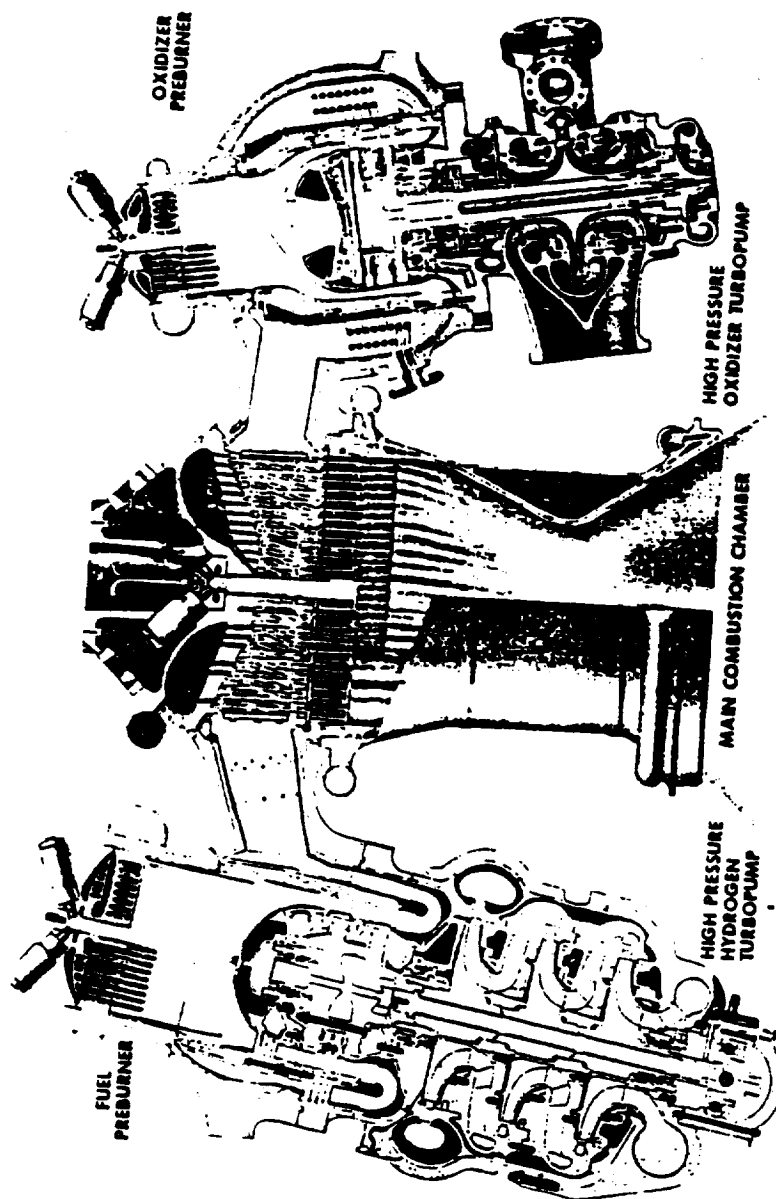


Fig. 3.2 SSME Powerhead Component Arrangement



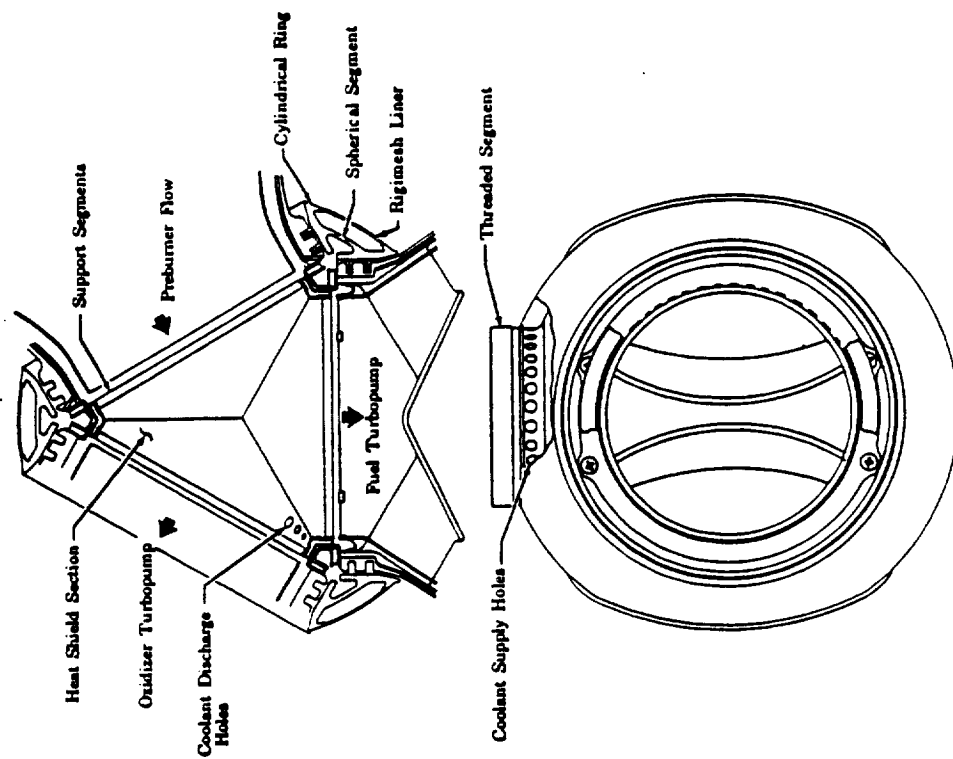


Fig. 3.3 Transition Case Center Body for XLR129-P-1 Engine

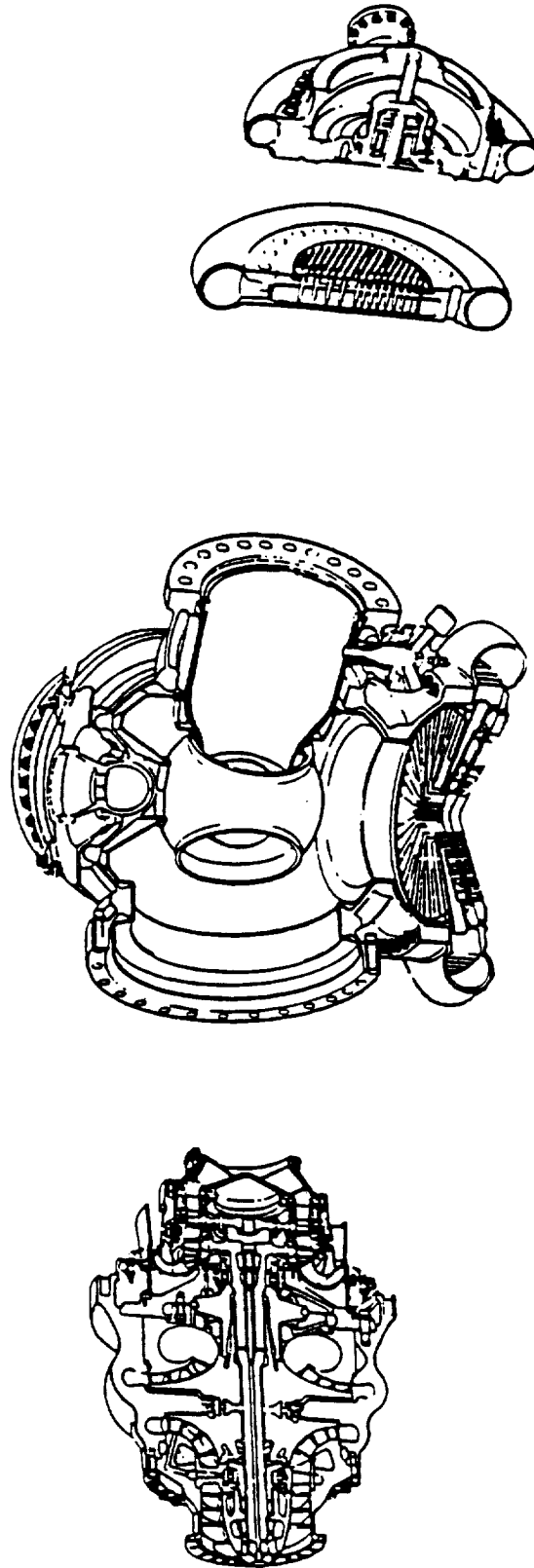


Fig. 3.4 XLR129-P-1 Engine Packaging Concept

cold hydrogen flows. Integrity of structural liner is very important for satisfactory engine operation through transients and steadystate. It must be emphasized that the environment is very severe with high flow rate, high velocity and high temperatures. A leak and adverse differential pressure can cause the hot gases to be driven into the cooling system. The reliability of structural liner is increased by having a scrub liner which acts as a barrier against hot gas impinging on the structural liner to minimize the thermal expansion and the possibility of structural liner buckling. Usually, stagnant gas is present in the gap between the liner elements.

Extensive engine experience has indicated few problems with the outer case structural shell of the hot gas manifold. However, the inner liners are subjected to environments and forces that are not well understood and it is considered more appropriate to a treatment based on probabilistic approach. Thus for the purposes of this contract, the transfer duct component analysis is limited to the analysis of structural and scrub liners. Depending upon the engine packaging concept the transfer ducts could also serve the function of transporting hot gas from preburner to a transition assembly, (Fig. 3.4). In this case, the liner environment will be very similar to the preburner liner environment of SSME. For this reason, this overview covers the transfer duct as well as preburner liner experience of SSME.

## 2. Geometry Definition

The shape of the transfer tube liners is determined by the geometry of the outer structural shell of the transfer tube. The geometry that has been used to date include elliptical and circular cross-sections. Elliptical shape has been proposed on the fuel side transfer duct for the two duct hot gas manifold (Fig. 3.5). Some of the other concepts that have been explored include bi-directional volute concept (Fig. 3.6) and elevated turbine discharge (Fig. 3.7). The crosssectional shape of the tube is determined by the area needed to transport the given amount of gas and simultaneously satisfying envelope, structural strength and flow requirements. At the inlet of the transfer tubes smooth fairing to the bowl liner is accomplished to reduce stress concentrations as well as to guide the flow (Fig. 3.8). Frequently these doubly curved complex shell regions can be stress critical.

The preburner liner in SSME (Fig. 3.9) serves the function of ducting the gas to the turbine inlet as well as to contain the coolant to cool the structural wall. A divergent ring liner concept is used to have more favorable heat transfer coefficients in the flame region. The preburner transfer duct concept explored in XLR-129-P-1 engine (Fig. 3.10) also has a smoothly faired scrub liner and a structural liner behind it containing coolant to cool the outer case.

Joint details of the liners account for the thermal expansion. When cooled structural liners are protected by scrub liners (Fig. 3.11) the ends of structural liners can be designed to be welded as the rise in bulk temperature can be controlled. The uncooled scrub liners can have significant increase in bulk temperatures and are usually cantilevered allowing for free expansion. However, engine firing experience has indicated that some motion limiters (Fig. 3.12) or vibration dampers (Fig. 3.10) are necessary to extend the fatigue life of liners. In new SSME designs integrally machined supports are used in scrub liners. For manufacturing purposes and thermal growth, the support design incorporates a nominal gap. The net thermal growth of the assembly allows for a small interference between scrub liner and structural liner. During steadystate operation, the supports expand thermally to contact the structural liner and provide mechanical support and dampers. If the gap

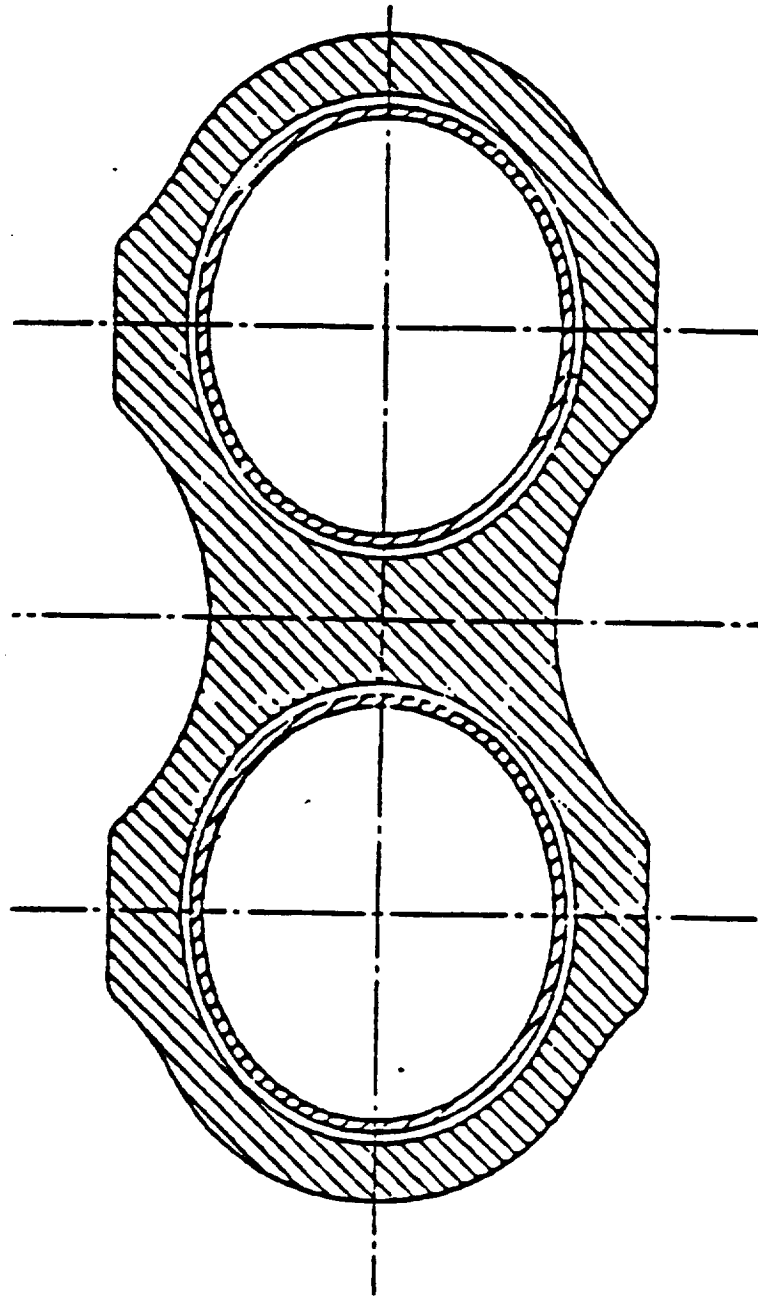


Fig. 3.5 Phase II+ HGM Fuel Transfer Tube Concept

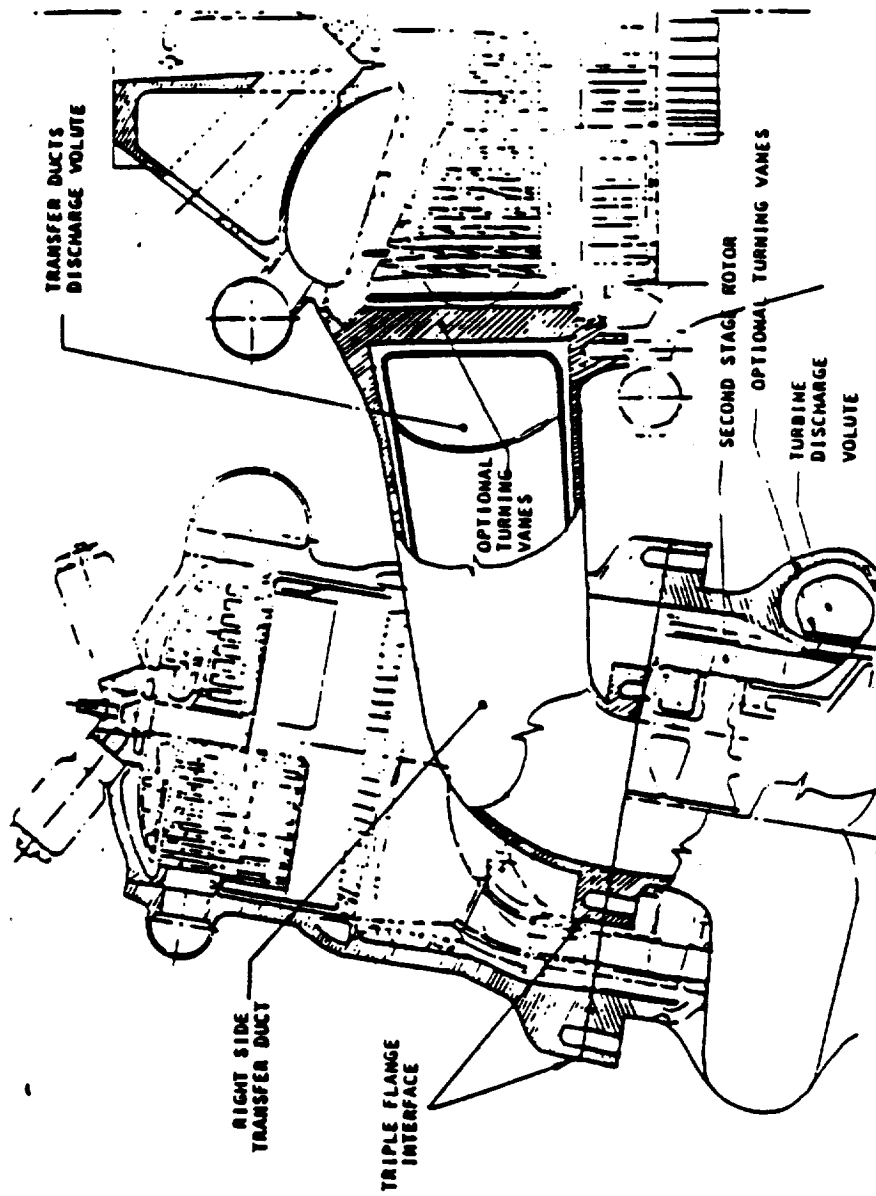
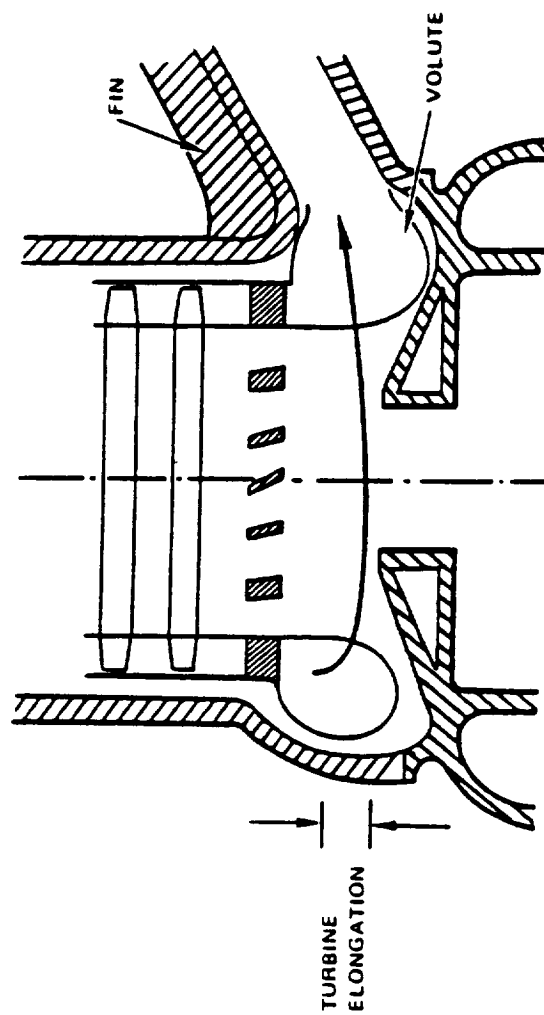


Fig. 3.6 Bidirectional Volute Transfer Tube Concept



Fig, 3.7 Elevated Turbine Concept

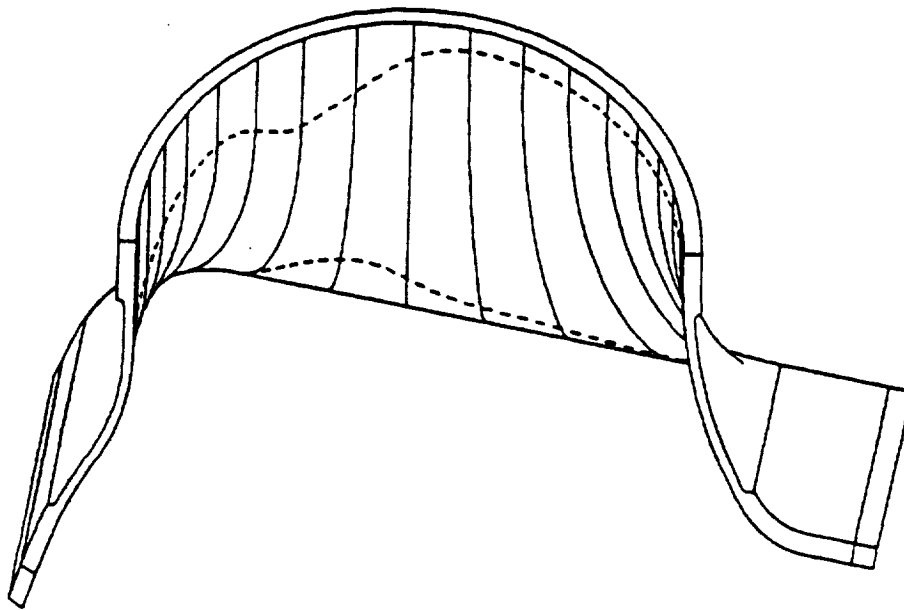


Fig. 3.8 Inlet Fairing to the Fuel Transfer Tube



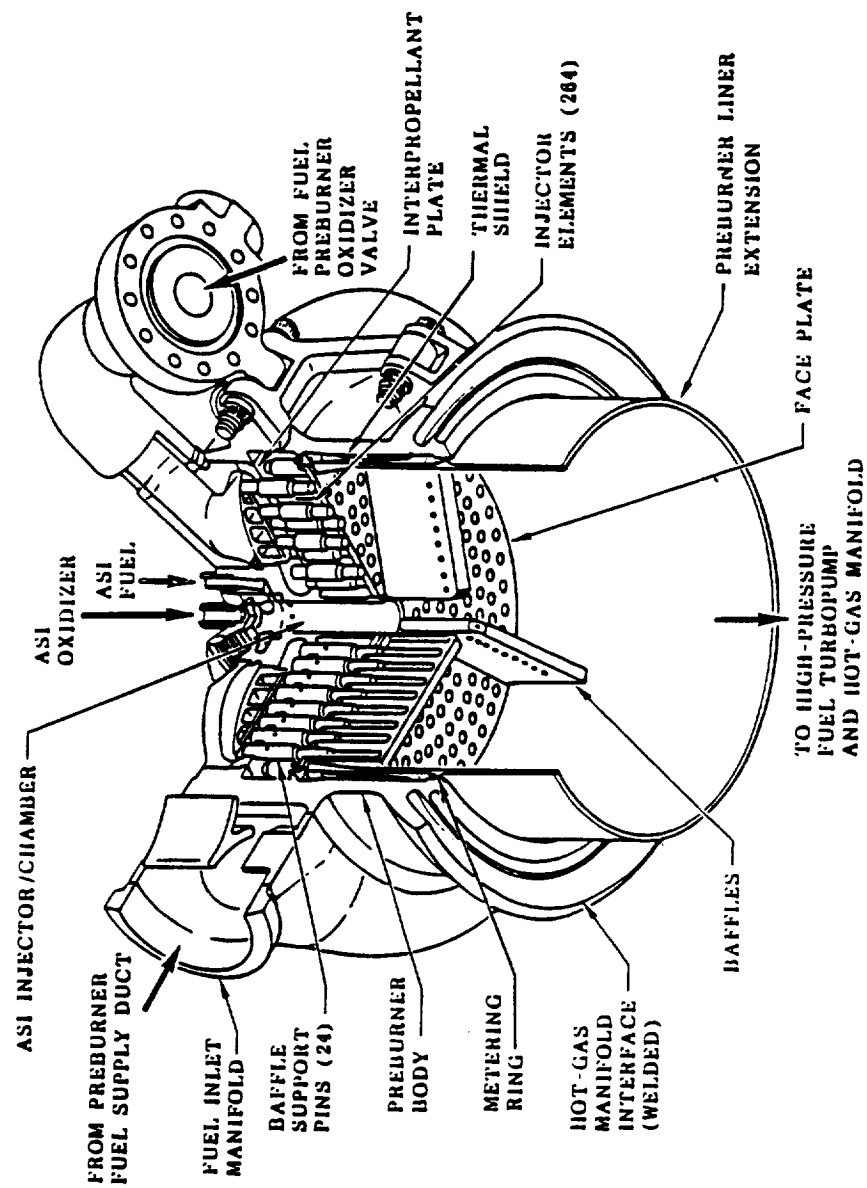


Fig. 3.9 Fuel Preburner Liner and Extension

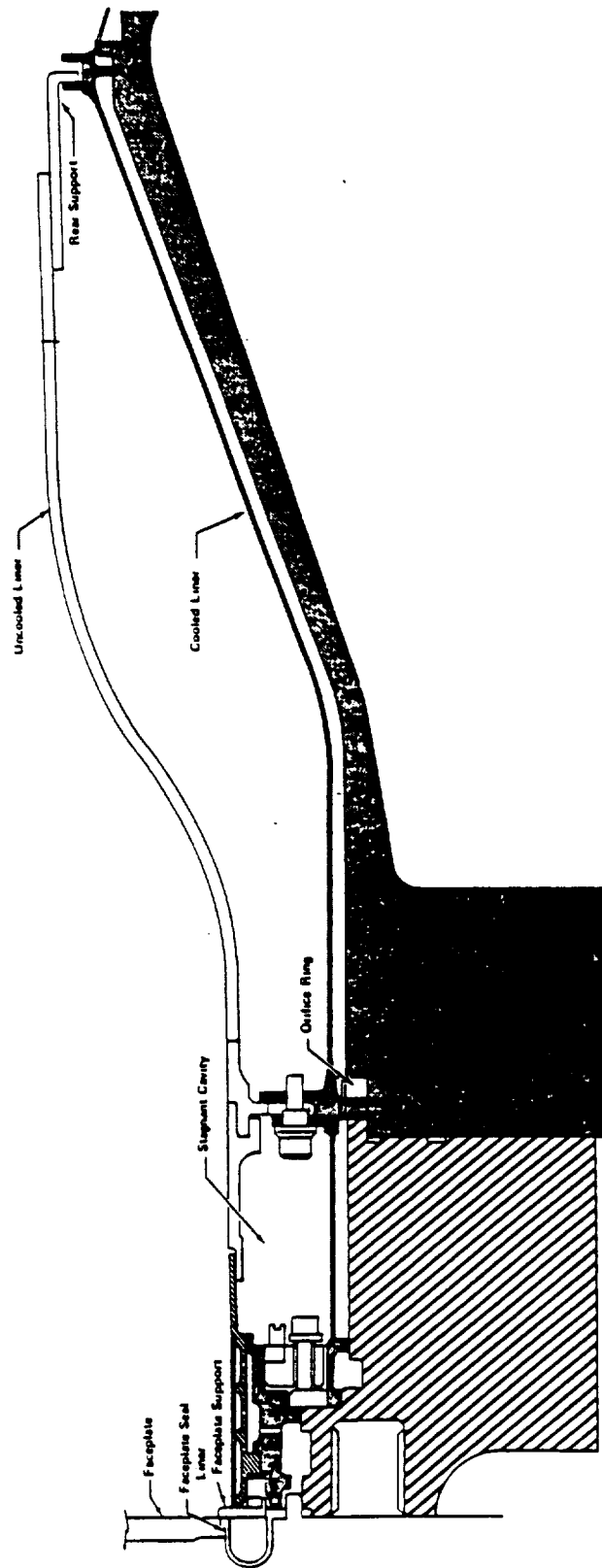


Fig. 3.10 XLR129-P-1 Cooled Liner Concept with Uncooled Liner Vibration Damper

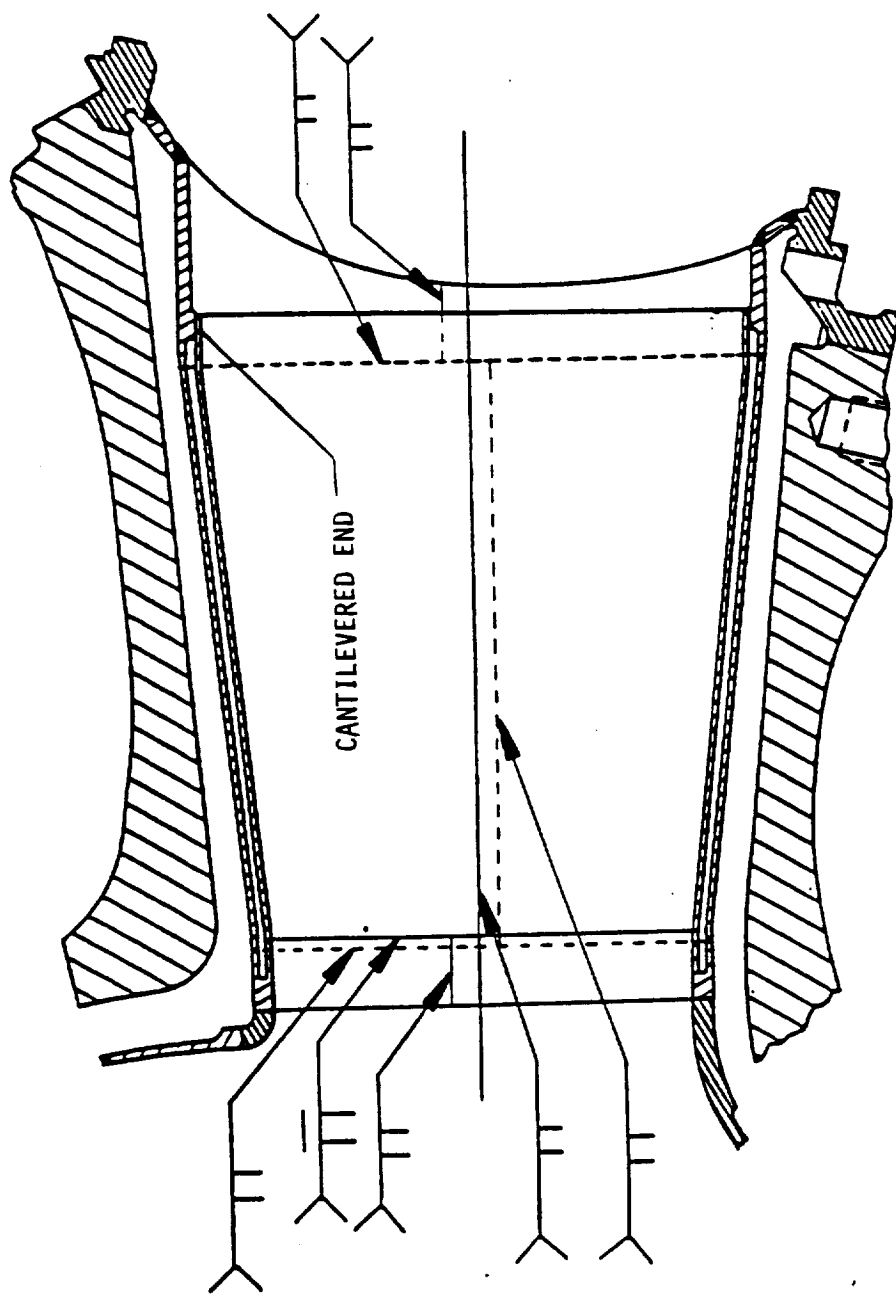


Fig. 3.11 Scrub Liner and Structural Liner Concept used in HGM Transfer Tube Design

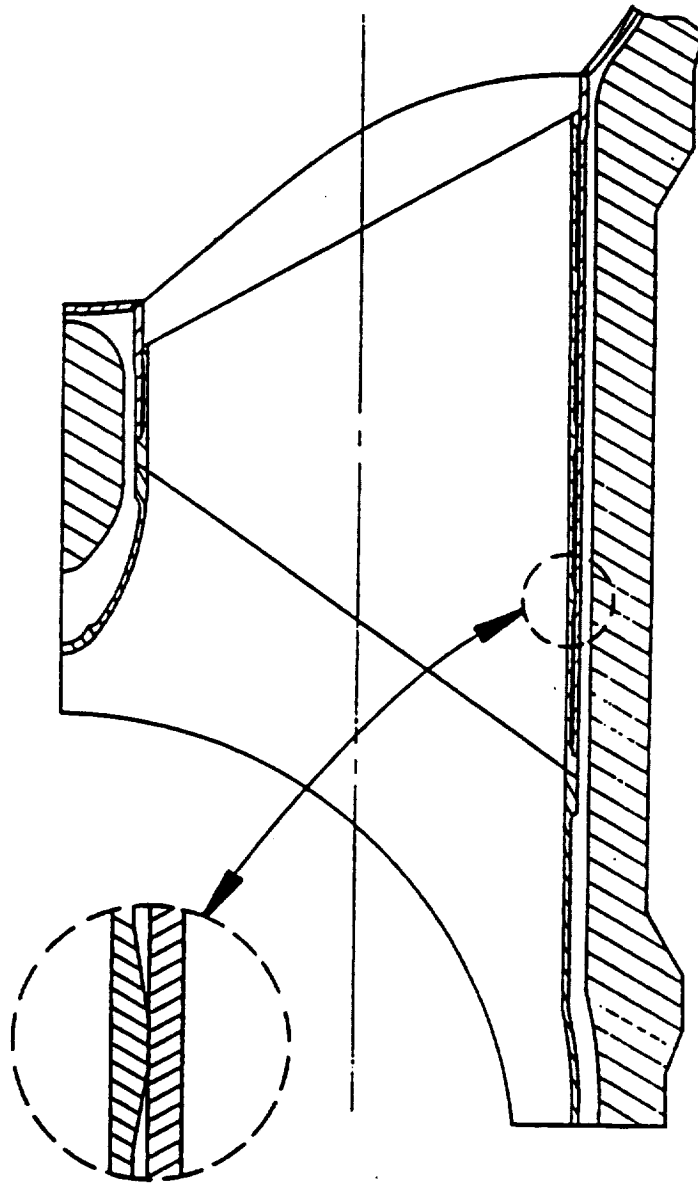


Fig. 3,12 Integrally Machined Motion Limiters in the New Transfer Tube Liner Designs

length is not tightly controlled, such compression only support greatly increases the complexity of structural analysis, especially when accurate vibration response calculations are required.

The finger like support tabs used in preburner liners allow for radial as well as axial expansion of the liners (Fig. 3.13). There are 24 legs in the fuel preburner and there are 8 legs in the oxidizer preburner. The liner material is coated with zirconium coating 0.013" thick on inner surface at forward end. The radial expansion of the liner is counted upon for the liner to bottom out on fuel preburner body resulting in metering of the coolant flow in the cavity, resulting in a favorable thermal gradient.

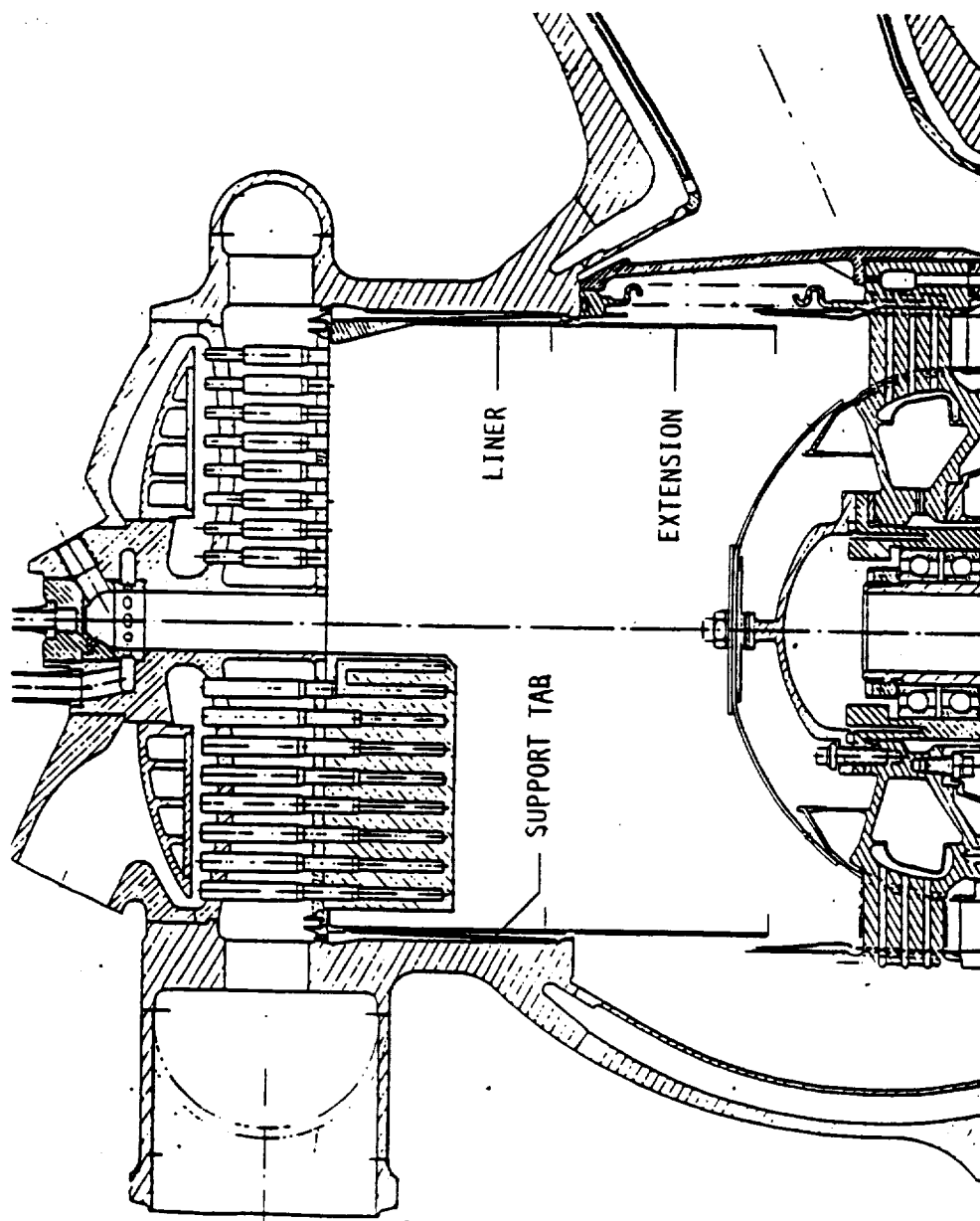


Fig. 3.13 Preburner Liner with Flexible Support Tabs

### 3. Material Considerations

The SSME transfer tube liner is made of Incoly 903 material. This material was chosen because of its superior strength properties at high temperature, low coefficient of thermal expansion, good low cycle fatigue properties and its superior performance in hydrogen environment. The preburner liner is made of Haynes 188 material.

Alternate concepts of liner design include the use of transpiration cooling. Transpiration cooling can be achieved through the use wire mesh laminate sheets called Rigimesh. This material has been used in face plate design in J2S, RL-10 and SSME engines. The use of this material has been considered for transfer tube or casing liners.

Rigimesh is produced through precision calendering and diffusion bonding of one or more layers of woven wire mesh into strong monolith structure. Rigimesh sheets are produced to specific permeability by having one or more layers subjected to multiple sintering and rolling operations. Manufacturing processes try to achieve uniform directional properties by orienting adjacent layers  $90^\circ$  apart. Tensile tests are conducted with specimens fabricated parallel, at  $45^\circ$  and at  $90^\circ$  to the primary weave of the plate. In general varying material strengths are obtained based on direction, and thus analysis must treat the material as orthotropic, with directionally dependant young's moduli.

Heat transfer analysis of Rigimesh include coupled models of solid metal and fluid interacting with independant thermophysical properties.

#### 4. Loading Environment

##### Transfer Tube Liners

##### Design Considerations

The transfer tube ducts were originally designed to withstand the sixty flight cycles at rated power level. However, during the development program to upgrade the SSME to 109% power level, fuel side center transfer duct failures were experienced. From the evaluation of failures, additional transfer duct design criteria were defined. The current design procedure for transfer tube liners include steady state analysis due to pressure and temperature, temperature cycling for multiple starts and cutoffs and, random pressure and mechanical loading. Adequate factor a safety is maintained for high cycle and low cycle fatigue, buckling due to thermal, mechanical and, pressure loading.

##### Static Pressure Loads

An accurate determination of the flow field in the hot gas manifold is a difficult task due to intricacy of the flow passages. The flow exits at a high velocity and the tight turnaround ducts might lead to separation of flow on the inner wall (Fig. 3.14). The swirling action of the gas at turbine exits, one sided discharge and compactness of the manifold lead to transverse pressure differential. Further, flow in all the transfer tubes need not be equal. Typical mass flow splits are 52% in the transfer duct favored by the swirl direction and 48% in the other duct for the two duct system, while the three duct system exhibits mass flow splits of 52,9 and 39%. The maximum engine scaled mach number observed in two duct configuration is 0.16, while the three duct HGM exhibited a maximum mach number of .26. Due to the severe environment in the transfer tubes any extensive measurements of static and dynamic pressure in the transfer tubes itself is not available from hot fire engine tests. Thus the pressure loading that is used in analysis is a combination of engine balance, scaled values from extensive airflow tests and the nearest available instrumentation to the point of interest from hot fire engine tests.



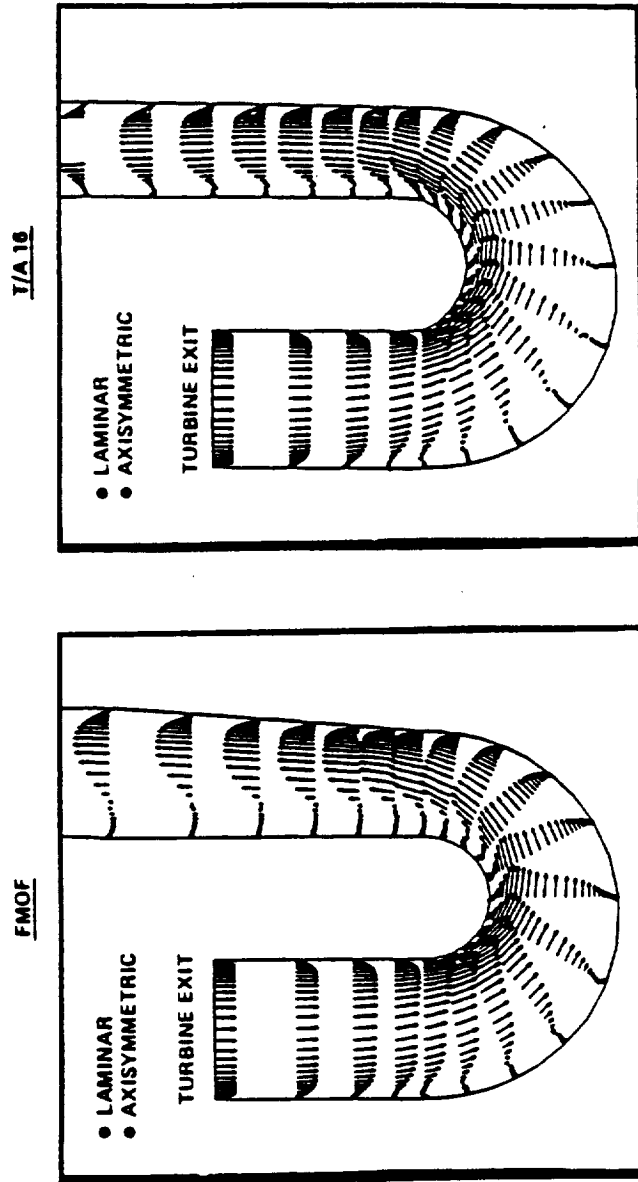


Fig. 3.14 CFD Velocity Vector Results for Two Turnaround Duct Configurations

One of the primary objectives of the SSME development program is to make design changes that improve the flow field in the hot gas manifold. In support of these design changes data from extensive air flow tests, computational fluid dynamics model results and water flow test data are available. Some of the results of airflow tests for static pressure for the two duct hot gas manifold design that has been used in new designs is presented below and in subsequent discussions.

The transfer duct geometry is characterized by a very short length compared to its diameter (Figure 3.15). Thus the simulation flow in the transfer duct to a flow through a long duct can be a gross approximation. The static pressure flow field in the transfer duct is affected by the geometry of the turnaround duct and the details of the inlet fairing to the transfer duct. The airflow model static and total pressure measured at the entrance of transfer duct is shown in Figure 3.16., where the variation in static pressure in the thirteen zones can be observed. The measurements were made using two dimensional probes. The flow rates used in the model testing is more than 100 lpm/sec. of ambient air, which is equivalent to 60% of the Reynolds number of the hot fire engine operating of FPL. Previous testing has shown that this simulation to be an accurate modeling of the hot fire engine.

In a transfer duct liner design, scrub liners (Figure 3.11) are not designed for any pressure differential as sufficient pressure relief passages are provided to avoid any pressure differential. On the other hand, the structural liners are designed for pressure differential between coolant pressure and the gas pressure. Since no measurements of coolant pressures in the transfer tube liners are available, those values are obtained from engine balance and transient simulation models. The differential pressures are evaluated for both steady state and transient. The differential pressure is of the order of 200 psi between the coolant and hot gas.

#### Temperature Loads

The transfer tube liners are subjected to severe heating and cooling conditions. Hot gas flows to the main injector through the interior of the

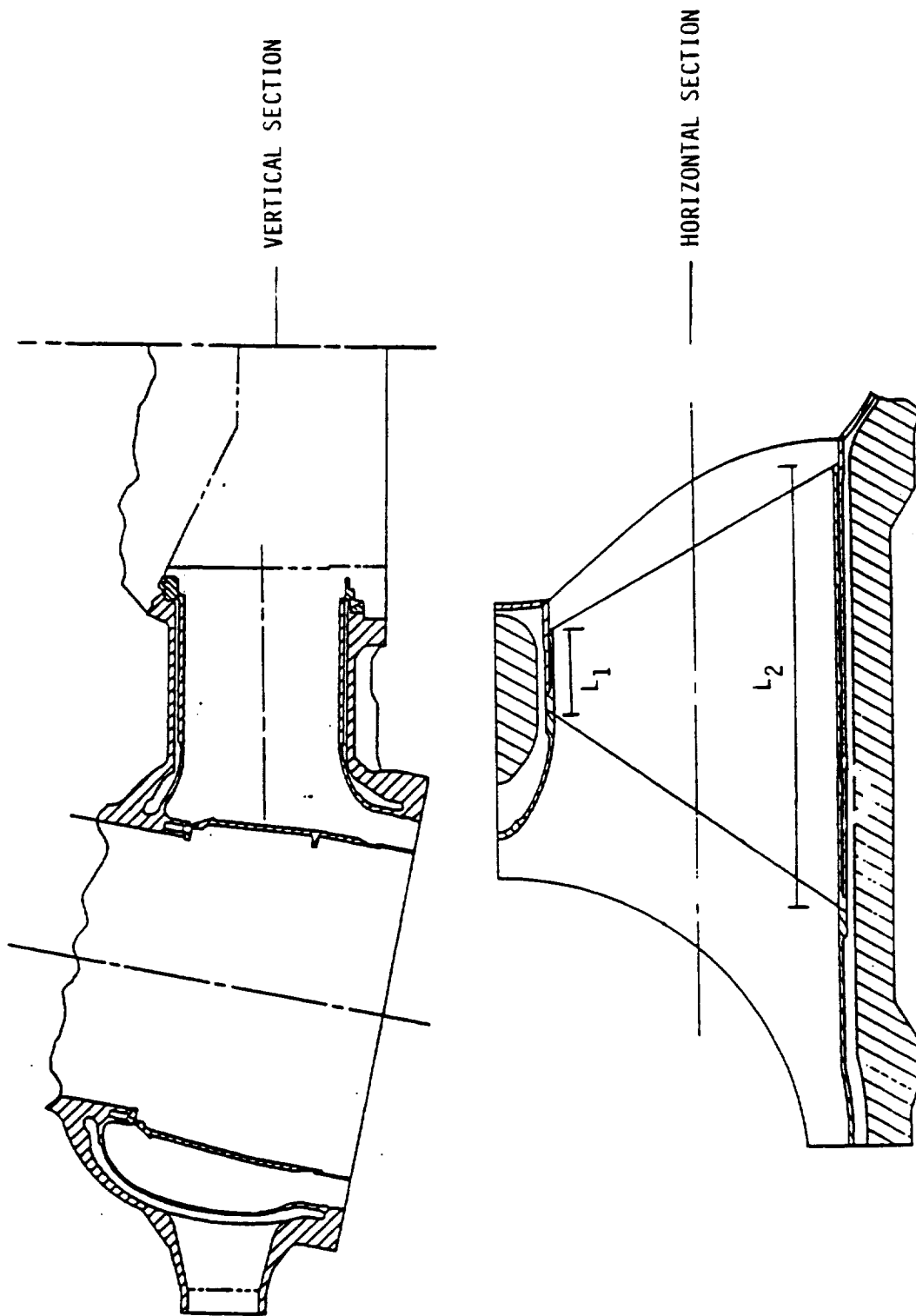


Fig. 3.15 Transfer Duct Length Compared to the Diameter

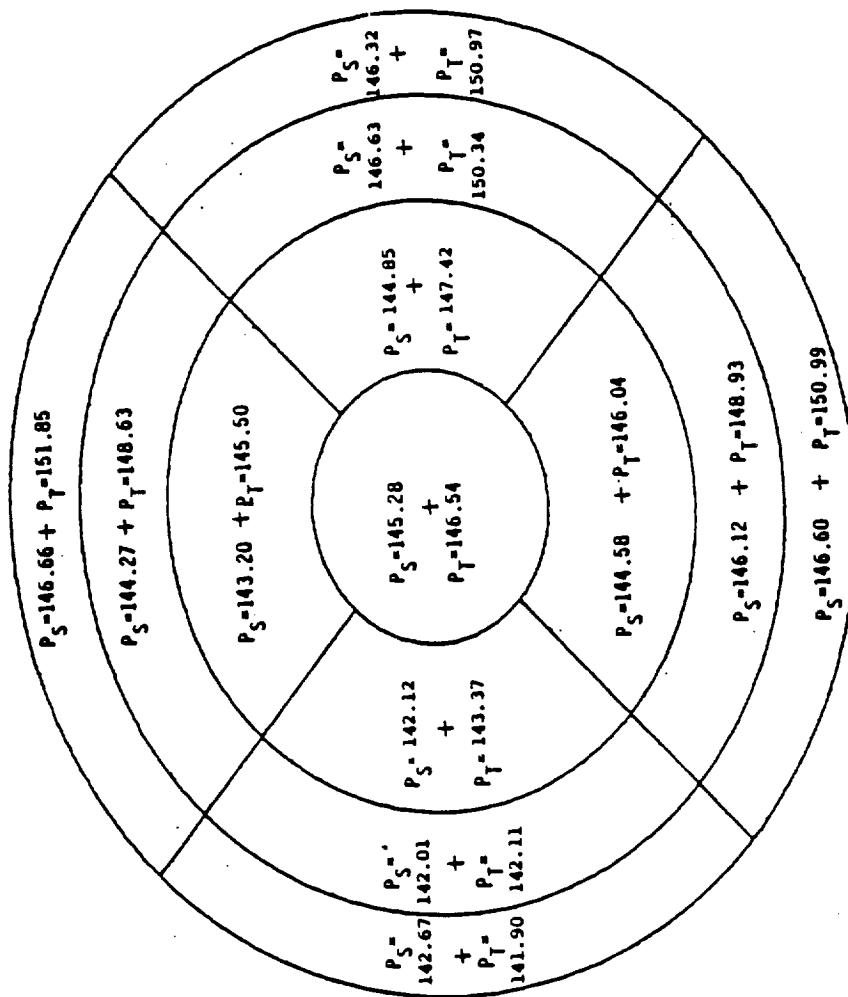


Fig. 3.16 Measured Static and Total Pressures from Airflow Model

liner while hydrogen coolant flows outside the liner in the annulus between the structural liner and hot gas manifold structural wall. In the new designs the inner scrub liner has partial circumferential ribs such that there are gas spaces between inner scrub liner and outer structural portion of the hot gas manifold liner (Figure 3.12). These gas spaces are connected to the hot gas environment in the liner center region by four slots equally spaced around the circumference of the down stream end of the scrub liner. While the scrub liner operates at high temperatures with thermal expansion connections at the end, the structural liner operates at correspondingly low temperatures but with ends welded.

Thermal loads on the liners are evaluated at start up., at steady state FPL and then at shut down. To model the above conditions in a heat transfer analysis, the following fluid conditions are required.

- 1) Coolant Temperature, pressure and mass flux in the annulus
- 2) Hot Gas Temperature, pressure and mass flux through the tube
- 3) Hot Gas Mixture Ratio
- 4) Hot Gas Condition (temperature, pressure, mixture ratio and mass flux) in the Gas Gap Between Structural Liner and Scrub Liner

Conditions 1 and 2 at the transfer duct are directly available from transient and steady state engine balance models. The hot gas mixture ratio can be calculated from the variation of flow rates of oxidizer and fuel to the preburners. These properties are needed to estimate the heat transfer coefficients on the liner surfaces and across the gaps between the scrub and structural liner portions.

In general condition in each gas gap, e.g. pressure, mixture ratio are assumed to be same as that of hot gas through the tube except for gas temperatures. The conditions in the gas gaps is based on condition of hot gas flow and on the physical constraints imposed by the design of gas path between the scrub and structural liner. For example for the two duct hot gas manifold design which utilizes four gas gaps and integrally machined portion limiters (Fig. 3.15), assumptions are different for the gas gaps. There are four such gas spaces on the fuel side and two on the oxidizer side. For the most downstream

gap, since these are slots allowing for flow between this gap and hot gas flow, it is assumed that the gas temperature equal to that of hot gas flow. However, gas temperatures on other upstream gaps are estimated as the capacitance weighted average temperature of the material represented by the nodes around that gap. This is done because of the physical restrictions on the gas flow for the upstream gaps. The gas temperature is most affected by the temperature of the surrounding liner material. The assumption of negligible flow in the upstream gas spaces, results in different heat transfer coefficients in the gaps. Heat transfer in the gaps without the flow is by free convection, while in the gap with flow forced convection is dominant. To determine the forced convection heat transfer coefficient, the mass flow flow through the most downstream gap is estimated. At the point of contact of scrub liner to structural liner at motion limiters, a contact conductance is assumed which is a function of contact pressure, surface finish and hardness of the material.

The calculated temperatures at various time slices are then used by stress analysis programs to calculate low cycle fatigue life by subjecting the structural model to thermal cycling.

Instrumented HPFTP turbine discharge measurements have shown that there is circumferential variation of temperature (Fig. 3.17). Such circumferential temperature variation must also be present in the transfer tube liners though the two dimensional axisymmetric analysis does not account for it.

#### Dynamic Loads

#### GENERAL

The major dynamic loads on transfer tube liners are the aerodynamic loads and to less extent mechanical vibration. Similar to many components in the gas path the life of the liner can be controlled by flow pressure oscillations. There are no high frequency measurements of pressure fluctuations at the transfer tube from hot fire engine tests. Hence the analysis is based on scaled values from air flow tests. Sometimes, the results are correlated to the hot fire engine measurements at CGIP location which is located in the main

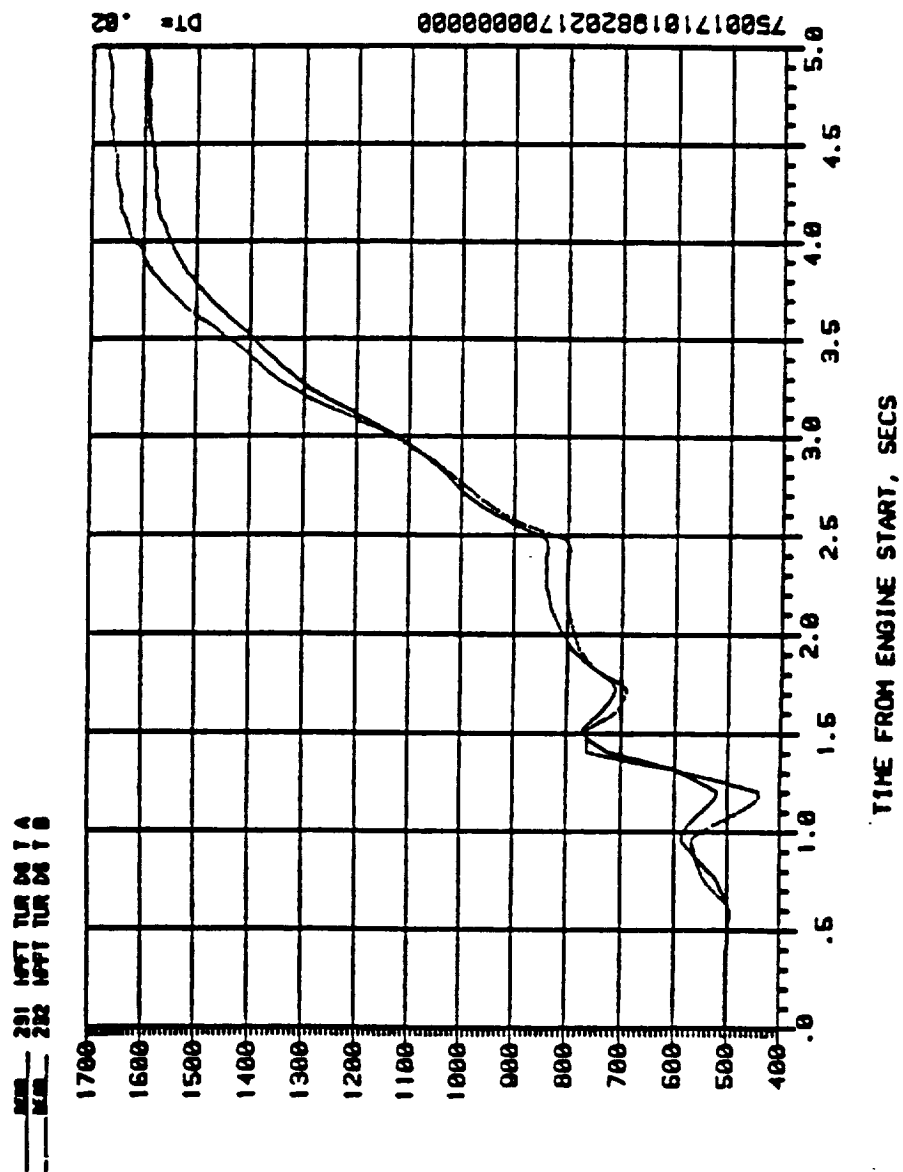


Fig. 3.17 Circumferential Temperature Variation at Turbine Discharge Measured at Probes A and B

injector bowl. However, the new HGM designs have provisions for measurement at transfer tubes and additional hot fire engine data should be available in Phase II + testing. (Fig. 3.18).

#### Mechanical Vibration

The mechanical vibration data that are used for transfer tube liner designs are obtained from SSME dynamic data base. G-1 vibration zone criteria was used for oxidizer side and R-6 vibration criteria was used on the fuel side. A typical PSD data for vibration zone G-1 is shown in Table 3.1. When data at higher frequencies than available in SSME data base are required, they are obtained from actual engine test data.

#### Pressure Oscillation

The pressure oscillation in transfer tube liners is closely linked to the hot gas flow circuit. Improved flow and pressure distribution through out the circuit, decreased turbulence, reduced velocity and less system pressure losses all help in a more favorable environment for transfer tube liners. The two sources of pressure oscillation on the transfer tube liners that have been identified are the boundary layer noise and the flow separation effects. It is known in the current SSME design, these are large regions of separated flow (Figure 3.19) in the center and outboard transfer tubes. In a failure analysis study of center transfer tube scrub liner failures at FPL, the pressure fluctuations due to separated flow was identified as the source for liner high cycle fatigue failure. It was postulated that the separated bubble was excited by accoustics emanating from turbine which in turn coincided with a sympathetic vibration mode of the scrub liner. The area of the separated flow was visualized by water flow tests (Figure 3.20). Tufts, bubble injection and dyes aid in establishing stream lines and separation patterns.

The high frequency pressure measurements are made at the top and bottom of transfer tube inlet (Figure 3.21). The measurements are done on the oxidizer and fuel transfer tubes. The air flow test results are scaled to 109% FPL and a typical set of pressure PSD diagrams on the oxidizer and fuel side transfer tubes are shown in Figure 3.22 and Figure 3.23. Analysis of data has indicated



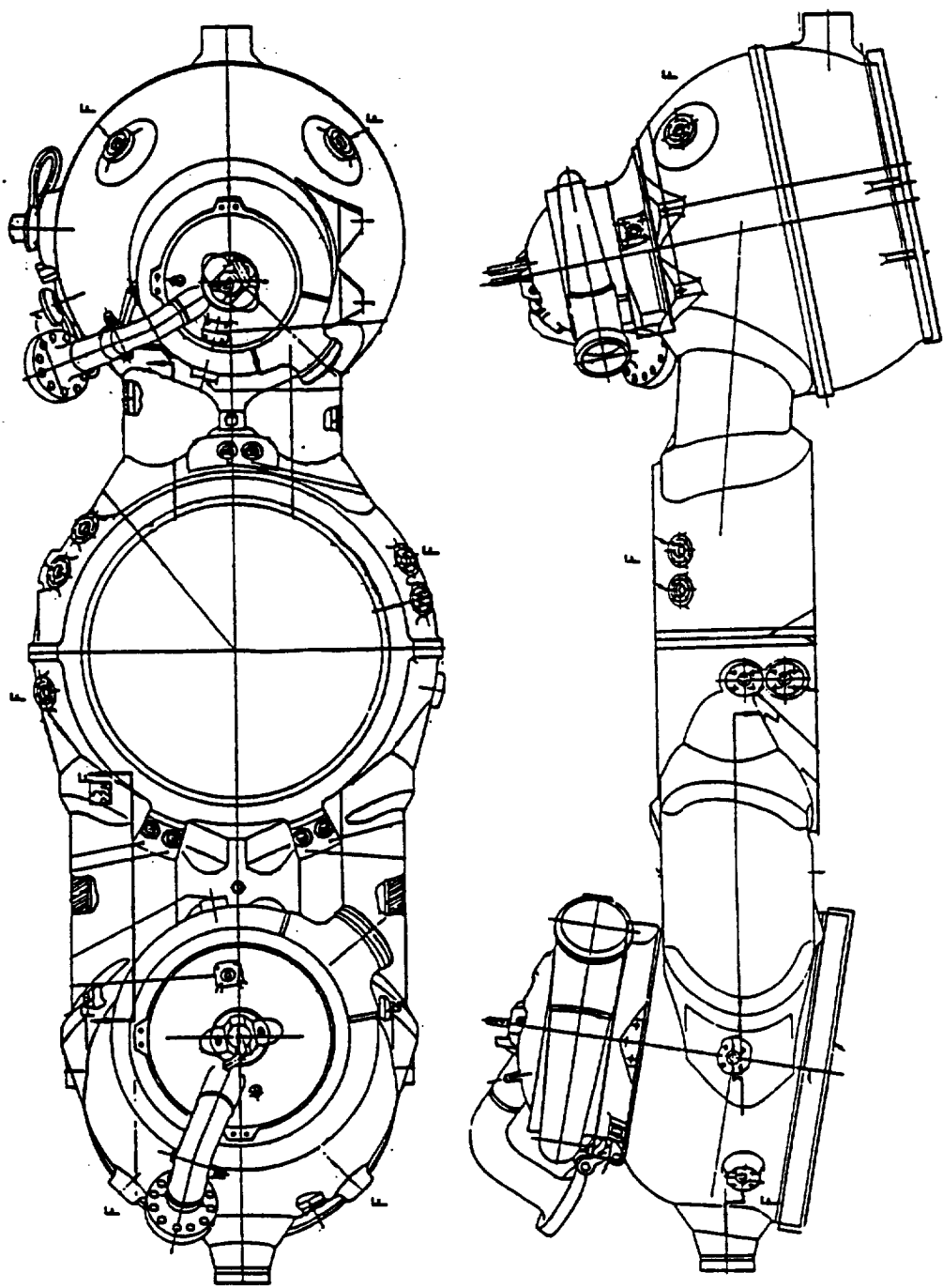


Fig. 3.18 New HGM Design with Additional Ports for Instrumentation

**X and Y Axes (Radial to pump centerline)**

**Steady-state random vibration amplitudes:**

20 Hz to 410 Hz @	0.033	$G^2/Hz$
420 Hz to 790 Hz @	0.041	$G^2/Hz$
930 Hz to 1180 Hz @	0.43	$G^2/Hz$
1450 Hz to 1740 Hz @	0.051	$G^2/Hz$
1870 Hz to 2000 Hz @	0.077	$G^2/Hz$

**Random Composite Reference Level = 15.46  $G_{rms}$**

**Z Axis (Parallel to pump centerline)**

**Steady-state random vibration amplitudes:**

20 Hz to 260 Hz @	0.011	$G^2/Hz$
270 Hz to 600 Hz @	0.017	$G^2/Hz$
800 Hz to 1070 Hz @	0.12	$G^2/Hz$
1180 Hz to 1280 Hz @	0.29	$G^2/Hz$
1310 Hz to 1380 Hz @	0.55	$G^2/Hz$
1410 Hz to 2000 Hz @	0.29	$G^2/Hz$

**Random Composite Reference Level = 18.33  $G_{rms}$**

**Table 3.1 SSME Vibration Zone Criteria Zone G-1**

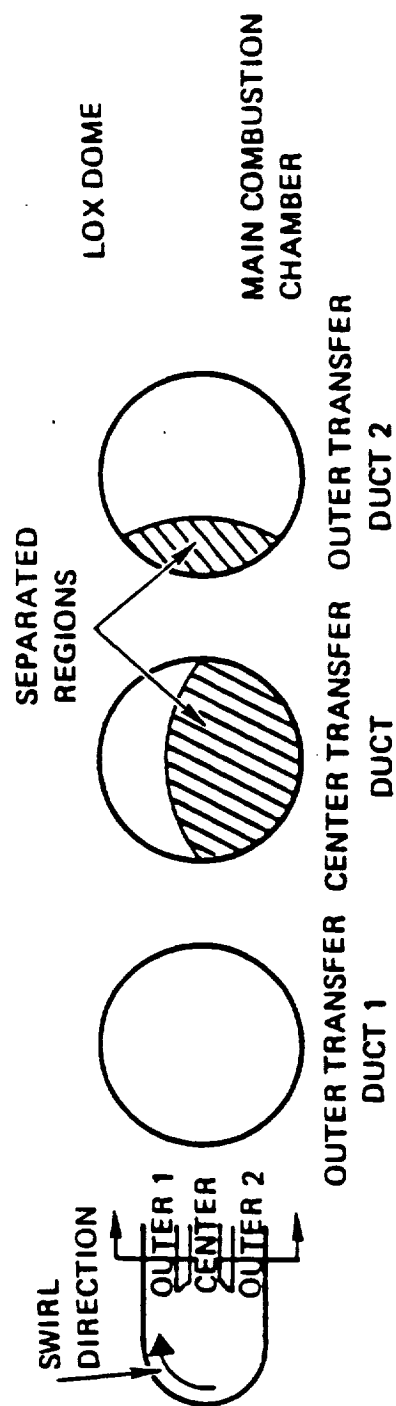


Fig. 3.19 Separated Flow Regions in the Three-Duct HGM Design

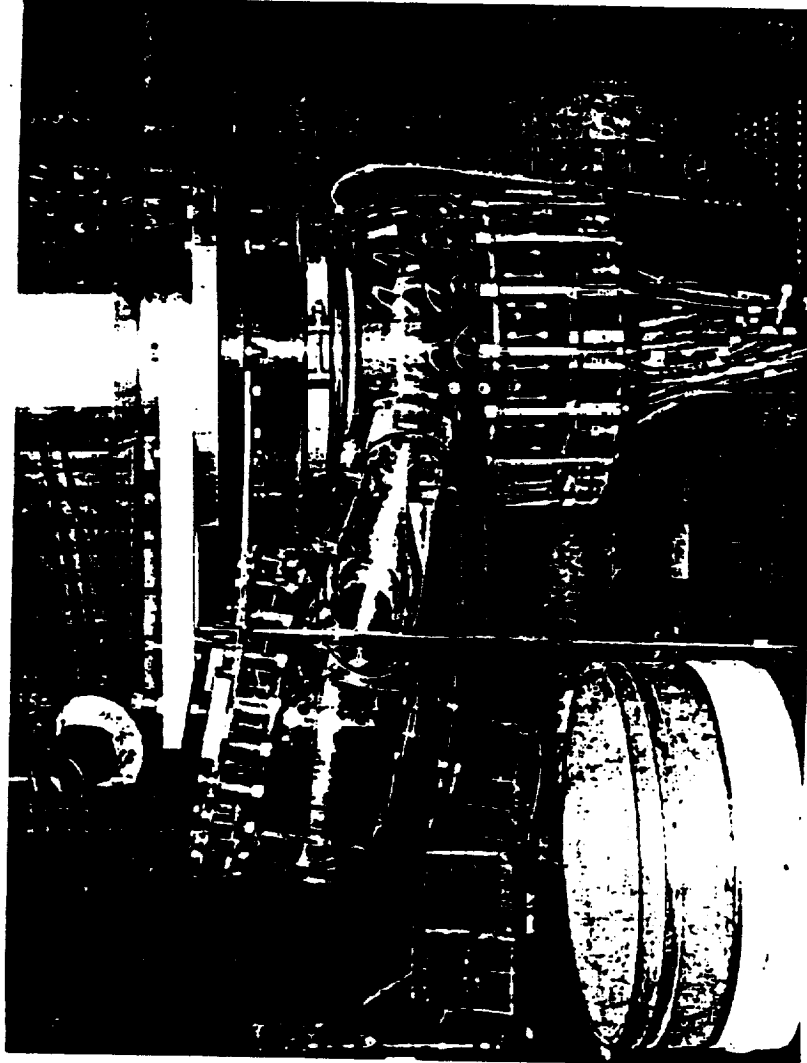


Fig. 3.20 Half Scale Plexiglass Three-Duct HGM Water Flow Model Showing the Three Transfer Ducts

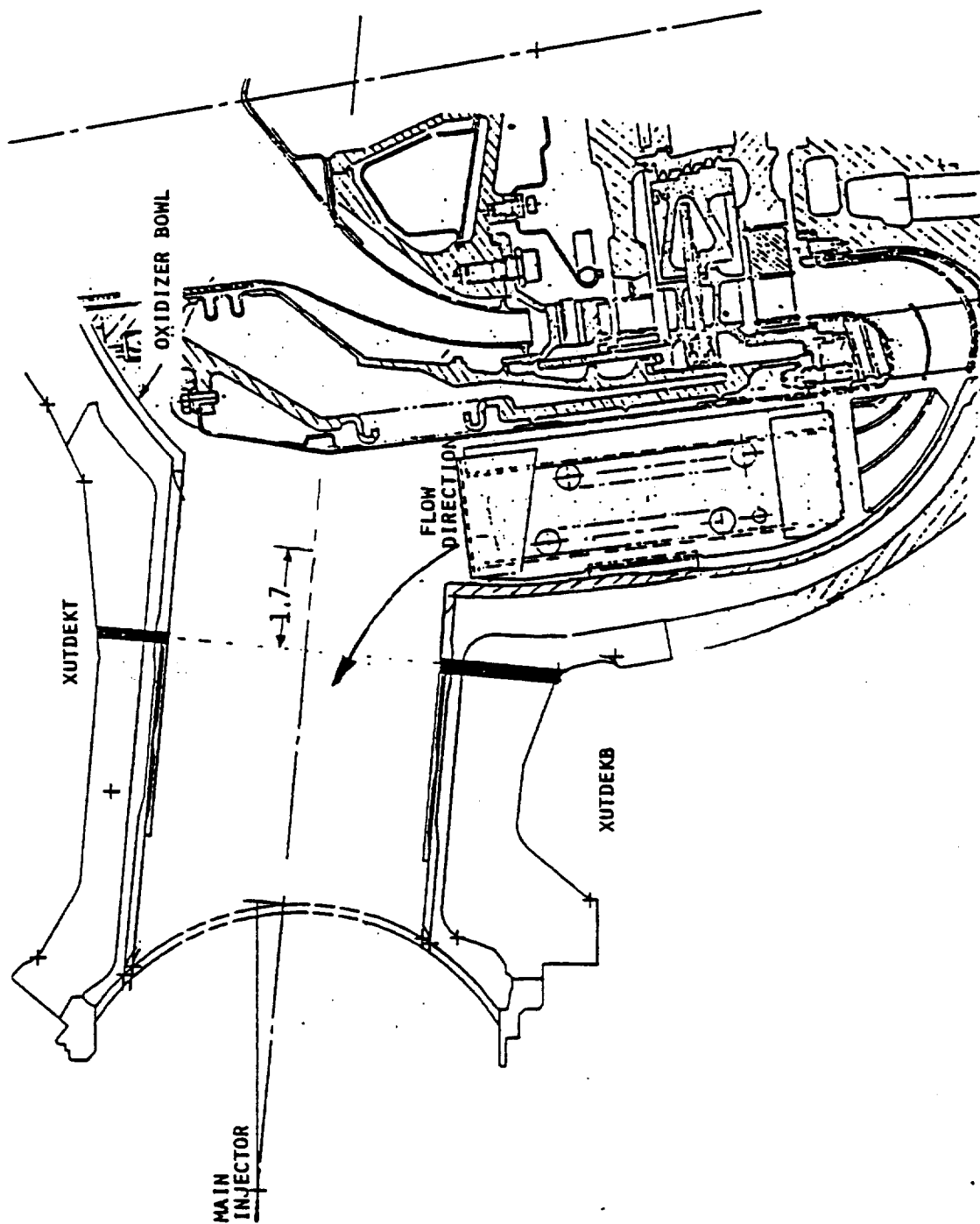


Fig. 3.21 High Frequency Pressure Measurements on the Oxidizer Transfer Duct for Air Flow Test

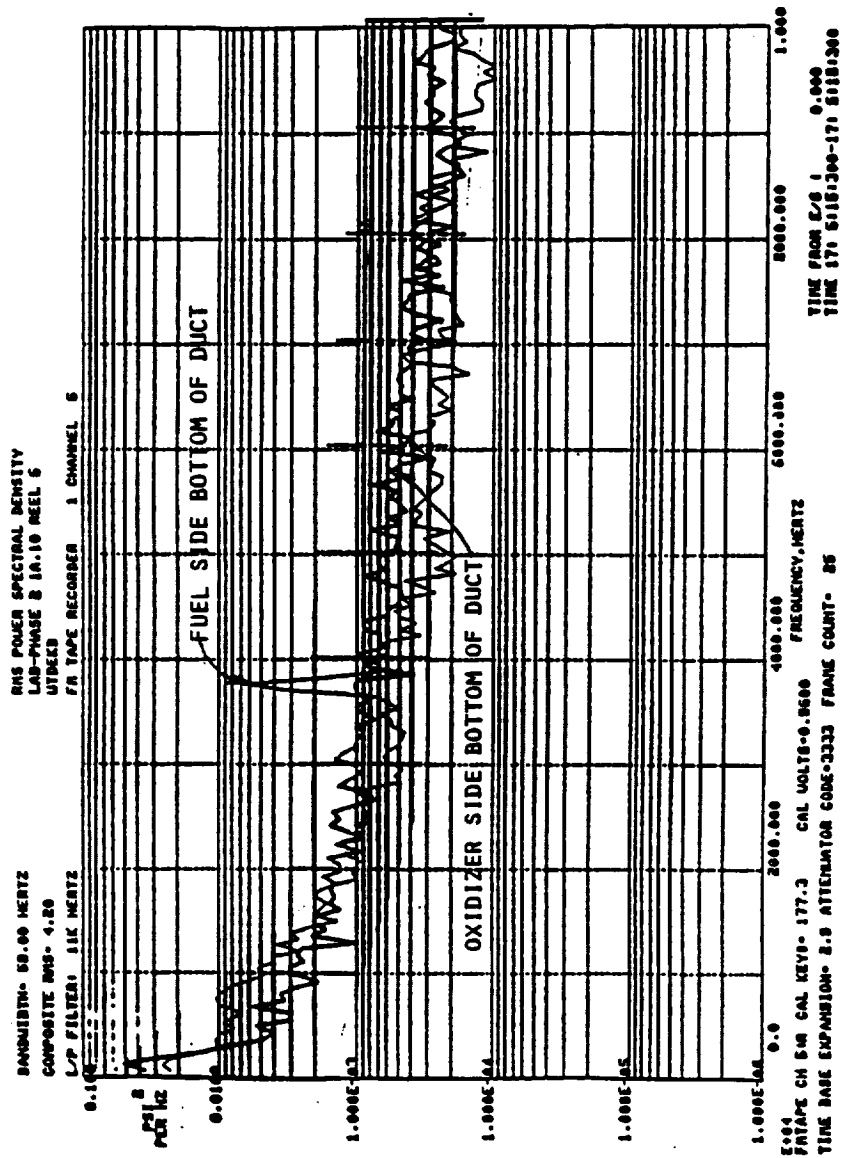


Fig. 3,22 Oxidizer Side Bottom Environment Similar to Fuel Side (Scaled to 109%)

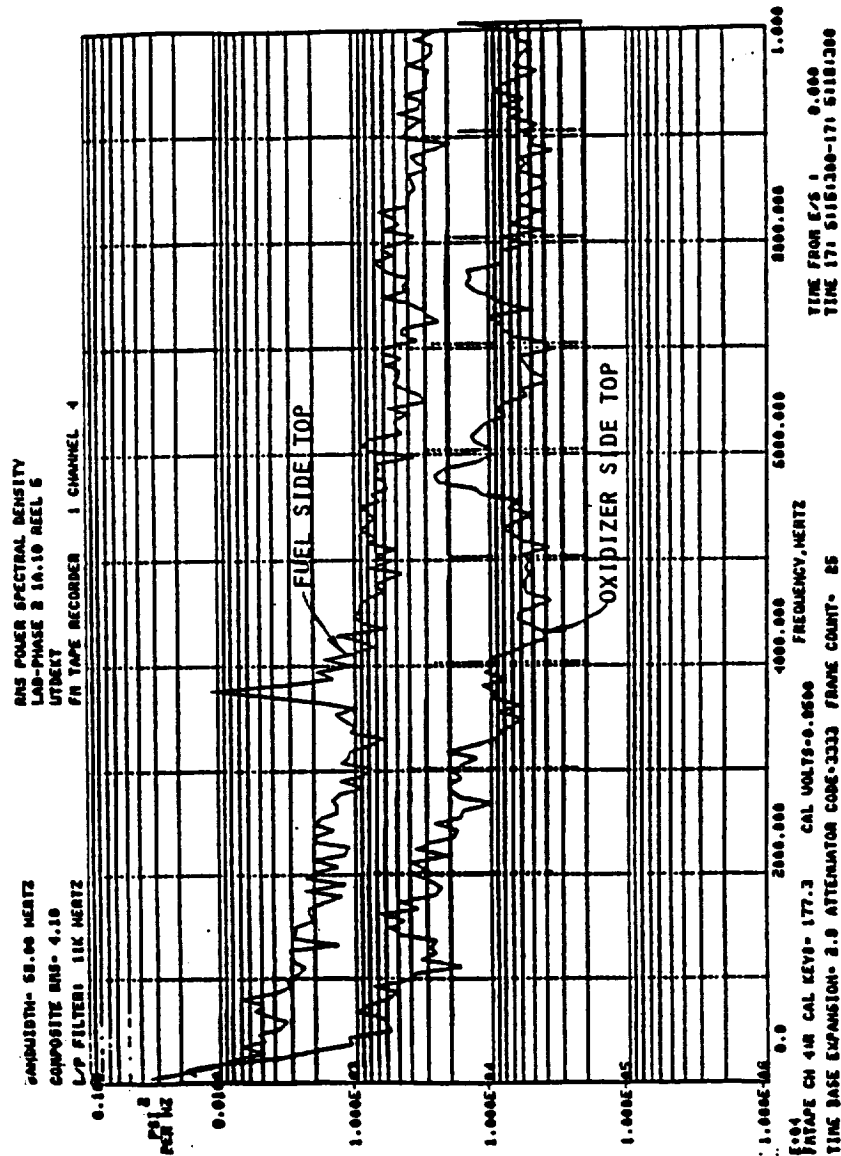


Fig. 3.23 Oxidizer Side Top Environment Reduced Compared to Fuel Side

the top and bottom measurements are uncorrelated. There are no pressure data available at the transfer duct exit. Due to limited measurements, the correlation distance circumferentially and along the length are unknown for the pressure fluctuations.

## Preburner Liners

### Design Considerations

The primary function of the preburner liners is to contain the hydrogen coolant obtained from preburner liner cavity in order to maintain a cooled structural wall. Additionally the coolant is used to cool the turbine bellows and the tips of the first stage turbine blades. The static loads to which the preburner liner is designed for are the temperature loads and cycling of them for multiple starts and cutoffs, the differential pressure between coolant and the chamber pressure. The dynamic loads for which the preburner liner is designed for include mechanical vibration and differential pressure oscillation.

### Temperature Loads

A heat transfer analysis is conducted for the preburner liners at steadystate temperatures taking into account the following considerations.

- . Temperature rise of backside coolant flow
- . Hotside film cooling
- . Hotside zirconium coating effectiveness
- . Flame front development
- . Hot gas flow changes near turbine inlet
- . Position dependent hot gas and coolant film coefficients
- . Transient cycling
- . Metering orifice/Structural wall interface
- . Hot gas and coolant temperature and flow as a function of power level and transient conditions.



The analysis is done using 2-D axisymmetric finite difference models, with a complete node compatibility with structural model. A divergent ring design is used to obtain a better flow and additional mass to distribute the heat away from localized hotspots. The liner is 0.4 inch thick near the face plate and tapers at a  $15^\circ$  angle until the wall thickness is 0.05 inches near the downstream end of the baffle. At this point the gradient across the wall is  $250^\circ\text{F}$ . The highest thermal gradient of  $500^\circ\text{F}$  occurs nearly 4 inches downstream of the face plate.

#### Static Pressure Loads

The liner is subjected to the differential pressure between coolant and chamber pressure. In SSME preburner liner designs, the differential pressure is a nominal value of about 24 psi. The metering orifices at the downstream end of the liner is a method of increasing the back pressure to prevent hot gas being driven into coolant cavity.

#### Dynamic Loads

The dynamic loads for which the preburner liners are designed for are mechanical vibration and combustion pressure oscillations. For SSME design, the effect of mechanical vibration on the preburner liners is small. This is because of the soft support system that is used for mounting the liners.

Potentially a more severe dynamic problem could be the pressure oscillations associated with combustion instabilities. Development of liquid rocket engines in the 1950S and early 1960S were often accompanied by high amplitude combustion instabilities resulting in severe hardware damage. Combustion instabilities in liquid rocket engines occur as a result of the unsteadiness in the combustion processes, which influence the conversion of the propellants in the liquid and/or gas phases to the product gas phase. The instabilities generally fall into two categories: rough combustion characterized by random oscillations and organized disturbances at discrete frequencies. In unstable combustion, the chemical energy release can couple with either the chamber acoustic modes or the feed system.

The combustion instability can be divided into three broad categories as:

- 1) Low Frequency (Chug)
- 2) Intermediate frequency (Buzz)
- 3) High frequency (Acoustic or Hybrid)

Low frequency instability is primarily caused by the interaction of combustion dynamics with propellant feed dynamics and generally is in the range of 250hz or below. Combustion oscillations at intermediate frequencies are caused by a variety of coupled process and occur at frequencies ranging from hundreds to approximately 1000. The coupling involves a portion of the feed system with the combustion response and the chamber wave motion can not be neglected.

High frequency combustion instability is considered to be a forced oscillation of the combustion chamber gases that are coupled to the resonant properties of the chamber geometry (acoustic) and to a portion of the feed system (hybrid) as well. The causes of hybrid instabilities may involve mechanical vibrations of the structure, eddy patterns from fluid induced flow oscillations or even flow disturbances caused by temporal variations in heat transfer. The wave motion in acoustic instability occurs at frequencies corresponding to the acoustic resonant modes of the chamber geometry. High frequency combustion instability is generally accompanied by high pressure amplitudes, accelerated heat transfer rates and frequently combustion chamber damage. Acoustic or high frequency instability has been by far the most challenging to suppress experimentally and to model analytically.

In the current SSME design, significant pressure oscillation of about 500 psi peak to peak occur during shutdown (chug) in low frequency range. However, the significant gap at the top of preburner liner acts as a pressure relief and the actual differential pressure seen by the liner is much smaller. The dynamic pressure measurements made at the coolant cavity support the chugging and pressure relief phenomena at shutdown. High frequency measurements of the chamber pressure are not available for current SSME design though plans for such measurements exist for test bed engine. The SSME engine experience indicates the high frequency pressure oscillation is small in the preburner liners.

## 5. Static Analysis

### Transfer Tube Liners

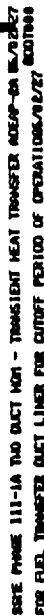
The low cycle fatigue life of transfer tube liners are evaluated to ensure adequate factor of safety. The analysis is done using two dimensional axisymmetric finite element models subjected to several mission duty cycles. The finite element models have sufficient details to capture the strain range at critical areas. Different material properties are assumed for the parent material, GTAW - as welded location and EB weld locations. A bilinear stress strain curve is normally used in the analysis. The typical gas temperatures at start transient, mainstage and shut down are shown in Fig. 3.24 and Fig. 3.25. The actual temperatures used in the finite element models are automatically transferred from heat transfer analysis to structural analysis through the use of common models. A typical duty cycle analysis can include the following stages:

- 1) Pressure and room temperature
- 2) Main stage pressure and temperature
- 3) Main stage temperature with no pressure
- 4) Shut down temperature with no pressure
- 5) Room temperature and no pressure

The cycle is repeated until a stable strain range is obtained. Past experience has indicated that two duty cycles are sufficient to obtain stable strain range values. Maximum effective strain range is calculated at all critical locations and factors of safety against low cycle fatigue is computed. (Fig. 3.26).

A closed form buckling analysis of the liner is made difficult due to its complex geometry of doubly curved shells and the operating stresses are near yield stress at many locations. Thus a finite element buckling analysis is performed on finite element model containing transfer tube liners and part of inlet and outlet toruses. Initially a linear eigen value buckling analysis is performed to obtain an estimate of buckling pressure and the lowest buckling mode at operating temperature.





**TIME. 0511**

$\Delta P = 210 \text{ PSI}$   
 $F.S. \text{ BUCK} = 4.17$

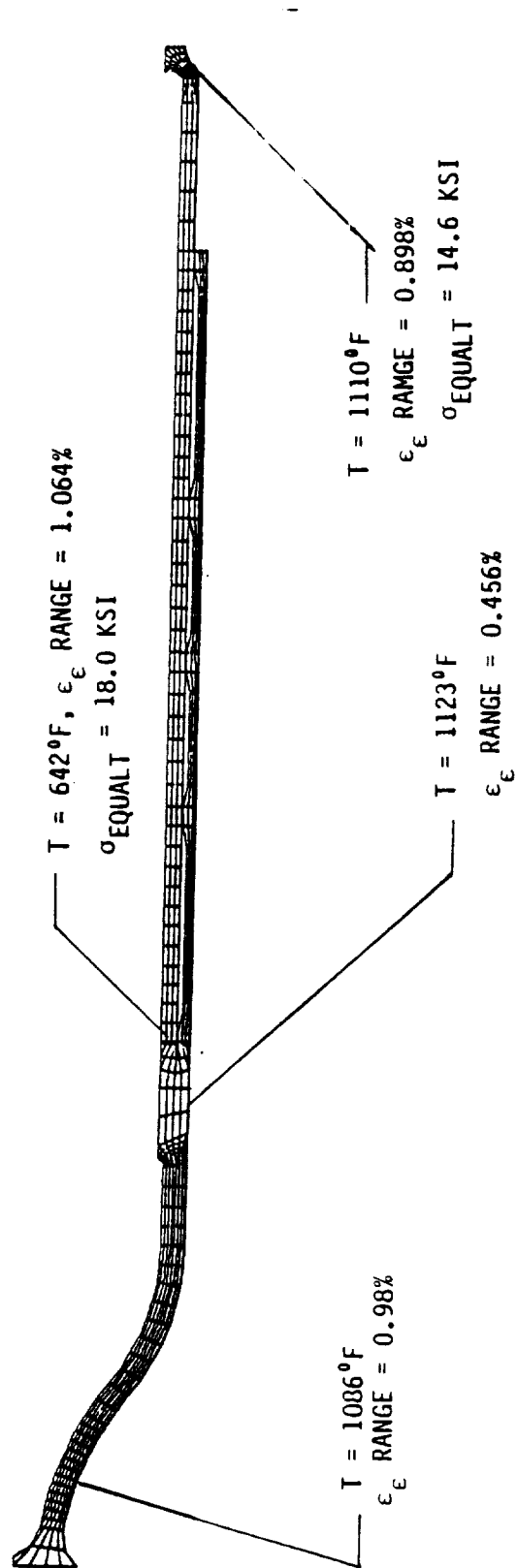


Fig. 3.26 LCF and HCF Analysis of Fuel Transfer Tube Liner

This analysis is followed by an incremental nonlinear analysis considering material and geometrical nonlinearity to obtain a better estimate of buckling collapse pressure. In many instances while the pressure is incremented, the temperatures are maintained at main stage to obtain a conservative design. In cases where the worst case is not obvious due to the interaction of temperature dependant material properties, temperature deflections and its effect on buckling load on shell, several limit cases are evaluated to bound to solution.

#### Preburner Liners

Static analysis of SSME preburner liner consist of temperature cycling and differential pressure loading between coolant and hot gas. A thermal cyclic analysis is done using 2-D finite element models. The cycling analysis include cycling from thermal steady state with pressure to ambient conditions until the solution is stabilized. Thermal data from heat transfer models with node to node compatibility is directly used. The maximum differential pressure on the SSME preburner liners is about 24 psi based on engine balance. The SSME preburner liners experience a maximum thermal gradient of about 500°F nearly 4" downstream of the faceplate and is the life limiting location at about 140 allowable starts.

## 6. Dynamic Analysis

### Transfer Tuber Liners

The dynamic analysis of the transfer tube liners are conducted to determine the high cycle fatigue life of scrub liners. A random mechanical support vibration analysis and a pressure analysis is done for the dynamic loads already described. The dynamic analysis is done on three dimensional linear elastic finite element models subjected to stationary random dynamic loading. The normal mode method is employed. The RMS (Standard deviation) nodal displacements, velocities, accelerations, element loads and stresses are computed. Briefly the solution is performed in the following phases. First a model analysis is run and the model vectors are saved. Out of this, N modes are selected for the analysis and a covariance matrix need to be computed. This symmetric matrix represents model responses to applied PSD forcing tables, the off diagonal terms representing the cross mode responses. When all the modes are considered, the covariance matrix might contain many off diagonal trivial terms for widely varying modes. On the other hand, neglecting all the cross coupling terms might give unacceptable inaccuracies. Their limited range of frequencies can be considered in computing cross mode coupling based on a frequency ratio, normally between 2 to 6. The sigma convariance matrices are then calculated by numerically intergrating based on frequency ratio chosen. The RMS modal and element stress responses are then calculated by modal superposition using sigma matrix and modal vectors. One of the key assumptions that need to be made in the analysis is the correlation distance for pressure oscillations. Due to lack of data certain assumptions are made in the analysis. In general, when detailed separated flow region data is not available, the shell is divided into four quadrants with the assumption that the pressure fluctuation in each quadrant is uncorrelated to other quadrants. The pressures are assumed to be correlated along the length of the liner for each quadrant. With an eccentric pressure load excitation, the above procedure gives conservative designs.

Past engine experience has indicated that the life of the scrub liners are extended by motion limiters. While the gaps are usually engineered for closing due to thermal expansion at operating temperatures, tight control of the gap widths may not be possible due to the difficulty of inspection of



double walled tubes. Thus any dynamic analysis procedure for response calculation, must ideally capable of accounting for nonlinearity due to gaps. A typical dynamic analysis include four pressure excitations, three base random and three base sine excitation cases.

#### Preburner Liners

Dynamic analysis of preburner liners are conducted using 3-D finite element models including the support legs, liner and liner extensionn. The dynamic analysis for base excitation is done using zone E structural loads criteria. An approximate analysis is done to determine the adequacy of the support legs based on maximum G loading that the liner experiences. In general, preburner liners must also be analysed for combustion pressure oscillation. Depending upon design, the liners might be subjected to large low frequency pressure oscillation due to chugging if pressure relief passages are not provided. For a well designed stable combustion system, the high frequency pressure oscillations must have low amplitude.

## 7. Failure History

### Transfer Tube Liners

Evidence of the transfer tube thermal protection liner unsatisfactory conditions, resulting from FPL testing operations, were first noted in mid 1980. The failures were manifested by thermal scrub liner cracking in the central fuel tube in many engines and were attributed to high cycle alternating stresses. The conditions started on all of the engines after a relatively short test period at full power level (FPL, 109% rated power level). The initial design was adequate for RPL operations as no transfer duct problems were experienced at that power level. The cracking occurred at the junction of the transfer tube to the fuel transfer tube liner inlets. (Fig. 3.27). The crack failure was attributed to the first bending mode and shell bending mode combination and was analytically shown restricted to center fuel transfer tube. This failure mode was eliminated by adding motion limiting support spacers (buttons Fig. 3.28) to the thermal protection liners. These devices are welded to the thermal protection liner and limit relative radial motion between the thermal protection and structural liners. Failures persisted in some engines with spacer configuration. The failure scenario was developed from the original condition where the support spacer installation allowed excessive gap between the support spacer ends and the structural liner. The gap indented due to support spacer deterioration by impacting of the structural liner, eventually allowing the thermal protection liner to fail in a similar manner to the earlier unsupported liner assemblies. Support spacer installation criteria was established to preclude service deterioration.

The interim solution of spacer pins is also very susceptible to failures because of inadequate weld joint strength. The pins and liners which are made of Incoloy 903 serve under high pressure hydrogen environment and require full penetration welds at liner to pin location. However, radiographic examination can not verify this condition due to the joint configuration and uncertainties expressed in radiographic image after a double wall shot. Other configurations that have been studied include upstream, midspan, and down stream doublers (Fig. 3.29). However, all new designs incorporate integrally machined supports on the inner liner (Fig. 3.30). The supports serve the function as deflection limiters.

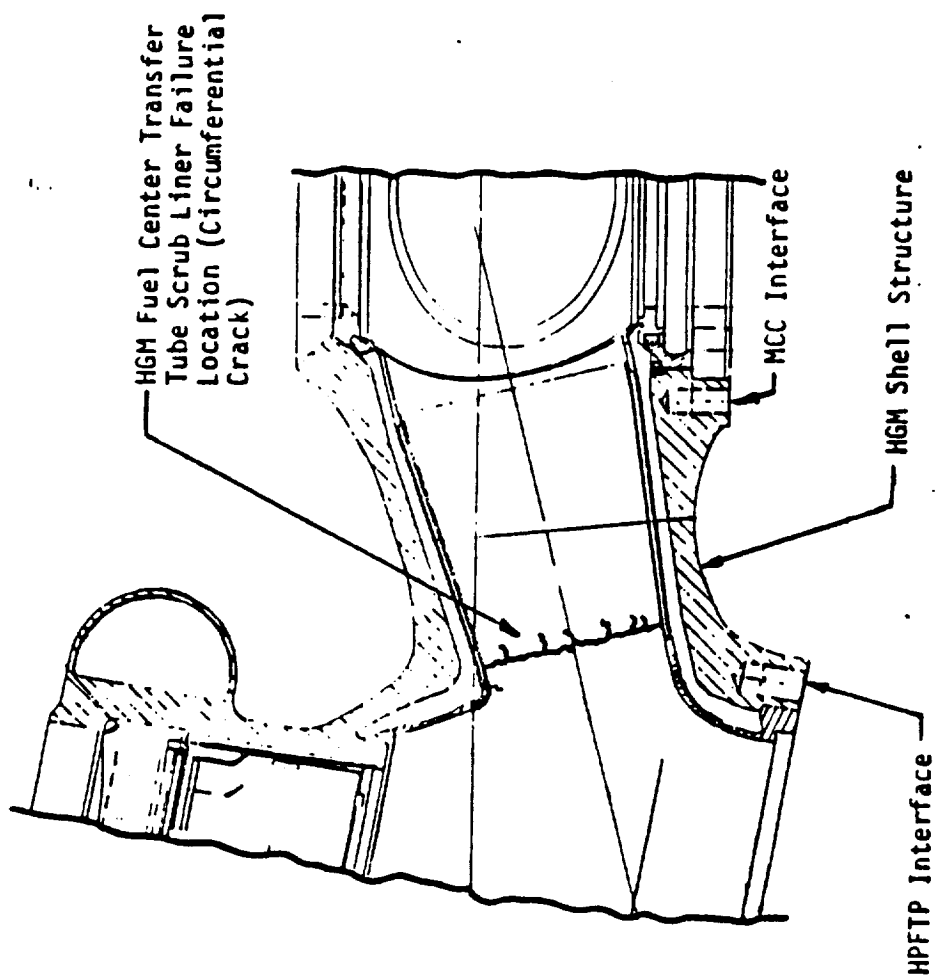


Fig. 3.27 Center Transfer Tube Liner Failure

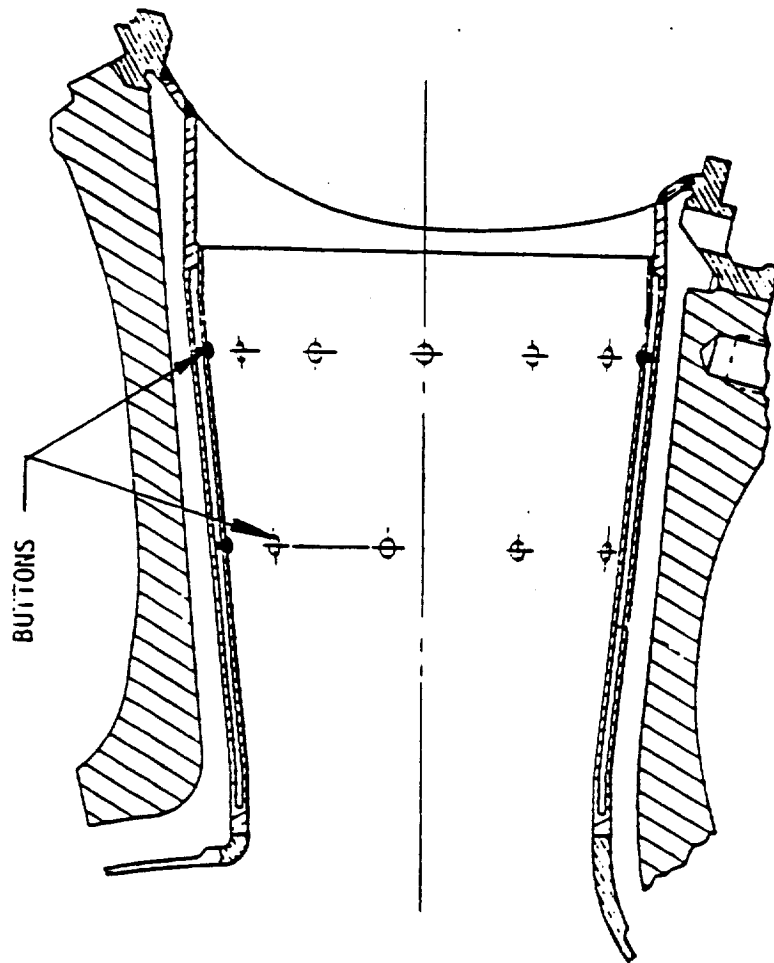


Fig. 3.28 Center Transfer Tube Liner with Motion Limiting Button Configuration

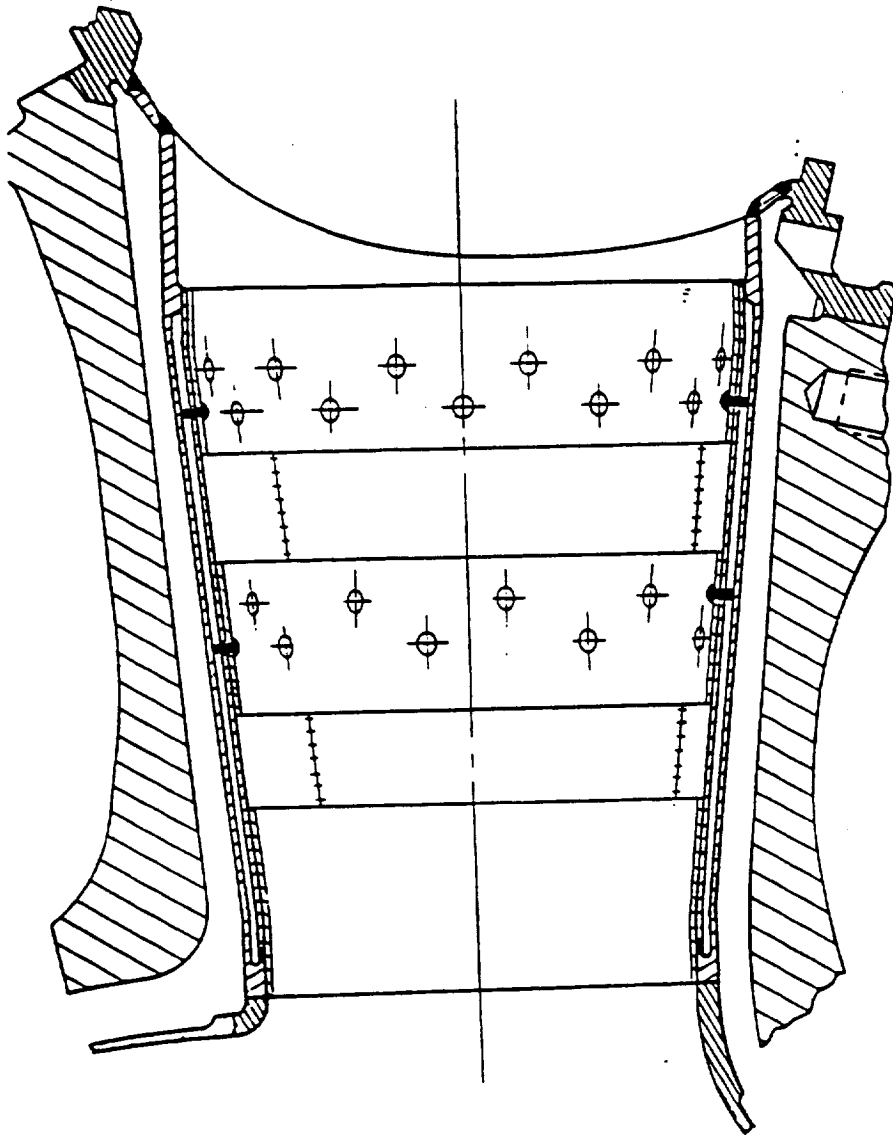


Fig. 3.29 Center Transfer Tube Liner with Doubler and Button Configuration

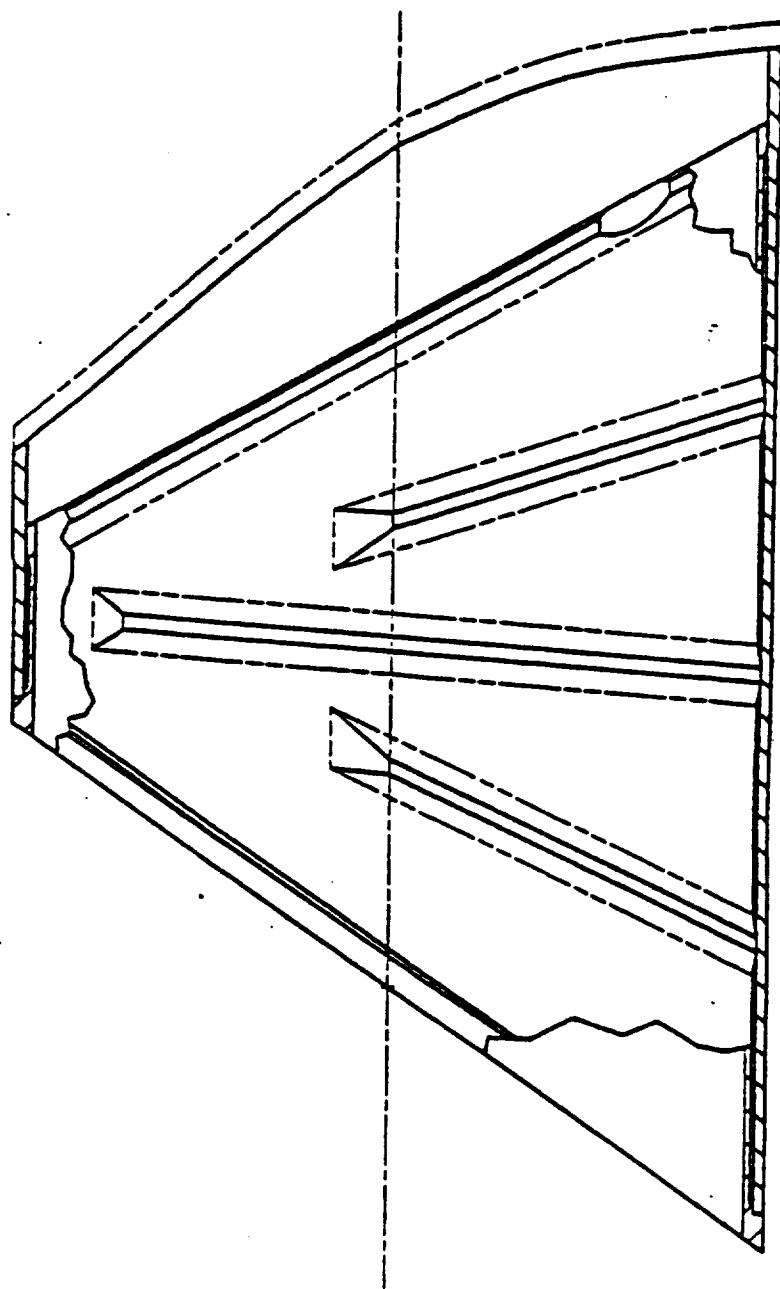


Fig. 3.30 New HGM Liner Design with Integrally Machined Motion Limiters

## Preburner Liners

Preburner liner failures were experienced on two engines with burn through of the structural wall when lox stream on the oxidizer post was diverted. Failure review concluded that the liner was inadequate to protect the wall under these conditions. The liner was redesigned to include the divergent ring to provide better flow and additional mass to distribute heat away from localized hot spots. The metering orifice at the downstream end was added to prevent back flow of the hot gas into the coolant liner.

## 8. Survey of Finite Element Models

Two basic types of finite element models are constructed for transfer tube liner analysis. The axisymmetric two dimensional models are used to do heat transfer and stress analysis duct to thermal cycling (Fig. 3.31). A common model is used between heat transfer and stress analysis such that temperature data is automatically transferred. The model contains part of the torus liner in the fuel and injector bowl. The model that is shown is for fuel side liner of the two duct hot gas manifold design.

Several three dimensional finite element models also exist that were used for buckling and dynamic analysis. The models incorporate scrub liner. Structural liner and part of the fuel and injector bowl. The available models include the center and outboard transfer tubes on fuel side for three duct manifold and fuel and oxidizer side tubes for the two duct hot gas manifold design. The fuel side transfer tube structural liner model used for nonlinear buckling analysis is shown in Fig. 3.32. The dynamic model consisting of structural and scrub liner of the fuel side transfer tube is shown in Fig. 3.33 an oxidizer side model is shown in Fig. 3.34. Similar models are also available for the current production three duct hot gas manifold design. Table 3.2 shows the relevant parameters of the finite element models for the transfer tube liners.

Similar to transfer tube liners 2-D and 3-D models are available for preburner liner. The 2-D axisymmetric model of the preburner liner is shown in Fig. 3.35. The three dimensional shell model of the preburner liner used for dynamic analysis is shown in Fig. 3.36. Table 3.3 shows the relevant parameters of the finite element models for the preburner liners.



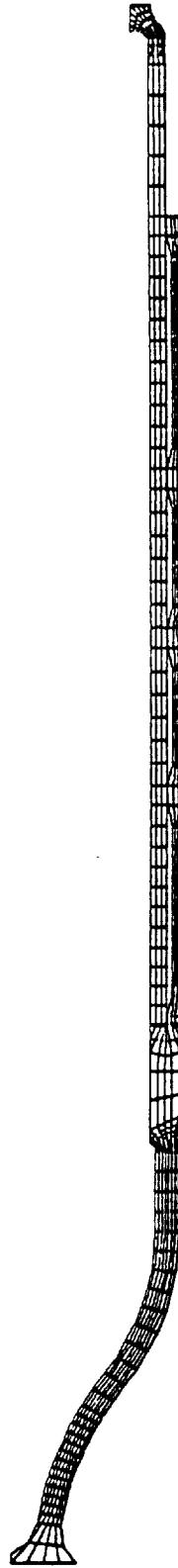


Fig. 3.31 2-D Axisymmetric Model of the Fuel Transfer Tube Liner

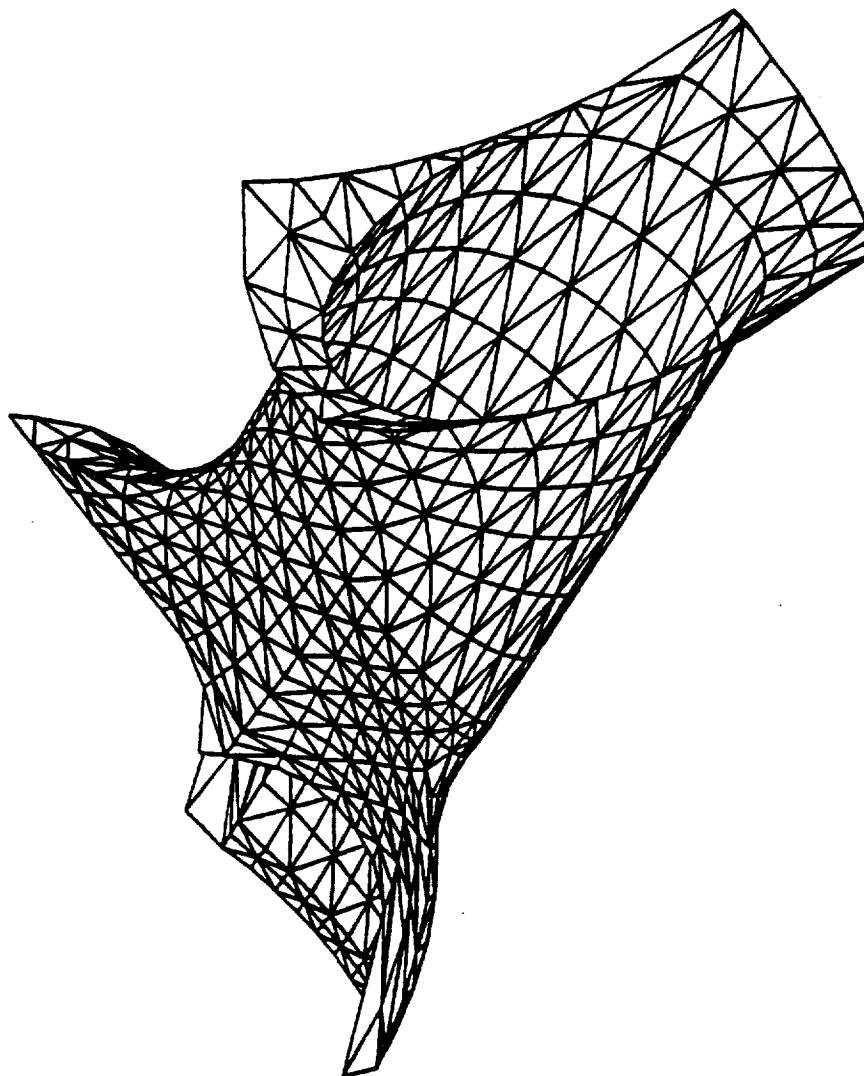


Fig. 3.32 3-D Shell Model of the Fuel Transfer Tube Structural Liner

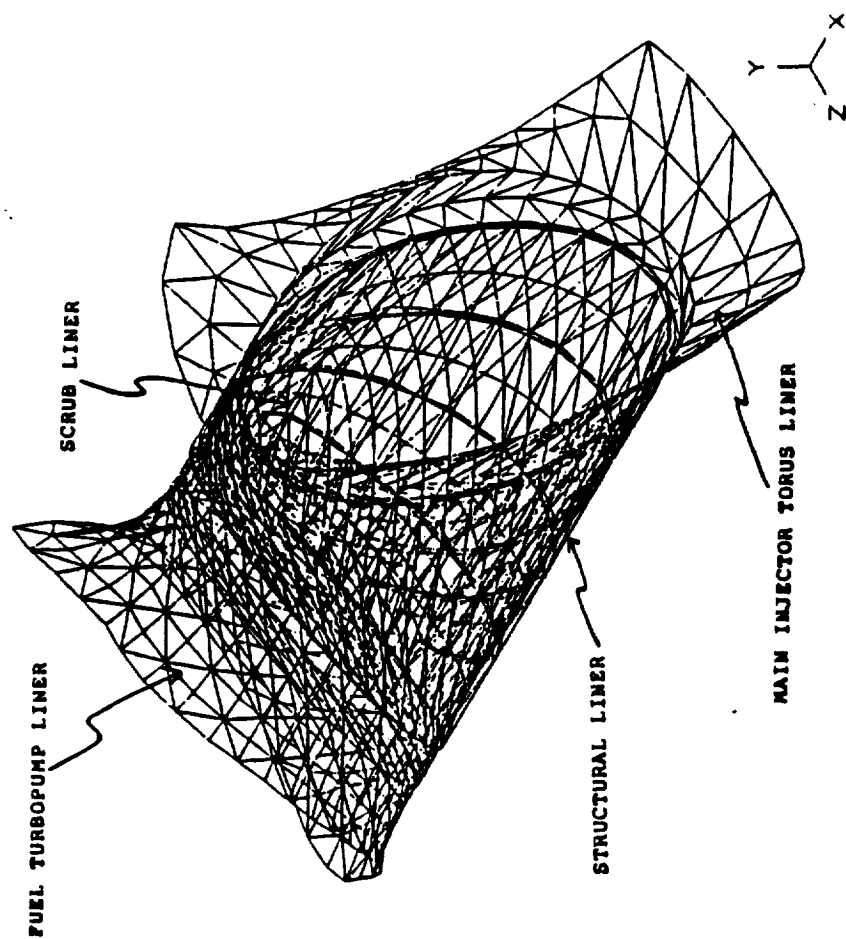


Fig. 3.33 3-D Shell Model of the Fuel Transfer Tube Liner Assembly

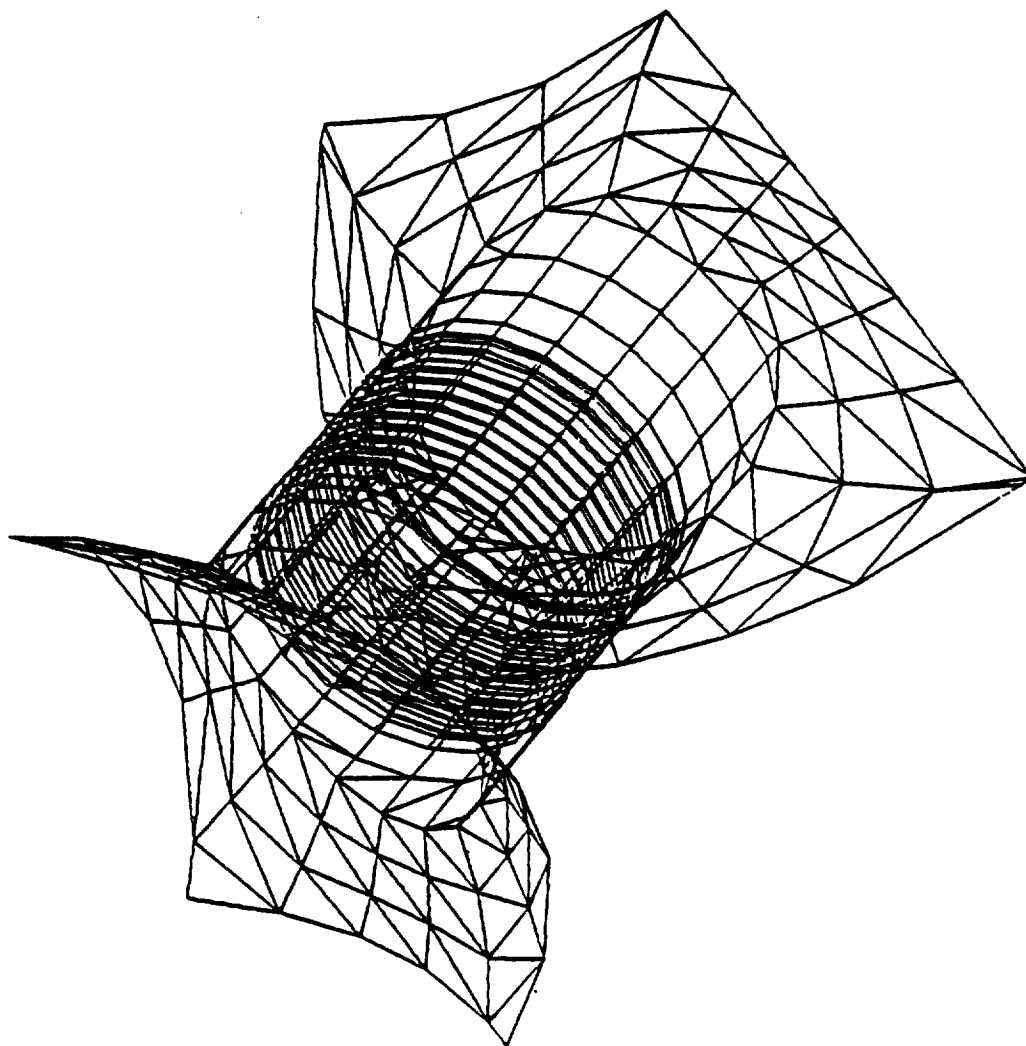


Fig. 3.34 3-D Shell Model of the Oxidizer Transfer Tube Liner Assembly



Fig. 3.35 2-D Axisymmetric Fuel Preburner Finite Element Model

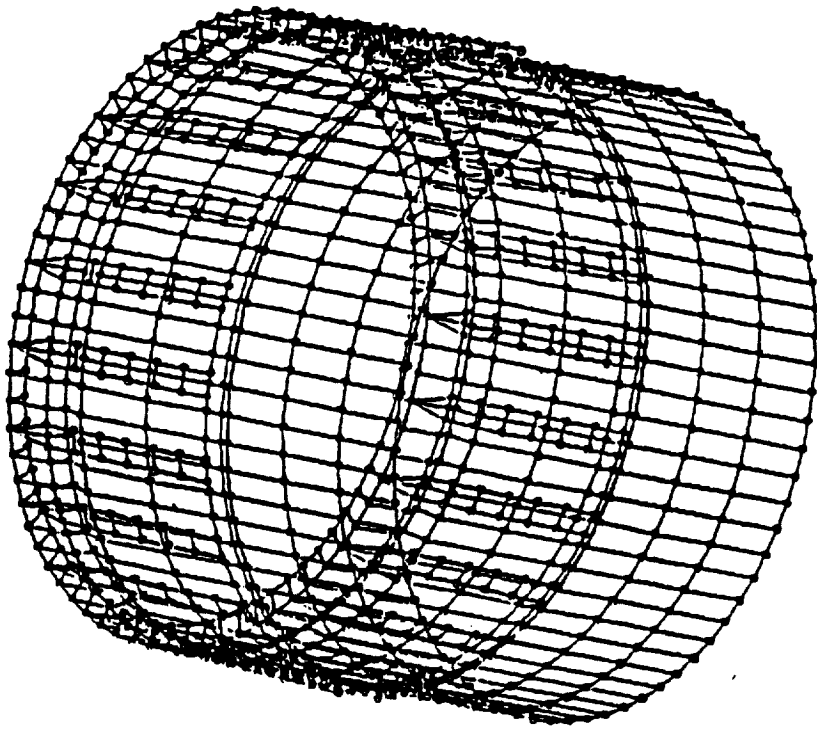


Fig. 3.36 3-D Shell Model of the Fuel Preburner Liner Assembly

TABLE 3.2 FINITE ELEMENT MODEL SURVEY FOR TRANSFER TUBE LINERS

PART	MODEL	SECURITY	ANALYSIS PROGRAM	AVAILABILITY		MODEL COST/STRAIN	FINITE ELEMENT TYPE/NO. OF ELEMENTS		NO. OF DIMENSIONS OF D.O.F.	ANALYSIS TYPE	STATE	TRANSFER	LOAD CYCLES	REASONS FOR ANALYSIS
				INPUT	RESULTS		TYPE	NO.						
	1) MODEL	1) TYPICAL	1) APTSA	1) POINT ONLY	1) PRELIMINARY		1) 3-D BEAM			1) LINEAR - STATIC	1) THERMAL	1) THERMAL		
	2) LOCAL	2) NON-COMMITMENT	2) APTSA	2) POINT ONLY	2) PRELIMINARY		2) 3-D BEAM			2) GEOM. NONLINEAR - STATIC	2) PRESSURE	2) PRESSURE		
	3) SECTION	3) SENSITIVITY	3) APTSA	3) POINT ONLY	3) POST-PROCESS		3) 3-D TRIANGLE			3) GEOM. NONLINEAR - STATIC	3) EXT. LOADS	3) EXT. LOADS		
	4) STIM		4) APTSA	4) POINT ONLY	4) POST-PROCESS		4) 3-D QUAD			4) GEOM. NONLINEAR	4) DYNAMIC	4) DYNAMIC		
							5) SOLID			5) MODAL ANALYSIS				
										6) HARMONIC ANALYSIS				
										7) RANDOM ANALYSIS				
										8) MODAL SUPERPOSITION				
										9) DIRECT TIME INTEGRATION				
FUEL	1	1	1	1, 2	1, 2	0. P.	3	5	613	4	1, 2	1, 2	0	ELCF ANALYSIS
FUEL	1	1	2	1, 2	1, 2	U. V. M.	2	3	1270	2, 2	1, 2	1, 2	1	BUCKLING ANALYSIS
FUEL	1	3	2	1, 2	1, 2	L. M.	2	1, 2, 3	2052	5, 6, 7	3, 4	3, 4	1	THCF ANALYSIS
COOLANT	1	1	3	1, 2	1, 2	E. R.	2	1, 2, 3, 4	846	5, 6, 7	3, 4	3, 4	1	THCF ANALYSIS

**TABLE 3.3 FINITE ELEMENT MODEL SURVEY FOR PREBURNER LINERS**

PART	MODEL	GEOMETRY	ANALYSIS	AVAILABILITY		MODEL	MODEL DETAILS		NO. OF MODELS/NO. OF R.O.F.	ANALYSIS	STATIC	TRANSIENT	LOAD CYCLES	REASONS FOR ANALYSIS
				SHORT	RESULTS		SIZE	TYPE						
	(1) MODEL	(1) TYPICAL	(1) STRESS	(1) PERMANENT FILE	(1) TYPICAL	(1) 2-D	(1) 2-D	(1) 2-D	(1) LINEAR - STATIC	(1) THERMAL	(1) THERMAL	(1) THERMAL	(1) THERMAL	
	(2) LOCAL	(2) LOCAL	(2) STRESS	(2) PERMANENT FILE	(2) PERMANENT FILE	(2) 2-D	(2) 2-D	(2) 2-D	(2) GEOM. NONLINEAR - STATIC	(2) PRESSURE	(2) PRESSURE	(2) PRESSURE	(2) PRESSURE	
	(3) SECTION	(3) SENSITIVITY	(3) STRESS	(3) ON TAPE	(3) ON TAPE	(3) 2-D	(3) 2-D	(3) 2-D	(3) GEOM. NONLINEAR - STATIC	(3) CYCLES	(3) CYCLES	(3) CYCLES	(3) CYCLES	
	(4) STRESS	(4) STRESS	(4) STRESS	(4) CARD DECK ONLY	(4) CARD DECK ONLY	(4) 2-D	(4) 2-D	(4) 2-D	(4) GEOM. NONLINEAR	(4) DYNAMIC	(4) DYNAMIC	(4) DYNAMIC	(4) DYNAMIC	
									(5) MODAL ANALYSIS					
									(6) MODAL ANALYSIS					
									(7) MODAL ANALYSIS					
									(8) MODAL ANALYSIS					
									(9) MODAL ANALYSIS					
									(10) MODAL ANALYSIS					
									(11) MODAL ANALYSIS					
									(12) MODAL ANALYSIS					
									(13) MODAL ANALYSIS					
									(14) MODAL ANALYSIS					
									(15) MODAL ANALYSIS					
									(16) MODAL ANALYSIS					
									(17) MODAL ANALYSIS					
									(18) MODAL ANALYSIS					
									(19) MODAL ANALYSIS					
									(20) MODAL ANALYSIS					
									(21) MODAL ANALYSIS					
									(22) MODAL ANALYSIS					
									(23) MODAL ANALYSIS					
									(24) MODAL ANALYSIS					
									(25) MODAL ANALYSIS					
									(26) MODAL ANALYSIS					
									(27) MODAL ANALYSIS					
									(28) MODAL ANALYSIS					
									(29) MODAL ANALYSIS					
									(30) MODAL ANALYSIS					
									(31) MODAL ANALYSIS					
									(32) MODAL ANALYSIS					
									(33) MODAL ANALYSIS					
									(34) MODAL ANALYSIS					
									(35) MODAL ANALYSIS					
									(36) MODAL ANALYSIS					
									(37) MODAL ANALYSIS					
									(38) MODAL ANALYSIS					
									(39) MODAL ANALYSIS					
									(40) MODAL ANALYSIS					
									(41) MODAL ANALYSIS					
									(42) MODAL ANALYSIS					
									(43) MODAL ANALYSIS					
									(44) MODAL ANALYSIS					
									(45) MODAL ANALYSIS					
									(46) MODAL ANALYSIS					
									(47) MODAL ANALYSIS					
									(48) MODAL ANALYSIS					
									(49) MODAL ANALYSIS					
									(50) MODAL ANALYSIS					
									(51) MODAL ANALYSIS					
									(52) MODAL ANALYSIS					
									(53) MODAL ANALYSIS					
									(54) MODAL ANALYSIS					
									(55) MODAL ANALYSIS					
									(56) MODAL ANALYSIS					
									(57) MODAL ANALYSIS					
									(58) MODAL ANALYSIS					
									(59) MODAL ANALYSIS					
									(60) MODAL ANALYSIS					
									(61) MODAL ANALYSIS					
									(62) MODAL ANALYSIS					
									(63) MODAL ANALYSIS					
									(64) MODAL ANALYSIS					
									(65) MODAL ANALYSIS					
									(66) MODAL ANALYSIS					
									(67) MODAL ANALYSIS					
									(68) MODAL ANALYSIS					
									(69) MODAL ANALYSIS					
									(70) MODAL ANALYSIS					
									(71) MODAL ANALYSIS					
									(72) MODAL ANALYSIS					
									(73) MODAL ANALYSIS					
									(74) MODAL ANALYSIS					
									(75) MODAL ANALYSIS					
									(76) MODAL ANALYSIS					
									(77) MODAL ANALYSIS					
									(78) MODAL ANALYSIS					
									(79) MODAL ANALYSIS					
									(80) MODAL ANALYSIS					
									(81) MODAL ANALYSIS					
									(82) MODAL ANALYSIS					
									(83) MODAL ANALYSIS					
									(84) MODAL ANALYSIS					
									(85) MODAL ANALYSIS					
									(86) MODAL ANALYSIS					
									(87) MODAL ANALYSIS					
									(88) MODAL ANALYSIS					
									(89) MODAL ANALYSIS					
									(90) MODAL ANALYSIS					
									(91) MODAL ANALYSIS					
									(92) MODAL ANALYSIS					
									(93) MODAL ANALYSIS					
									(94) MODAL ANALYSIS					
									(95) MODAL ANALYSIS					
									(96) MODAL ANALYSIS					
									(97) MODAL ANALYSIS					
									(98) MODAL ANALYSIS					
									(99) MODAL ANALYSIS					
									(100) MODAL ANALYSIS					
									(101) MODAL ANALYSIS					
									(102) MODAL ANALYSIS					
									(103) MODAL ANALYSIS					
									(104) MODAL ANALYSIS					
									(105) MODAL ANALYSIS					
									(106) MODAL ANALYSIS					
									(107) MODAL ANALYSIS					
									(108) MODAL ANALYSIS					
									(109) MODAL ANALYSIS					
									(110) MODAL ANALYSIS					
									(111) MODAL ANALYSIS					
									(112) MODAL ANALYSIS					
									(113) MODAL ANALYSIS					
									(114) MODAL ANALYSIS					
									(115) MODAL ANALYSIS					
									(116) MODAL ANALYSIS					
									(117) MODAL ANALYSIS					
									(118) MODAL ANALYSIS					
									(119) MODAL ANALYSIS					
									(120) MODAL ANALYSIS					
									(121) MODAL ANALYSIS					
									(122) MODAL ANALYSIS					
									(123) MODAL ANALYSIS					
									(124) MODAL ANALYSIS					
									(125) MODAL ANALYSIS					
									(126) MODAL ANALYSIS					
									(127) MODAL ANALYSIS					
									(128) MODAL ANALYSIS					
									(129) MODAL ANALYSIS					
									(130) MODAL ANALYSIS					
									(131) MODAL ANALYSIS					
									(132) MODAL ANALYSIS					
									(133) MODAL ANALYSIS					
									(134) MODAL ANALYSIS					
									(135) MODAL ANALYSIS					
									(136) MODAL ANALYSIS					
									(137) MODAL ANALYSIS					
									(138) MODAL ANALYSIS					
									(139) MODAL ANALYSIS					
									(140) MODAL ANALYSIS					
									(141) MODAL ANALYSIS					
									(142) MODAL ANALYSIS					
									(143) MODAL ANALYSIS					
									(144) MODAL ANALYSIS					
									(145) MODAL ANALYSIS					
									(146) MODAL ANALYSIS					
									(147) MODAL ANALYSIS					
									(148) MODAL ANALYSIS					
									(149) MODAL ANALYSIS					
									(150) MODAL ANALYSIS					
									(151) MODAL ANALYSIS					
									(152) MODAL ANALYSIS					
									(153) MODAL ANALYSIS					
									(154) MODAL ANALYSIS					
									(155) MODAL ANALYSIS					
									(156) MODAL ANALYSIS					
									(157) MODAL ANALYSIS					
									(158) MODAL ANALYSIS					
									(159) MODAL ANALYSIS					
									(160) MODAL ANALYSIS					
									(161) MODAL ANALYSIS					
									(162) MODAL ANALYSIS					
									(163) MODAL ANALYSIS					
									(164) MODAL ANALYSIS					
									(165) MODAL ANALYSIS					



## 9. Scoping of Analysis Requirements

### Static Analysis

- 1) Two dimensional and three dimensional material nonlinear analysis.
- 2) Geometric nonlinearities for gap element capabilities.
- 3) Linear eigen value buckling analysis.
- 4). Large deflection plastic buckling analysis of general doubly curved shells.
- 5) Temperature gradient capabilities along the thickness of shell element.

### Dynamic Analysis

- 1) Modal extraction analysis for shell structures.
- 2) Random base excitation analysis
- 3) Random pressure analysis
- 4) Facilities for input for correlation distances of pressures
- 5) Facility to account for nonlinear gap elements

## Section 4

### SSME Ducts and High Pressure Oxidizer Duct

## INTRODUCTION

The SSME fluid component system contains many propellant valves and ducts. The propellant valves are (Figure 4.1):

- 1) Main Fuel Valve
- 2) Main Oxidizer Valve
- 3) OPB (Oxidizer Preburner) Oxidizer Valve
- 4) FPB (Fuel Preburner) Oxidizer Valve
- 5) Chamber Coolant Valve
- 6) Fuel Bleed Valve
- 7) Oxidizer bleed Valve

The major propellant ducts are (Figure 4.2 through 4.10):

- 1) LPFTP (Low Pressure Fuel Turbopump) Turbine Drive Duct
- 2) LPFTP Turbine Discharge Duct
- 3) LPFTP Discharge
- 4) LPOTP (Low Pressure Oxidizer Turbopump) Turbine Drive Duct
- 5) LPOTP Discharge Duct
- 6) HPFTP (High Pressure Fuel Turbopump) Discharge Duct
- 7) HPOTP (High Pressure Oxidizer Turbopump) Discharge Duct
- 8) Preburner Fuel Supply Duct
- 9) Preburner Oxidizer Supply Duct

Figure 4.3 through Figure 4.10 shows the various views of the engine incrementally in a counter clockwise manner. They help in understanding the

(2131e)

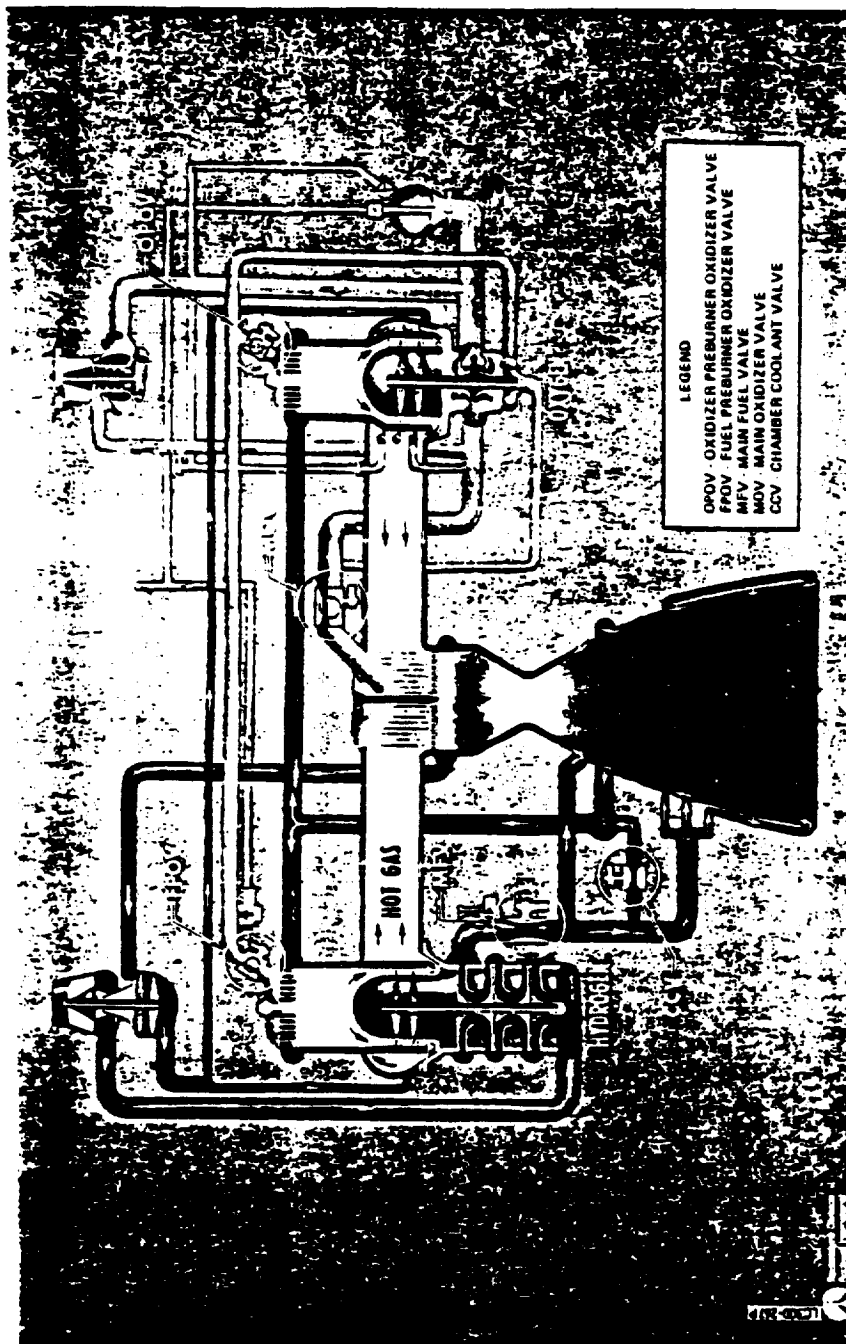


Fig. 4.1 SSME Propellant Flow Schematic

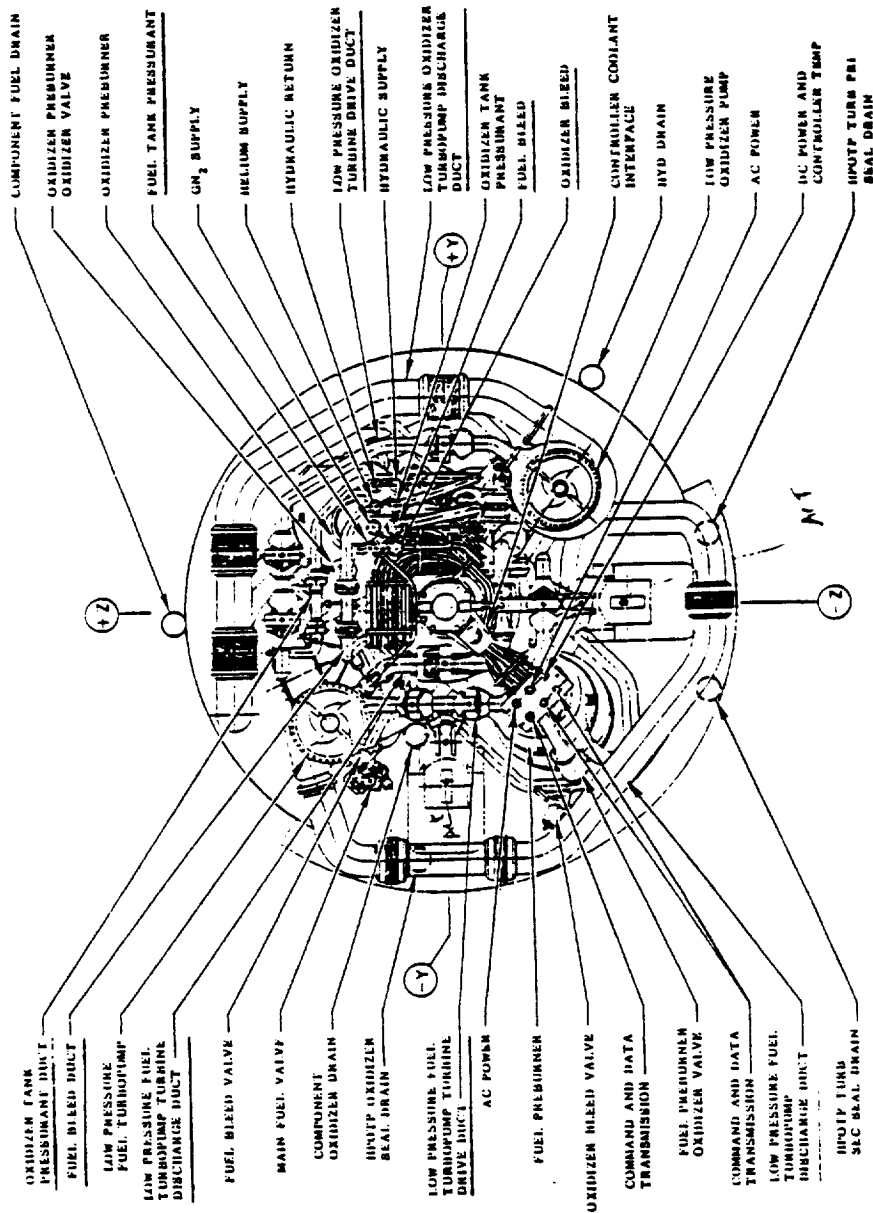


Fig. 4.2 SSME Propellant Ducts



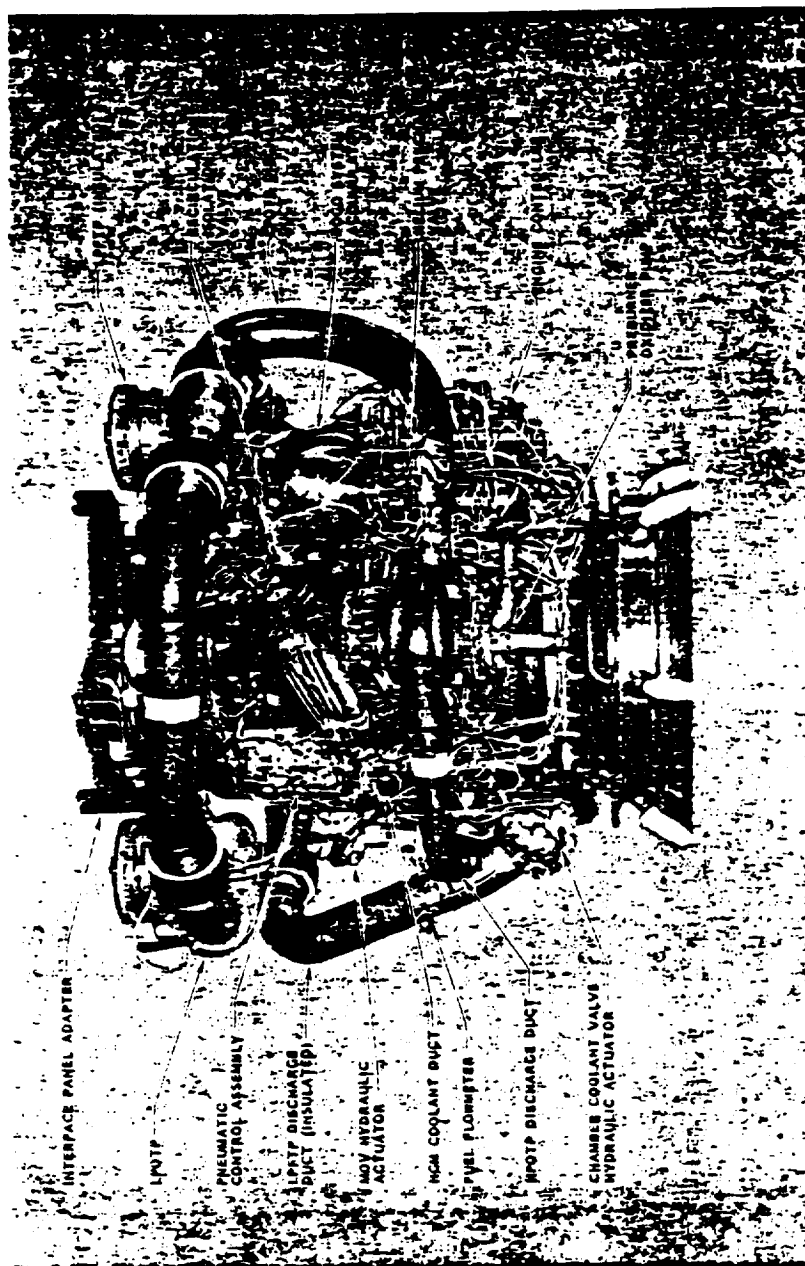


Fig. 4.4 Typical SSME View 2

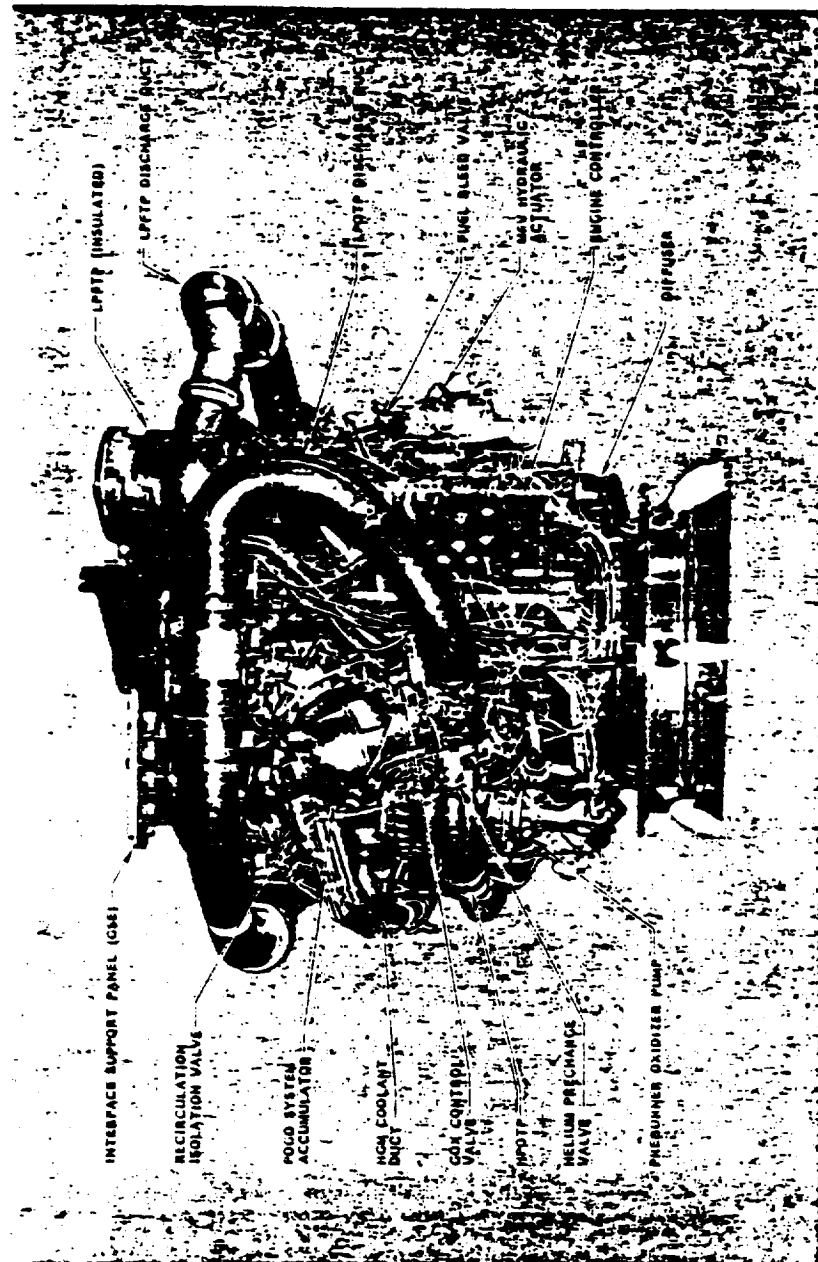


Fig. 4.5 Typical SSME View 3



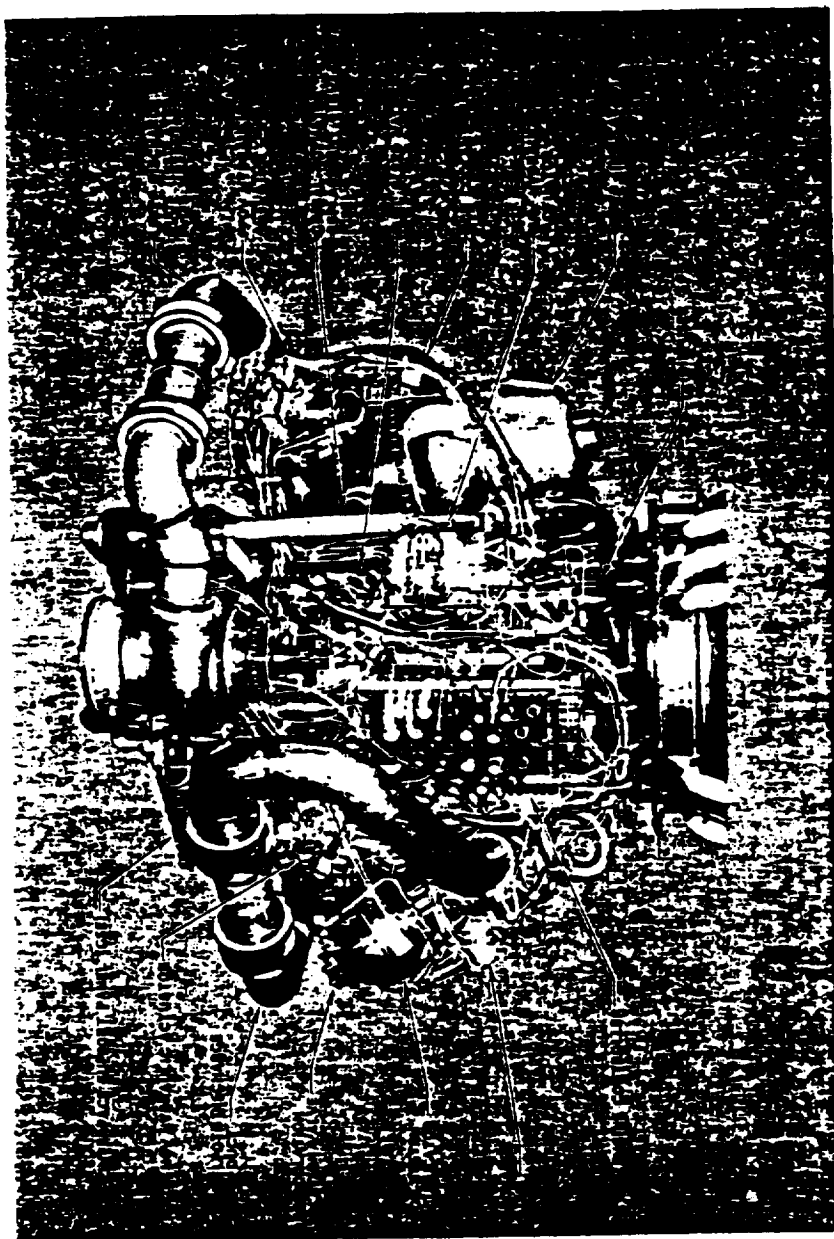


Fig. 4.6 Typical SSME View 4

ORIGINAL PAGE IS  
OF POOR QUALITY



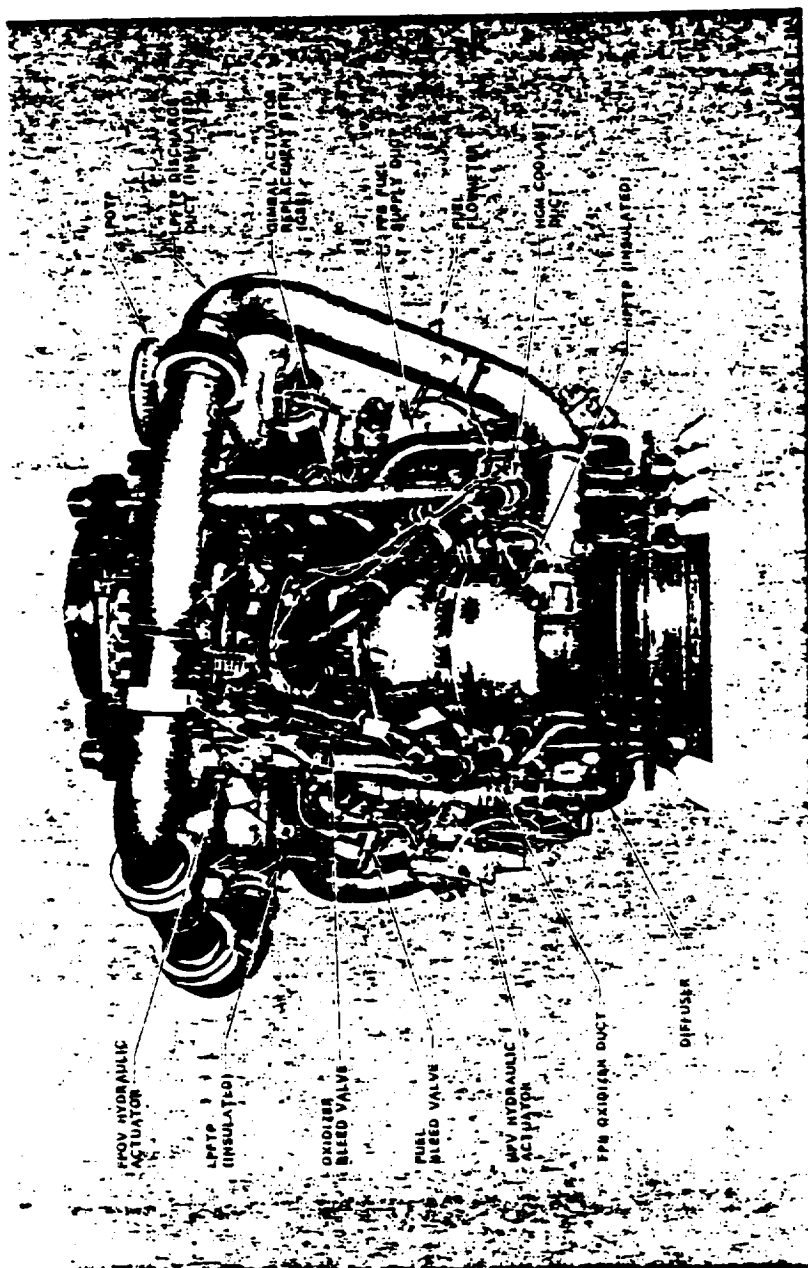


Fig. 4.8 Typical SSME View 6



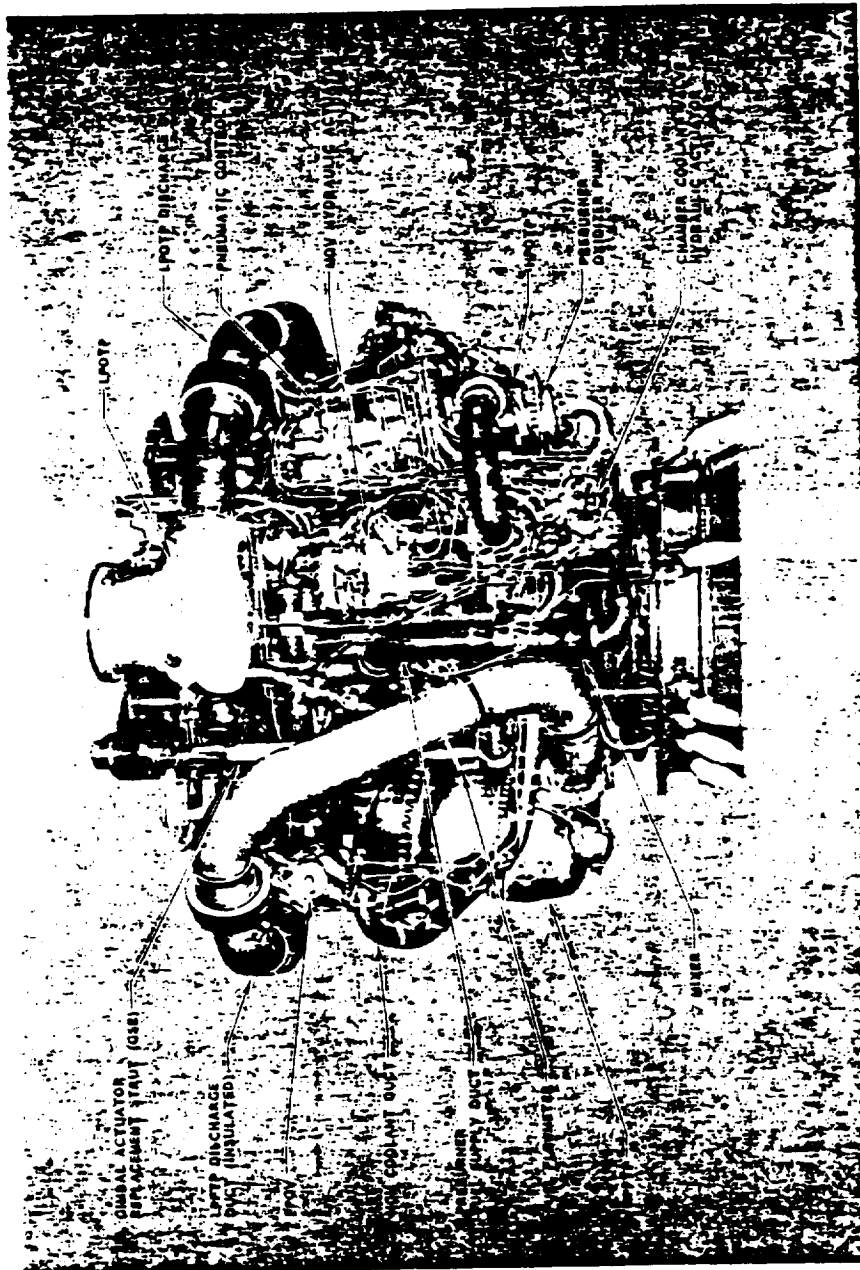


Fig. 4.10 Typical SSME View 8

geometry of the ducts in 3-D space. A more complete line diagram for the flight configuration is shown in Figure 4.11. Classification of the ducts can also be made based on the following (Table 4.1):

- a) Articulating Main Ducts
- b) Fluid interface lines to the orbiter
- c) Component Interconnects

The major difference between articulating ducts, fluid interface ducts and hard lines is that the former lines are flexible to angular and translational deflections. The angular deflections are caused due to gimbaling of the engine. The deflection capability is required by the engine alignment requirement that the engine thrust vector shall be within 30 minutes of arc to the engine center line and laterally within 0.6 inch of the gimbal center. In order to permit conformance with the lateral alignment requirement, an adjustment capability of  $\pm 0.50$  inch was designed into the gimbal bearing thrust chamber interface. The design should also be capable of absorbing torsional deflections caused by gimbal bearing torsional flexibility and Hooke's joint effect.

Articulating metal-bellows flex joints are used in main propellant ducts that cross the gimbal plane and are capable of accommodating engine gimbaling motions. These ducts service the vehicle-mounted low pressure turbopumps and are configured to wrap around the main gimbal bearing thrust axis. This can be visualized by following a typical duct through Figure 4.3 through Figure 4.10 as one goes around the engine.

The articulating lines used as fluid interface lines are similar to the main propellant ducts with wrap around configuration, but smaller in diameter. The term wrap around derives from the line centerline geometry that wraps around the engine gimbal assembly.

Flexible hoses are used for small diameter vehicle to engine lines such as hydraulic supply.

(2131e)

Figure 4.11 Flight Configuration  
Original Mailed to NASA Program Manager

TABLE 4.1 SUMMARY OF INTERCONNECTS

ARTICULATING MAIN PROPELLANTS	FLUID INTERFACE LINES	COMPONENT INTERCONNECTS
LPFTP PUMP DISCHARGE	<u>ARTICULATING</u>	<u>HARD LINES</u>
LPFTP TURBINE DRIVE		
LPFTP TURBINE DISCHARGE	FUEL BLEED	HPFTP DISCHARGE
LPOTP PUMP DISCHARGE	OXIDIZER BLEED	PREBURNER FUEL SUPPLY
LPOTP TURBINE DRIVE	OXIDIZER TANK PRESSURANT	HPOTP DISCHARGE
		PREBURNER OXIDIZER SUPPLY
	<u>FLEX HOSES</u>	HEAT EXCHANGER SUPPLY
	HYDRAULIC SUPPLY	HGM COOLANT DUCT
	HYDRAULIC RETURN	PREBURNER PUMP SUPPLY
	ENGINE GASEOUS NITROGEN	
	SUPPLY	<u>FLEX HOSES</u>
	ENGINE HELIUM SUPPLY	PNEUMATIC SHUTDOWN CONTROL
		FUEL PUMP LIFTOFF SEAL
		CONTROL
	<u>HARD LINES</u>	
	FUEL TANK PRESSURANT	



Hard lines are defined as lines with no flex joints. They are used for non-gimbaling applications which connect to the fluid interface panel and for all non-gimbaling engine component interconnections.

Bolted flange joints with static seals are used throughout the engine for connecting ducts and components. Separable static seal joints are necessary for servicing and maintenance of the engine. The deflection loaded, pressure assisted Naflex-type static seal concept is used for static seal joints within component assemblies and at the interconnection of components.

The high pressure oxidizer duct (HPOD) supplies high pressure oxidizer to the main combustion chamber injector dome which initiates ignition of the hydrogen rich gases in the main combustion chamber and also provides oxidizer to support combustion in the main combustion chamber. The duct receives pressurized oxidizer from the HPOTP main discharge and routes it through the main oxidizer valve which regulates the LOX flow into the main combustion chamber injector dome. Oxidizer is also tapped from this duct and delivered to the preburner boost pump which further boosts the pressure for use in the two preburners.

#### GENERAL DESIGN CONSIDERATIONS

The principal design consideration controlling the design configuration of the ducts are:

- 1) Accommodation of engine gimbaling deflections
- 2) Meeting low cycle fatigue criterion as applied to engine gimbaling cycle
- 3) Meeting high cycle fatigue criterion as applied to engine vibration environment

(2131e)

- 4) Separation of bellows mechanical and flow induced excitation vibration frequencies
- 5) Accommodation of thermal deflections, misalignments, installation adjustments and operational deflections
- 6) Accommodation by bellows of each specific joint angle resulting from engine gimbaling deflections
- 7) Withstanding operational fluid pressures and temperatures initially estimated by engine balance, scaled values from other engine experience and then subsequently based on actual engine experience
- 8) Additional design requirements on bellows for buckling (squirming) for high pressure lines.
- 9) Use of flow sleeves or liners on articulating lines to prevent coupling of natural and flow vibration frequencies

For high pressure oxidizer duct which is a hard line design considerations involving gimbaling and flex joints do not apply.

#### MATERIAL CONSIDERATIONS

The material selection of the ducting is based on number of factors including environment, strength, and fatigue properties (Table 4.2). High strength alloys which have favorable weight to strength ratios are invariably used. The duct environment can include:

(2131e)

TABLE 4.2 SUMMARY OF MAJOR PROPELLANT DUCTS

DESCRIPTION	HARD OR FLEXOR BASE	FPL (MAX) DOES NOT INCL. SURGE		I.D.	THICKNESS RANGE	MATERIAL	ELBOW		
		PSI PRESSURE	TEMPERATURE				TYPICAL RADIUS	MAX. ANGLE	THICKNESS
<u>HYDROGEN</u>									
1) LOW PRESSURE FUEL PUMP DISCHARGE	FLEX	311 (343)	45	5.20	28/.150	INCO 718 ALLOY 21-6-9	TO 6+13	90°	.026/.063
2) LOW PRESSURE FUEL PUMP TURBO DRIVE	FLEX	5307	472	2.00	.118/.270	INCO 903 TI 6-6-2	2.80/6.00	90°	.118/.166
3) LOW PRESSURE FUEL PUMP TURBINE DISCHARGE	FLEX	3871	457	2.70	.096/.274	INCO 903 TI 6-6-2	6.80	90°	.095/.170
4) HIGH PRESSURE FUEL PUMP DISCHARGE	RIGID	7221	110	3.40	.131/.203	TI 5.25	4.00	90°	.131/.203
5) PREBURNER FUEL SUPPLY	RIGID	6437	289	2.00 ↓ 3.60	.089 ↓ .192	INCO 903	2.50 ↓ 6.00	50°	.089 ↓ .193
6) HOT GAS MANIFOLD COOLANT DUCT	RIGID	3784	457	2.30 ↓ 2.70	.069 ↓ .155	INCO 903	4+6	95°	.071 ↓ .110
7) FUEL BLEED	FLEX & RIGID	300	110	1.245	.060	ALLOY 21-6-9	1.50/2.50	90°	.040/.060
8) FUEL TANK PRESSURANT	RIGID	3871	457	.560	.0855	ALLOY 21-6-9	2 .50	90°	.077/.096

A

TABLE 4.2 SUMMARY OF MAJOR PROPELLANT DUCTS

DESCRIPTION	HARD OR FLEX	FPL (MAX)		I. D.	THICKNESS RANGE	MATERIAL	ELBOW		
		PSI PRESSURE	°R TEMPERATURE				RADIUS	MAX. ANGLE	THICKNESS
OXIDIZER									
1) LOW PRESSURE OXIDIZER PUMP DISCHARGE	FLEX	554 (695)	178	6.30	.032+.160	INCO 718	12.00	90°	.032+.160
2) LOW PRESSURE OXIDIZER PUMP TURBINE DRIVE	FLEX	4902	205	2.30	.090+.287	INCO 718 11 6-6-2	3.50	90°	.086+.180
3) HIGH PRESSURE OXIDIZER PUMP DISCHARGE	RIGID	4902	205	-4.000	104+.270	INCO 718	4.50	90°	.104+.127
4) PREBURNER PUMP OXIDIZER	RIGID	4801	205	2.3	.084+.120	INCO 718	2.75	90°	.084+.134
5) HEAT OXIDIZER SUPPLY	RIGID	4770	205	.555	.026+.075	INCO 718 INCO 628	2.00	90°	.026+.035
6) OXIDIZER BLEED	RIGID	230	554	.68	.030+.063	CRES 321 INCO 718	2.25	MOCK-UP	.026+.030
7) OXIDIZER TANK PRESSURANT	FLEX & RIGID DUCTS	4460	990	1.00	.138+.285	INCO 718	3.50	90°	.142+.172
8) PREBURNER OXIDIZER SUPPLY	RIGID	8309	221	1.982 1.097	.096+.205	INCO 718 INCO 675	4.50	90°	.101+.209

- 1) Gaseous Hydrogen
- 2) Liquid Hydrogen
- 3) Hydrogen Rich Combustion Products
- 4) Liquid Oxygen
- 5) Gaseous Oxygen

Since hydrogen embrittlement is a consideration for hydrogen lines, Inconel 903 is used extensively in fuel lines. Where the temperature is cryogenic, ARMCO 21-6-9 is also used for fuel lines. ARMCO 21-6-9 material exhibit superior strength properties at cryogenic temperature, when compared to its room temperature properties. In the case of LOX Systems, Titanium is never used where it can be expected to LOX. Bellows are normally made out of Inconel 718 or 903 material. The high pressure oxidizer duct is made of INCO 718.

#### GEOMETRICAL CONSIDERATIONS

The geometrical definition of the diameter of the lines is based engine flow requirements. However, the actual line routing is controlled by the following factors:

##### Flex Lines:

- 1) Bellows are positioned 90 degree apart lying on gimbaling axis to reduce angulation at bellows.
- 2) At least three bellows are needed to accommodate general gimbaling motion.

(2131e)

#### Hard And Flex Lines:

- 3) Flexibility requirements of the duct might dictate additional elbows.
- 4) The line should meet the engine enveloping requirements.

These considerations result in the typical wrap around geometry of the lines (Figure 4.3 through Figure 4.10).

In general thickness of tube changes spatially due to strength and manufacturing requirements. While individual parts may be heat treated, assemblies that have flex joints are not heat treated. This is because the assemblies contain different materials and the bearing surfaces on the flex joints have dry lubrication. The "as welded" condition at welded joints dictate the use of larger thicknesses at weld joints. In addition, the elbows are formed resulting in thinner section at the extrados of the elbow. Sometimes, variable thickness transition pieces are also used to connect elbow to straight sections.

The liquid hydrogen fuel lines have insulation since they are sensitive to a rise in temperature. The insulation covers the entire line including flanges and bellows. A typical insulation of the duct is shown in Figure 4.12 and 4.13. It comprises of polyurethane foam enclosed in a nickel plate shell. The joints are sealed to be leak proof. This is necessary to prevent air from entering into insulation space. Trapped air will liquefy under cryogenic temperatures. At engine shutdown, the trapped liquid air will become gas and exert high pressures on the structural duct due to insufficient escape passage. Instances of such buckling have occurred in LPFTP discharge duct. A typical insulation at the flange is shown in Figure 4.14. Double annular bellows are used for flex fuel lines with a vacuum in between the bellows. A burst diaphragm is used in the insulated bellows to allow for escape of vapor

(2131e)

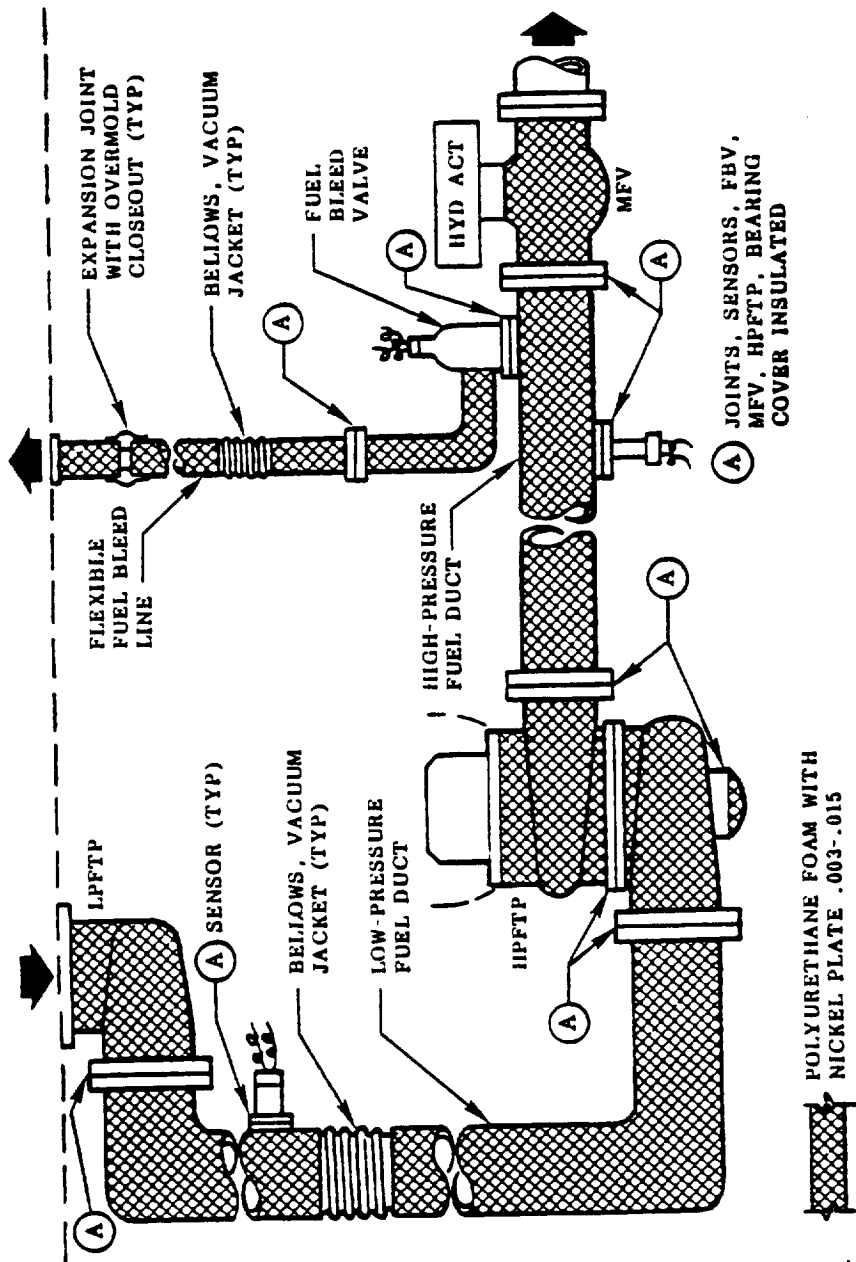


Fig. 4.12 Fuel System Insulation

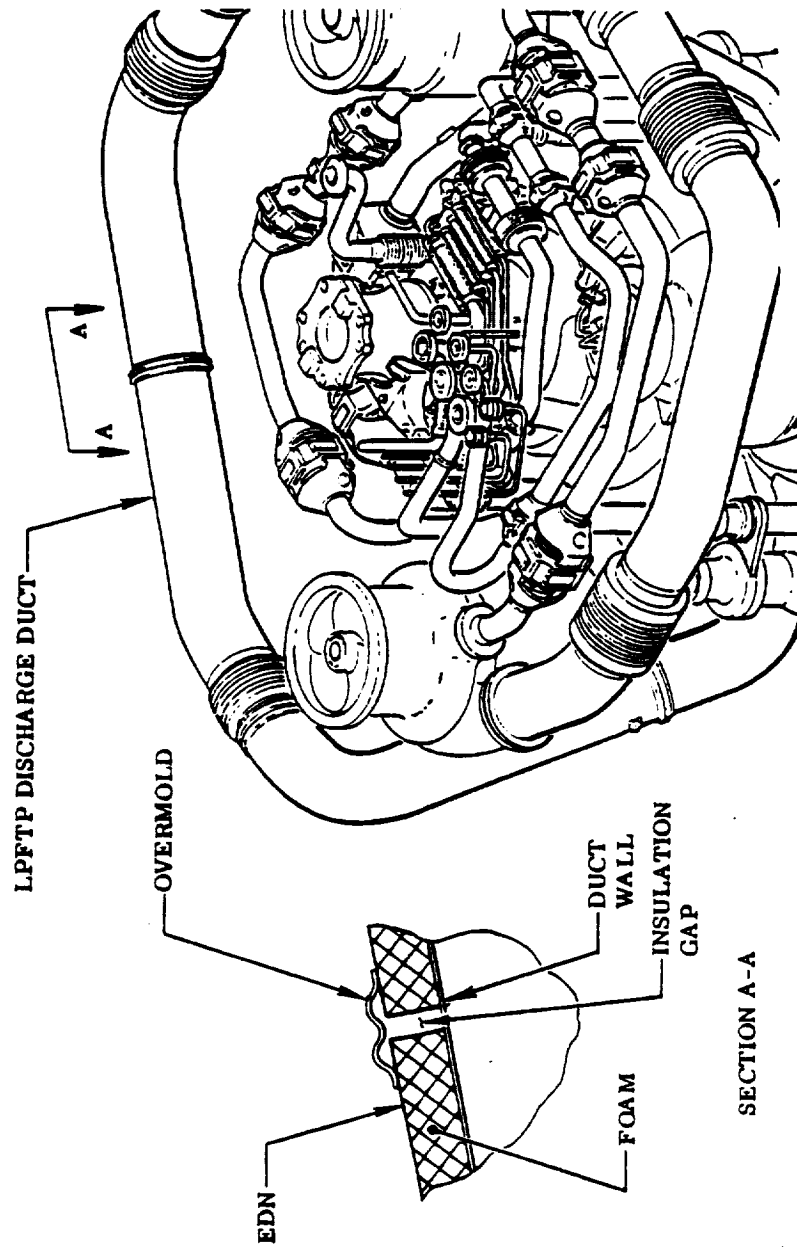


Fig. 4.13 Typical Duct Insulation



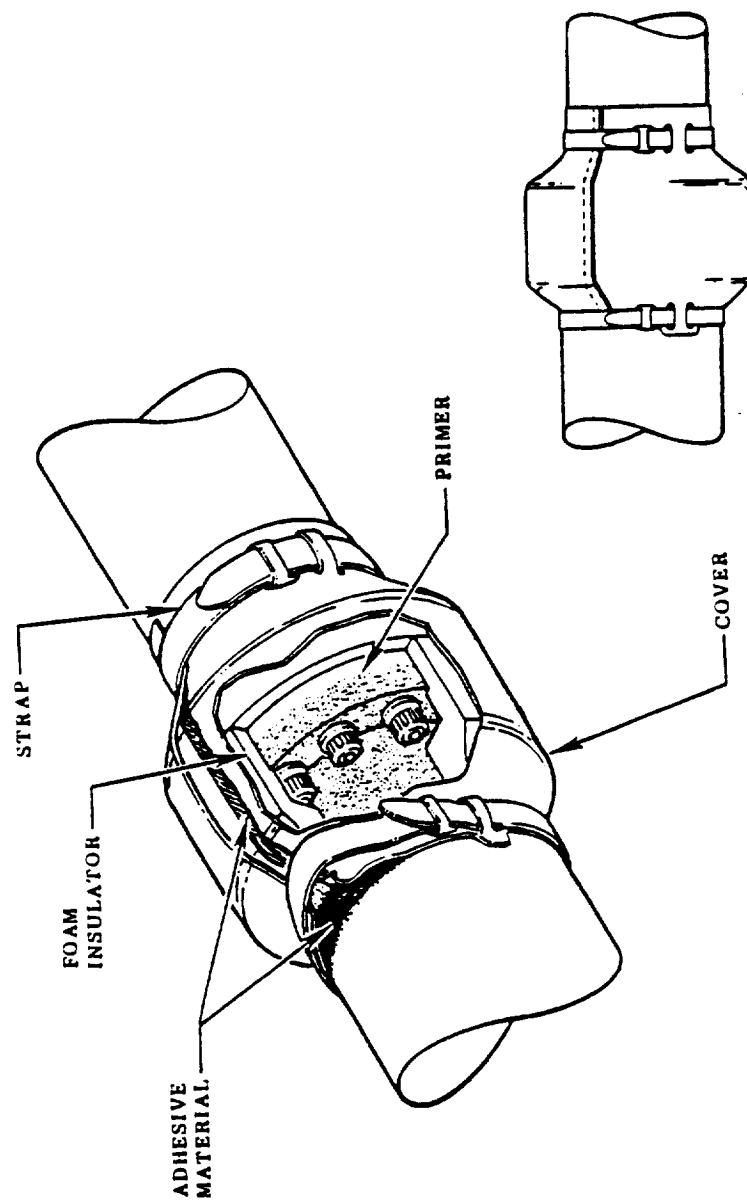


Fig. 4.14 Typical Joint Insulation

in the event of a vacuum jacket leak. The insulation affects the structural analysis in the sense that their weight is considered in the analysis. They have negligible structural strength contribution to the duct.

The location of the high pressure oxidizer duct relative to the engine is shown in Figure 4.15. Notable features of the geometry are the several 90° elbows, tap off for the preburner boost pump, ports and stops used for flow measurement (flow meter), the block for mounting ultrasonic flow measurement devices (Figure 4.16). Geometry of the HPOD has evolved based on engine experiences. Early designs of HPOD contained flow meters but the measurement attempts were unsuccessful. Thus the flow meters were removed but the ports were left intact for possible future uses. Measurement of LOX flow using ultrasonic devices mounted on blocks were attempted (Figure 4.16) on development of engines. The brazed blocks were sources of stress riser resulting in failure of duct. Thus the current HPOD's do not contain flow meter ports or blocks. However, future designs might contain integrally mechanized blocks (avoiding brazed joints) for ultrasonic measurement.

#### BELLOWS GEOMETRY

Two types of bellows configurations are used in articulating main propellant ducts. They are:

- 1) The external double shear pin gimbal ring.
- 2) The internal tripod, ball and socket.

Typical flex bellow applications are illustrated in Figure 4.17. A summary of typical SSME Bellows application is presented in Table 4.3. The external gimbal ring is used in all high pressure articulating lines under 3.25 inches I.D.. The larger diameter pump discharge lines use the internal ball and

(2131e)

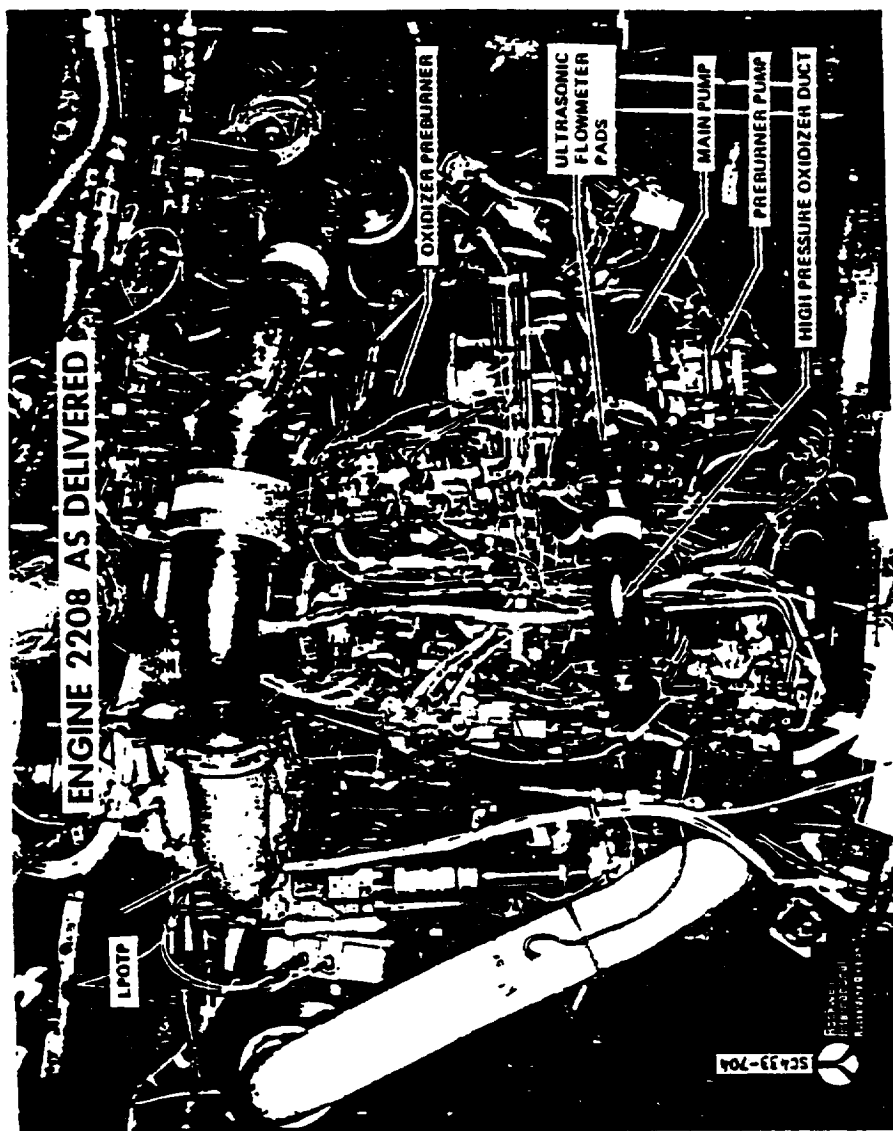


Fig. 4.15 HP0D Location Relative to the Engine

ORIGINAL PAGE IS  
OF POOR QUALITY

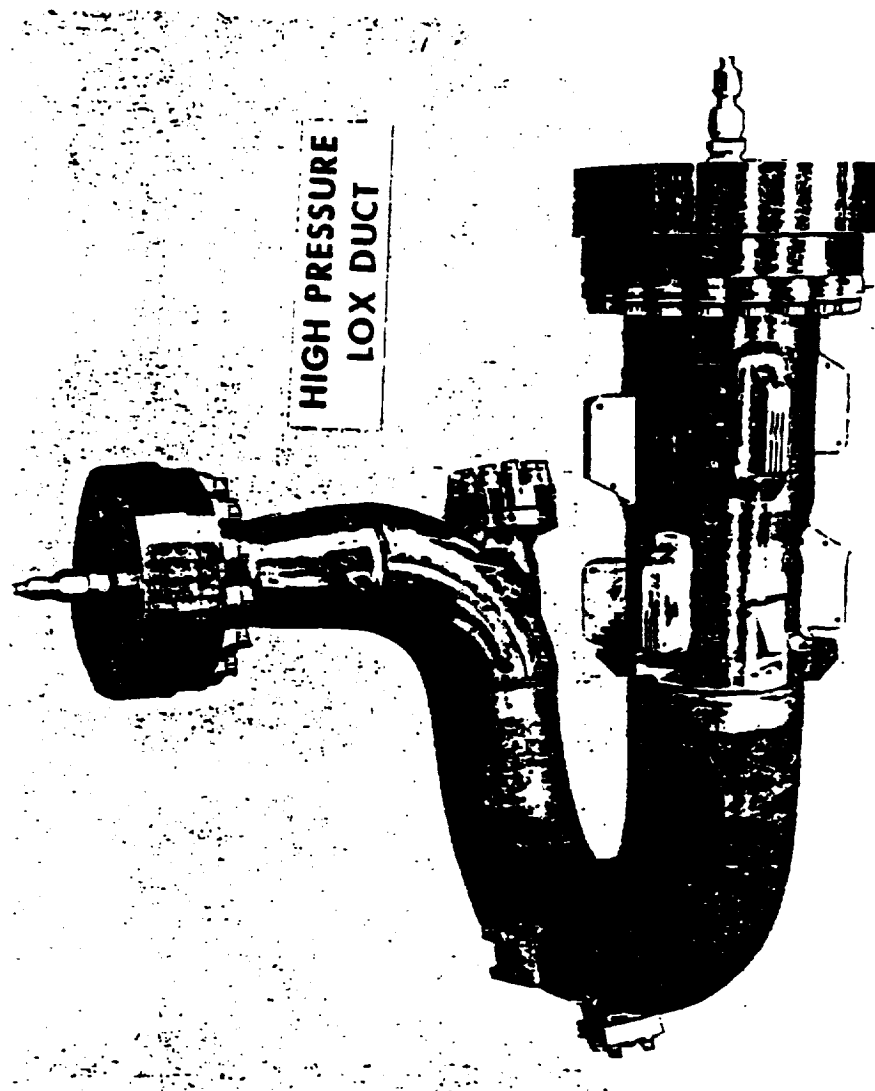


Fig. 4.16 High Pressure Oxidizer Discharge Duct

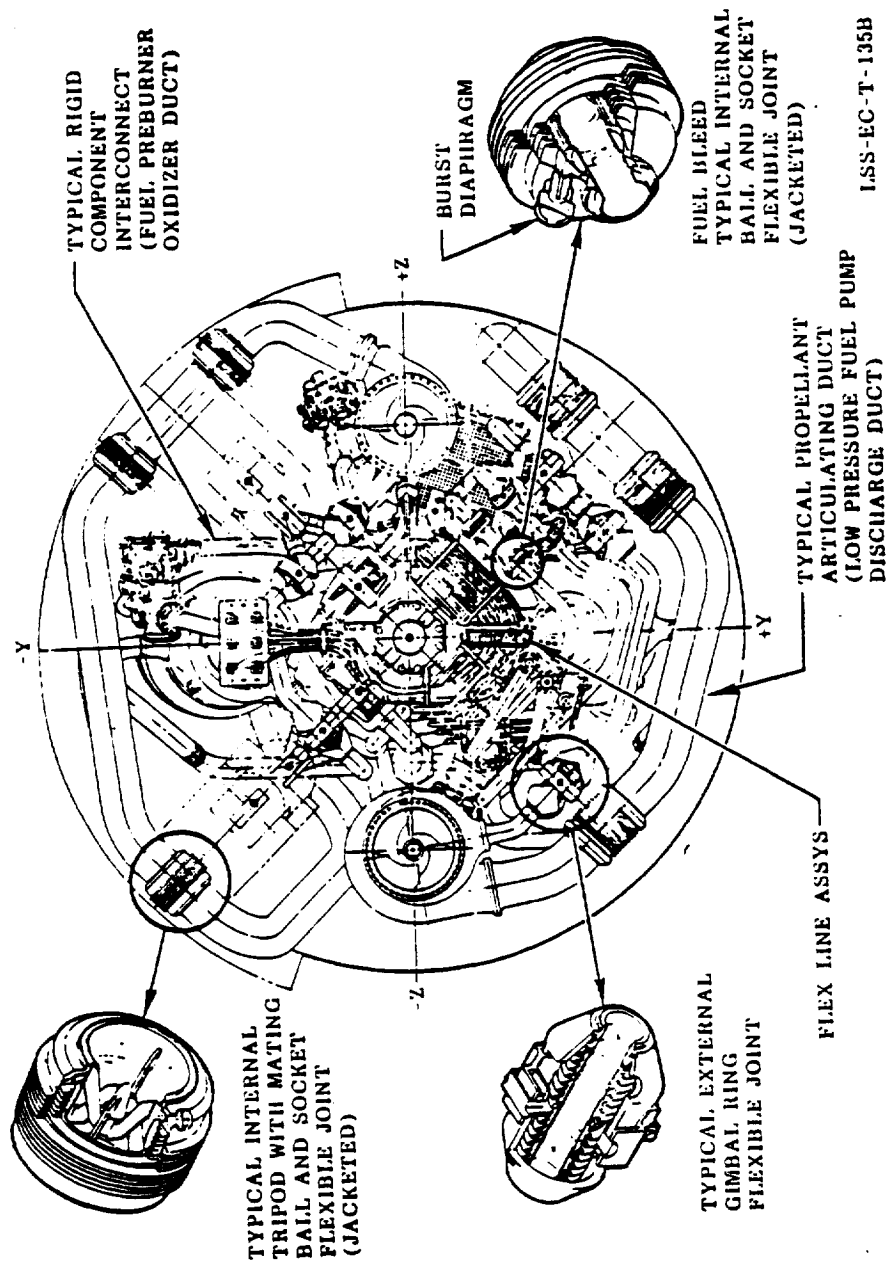


Fig. 4.17 Typical Flex Bellows Application

TABLE 4.3 SSME BELLOWS APPLICATION

DUCT OR LINE DESCRIPTION	FLUID CONTAINED	TYPE OF JOINT
LOW PRESS. OXID PUMP DISCHARGE	LIQUID OXYGEN	INTERNAL BALL AND SOCKET
LOW PRESS. OXID PUMP TURB DISCHARGE	LIQUID OXYGEN	EXTERNAL GIMBAL RING
OXID. TANK PRESS.	GASEOUS OXYGEN	EXTERNAL GIMBAL RING
LOW PRESS. FUEL PUMP DISCHARGE	LIQUID HYDROGEN	INTERNAL BALL AND SOCKET
LOW PRESS. FUEL PUMP TURB DRIVE	GASEOUS HYDROGEN	EXTERNAL GIMBAL RING
LOW PRESS. FUEL PUMP TURB DISCH.	GASEOUS HYDROGEN	EXTERNAL GIMBAL RING
FUEL RECIRCULATION	LIQUID HYDROGEN	INTERNAL BALL AND SOCKET

(2133e)

socket on a tripod mount, and the fuel bleed line uses a flow through ball and socket linkage. Exploded views of typical bellows are presented in Figure 4.18 through Figure 4.21.

While a detailed coverage of the design aspects of the bellows is beyond the scope of this overview, the following considerations are used in arriving at an acceptable design.

- 1) All flex joints used in the wrap around lines have sleeves or liners in the internal diameter. The sleeves serve two purposes. a) reduce pressure loss and b) avoidance of flow induced pressure vibration. The possibility of high frequency pressure vibration is great when relatively stiff, high pressure bellows with high flow velocities are involved.
- 2) Double bellows with vacuum in the annular space is used for cryogenic temperature fuel lines.
- 3) The length of bellows and tension restraint linkage for each joint is designed specifically for its operational deflection cycle.
- 4) Initially curved bellows go through a change in shape of centerlines as the result of application of internal pressure resulting in increased bending stress. This effect is significant in lines which operate under high pressure.
- 5) The designed bellow satisfies the following requirements:
  - a) Predictable low cycle and high cycle fatigue life.

(2131e)

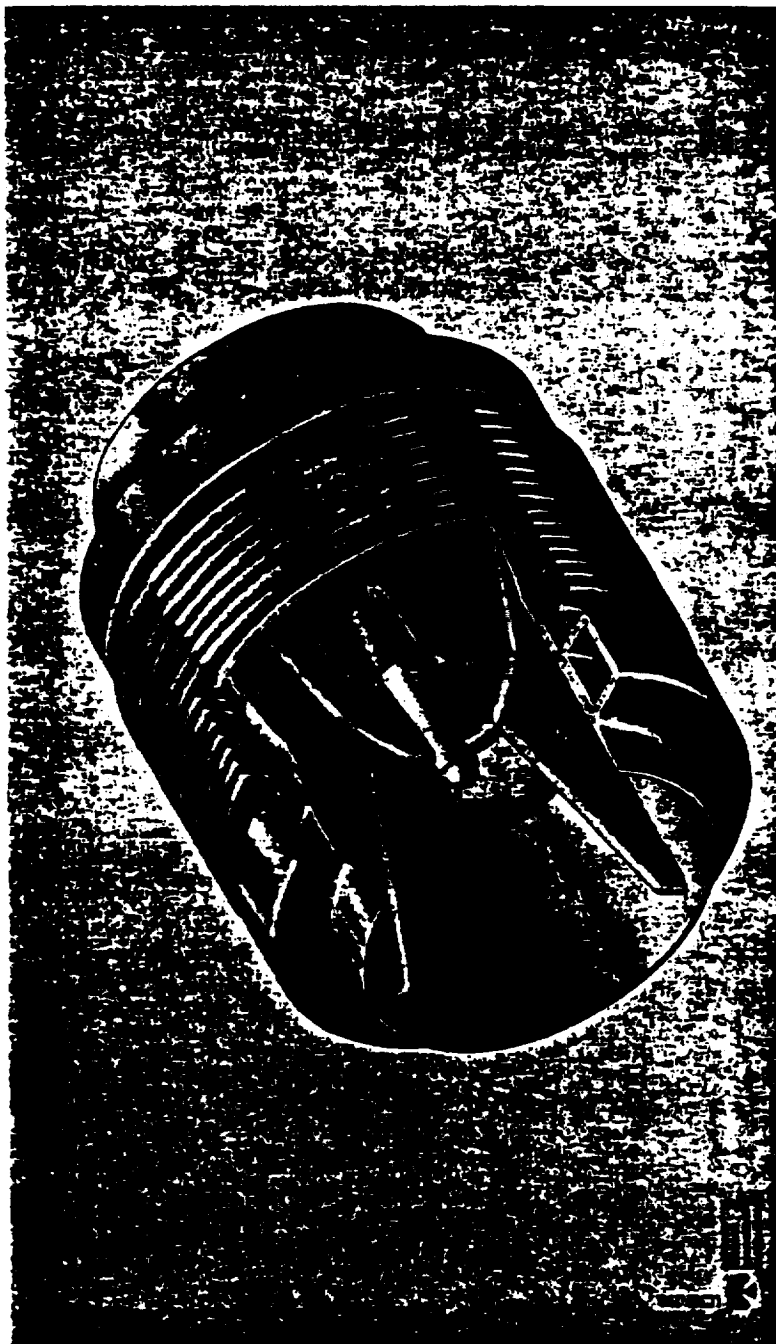


Fig. 4.18 LP0TP Discharge Flex Joint (Internal Tripod)



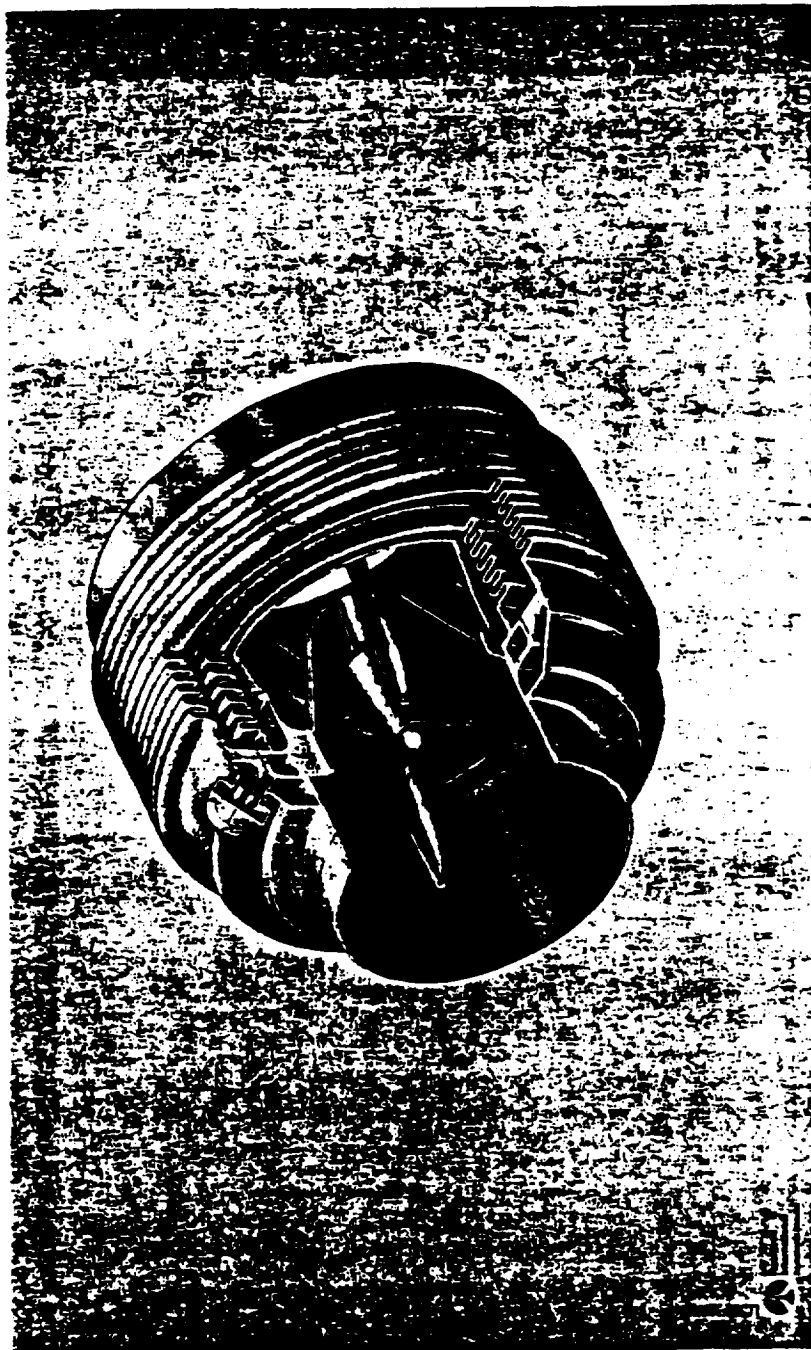


Fig. 4.19 LPFTP Discharge Flex Joint (Internal Tripod with Insulating Jacket)

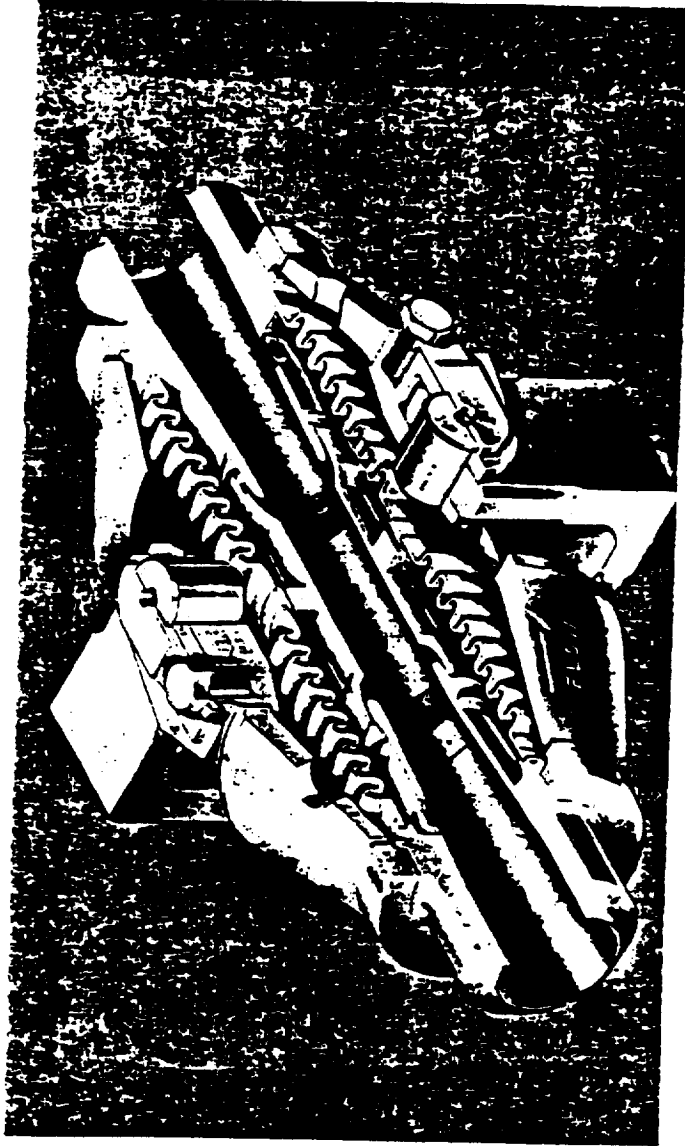


Fig. 4.20 Oxidizer Tank Pressurization Duct Flex Joint (External Gimbal Ring)

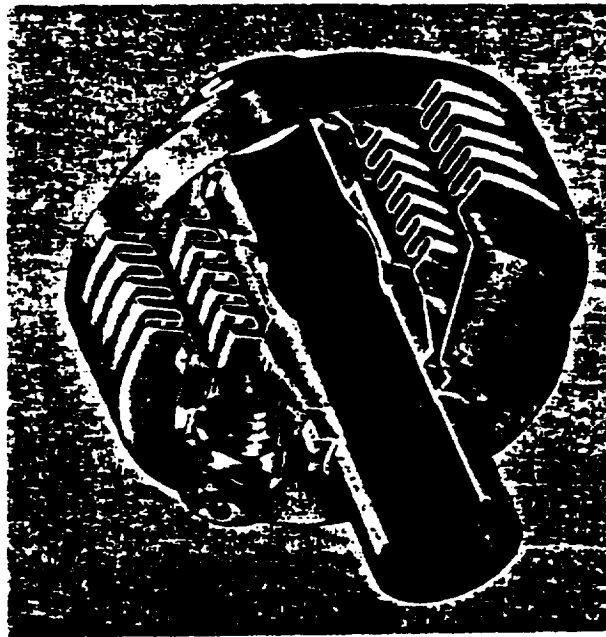


Fig. 4.21 Fuel Bleed Line Flex Joint (Internal Ball Joint with Insulating Jacket)

- b) Predictable spring rate
- c) Buckling stability
- d) Small pressure drop
- e) Predictable response to vibration input.

#### LOADING ENVIRONMENT

The static loads considered in the duct analysis are:

- 1) Internal Pressure
- 2) Misalignment, thermal and gimbal displacement
- 3) Flow momentum loads
- 4) Acceleration loads
  - a) Vehicle Acceleration
  - b) Gimbal Acceleration

The above loads occur during engine steady state operation but is assumed to occur during the entire mission history profile at constant magnitudes for analysis purposes. It should be noted that steady state loads dictate the design. Transient loads are considered but have lesser impact on the design.

#### STATIC PRESSURES

The steady state pressures in the ducts are initially obtained from engine balance and subsequently refined from hot fire engine tests. Table 4.2 illustrates the typical design pressures for major propellant ducts in SSME.

(2131e)

During shutdown, the ducts experience a surge in pressure. This effect is more pronounced on the oxidizer side of the engine system. The surge pressures do not impact the high pressure ducts as much as the low pressure ducts. A typical cutoff transient of the LPOTP shaft speed is illustrated in Figure 4.22, where the power up of the pump at cutoff sequence must be noted. Corresponding typical pressure transients at cutoff are shown in Figure 4.23 for low pressure oxidizer discharge duct. Normally two pressure surge peaks are seen after the cutoff command. The first peak (Fig. 4.23) occurs at approximately cutoff plus 0.3 seconds. The magnitude of this surge is controlled by the system power down. Magnitude of this surge is proportional to cutoff power level. The second peak occurs at approximately cutoff plus 2.0 seconds. This is driven by the main oxidizer valve schedule. The magnitude of this pressure surge is inversely proportional to the cutoff power level. The magnitude of the pressure surge, is related to minimum pressure prior to power up, the lower the dip, the higher the surge. This surge pressure which is a significant percentage of LPOTP discharge duct is accounted for in the analysis (Table 4.2). The surge phenomenon is also observed in high pressure ducts such as HPOD. However, the surge pressure occurs at a reduced power level and hence total pressure is less than the maximum pressures the ducts experience at steady state (Figure 4.24).

#### THERMAL LOADS

The ducts primarily experience two types of temperature loading 1) Steady state temperature and 2) engine prechill condition temperature. The steady state temperatures are listed in Table 4.2 and is assumed to be uniform across the wall thickness. Engine prechill condition occurs when the pre valves located in the orbiter above the low pressure turbopump are opened approximately one hour prior to firing. On opening of the pre valves, the propellants flow through the low pressure turbopumps, and through the high

(2131e)

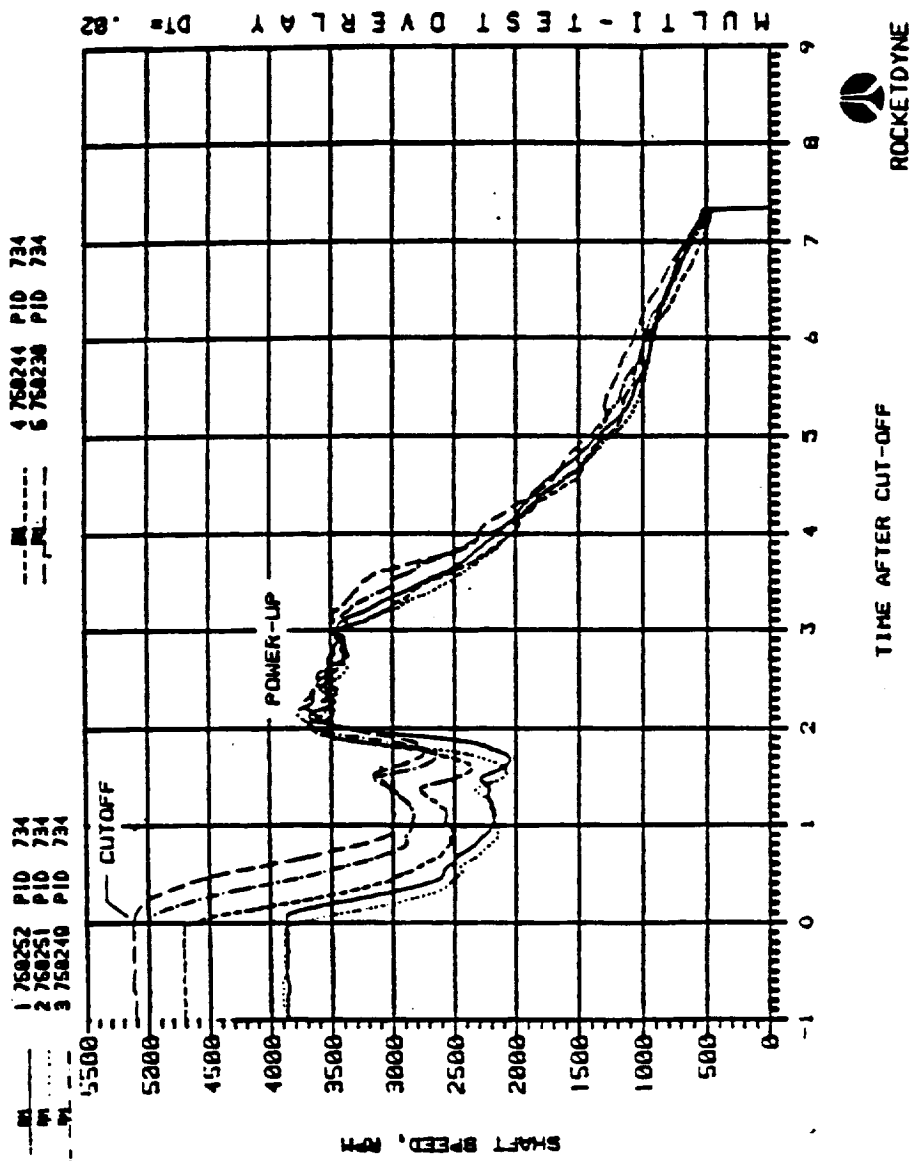


Fig. 4.22 LPOTP Shaft Speed For Various Cutoff Power Levels

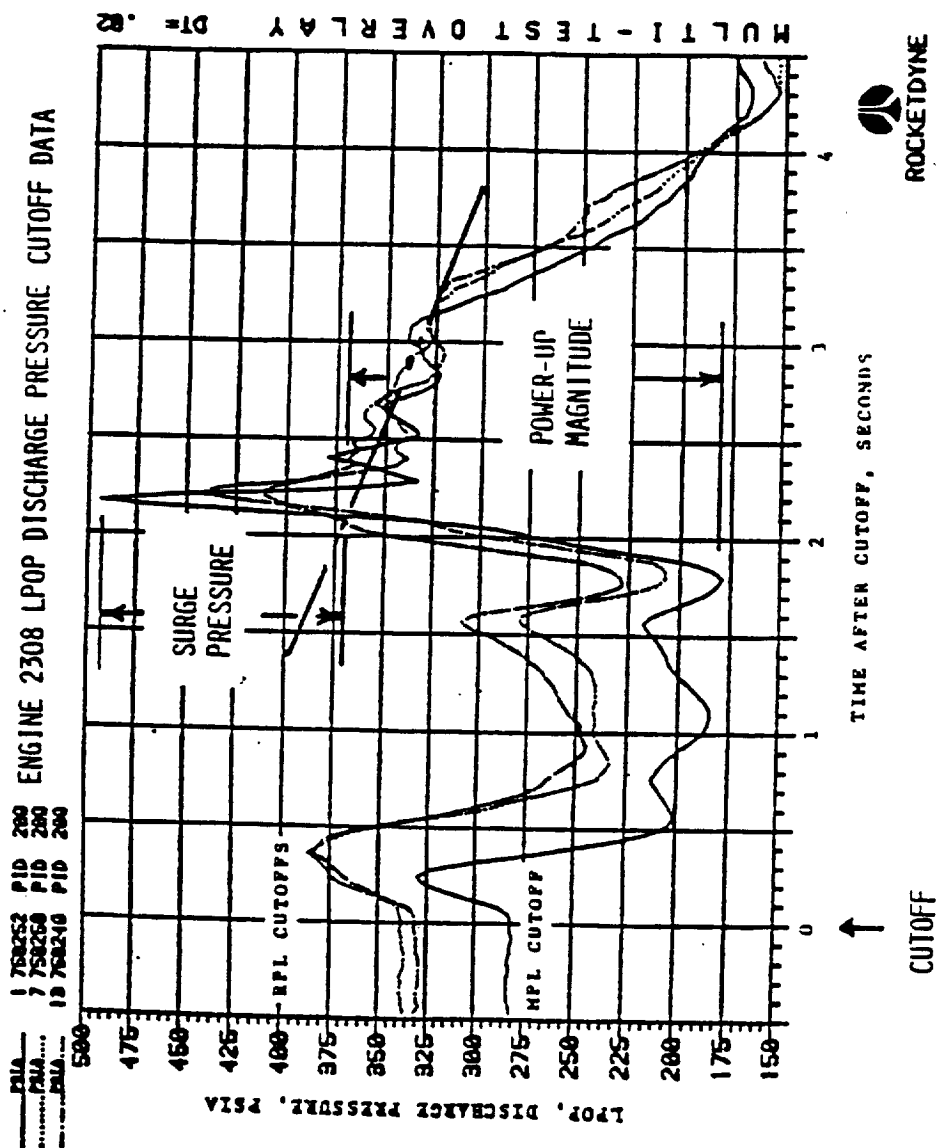


Fig. 4.23 LPOTP Discharge Pressure Cutoff Data

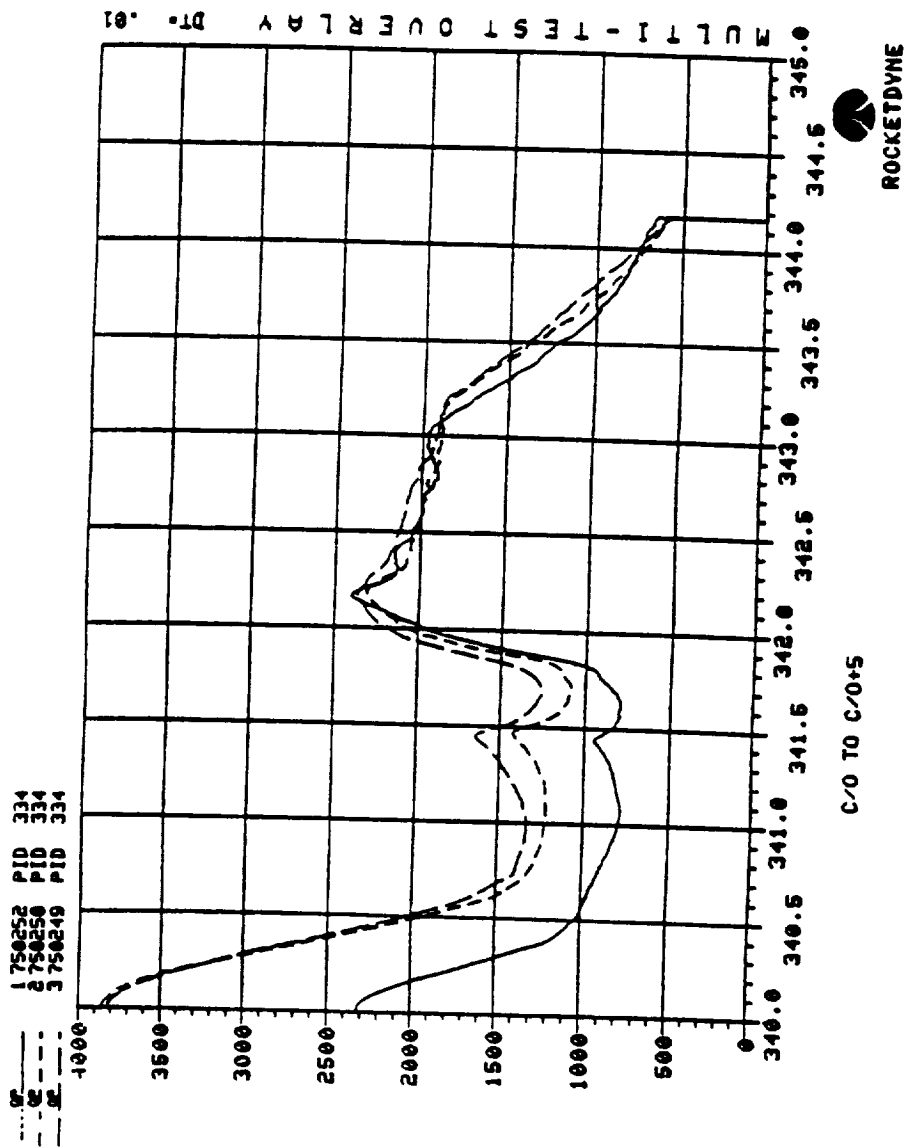


Fig. 4.24 HPOTP Discharge Pressure at Cutoff Data



pressure turbopumps and then to the main propellant valves. On the liquid oxygen side, the system also fills the preburner valves. The cryogenic propellants are held in the ducts for sufficient time to chill the engine and attain liquid conditions in the respective propellant systems. The chill process is aided by bleedlines which remove the gas as it is formed. It must be noted that while the ducts experience cryogenic temperatures ( $37^{\circ}\text{R}$  for Hydrogen and  $164^{\circ}\text{R}$  for Oxygen), the pressure experienced by the ducts in this condition is minimal, and thus these temperatures do not control the design.

#### MISALIGNMENT LOADS

The duct misalignment loads are considered in the design of rigid ducts. The design is based on worst case tolerance stackup in the duct assembly. The sequence of assembly of the ducts is tightly controlled through the specifications. The acceptable tolerances are specified in the form of interaction curves at flange joints. As examples, the interaction curves for high pressure oxidizer duct inlet and outlet are shown in Figure 4.25 and Figure 4.26. In general, only misalignment that fall outside the specification are recorded for MR action. One exception to the above rule is the ASI (Augmented Spark Igniter) fuel and LOX lines where the entire misalignment data is available. Shop experience indicates that due to the method for manufacture of larger ducts using jig fixtures, unacceptable misalignment (outside the specification) is very rarely encountered. Further, the misalignments found in practice in the large ducts are within the tolerances of the play in the bolt holes of the flanges and the large rigid ducts are not generally subjected to any significant preloads during assembly. The small ASI fuel and LOX lines are formed and any unacceptable misalignments in the flanges are first corrected by further forming the tube away from welded areas. However, statistical analysis of misaligned ASI tubes might give an indication on the nature of distribution of misalignments subjected to these types of manufacturing methods. Effort has been initiated to collect this data for all delivered flight engines.

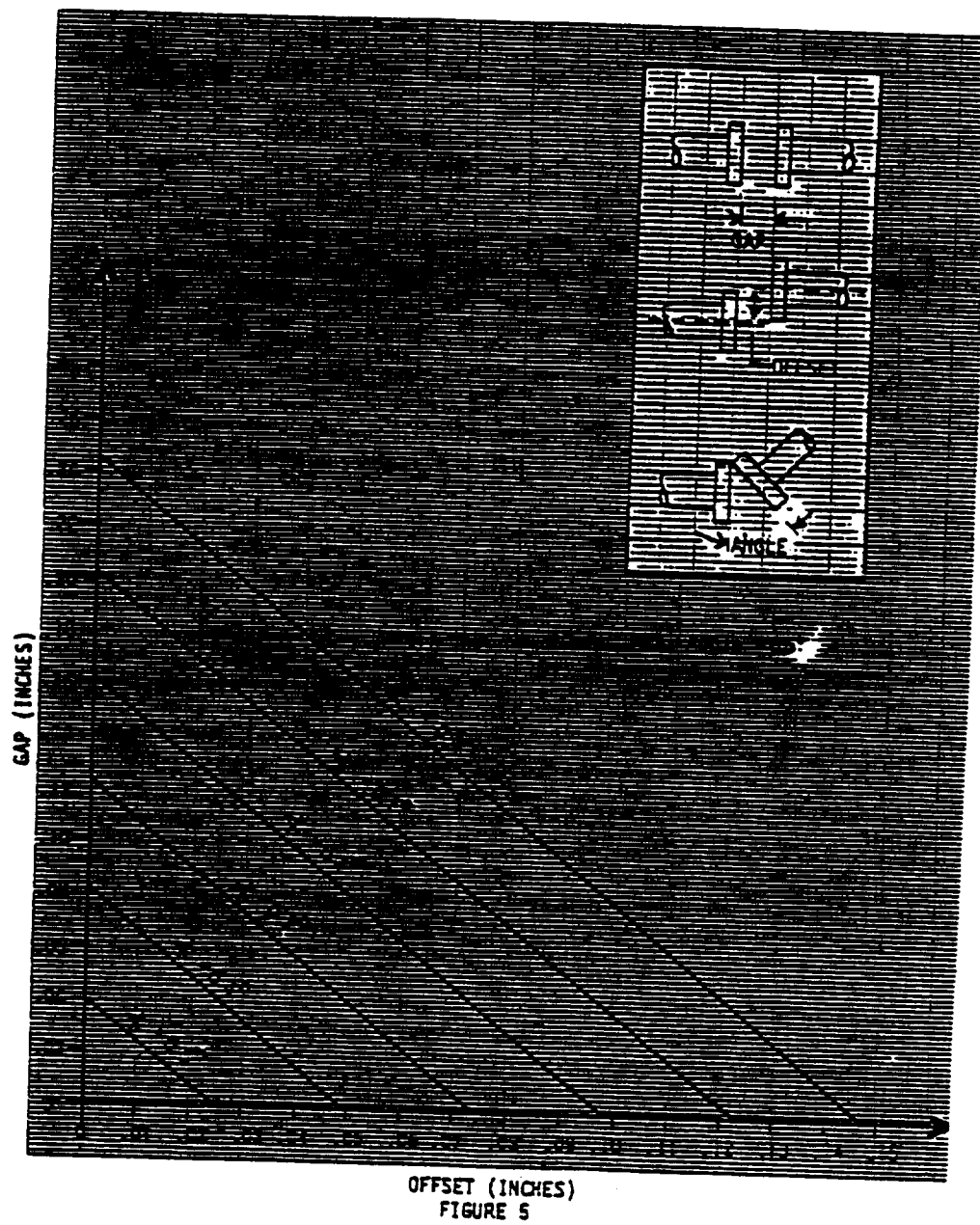


Figure 4.25 Allowable misalignment at HPCD Inlet

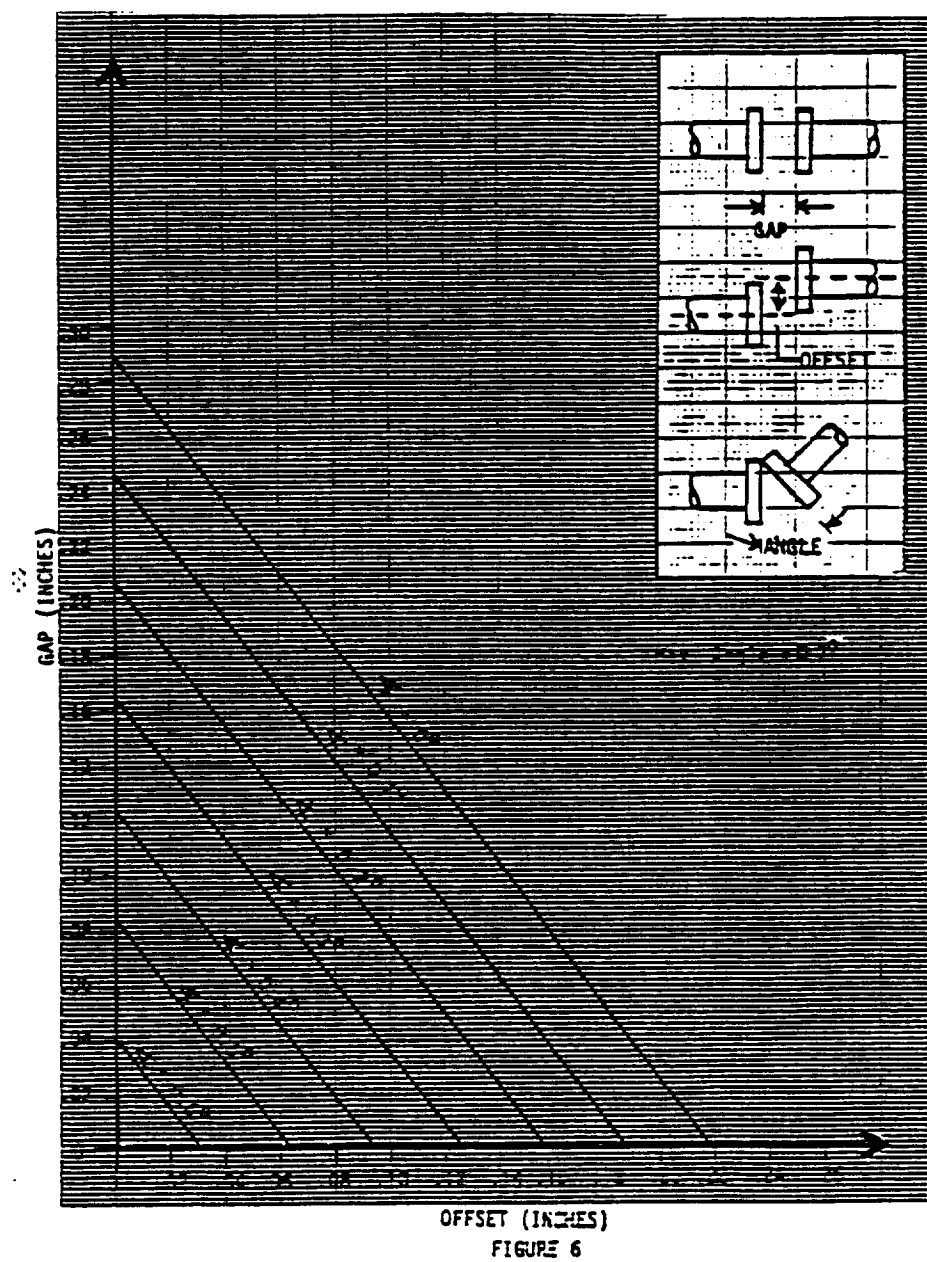


Fig. 4.26 Allowable Misalignments at HPOD Outlet

### GIMBALING LOADS

All lines which are subjected to deflections due to gimbaling have flex joints. The angulations at the joints are calculated using space frame analysis programs treating the ducts as a series of linear beams. The maximum angle is  $11^{\circ}$  about any of the gimbaling axis. This maximum gimbaling occurs only in an abort cycle. In addition the joint angulations are also calculated for maximum torsional twist of  $1^{\circ}$  about the engine axis. The rigid ducts like HPOD are not subjected to gimbaling deflections and are not designed for any gimbaling deflections.

### ACCELERATION LOADS

Ducts are designed for acceleration loads due to gimbaling acceleration and vehicle acceleration. The gimbaling acceleration is bounded by calculating the maximum g load that it can produce at any point in the duct. This has been calculated to be 5g and this load is applied over the entire duct. The vehicle acceleration loads come from SSME load criteria and is calculated to be 5g. Thus the ducts are designed for a total of 10g acceleration load subjected to on any axis. The fluid weight in the ducts must be considered in the analysis.

### FLOW MOMENTUM LOADS

The flow momentum loads are calculated using the flow rate of the fluid, density of the fluid at operating temperature and pressure, flow area and gravitational constant. The flow loads calculated is applied as an axial load on the duct beam elements.

## DYNAMIC LOADS

The dynamic loads that are considered in the duct analysis are:

- a) Random base vibration loads
- b) Periodic pump generated base excitation loads
- c) Shock transients
- d) Random pressure loading or equivalent sinusoidal pressure loading at pump wake frequencies.

Initial random base excitation data was predicted by scaled values from J2-S engine data. Subsequently, the data is being continually revised as more actual engine measurements become available. The loads are defined based on vibration zone classification (Figure 4.27). As an example for the case of HPOD the appropriate zones are A and G respectively (Figure 4.27). Typically SSME loads criteria defines the spectra up to 2000HZ. However, when the need arises, the spectra is extended to a higher frequency range using actual engine measurement data (Figure 4.28). This can happen when the excitation of local shell modes of the duct are the subject of the study.

## SHOCK TRANSIENTS

These loads are predicted from the actual engine firing test data from SSME. The primary shock transients occur at start and cutoff, and to a lesser extent, by preburner pops. The primary contributor to the start and cutoff transients is the nozzle side load caused by flow separation. During engine start and cutoff, the flow inside the SSME nozzle is constantly changing. Unsteady flow separation occurs in the nozzle during this time

(2131e)

Figure 4.27 Major Sources of Vibration (Criteria) Zone Locations  
Original Mailed to NASA Program Manager

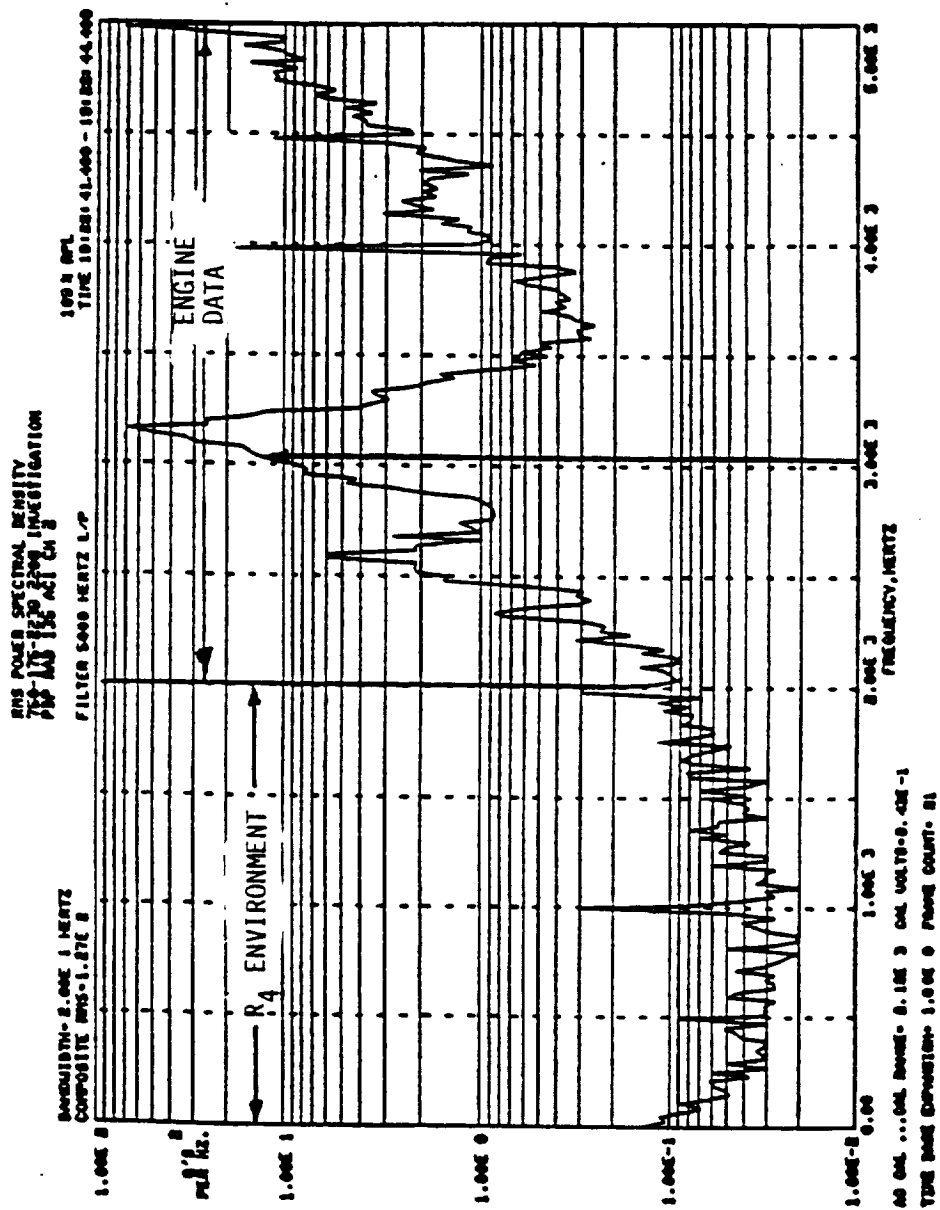


Fig. 4.28 HP0D Base Vibration Environment

period. The axial location of this flow separation move towards the exit of the nozzle as combustion chamber pressure is increased, and back into the nozzle as chamber pressure is decreased. Side loads are developed in the nozzle walls because the flow separation patterns are not symmetrical. The start transient is more severe than the cutoff transient due to comparatively longer cutoff time sequence as well as due to the higher altitude. The SSME shock spectra criteria was developed by enveloping sixty starts and sixty cutoff engine data measured on the ground. A typical shock spectra is shown in Table 4.4 for Zone A and Zone G that govern the HPOD environment. It must further be noted that the shock transients are not a strong function of power level.

#### DYNAMIC PRESSURE LOADS

Dynamic pressure loads have been used in the analysis when detailed local shell stresses were the object of study. As an example, the high frequency pressure measurement made just downstream of HPOTP discharge is discussed here. Power spectral density plots of engine tests at 100% and at 109% are presented in Figure 4.29 and Figure 4.30 respectively.

Primary characteristics are at rather flat low level power at about  $1/3 \text{ psi}^2/\text{HZ}$  from 0 to 10KHZ. Superimposed on this background are two characteristic signals, speed harmonics and a broad random hump in the 6000 to 9000 HZ range. At 100% power level the random hump and 16/rev harmonic are distinct, while at 109% they superimpose at 8KHZ. Total power ( $\text{psi}^2$ ) at 109% is twice the 100% power level value.

Speed harmonics have narrow power spikes typical of sinusoidal components. The fact that the first three or four multiples of 8/rev show an increase with frequency and then decrease indicate a wave form like positive-negative pulse with a duration of about 25% of the period between the 8/rev pulses. This

(2131e)



<u>ZONE</u>	<u>AXIS</u>	<u>ZONE</u>	<u>AXIS</u>
A	X, Y, Z	G	X, Y, Z
10 HZ @	1.0 g Peak	10 @	2. g Peak
30 HZ @	40. g Peak	30 @	28. g Peak
800 HZ @	60. g Peak	60 @	53. g Peak
2000 HZ @	150. g Peak	220 @	104. g Peak
		320 @	200 g Peak
		950 @	157 g Peak
		2000 @	333 g Peak

Table 4.4 HP0D Zone A and Zone G Shock Spectrum





type of excitation tends to propagate as a plane wave down the duct and would be attenuated by a reflection at the constriction formed by the main oxidizer valve.

The broad random hump is explained by the attenuated power radiated by lateral acoustics driven in the constant velocity pump volute by the blade wakes. The variable diameter volute causes local resonances at different frequencies with the broad hump being the sum of all components. As the power level is increased, local frequencies will remain the same, although the magnitude would increase. This tendency is seen in Figure 4.29 and Figure 4.30. The broad hump would tend to decrease with distance. However, data at these frequency ranges may have to be used when local shell modes are of concern, near the HPOTP discharge.

#### LOAD COMBINATIONS

The loads are combined in a conservative manner to calculate life. Currently all maximum expected static loads are combined together to maximize the total static load. Loads are then used in fatigue analysis. Assumption is made that the engine operates at FPL for a full 7.5 hours of operation, though the engine is throttled back during launch. Further, the maximum vehicle acceleration loads do not occur all the time in all axes, and the maximum gimbaling acceleration only occurs during an engine abort cycle. Some of the conservatism in the analysis technique may be eliminated using a probabilistic approach.

#### STATIC ANALYSIS

A static analysis is performed on the ducts for the application of loads described above, using frame analysis. The analysis is performed for the

(2131e)

worst case combination. The load time history is considered such that transient loads present at start or cutoff are not applied simultaneously with main stage operating pressures, maximum gimbal accelerations, main stage vibration and acoustic loads.

A normal static finite element analysis is performed using beam finite elements. The elbow elements are analyzed using ASME flexibility factors. The flexibility decrease due to internal pressure is also accounted for. Approximate hand analysis of the ducts includes standard equations for curved beams for hollow circular cross-sections and considering the ovality effect and Torus effect. Curved beam effect is caused by the shift of neutral axis with respect to centroid of the bend. Torus effect is caused by the balance of shell cross-sectional forces to offset the pressure load acting across the shell surface. Ovality effect is caused by the external moment forcing the cylindrical section to go oval at the elbow. Two dimensional axisymmetric models are also constructed for flanges. The local flange models are analyzed for bolt preload, external load, pressure load, and seal load. The local flange models provide the maximum surface strains for low cycle fatigue calculation. Flange rotations are checked to ensure the outer edge of the flange will not contact mating flange face. Local finite element models are also constructed to determine stress concentrations due to ports and bosses. Recognizing the approximations in the empirical approach of treating elbow flexibility with flexibility factors, limited amount of testing has been done using advanced elbow finite elements for some SSME ducts. These advanced elements use a combination of fourier and polynomial interpolations, the first is used circumferentially and the second is used along the axis of the tube. An important development in these elements is the coupling between straight pipe runs and pipe bends. If the stiffening effect of the straight runs are neglected, the strain response of the bends may be overpredicted. The advantages of these elements are their formulation in the large deflection domain, and their appearance to the user as stick models though in fact they model the shell behavior as though the pipe has been modeled using shell elements. Limited static analysis results show good correlation with results of shell element models for SSME ducts.

## DYNAMIC ANALYSIS

Dynamic analysis on ducts are performed using classical beam finite elements and elbow finite elements with ASME flexibility factors with the effect of internal pressure included. The types of dynamic analysis performed are:

- 1) Model analysis
- 2) Random base excitation analysis
- 3) Periodic base excitation analysis
- 4) Pressure excitation analysis due to pump blade wave frequencies
- 5) Shock spectra analysis

Random base excitation analysis are done using PSD diagram in the frequency domain. For analysis purposes, the assumption is made that the vibration environments at each end of the duct are uncorrelated with respect to one another. In actuality, some of the vibration environment at both ends of the duct is generated from the same source (i.e. main combustion process). In addition, a portion of the vibration environment at discharge end of the duct is generated by mechanical and/or fluid transmission through the duct itself. Due to the inability to predict or account for these load correlation factors properly, the conservative uncorrelated vibration assumption is used.

Steady state response due to sinusoidal excitations are calculated using normal mode method. The technique is a two step process for each axis of motion. In the first pass, the maximum stresses and the associated phase angles are calculated for selected critical elements for all given sinusoidal frequencies. In the second pass, the frequencies and phase angles are entered such that responses are calculated in a consistent manner with phasing information.

(2131e)

The shock spectra analysis is performed using normal mode method applied to shock analysis. In this method, all phasing relationships among the several modes are lost and only the maximum absolute values are retained for each mode. Hence, RSS (the square root of the sum of the squares) method is commonly used to obtain a rational assessment of displacements and internal loads.

### GEOMETRICAL UNCERTAINTIES

Geometrical uncertainties in the duct system can include variations in thicknesses, and weld mismatches, and spatial geometry variations. One area that has received much attention is the weld mismatches. Mismatch between segments of welded ducts can result in substantial local increases in stress. This increase in stress must be accounted for in fatigue analysis. Mismatches can be present even before the welding has occurred, called "fitup" discrepancies or they can be the result of the welding process itself due to differential shrinkage, or excessive welding. There are numerous factors that control the final resulting mismatch. In SSME, weld mismatch data can probably be broadly grouped into the following categories, each having its own characteristics. They are:

- 1) Sheet metal welds
- 2) Thin wall duct welds
- 3) Rigid parts or thick walled ducts
- 4) Parts which have complex geometry

In general, the amount of weld offsets vary with clock positions at a joint. Some limited amount of data has been collected and is available to study the weld offsets in thin walled ducts. Some limited amount of data is also available for parts with complex geometry such as main combustion chamber inlet neck.

(2131e)

## FAILURE HISTORY

The inservice failures of ducts include LPFTP discharge duct buckling, failure of flow guide in HPOD and failure of development HPOD with brazed bosses for ultrasonic measurement.

The low pressure fuel turbopump discharge duct buckling was due to leak in the insulation jacket. The trapped air will liquefy under cryogenic temperatures. At engine shutdown, the trapped air due to insufficient escape passage can exert pressure resulting in duct shell buckling. This failure is not catastrophic to the engine.

The original configuration of the HPOD at discharge incorporated an integral flow guide to provide a smooth transition of fluid into the main oxidizer valve. The cantilevered flow guide failed at the base due to resonance excited due to acoustic cavity behind the guide. The redesign eliminated the acoustic cavity.

A high pressure oxidizer duct was modified by adding special brazed-on ultrasonic flowmeter blocks to the exterior duct wall of the special development duct (Figure 4.31). This duct failed during engine testing (Figure 4.32). Failure investigation of this special HPOD involved model simulation to determine failure initiation, supplementary hot-fire test simulation, and extensive instrumentation of the HPOD.

Instrumentation of the duct included locations for tri-axial accelerometers at both inlet and outlet flanges of the duct and selected locations for strain gages on the exterior of the duct. Re-analysis of the flowmeter attachments was updated using measured vibration environments, including dynamic response of the brazed-on flowmeter blocks due to mechanical vibration and pressure oscillations. It was determined that the failure mechanism resulted from

(2131e)



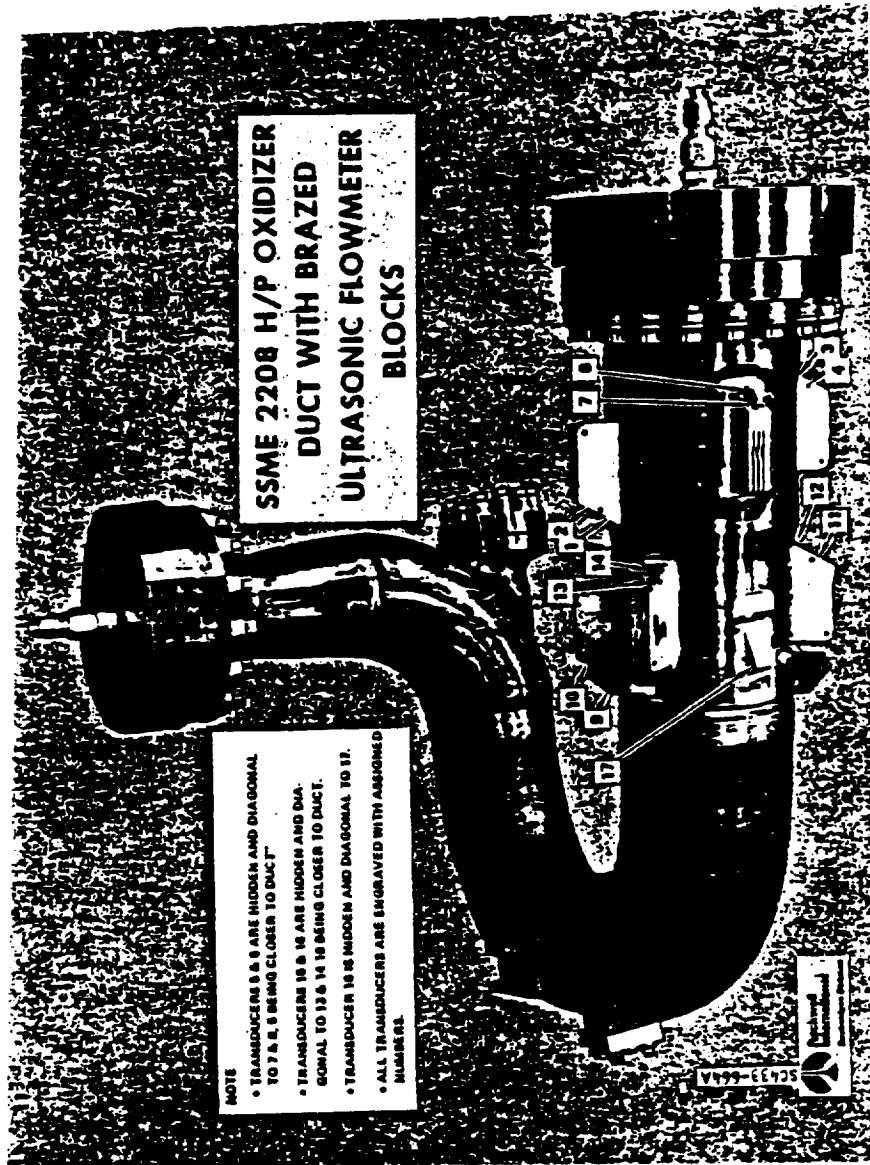


Fig. 4.31 HP0D with Brazed Ultrasonic Flowmeter Blocks



Fig. 4.32 Engine 2108 HP0D Failure

alternating lateral vibrational loads of the block and pressure effects (Figure 4.33). The peak stress location was at the block-to-duct braze fillet intersection. High stresses were attributed to the tight fillet radius at this location. A two-dimensional plane strain analysis of the flowmeter block to duct shell was performed to determine the fillet radius stress concentration, which was determined to be 3.5 in the hoop direction. The current configuration completely eliminated the ultrasonic measurement bosses. Analysis has shown integrally machined bosses with generous fillet radius have the desired factor of safety for fatigue life.

#### SURVEY OF FINITE ELEMENT MODELS

Various finite element models exist for the analysis of SSME duct systems. The survey here is limited HPOD and related LOX systems. Due to the interaction between the various ducts, typical finite element models not only contain the duct in question but would also include other branching lines and they would be modeled till they connect to a rigid part. As in other components, global and local models exist. The global models are used to obtain gross cross-sectional forces. Local models are constructed to determine stress concentration factors.

The model shown in Figure 4.34 was constructed to determine the natural frequencies, mode shapes, and the response of the SSME high pressure oxidizer discharge duct and preburner supply duct to the FPL dynamic test environment. The model also contains a portion of HPOTP where HPOD bolts to pump flange (Figure 4.35). This was done to simulate flexibilities at flange interface so that loads at the end of the duct can be obtained more accurately.

The model in figure 4.36 is a hybrid stick-shell model that was constructed to determine the dynamic loads/stresses in the discharge duct. The area of interest was the response of ultrasonic flowmeters to the dynamic motion of

(2131e)

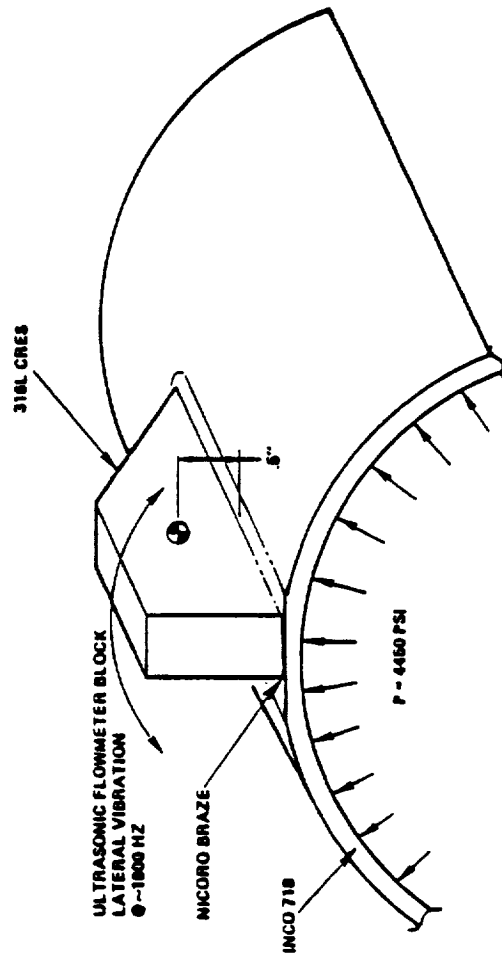


Fig. 4.33 HP0D Failure Mechanism

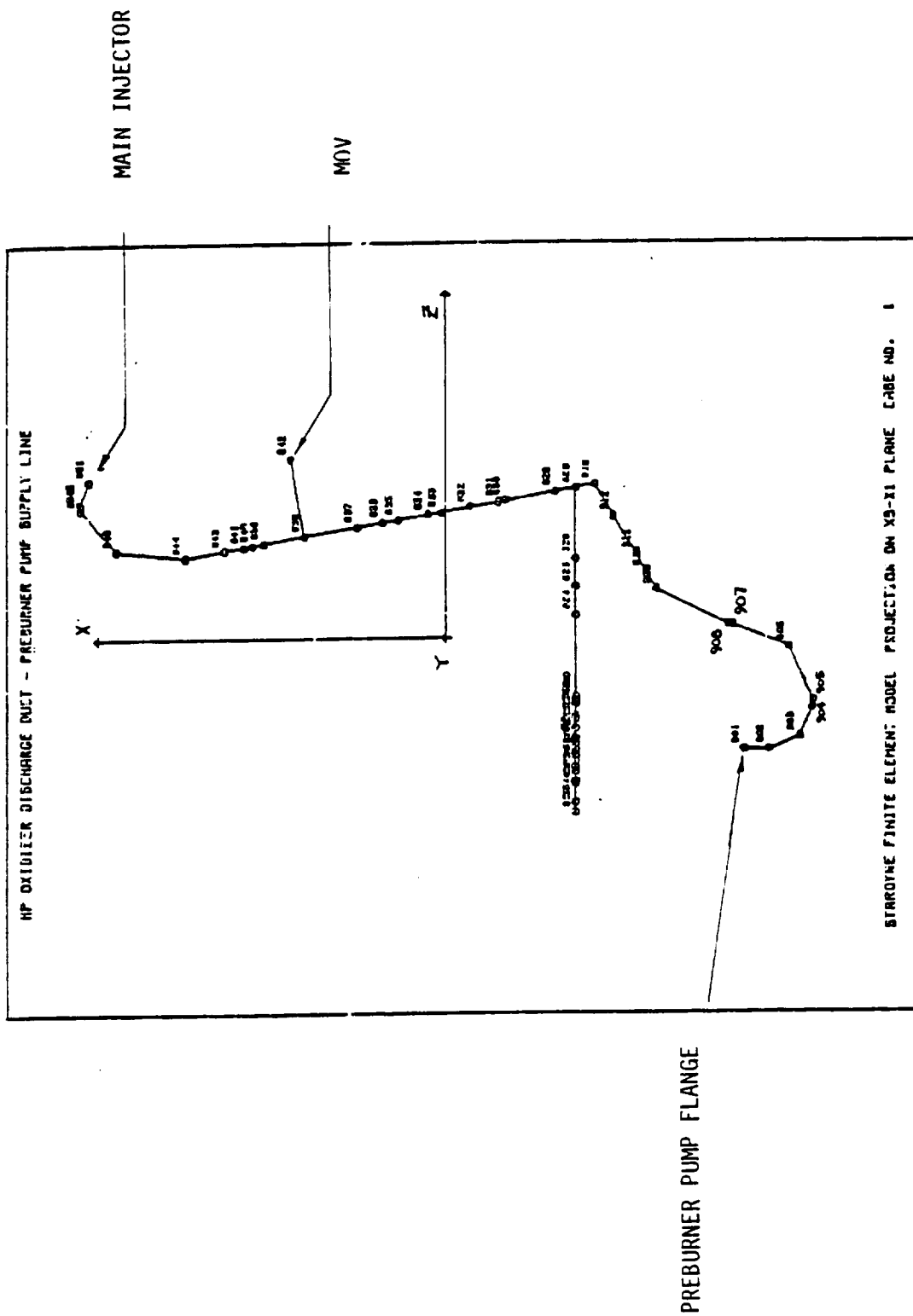


Fig. 4.34 HP0D and Preburner Pump Supply Line Model

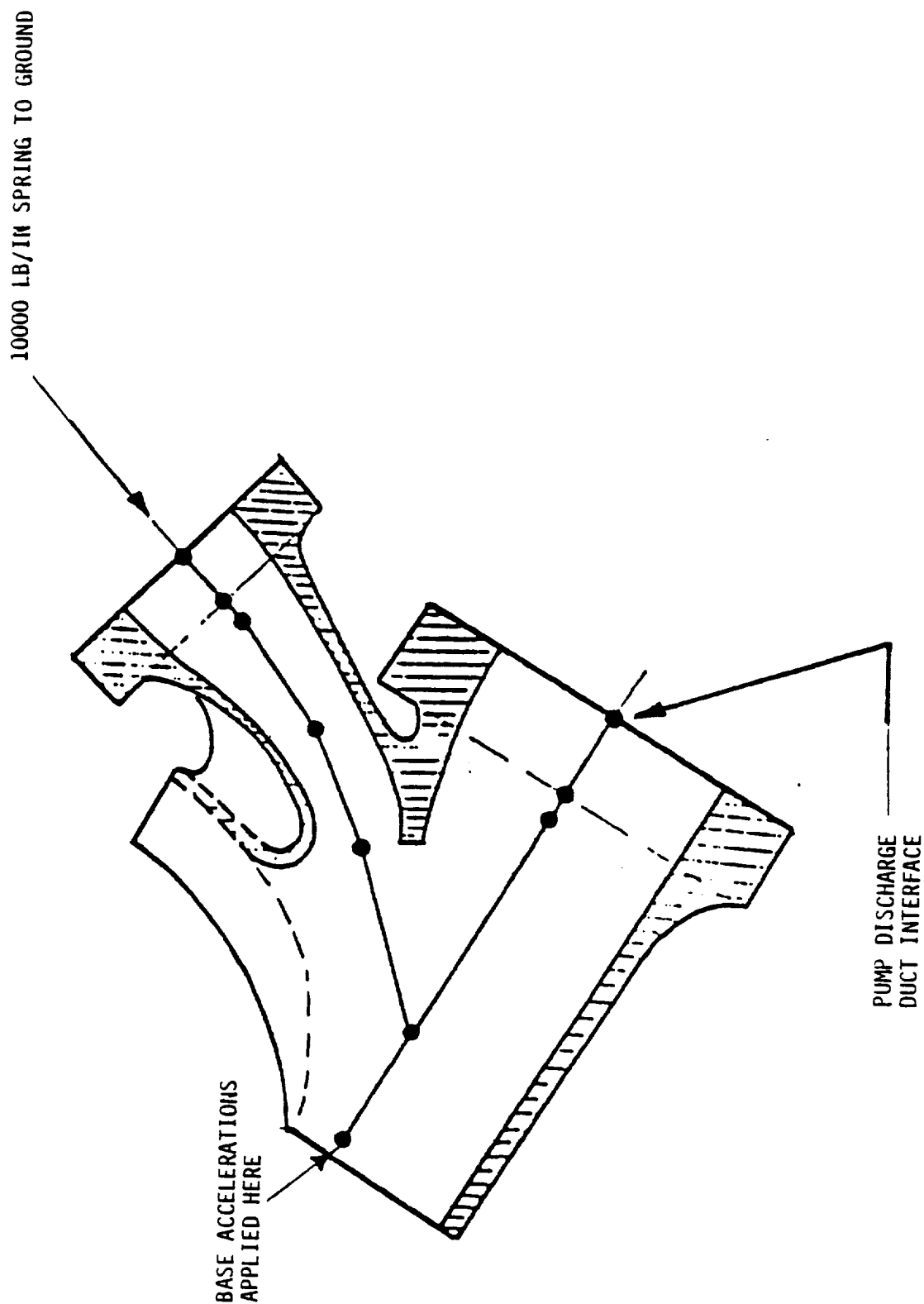


Fig. 4.3.5 Finite Element Model Detail at HPOTP Discharge Outlet

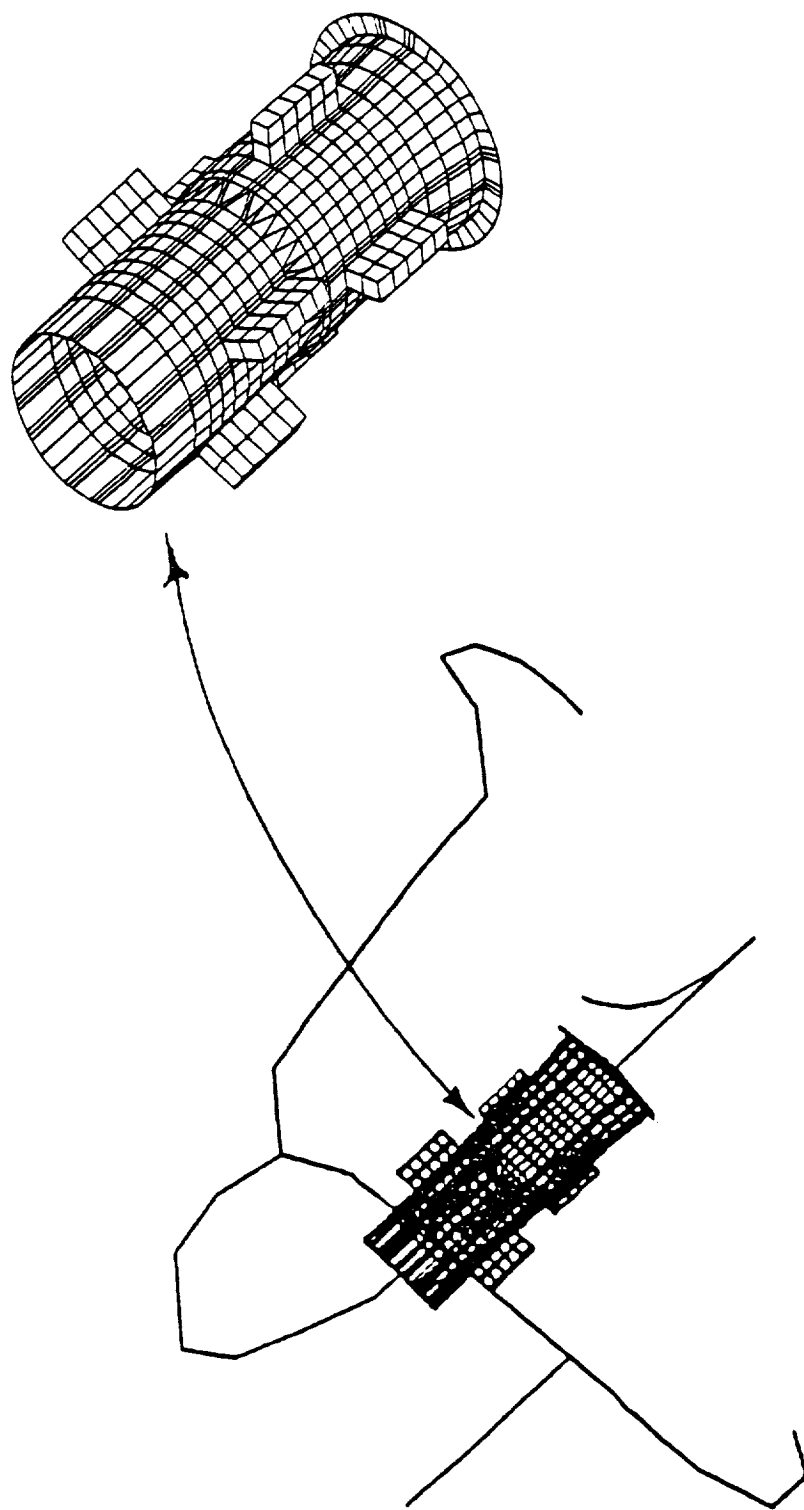


Fig. 4.3.6 Hybrid Stick - Shell Model of the HPD

the duct. The model was analyzed for a sinusoidal pressure excitation with a sinusoidal distribution along the circumference (Figure 4.37) with a frequency matching the first acoustic mode of the duct. It was concluded that integrally machined ultrasonic bosses with generous fillet radius would not present a fatigue problem.

The model shown in Figure 4.38 contains several components forming the LOX system modeled as pipe or elbow elements. They are:

- 1) LPOTP discharge duct
- 2) LPOTP turbine drive duct
- 3) Preburner pump supply duct
- 4) Heat exchanger supply duct with antiflood valve
- 5) Fuel and Oxidizer preburner LOX supply duct
- 6) Preburner valves(OPOV and FPOV) with actuators
- 7) High pressure oxidizer discharge duct
- 8) Main oxidizer valve and the actuator

A better visualization of the same model is obtained in Figure 4.39. This figure (Figure 4.39) depicts the model as flat faceted shells for the purposes of visualization only. This model represents visually the variation in diameters of the duct systems and the modeled elements (with equivalent stiffness) for valves etc.

This model was used to study the dynamic response of the system to mechanical vibration, shock and superimposed sine environments. The flex joints are modeled as a three element finite element assembly with appropriate properties to simulate linkage and bellows. Appropriate pin codes are used to model the linkage.

The local 2-D model was used to determine the local stresses present in the HPOD due to the ultrasonic bosses (Figure 4.40).

(2131e)



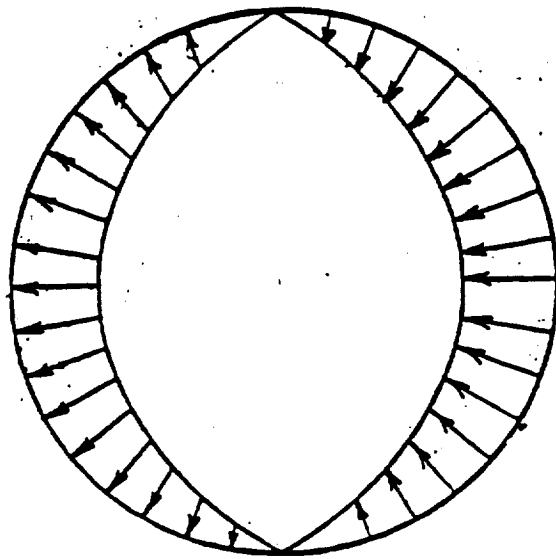


Fig. 4.37 Sinusoidal Pressure Loading on Shell



Fig. 4.38 Line Element Finite Element Model of the Lox System

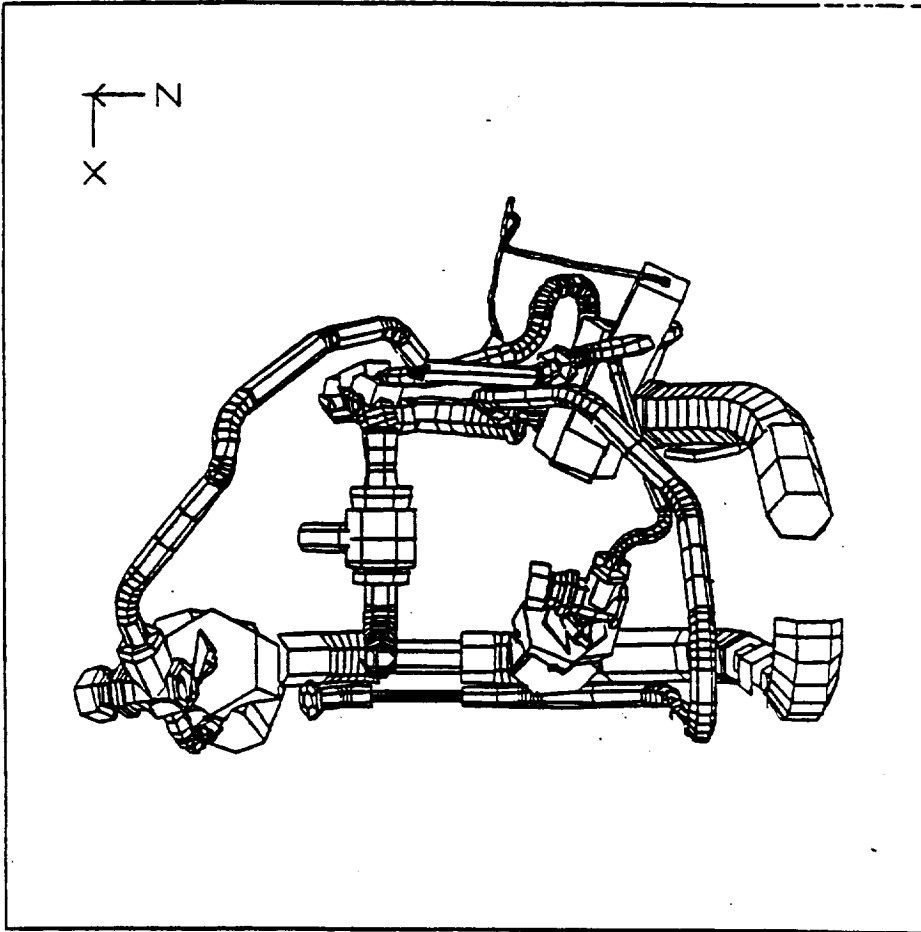


Fig. 4.39 Flat Facetted Representation of Lox System Model For Visualization

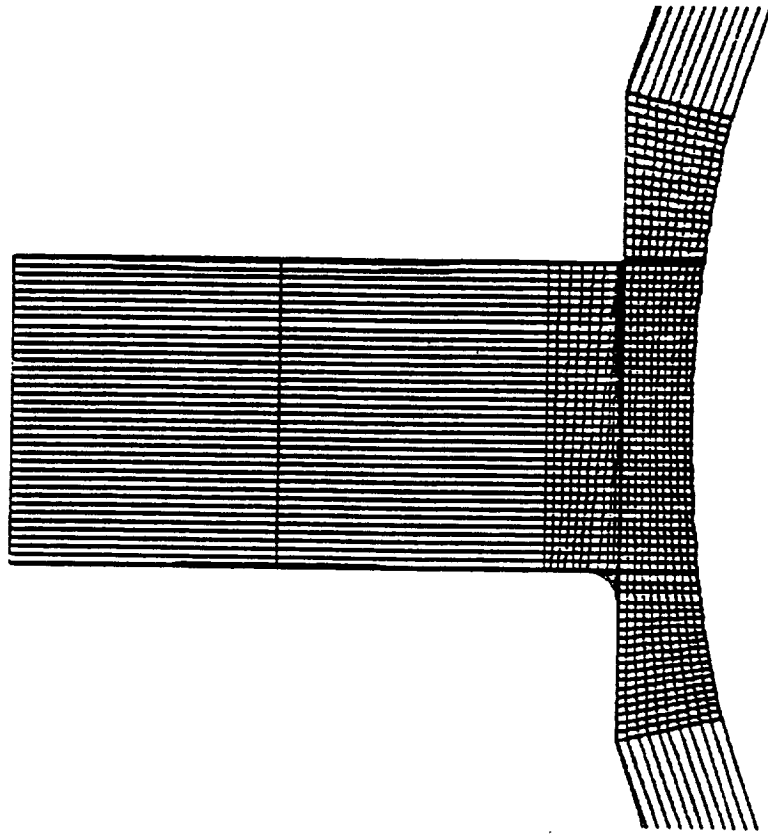


Fig. 4.40 Local Model of the Ultrasonic Block

A local axisymmetric flange model (Figure 4.41) was used to determine the local stresses at the flange due to preloads and external loads.

The statistics of the models discussed above are presented in Table 4.5

#### SCOPING OF ANALYSIS REQUIREMENTS

##### Static Analysis

- 1) Linear beam finite elements with pipe cross-sections
- 2) Ovality considerations for elbow with flexibility and internal pressure factors
- 3) Temperature dependent material properties
- 4) Provision for pin codes in modelling linkages
- 5) If possible incorporation of more advanced elbow elements
- 6) Provision to prescribe load as well as prescribed displacements

##### Dynamic Analysis

- 1) Modal extraction analysis for beam type structures and shell structures
- 2) Multiple base uncorrelated random excitation analysis
- 3) Sinusoidal base excitation analysis
- 4) Random and sinusoidal pressure analysis

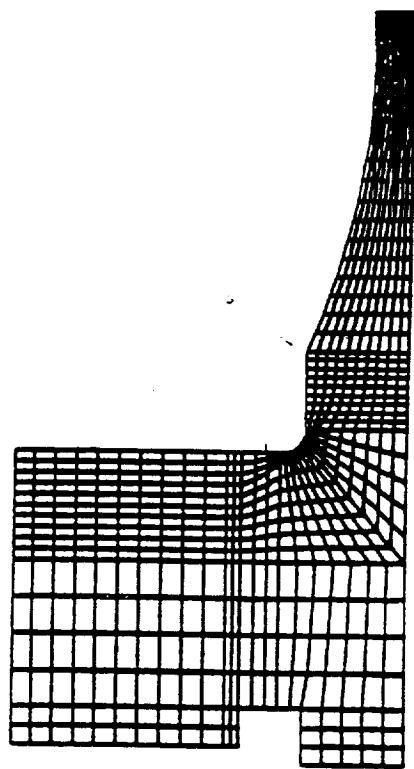


Fig. 4.4.1 Local Flange Model of HP0D

375

[illegible]

Section 5  
Nozzle Feed Line



## PSAM PROJECT

### NOZZLE FEED LINE

#### INTRODUCTION

Nozzle feed line is part of the nozzle cooling system, supplying coolant to the nozzle. Several cooling methods such as radiation, ablation, film cooling, dump cooling or regeneration cooling can be employed in the nozzle design. It is also possible that different cooling systems can be employed in different regions of the same nozzle. When regenerative cooling type is used, the nozzle structure is usually made out of tube bundles reinforced by an external outer shell and circumferential hat bands. The coolant which flows in the tubes is normally the fuel such as hydrogen in SSME. The integrity of the nozzle feed line is critical, as any failure in the feed line will result in an excessively LOX-rich mixture causing fires and extensive damage to a major portion of the engine. In SSME, the nozzle feed line which is made out of INCONEL 718 material, carry the coolant at approximately 6000 psi and 93°R at steady state.

#### GEOMETRICAL CONSIDERATIONS

The actual geometrical details of the nozzle feed line depend upon the cooling concept used in the regeneratively cooled nozzle. It can employ single pass, pass and half, or double pass methods. In SSME, the concept used is the single pass method in which the coolant is introduced to the lower inlet manifold, using three lines with branching ducts which are spaced 120° apart (Fig. 5.1). The attachment of the nozzle feed line to the nozzle is made at selected hat bands. The intermediate supports allow the feed line to move freely along the axial direction, and the end support brackets provide a rigid condition. The redesigned nozzle feed line contains a loop to provide flexibility in the axial direction to accommodate the thermal contraction.

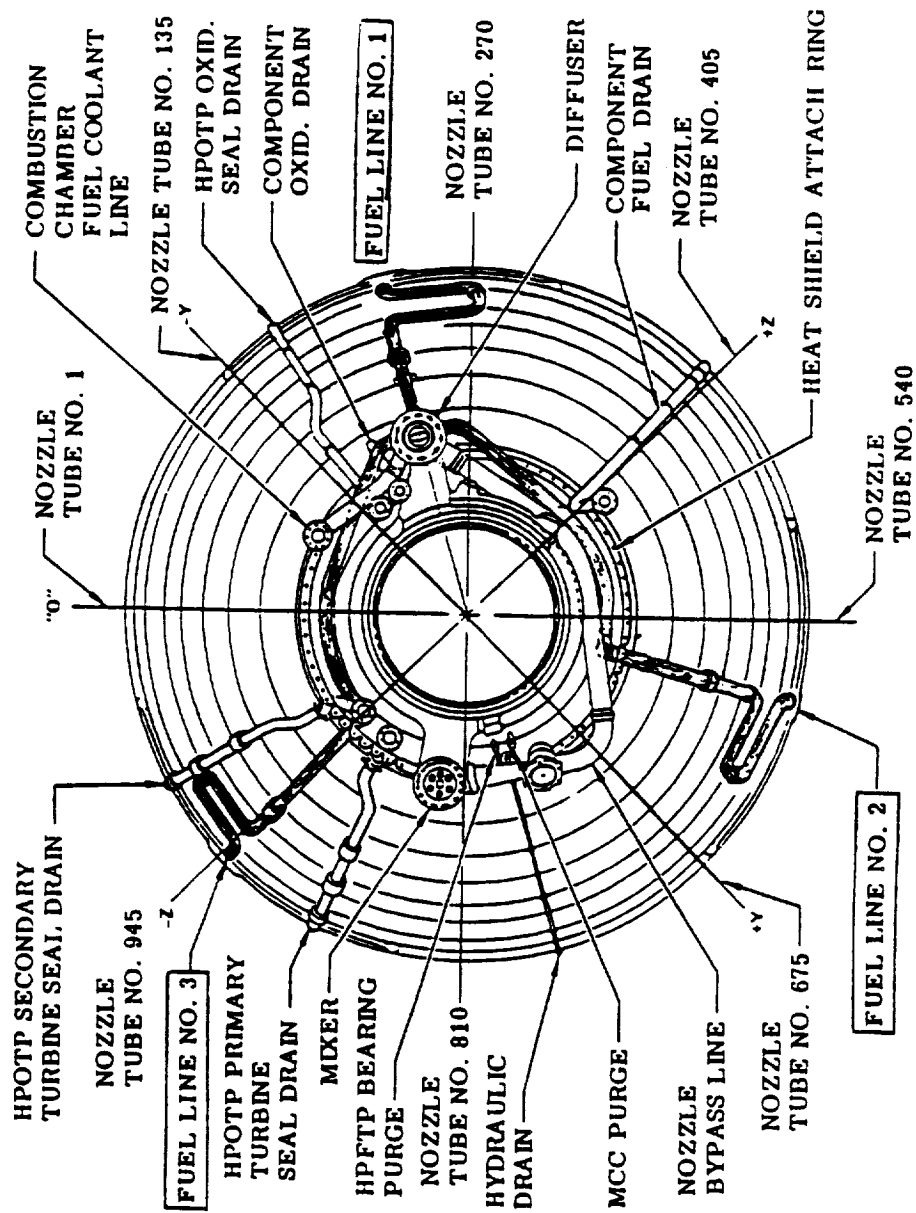


Fig. 5.1 Flight Nozzle Features

## LOADING ENVIRONMENT

The nozzle feed line is subjected to the following steady state and transient loads.

1. Steady State Loads
  - . Pressure
  - . Temperature
  - . Random vibration
2. Transient
  - . Pressure
  - . Thermal
  - . Side load
  - . 20-g inertial
  - . Oscillating pressure shock transient.

The internal pressure furnishes a high mean stress and is one of the primary loads on the line. The largest thermal gradient usually occurs during transient (Fig. 5.2) and can be of the order of  $200^{\circ}\text{R}$ . However, it is not generally a significant load as it occurs during lower transient pressure values. However, the combination of temperature and pressure at transient must be considered for HEE (Hydrogen Embrittlement Effect) susceptibility. The thermal shrinkage is accommodated normally through sliding joints and "steam loops" and is normally a secondary load. For nozzles with full flowing conditions, steady state random vibration loads are low. However, accelerometer measurements at hat bands are available from engine firings (Fig. 5.3). The vibratory loads in the form of PSD can be used for multibase vibration analysis of the nozzle feed line. The other primary load that needs to be considered is the transient aerodynamic load at start and cutoff which plays a critical role in the nozzle feed line design. Early designs of SSME nozzle feedline did not consider the shock transient load in the 200 to 400 Hz regime.

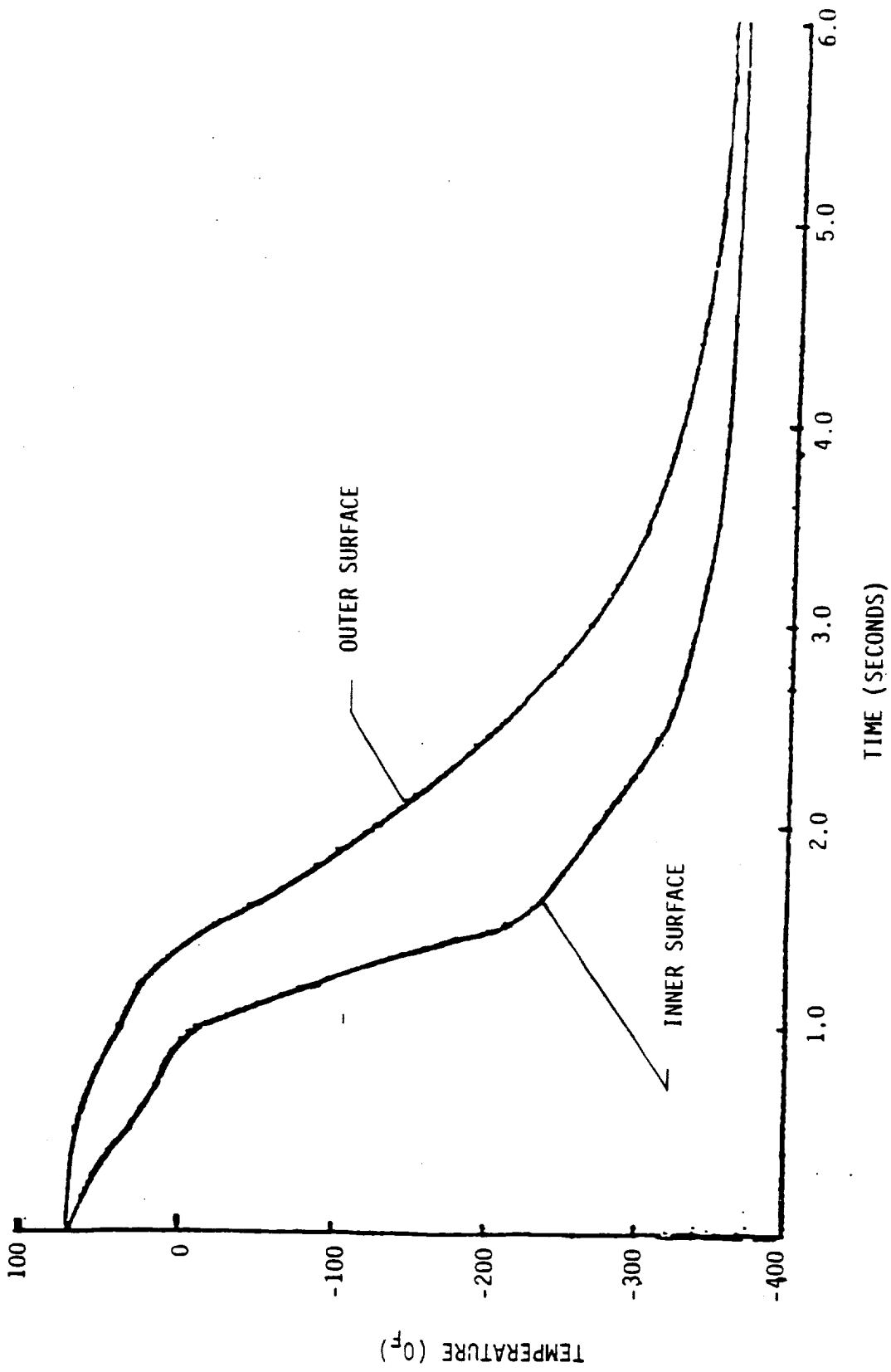


Fig. 5.2 Nozzle Feed Line Start Transient Temperature Profile

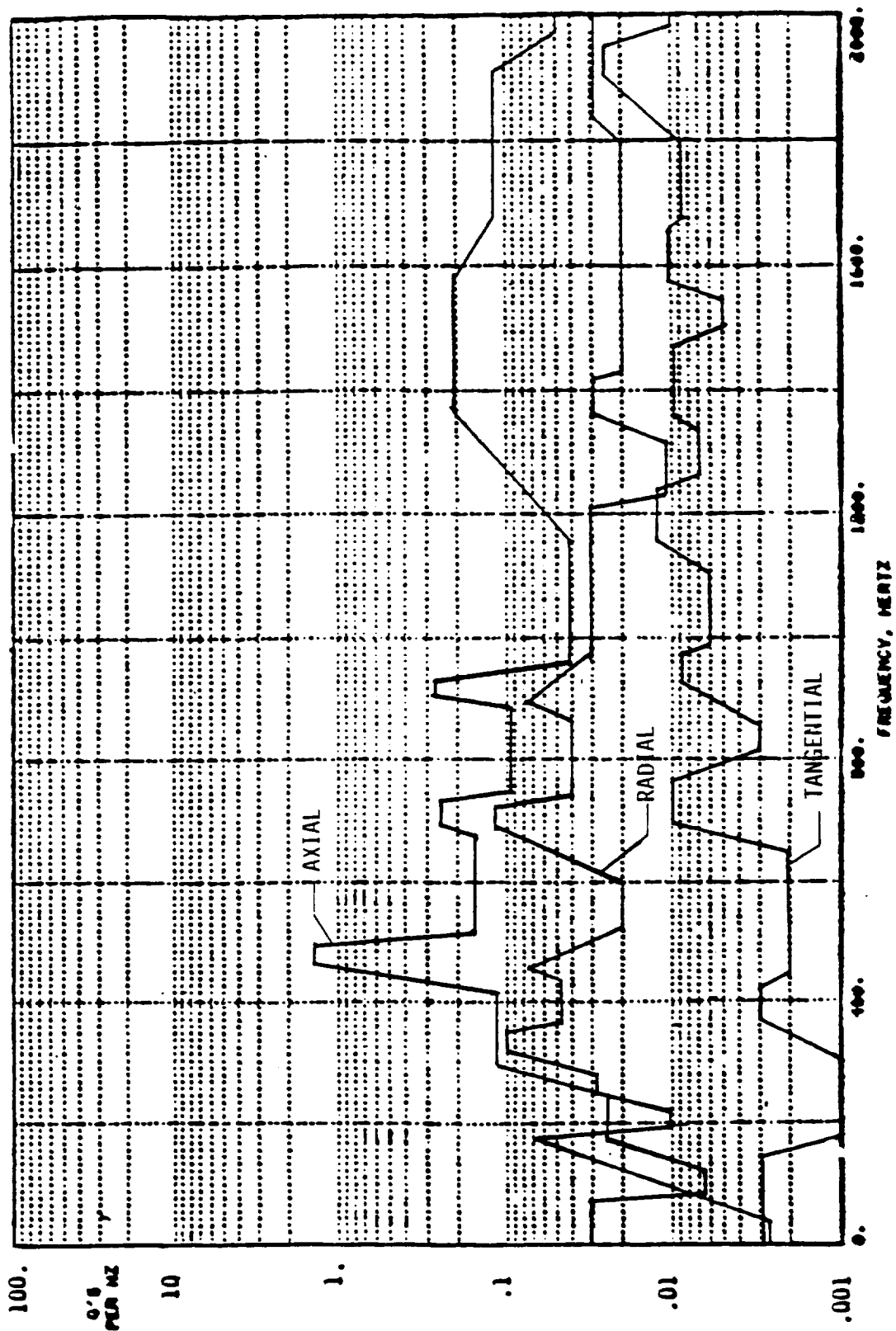


Fig. 5.3 R.M.S. Power Spectral Density Plots for Acceleration at Steady State at Hatband 9

### AERODYNAMIC TRANSIENT LOADS

The primary aerodynamic transient load is due to the unsteady flow separation effects. The different aspects of the flow separation is conveniently divided as by sideloads, oscillating shock loads and breathing mode loads. Such a classification is made as their effects are in different frequency ranges.

### SIDE LOADS (JET SEPARATION)

Rocket engines incorporating high nozzle expansion ratios and operating in an environment wherein significant ambient pressure level exists, encounter a region of asymmetric flow during their start and cutoff transients as the nozzle fills or empties. This causes an imbalance of pressure forces in the nozzle wall and may result in side loads of significant magnitude. The effect of this side load can be seen by the pendulum mode deformation of the nozzle in SSME firings at transient. The engine start and cutoff sequences are planned to minimize the side loads. Dwelling at thrust levels where separation is expected will result in large side loads leading to structural damage.

Exact theoretical evaluation of the side load, which is due to asymmetry, is beyond the scope of the current state-of-the-art. Hence, side load data is measured from many engine tests using load cells at gimbal point or through strain gaged actuators or stiff arms. It must be noted that the strain gages measure the equilibrating forces, while the forces themselves are applied internally to the nozzle as pressure gradient which varies with time. Dynamic pressure measurements of the nozzle wall pressure from actual engine firings are not available. However, nozzle pressure measurements from airflow tests on subscale models are used with appropriate scaling to obtain approximate oscillating engine pressure values. The magnitude of the side loads vary significantly from test to test. This is illustrated by the statistical summary (Fig. 5.4) of the maximum moment generated from 186 engine tests of the J-2 engine about the gimbal point. The J-2 engine which was an upper stage Saturn engine, similar to SSME encountered an overexpanded flow in the nozzle when fired during sea level. The results indicate a large spread in the measured magnitude of the side load and any realistic design must consider

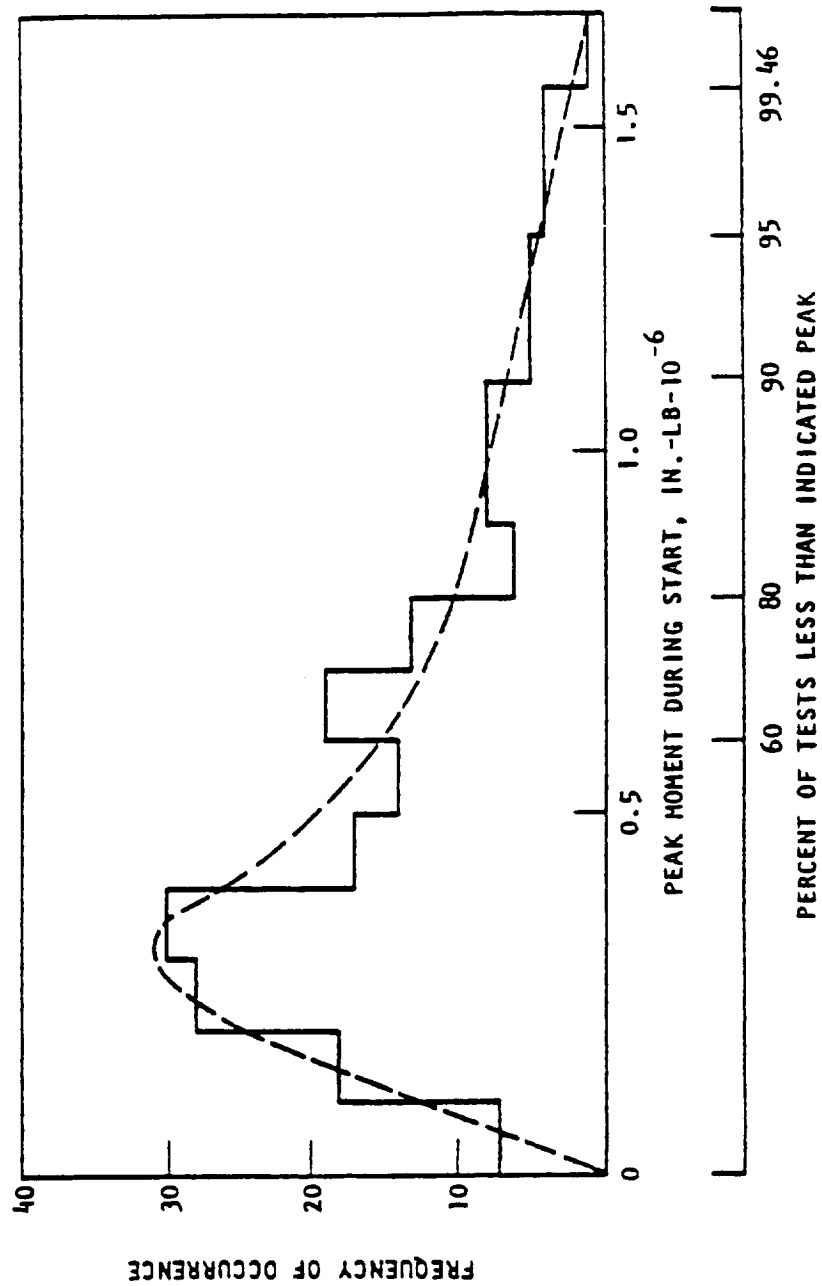


Fig. 5.4 Distribution of J-2 Engine Side Load Moments About Gimbal Point  
(Summary from 186 Engine Tests)

this inherent variation from firing to firing. Side load phenomenon is primarily a low frequency transient (up to 20 Hz) with oscillatory response due to ringing of the low damped structure. In the SSME engine, extensive analysis of strain gage measurements has indicated that side loads do not cause significant loading on the nozzle feed line itself. However, the effect of sideloads on nozzle and its attachments must be considered in all over expanded nozzle design.

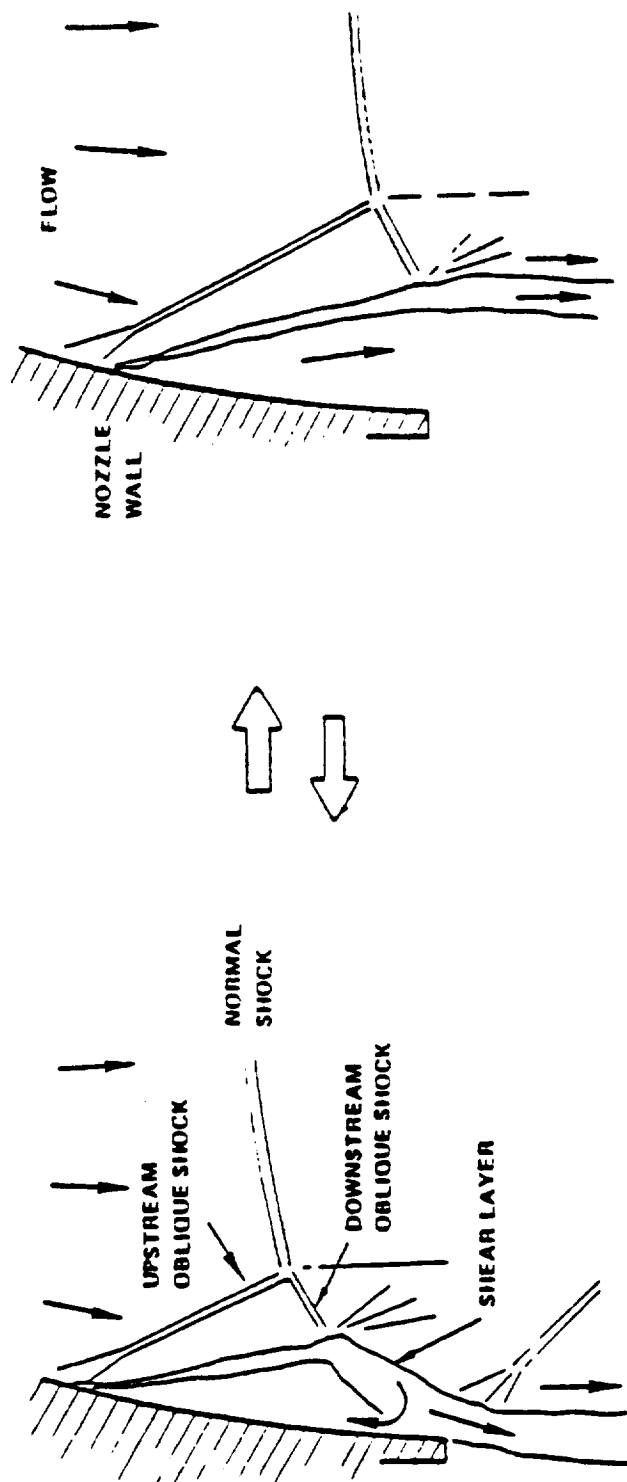
#### OSCILLATORY SHOCK TRANSIENTS

Shock transients which is the result of flow separation phenomenon occurs when supersonic flow from a nozzle discharge into ambient pressure which is higher than the nozzle gas pressure at exit plane. The nozzle flow adjusts itself to the back pressure through oblique shocks near the wall and a normal shock in the interior flow. For large area expansion nozzles with shallow exit angles as is the case in SSME bell contour nozzle, this can result in large pressure fluctuations at the nozzle exit. This happens when separated free shear layer impinge on the nozzle at a steep angle (Fig. 5.5). Due the steep impingement angle, more flow returns into the separated zone than that can be aspirated through mixing with the surrounding flow. Thus the pressure builds up and enlargement of the separation bubble occurs. As the separated region grows and reaches nozzle exit, the accumulated gas is discharged to ambient with the free shear layer detaching from the nozzle. Free jet pumping of the region between the shear layer and the wall causes subambient pressures in the region. As a consequence, the shear layer is pushed back on the nozzle wall and the cycle continues. This explanation of the phenomenon is supported by air flow tests on scaled models where exit wall pressures as low as one fifth and as high as twice the ambient pressure has been seen in data (Fig. 5.6). The frequency range of this transient in SSME is in the 100 to 500 Hz.

#### BREATHING MODE LOADS:

These loads also due to asymmetric flow separation effects and excites the nozzle in the low frequency range (<100 Hz). The presence of these loads can be seen in the motion pictures of engine firings near the exit of the





- SHEAR LAYER IMPINGES ON NOZZLE EXIT
- WALL PRESSURE INCREASES ABOVE AMBIENT
- SHEAR LAYER IS FORCED OFF NOZZLE WALL EXIT
- FREE JET PUMPING LOWERS WALL PRESSURE
- SHEAR LAYER IS PULLED BACK AGAINST WALL AND PROCESS REPEATS

Fig. 5.5 Driver Mechanism for Oscillatory Pressure Pulse on the Nozzle

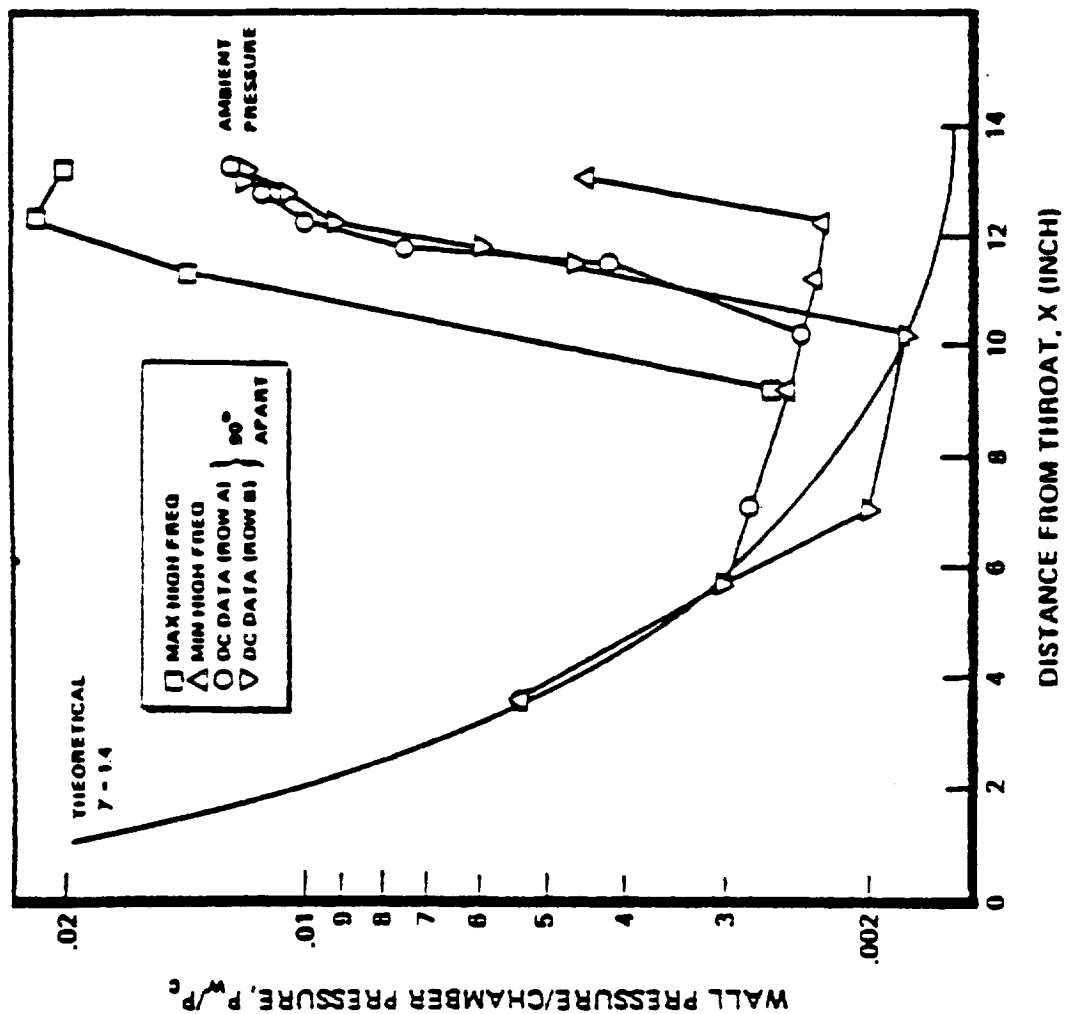


Fig. 5.6 Typical Wall Pressure Results from Air Flow Tests on Sub Scale SSME Nozzle Model for  $P_c/P_A = 106$

nozzle as a flickering white band, referred to as "teepees". The dynamic nature of these shocks must be emphasized by their circumferential movement and appearing and disappearing at random intervals of time accompanied by inflow of ambient air at transient. Motion pictures of SSME firings will show a relatively large (2 inch) diametrical ovalization of the nozzle aft manifold due to the breathing mode. For SSME nozzle feedline design, laboratory experiments have shown relatively low stresses are obtained in the critical areas of the feedline with 2-inch motion. Depending upon the feedline design, this mode has to be considered in the nozzle feed line designs.

#### Low Cycle Fatigue

Life estimates using static and dynamic analysis rely on the experimentally observed measurements from many engine firings. The presence of high level transient spikes is supported by strain gage and accelerometer data. The strain gage response on the nozzle feed line (Fig. 5.7), and the accelerometer response mounted on the oxidizer preburner (Fig. 5.8) show the maximum transient loads occur after few seconds of start or cutoff. These shock transients are seen by major components on a number of locations throughout the engine as evidenced by the test stand load cell response (Fig. 5.9).

Experimental observations on strain gage readings mounted axially near the steerhorn tee and manifold show a considerable variation in the maximum strain gage from test to test (Fig. 5.10). It can be observed that in majority of tests, a peak to peak strain is at a value that contribute very little to low cycle fatigue damage. In order to obtain realistic life estimates, strain ranges that can cause low cycle fatigue damage are analyzed from actual tests to provide a cumulative damage spectrum. A typical spectrum is shown in Table 5.1, and consists of listing of peak to peak strain levels and the corresponding number of cycles that were recorded at the indicated strain level. In this case, out of 41 tests, a total spectrum of 85 strain cycles above the range of 7000 microinches per inch was obtained.

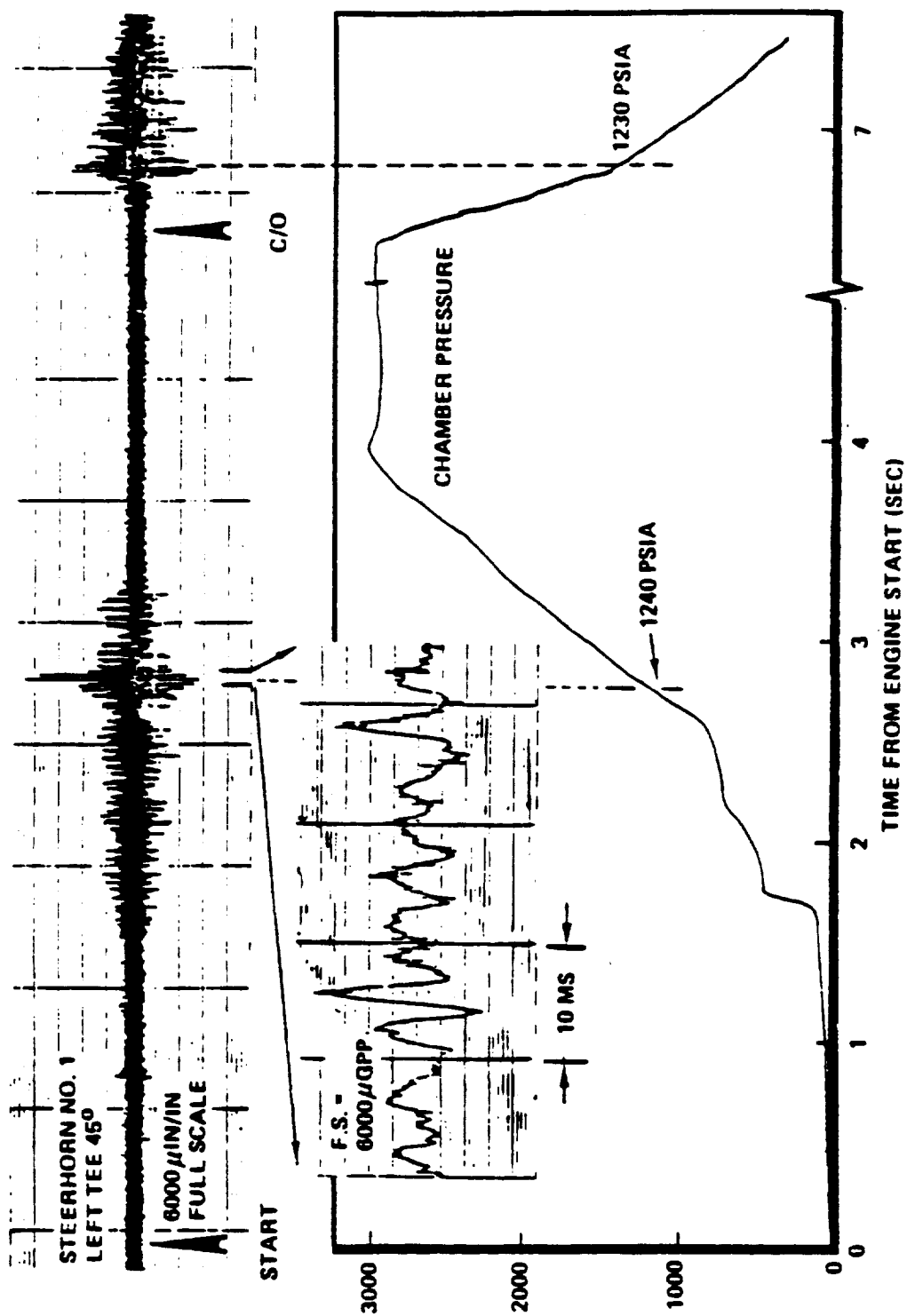


Fig. 5.7 Steerhorn Strains at Tee in Transient Operation

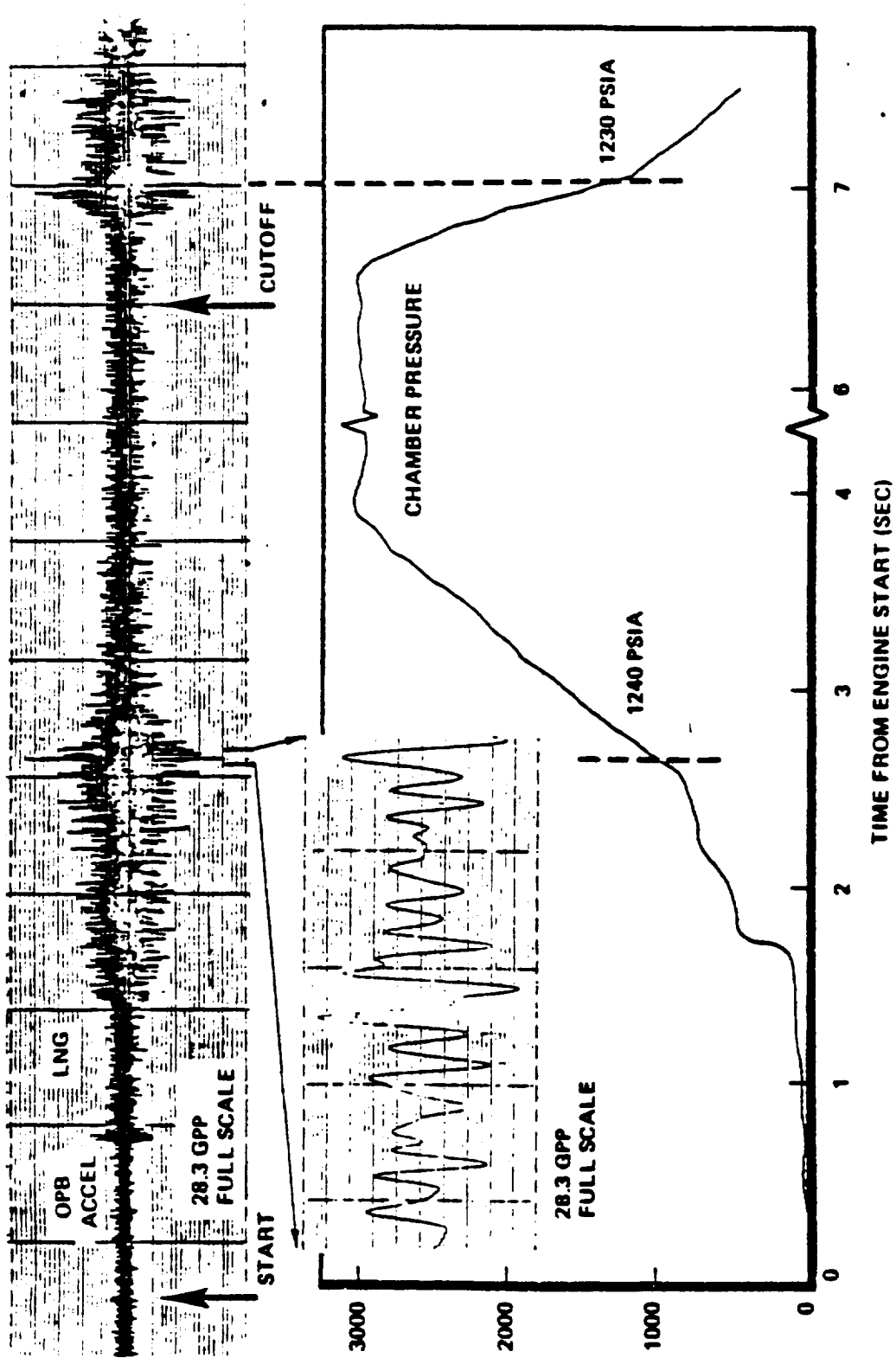


Fig. 5.8 Oxidizer Preburner Accelerations in Transient Operations

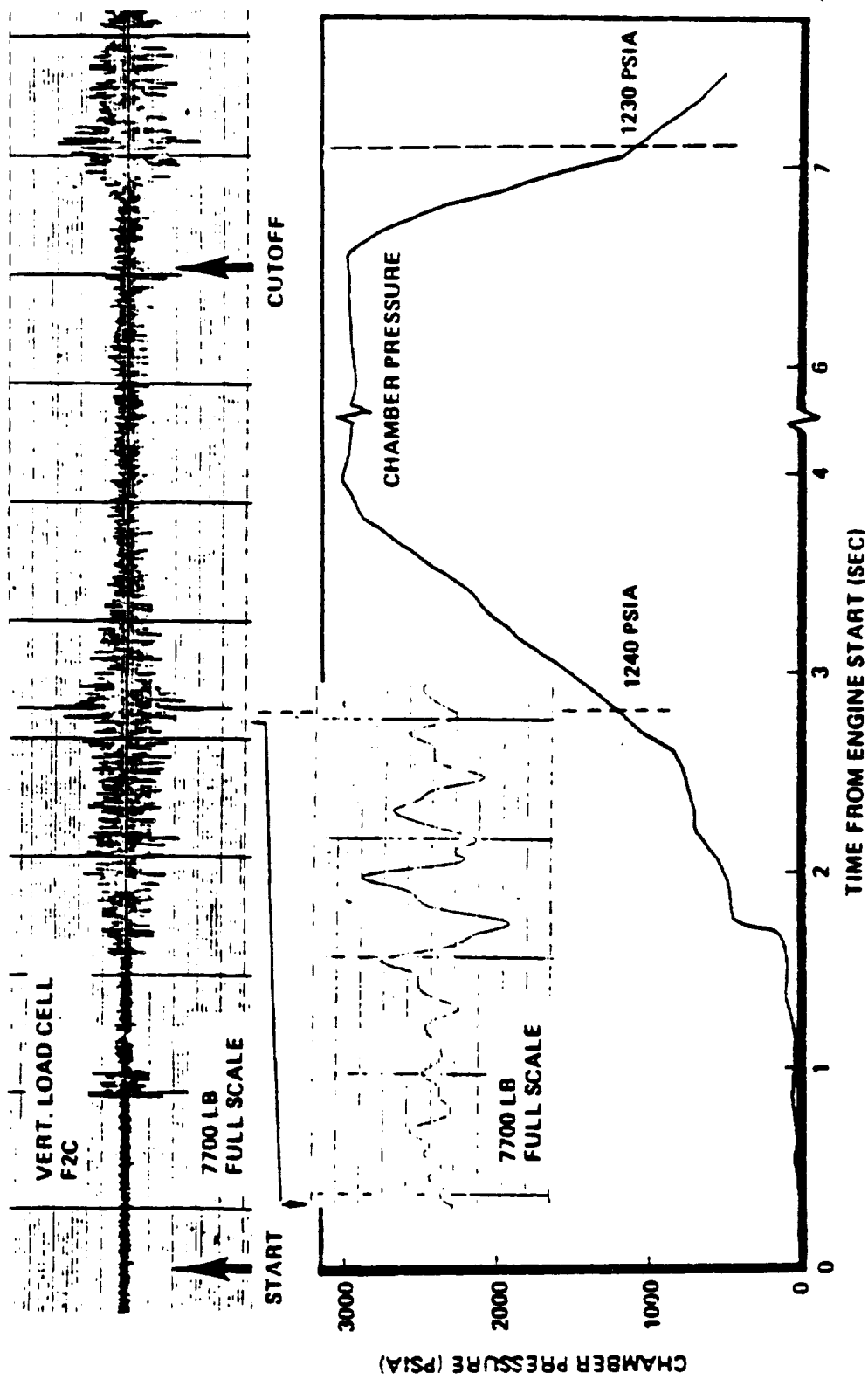


Fig. 5.9 Vertical Load Cells in Transient Operation

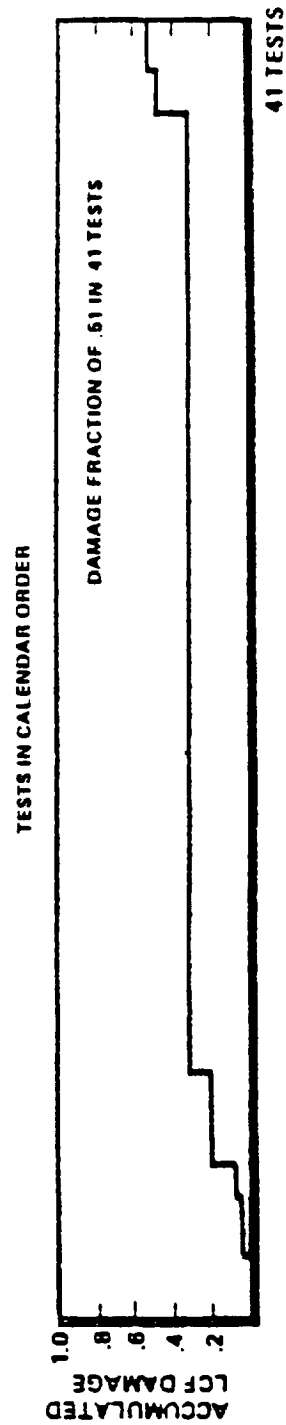
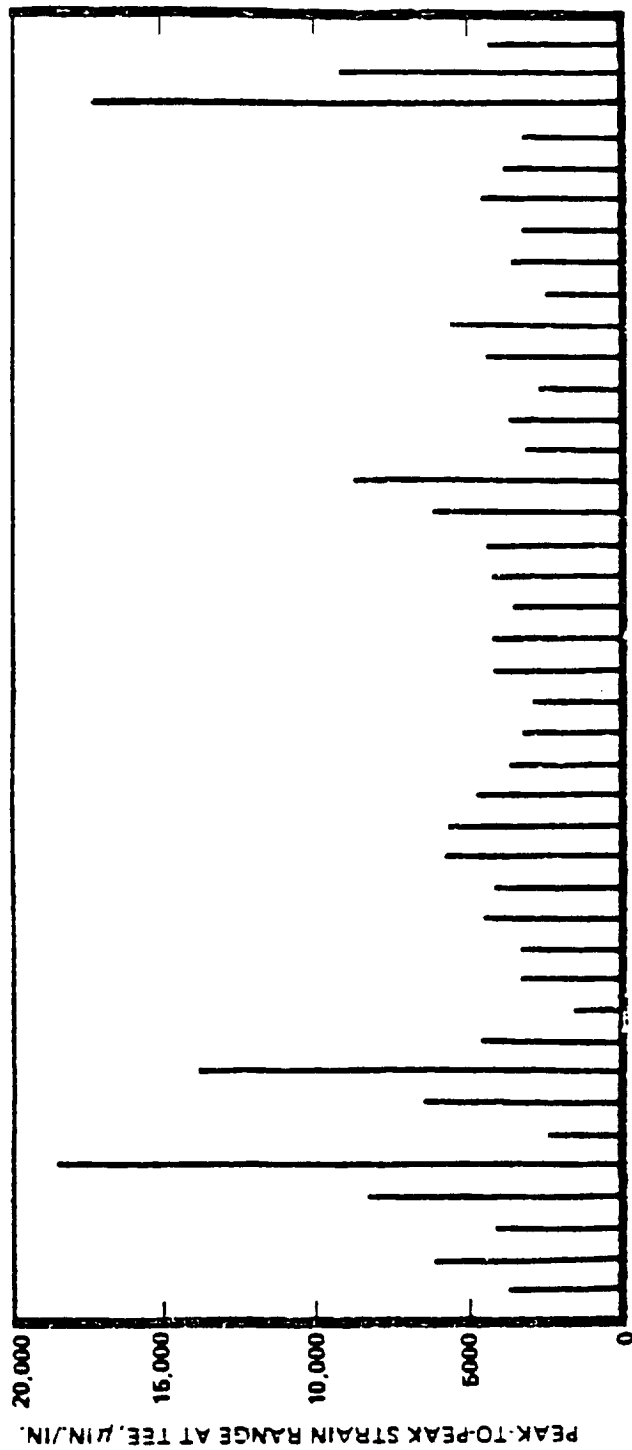


Fig. 5.10 History of Maximum Strains at the Nozzle Feed Line Tee  
(Summary of 41 Tests)

Strain, microinch per inch	No. of Cycles
19,500	1
15,000	2
13,500	1
12,500	1
12,000	2
11,500	4
10,500	13
8,500	25
7,500	36

Table 5.1 Cumulative Damage Spectrum (Summary of 41 Tests)



An analysis of the observed maximum strain ranges can be used to provide a framework of probabilistically estimating future maximum strain ranges. Kulomgrov-Smirnov goodness of fit test has indicated that the maximum strain range distribution do not deviate significantly from the log normal distribution. Using the distribution information, the design maximum strain range for evaluating safety factors for 99% best estimate (the level exceeded once in 100 tests) and the  $3\sigma$  level or 99.87% probability (the level exceeded once in 750 tests) as an upper limit that the hardware must survive without failure can be established.

#### STATIC AND DYNAMIC ANALYSIS

Static analysis include evaluation of stresses due temperature and internal pressure. However, the major loads in the nozzle feed line are the transient aerodynamic loads.

Dynamic analysis consists of random base excitation loading and pressure pulse loading. The base excitation loading is analyzed as a multibase excitation, both for transient and steady state conditions. A sample input accelerometer time history is shown in Fig. 5.11. The pressure pulse loading is essentially transient phenomena, the characteristic pulse frequency, amplitude and number determined from a statistical survey of several test cycles on subscale model tests. A typical pressure pulse that is used is shown in Fig. 5.12. The amplitude of the pulse is varied from a maximum at the nozzle exit to zero approximately 30 inches upstream of the nozzle. For SSME, scaled results indicate pressure pulses as high as 38 psi at a frequency range of 100 Hz. The last 30 to 36 inches of the SSME nozzle experience approximately 7 pulses during start and 3 pulses during cutoff. This corresponds to an outward oscillating load on the structure of the order of 200,000 lbs. While single line math models have been used to study the response of nozzle feed line in the post, accurate dynamic response calculation require the use of models that contain the nozzle, nozzle feed line and other lines that are attached to the nozzle structure. Accurate determination of the modes of the nozzle structure is an important aspect of the dynamic analysis. The responses of

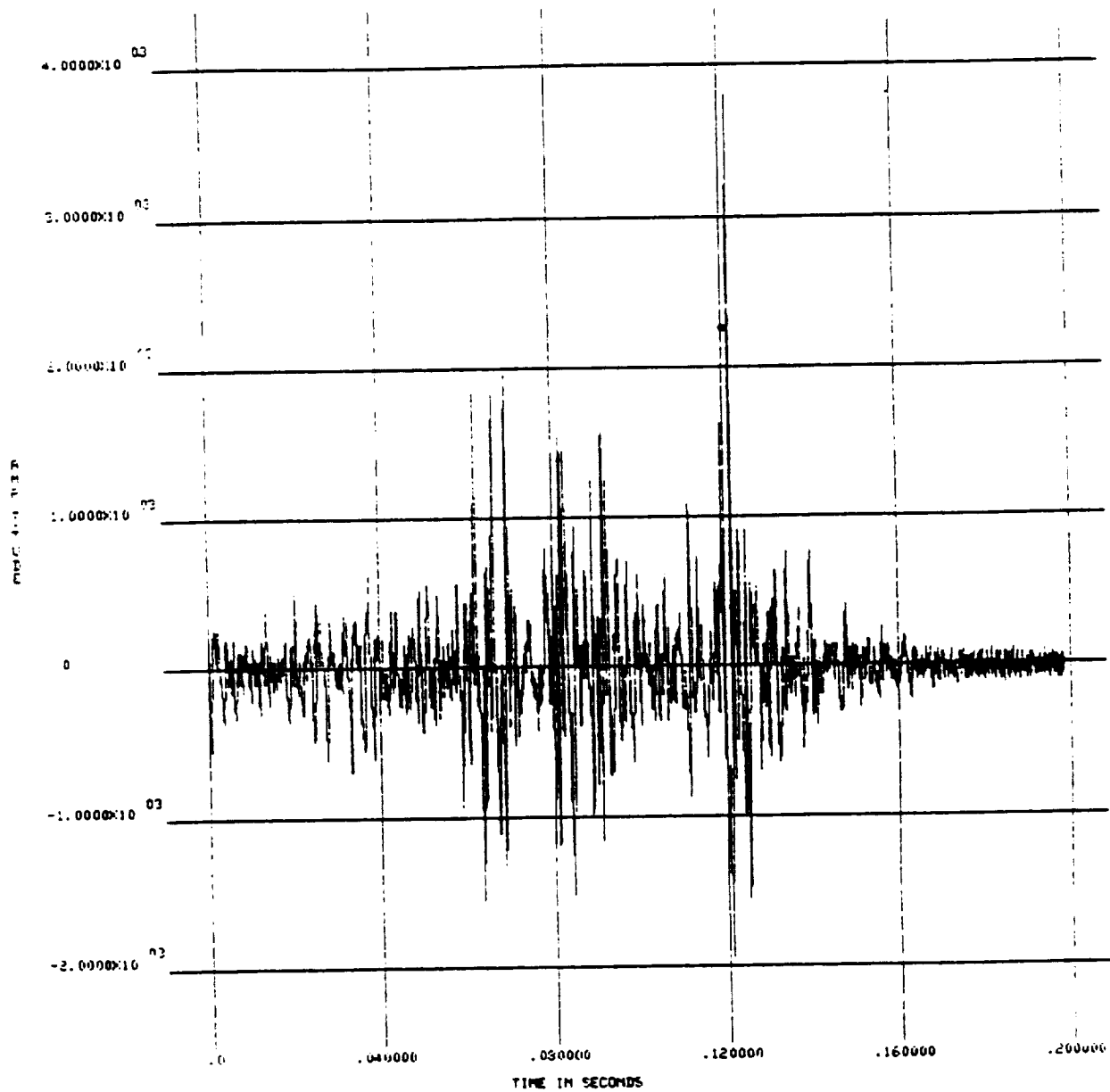


Fig. 5.11 A Typical Digitized Accelerometer Time History Data on the Nozzle

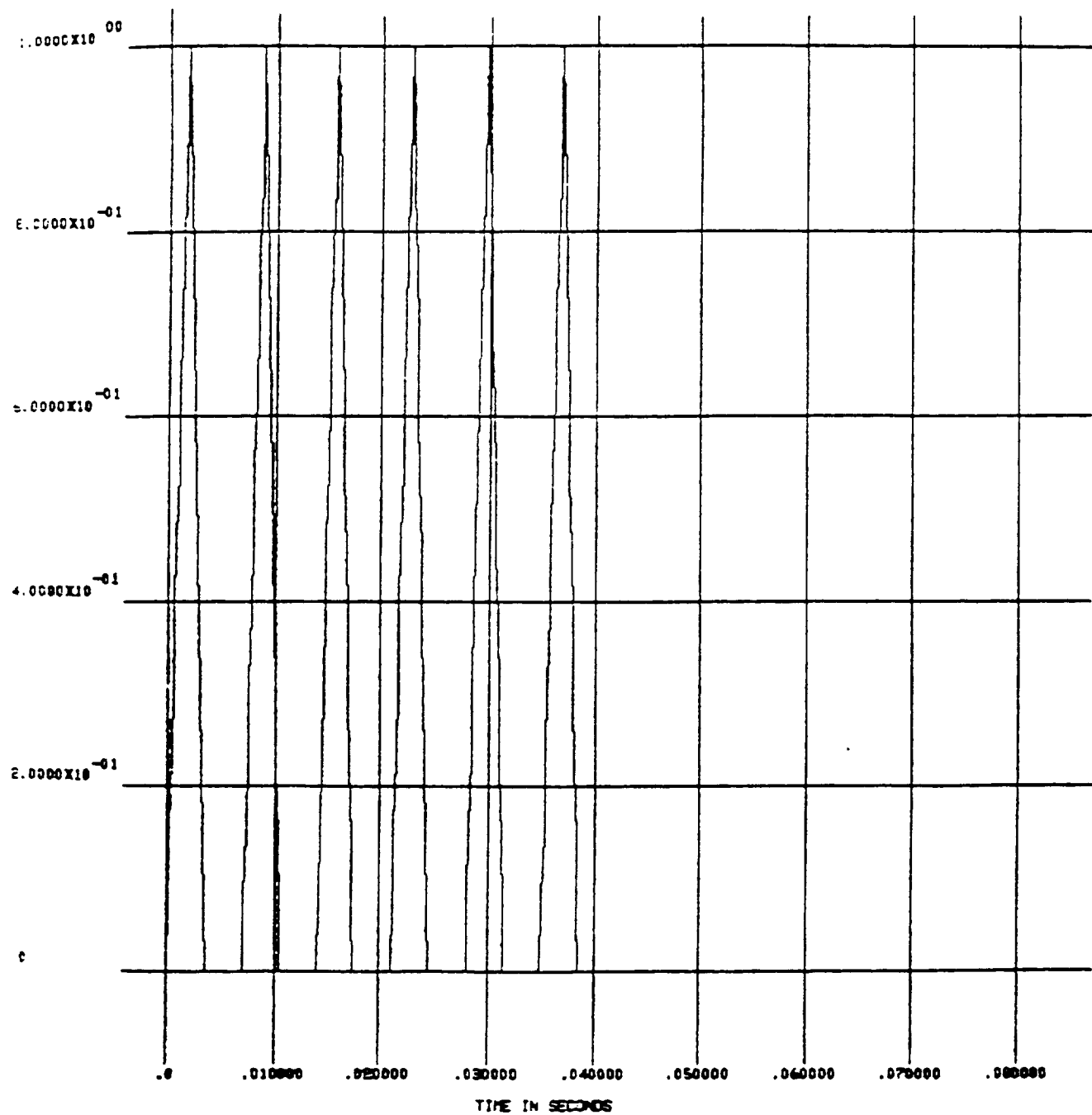


Fig. 5.12 A Typical Pressure Pulse Forcing Function Applied on the Nozzle

the nozzle feed line can be dominated by the responses of the more massive nozzle shell modes. For example, the SSME nozzle has about 400 modes in the frequency range of interest, 0 to 500 Hz, with a high gain shell mode illustrated in Fig. 5.13. The tubes contribute significantly to bending stiffness and the jacket contributes significantly to membrane stiffness.

#### FAILURE HISTORY

The SSME development program experienced two similar-appearing fuel feed line failures during the shutdown portion of two separate engine tests (Fig. 5.14). An in-depth investigation was carried out which determined the cause of the failure and established alternative designs. The investigation included detailed metallurgical examination, structural and aerodynamic analysis, extensive strain measurements on actual engine tests, redesign and follow up. The original nozzle feed line design (Fig. 5.15) experienced high strains at tee's due to aerodynamic oscillating shock transient pressure pulse already discussed earlier. The metallurgical examinations revealed the feed line rupture in one incident was the result of fatigue failure due to accumulated damage after 46 tests. The second failure was due to the combination of soft weld and high transient strains. In the redesigned nozzle feed line (Fig. 5.16), the maximum strain at the tee was reduced by 50% by modification of support restraint system and geometry of the feed line. The theoretical calculations of reduced strains in the nozzle feed line is supported by experimental measurements from actual engine tests.

#### SURVEY OF FINITE ELEMENT MODELS

Several different finite element models have been constructed to analyze the nozzle feed line. They include old single nozzle feed line design (Fig. 5.17), the three line nozzle feed line model incorporating current nozzle feed line design (Fig. 5.18), and the combined nozzle feed line and nozzle model incorporating new designs (Fig. 5.19 & Fig. 5.20). The single line models without the nozzle are primarily used to study the response of the nozzle feed line due to the measured base accelerations input at the hat band support

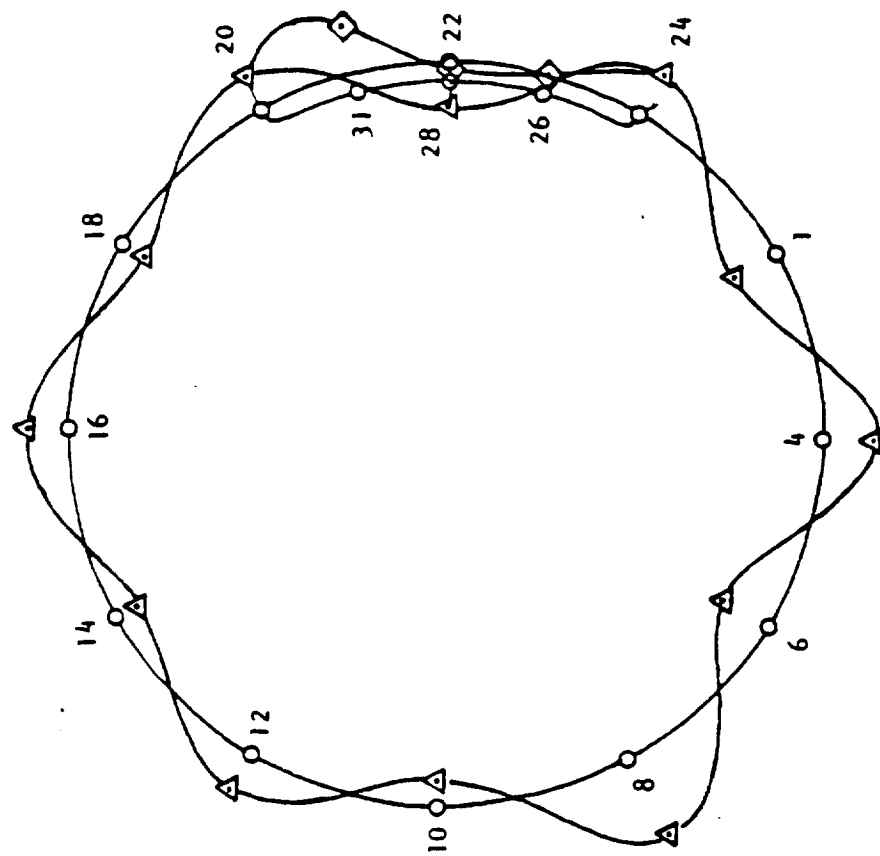


Fig. 5.13 SSME Nozzle Mode Shape, Sixth Mode, 259 Hz



Fig. 5.14 Ruptured Section of the Nozzle Fuel Feed Line

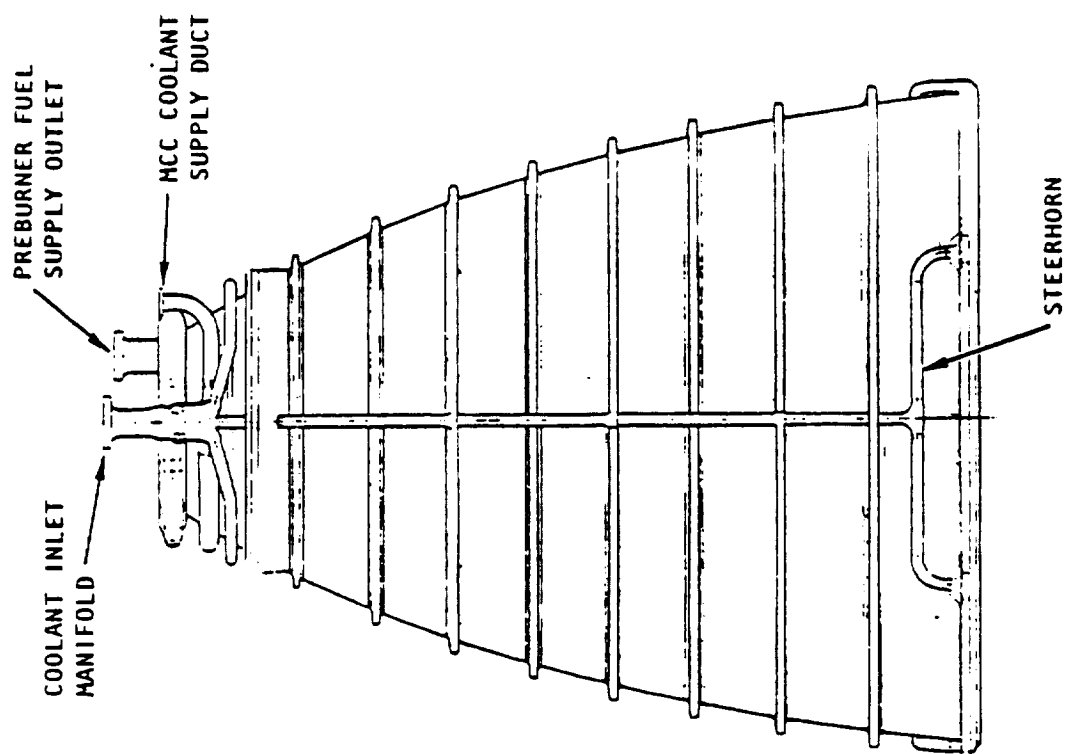


Fig. 5.15 Old Design of SSME Nozzle Fuel Feed Line

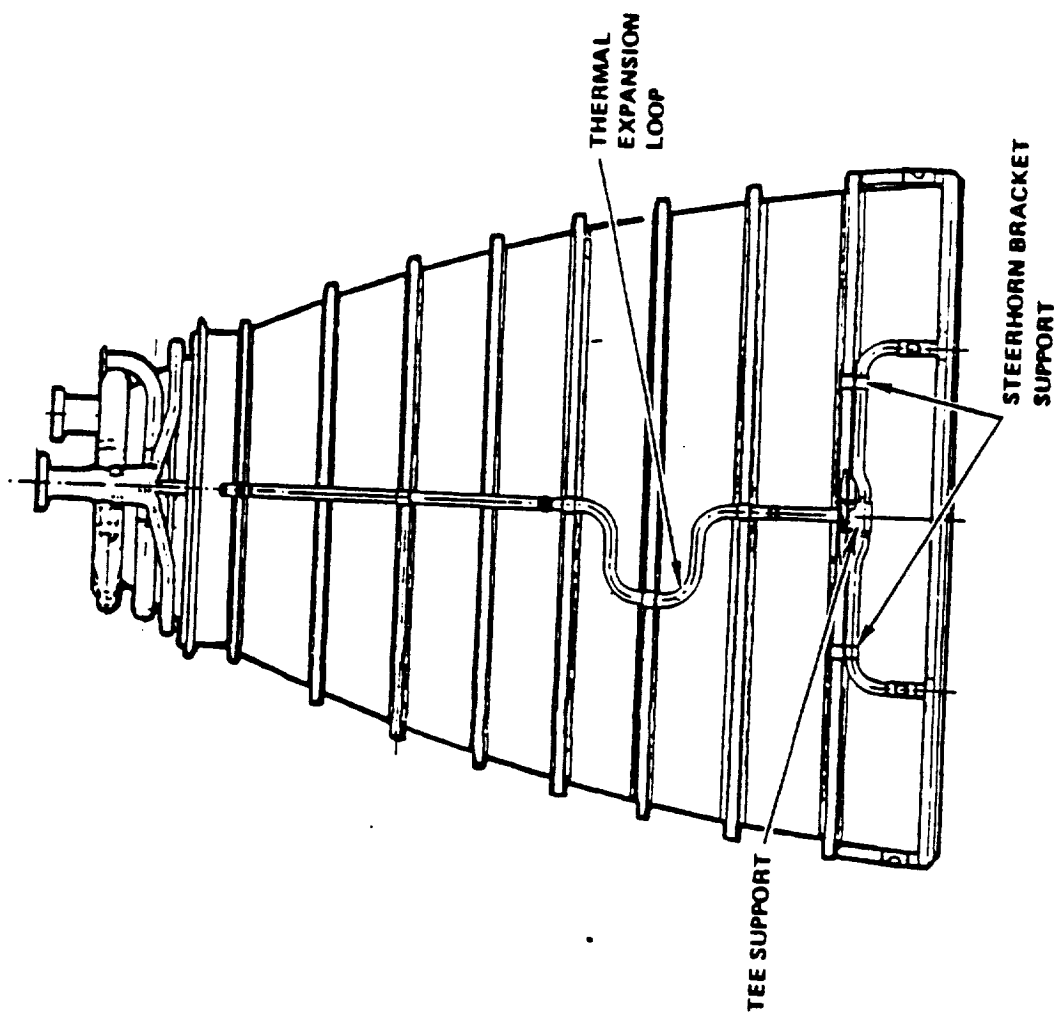


Fig. 5.16 Current Design of the Flight Nozzle Fuel Feed Line



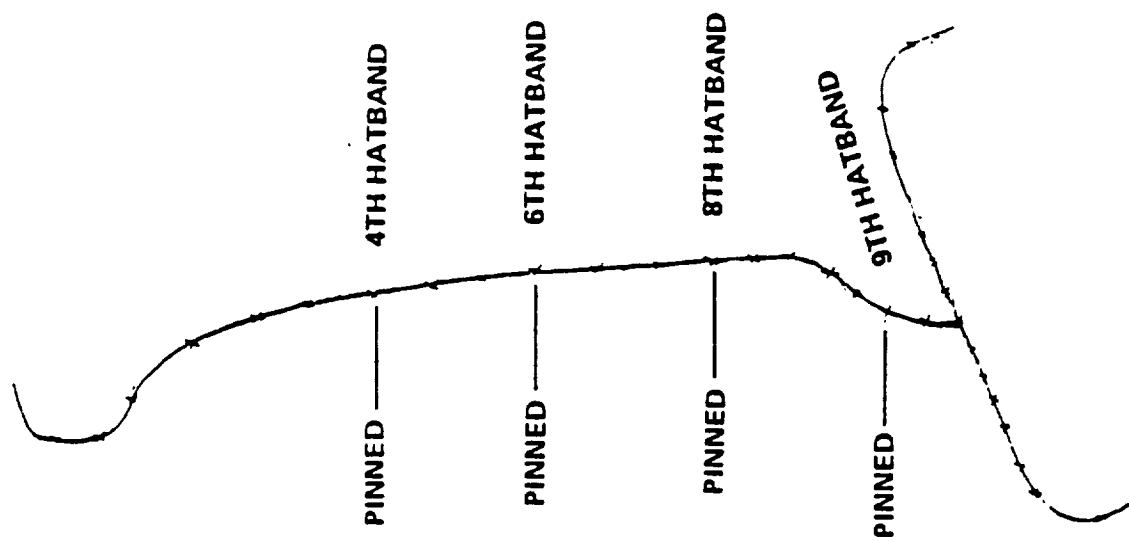


Fig. 5.17 Single Line Finit Element Model of the Nozzle feed Line with Old Design

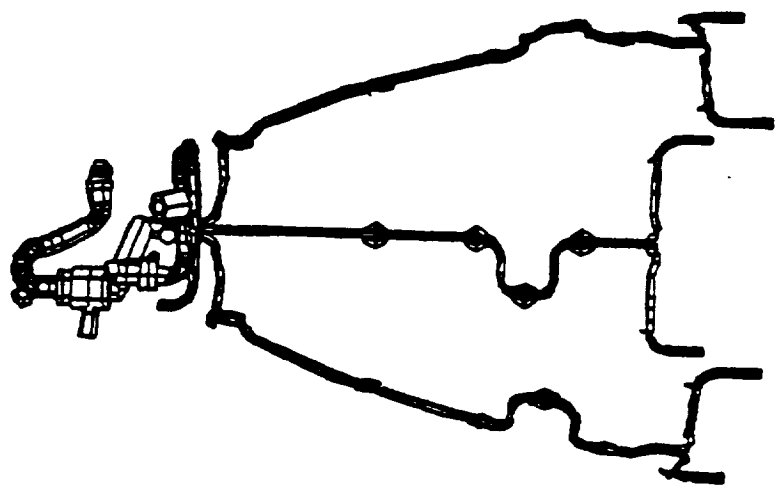


Fig. 5.18 The Three Line Finite Element Model of the Nozzle Fuel feed Line Design

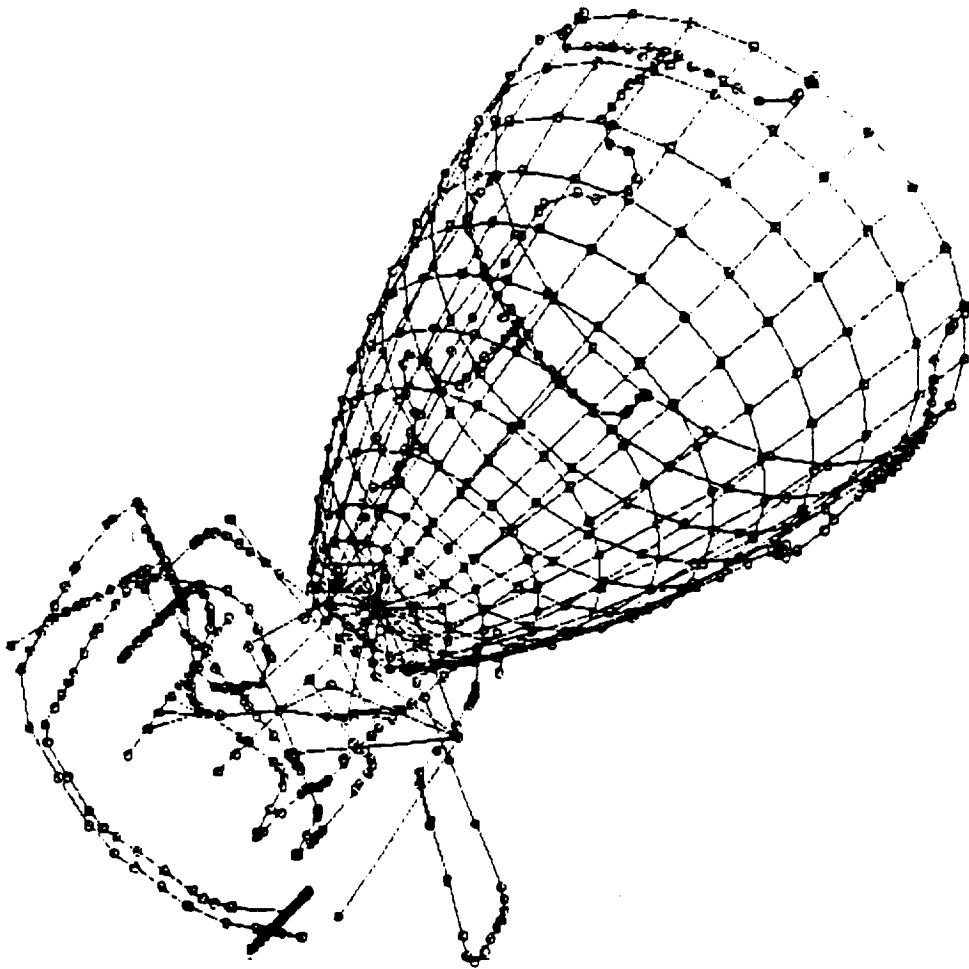


Fig. 5.19 A Typical Finite Element Model of the Fuel Feed Line, Nozzle and other Attachments to the Nozzle

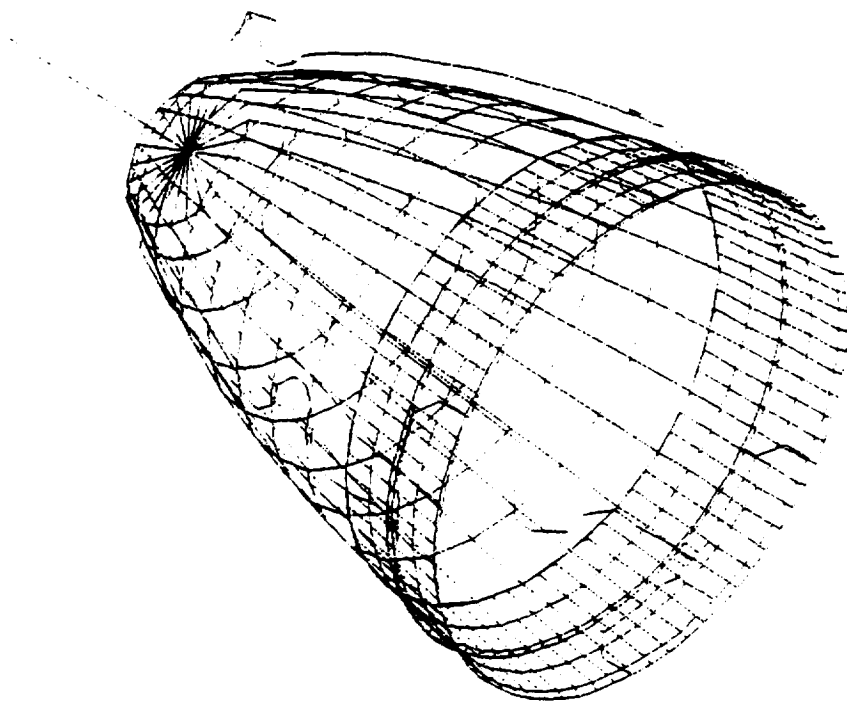


Fig. 5,20 A Typical Finite Element Model of the Fuel Feed Line,  
Nozzle and other Attachments to the Nozzle

locations. The finite element models that include the nozzle are used to study the response of nozzle feed line due to pressure pulse that is applied on the nozzle wall near the exit. The modeling of the nozzle requires orthotropic plate elements with appropriate stiffness to model tube wall, jacket and braze material. Experience has shown that modeling of hat bands using shell elements provide improved solutions over models that model hat bands as beam elements. The details of the two finite element models incorporating the current nozzle feed line design are shown in Table 5.2.

### SCOPE OF ANALYSIS REQUIREMENTS

#### Static Analysis

1. Linear beam finite elements with pipe cross sections
2. Orthotropic plate elements to model nozzle wall
3. Ovality considerations for elbow with flexibility and internal pressure factors
4. Temperature dependent material properties
5. Provision for selective deletion of restraints to model sliding joints
6. Inclusion of linear springs at support degrees of freedom to model support flexibility

#### Dynamic Analysis

1. Model extraction analysis
2. Multibase correlated and uncorrelated random excitation analysis
3. Pressure pulse excitation
4. Transient analysis using normal mode method or using direct time integration
5. Shock spectra analysis.

TABLE 5.2

[illegible]

Section 6  
Main Combustion Chamber Liner

## INTRODUCTION:

The combustion chamber liner is part of the thrust chamber assembly of a rocket engine where the essence of rocket propulsion, the acceleration and ejection of matter imparting propulsive force to the vehicle takes place. The design goals for a main combustion chamber design are maximum performance, combustion stability, durability, and minimum size and weight. A typical cutaway view of the SSME main combustion chamber is shown in Fig. 6.1. The SSME combustion chamber liner can be considered as the fourth candidate component for probabilistic structural analysis. The combustion liner is subjected to severe thermal cycles and durability calculations for the chamber liner require the simulation of thermal ratchet condition called "cyclic creep". The methodology should also account for large deformation analysis where the geometry of the structure needs to be continually updated as the structural analysis proceeds in the time domain. Some of these features are not necessarily exercised in the analysis of other components previously discussed.

### Geometrical Design Considerations

The geometrical shape of the top of the combustion chamber design can be spherical, cylindrical or near spherical design. Lower part of the combustion chamber is part of the nozzle shape usually a converging-diverging type. The flow velocities in convergent nozzle section is relatively low compared to the divergent nozzle section where very high flow velocities are involved.

Because of high combustion temperature (6000°F) and high heat transfer rates, thrust chamber cooling is a major design consideration. For example, the heat flux requirement has markedly increased from Redstone era to the J-2 and then to an almost 3-fold increase in SSME (Fig. 6.2). J-2 and RL-10 engines thrust chamber construction employed a regenerative cooling scheme using tubular construction. SSME has a channel wall design (Fig. 6.3) where liquid hydrogen is used as a coolant, a design concept that is very successful in high heat flux environments such as in SSME. The design consists of an outer structural jacket forming the shape of the combustion liner and carrying internal pressure and external loads from interfacing components. The liner is



attached only at the ends to the structural jacket. Structurally, the liner is required to strain out to contact the structural jacket, to react the differential pressure load between the coolant and the combustion gases.

#### Loading Environment

The liner loading is different than most other structures on the engine. It lays up against a structural jacket that is designed to take the primary loads on the engine. The liner has to support itself, act as a thermal barrier, heat exchanger, and duct hydrogen flow internally. The jacket is structurally designed to take all the internal pressure loads even though the liner's inherent structure supports some of it. The loads that need to be considered in the structural analysis of MCC liners are the chamber and coolant pressure, temperatures at the hot gas wall and the jacket, and the imposed end radial and tangential displacements due the displacements in the structural jacket. Dynamic loads do not play a significant part in channel wall liner design.

#### Thermal Loads

Thermal loads play a critical role in the analysis and design of chamber liner wall. It is subjected to severe thermal cycling. During prechill and cutoff conditions, the complete liner is approximately at  $-400^{\circ}\text{F}$ . During steady state operation, the temperature profile on the hot gas wall varies along the length (Fig. 6.4), the maximum temperature ( $1100^{\circ}\text{F}$ ) occurring at couple of inches upstream of the thrust section. It is known that due to injector anomalies, the temperatures can be higher at localized hot spots. The temperature distribution at a cross-section of the channel wall liner can be determined using 2-D finite difference models and a typical temperature distribution is shown in Fig. 6.5. Localized hot spots can be simulated by modifying the heat transfer film coefficients in a localized zone. Structural analysis can be performed at these localized hot spots to estimate cycle life to cracking.

#### Pressure Loads

The chamber liner is also subjected to differential pressure between the coolant passages and the main combustion chamber pressure. A typical time history of the chamber pressure and a typical time history of the coolant pressure are shown in Fig. 6.6.

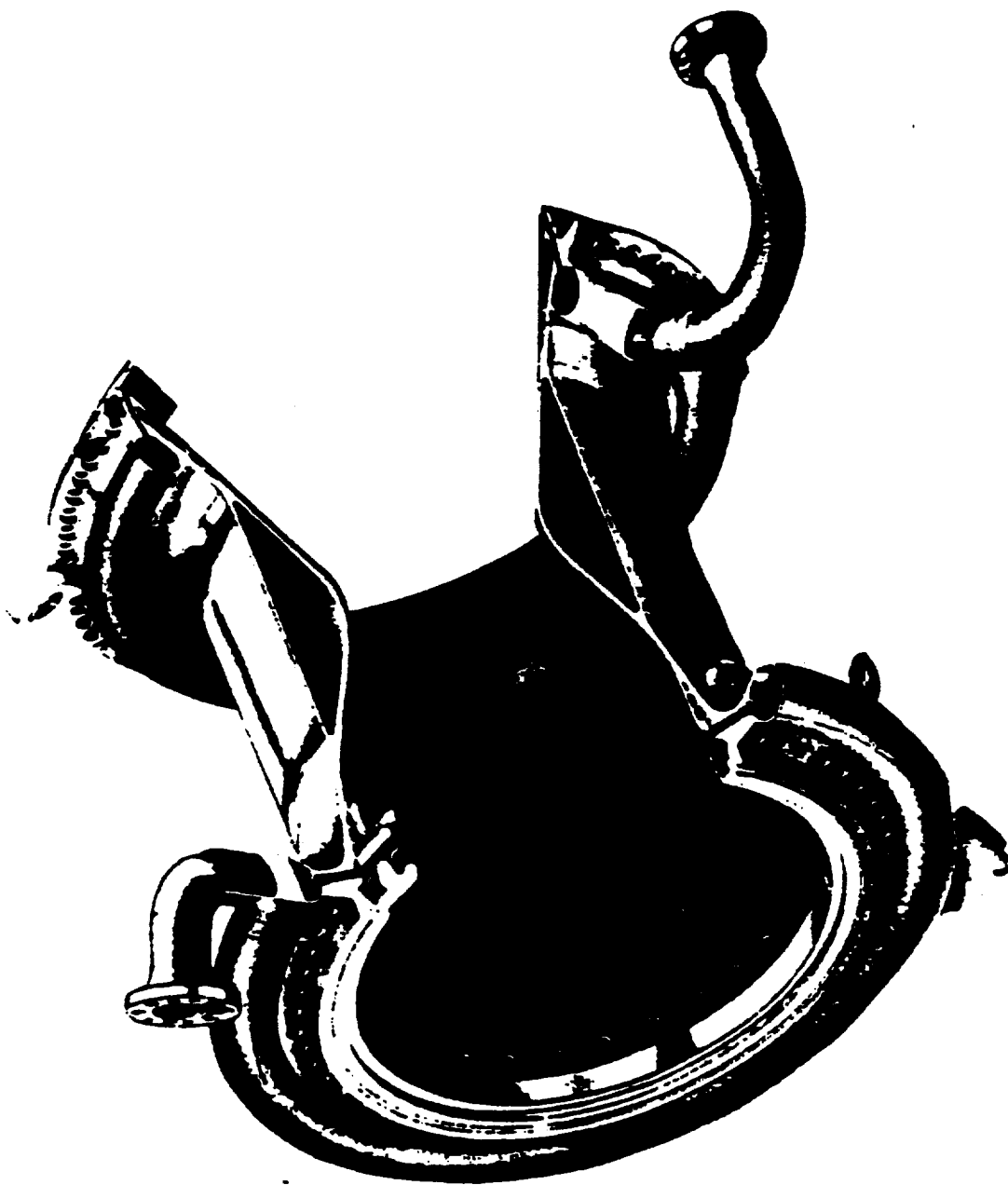


FIGURE 6.1 SSME MAIN COMBUSTION CHAMBER

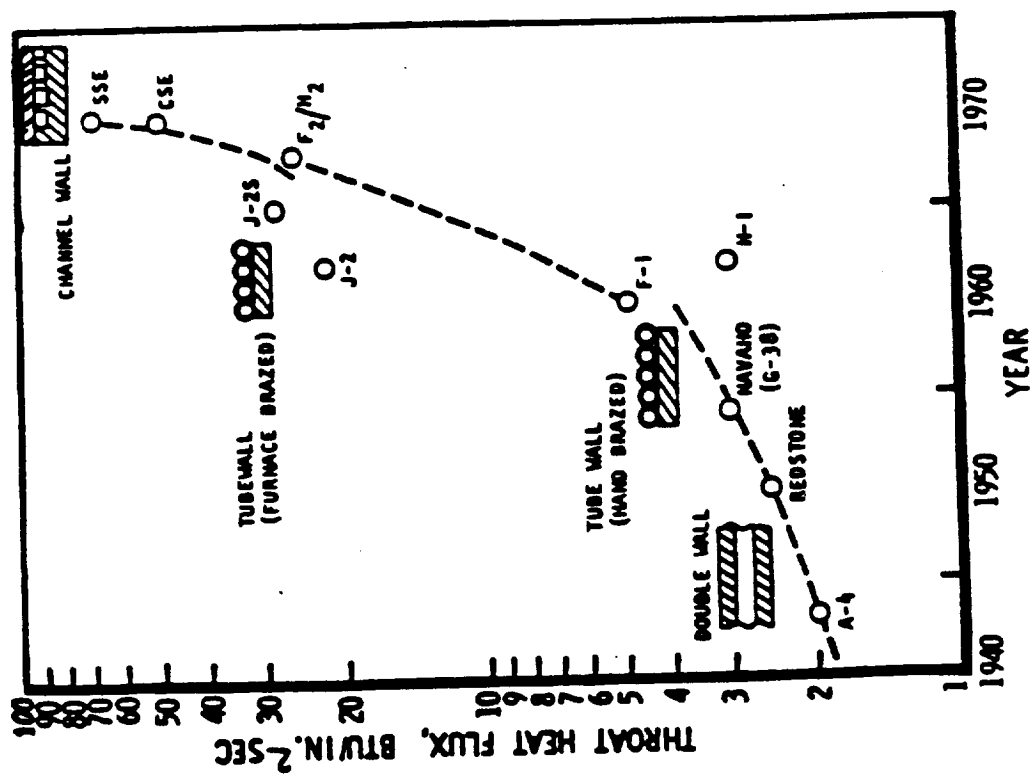


FIGURE 6.2 THROAT HEAT FLUX CHRONOLOGY

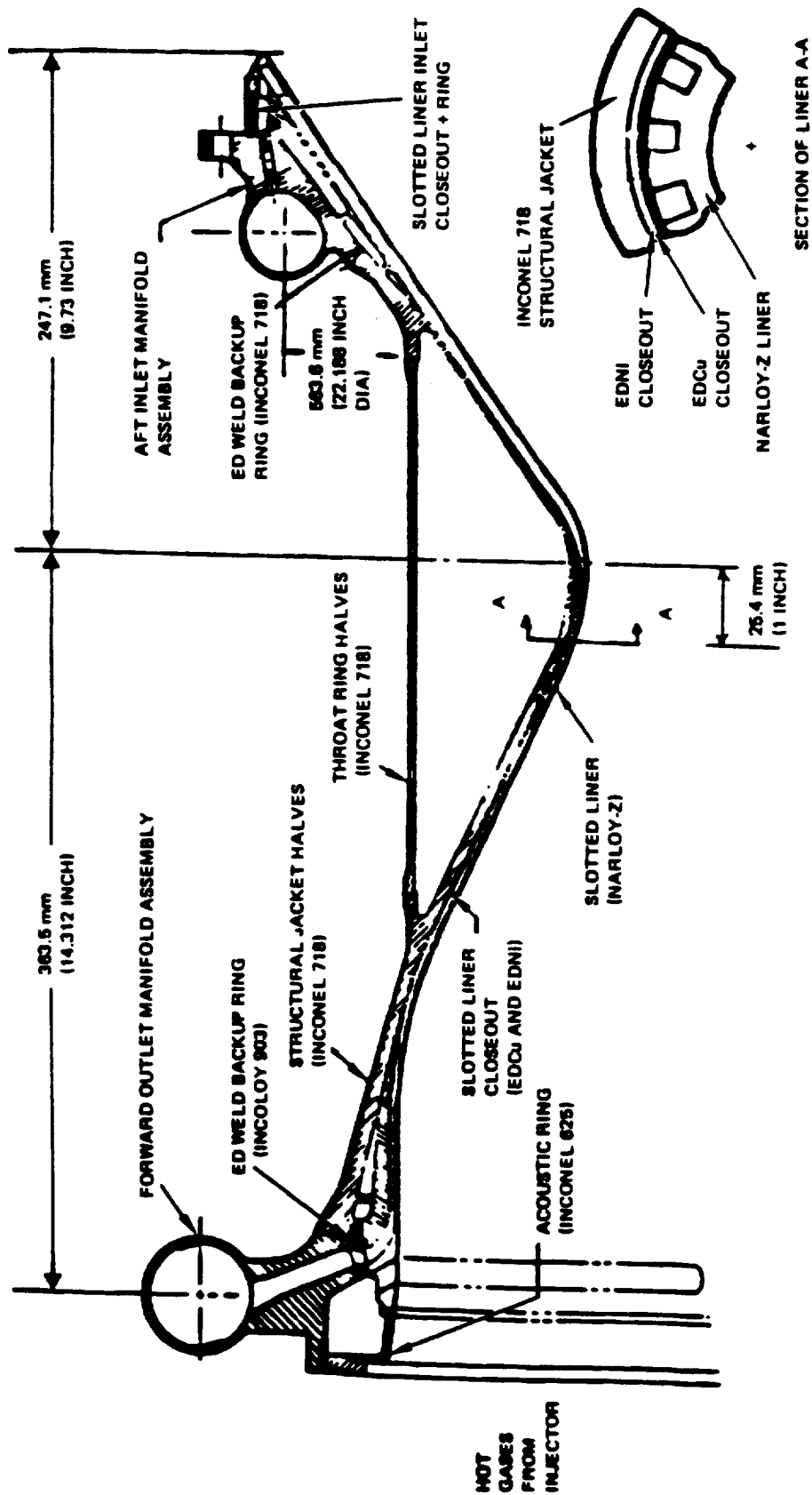


FIGURE 6.3 SSME MAIN COMBUSTION CHAMBER CROSS SECTION

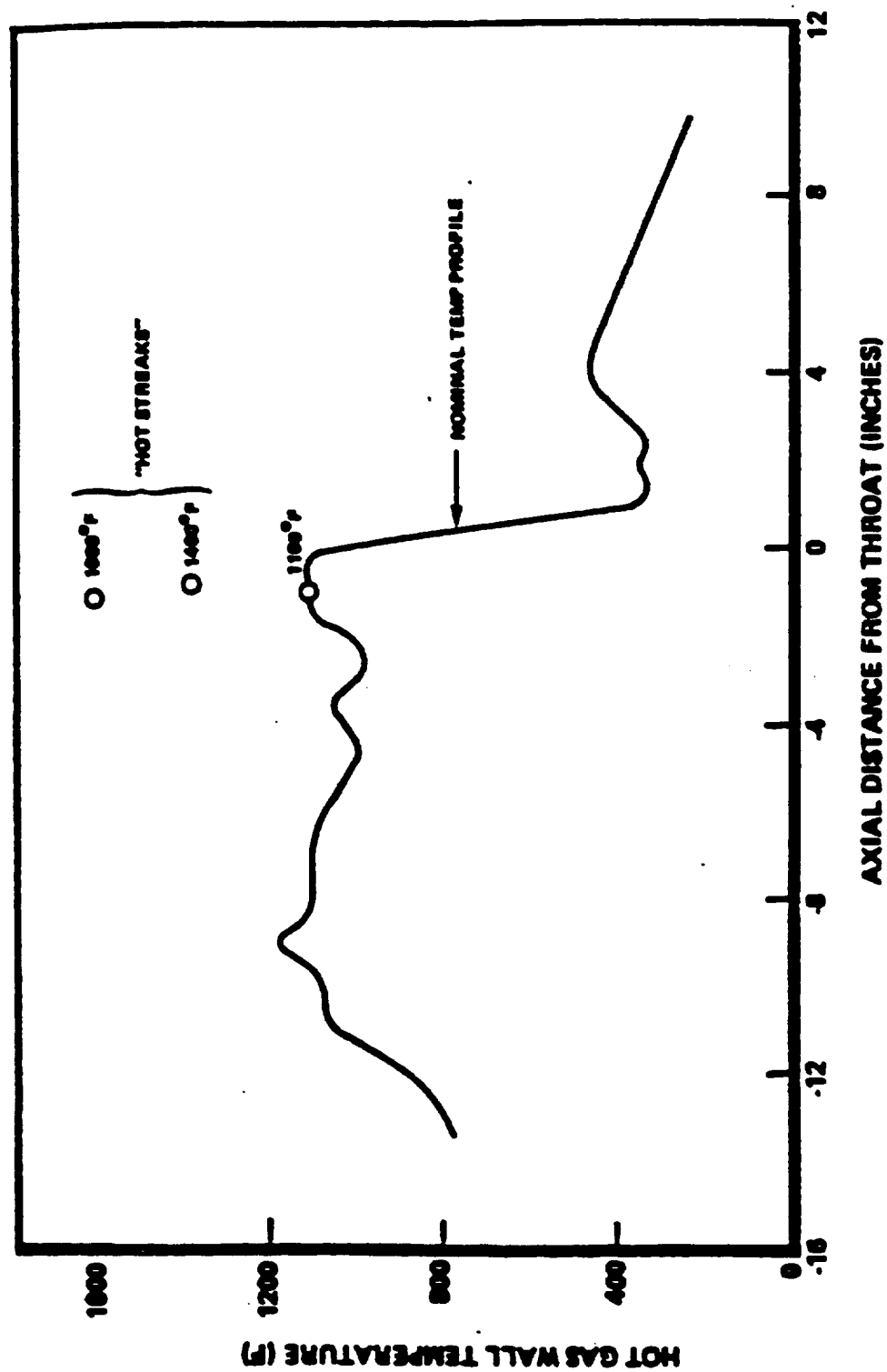


FIGURE 6.4 TYPICAL SSME MCC WALL TEMPERATURE AT RPL

1355	1350	1353	1350	1355	1355	HOT GAS WALL
865	852	852	852	855	855	
565	555	555	552	570	672	COOLANT WALL
991	953	925	953	935	930	
252	237	133				
99	78	12				
-11	-25	-72				
-92	-31	-123				
-127	-130	-135				
-155	-155	-173				
-171	-173	-133				
-179	-182	-191	-199	-232	-203	CLOSE-OUT
-167	-133	-131	-133	-196	-196	
-163	-182	-131	-132	-182	-181	

S.I. Conversion  
K = 5/9 (F + 460)

COOLANT CHANNEL

FIGURE 6.5 TYPICAL COOLANT CHANNEL TEMPERATURE DISTRIBUTION AT RPL

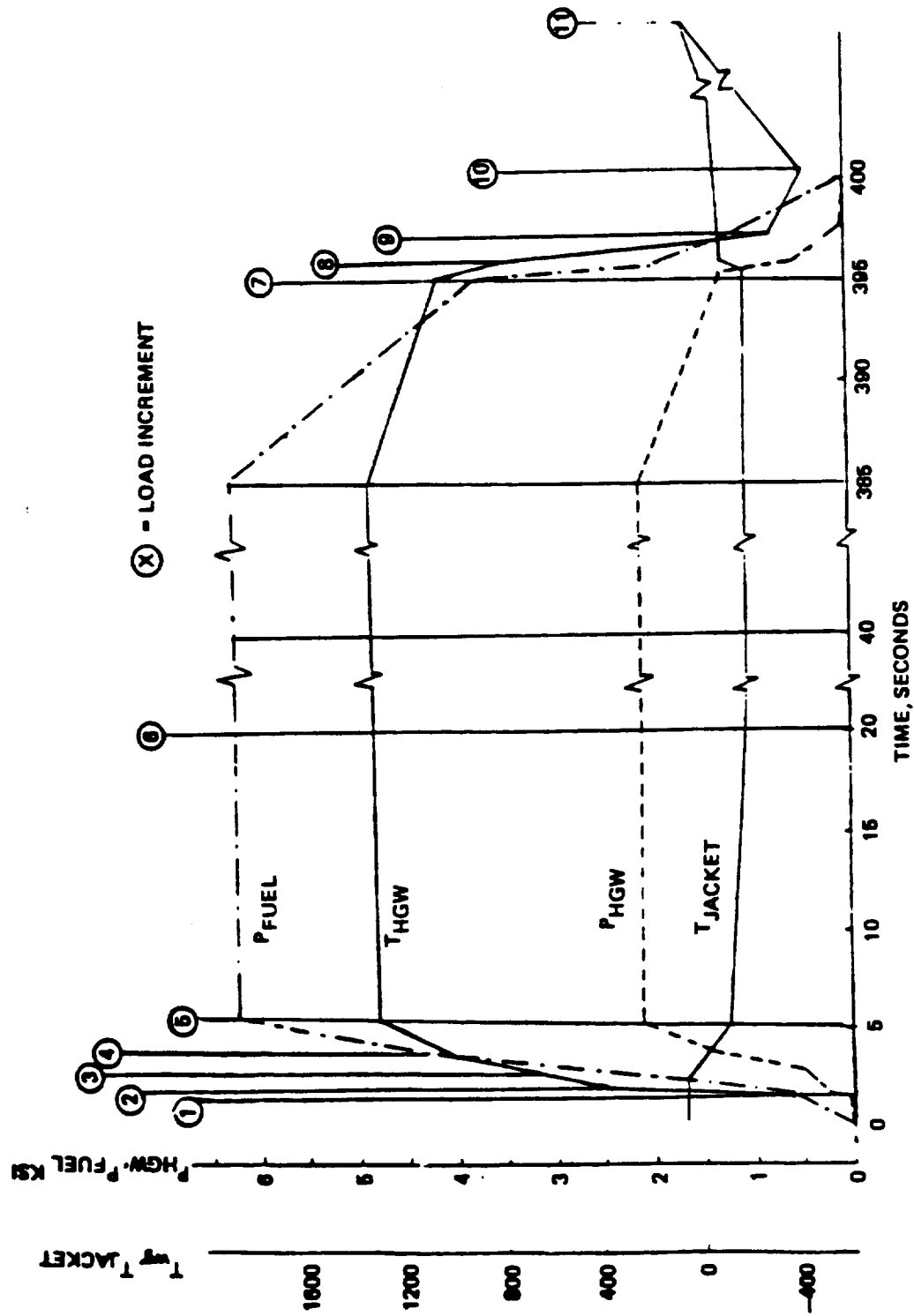


FIGURE 6.6 SSME MCC TEMPERATURE AND PRESSURE TIME HISTORY

### Imposed End Displacements

The effect of other loads on MCC are passed to the liner as radial and axial deflection of the structural shell at the attached end points. It must be noted that the liner is not attached all along the MCC, its motion is restricted by the motion of the external jacket as described below.

The MCC as manufactured can have a maximum radial gap between the liner outer diameter and the structural jacket inner diameter of 0.020 inch. During the start prechill, the cold hydrogen flowing through the liner coolant channels causes a thermal contraction of the liner which increases the liner/jacket radial gap. During this time, there is a negligible cooling effect on the jacket due to the cold radiation from the liner. Then, upon ignition, the combustion pressure increases and the weak liner expands radially, like an inner tube in a tire. At a fairly low pressure it contacts the jacket inner diameter. Once liner/jacket contact is made, the jacket mean temperature experiences a fairly rapid drop in temperature to approximately  $-100^{\circ}\text{F}$ , while combustion pressure is increasing to its steady-state value. During this time, there is a net radial growth of the jacket from the positive radial displacement of the jacket due to combustion pressure. This displacement is partially offset by the negative radial motion of the jacket as it drops in temperature. After steady-state combustion pressure is reached at 4.9 seconds, the jacket continues to get colder over the next 150 seconds, resulting in a decrease in the jacket radial displacement and axial strain.

At this point, pressure and thermal equilibrium loads in the jacket have been achieved. During shutdown, combustion pressure is throttled down to 65% of rated power level, and then the engine is shut down. During shutdown, the purge flow of hydrogen through the coolant channels rapidly chills the liner to  $-400^{\circ}\text{F}$ , and the liner separates from the jacket. When combustion pressure reaches zero, the mean temperature of the jacket has warmed up to approximately  $-80^{\circ}\text{F}$ . The jacket eventually warms back up to room temperature and returns to essentially a line-to-line contact position with the jacket.



### Hot Spot Cracking

It is known that localized hot spots trigger cyclic creep mode of local channel cracking. Hot fire tests of this class of chambers show that locally the hot gas wall material at the center of the channel progressively thins from the inside of the channel and the material moves and thickens the adjacent material (Fig. 6.7). This phenomena is attributed to a thermal ratchet condition termed "cyclic creep". In some cases the center of the channel thins sufficiently such that the wall fractures with an attendant coolant loss. Small cracks have occurred mid-land on SSME, but they have not grown large enough to cause a problem. The cyclic creep mode of local channel cracking has usually been associated with local hot spots from injector effects.

Detailed measurement of channel geometries indicate that material volume is essentially conserved; the thinned section is balanced by the thickened shape at the channel corner. The cyclic creep phenomena requires a biased load--structural duty cycle to cause an increase to the average maximum hoop strain in the mid channel for each duty cycle. The observed thinning and distortion of the channels show that the mid channel thinning is the result of local biased negative radial strain and a compatible increase in a local hoop strain. The reshaping of the corner is dominantly a large shear strain that resolves into plus and minus principal strains that thicken the corner zone. It has been observed that one of the necessary conditions for the thermal ratcheting to occur is the presence of localized hot spots.

During the development of SSME, provisions for film cooling of the chamber liner wall were made with the addition of film coolant holes. This reduced the overheating experienced in the local circumferential areas of the combustion chamber. It was also discovered that surface roughening caused by hot fire operation contributed to escalating hot loads and further roughening and degradation of the hot gas wall. Polishing of the MCC liner between tests with fine grit sand paper is used as a method for reducing deterioration of the hot gas wall. The smoother hot gas wall surface is credited with reducing local distress, especially on long duration tests.

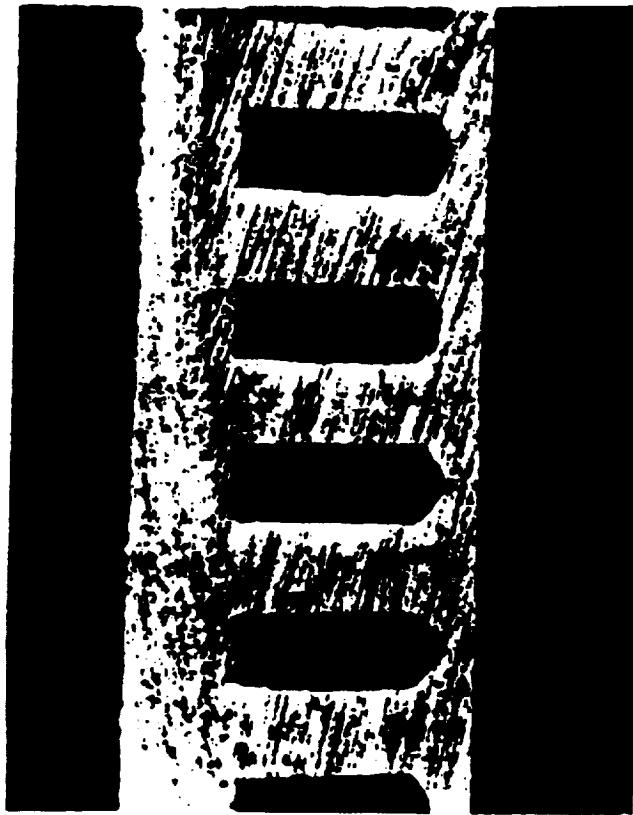


FIGURE 6.7 THROAT SECTION OF THE SSME-MCC SHOWING THE THINNED HOT GAS WALL

### Static Analysis

Channel wall combustion chambers are initially sized by hand solutions followed by local detailed finite element analysis of a channel cross section. The finite element analysis utilizes a duty cycle considering the prechill, start, mainstage and cutoff conditions for temperature, pressure and any movement of the support jacket. The conditions that maximize the strain range are utilized in defining the duty cycle. In order to adequately analyze this type of structure, the standard structural considerations of strength, creep and low cycle fatigue must be supplemented by a cyclic thermal ratchet analysis.

A duty cycle analysis may require tens or hundreds of cycles prior to a failure condition. In cases where a stabilized condition occurs in one or two cycles, the analysis can be terminated at this point, and the failure or cracking condition accurately extrapolated. For the structural response of the MCC, this is not possible, since the cyclic strain condition does not stabilize; and the gradual geometric distortions are significant in changing the rate of strain cycling and maximum strain. It might also be prohibitively expensive to consider analyzing every duty cycle. A compromise is to utilize an approximate methodology that analyzes a series of duty cycles to determine the conditions consistent within a particular portion of the distortion sequence, extrapolates the geometry to a geometric condition further into the deformation pattern, and then analyzes another series of duty cycles to determine local conditions at this point. It should be noted that this is a specialized analysis technique, not a general methodology applicable to a large class of problems. The extrapolation technique requires that the geometric distortions further into the life cycle can be linearly approximated from a sequence of previous distortions. The analysis technique requires a balance of the cost in performing sufficient duty cycles to determine a local, stabilized condition and the extent of the extrapolation further into the duty cycle where the rate of cyclic change is not significantly different. In one study a standardized approach of developing a 5 duty cycle detailed analysis followed by a 15 duty cycle extrapolation of the geometric shape was utilized. The model was then rerun based on the distorted geometry for the next sequence of cycles.

This procedure develops the distorted geometry shape for the analysis, but a major drawback is it does not track the strain history through the total history. The strain history is tracked only within each of the individual 5 duty cycle analyses. However, it is rather a simple task to track the accumulated thinning of the channel wall.

The 2-D finite element analysis results using the above approximate procedure can simulate the cyclic creep phenomenon at localized hot spots (Fig. 6.8). The gradual change in the cross section can be noted as the cycling progresses.

Figure 6.9 is a typical multiple duty cycle plot of the stress-and-strain history of the element located mid-channel at the hot wall. The effective stresses and strains are plotted with their sign obtained from the hoop stress components. (Note: effective stress and strain are only magnitude quantities).

The duty cycle increments and hot wall temperatures are noted on the first cycle to help follow the duty cycle. The point first goes in tension during the prechill operation, followed by a rapid drop to a high compressive state, then reduces in stress magnitudes as the material strength decreases with temperature and from creep/relaxation effects to the maximum compressive strain (Point 6). The stress decrease from increment 2 to 6 is mainly due to changes in yield stress with temperature. During the throttle back to 65% of thrust, the point moves to a tension stress state even though the total strain is a high compressive plastic strain. As cutoff starts, the element is driven to a high tension, high positive strain point. Finally, after the test duty cycle and the part is stabilized at room temperature, the element is in compression with a large tensile, plastic strain. Each duty cycle progressively shifts to a more positive strain position. This is indicative of a thermal ratchet or cyclic creep phenomenon and resultant channel wall thinning.

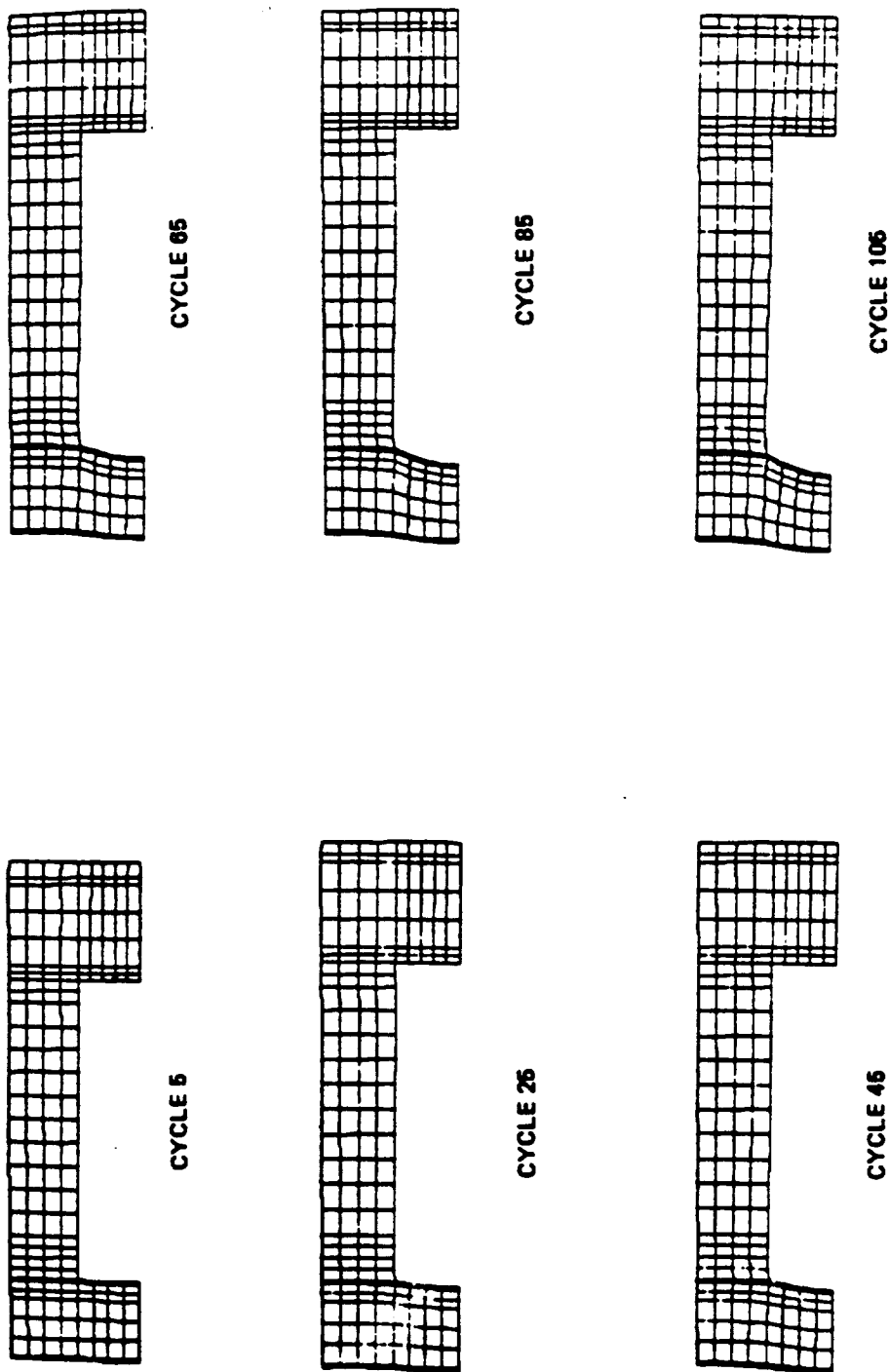


FIGURE 6.8 GEOMETRIC SHAPE CHANGE WITH CYCLING OF BASIC SSME CHANNEL CONFIGURATIONS AT 135% FPL hg

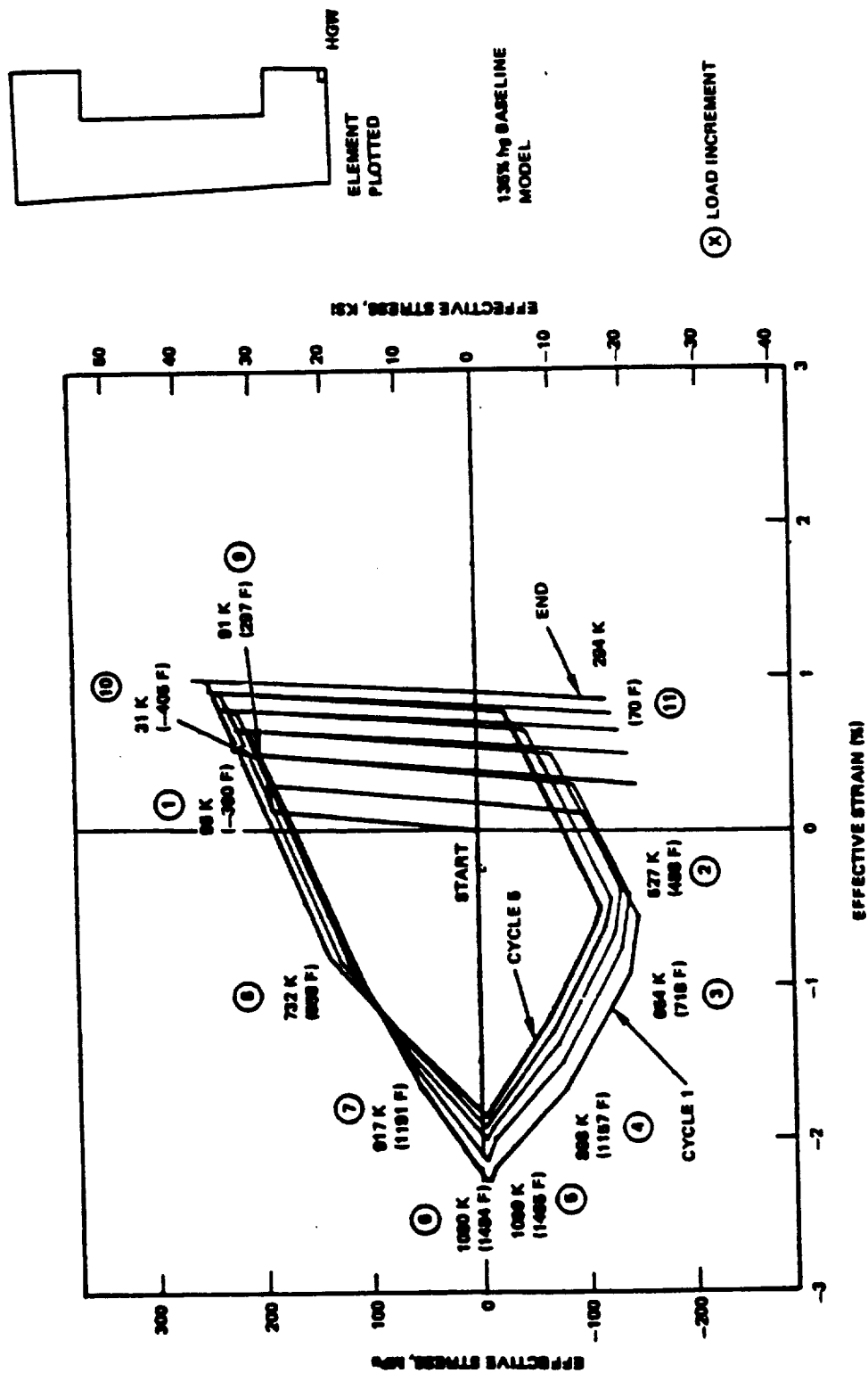


FIGURE 6.9 MIDCHANNEL HOT-GAS WALL MULTIPLE DUTY CYCLE STRESS/STRAIN HISTORY

The maximum strain capability of the MARloy-Z material in the channel wall is approached from the tensile instability failure criterion. The maximum hoop strain is related to the radial strain and the thinning of the channel wall. Tensile instability is defined in this case as where the incremental strain hardening of the deforming metal of the wall is less than the incremental increase of true stress due to local wall thinning. Once the instability condition is reached, further increase in load results in rapid failure of the channel wall. The criterion defines a critical strain limit for the material. The biaxial stress state critically affects the available ductility even for ductile materials. The maximum tensile stress in MCC occurs in 600F to 700F range during the cutoff portion of the duty cycle as the temperature starts to fall off and there is still pressure in the channel. If a simplified assumptions of axial strain being zero and the ratio of hoop to axial strain as 2:1 are made, then a tensile instability failure can occur at a range of thickness reduction of 5 to 10%.

A review of typical cross sections from hot fired MCC's show that failure can occur at an estimated 5 to 10% thinning of the channel wall. There is a wide variation in this thinning for different MCC chambers data base, but a 5 to 8% thinning limit is a reasonable criterion for the minimum strain at a failure for the SSME. The variation in test results may be attributed to conditions in the heat input at hot spots, flow variation in a specific combustor and the sensitivity of instability analysis to small changes in material orthotropic properties. The 5 to 8% strain limit compared to the uniaxial strain limit of 50% is consistent with a literature survey study Rocketdyne has previously made of available biaxial test results vs uniaxial test results.

While the approximate 2-D analysis indicate the cyclic creep phenomena from the structural standpoint, a good simulation of heat spot effects require a 3-D modeling approach. This is because the 2-D model essentially assumes the hot spot effect is axisymmetric while in reality hot spots roughly take the shape of 3:1 to 4:1 ellipse, with long axis along the meridian and the short axis covering 5 to 10 channel widths (Fig. 6.10). The 3-D effects can be explained as follows:

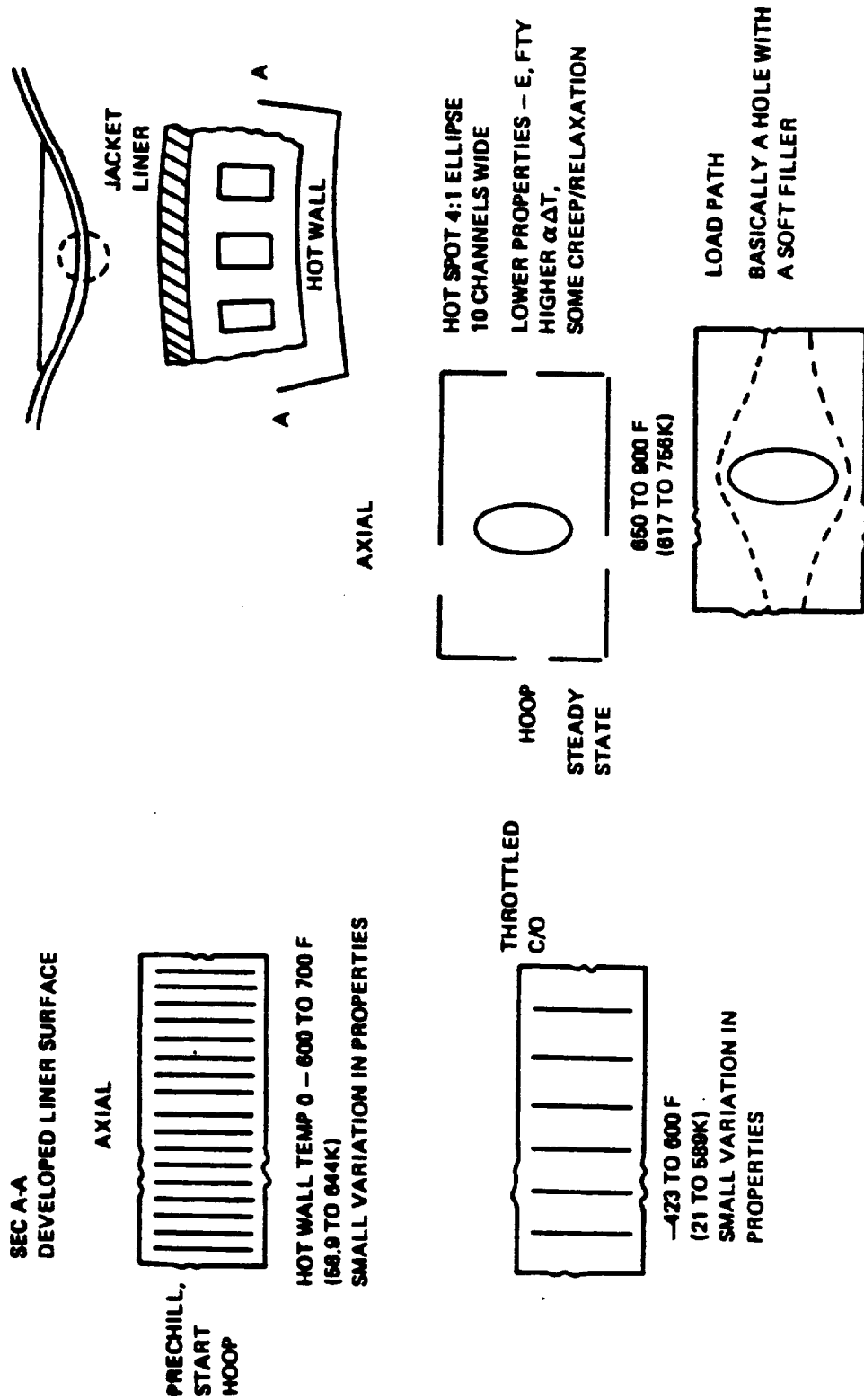


FIGURE 6.10 3-D HOT SPOT EFFECTS



A pictorial view of a developed liner with a hot spot near the throat throughout a duty cycle is shown in Fig. 6.10. The liner has two axisymmetric surfaces with axial land members. This results in an orthotropic stiffness path that makes a hot spot analysis more difficult. During the prechill portion of the duty cycle and up to say 600 or 700F, the liner wall temperatures and stiffnesses are relatively uniform with little variation from local injector effects. As the temperature rises, the hot spot markedly affects the stiffnesses and thermal loads. At steady state, the hot spot is essentially an elliptical hole to the overall liner, since its stiffness is much less than the surrounding zone of material. A local hole will result in a distorted shape and load path around this location and strain concentrations at its edges. Within the hot spot, the hole distortion is additive to the local hot spot strains. As the engine is throttled back and goes through the ensuing cutoff conditions, the liner cools and again becomes essentially a stiff membrane that locks in a portion of the strain distortions from the hot spot. This hot spot duty cycle has the potential to both add in large local strains in the axial and hoop directions over an axisymmetric model analysis, and add a biased strain to each duty cycle. A detailed 3-D model of a total liner to develop this hot spot duty cycle strain history is a large study in manhours and computer dollars.

The primary probabilistic factor in the liner analysis is the randomness and variability of hot spots. Hot spots are related to injector effects that are caused by slight manufacturing variations in the injector, contamination restricting flow in the channel or degradation of the injector with operation. The variability in material properties that affect most analysis are the variation in nonlinear material properties, including the cyclic stress-strain behavior.

#### Survey of Finite Element Models:

The availability of the finite element models for MCC liner is limited to 2-D models. Many different 2-D finite element models used for various

design concepts and sensitivity analysis are available (Fig. 6.11). The typical 2-D models are small by comparison (175 elements and 218 nodes), but are subjected to typically many duty cycles. They also model the many different materials (NARloy-Z, EDcu, EDN1) that make up the liner cross section.

**Scope of Analysis:**

1. 2-D elements to analyze plane strain condition. 3-D solid elements if 3-D analysis is deemed necessary to model localized hot spot condition.
2. Material library should include elastic-plastic analysis capability with provision for inputting cyclic strain hardening/softening capability for materials exhibiting such a behavior. All properties are temperature dependent.
3. Large deformation analysis as the geometry changes of the channel construction is the key element in simulating the cyclic creep condition.
4. Efficient nonlinear solution strategies using incremental and iterative techniques.

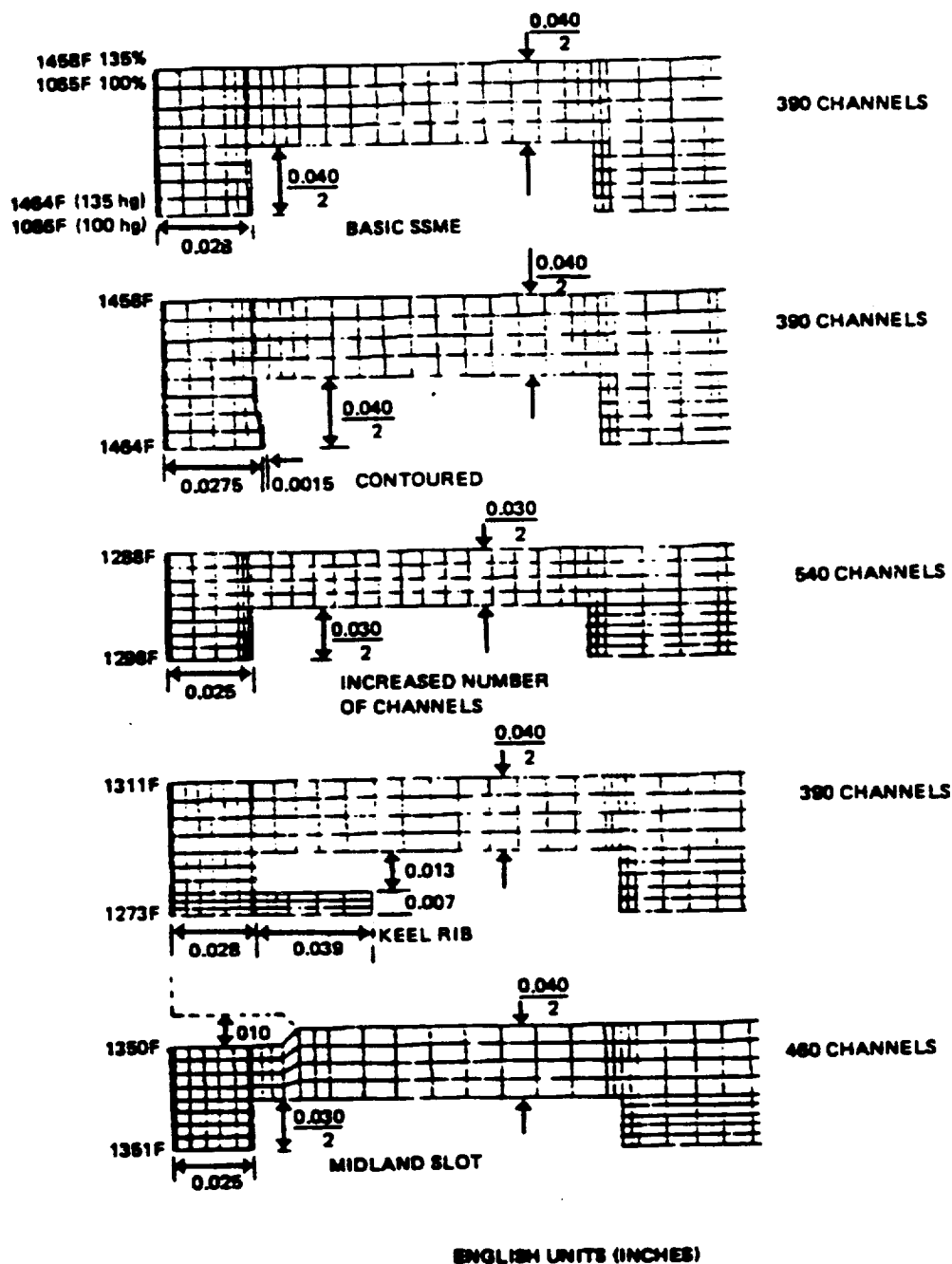


FIGURE 6.11 AVAILABLE FINITE ELEMENT MODELS  
FOR MCC LINER FOR VARIOUS DESIGN CONCEPTS

REPORT DOCUMENTATION PAGE			Form Approved OMB No. 0704-0188	
<small>Public reporting burden for this collection of information is estimated to average 1 hour per response, including the time for reviewing instructions, searching existing data sources, gathering and maintaining the data needed, and completing and reviewing the collection of information. Send comments regarding this burden estimate or any other aspect of this collection of information, including suggestions for reducing this burden, to Washington Headquarters Services, Directorate for Information Operations and Reports, 1215 Jefferson Davis Highway, Suite 1204, Arlington, VA 22202-4302, and to the Office of Management and Budget, Paperwork Reduction Project (0704-0188), Washington, DC 20503.</small>				
1. AGENCY USE ONLY (Leave blank)	2. REPORT DATE April 1992	3. REPORT TYPE AND DATES COVERED Final Contractor Report		
4. TITLE AND SUBTITLE Probabilistic Structural Analysis Methods for Select Space Propulsion System Components (PSAM) Volume II—Literature Surveys of Critical Space Shuttle Main Engine Components		5. FUNDING NUMBERS  WU-590-21-11 C-NAS3-24389		
6. AUTHOR(S) K.R. Rajagopal				
7. PERFORMING ORGANIZATION NAME(S) AND ADDRESS(ES)  Southwest Research Institute 6220 Culebra Road San Antonio, Texas 78228		8. PERFORMING ORGANIZATION REPORT NUMBER  None		
9. SPONSORING/MONITORING AGENCY NAME(S) AND ADDRESS(ES)  National Aeronautics and Space Administration Lewis Research Center Cleveland, Ohio 44135-3191		10. SPONSORING/MONITORING AGENCY REPORT NUMBER  NASA CR-189158		
11. SUPPLEMENTARY NOTES  Project Manager, C.C. Chamis, Structures Division, NASA Lewis Research Center, (216) 433-3252. K.R. Rajagopal, Rockwell International, Rocketdyne, Canoga Park, California 91303.				
12a. DISTRIBUTION/AVAILABILITY STATEMENT  Unclassified - Unlimited Subject Category 39		12b. DISTRIBUTION CODE		
13. ABSTRACT (Maximum 200 words)  This annual report summarizes the technical effort and computer code developed during the first year. Several formulations for Probabilistic Finite Element Analysis (PFEA) are described with emphasis on the selected formulation. The strategies being implemented in the first-version computer code to perform linear, elastic PFEA is described. The results of a series of select Space Shuttle Main Engine (SSME) component surveys are presented. These results identify the critical components and provide the information necessary for probabilistic structural analysis. The report is issued in three volumes: Volume I - summarizes theory and strategies; Volume II - summarizes surveys of critical space shuttle main engine components; and Volume III - summarizes literature surveys and technical reports available at that time.				
14. SUBJECT TERMS  Finite elements; Strategy; Computer code; Space shuttle main engine; Select components; Literature; Survey		15. NUMBER OF PAGES 430		
		16. PRICE CODE A19		
17. SECURITY CLASSIFICATION OF REPORT Unclassified	18. SECURITY CLASSIFICATION OF THIS PAGE Unclassified	19. SECURITY CLASSIFICATION OF ABSTRACT Unclassified	20. LIMITATION OF ABSTRACT	

National Aeronautics and  
Space Administration

**Lewis Research Center**  
Cleveland, Ohio 44135

Official Business  
Penalty for Private Use \$300

**FOURTH CLASS MAIL**

ADDRESS CORRECTION REQUESTED



Postage and Fees Paid  
National Aeronautics and  
Space Administration  
NASA 451

**NASA**

---

